
Electron Beam Dynamics in Dielectric Laser Accelerators

Elektronenstrahldynamik in dielektrischen Laserbeschleunigern
Habilitationsschrift von Dr.-Ing. Uwe Niedermayer
Fachbereich Elektrotechnik und Informationstechnik



TECHNISCHE
UNIVERSITÄT
DARMSTADT

Institut für Teilchenbeschleunigung
und Elektromagnetische Felder

Fachgebiet Beschleunigerphysik

Electron Beam Dynamics in Dielectric Laser Accelerators
Elektronenstrahldynamik in dielektrischen Laserbeschleunigern

Habilitationschrift von Dr.-Ing. Uwe Niedermayer

Einreichung des Habilitationsgesuches: 18.03.2022

Habilitationsvortrag: 01.11.2022

Bitte zitieren Sie dieses Dokument als:

URN: urn:nbn:de:tuda-tuprints-228468

URL: <http://tuprints.ulb.tu-darmstadt.de/22846>

Dieses Dokument wird bereitgestellt von tuprints,
E-Publishing-Service der TU Darmstadt

<http://tuprints.ulb.tu-darmstadt.de>

tuprints@ulb.tu-darmstadt.de

Diese Arbeit ist urheberrechtlich geschützt unter deutschem Urheberrecht.

This work is protected under german copyright law.

Abstract

Dielectric Laser Acceleration (DLA) is a nascent scheme of electron acceleration, which is particularly promising due to its high acceleration gradients. Although these gradients are lower than what is obtained in plasma-based schemes, they are the highest in structure based schemes, which are limited by material breakdown. DLAs can be implemented on microchips, leveraging on the nano-technology available in the semiconductor industry. This work aims to tackle the electron beam dynamics in DLAs systematically, with the goal to turn the already experimentally demonstrated record gradients into large energy gain. In other words, the goal is to increase the length of the acceleration channels while keeping a full 6D (3 coordinates and 3 momenta) confinement of the electron beam. This is particularly challenging, since DLAs are based on optical near-fields, requiring the transversal size of the channel to be tiny, down to a tenth of the laser wavelength at subrelativistic electron energies.

In order to keep the electron beam in this nanophotonic channel, enormous focusing strengths are required. Conventional techniques, usually involving solenoid- or quadrupole magnets, are too weak, since their aperture cannot be de-magnified in the same ratio as the DLA cells are de-magnified compared to conventional radiofrequency (RF) accelerator cavities. The solution to this problem is brought up in this work. It borrows from the Alternating Phase Focusing (APF) scheme as introduced for heavy ion accelerators in the 1950'. APF uses the laser fields themselves to focus the electron beam and thereby enables to omit external focusing devices entirely. While only a small amount of the large available acceleration gradient is sacrificed, full 6D confinement is obtained in length scalable structures. Thus in principle arbitrary high energy can be obtained provided the required laser parameters are available.

This work comprises two parts: A theoretical one introducing the DLA structures and a semi-analytic highly numerically efficient simulation approach named DLATrack6D. From this approach, the Hamiltonian and the entire dynamics in DLAs is derived. This leads to the recipe to design scalable APF DLA structures, especially suitable for fabrication on Silicon-On-Insulator (SOI) wafers, which are very common in commercial nanophotonics. More conventional structures are also created on the basis of pure silicon technology. These devices are also experimentally investigated in the second part of this work, where simulations and experimental results are matched. The requirements and experimental achievements of subrelativistic DLAs in ultralow-emittance injector chambers are discussed.

While low energy DLAs mostly aim at ultrafast (attosecond!) dynamics, high energy DLAs particularly exploit the available high acceleration gradient, in order to provide high energy electrons in small scale facilities. Furthermore DLA devices can also be used

as a versatile bunch-shaping tool in large-scale, high-energy conventional accelerator facilities. For that purpose, the beam current limit as being imposed by wakefields due to the structure surfaces that come very close to the beam is investigated. Our semi-analytic tracking code DLATRACK6D is supplemented with a wakefield module to assess collective effects and coherent beam instabilities. Moreover, the wakefields of DLAs can also be used in beneficial ways to shape the longitudinal phase space in high energy conventional accelerator facilities.

Application goals for DLA are Ultrafast Electron-Microscopy and -Diffraction (UEM/UED) at boosted energy and on a longer time scale the high acceleration gradients can be exploited for a high energy electron-positron collider for elementary particle physics. High energy ultrashort electron pulses can also be used for radiation generation, potentially in DLA-based microchip undulators. Another imaginable goal would be to accumulate electrons from a continuously running DLA injector in a storage ring. All these applications require a length scalable DLA and stable 6D-confined electron beam dynamics therein.

Zusammenfassung

Die dielektrische Laserbeschleunigung (engl. Dielectric Laser Acceleration, DLA) ist ein im Entstehen begriffenes Verfahren der Elektronenbeschleunigung, das aufgrund seiner hohen Beschleunigungsgradienten besonders vielversprechend ist. Diese Gradienten sind zwar geringer als bei plasmabasierten Verfahren, aber die höchsten in struktur-basierten Verfahren, die durch die Durchbruchfeldstärke der Materialien begrenzt sind. DLAs können auf Mikrochips implementiert werden, indem die in der Halbleiterindustrie verfügbare Nanotechnologie genutzt wird. In dieser Arbeit wird die Elektronenstrahldynamik in DLAs systematisch entwickelt, mit dem Ziel, die bereits experimentell nachgewiesenen Rekordgradienten in einen großen Energiegewinn umzuwandeln. Mit anderen Worten, das Ziel ist es, die Länge der Beschleunigungskanäle zu vergrößern und gleichzeitig einen vollständigen 6D-Einschluss (3 Koordinaten und 3 Impulsrichtungen) des Elektronenstrahls zu gewährleisten. Dies ist eine besondere Herausforderung, da DLAs auf optischen Nahfeldern basieren und die transversale Größe des Kanals deshalb winzig sein muss, bis hinunter zu einem Zehntel der Laserwellenlänge bei subrelativistischen Elektronenenergien.

Um den Elektronenstrahl in diesem nanophotonischen Kanal zu halten, sind enorme Fokussierungskräfte erforderlich. Herkömmliche Techniken, die in der Regel Solenoid- oder Quadrupolmagnete verwenden, sind zu schwach, da ihre Apertur nicht in demselben Verhältnis verkleinert werden kann wie die DLA-Zellen verglichen mit konventionellen Radiofrequenz (RF) Beschleunigungskavitäten. Die Lösung für dieses Problem wird in dieser Arbeit vorgestellt. Sie lehnt sich an das Alternating Phase Focusing (APF)-Verfahren an, das in den 1950er Jahren für Schwerionenbeschleuniger entwickelt wurde. In der APF-Technik werden die Laserfelder selbst zur Fokussierung des Elektronenstrahls verwendet, sodass auf externe Fokussierelemente völlig verzichtet werden kann. Während nur ein kleiner Teil des großen verfügbaren Beschleunigungsgradienten geopfert wird, wird der volle 6D-Einschluss in längenskalierbaren Strukturen erreicht; daher können im Prinzip beliebig hohe Energien erzielt werden, sofern die erforderlichen Laserparameter verfügbar sind.

Diese Arbeit besteht aus zwei Teilen: Erstens, ein theoretischer Teil, in dem die DLA-Strukturen sowie ein semi-analytischer, numerisch hocheffizienter Simulationsansatz namens DLATRACK6D, vorgestellt werden. Aus diesem Ansatz wird die Hamiltonfunktion und die gesamte Dynamik in DLAs abgeleitet. Dies führt zu einem Rezept für den Entwurf skalierbarer APF-DLA-Strukturen, die sich besonders für die Herstellung auf Silicon-On-Insulator (SOI)-Wafers eignen, welche in der kommerziellen Nanophotonik sehr verbreitet sind. Es werden auch konventionellere Strukturen auf der Basis reinen Siliziums diskutiert. Diese neuartigen Beschleuniger-Bauelemente werden im zweiten Teil

dieser Arbeit auch experimentell untersucht, wobei Simulationen und experimentelle Ergebnisse abgeglichen werden. Die Anforderungen und experimentellen Ergebnisse von Injektoren mit ultraniedriger Emittanz, die für subrelativistische DLAs erforderlich sind, werden behandelt.

Während aktuelle Niederenergie-DLAs vor allem auf ultraschnelle (Attosekunden!) Dynamik abzielen, nutzen Hochenergie-DLAs hauptsächlich den verfügbaren hohen Beschleunigungsgradienten aus, um hochenergetische Elektronen in kleinen Anlagen bereitzustellen. Es wird erörtert, wie ein solcher Hochenergiebeschleuniger aufgebaut werden kann und wie ein DLA-Chip als vielseitiges Werkzeug in großen konventionellen Beschleunigeranlagen zum Einsatz kommen kann. Zu diesem Zweck wird auch die Begrenzung des Strahlstroms untersucht, die durch die Kiefelder der sehr nahen Strukturen verursacht wird. Unser vereinfachtes Tracking-Modell DLATRACK6D wird durch ein Kiefeld-Modul ergänzt, um kollektive Effekte und kohärente Strahlinstabilitäten zu untersuchen. Darüber hinaus können die Kiefelder von DLAs auch vorteilhaft zur Verformung des longitudinalen Phasenraums in konventionellen Hochenergie-Beschleunigeranlagen genutzt werden.

Anwendungsziele für DLA sind ultraschnelle Elektronenmikroskopie und -beugung (UEM/UED) bei erhöhter Energie. Auf einem längeren Zeithorizont können die hohen Beschleunigungsgradienten für einen Hochenergie- Elektron-Positron-Collider in der Elementarteilchenphysik genutzt werden. Hochenergetische ultrakurze Elektronenpulse können auch in der Strahlungserzeugung, z. B. in DLA basierten Mikrochip-Undulatoren eingesetzt werden. Ein weiteres denkbares Ziel wäre es, Elektronen aus einem kontinuierlich betriebenen DLA-Injektor in einem Speicherring zu akkumulieren. Alle diese Anwendungen erfordern in der Länge skalierbare DLAs mit einer stabilen 6D-Elektronenstrahldynamik.

Contents

1. Introduction	1
1.1. Charged Particle Accelerators	1
1.2. This Work in Relation to the Field of Research	4
1.3. Dielectric Laser Acceleration	7
2. Beam Dynamics in DLA	13
2.1. Fields and Forces in Vacuum	13
2.2. Modeling and Simulation of Periodic Structures	16
2.3. Alternating Phase Focusing	20
2.4. Lattice Design vs. Ponderomotive Averaging	26
2.5. Low Energy DLA	28
2.5.1. Attosecond Bunching	28
2.5.2. Scalable Acceleration	30
2.6. High Energy DLA	34
2.6.1. Scalable Acceleration	34
2.6.2. Wake Fields and Collective Effects	36
3. Experimental Setups and Selected Results	41
3.1. Electron Microscopes	42
3.2. Dedicated DLA Test Chambers	45
3.3. Immersion Lens Electron Sources	49
3.4. Interaction Chambers in Large-Scale Facilities	52
4. Conclusion	57
4.1. Summary	57
4.2. Applications of DLA	59
4.3. Outlook	60
5. Selected Paper Contributions (chronological order)	63
5.1. Designing a Dielectric Laser Accelerator on a Chip	64
5.2. Beam dynamics analysis of dielectric laser acceleration using a fast 6D tracking scheme	71
5.3. Alternating-Phase Focusing for Dielectric-Laser Acceleration	86
5.4. Laser-Driven Electron Lensing in Silicon Microstructures	97
5.5. Challenges in simulating beam dynamics of dielectric laser acceleration	108



5.6. Dielectric laser electron acceleration in a dual pillar grating with a distributed Bragg reflector	123
5.7. Net Acceleration and Direct Measurement of Attosecond Electron Pulses in a Silicon Dielectric Laser Accelerator	127
5.8. Generation and Characterization of Attosecond Microbunched Electron Pulse Trains via Dielectric Laser Acceleration	133
5.9. Laser-Driven Modulation of Electron Beams in a Dielectric Micro-Structure for X-Ray Free-Electron Lasers	145
5.10. Tracking with wakefields in dielectric laser acceleration grating structures	154
5.11. Three Dimensional Alternating-Phase Focusing for Dielectric-Laser Electron Accelerators	167
5.12. Low-Energy-Spread Attosecond Bunching and Coherent Electron Acceleration in Dielectric Nanostructures	181
5.13. Design of a Scalable Integrated Nanophotonic Electron Accelerator on a Chip	187
5.14. Electron phase space control in photonic chip-based particle acceleration	198
5.15. High Gradient Silicon Carbide Immersion Lens Ultrafast Electron Sources	210
Acknowledgements	217
A. List of Acronyms	219
B. Outline of the FemtoTrack Code	221
Bibliography	223

1 Introduction

The first chapter starts with a brief introduction to particle accelerators for non-experts. We follow established accelerator physics textbooks [1, 2, 3, 4, 5], however excluding circular accelerators, as those are not relevant in this treatise. Then, this work will be put into the perspective of the nascent field of research on Dielectric Laser Accelerators (DLAs). The introduction of crucial properties of DLAs, their modeling, and current experimental setups concludes this chapter.

1.1 Charged Particle Accelerators

Accelerating small particles to high velocities became a scientific challenge in the beginning of the 20th century, especially due to the novel theories of the composition of matter delivered by quantum mechanics and the special theory of relativity. In order to look inside smaller and smaller structures of matter, one has to shine “light” on these structures, which has a wavelength that is shorter than the size of the structures to observe. Usage of electromagnetic wave-based light is limited here, as for the size of molecules (~ 1 nm) already X-ray is required and “looking” into atomic nuclei (~ 1 fm) requires Gamma-radiation. Instead of light beams, also particle beams can be used, and the corresponding wavelength is the de-Broglie wavelength given by

$$\lambda_B = \frac{h}{p} \approx \frac{hc}{W}, \quad (1.1)$$

where $h \approx 6.6 \cdot 10^{-34}$ Js is Planck’s constant, $c \approx 3 \cdot 10^8$ m/s is the speed of light, and p and W are the particle’s momentum and total energy, respectively.

Elementary particles, such as electrons, provide a particularly high q/m (charge/mass) ratio and can therefore be accelerated by an electrostatic or electromagnetic field in vacuum to high momenta swiftly, providing a correspondingly small de-Broglie wavelength. Acceleration of a particle means increasing its kinetic energy, which is given by

$$W_{\text{kin}} = q \cdot U = (\gamma - 1)mc^2 \quad (1.2)$$

where U is the voltage the particle has crossed after being at rest and q is its charge. Therefore, energy is usually given in units of Electronvolts, i.e., $1 \text{ eV} = 1.6 \cdot 10^{-19}$ J is the energy an electron has gained when traveling through a capacitor charged to 1 V, where $q = -e = -1.6 \cdot 10^{-19}$ C is the charge of the electron. The relativistic factor

$\gamma = 1/\sqrt{1 - v^2/c^2}$ describes the mass increase of a particle at velocity v , observed from the rest frame. At velocities significantly smaller than the speed of light, Newtonian mechanics holds ($W_{\text{kin}} = mv^2/2$) and the total energy is dominated by the rest mass. The rest mass expressed in units of energy amounts to $m_e c^2 = 0.511$ MeV for electrons and to $m_p c^2 = 938$ MeV for protons. At velocities very close to the speed of light, most of the energy is kinetic, and the rest mass can be neglected. In between, Eq. 1.2 has to be precisely evaluated. Note that acceleration toward the speed of light requires infinite amounts of energy and therefore c is an upper bound for v , while the momentum $p = \gamma m v$ is still unbounded.

First particle accelerators were build in electrostatic fashion, i.e., one tried to obtain high DC voltages to pass the particles through. Examples of such are the the Cockcroft-Walton accelerator, where capacitors are charged in parallel and discharged in series¹, or a Van de Graff accelerator, where high voltage is created by accumulating charges by a mechanically driven rubber conveyor belt. However, since the voltage source can be used only once in a DC setup due to the electric field fulfilling $\oint \vec{E} \cdot ds = 0$, the energy gain in electrostatic accelerators is rather limited.

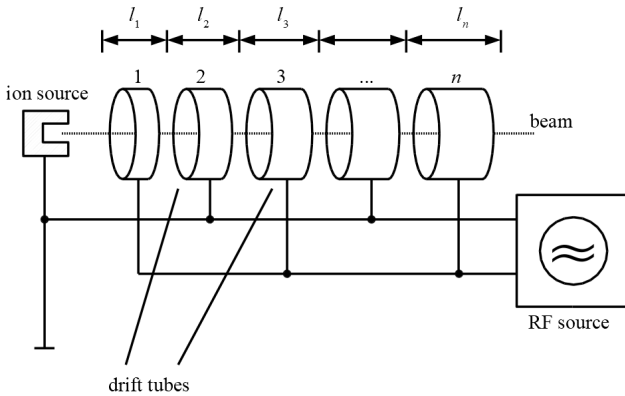


Figure 1.1.: Principle of a Wideroe Linac. Picture from [6].

Radiofrequency (RF) driven drift tube accelerators allow to use the AC voltage in every gap between the drift tubes, since every gap corresponds to a new RF period. The lengths of the tubes however has to be matched with the increasing velocity. Figure 1.1 shows this setup, which is known as Wideroe linear accelerator (linac). A drawback of this construction is that most of its RF power is radiated away, since the drift tubes act like antennas. This is solved by the Alvarez type linac, where the drift tubes are enclosed

¹ This can be achieved with an AC driver and diodes (Greinacker circuit) or by a DC driver with sparc gaps (Marx generator)

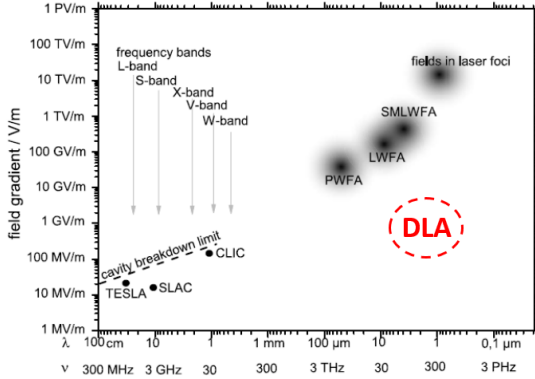


Figure 1.2.: Achievable gradients as function of frequency. The broad black dots indicated the different plasma-based schemes. Picture from [9], DLA annotation added here.

by a cavity, requiring considerations of not only the fundamental (accelerating) mode but also higher order modes acting on the particle beam.

Crucial in the pursuit for higher energy gain in limited size is to increase the “gradient”, i.e. the electric field strength, since the voltage is roughly speaking given by $U = E \cdot d$. While in electrostatic accelerators the limitation is given by the residual gas pressure (Paschen’s law), in AC accelerators material-dependent surface breakdown limits the attainable field strength. This is sometimes described by the empirical Kilpatrick limit [7], which is frequency dependent and practically limits contemporary RF accelerators to about 35 MeV/m gradient².

Instead of worrying about material breakdown, one can also resort to already broken down material, i.e. plasma. Driving a laser or charged particle impulse through a plasma generates a wake field, which can be tailored to attain enormous magnitude, without any classical theoretical limit. A trailing particle bunch can exploit this field strength and be accelerated with an enormous gradient. However, plasma wakefield accelerators have just recently come to practical use since they are technically challenging and suffer from fluctuations of the plasma parameters. Moreover, their beam dynamics design is inherently nonlinear. Figure 1.2 illustrates the enormous gradients of various plasma acceleration schemes as compared to conventional accelerators.

Dielectric laser Accelerators (DLAs) attempt a compromise between plasma accelerators and RF accelerators. They are still bound by the material breakdown limit, which is however much higher than for RF accelerators at the usually employed infrared laser

² There are some exceptions, as e.g. cryogenic copper cavities [8], which are however yet in prototype status

frequencies ($\lambda = 0.8 \dots 6 \mu\text{m}$ corresponding to $f = 50 \dots 375 \text{ THz}$). The gradients at which we aim are indicated in Fig. 1.2, which is roughly an extrapolation of the RF breakdown limit to optical frequencies. An extra boost in gradient is also provided by the ultrashort (femtosecond) pulses of modern laser systems, which enable high peak power at given moderate pulse energy.

1.2 This Work in Relation to the Field of Research

This work is a cumulative Habilitation thesis, which means most of its content is in the already published scientific papers reprinted in Chapter 5. The Chapters 2 and 3 produce required scientific content to fill the gaps between the different papers. The text presented here, together with the reprinted papers and the not reprinted but only cited papers, aims to produce a cohesive framework which can be used to understand beam dynamics in Dielectric Laser Acceleration (DLA) and allow the reader to design DLA structures for specific application goals. Furthermore, this text should help the application-oriented reader to quickly navigate inside huge amount of recent publications in the field of miniaturized particle accelerators, advancing the field from a first-principle concept to practical usefulness and readiness.

The underlying research of this work was conducted to a large extend within the Accelerator on a Chip International Program (ACHIP) [10], funded in the years 2015-2022 by the American Gordon and Betty Moore Foundation [11]. The goals of ACHIP are to create an electron accelerator on a chip that attains 1 MeV energy gain and to explore the transverse dynamical properties of the electrons in the acceleration channel. The second goal particularly includes focusing, which is crucial to reach the first goal. Moreover, understanding transverse beam dynamics also includes applications of a DLA accelerated beam, e.g. laser driven undulators, creating small table-top radiation sources with unprecedented parameters. An overview of an idealized ACHIP outcome can be seen in Fig. 1.3.

The development of novel particle accelerators has a very interdisciplinary character, mainly in the subjects physics and electrical engineering. For the structure synthesis of nanophotonic particle accelerators this is particularly decisive, as all the fields illustrated in Fig. 1.4 are required to contribute. Beyond the obviously connected field of accelerator physics and laser physics for the advanced ultrashort light pulses driving the structures, the fabrication of the structures themselves borrow a lot from integrated electronics and photonics. Particularly the technology based on silicon is strongly used and available university-scale nanofabrication facilities as well as so-called foundry companies are employed. The lasers in the optical and infrared spectrum as being used equip chip-based accelerators intrinsically with ultrafast, attosecond ($1 \text{ as} = 10^{-18} \text{ s}$) timing capabilities. Note that the ratio of $2 \times 10^{-18} \text{ s}$ to 1 s is about the same as 1 s to the estimated age of the universe. Such ultrashort processes can never be directly recorded; data collection requires mapping the time axis onto another axis as e.g. a spatial coor-

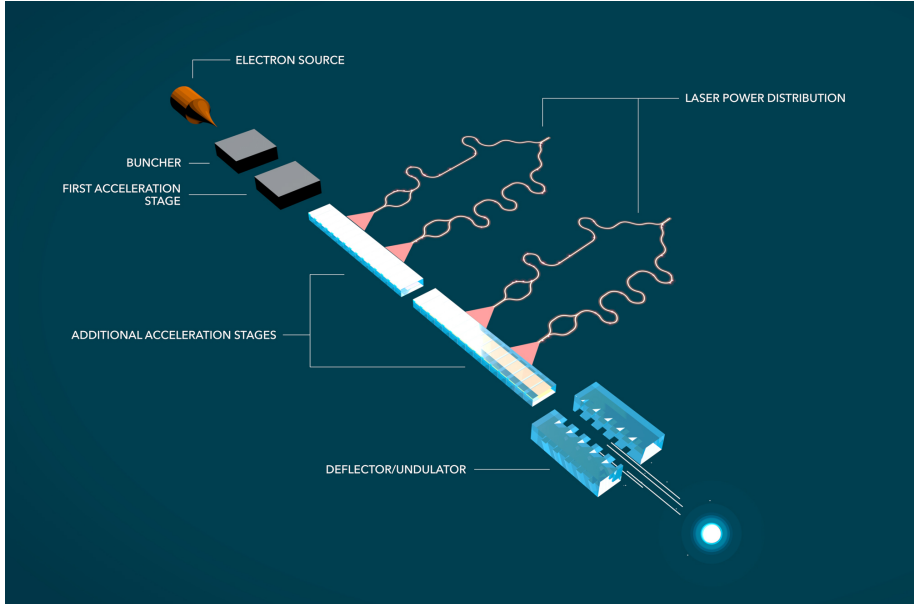


Figure 1.3.: Artist view of the ACHIP goals. Picture from www.achip.stanford.edu

dinate, which can be magnified. This lack of direct access to the underlying phenomena additionally emphasizes the role of computation and simulation in this field. In contrast to conventional accelerator physics or engineering in general, Computer Aided Design (CAD) and simulation methods are not only required to speed up prototyping, but also are absolutely essential to come up with on-chip electron acceleration structures that work in a predictable manner. The mathematical methods themselves are more-or-less available in the literature. However, the numerical schemes and codes are not specialized on this nascent field of nanophotonic ultrafast electron dynamics. Therefore, the challenges are primarily in engineering the codes, such that they can be applied to engineer the nanophotonic structures. In other words, we tackle an engineering challenge rather than a challenge in pure mathematics or fundamental physics. Once the structures are engineered and fabricated, the achievements of experimental physicists to obtain the best real-life performance in the state-of-the-art laser and accelerator laboratories can however hardly be overestimated.

This work is mostly of theoretical nature with the goal to design practically feasible accelerator structures. It should be emphasized, that it was the goal from the beginning to avoid lengthy theoretical treatises with no practical outcome; at the risk of fabricating structures that do not directly work as planned. The loop of design-fabricate-test-

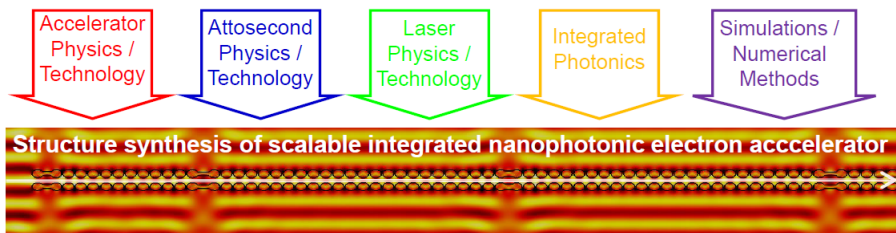


Figure 1.4.: Illustration of the many interdisciplinary connected fields involved in the pursuit of creating an electron accelerator on a chip.

redesign was pursued in a rather quick pace (at least before the Corona pandemic, which caused delays in the fabrication). While the testing capability in the laboratories continuously improved, the design and simulation capabilities could be developed in parallel according to the upcoming needs or upcoming practical issues. A requirement for this is the strong interaction between theoreticians and experimentalists, which is excellent within ACHIP

My theoretical work was performed mostly at TU Darmstadt together with the local DLA group. Moreover, both UCLA and Stanford University provided me the opportunity of guest scientist stays, in which the work towards scalability in laser-driven accelerators on a chip could be significantly pushed forward. Especially the experimental aspects, such as e.g. nanoscale alignment, often unknown or oversimplified by theoreticians, could be taken into consideration by explicitly working on the experiments, e.g. at Stanford. The collaborative work with PSI is also a special highlight, where the TU Darmstadt group could participate in beam time in the newly commissioned SwissFEL facility, both in person and by remote access to the controls of the entire accelerator. Furthermore, the collaboration also encouraged to reach out for further research funding, such that after the conclusion of ACHIP the research on small scale accelerators and their applications can be continued.

The structure of this treatise is as follows: Chapter 1 introduces Dielectric Laser Acceleration (DLA) and the sub-topics this thesis elaborates on. Chapter 2 discusses the electron beam dynamics from a bottom up theoretical perspective, with clear prospect to experimental implementation. The way of discussing the theory is kept rather brief and abstract, for more details the reader can refer to the respective papers reprinted in Chapter 5. Chapter 3 takes a practical view on the experimental setups created within ACHIP and on how experimental confirmation of the theory could be obtained. Key experiments both in small scale (sub-relativistic) laser laboratories and dedicated DLA interaction chambers in large scale accelerator facilities are highlighted. Chapter 4 concludes with a summary and an outlook to continued activities in modeling ultrashort electron bunches, also with a prospect on continuation of the pursuit of electron accel-

eration in nanophotonic structures beyond the ACHIP horizon of 2022. Furthermore, applications of the DLA structures available today, as well as an outline for applications of future developments will be given.

1.3 Dielectric Laser Acceleration

The combination of dielectric structures and coherent light allows to reverse electromagnetic radiation effects in order to attain particle acceleration. These radiation effects are the well known Cherenkov effect, in which charged particles moving faster than the speed of light in a material emit a shock wave, and the Smith-Purcell effect [12] in which the (relativistic) Coulomb field of charged particles is scattered off a grating structure. Both effects can be inverted, such that energy is transferred from a coherent radiation field to the charged particles as was being proposed already in 1962 [13, 14]. The combination of these effects, i.e., the use of dielectric gratings in conjunction with laser light sources, has been named Dielectric Laser Acceleration (DLA) after it became a viable approach to accelerate electrons with very high gradients, about tenfold higher than in conventional RF accelerators. These record gradients in damage threshold limited structures were enabled especially by modern ultrashort-pulsed laser systems, mostly in the infrared spectrum, and nanofabrication techniques for the dielectric materials, as adopted from the semiconductor industry. Dielectric materials have a significantly higher laser damage threshold fluence (fluence = pulse energy per cross-section area) than metals, among the most suitable are silicon (Si) and fused silica (SiO₂) for low and high energy electron acceleration, respectively [15]. Due to the high technical demands of the experiments, demonstration of electron acceleration in DLA came only in 2013, more than 50 years later than the original proposal [16, 17]. The promising results of gradients on the order of 300 MeV/m, generating only energy spread of rather small magnitude so far, lead to the funding of the ACHIP collaboration, with the goal of constructing a miniaturized accelerator attaining MeV energy gain. A summary of DLA research as it stood in 2014 is given in [18].

Key to the high gradients in DLA is the synchronization of optical near fields to relativistic electrons, expressed by the Wideroe³ condition

$$\lambda_g = m\beta\lambda, \tag{1.3}$$

where λ_g is the grating period, λ is the laser wavelength, and $\beta = v/c$ is the electron velocity in units of the speed of light. The integer number m represents the spatial harmonic number at which the acceleration takes place. The zeroth harmonic is excluded by means of the Lawson-Woodward theorem (see e.g. [18, 19]). Usually the first harmonic is chosen for acceleration, as it provides the highest gradient. This similarity relates DLAs

³ The same condition applies to conventional drift-tube linear accelerators, see Fig. 1.1

quite closely to conventional RF accelerators. More precisely, the subrelativistic electron accelerators on a chip can borrow a lot from proton or heavy ion accelerators, just scaled down by the proton/electron mass ratio of ≈ 2000 . A beam dynamics approach in this spirit is presented in Paper 5.1, which however turned out to be unfeasible, since conventional focusing elements, required to keep the beam in the channel, cannot be scaled down that strongly.

An experimentally common setup is to illuminate the dielectric grating structures laterally with laser pulses polarized in the direction of electron beam travel. The ultra-short pulses required by the material damage threshold fluence restrict however the interaction length to the laser pulse length. A technique to elongate the interaction of the laser pulse with the electron, without elongating its interaction with the dielectric structure is given by pulse front tilting (PFT), see Fig. 1.5. The tilted pulse can be created by various dispersive optical elements, such as prisms or gratings [20]. Figure 1.5 illustrates the action of a tilted pulse on a short electron packet, where the PFT angle needs to be matched with the electron velocity by the condition [21]

$$\tan \alpha = \frac{1}{\beta}. \quad (1.4)$$

Experiments were performed to demonstrate the advantage of PFT, starting from repeating the first experiment at SLAC with increased peak laser power, such that the gradient could be increased from 300 MeV/m [16] to 690 MeV/m [22]. Experiments with PFT were also conducted at low energy [23], however, for subrelativistic electrons the acceleration leads to a velocity increase that has to be taken into account in Eq. 1.4.

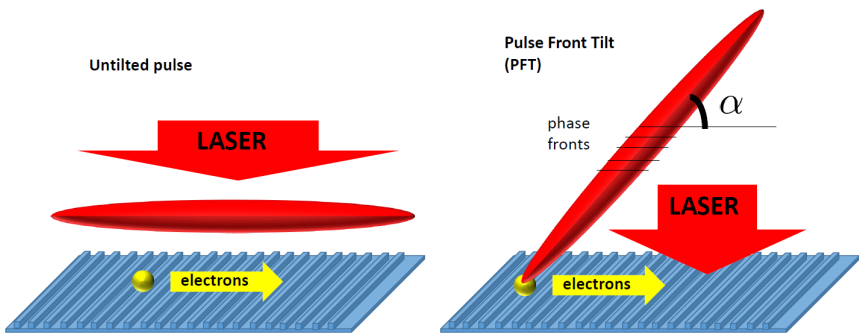


Figure 1.5.: Dielectric laser acceleration with a short laser pulse polarized in the direction of electron travel. Left: uncorrelated pulse, Right: Pulse with a correlated (tilted) envelope and still flat phase fronts.

Therefore the required pulse is rather “banana”-shaped, which is challenging to create in practice. Techniques using Acousto-Optic Modulators (AOM) are available to address this challenge [24], but experiments demonstrating that the phase fronts can be kept flat or even be predictable are yet missing. A technically quite involved way of approaching this issue is to drive the DLA with an on-chip photonic waveguide system, where arbitrary PFT shapes can be created by engineering the group delay in the individual branches [25]. The principle of waveguide-driven DLA has already been tested [26], however only with a single, strictly periodic segment creating only energy spread thus far. A simpler, still suitable approach is to approximate the curved pulse by linear pieces (see Paper 5.11 Supplement). Naturally, such a setup leads to a staged accelerator, where each stage has its individual PFT angle and requires a theoretical minimum pulse length, which is on the same order as the practically used pulses are today (hundreds of fs). With an extremely short 45 fs (FWHM) tilted laser pulse and a relativistic 8 MeV beam, the current record gradient of 850 MeV/m could be achieved at the UCLA Pegasus facility [27]. This gradient was not limited by damage threshold but rather by self-phase-modulation in the bulk of the fused silica grating, i.e. a nonlinear effect occurring when a high amplitude pulse travels over long distance inside a dielectric material. Moreover, in a similar setup, the record energy gain in DLA could be demonstrated as 315 keV [28], which is impressive on its own, but represents a relative energy gain of less than 5% for the 8 MeV beam from the photoinjector.

As in every novel particle acceleration scheme, the challenge in DLA is to make it length scalable, i.e., to turn the large gradients into significant energy gain, while preserving as much as possible of the beam quality. This requirement constitutes the transition of a novel acceleration technique to something practically useful. For DLA the scalability challenge is strongly connected to the challenge posed by the small apertures required by the driving evanescent near-fields. For subrelativistic electrons, a feasible aperture is roughly $\lambda/10 - \lambda/5$ and for relativistic electrons one obtains roughly $\lambda/2 - \lambda$, where in both cases a material with refractive index $n > 1/\beta$ (fulfilling the Cherenkov condition) is considered. For the typical infrared laser systems at $\lambda = 2 \mu\text{m}$ used for subrelativistic setups in ACHIP, this results in an aperture of only 200-400 nm. In order to obtain scalable acceleration, the beam has to be transported in this tiny channel without hitting the channel boundary. The unification of high gradient acceleration and small beam envelope electron transport is the main challenge of beam dynamics analysis and length-scalable structure synthesis in DLA.

The quest of six-dimensional (3 coordinates and 3 momenta) confinement leads naturally to full six-dimensional beam dynamics simulations. Executing these simulations in the full 3D laser fields is numerically heavy, also due to the vastly different size of the accelerator setup and the electron bunch. However, the periodicity of the structures can be exploited such that the field can be semi-analytically represented. Moreover, the transverse forces (kicks) acting on the electrons can be obtained from the longitudinal one using the Panofsky-Wenzel theorem [29]. This constitutes the approach of the fast tracking code DLAttrack6D, presented in Paper 5.2. In DLAttrack6D each grating cell is

allowed to adiabatically differ from its neighbor, as required for acceleration, i.e., the periodicity condition is relaxed to quasi-periodicity. In order to maintain the mathematical advantages of the periodicity, this requires non-resonant structures, providing sufficient cell-to-cell independence. The transverse dependence of the near field can be modeled analytically, when the center peak acceleration gradient is known⁴. Thus, the entire DLA structure can be represented by a vector of complex numbers assigning laser amplitude and phase to each cell. The evolution of an initially defined bunch distribution can be simulated by just applying one three-dimensional kick per DLA cell in a symplectic (Hamiltonian-preserving) manner, which can be computed on any standard PC.

Furthermore, the DLATRACK6D approach allows us to directly find the 6D Hamiltonian in the co-moving (Galilean) frame, which governs the motion for each electron. This gives rise to a closed description of the dynamics, while the laser and grating structure properties can be kept parametric. By introducing phase jumps, the grating can be perceived as a focusing lattice based on the alternating phase focusing (APF) technique introduced for proton and ion linacs in the 1950'. In Paper 5.3, APF for DLA is conceived and it is shown that the grating segments can be interpreted as thick quadrupole lenses creating a FODO lattice. This lattice can be analytically integrated in order to determine the Courant-Snyder lattice envelope functions (betafunctions). A specialty of the approach presented here is that also in the longitudinal plane a betafunction is determined, which describes a natural, matched oscillation of the bunch length. Within the linear range, the three planes (x, y, s) decouple and the individual normalized emittances are preserved. Especially for sub-relativistic DLAs, this is a major breakthrough with respect to the previous beam dynamics concepts, relying on conventional (fish-bucket) longitudinal dynamics [3] and ponderomotive focusing schemes based on non-synchronous sub-harmonics [30]. The APF for DLA scheme enables the large field strength to be converted into large average gradients over arbitrary long distances by a lattice design procedure that confines, transports, and accelerates a 6D phase space volume which ought to be maximized.

The tight 6D acceptance requirement of DLAs requires using injectors with small emittance or high brightness, respectively⁵. At low energy, electron microscopes have been utilized to provide electron beams that can be focused into the tiny aperture of the chip. While equipping a Scanning Electron Microscope (SEM) with the opportunity to laser trigger the source is sufficient for first experiments [23], resorting to Transmission Electron Microscopes (TEM) or Scanning Transmission Electron Microscopes (STEM) might be required in the future as they provide lower beam emittance. Especially advanced TEMs with aberration correction attain atomic resolution [31, 32], which is certainly sufficiently low emittance to inject into a DLA. Size and cost of such sophisticated equipment however suggest that creating dedicated DLA test chambers might be a viable alternative.

⁴ This has to be obtained/optimized numerically using periodic boundaries.

⁵ A convenient definition of brightness is charge divided by (6D) emittance.

Both the commercial as well as the home-made setups require nanoscale tip electron emitters. The emitter essentially represents a point, from which the electrons are emitted under large angles. The downstream electrostatic lenses have to provide acceleration and focusing back towards the optical axis. This focusing suffers of unavoidable spherical and chromatic aberrations⁶, which will blow up the initially small emittance from the nanotip [34]. These aberrations cannot be completely mitigated, but only be reduced by clever setup of the electrostatic lensing system. A recent development of such is the “Immersion Lens” setup [35], which trades a part of the initial longitudinal electric field for transverse focusing, leading to small emittance beams with 1-20 electrons in about 800 fs long bunches, see Paper 5.15. The brightness properties of these beams are sufficient to inject into a DLA only under large losses, but current developments promise significant improvement in this regard soon.

The adiabatic damping effect of the geometric emittance at preserved normalized emittance⁷ together with the slower roll-off of the DLA nearfield makes the structure aperture larger and the beams smaller at higher energy. Thus, if available, higher energy beams are a way to circumvent the most critical challenges of DLA experiments. However, such beams require state of the art RF accelerator systems as sources, which are available in the ACHIP realm at the ARES⁸ linac at DESY or at the SwissFEL linac at PSI. As shown in Paper 5.9, the projected purpose of a DLA interaction chamber in a FEL linac can also be bunching on the infrared scale, before injecting into the undulator. The resulting increased peak current leads to intensity increased X-ray pulses in well defined trains for the users. As an outlook in these facilities, one would also expect to see an experiment on a laser-driven DLA-structure based undulator on a chip; a novel way of radiation generation based on available high brightness electron beams.

Between the high-energy high-charge setups in the large-scale accelerator facilities and the low-energy ultralow-emittance setups in the laser laboratories are RF photoinjectors. By tailoring the trigger laser pulse to be short and small, the emittance can be sufficiently reduced to inject into a DLA at the gun-energy, usually in the single digit MeV range. The emittance reduction can be obtained either from emitting less electrons, or by a filter aperture between the gun and the DLA. Examples of such facilities are Pegasus [36] or the PITZ (Photo Injector Test facility at DESY in Zeuthen) near Berlin in Germany. Although the beam in these facilities is already relativistic, it is not sufficiently stiff to obtain significant acceleration by DLA without a length-scalable focusing scheme.

⁶ This is also referred to as Scherzer’s theorem [33].

⁷ See any accelerator physics textbook, e.g. [4].

⁸ ARES: Accelerator Research Experiment at SINBAD; SINBAD: Short and INovative Bunches at DESY.



2 Beam Dynamics in DLA

The following will discuss electron dynamics in DLAs in a bottom-up manner, starting from first principles. We will use modern notation of Maxwell's equations as is currently being taught in electrodynamics classes in physics and electrical engineering (see e.g. [37]). Theory will be kept to a minimum, in order to swiftly proceed to a Hamiltonian beam dynamics approach that can be practically implemented on producible chips.

2.1 Fields and Forces in Vacuum

Classical electromagnetic fields are described by Maxwell's equations

$$\nabla \times \vec{E} = -\partial_t \vec{B} \quad (2.1a)$$

$$\nabla \times \vec{H} = \partial_t \vec{D} + \vec{J} \quad (2.1b)$$

$$\nabla \cdot \vec{D} = \rho \quad (2.1c)$$

$$\nabla \cdot \vec{B} = 0, \quad (2.1d)$$

where the field strengths \vec{E} and \vec{H} , the flux densities \vec{D} and \vec{B} , and the source charge and current densities ρ and \vec{J} are functions of position \vec{r} and time t . In vacuum, the linear relations

$$\vec{D} = \epsilon_0 \vec{E} \quad (2.2a)$$

$$\vec{B} = \mu_0 \vec{H} \quad (2.2b)$$

render electric and magnetic field strengths equivalent to their respective flux densities. In dielectric materials, the relation can be written as $\vec{D} = \epsilon_0 \epsilon_r \vec{E}$, with the relative permittivity or refractive index $\epsilon_r = n^2$, both being functions of angular frequency ω and position \vec{r} . As long as nonlinearities and dispersion are negligible, i.e., when the field amplitude is not extremely high and the pulse duration is not extremely short, the refractive index can be seen as a constant number. For brevity, the discussion of losses, dispersion, and nonlinearities will be omitted and redirected to specialized textbooks on optical materials [38] and nonlinear optics [39].

The change of the momentum $d\vec{p} = \vec{F} dt$ of a point-like particle with charge q is given by the Lorentz-force

$$\vec{F} = q(\vec{E} + \vec{v} \times \vec{B}). \quad (2.3)$$

Within a time interval T , the force can be lumped into a momentum kick

$$\Delta\vec{p}(x, y, s) = \int_T \vec{F}(x, y, z = \nu t - s; t) dt, \quad (2.4)$$

which under the conditions of the Panofsky-Wenzel theorem [29] is irrotational. Since this theorem is crucial here, we will show it explicitly. The relative nabla-operator $\nabla' = (\partial_x, \partial_y, -\partial_s)$ can be substituted in Maxwell's equations, evaluating them in the special case where the z -coordinate and the time are tied together by $z = \nu t - s$. As common in the computation of wake fields [40], we chose the negative sign for s here, which measures the longitudinal coordinate *behind* a reference particle¹. For the relative curl of the kick one obtains

$$\begin{aligned} \nabla' \times \Delta\vec{p} &= q \int_T dt [\nabla' \times \vec{E} + \nabla' \times (\vec{v} \times \vec{B})] \\ &= q \int_T dt [-\partial_t \vec{B} + \underbrace{\vec{v} \nabla' \cdot \vec{B}}_{=0} - \underbrace{\vec{B} (\nabla' \cdot \vec{v})}_{=0} + \underbrace{(\vec{B} \cdot \nabla') \vec{v}}_{=0} - (\vec{v} \cdot \nabla') \vec{B}] \end{aligned} \quad (2.5)$$

where the first vanishing term is due to the absence of magnetic charges and the other two are due to the velocity being a constant. The remaining terms are a convective derivative and a partial time derivative, summing up to the total time derivative. This yields

$$\nabla' \times \Delta\vec{p} = -q \int_T dt \frac{d\vec{B}}{dt} = -q \vec{B}|_T, \quad (2.6)$$

such that only the boundary terms remain. The conditions for Panofsky-Wenzel theorem, i.e. for the above expression to be well defined and to evaluate to zero, are subsequently

1. *Kick approximation*: The continuous force can be lumped into a single kick.
2. *Rigid beam approximation*: The velocity is constant and changes instantly when the kick is applied (after the interaction with the field).
3. *Vanishing boundary terms*: \vec{B} has to be either zero or identical at boundaries of the interval T . The former is commonly used in wakefield calculations and the latter is being exploited in the periodic structures here.

¹ The mathematical advantage of this is that the wake Green function is a causal impulse response.

Having established that the kick in one cell in a periodic structure is irrotational, the force can be obtained from a scalar potential $V(x, y, s)$ as

$$\frac{d\Delta\vec{p}}{dt} = -\nabla'V. \quad (2.7)$$

The potential is calculated by integration, i.e. $V(x, y, s) = \int \Delta\dot{p}_z(x, y, s)ds$, which by insertion into Eq. 2.7 and omission of the time derivative on both sides leads to the commonly known expression of the Panofsky-Wenzel theorem: *The transverse derivative of the longitudinal wake is the longitudinal derivative of the transverse wake*, or mathematically

$$\Delta\vec{p}_\perp = \underbrace{-\nabla_\perp \int ds}_{\text{Panofsky-Wenzel operator}} \Delta p_z. \quad (2.8)$$

In order to calculate a potential from which the kicks in any DLA structure can be derived explicitly, we introduce a reference particle at $(0, 0, s_{\text{ref}})$. Within each DLA cell, the reference particle gains energy exactly such that it follows the design acceleration ramp, where the reference energy in each cell is denoted by W_0 . Thus, the energy offset $\delta = (W - W_0)/W_0$ remains unchanged at the reference phase, i.e. for the energy kick $\Delta\delta$ holds $\Delta\delta(0, 0, s_{\text{ref}}) = 0$. Assuming further, that the DLA cells are short and the kicks are small, we can approximate the force by

$$\Delta\dot{p}_z \simeq \frac{\Delta(\Delta p_z)}{T} = \frac{W_0}{\lambda_g} \Delta\delta, \quad (2.9)$$

which allows to determine the potential $V(x, y, s; s_{\text{ref}})$ by integration over s . This potential can depend parametrically on s_{ref} and other quantities, which are allowed to change along the DLA grating structure (see also Paper 5.3 Supplement). Note an ambiguity in the notation of Δp_z : in Eq. 2.8 it means a momentum kick, while in Eq. 2.9 it means the deviation of the momentum w.r.t. the reference particle. Since the reference particle itself does not experience a momentum kick in the reference system, the change in momentum deviation is the same as the change in momentum itself, i.e. there is no ambiguity in $\Delta\dot{p}_z$. Moreover, the change in momentum can be related to the change in energy (deviation) by the differential $\Delta p_z/p_z = \beta^{-2}\Delta W/W$, which was exploited to calculate Eq. 2.9.

Through the analytical determination of $\Delta\dot{p}_z$ one obtains the entire 6D Hamiltonian in the limit of small kicks and short periods. Although this limit cannot be taken, it is well approximated by the large number of short cells in DLA. This small kick is also in agreement with the kick approximation, which must hold in each cell. Thus, the Hamiltonian

obtained in this way governs the motion of an electron in the (long) vacuum channel of a DLA structure accurately, while the motion within each (short) cell is linearly approximated. Furthermore, using the paraxial approximation and the fact that the motion is non-relativistic in a (Galilean) frame co-moving with the relativistic reference particle, a simple expression for the Hamiltonian is obtained as

$$H = T_{\text{kin}} + V = \frac{\Delta \vec{p}^2}{2m_e \gamma} + \frac{W_0}{\lambda_g} \int_{\lambda_g} \Delta \delta(x, y, s; s_{\text{ref}}) ds, \quad (2.10)$$

where the three-dimensional momentum deviation is given by $\Delta \vec{p} = (p_x, p_y, \Delta p_z / \gamma^2)$ and $m_e \gamma = m_e / \sqrt{1 - \beta^2}$ is the relativistic mass of the electron. The Hamiltonian is separable, with a kinetic energy T_{kin} only dependent on the momentum and a potential V which depends only on the position. The potential is however allowed to change (parametrically) for each DLA cell, where the cell index takes the role of time. The entire dynamics of an ensemble of independent particles with arbitrary initial conditions can be derived by means of Hamilton's equations $\dot{\vec{x}} = \nabla_{\vec{p}} H$ and $\dot{\vec{p}} = -\nabla_{\vec{x}} H$; only $\Delta \delta(x, y, s)$ needs to be known from the electromagnetic field. Analytic modeling of $\Delta \delta(x, y, s)$ and the tracking of a large particle ensemble in a lightweight algorithm is shown in Paper 5.2, resulting in the semi-analytic tracking code DLATRACK6D.

The potential V necessarily contains nonlinearities due to the exponential near-field decay of the synchronous accelerating fields in DLA, which poses a challenge to simulation and beam dynamics design. In the next section, analytical models for the potential will be introduced, such that only one complex number per DLA cell suffices to describe any DLA structure completely in the vacuum channel where the electron beam runs. Moreover, linearization at the reference particle, placed at the appropriate fixed points, leads directly to analytically integrable dynamics in an Alternating Phase Focusing (APF) setup.

2.2 Modeling and Simulation of Periodic Structures

In periodic or quasi-periodic structures, the (differential) energy gain $\Delta \delta = (\Delta W(x, y, s) - \Delta W(0, 0, s_{\text{ref}})) / W_0$ can be expressed in a particularly simple manner. The electric field can be written in frequency domain (Phasor) notation as $E(\vec{r}, t) = \text{Re}\{\mathcal{E}(\vec{r}, \omega) e^{i\omega t}\}$. Exploiting the periodicity of length λ_g , it can be expanded in spatial Fourier series and only the synchronous component contributes to the kick, all higher harmonics vanish (see Paper 5.2). By means of the Lawson-Woodward theorem (see e.g. [18]), the zeroth Fourier component (i.e. a plane wave) does not contribute; moreover, the 1st harmonic usually has the highest amplitude. Therefore one can write with no loss of generality

$$e_1(x, y) = \frac{1}{\lambda_g} \int_{\lambda_g} \mathcal{E}_z(x, y, z) e^{2\pi i z / \lambda_g} dz \quad (2.11)$$

and the energy gain in each DLA cell results as $\Delta W(x, y, s) = q\lambda_g \text{Re}\{e_1 e^{2\pi i s/\lambda_g}\}$. This energy kick can be directly inserted into the Hamiltonian, Eq. 2.10. Alternatively, it can be transformed to the momentum kick by the differential $\Delta p_z/p_z = \beta^{-2}\Delta W/W$ and the transverse momentum kick is obtained by executing the Panofsky-Wenzel operator in Eq. 2.8.

What remains to determine is the transverse distribution $e_1(x, y)$. This can be approached by numerical calculation of the Frequency Domain (FD) field $\mathcal{E}_z(x, y, z)$ by the Finite Element Method (FEM) or Finite Differences in the Frequency Domain (FDFD). Open source codes of such are available [41, 42]; their largest challenge is the proper implementation of open boundary conditions (perfectly matched layer, PML [43]) on the entry and exit side of the laser. The simulation can however also be performed in Time Domain (TD), by Finite Integration (FIT) or Finite Difference in Time Domain (FDTD), and on-the-fly Fourier transform of the field. Both the FIT and the FEM determination of e_1 can be done in agreeing manner by commercial codes as e.g. CST Studio Suite [44]. Fast parameter studies, both in 2D and in 3D are possible. We also conceived a tool to determine $e_1(x, y)$ for a two-dimensional array of x and y values, see Paper 5.2 for the concept, which has been implemented later in a more efficient way by Jan Lautenschläger in Matlab [45].

The distribution of $e_1(x, y)$ in a large part of the channel cross section of symmetric structures can also be semi-analytically modeled, by only determining $e_1(0, 0)$ numerically and inferring the transverse dependence analytically. Transforming the vacuum electromagnetic wave equation to spatial and temporal frequency domain (see Paper 5.11 Supplement), one obtains the dispersion relation

$$k_x^2 + k_y^2 = \frac{\omega^2}{c^2} - k_z^2 =: -\kappa^2, \quad (2.12)$$

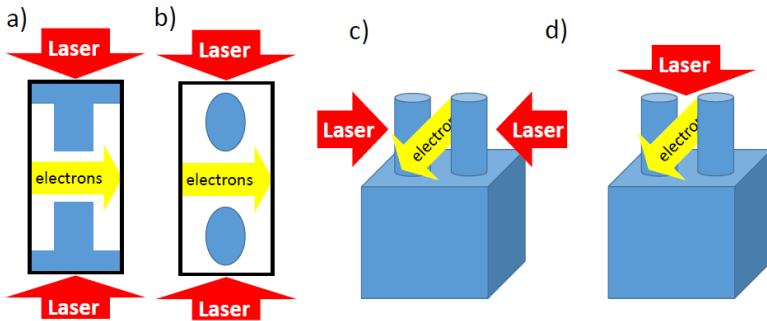


Figure 2.1.: DLA structures made from a single material. (a) and (b): 2D idealizations, (c) and (d): practical realizations where 3D effects are inevitable.

where the synchronicity condition (Eq. 1.3) requires $k_z = \omega/(\beta c)$. The transverse wavenumbers k_x and k_y can be real or imaginary and they can be engineered by means of shaping the dielectric structure and the laser incidence, see e.g. Fig. 2.1. Note that since massive particles are always sub-luminal ($\beta < 1$), the right hand side of Eq. 2.12 must always be negative, i.e., $\kappa = \omega/(\beta\gamma c)$. If two-dimensional structures are considered (see Fig. 2.1 a) and b)), i.e., $k_x = 0$, then k_y is imaginary. This implies that the near-field, which causes synchronous acceleration and deflection, must exponentially decay from the grating surface. Optimization of such structures in 2D were carried out by conventional [42], but also by automatic, inverse design methods [46, 26]. Practically, it turned out that simple elliptical pillar structures are most reliable and predictable in their performance close to the laser damage threshold.

Elliptical pillar based (silicon) structures can be implemented by electron beam lithography on a photo-lithographically created elevation (“mesa”) [47]. Such a setup is schematically drawn in Fig. 2.1 c) and d). In these structures, the pillars are limited in height; thus, the assumption of $k_x = 0$ is difficult to retain. The 2D assumption would require the pillar height to be larger than the laser spot size. This can be fulfilled for grating type structures as shown in Fig. 2.1 a) or Fig. 1.5, but not for pillar type structures produced by electron beam lithography as indicated in Fig. 2.1 c) and d). Thus, resorting to structures that exploit the vertical dependence of e_1 (rather than trying hard to avoid it) appears feasible, which results in abandoning the 2D setups for a general 3D focusing scheme.

The simplest three-dimensional structures are tilted gratings, in which k_x is real and directly determined by the tilt angle. Therefore, one can easily solve for k_y , resulting in larger imaginary k_y , i.e., faster roll-off of the synchronous near field from the surface (this is a drawback of tilted gratings). A similar effect is created by altering the incidence angle of the laser around the electron beam axis, while keeping the polarization aligned with the electron beam (see Paper 5.5). These structures create a phase dependence of e_1 on x , which leads to a constant deflection in x over many periods. This effect can be exploited to create phase dependent deflectors and undulators, see Paper 5.2 for an approach to electron dynamics therein and [48, 49, 50] for first laser-driven undulator concepts.

In order to conceive structures that provide focusing in both transverse directions in a predictable fashion, the structures need to be symmetric in both transverse planes. Examples of such structures made from a single material are shown in Fig. 2.2. In these symmetric structures, the synchronous field must be cosh-shaped in both transverse planes, i.e. a superposition of two exponentials from each side. In case the decay is so slow that a reflection occurs at the opposite side, the synchronous field can be written as an infinite sum, resulting however again in a cosh-shaped global dependence, see [51]. In a (large) environment around the fixed point at the center, not too close to the boundary of the channel, the synchronous field can be written as

$$e_1(x, y) = e_{10} \cosh(ik_x x) \cosh(ik_y y) \quad (2.13)$$

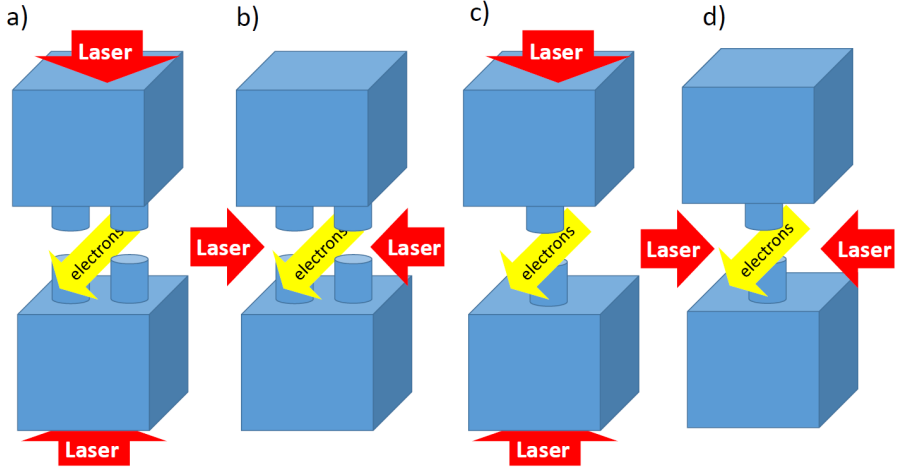


Figure 2.2.: Symmetric 3D APF DLA structures made from a single material.

where $e_{10} = e_1(0, 0)$ is referred to as the structure constant and at least one of the focusing constants k_x or k_y needs to be numerically determined. As discussed in Paper 5.11, e_1 is subject to a Helmholtz equation $(\Delta_{\perp} + \kappa^2)e_1(x, y) = 0$, however, boundary conditions at the channel boundary are not available, so it cannot be solved in this way. An easy and effective way to solve for $e_1(x, y)$ is to numerically solve for e_1 at the origin to obtain e_{10} , and subsequently determine k_y by solving at a transversally displaced position. The second decay constant, k_x , can then be determined analytically using Eq. 2.12. This procedure has been checked by performing numerical determination of e_1 at all values of (x, y) , and obtaining k_x and k_y from a fit, resulting in only small difference to the simplified two point determination for optimized structures (see papers 5.11 and 5.13). The fully symmetric structures in Fig. 2.2 are difficult to fabricate in practice. However, they can be well approximated by structures based on two materials which provide an as high as possible refractive index contrast. This idea was first conceived for structures with pillars made of two materials, see Fig. 2.3 (a)-(c) and Paper 5.11. Since Fig. 2.3 (a)-(c) are still hard to fabricate, the two-bead structures as introduced in Paper 5.13 and depicted in Fig. 2.3 (d) have been conceived, providing a quadrupolar $e_1(x, y)$ distribution on a setup that can be fabricated on a Silicon On Insulator (SOI) wafer by standard nanophotonics techniques. The feasibility of DLA structures on SOI wafers in fabrication and laser acceleration testing has already been demonstrated by Sapa et al. [26] for the purpose of feeding the DLA from a nanophotonic waveguide.

Once the structure of each cell is fixed and $e_1(x, y)$ is determined, an entire ensemble of electrons can be tracked by a rather simple one-kick-per-DLA cell method as

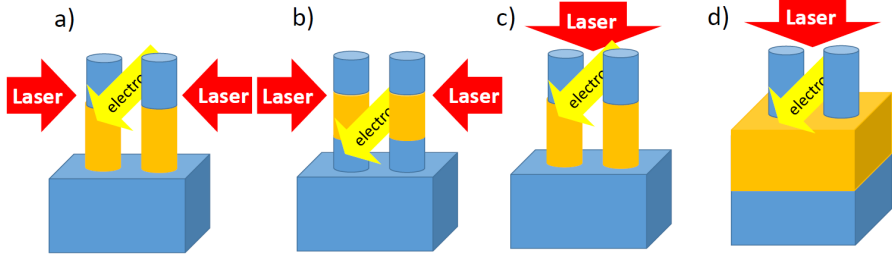


Figure 2.3.: DLA structures based on two materials with high refractive index contrast. Practically, these structures can be fabricated using SOI wafers. In d), the fabrication process is standard in nanophotonics, i.e. only the device layer needs to be patterned by electron beam lithography.

implemented in the code DLAttrack6D, see Paper 5.2. In order to avoid the numerically artificial increase of the electron beam emittance, the tracker has to be symplectic. DLAttrack6D uses the symplectic Euler method, which is natural to the one-kick-per-cell approach via the Panofski-Wenzel theorem. By avoiding artificial emittance increase, the naturally occurring emittance increase due to the field nonlinearities can be properly quantified. First tracking results with DLAttrack6D are shown in Paper 5.2, but more important, this formal approach leads to 2D and 3D APF methods that finally make DLA length-scalable, both at subrelativistic and relativistic energy. Amendments to DLAttrack6D for different laser incidence angles as well as for antisymmetric, laterally driven dual pillar deflection structures are shown in Paper 5.5. Later developments in DLAttrack6D include also automatic loading of entire accelerator lattices from text files.

2.3 Alternating Phase Focusing

Alternating phase focusing (APF) is a beam dynamics scheme, which stems originally from low energy proton and heavy ion accelerators, already established in the 1950'. It is based on changing the synchronous phase φ_s in each acceleration cell and thereby alternating between acceleration focusing and acceleration defocusing of the RF fields. By smart choice of the distances between cavities, their amplitude and phase, and the respective reference beam energy, both longitudinal and transverse beam stability is obtained entirely without any (external) transverse focusing equipment. With the advent of Radio Frequency Quadrupoles (RFQs) in the ion accelerator field, the focusing strength could be enhanced and combined with adiabatic bunching and acceleration. RFQs however come at the price of rather complicated three-dimensional structures, demanding fabrication accuracy on multiple length scales [4]. Such structures are

currently not feasible to be created on chip. There are also “intermediate” beam dynamics schemes, which make partial use of both magnetic quadrupole focusing and RF focusing of the acceleration structures. Examples of such schemes are KONUS [52] and EQUUS [53] beam dynamics schemes, mostly employed in the medium energy section of proton and heavy ion linacs. For DLA, these schemes are also not feasible, since they still require external electric or magnetic quadrupole focusing to some extent. Thus, one has to resort to purely electromagnetic schemes for focusing in DLA, which can convert the high laser field strength accurately to acceleration and focusing forces. As of today, the only known schemes fulfilling beam dynamics needs on an accelerator chip are APF and spatial harmonic focusing, which will be discussed in the next section.

APF for DLA was conceived in Paper 5.3. Instead of defining the synchronous phase individually for each cavity or DLA cell, a formalism based on segments, in which the synchronous phase is kept constant, is introduced. By fractional cell length drifts, the synchronous phase can be almost instantaneously changed (jumped) from one constant value to another. Thus, the constant synchronous phase in each segment makes it easy to calculate the acceleration ramp (reference energy) and the focusing strength (focusing lattice function) for each DLA cell along the accelerator chip.

The focusing strengths in all directions are connected by Earnshaw’s theorem [54], which originally proved that static fields cannot keep a stable equilibrium of charged particles. For focusing in accelerators, this means that the potential $V(x, y, s)$ (Eq. 2.7), derived by the Panofsky-Wenzel theorem, has no extrema; the fixed points are unstable saddle points. Similar as in conventional accelerator FODO lattices or in Paul traps (see e.g. [55]), the sign of the saddle can be flipped by jumping the phase, eventually enabling confinement in all directions. A special case of this approach is the 2D APF for DLA scheme as presented in Paper 5.3, where one transverse and the longitudinal plane are alternatingly focused. The other transverse plane can be constantly focused by a single external quadrupole magnet, which has a length that spans the entire accelerator chip (see also Fig. 2.5). This scheme is exactly what is practiced in conventional accelerators, just with interchanged coordinate axes. In conventional (Wideroe or Alvarez) ion accelerators, the synchronous phase is set such that constant longitudinal focusing is obtained, while the two transverse planes are alternatingly focused by a FODO lattice of quadrupole magnets. In the 2D APF scheme the constant focusing is applied by the single quadrupole vertically, while the longitudinal and horizontal planes are alternatingly focused by laser fields. Note that the laser fields are much stronger than the quadrupole, such that the magnetic defocusing in the horizontal plane can be neglected. Including the defocusing force in the formalism as an additive term in the potential is also possible when needed, the complete potential then reads (see also Paper 5.3)

$$V = q\text{Im}\{e_{10}\left[\frac{\lambda_g}{2\pi} \cosh\left(\frac{\omega y}{\beta\gamma c}\right) e^{2\pi i s/\lambda_g - i s e^{i\varphi_s}}\right]\} + K_M(y^2 - x^2) \quad (2.14)$$

where $\varphi_s = 2\pi s_{\text{ref}}/\lambda_g$ is the synchronous phase and $K_M = q\beta c B_0/b$, with the quadrupole magnet pole tip to beam axis distance b and field strength B_0 at the pole tip.

The linearized equations of motion following from the Hamiltonian (Eq. 2.10) with the above potential are Hill's equations. This is similar to conventional accelerators, however, here we also have Hill's equation in the longitudinal direction. Hill's equations describe the particle motion in a lattice function $K(z)$ in a linearized fashion as

$$\xi'' + K_\xi(z)\xi = 0 \quad (2.15)$$

where $\xi = \{x, y, s\}$. While the motion in x is just a simple harmonic oscillator due to $K_x = -K_M = \text{const}$, the motion in the y and s coordinates retains the z -dependence in the focusing functions. This can subsequently be solved by the Courant-Snyder lattice integration formalism [56], i.e., by determining the envelope functions for all initial conditions of the particles. Since in our APF scheme the lattice functions are piecewise constant, the procedure of integration is the same as for a conventional lattice of thick quadrupoles. As described in Paper 5.3 Supplement, the envelope functions $\eta_\xi(z) = (\hat{\beta}_\xi, \hat{\alpha}_\xi, \hat{\gamma}_\xi)$ are determined by a linear map \mathbf{T} of their initial conditions². These initial conditions are obtained from the assumption that a lattice cell is periodic, and thus $\eta(L) = \mathbf{T}\eta(0) = \eta(0)$ is an eigenvalue problem of the 3×3 envelope function map matrix \mathbf{T} , which can be analytically solved using symbolic algebra (Mathematica [58]). For the first time, in the APF for DLA scheme this formalism is also applied to the longitudinal plane ($\xi = s$), and longitudinal envelope functions are obtained, describing a natural, matched bunch length oscillation. This could be called a longitudinal betatron oscillation resembling the conventional transverse betatron oscillation and contrasting the conventional longitudinal synchrotron oscillation.

A first lattice integration in this way is shown in Paper 5.3, where the energy range from 83 keV to 1 MeV is covered in an idealized fashion (i.e. disregarding the PFT angle change and disregarding 3D effects). The lattice functions of a single "stage" of such an on-chip silicon accelerator, providing a first attempt towards "energy-doubling" in an experimentally feasible manner, are shown in Fig. 2.4, where the parameters of four different configurations are summarized in Tab. 2.1.

The different configurations are sorted with respect to the design peak gradient, in order to test the damage threshold of the rather long structures with tilted laser pulses in the 600-700 fs realm. These structures have been designed and numerically simulated in 2D with great success, and submitted to Stanford University for fabrication and testing. Although the structures are longer than the Rayleigh length of the electron beam, the external quadrupole magnet is not planned for the first experiment. Instead, the experiment is outlined with cut structures, in order to empirically find the length lim-

² The beam envelope is described by $a(z) = \sqrt{\hat{\beta}(z)}\epsilon$, with the geometric emittance ϵ . The other Courant-Snyder functions describe momentum-envelope ($\hat{\gamma}$) and correlation ($\hat{\alpha}$), and can be calculated from the betafunctor $\hat{\beta}$ by $\hat{\alpha} = -\hat{\beta}'/2$ and $\hat{\gamma} = (1 + \hat{\alpha}^2)/\hat{\beta}$, see e.g. [57].

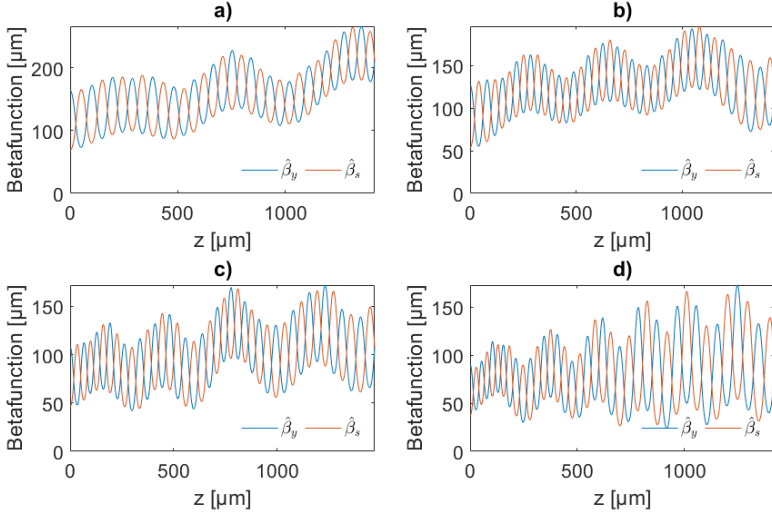


Figure 2.4.: Designs for first high energy gain subrelativistic DLA experiments, submitted to Stanford for fabrication and testing. Lattice data courtesy of T. Egenolf. The parameters are $W_0 = 96$ keV, $\lambda_0 = 1980$ nm, length 1.44 mm (limited by fabrication process) and the 4 different designs are for different laser field strengths as detailed in Tab. 2.1.

itation. Preliminary results from testing these structures in the “Glassbox” interaction chamber at Stanford University have been obtained in 2022, where the design energy gain for the Fig. 2.4 c) structures, trimmed in length to $480\mu\text{m}$ (16.5 keV) and to $708\mu\text{m}$ (24.1 keV) has been successfully reached. Structures of 1 mm length are currently (au-

Table 2.1.: Parameters of the APF lattices in Fig. 2.4. The injection geometric emittance is $\varepsilon_y = 25$ pm and the bunch length is 10 nm. Angle distribution and energy spread are matched, see Paper 5.3 Supplement. The throughput fraction is calculated by DLAttrack6D under the 2D assumption.

Design	G_{peak}	E_L	Initial $\hat{\beta}_y/\hat{\beta}_s$	W_{out}	throughput
a)	30 MeV/m	91 MV/m	163/96 μm	117 keV	31%
b)	50 MeV/m	152 MV/m	126/54 μm	132 keV	26%
c)	70 MeV/m	212 MV/m	107/46 μm	147 keV	51%
d)	100 MeV/m	303 MV/m	90/38 μm	167 keV	71%

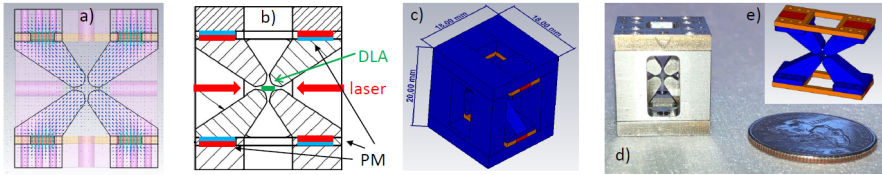


Figure 2.5.: Design and simulation of the Permanent Magnet Quadrupole (PMQ) in CST EM Studio [44] (a), (c), (e)) and annotated construction drawing b). The permanent magnets are commercial low cost $3 \times 3 \times 1\text{mm}^3$ NeFeB blocks. The brown sheet around the magnets in e) is low permeability material. Photograph (d) courtesy of J. England.

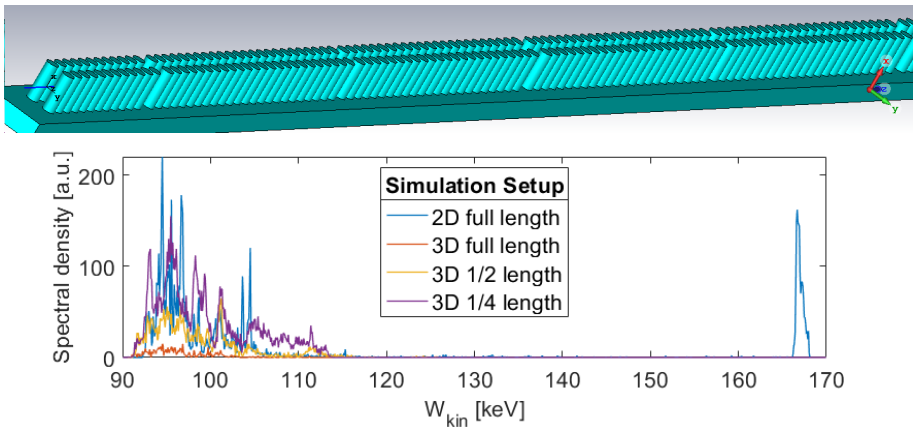


Figure 2.6.: Top: first 5 segments of the structure with $3\mu\text{m}$ pillar height, as it will be fabricated on a “mesa”. Bottom: energy spectra obtained from 2D and 3D simulation with a transversally matched, unbunched incident electron beam. In the 3D setup severe beam loss occurs, requiring to trim the structures in length to see any signal.

tumn 2022) under test, which is roughly the length limit of the 2D structures, since the full length (1.44 mm) structures were already unsuccessfully tested. Note that due to the finite height of the pillars, there are unmatched vertical focusing/defocusing forces which are hardly possible to assess in simulations. Therefore estimating the length limit by the vertical Rayleigh range is likely an inappropriate oversimplification.

A permanent magnet quadrupole (PMQ) for the vertical confinement has however already been designed, fabricated, and tested, see Fig. 2.5. The manufacturing of the

pole pieces requires high accuracy, on the order of 50 μm , which could be obtained by Electric Discharge Machining (EDM) at SLAC. The permanent magnets are low-cost commercially available $3 \times 3 \times 1 \text{mm}^3$ NeFeB blocks, that have been measured and sorted, in order to ensure equal strength, which in turn ensures that the symmetry axis of the magnetic field coincides with the symmetry axis of the quadrupole magnet structure.

Even if the quadrupole magnet were installed and thus the electron beam is kept in a small vertical range, it remains questionable if the 2D assumption for the synchronous field between the pillars can be held, i.e., if $\partial_x e_1 = 0$ holds to sufficient accuracy. Preliminary 3D simulations on the 2D structures with 3 μm pillar height indicate that the fluctuations of e_1 along the vertical coordinate deteriorate the beam quality so strongly, that only about 10 to 20 keV of energy gain is possible, see Fig. 2.6. To demonstrate that this is a principle issue, the plot shows a full-field 2D simulation in CST Particle Studio [44], where the design output energy is nicely reached as designed. This indicates that there were no errors in the lattice design itself and neither in the DLAttrack6D cross-check. Extending the full-field simulation to 3D, in a structure with 3 μm pillars as depicted in Fig. 2.6, the result is that especially those electrons following the acceleration ramp are lost. Obviously, the amount of lost electrons is reduced by shortening the structure, however a peak at the acceleration ramp is unfortunately still not obtained in the 3D simulation. By tweaking the laser incidence angles, electron beam vertical position and laser amplitude this can however improve in the experiment, such that at least for reduced length a peak at the ramp appears.

As a consequence of this rather unpredictable behavior especially at low energy, the laser based focusing scheme must be extended to 3D. This avoids both the issues with the quadrupole magnet itself and its alignment, as well as the requirement to ensure vertical invariance of the laser fields. Three-dimensional APF for DLA has been conceived in Paper 5.11. The idea of the setup is that e_1 fulfills a Helmholtz equation

$$(\Delta_{\perp} + \kappa^2)e_1(x, y) = 0 \quad (2.16)$$

where κ is given by the dispersion relation, Eq. 2.12. The potential generalizes to

$$V = q\text{Im}\{e_{10}[\frac{\lambda_g}{2\pi} \cosh(ik_x x) \cosh(ik_y y) e^{2\pi is/\lambda_g} - ise^{i\varphi_s}]\} \quad (2.17)$$

such that Hill's equations (Eq. 2.15) are obtained for all three coordinates x, y, s , with the respective lattice functions K_x, K_y, K_s . As discussed in Paper 5.11, the dispersion relation 2.12 implies $K_x(z) + K_y(z) + K_s(z) = 0$ which directly reflects Earnshaw's theorem. Moreover, in a 2D scheme, $K_x = 0$ implies $K_y = -K_s = K$, i.e. $\hat{\beta}_y$ and $\hat{\beta}_s$ are roughly shifted by a half lattice period, see Fig. 2.4. In the 3D scheme all lattice functions are disparate and must be subjected to a multi-objective optimization as being detailed in Sect. 2.5.2.

2.4 Lattice Design vs. Ponderomotive Averaging

Before the APF for DLA approach, a ponderomotive focusing approach for DLA was proposed by Naranjo et al. [30]. This approach is based on preceding work on electron focusing properties in RF linacs [59, 60, 3]. The key idea is that non-synchronous spatial harmonics exert an alternating transverse force on the particles, similar to a focusing lattice. The accelerating harmonic is usually referred to as the fundamental harmonic, fulfilling Wideroe's condition Eq. 1.3. Thus, since the focusing harmonics are lower in wavenumber, they can be better understood as non-synchronous spatial sub-harmonics. Here, the focusing function as it appears in Hill's equation, is sinusoidally following each of these spatial sub-harmonics, as compared to the piecewise constant focusing function in APF. For a single focusing (non-synchronous) harmonic, this special case of Hill's equation with sinusoidally changing frequency is referred to as Mathieu equation, solvable by special functions (i.e. Mathieu functions), defined as the solution of this respective equation. The corresponding (nonlinear) envelope equation does not have a closed solution known to the author today. Therefore, in spatial harmonic focusing, the lattice cannot be analytically integrated, i.e. the lattice/envelope functions cannot be determined analytically, which is a requirement for pragmatic optimization procedures. Nevertheless, it can be shown that the motion is bounded [30], and the *average* $\hat{\beta}$ -function can be determined [61]. Subsequently, an entirely numerical approach to beam dynamics in spatial harmonic focusing is required and has been made by UCLA's code SHarD [62].

To explain the spatial harmonic focusing technique, we simplify the math of [30] following [63]. Assume there are only two spatial harmonics, one synchronous for acceleration (e_1) and one non-synchronous for focusing (e_2), travelling at the slower phase velocity $v_2 = \beta_2 c$. The equations of motion can be written as (linearizing the cosh-potential)

$$\varphi'' = -\frac{q}{m_e c^2} \frac{k_z}{\beta^2 \gamma^3} (e_1 \sin(\varphi) + e_2 \sin(\varphi + \delta_k z)) \quad (2.18a)$$

$$y'' = \frac{q}{m_e c^2} \frac{k_z y}{\beta^2 \gamma} \left(e_1 \frac{1}{\gamma^2} \cos(\varphi) + e_2 (1 - \beta \beta_2) \cos(\varphi + \delta_k z) \right) \quad (2.18b)$$

where $\varphi = \omega s / \beta c$, $k_z = 2\pi / \lambda_g$, and $\delta_k = 2\pi / \lambda_s$ with the sub-harmonic period λ_s . we assume the longitudinally stable case, i.e. φ stays close to φ_s . However, $\delta_k z$ changes largely over the length of the accelerator. Therefore the motion can be split into fast and slow (secular) parts as $y = y_f + y_s$, where $y_s \gg y_f$ but $y_s'' \ll y_f''$, i.e., the fast motion can be highly chaotic, but is small in amplitude. It can be written as

$$y_f'' = \frac{q}{m_e c^2} \frac{k_z y_s}{\beta^2 \gamma} e_2 (1 - \beta \beta_2) \cos(\varphi + \delta_k z), \quad (2.19)$$

in which y_s can be regarded as a constant. Thus, integrating over z twice provides y_f explicitly. Inserting y_f and y_f'' from Eq. 2.19 into the equation of motion (Eq. 2.18b) and averaging over one λ_s period yields

$$y_s'' = \frac{q}{m_e c^2} \frac{k_z y_s}{\beta^2 \gamma} \left(\frac{e_1 \cos(\varphi_s)}{\gamma^2} - \frac{q}{m_e c^2} \frac{e_2^2 (1 - \beta \beta_2)^2}{\beta^2 \gamma} \frac{k_z}{4 \delta_k^2} \right), \quad (2.20)$$

which is the equation of *secular* motion. The focusing term has a negative sign, which means the particles are driven towards the center of the channel, where the absolute field strength is lower than close to the grating surface. Since we assumed longitudinal stability, i.e., the conventional fish-type bucket, Earnshaws theorem demands the positive sign for the acceleration defocusing term. Thus, for transverse stability, the ponderomotive focusing term in Eq. 2.20, must overcome the acceleration defocusing term in magnitude. Explicitly, from Eq. 2.20 this can be written as

$$e_2 \gg \frac{2 \beta \delta_k}{\gamma (1 - \beta \beta_2)} \sqrt{\frac{m_e c^2}{q} \frac{\gamma}{k_z} e_1 \cos(\varphi_s)}, \quad (2.21)$$

where the exact minimum magnitude depends crucially on the choice of δ_k and β_2 , as well as the relativistic beam parameters. Note the scaling of the minimum e_2 with $\sqrt{e_1}$, which favors this scheme at high gradients. Practical numbers for DLA experiments with RF-photoinjectors ($\gamma = 10$, $(1 - \beta \beta_2)^{-0.5} = 2$, $\lambda_g = 1 \mu\text{m}$, $\delta_k/k_z = 1/100$, $\cos \varphi_s = 0.5$) imply that the e_2 magnitude needs to be on the same order as e_1 or higher. The smallest gradient e_1 for the break-even, in order to work with $e_2 < e_1$, is at about $e_1 = e_2 = 1 \text{ GV/m}$. These very high values for e_2 are obviously also constrained by the damage threshold of the structures. Since e_2 does not contribute to acceleration, the limitation of the focusing gradient rather than the acceleration gradient by the damage threshold of the structure is the main drawback of the spatial harmonic ponderomotive focusing scheme.

The main advantage of the ponderomotive scheme is that it works for highly relativistic electrons on generic, strictly λ_g -periodic, grating structures. The required laser pulses can be prepared on the optical table by chirping the frequency to account for the acceleration and by creating the focusing sub-harmonics by a spatial light modulator (SLM). Due to the smoothness of the sinusoidal focusing functions, spatial harmonic focusing requires less bandwidth than creating APF lattices by laser pulse shaping on these generic gratings.

An interesting property of the spatial harmonic scheme is that it preserves the *average* beam size if the normalized (RMS) emittance is conserved³. Since the average $\hat{\beta}$ -function scales as $\hat{\beta} \propto 1/\sqrt{K}$ and the beam size is $a = \sqrt{\varepsilon \hat{\beta}}$ with $\varepsilon = \varepsilon_n/(\beta \gamma)$, the

³ Conservation of the normalized (RMS) emittance is a consequence of Liouville's theorem in a *linear* focusing lattice [57].

scaling of the focusing term $K \propto \gamma^{-2}$ implies $a = \text{const.}$ Compared to this, 2D APF has $K \propto \gamma^{-3}$, thus the beam size increases as $a \propto \gamma^{1/4}$. This slow increase can be easily compensated in the structure design, keeping in mind that at higher energy the roll-off of the evanescent wave decay constant is slower, allowing for a higher aperture. In 3D APF, the focusing constant scales as $K \propto \gamma^{-1}$, see Paper 5.11. Thus the beam spot shrinks as $a \propto \gamma^{-1/4}$, which can be translated into increased gradient by reducing the aperture or to improved longitudinal stability by staying longer on the longitudinally focusing phase.

On the long run, APF will definitely outperform spatial harmonic focusing, since the requirement of large laser power in the focusing harmonic harmonics basically loses the advantage DLA has over conventional accelerators. Moreover, for an accelerator ready for applications one would need analytically accessible dynamics, which needs to be free of chaotic motion at least for small particle amplitudes, in order to design the accelerator in an entirely deterministic manner. On the short run, for proof of principle experiments, the advantage of using generic grating structures and loading the focusing scheme on the laser pulse just as a completely variable “software”, has advantages. Moreover, the optimization of the required harmonics can be done, both in experiments and in online simulations. These online simulations give rise to a “digital twin” model, with heuristically determined model parameters. Modern machine learning and artificial intelligence techniques can be utilized to obtain these parameters from the plethora of experimental, simplified numerical (DLAtrack6D) or expensive full-field numerical data. In the final setup, in order to increase the laser power efficiency, the chosen focusing lattice can then be re-optimized based on the APF formalism and fabricated on a dedicated chip, which is illuminated by a (locally) flat phase front tilted laser pulse.

2.5 Low Energy DLA

A particularly interesting feature of low energy DLA is that the electron beam is so soft, that involved dynamical processes can occur in structures that contain only as few as 20 periods or even less. This gives rise to attosecond science [64] on simple, dedicated DLA structures. One goal of these dynamical processes is to prepare the electron pulses such that they fit into the optical acceptance buckets and can be accelerated in a length-scalable DLA from sub-relativistic to highly relativistic energy.

2.5.1 Attosecond Bunching

At low energy, the energy dependency of the velocity leads to intrinsic dispersion in drift sections. This enables ballistic bunching using energy modulation correlated with the longitudinal position s in the beam. A modulator-drift buncher, followed by a chirped accelerator on a single chip is proposed in Paper 5.1. The required drift length can be easily calculated from the energy modulation $\Delta W = qe_1 N \lambda_g \sin(\omega \Delta t)$ under the

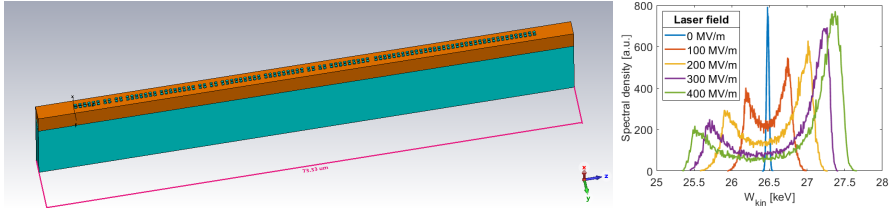


Figure 2.7.: 3D APF buncher on a SOI wafer. Left: simulated 73 μm long setup, where also lateral grounding traces can be attached (cf. Paper 5.13). The electron beam enters from the left and the laser impinges from the top. Right: energy spectrum for different laser field amplitudes. One can clearly see that for the nominal value (400 MV/m) the initially larger energy spread turns into a shifted peak with smaller spread, indicating that the beam was properly bunched with small energy spread and accelerated.

assumption that the particle phase remains constant in all N cells of the modulator (if this is not fulfilled, DLAttrack6D can be used to calculate the proper energy modulation and dephasing). Using the energy velocity differential $\Delta v/v = \beta^{-2}\gamma^{-2}\Delta W/W$ the required drift length results as

$$L = \beta c T = \beta c \frac{v \Delta t}{\Delta v} = \frac{\beta^2 \gamma^3 m_e c^2}{2\pi q e_1 N} \frac{\omega \Delta t}{\sin(\omega \Delta t)}, \quad (2.22)$$

where T is the time required to reach the bunched state and β, γ refer to the synchronous energy. The last factor in Eq. 2.22 is an inverted sinc-function which takes the limit 1 for small initial time difference Δt . In this case, the phase space around the fixed-point becomes exactly vertical and thus the shortest micro-pulses are achieved. However, this corresponds to a rather small fraction of the electrons being bunched. A larger fraction of the electrons is captured at a longer drift section, e.g. at $\omega \Delta t = \pi/2$, where the most-modulated particle and the non-modulated particle (i.e. the particle at the fixed point) arrive at the same time. In this case the inverse sinc function takes the value $\pi/2$, describing the increased drift length.

A problem with these ballistic bunchers is the remaining energy spread in the ultra-short bunches. First, this leads to rapid debunching after the longitudinal focus. Second, and more importantly, such high energy spread can exceed the acceptance of a downstream accelerator. A way to mitigate the large energy spread is to use an APF based bunching scheme, which relies on modulating the beam, drifting, and demodulation, before the longitudinal focus is reached. Such a scheme was theoretically proposed in Paper 5.3 and experimentally demonstrated in Paper 5.12. However, the experiment could not reach the energy spread as low as predicted by 2D simulations. The main

reason for this is that the structures were designed in 2D, but 3D effects manifested themselves in the experiment, where the pillar height was only 3 μm . The results were however sufficiently good to observe for the first time in DLA “coherent acceleration”, i.e. a phase dependent shift, rather than just a broadening, of the peak in the energy spectrum.

In order to achieve the goal of sufficiently small energy spread combined with sufficiently small bunchlength such that the bunch can be scalably accelerated on a chip, a 3D APF buncher is required. Such a design, together with full 3D simulations, is shown in Fig. 2.7. The setup is based on 26.478 keV reference energy and relies on 3 modulation/drift/demodulation stages. The 3D APF structure is designed on a top-illuminated SOI wafer, including horizontal and vertical focusing. By design, no long drift is required before injection into the acceleration stage. The setup has been conceived using DLAttrack6D (Paper 5.2) and subsequently fully simulated in CST Studio [44]. Field simulations were carried out both in FD and in TD and also particle tracking was performed in both fields. The energy spectra from the full TD-PIC simulation are very similar to the ones from DLAttrack6D; moreover at design laser amplitude the peak shift indicates that the energy spread and the bunch length match the design. Such a buncher can be used to inject a beam into the scalable accelerators presented in Papers 5.11 and 5.13, thereby increasing the injection efficiency from roughly 5% (unbunched) to about 50% (well bunched). The design procedure for the lattice of the downstream accelerator is detailed in the next section.

2.5.2 Scalable Acceleration

In order to obtain a length-scalable accelerator at low energy, a design procedure has to tackle focusing and acceleration simultaneously. For the 2D APF scheme, this procedure has been developed in Paper 5.3 and for 3D APF in Paper 5.11. The strategy is outlined in Fig. 2.8, where we for brevity directly work on the 3D scheme (the 2D scheme is obtained by setting $k_x = 0$). We start with fixed parameters of the setting: the laser (center-) wavelength, the peak electric field of the laser E_L , limited by the material damage threshold and the electron injection energy W_{inj} . The synchronous phase φ_{sync} does not need to be fixed throughout the accelerator; however we employ an off-crest setting of constant value alternating between the focusing and defocusing phases while the acceleration is constant. This is not necessary, however it greatly simplifies the procedure, since more or less all parameters hinge on φ_{sync} .

First, a baseline structure needs to be selected. This single cell needs to provide a high structure constant e_{10} simultaneously with a high bandwidth. In other words, resonant structures have to be avoided, since they are strongly disturbed in their field flatness when the APF phase jumps are introduced. Moreover, in this selection also the compromise of gradient vs. transverse aperture has to be made. Once this baseline is found, numerical analysis, scanning over the relativistic speed β (or the period length λ_g) needs

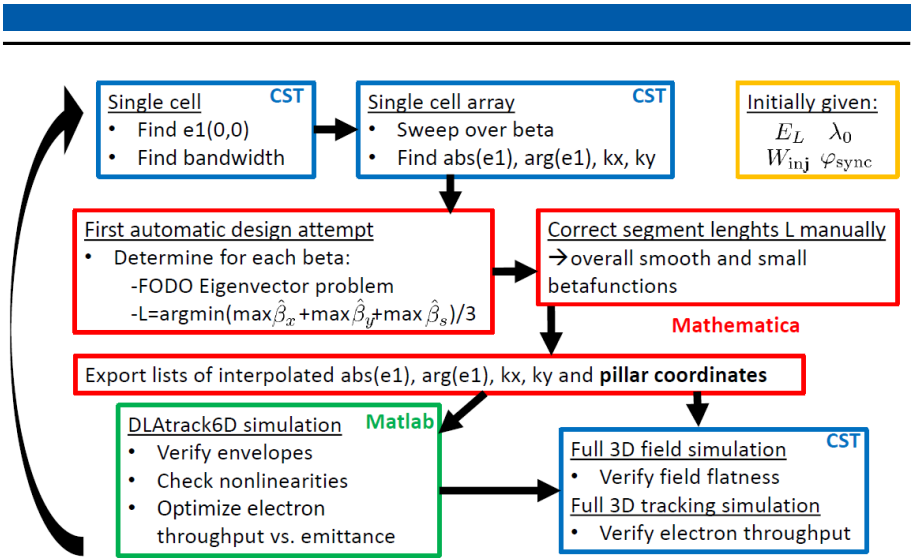


Figure 2.8.: Lattice design procedure for the 3D APF scheme

to be performed, in order to check if e_{10} remains within reasonable bounds, i.e. does not drop to extremely small values. In this scan, also the phase of e_{10} and the focusing constants k_x and k_y are determined and exported in lists.

Then, a first automatic design attempt is made, in order to find the APF focusing period lengths. This attempt is based on solving the FODO-cell eigenvector problem to obtain the initial values of the lattice functions. With the lattice function mapping matrices, known from the DLA-cell parameters, the maximum of the betafunction can be determined. Crucially, this maximum needs to be minimized depending on the APF cell length, in order to scrape as few particles as possible on the aperture. For 2D APF, this is a simple extremum calculation procedure, since the focusing function in the longitudinal and the transverse direction are identical and subsequently also the betatron phase advance is identical. In the 3D APF setup, all three focusing functions are different, so minimizing the maxima of the three betafunctions becomes a multi-objective optimization problem. Under the usual circumstances, the arithmetic average of the three betafunctions takes a minimum for a cell length that is practically achievable. Thus, this particular cell length is an element of the Pareto-front of the 3-objective optimization and taken as an initial guess for further optimization.

A severe issue at low energy is that the optimal APF cell lengths cannot be exactly realized, since they would be a non-integer number of DLA cells in length. Therefore, a mismatch between the APF cells always remains, which can accumulate errors over multiple APF cells. A way to mitigate this effect is to manually correct segment lengths from start to end, while overviewing the betafunction of the entire accelerator. Balancing

the errors between the three planes leads to smooth and small betafunctions, allowing a beam of given emittance to propagate along the accelerator with small losses and to accelerate according to the design acceleration ramp.

Once the accelerator is designed, the lattice in the form of pillar coordinates is exported. Moreover, from interpolation of the velocity sweep given by the input data, also the interpolated e_{10} and focusing constants can be exported. This allows to verify the beam envelopes and investigate the nonlinear behavior quickly in DLAttrack6D (Paper 5.2). Especially, these fast simulations allow to assess the maximum of the three initial emittances required to obtain a decent fraction of the injected beam to be accelerated and arriving at the design output energy.

Once the quick DLAttrack6D simulation is successfully completed, the full design can be verified by 3D field and particle simulations. First, a field simulation can be performed and the frequency domain electric field on axis can be exported. The on-axis field can subsequently be windowed in the respective DLA cells, i.e. the z-coordinates (start and stop) of each cell are taken to reconstruct e_{10} from the field of the full structure. The reconstructed array of e_{10} can then be compared with the design, both in its amplitude and phase. This comparison should be mostly accurate, except a Gibbs phenomenon occurring at the APF phase jumps. The required low quality factor of the DLA cells ensures that only one cell neighboring the APF jump is affected by the Gibbs phenomenon.

With the field properly checked and sufficient quality assured, a full start to end particle simulation in this field can be performed. This simulation is computationally very heavy, since its size is the entire structure, but the extremely small scale details within the tiny electron bunch have to be resolved. CST Particle Studio [44] chooses the time step according to the Courant-Friedrichs-Lewy (CFL) criterion on the spatial mesh used for the tracking. The precomputed fields are interpolated on this mesh, thus preserving the field resolution results in an extremely small time step. Nonetheless, using the powerful 18 core desktop PCs available in our institute, such a simulation over 500 DLA cells on a 400 μm long SOI structure is doable in about two days (cf. Paper 5.13). Hitting the initial conditions for the injected particle ensemble precisely is a challenge, the unphysical errors caused by the particle injection window have to be taken into account and manually corrected. Single simulations with the proper design parameters could be performed, assessing discrepancies to the analytical design and the DLAttrack6D simulations. However, for parameter sweeps assessing experimental errors, the full simulations are prohibitively heavy.

As indicated in Fig. 2.8, the design and simulation procedure is not always successful at the first attempt. Latest at the full start-to-end 3D field and particle simulation, conceptual and/or implementation errors can be revealed, leading to iterative restart of the procedure, together with fixing errors and design improvements. The results of the simulations in idealized symmetric structures are presented in Paper 5.11 and for more practical structures that can be fabricated in the device layer of SOI wafers in Paper 5.13. A first design attempt of these realistic structures was unsuccessful, since

the gradient of phase of the structure constant, i.e. $\partial_x \arg e_1$, was neglected. The physical consequence of phase gradient is a constant deflection force similar to a homogeneous magnetic field. However, the value of the phase gradient changes with the DLA cell length or synchronous velocity. Therefore, by means of an external homogeneous magnetic field, only partial compensation can be obtained. A better way is to avoid the phase gradient a-priori, i.e. the initial structure cell should be designed such that $\partial_x \arg e_1|_{x=0,y=0} = 0$. This can be done in two ways: either changing from elliptical to rather rectangular (hyper-elliptical) pillars or adjusting the phase by the longitudinal position of the lateral grounding traces. The second option can be done easier in a cell-length adapted fashion, ensuring that the phase gradient vanishes for all DLA cells in the entire accelerator structure.

Extrapolating the procedure to multistage setups, a mock-up design is depicted in Fig. 2.9. The stages are defined by individual PFT angles following Eq. 1.4, corresponding to ranges of beam velocity. Between the stages, some separation space for the different laser pulses is required. This space can also be used to account for vertical electrostatic deflectors, in order to correct for residual phase gradient deflection errors. The deflector plates would be attached by a second wafer from the top, contacted through the SOI device layer. The Silicon substrate of the SOI wafer serves as ground electrode. Since the distance between the electrodes is so small, biasing the

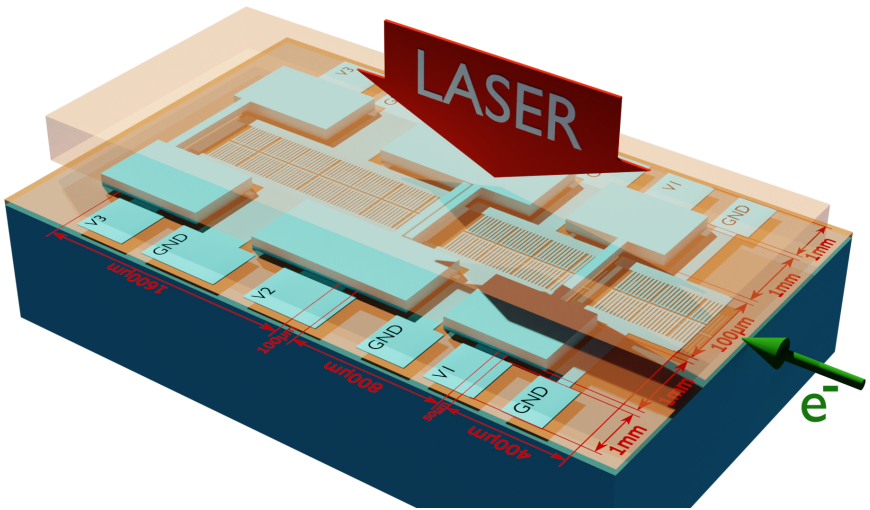


Figure 2.9.: Mockup picture of a multistage 3D APF SOI chip with electrostatic vertical steering between the stages. Courtesy of Jan Lautenschläger.

deflectors with about 30 V is estimated to suffice for the necessary corrections, see Paper 5.13.

2.6 High Energy DLA

On the one hand, DLA at very high energy simplifies focusing, since the electron beam is very stiff. This stiffness also helps in the longitudinal plane, allowing to choose the synchronous phase only slightly off-crest, or even entirely on-crest, for highest gradient acceleration. On the other hand, the stiffness of the beam complicates bunching, as dispersion needs to be introduced by a dedicated device as e.g. a magnetic chicane. As it is the case at low energy, a scalable DLA has a small longitudinal acceptance, requiring a bunched beam. In a large scale accelerator facility, a DLA can also be used as a modulator, in order to bunch the beam at the optical or infrared wavelength. A proposal to modulate a high energy beam on the sub-fs scale with a DLA is shown in Paper 5.9. The purpose of such a buncher in a Free Electron Laser (FEL) facility would be to create higher peak current in the undulator, leading to brighter X-ray arriving in well-defined pulses distanced by the modulating laser period. High brightness ultrashort bunches can be further accelerated in a scalable DLA; a first concept based on 3D APF using a single material is presented in the next section. Moreover, the PhD work of T. Egenolf in the DLA group at TU Darmstadt looks thoroughly into intensity limitations of high energy DLAs and created tools for this purpose on future structures. As a first practical step, we will look into the wakefields of ultrashort bunches in upscaled DLA structures, working in the THz range.

2.6.1 Scalable Acceleration

In order to improve upon conventional accelerators, the high acceleration gradients are crucial for high energy DLA. Therefore, a single material with the highest possible damage threshold should be used. Among the best choices, also practically demonstrated, is Fused Silica (SiO_2). Although etching this material is elaborate (it requires Hydrofluoric acid), a decisive advantage is that it is quite common in the semiconductor industry and established fabrication techniques can be used. In particular, to create symmetric structures, the process of direct bonding was used [16]. Many of the relativistic acceleration experiments in ACHIP still run on the original structures developed for the SLAC experiment [16] or direct descendants thereof. While at medium energy first dynamical effects are visible [65], the high energy experiments at DESY have not yet pushed the interaction length to the point where focusing inside the chip is required. Keeping the generic structures and using the spatial harmonic focusing scheme, imprinted by a liquid crystal phase mask or SLM is certainly possible, however it is unlikely that the drawbacks coming with this render the scheme still better than conventional accelerators. Particularly, the requirement of large amounts of laser power in the focusing harmonic, as well

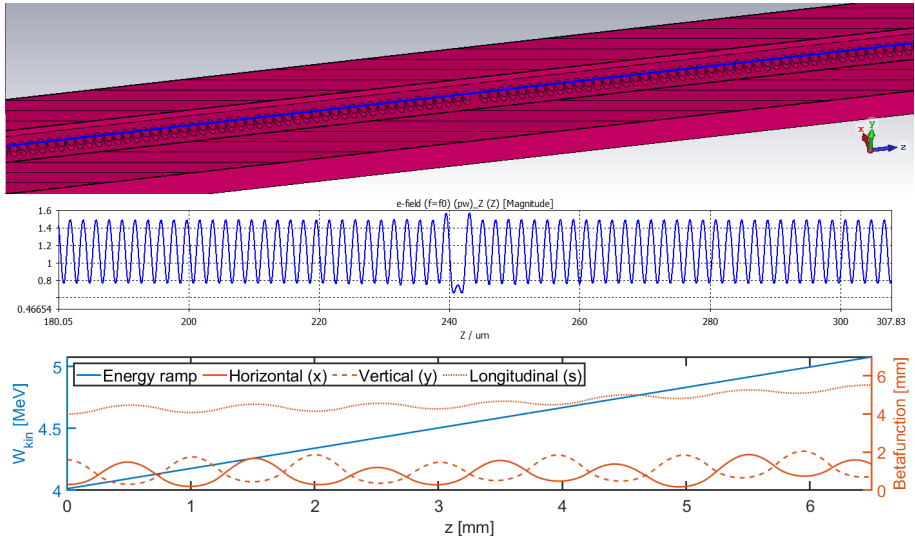


Figure 2.10.: APF counter-phase structure for relativistic acceleration. Top: half of the simulated structure (The laser comes from top and bottom as in Fig. 2.2 (c), the blue line is the beam axis), center: normalized electric field on axis, bottom: energy ramp and betafunctions of the six-dimensional confinement.

as the absence of focusing in the invariant plane indicate a soon advent of a scalable DLA based on the 3D APF scheme.

An outline of such a scalable accelerator design at 4 MeV is shown in Fig. 2.10. The parameters of this setup are as follows: synchronous phase 30 degrees off crest, 500 MV/m incident laser field from both sides, 3345 DLA cells (about 6 mm total length). The resulting energy gain is 1 MeV, i.e. an *average* gradient of about 158 MeV/m. The aperture was chosen rather by rule of thumb as 800 nm and not yet optimized. The initial normalized emittance of 0.08 nm rad and the bunchlength of 0.08 fs results in an accelerated electron yield of about 70 % (DLAtrack6D). The remaining challenge of these structures is their fabrication, requiring multiple lithography steps and bonding. Similarly long, bonded grating structures have been fabricated recently [47], which raises some optimism that it is also possible to fabricate and bond these three-dimensional structures. A general challenge in these long structures is that the channel must be straight, i.e., it must be prevented from thermal warping. Ideas of locally heating the structures or techniques based on Microelectromechanical Systems (MEMS) are being considered to straighten the channel in a length-scalable fashion.

2.6.2 Wake Fields and Collective Effects

Connected to the acceleration of high energy electrons is the question of the intensity (or charge) limit. While tip-based sources for low energy DLA pose a rather low intensity limit by space charge right after emission, high energy DLA leverages the extensive development efforts of conventional accelerators. By using conventional photo-injectors and pre-accelerators to increase the injection energy while keeping the normalized emittance nearly constant, the geometric emittance can be sufficiently reduced to inject into a DLA with acceptable losses. In this case, the DLA can be run on high charge, requiring to assess collective effects, as was done in Paper 5.10.

The simplest collective effect is beam loading, i.e., the wake potential significantly alters the laser-driven potential which confines and accelerates the electrons longitudinally. A coarse estimate of the maximum charge can be given by comparing the magnitude of the wake potential and the accelerating voltage; if they are equal, acceleration of the reference particle is entirely prevented. For the 2D fused silica grating structures and usual bunch lengths, this results in about 10^4 to 10^5 electrons per optical microbunch. However, this is a large overestimation of the intensity limit as collective instabilities kick in much earlier. Controlling the collective instabilities and approaching the beam loading limit is however necessary in order to efficiently extract energy from the drive laser pulse. Therefore, a more thorough assessment of collective instabilities driven by resonant wake effects in DLA is necessary [51].

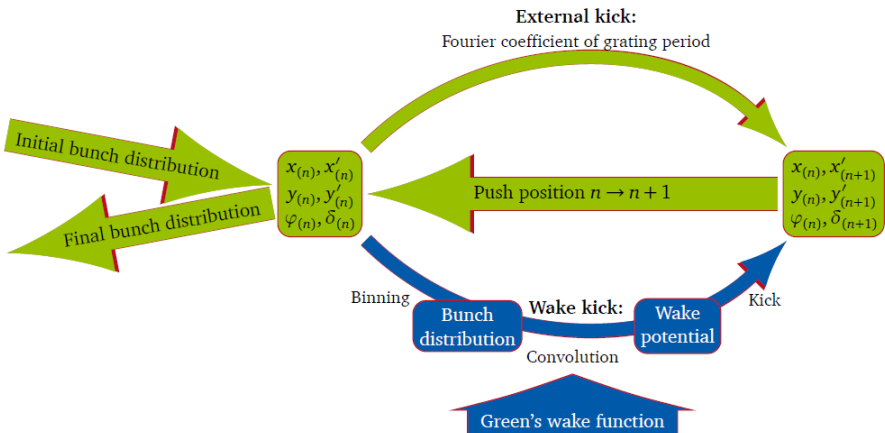


Figure 2.11.: DLAttrack6D tracking scheme. The green part is the original code as conceived in Paper 5.2 and the blue part is the wakefield extension, as introduced in Paper 5.10. Picture courtesy of T. Egenolf.

Similar as the laser kicks, the wake kicks also fulfill the Panofsky-Wenzel relation $\nabla' \times \Delta \vec{p} = 0$. This allows also to check the validity of numerically determined wake potentials as was done in Paper 5.10. When choosing the bunch length as short as possible in a numerical simulation, one obtains an approximation to Green function of the wake. Convolution of this Green function with the beam distribution results in the wake potential from which one can directly calculate kicks and apply them in a tracking scheme as DLAttrack6D, see Fig. 2.11. The beam distribution originates from binning the particles to obtain a (smoothed) histogram of sufficient resolution. Note that the convolutions have to be executed in all three dimensions and that this approach makes the additional simplifying assumption that the bunch is uncorrelated (not tilted) in x , y , and s . A straightforward finding of this procedure is that in order to mitigate the coherent deflection effect of the transverse wakefield, the structures must be symmetric. Symmetrizing the driving laser field by means of a Bragg mirror is insufficient at high intensity, since the wakefields are broadband in character and subsequently reflected asymmetrically due to the frequency-dependent reflectivity of the Bragg mirror.

Paper 5.10 shows the wakefield extension to the original DLAttrack6D and its testing and validation (see Fig. 2.11 for an illustration). Moreover, the paper discusses the determination of the betatron phase advance for an ensemble of particles and the subsequent determination of the betatron-tune spectrum. The tune spectrum is crucial for the damping of intensity-dependent collective instabilities. As an example, the paper discusses the strong head-tail instability, its simulation and its analytical description by Chao's two-particle model [66]. The new wakefield module was implemented by T. Egenolf in a rewritten version of DLAttrack6D in Python. With the new wakefield module in DLAttrack6D, a stability diagram as function of emittance and intensity is obtained for a 6.5 MeV beam with realistic distribution but very small emittance in order not to have to consider particle scraping on the aperture.

Usually wakefields are detrimental to the beam quality as they cause potential well distortions and collective instabilities. Under particular circumstances the wakefields can also be used to change the energy spectrum of a high energy high intensity beam in a beneficial way. An example of such are wakefield dechirpers, i.e., structures that passively remove residual correlated energy spread before the entry of a FEL undulator, see particularly the works of K. Bane et al. [68, 69]. The correlated energy spread is required for bunch compression in dispersive chicanes, which is the common technique to compress electron bunches in high energy linacs, down to the space charge limit [5, 70, 71]. In ACHIP, we constructed experiments with DLA structures re-scaled to 50 μm period length, for the purpose of shaping the longitudinal phase space, in order to obtain beams with a particularly sharp peak in the energy spectrum.

Starting a general campaign on wakefield microstructures, tunable grating structures⁴ have been conceived by B. Hermann et al. at PSI, see Fig. 2.12, where the wakefield simulations were performed by T. Egenolf at TU Darmstadt, see also [51]. The structures

⁴ See also Paper 5.9 for a periodicity-tunable structure.

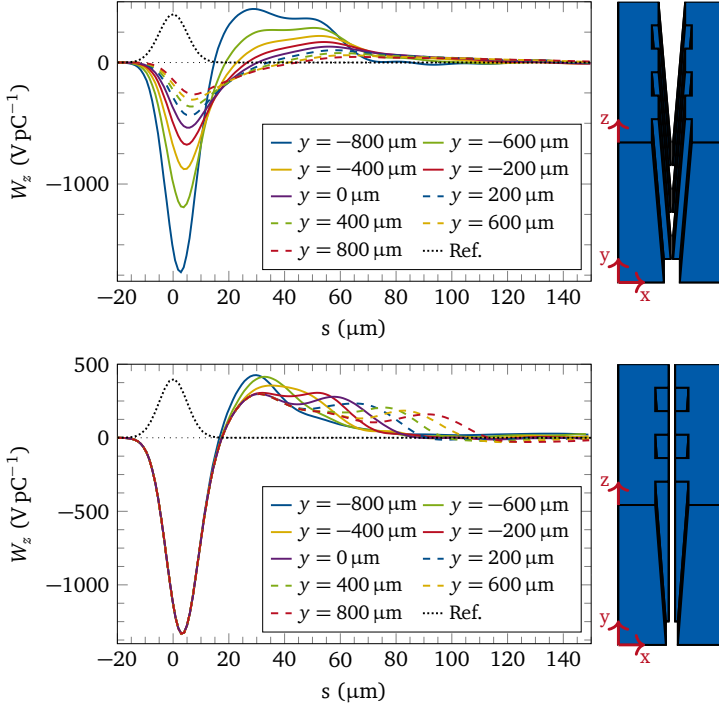


Figure 2.12.: Calculated wake potential of the THz grating structure with variable aperture (top) and variable groove depth (bottom). Courtesy of T. Egenolf [51].

are being tuned by placing them into the beam at different vertical positions. The curves show how the wake potential changes in strength and timing. Once the beam is aligned in the horizontal center, the wakefield and thereby the energy spectrum of the beam can be altered and optimized by vertically moving the structure.

The strength of the wake is maximized when the electron bunch length is minimized. Moreover, one would want a longitudinal distribution that has a strong and sharp peak in the head of the bunch, which creates the wake, and a long weak tail, which probes the wake. The probing of the wake ideally does not “load” the wake, which is ensured by concentrating the charge in the head. It is also advantageous, when head and tail of the bunch can be identified in the energy spectrum. Practically, such bunches are available at SwissFEL at 3.2 GeV. Their shape can be tuned by choosing the strength of the compressor chicane and the synchronous phase in the accelerator stages, in conjunction with the space charge effects at the initially defined total bunch charge [67].

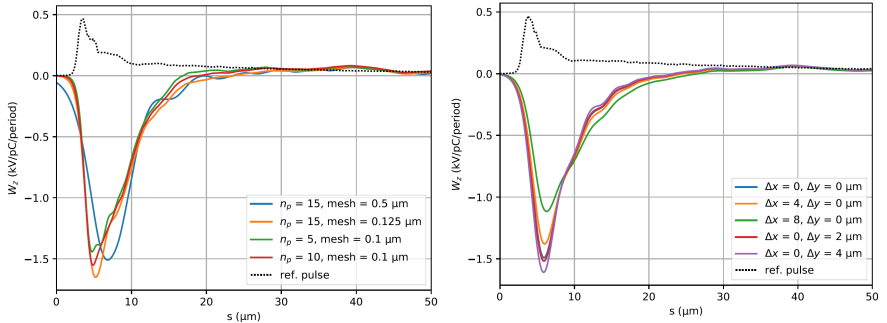


Figure 2.13.: Wake potential simulation of the structure in Fig. 2.12 (top) for the real ultrashort electron pulse at SwissFEL. The left plot shows a mesh resolution study, where an equidistant mesh was used. The number of structure periods is n_p ; if it is too small boundary effects are non-negligible. The right plot shows the wake for different horizontal positions in the V-shaped structure. Data by U.N., plots courtesy of B. Hermann [67]

The ultrashort bunches pose a challenge to the wake simulation, which has been addressed by many authors and techniques, e.g. [72]. For simplicity, we follow a brutal force approach here by just resolving the bunch shape as good as possible. Usually one would at least require 10 mesh lines per sigma of a Gaussian bunch, which renders 3D simulations of these grating structures that are much larger than the bunch numerically extremely heavy. Since the Green function wake cannot be obtained by approximating the excitation by an even shorter Gaussian impulse, we instead simulate the wake for each realistic bunch distribution individually. The required total mesh size is on the order of 10^9 hexahedral cells, about the highest currently doable on our high performance single PCs with the CST Studio software [44]. Moreover, these simulations run for very long time (up to a week) due to the time-step restriction by the CFL criterion. Figure 2.13 (left) shows an attempt of convergence study, indicating that a mesh size of about $0.125 \mu\text{m}$ and a total of 15 periods are required (orange line). Note that the critical feature of the wake is the timing, i.e., the rise steepness seems to be converged for all curves except the blue one. Figure 2.13 (right) shows a scan over the beam position, confirming that the wake strength can be tuned by the vertical position, even for such extremely short bunches. However, the dependence on the horizontal position is non-negligible, requiring to ensure that the beam is precisely injected in the center of the structure, also with proper angle alignment. Measurements of tunable wakefield-modified energy spectra in the real setup at SwissFEL are discussed in Sect. 3.4.



3 Experimental Setups and Selected Results

The different experimental setups, in which measurements of the structures proposed in the course of this work were executed, are discussed. Regarding low beam energy DLA structures, the experimental chambers turn from SEMs to dedicated DLA test chambers, in order to improve the beam brightness and operation stability. The theoretical minimum normalized single particle emittance is given by the Heisenberg uncertainty principle as

$$\epsilon_n = \Delta x \Delta x' \beta \gamma \geq \frac{\hbar}{2m_e c} = \frac{\lambda_C}{4\pi} \approx 0.19 \text{ pm} \quad (3.1)$$

where $\lambda_C \approx 2.426 \text{ pm}$ is the Compton wavelength of the electron and $\Delta x' = p_x/p$ is the angle in paraxial approximation. Experimental measurements approach this limit quite close, e.g. Ehberger et al. [34] obtain $\epsilon_n \approx 1.05 \text{ pm}$ at 44eV, right after a tungsten nanotip. However, this ultralow emittance is difficult to preserve when accelerating to the keV range while keeping the electron beam focused. This problem was already fundamentally stated by Scherzer [33] in his famous theorem about the impossibility of aberration free focusing in cylindrically symmetric setups.

Up to today, electron microscopes have evolved significantly. Especially, it even became possible to correct the aberrations by breaking the symmetry and using higher order multipole correctors [73, 32]. These devices enabled TEMs to attain atomic resolution, which is surely sufficiently low emittance to inject into DLAs. Introductory texts on TEMs can be found here [74, 75], state of the art emittance values are reported in [76]. Corresponding to their tremendous capabilities, advanced TEMs put a huge constraint on size and cost for the equipment. Therefore, dedicated DLA interaction chambers were constructed, attempting a compromise between size and cost of highly professional TEMs with ultralow emittance and the insufficient emittance provided by available SEMs. These setups leverage on so-called immersion lenses [35], an improved, aberration-reduced version of the Wehnelt cylinder commonly used in electron microscopes and even in ordinary Cathode Ray Tubes (CRT).

The injectors for high energy DLAs can exploit adiabatic emittance damping. By keeping the normalized emittance carefully constant, the beam spot can be naturally decreased at high energy. Moreover, also the aperture of DLAs grows with energy. Thus, higher injection energy is always preferable, however, size and cost of the large

scale facilities put a constraint on what can be done in practice, making intermediate size setups as e.g. photo injector test facilities highly interesting for DLA experiments.

3.1 Electron Microscopes

Among the many DLA experiments that were conducted in electron microscopes [17, 77, 78, 23, 26], we will summarize here only three, which were reported in papers 5.6, 5.8, and 5.14. These experiments were conducted at an ≈ 30 keV SEM at FAU Erlangen. The normalized emittance provided by this setup is roughly 100 pm, i.e. a geometric emittance of roughly 300 pm. The DLA structures were fabricated from silicon, first just on the silicon wafer surface and then later on a mesa structure, similar as the structures fabricated at Stanford University [47]. Details of the fabrication process at FAU Erlangen are discussed in [79]. The first experiment, Paper 5.6, demonstrates the utility of the Bragg mirror or Distributed Bragg Reflector (DBR) approach. The staggered acceleration structures were first designed by M. Kozak as a sinusoidal structure with a cut-through electron channel. These structures however perform only as designed when the corners are really corners; in reality they are however always rounded. Therefore one has to resort to structures that are round by design such that the numerical optimization is faithfully reproduced by the nano-fabricated chip. The resulting structures were first presented in [80], borrowing from the single cell Bragg mirror design introduced in Paper 5.1. Subsequent beam based measurement results are presented in Paper 5.6, elaborating on the practical efficacy of the DBR setup. As compared to without the DBR, the energy gain was only 57% higher (ideally 100% would be expected), indicating that also the symmetry of the synchronous field across the channel is impaired, which becomes a critical issue when the setup shall be scaled in length.

A second experiment, shown in Paper 5.8, combines two of these staggered-pillar DBR structures to create a buncher and analyzer setup. The detection of the bunches happens only indirectly, since the only observable quantity in this experiment is the energy spectrum. However, since the laser phase difference between the modulator and the analyzer structures is known, the bunch length can be inferred from a simulation, matching the measured spectrum and the phase difference. The bunch length, or electron arrival time spread, could be nailed down in this way to 0.27 fs. Moreover, exploiting the maximal possible modulation strength and assuming sub-eV initial energy spread, the theoretically achievable minimum bunch length could be estimated below one attosecond. This estimate however disregards all nonlinearities in the system and is thus rather unrealistic. Furthermore, since such extremely short pulses with maximally high energy spread would immediately de-bunch, it is not only challenging to create them, but also to properly detect them.

The third experiment, shown in Paper 5.14, demonstrates the first APF transport channel on a nanophotonic DLA chip. The design is also shown in Paper 5.5 and depicted in Fig. 3.1. This experiment measures a laser-power dependent transmission curve. At

zero laser power, the electron beam is mostly scraped on the aperture, due to its natural defocusing. At higher power, the maximum of the betafuncion attains a minimum, which means the beam is optimally transported. Increasing the laser power further, the beam is overfocused, i.e. the betafuncion minima become small, but the betafuncion maxima increase again, leading to more beam loss. This overfocusing can be driven so far that the transmission is even lower than with laser off; eventually approaching zero transmission. The simulated throughput of electrons as function of the laser field strength is shown in Fig. 3.2. Note that this structure employs DLA cells of constant length, and thus e_1 is identical for each cell and directly proportional to the incident laser field strength, with a structure constant of roughly $e_{10}^{\text{norm}} = 0.2$. However, a severe issue is created from the fact that due to practical considerations of the setup, the laser incidence angle is about 5° to the surface, which leads to a dependence of the amplitude and phase of e_1 on the vertical coordinate. Moreover, as e_1 must fulfill the Helmholtz equation, vertical and horizontal dependencies are interconnected, leading also to deviations in the focusing constants. Preliminary simulations, which are not reported in the paper, indicate that the transmission curve is strongly affected by the vertical coordinate of the beam injection. In practice, the vertical coordinate is however fixed during measurements, and thus a transmission curve as in Fig. 3.2 could be nicely reproduced by adjusting the DBR distance and the laser power normalization.

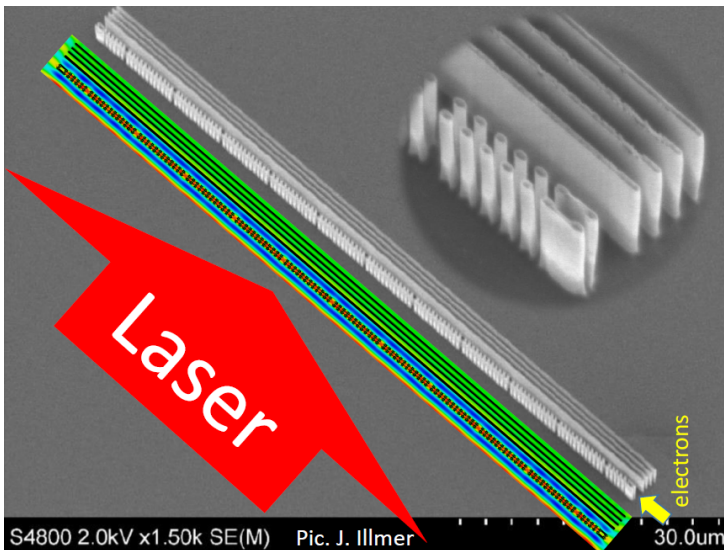


Figure 3.1.: APF transport structure and field simulations. The structure is $77 \mu\text{m}$ long and fabricated on a silicon wafer. The height of the structure is about $3 \mu\text{m}$.

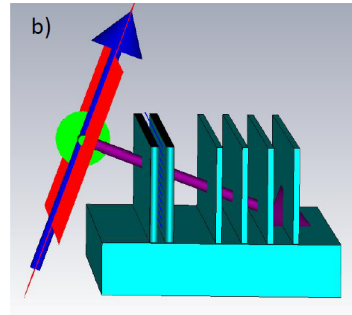
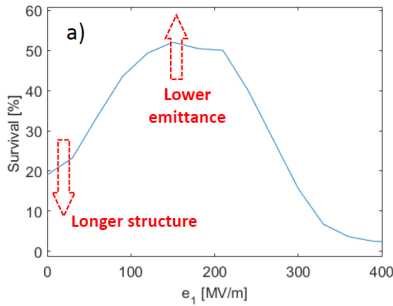


Figure 3.2.: Simulated survival rate (or transmission rate) for the electron beam with 300pm geometric emittance in the transport structure (a). The transmission ratio (optimum power/laser off) can be improved by longer structures (lower laser off transmission) and lower beam emittance (higher optimum transmission). Due to the flat wafer, the laser must impinge with a small angle of about 5° , which is depicted in strongly in exaggerated fashion in (b) (the blue arrow is \vec{H} , green is \vec{E} , and purple is \vec{k}), which leads to differences of e_1 along the vertical coordinate.

The attempt to show overfocusing with these structures however failed, since the damage threshold was reached earlier than the overfocusing regime. Therefore, a second structure was designed which has a smaller transmission ratio but reaches the maximum transmission ratio at lower laser power. This could especially measure the overfocusing regime. The new structure was fabricated by a different process, resembling the mesa-structures from Stanford. This setup allows to reduce the vertical dependence of e_1 by perfectly horizontal laser incidence, but due to the height of the pillars being much smaller than the laser spot, the vertical dependence is still present to some extent. Again, by means of optimization of the DBR distance, at least for one vertical position in the channel, nice horizontal symmetric fields can be obtained.

Extrapolating these results to periodicity-chirped structures for scalable acceleration, the optimization must be conducted for each cell individually. The distance of the Bragg mirror must therefore be variable, i.e., adjustable along the accelerator. This adds further complexity to the already mentioned issue of vertical fluctuations in laterally perfectly symmetric structures with dual-lateral drive, which suffer from e_1 fluctuation when being length-chirped and fully 3D simulated (cf. Fig. 2.6). Therefore, in a subrelativistic scalable accelerator demonstrator, it rather unlikely that DBRs created in this way can be successfully used.

3.2 Dedicated DLA Test Chambers

Dedicated experimental chambers for DLA in the sub-100 keV range have been created especially at Stanford University. Due to their compactness, the setups have been named “Shoebbox”. Technologically, these setups borrow from both electron microscopes and from ordinary television Cathode Ray Tubes (CRTs), in order to obtain a high brightness electron beam in a rather simple, home-made, cost-efficient and small-scale setup. Figure 3.3 shows the CAD design of the 57 keV “Shoebbox” setup and the laser and electron optics schematic. The drive laser provides 1024 nm for the nanotip cathode and feeds an Optical Parametric Amplifier (OPA) that provides 1980 nm for the DLA. The 280 fs cathode laser pulse creates an electron pulse roughly twice as long, fitting well to the DLA laser pulse length. The electron beam is emittance-filtered by a 50 μm aperture in the ceramic high voltage break. Then, the electron beam is focused by a solenoid into the DLA chip, which is itself suspended on a hexapod manipulator stage with about 100 nm accuracy. After the DLA, there are two Micro Channel Plate (MCP) detectors: one measures the energy by means of a magnetic dipole spectrometer, the other allows to determine the angle spectrum, to measure electron diffraction by a crystalline sample or deflection exerted by the DLA. Photographs of the setup in the laboratory are shown in Fig. 3.4. Two optical microscopes, one at the nanotip emitter and one at the DLA, help with the alignment of the two chips with the laser beams. The laser-optical setup enables driving the DLA from both lateral sides and on two stages. The optical path lengths are chosen equal, with the opportunity to adjust the phase between left and right globally, and then for the two stages individually. The delay lines for this purpose are also automatized, which enables precise relative phase control. The electron beam can be steered with two sets of deflection coils horizontally and vertically, in order to hit the aperture of the chip and fine-tune the horizontal and vertical injection positions.

The experiments conducted in the “Shoebbox” are reported in Papers 5.4, 5.7 and 5.12. The first experiment, Paper 5.4, is a focusing experiment, demonstrating the cross-shaped transverse phase space that is created by a DLA structure, as already shown in Paper 5.1. The structure here is 14 cells long and strictly periodic; the focusing demonstration is attained by sending the beam through an aperture, which is significantly smaller than the aperture of the DLA. Therefore, when the DLA provides focusing, even only for a particular range of electron arrival phase, the transmission should be increased as compared to laser off. In other words, if one arm of the “cross” of the density plot is transported through the aperture at optimal laser amplitude, the transmission is larger than in the case where the “cross” has not been created at all and the initial beam is scraped on the aperture. A simulation of this principle in DLATRACK6D is shown in Fig. 3.5, where for better visibility the initial angle spread has been reduced by factor 3 but all other parameters are identical to the experiment in Paper 5.4.

The second experiment in the Shoebbox, Paper 5.7 is a bunching - analyzing experiment, which was conducted almost at the same time as the similar experiment at Erlangen, Paper 5.8. The crucial advantage is here, that the two stages can be indi-

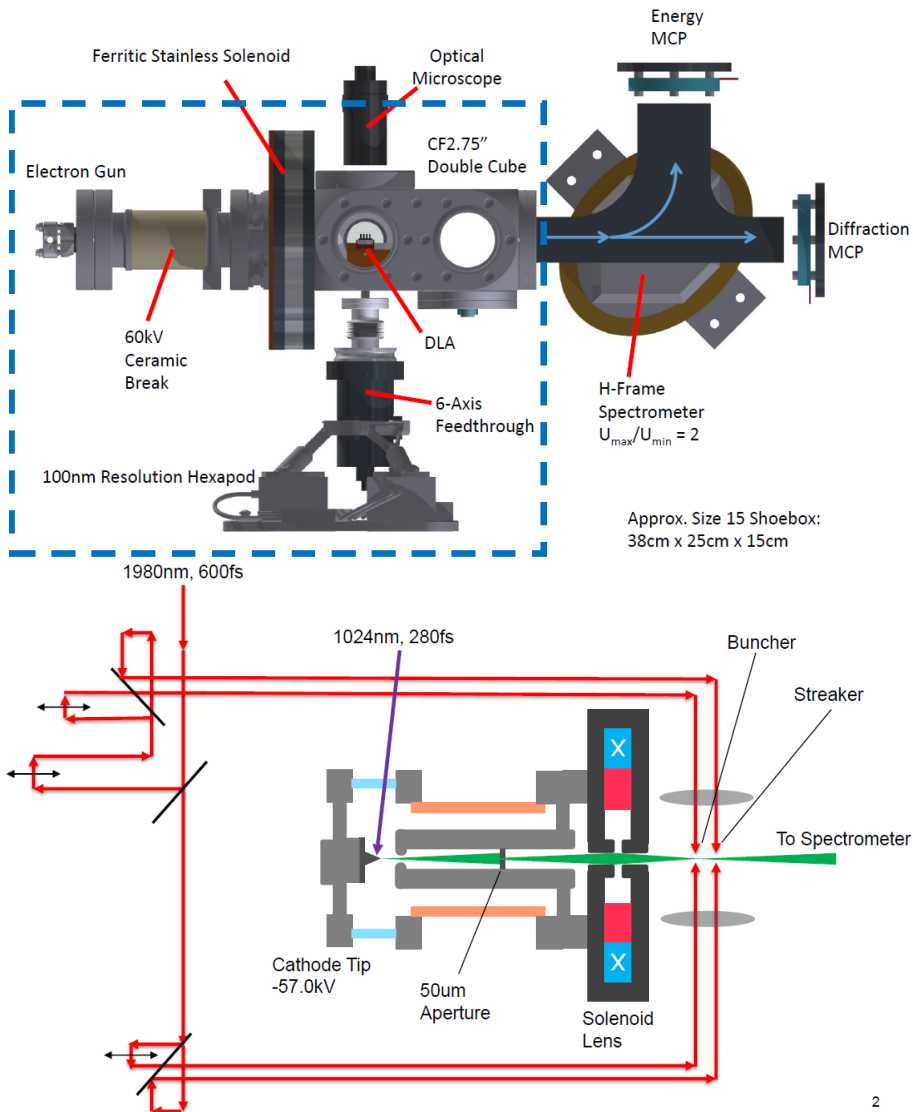


Figure 3.3.: CAD design and laser and electron beam schematic of the Stanford "shoe-box". Pictures courtesy of K. Leedle.

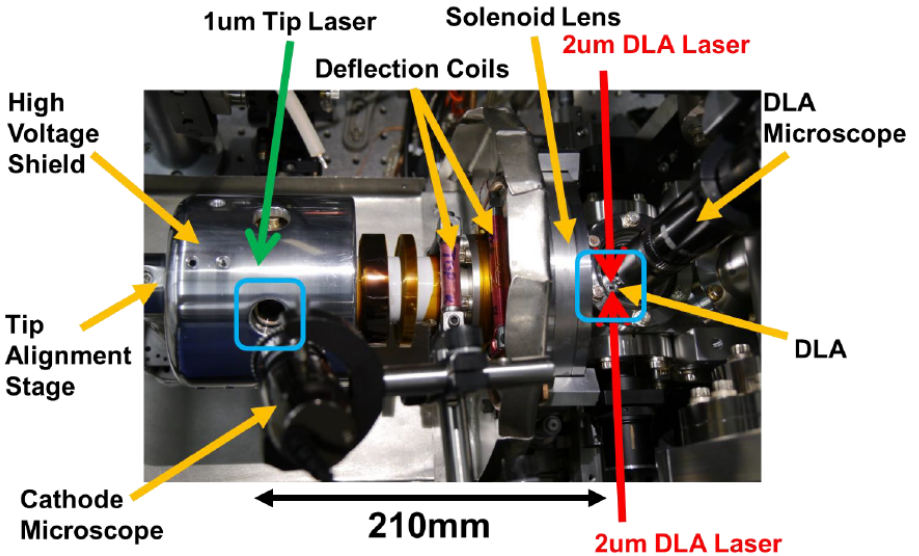
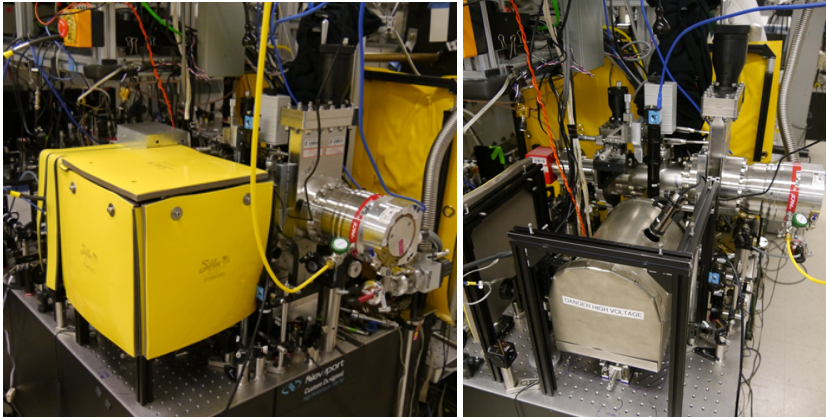


Figure 3.4.: Operational “shoebox” setup with yellow X-ray shielding mat (top left) and opened (top right). A more detailed view is in the bottom photograph, where the outer high voltage shield is also removed. Pictures courtesy of K. Leedle.

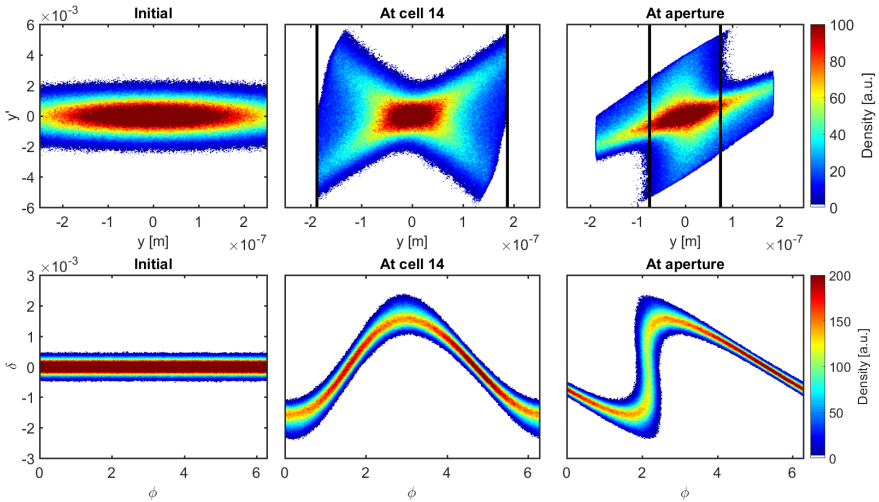


Figure 3.5.: Principle of phase-dependent ($\varphi = 2\pi s/\lambda_g$) electron lensing with DLA structures. The lower/upper plots show the longitudinal/transverse phase space along the DLA structure, where $y' = p_y/p_z$ and $\delta = \Delta W/W$. In order to make the effect better visible, the initial angle spread in this DLATRACK6D simulation was chosen a factor 3 smaller than in the experiment in paper 5.4

vidually phase-controlled from both lateral sides. This enables to turn the second stage from being an accelerator into being a streaker. As discussed in Paper 5.5, by changing the relative phase between the two lateral side lasers by 180° , the field profile across the channel changes from cosh to sinh, creating a phase-dependent deflection. This maps the longitudinal profile on the angle coordinate y' , resulting in a respective position change on the MCP. Similar to a conventional oscilloscope, this creates a streak on the screen, which corresponds to the temporal bunch profile; the process is therefore called “streaking”. The electron pulses could be measured by this technique, directly, to have a length of 0.7 fs.

The third experiment in the Shoebox, Paper 5.12, is the demonstration that an APF type buncher, as proposed in Paper 5.3, can create attosecond pulses with small energy spread, and then accelerate them without debunching or energy broadening. We called this “coherent acceleration” in contrast to “net acceleration” in Paper 5.7. In this experiment we could show for the first time that an attosecond bunch can be moved as a whole on the energy axis, just by changing the relative laser phase between the two stages on the chip. As discussed in Sect 2.5.1, an APF buncher achieves short bunches with small energy spread by modulating and demodulating the longitudinal phase space, before the

drift has turned the modulation into irreversible phase space filamentation. The experiment uses only a single modulator-drift-demodulator stage, thus, the nonlinear effects in the longitudinal plane are notably present. The bunching process is still far away from being adiabatic, but it is already a significant improvement as compared to the ballistic bunching without demodulation. Electron pulses of this kind are required to inject into a scalable APF DLA accelerator. The experiment however also revealed that the energy spread was not as small as predicted by the 2D simulations. Therefore, a setup using the 3D APF on SOI scheme was created, which also uses three modulator/demodulator stages. The 3D simulations shown in Sect. 2.5.1 indicate that the designed energy spread of about 200 eV (FWHM) can be maintained.

3.3 Immersion Lens Electron Sources

Future DLA experiments at Stanford will be conducted in immersion lens based setups conceived in [35]. The idea of this setup is to mount the electron source tip slightly behind a cylindrical lens, which is lower in the electric potential than the emitter itself, a similar concept as the Wehnelt-cylinder in classical CRTs. As a consequence, the electrons emitted under a large angle are pushed back toward the optical axis. Due to the close proximity of the lens and the cathode, the angle is decreased before the particles attain a large offset, thus the spherical aberration is reduced. A drawback of the setup is, that right after emission, the electrostatic acceleration gradient is reduced, which increases the detrimental effect of space charge on the brightness.

Paper 5.15 demonstrates an improvement of the immersion lens setup by using silicon carbide (SiC) electrodes, which allows higher field strength on the lens surface and enhances the breakdown stability. Two different beamline setups are considered: one is called "Glassbox" due to its shape of the vacuum chamber, which allows to look at the DLA on the hexapod from all sides, see Fig. 3.6. The hexapod-nanopositioner in the Glassbox can be loaded by four sets of DLA chips, which can be changed without breaking the vacuum. The immersion lens and the emitter chip can be visually seen from the front, while the alignment is done from the back of the cathode; the anode is aligned from behind the DLA. In this setup, the testing of the structures presented in Fig. 2.6 at 96 keV injection energy is performed in 2022, cf. Sect. 2.3. However, the measured emittance is still about a factor 5 higher than the acceptance of the APF-DLA, thus the yield of accelerated particles is rather low.

The second setup presented in Paper 5.15 leverages on the development of the "Shoebbox", as shown in Sect. 3.2, by adding an immersion lens to the cathode. As compared to the "Glassbox", this setup uses a weaker immersion lens in combination with a solenoid, that finally focuses the beam into the DLA. The weaker immersion lens allows for a higher acceleration gradient right after the tip and also leads to smaller aberrations, however in the solenoid additional aberrations are introduced. Overall, the Shoebbox shows particularly lower bunch length, but also lower emittance indicating the advan-

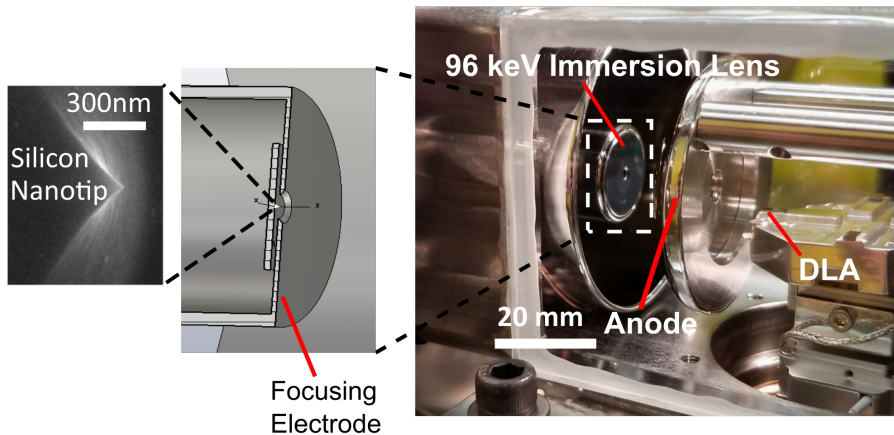


Figure 3.6.: Stanford Glassbox immersion lens setup. Picture adapted from [63].

tages of this setup. Moreover, the high voltage power supply at 57 kV is smaller and cheaper than the 96 kV one for the Glassbox.

The simulations in Paper 5.15 were executed with CST Studio [44]. First, the static fields were computed, then a Particle in Cell (PIC) simulation, dividing the beam channel into sections, was performed to track the beam. Note that at the tip a significantly higher resolution than at top energy is required, due to the low energy and the small size of the tip. Subsequently, the CFL criterion requires the time step also to be tiny. The fields of the nanotip emitter were simulated separately, in a cylinder with the top and bottom surface potential fitted to the large simulation result. The initial distribution has to be prepared, based on educated guessing and parameter fitting. Especially the emission cone, the angular distribution, and the emission energy distribution are unknown and can be obtained from fitting to the experimental results. This requires however to run the simulation many times, and we were using a Matlab interface to control CST Studio, see [81], alongside with automatized evaluation scripts for this purpose. Figure 3.7 shows the example of tracking data which reproduced the experimental parameters of the Shoebox with negligible space charge. The initial conditions are: Gaussian energy spectrum with 1.5 eV mean and $\sigma_E = 0.3$ eV (truncated at 0 eV and re-normalized), cosine-shaped angle distribution of the width of the hemispherical tip reduced by a factor 0.7 and cylindrically symmetric. For simplicity, the emission was considered to be always perpendicular to the hemispherical surface of the tip. Similar simulations and parameter fitting was done for the Shoebox, with a magnetostatic simulation of the solenoid and further tracking steps added, see Paper 5.15.

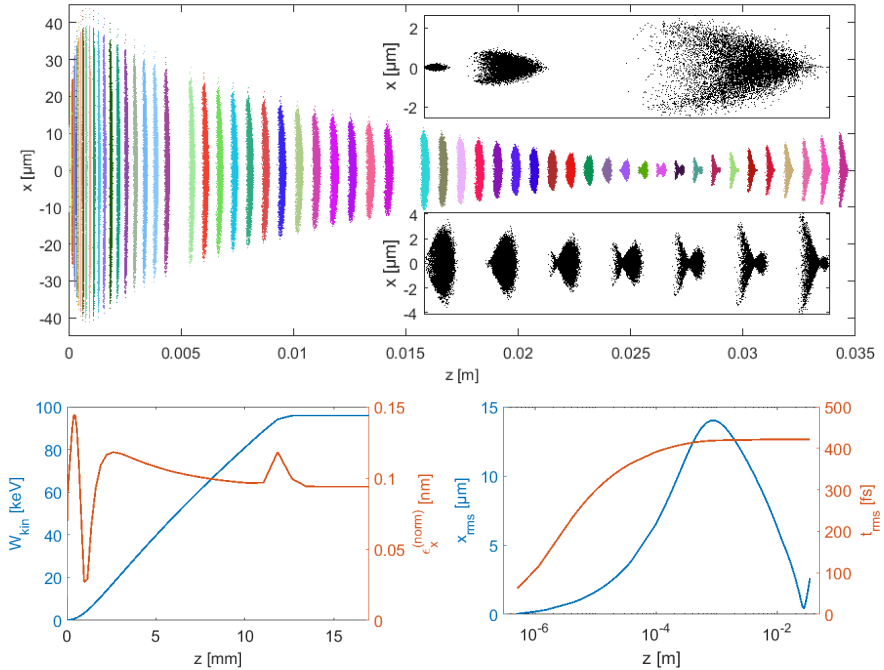


Figure 3.7.: Tracking simulation of the Glassbox without space charge (10000 individual particles). The insets of the top plot show enlargements of the emission (upper inset) and of the focus (lower inset). The bottom plots show statistical evaluations of the ensemble. The emittance and the bunch length are mostly created in the first few hundred micrometers after emission, before the beam waist reaches its maximum size. Note the log-scale in the bunch length plot.

In order to assess the brightness of the beams as function of the bunch charge, full space charge simulations were conducted with the CST PIC solver [44]. Already one single simulation of this kind is computationally very expensive, but in order to match with the experiment, statistics has to be obtained over many shots. With the current setup this is extremely ineffective, since it could only be executed as repetition of the single shot simulation in the full external fields, with individual calculation of the full space charge field. Therefore, only 50 shots were simulated, resulting in rather poor statistics. The statistics were however sufficiently good to reproduce the reduction of the brightness as function of charge to a constant value, as one would expect. Moreover

the simulation revealed that the brightness reduction is not as strong as measured, suggesting that a stronger source trigger laser pulse creates not only more charge but also a wider emission cone angle. In future, these simulations have to be improved, in order to obtain better statistics and more reliable convergence tests. This will be done with a new dedicated tracking code, as is outlined in Sect. 4.3 and Appendix B.

While the Glassbox is a dedicated DLA test beamline, which also benefits from the advantage of higher injection energy, the new “Shoebox” serves as a beamline for electron diffraction, with or without DLA. Finally, the Shoebox is outlined to demonstrate that DLA can enable electron diffraction at optical time scales and at boosted energy. Since many of the parameters of the current setup were chosen rather heuristically, it can be expected that optimization will bring up the Shoebox brightness parameters for efficient injection into a DLA soon. While the first scalable DLA structures as described in Sect. 2.5.2 are being tested in Glassbox currently, the Shoebox will require new structures to be designed, most probably as a 3D APF DLA on a nanophotonic SOI wafer.

3.4 Interaction Chambers in Large-Scale Facilities

Within the ACHIP program, several DLA test chambers in large scale facilities have been built. Starting from the DLA proof-of-principle experiment at SLAC [16] and its repetition with a tilted pulse [22], high energy facilities such as ARES [82] at DESY and the photo-injector test facility Pegasus [36] at UCLA embarked on DLA. The UCLA group pursues the spatial harmonic approach, in order to obtain MeV gain in generic grating structures with single digit MeV injection energy [61, 62]. As discussed in Sect. 2.5.1 and Paper 5.9, a high energy beam can be optically microbunched using a DLA and a chicane. On the other hand, optical (sub-fs) bunches can also be created by conventional means [83] and then injected and accelerated in a DLA. This approach is pursued at ARES [84, 82]. On the optical scale, RF jitter varies the arrival time of the bunch by up to 10 fs, which renders the injection reference phase (or s_{ref}) as a random variable. An analytical model of the energy spectrum of a relativistic DLA is presented in [85]. This allows to fit a measured energy spectrum on the analytical model, and thereby retrieve the exact injection phase a-posteriori for each shot. This can be used to statistically model the RF jitter.

Another bunching concept is based on an undulator, which modulates the beam followed by a chicane. The undulator is driven by the same laser that drives the downstream DLA, thus intrinsic synchronization is obtained [86]. Such a scheme can also be performed with two [87] or more stages, where any of the stage can be a DLA or an undulator. Such a multistage concept to produce arbitrary periodic shapes in the longitudinal phase space was already presented by E. Hemsing and D. Xiang [88]; a similar concept as the APF multistage buncher in Paper 5.12. Due to the necessity of magnetic chicanes to obtain dispersion at high energy, a high-energy multistage setup is however much larger and much more elaborate than its low energy counterpart.

The highest energy electron beam in the ACHIP realm is available at the newly commissioned SwissFEL facility at PSI. Since the drive laser has not been installed yet, ACHIP experiments were restricted to work with passive structures so far. Due to the high current ultrashort bunches at SwissFEL, passive structures reveal already interesting beam dynamics and phase space shaping opportunities. As soon as active DLA experiments are possible, particularly the DLA high energy buncher experiment in Paper 5.9 will be approached. In the following we will discuss the ACHIP chamber at SwissFEL and the wakefield experiments conducted therein in 2019-2021, which is reported in detail in [67].

A schematic of SwissFEL is outlined in Fig. 3.8. After the high-brightness photoinjector gun and the 300 MeV injector linac, there are two bunch compressors and three main linacs. After linac 2, at 3.2 GeV, there is a switch yard selecting if the bunch goes to the low energy soft X-ray beam line “Athos” or to the high energy (6 GeV) hard X-ray beam line “Aramis”. The ACHIP chamber is located right after the switch yard in the Athos branch. Two X-band transverse deflecting cavities (TDC) [89] are available, one after the first bunch compressor chicane (BC1) at 300 MeV and another after linac 3 in the Aramis branch. Another TDC will be installed in the Athos beam line soon, but was not yet available during our experimental campaign.

Figure 3.9 shows the inside of the ACHIP chamber. Two sets of movable quadrupole magnet triplets allow to strongly focus the beam into the microstructures mounted on a hexapod-positioner in the center. The electron optics is designed such that the beam is focused hard to minimal size, and then again matched to the usual optics in the Athos beam line (see Fig. 6 in Paper 5.9 for the betafunctions). As visible, five different structures are mounted on the hexapod, including a nanofabricated wire scanner to measure the beam size in both transverse dimensions [90].

The first DLA structures tested in the ACHIP chambers are scaled to the THz range ($50 \mu\text{m}$ periodicity) and 3D-printed with a special additive fabrication technique [91], see Fig. 3.10. This structure contains both the variable gap and the variable groove depth setups as outlined in Fig. 2.12; the material is fused silica with $\epsilon_r = 2.1$, see [92].

In order to measure the effect of a wakefield, the beam current distribution is ideally very strong in a short head and weak in a long tail as seen in Fig 2.13. The accelerator

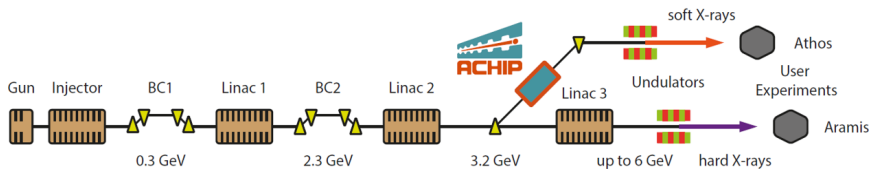


Figure 3.8.: Layout of the almost 1 km long SwissFEL facility, with the ACHIP chamber in the soft X-ray branch (Athos). Courtesy of B. Hermann.

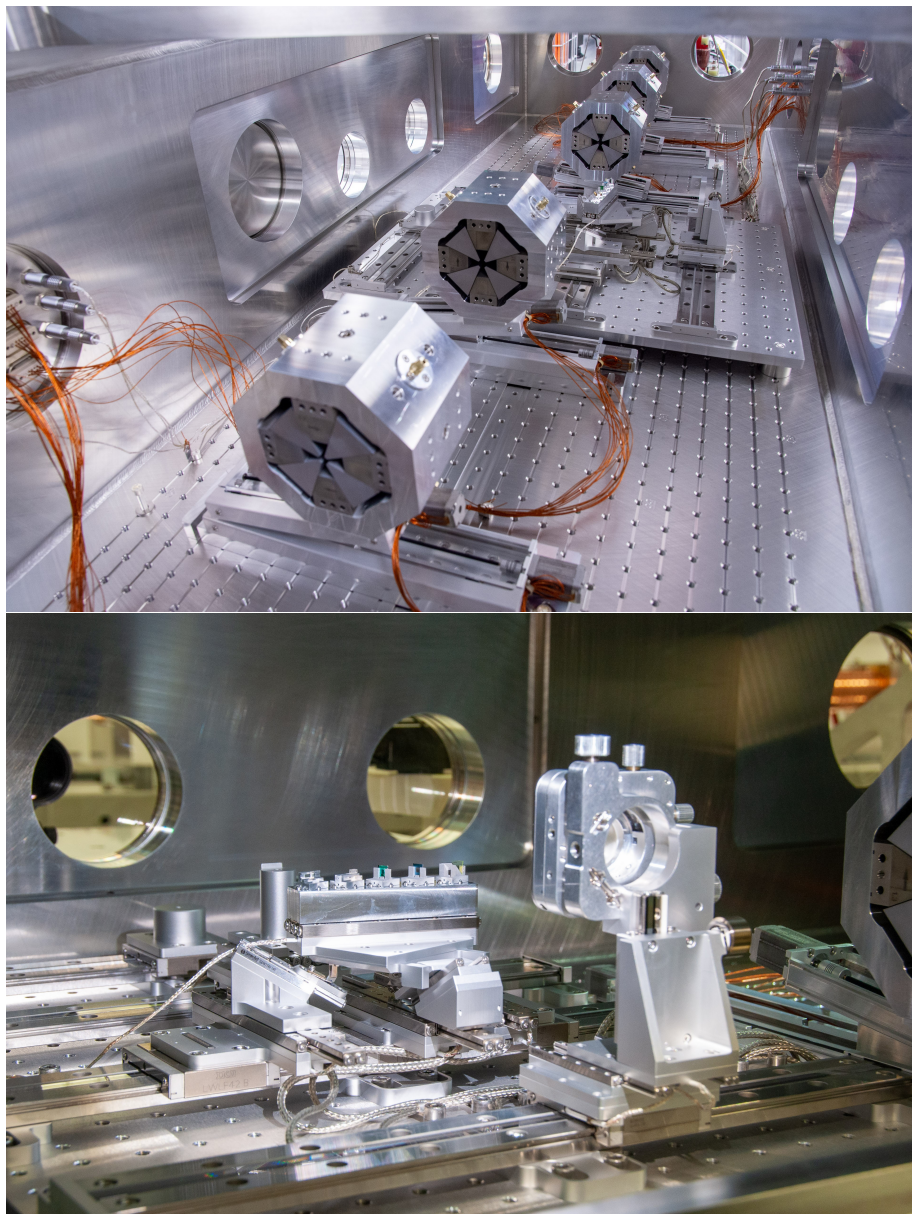


Figure 3.9.: Movable permanent magnet quadrupole triplets inside the ACHIP chamber and hexapod with five different structures. Courtesy of B. Hermann.

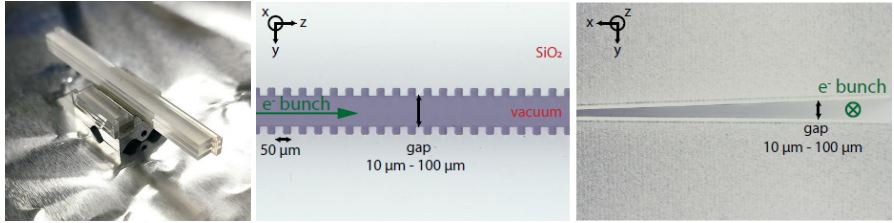


Figure 3.10.: THz variable gap grating structure, which includes both setups shown in Fig. 2.12 (left) and microscope images (center and right). Courtesy of B. Hermann [67].

parameters were set in order to obtain such a configuration. However, it was difficult to verify the bunch distribution, since at our beam time there was no TDC in Athos. Instead, the bunch profile was measured in the injector TDC and numerically propagated forward using Elegant [93]. This method was cross-checked by propagating to the Aramis TDC, where the result could be confirmed by another measurement. Moreover, the bunch profile (especially in case of strong compression) depends on the uncorrelated energy spread of the bunch after BC1. This so-called “slice energy spread” is also obtained from the TDS, but it needs to be corrected due to different kinds of errors such as the energy

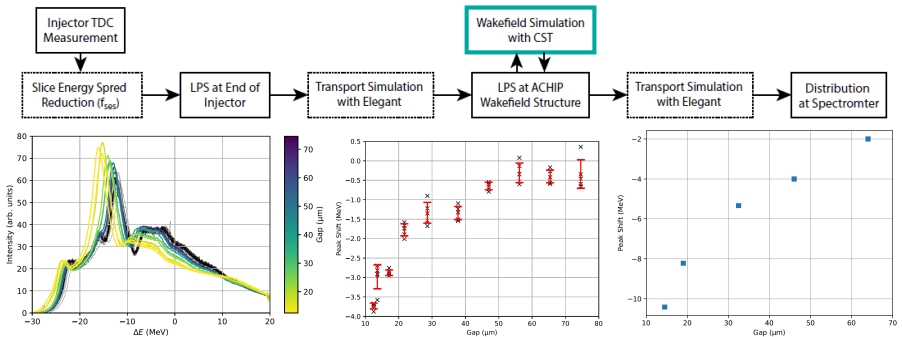


Figure 3.11.: Top: Procedure to obtain the longitudinal phase space (LPS) at the ACHIP chamber, where the structure wake potential acts on the energy spectrum. The modified LPS is then further transported to the spectrometer downstream in Athos. Left: Measured energy spectra as scan of different gap sizes chosen by the position of the V-shaped structure. Center: shift of the main peak of the energy spectrum. Right: simulation of the peak shift with the simulated wake potential. Courtesy of B. Hermann [67].

resolution of the spectrometer imaging system, but also due to less obvious blow-up effects as the finite beam size in the TDS or mismatch effects [67]. The entire procedure of reconstruction of the altered energy spectrum, together with the measurement results, is shown in Fig. 3.11. As a figure of merit we use the main peak of the energy spectrum (note that this main peak does not coincide with the main peak of the current profile), which shifts when the structure is moved such that the gap width changes and the wakefield is altered.

The measured peak shift is about 3.7 MeV at the smallest gap of about 12 μm . The corresponding simulation result is about 10.3 MeV, almost a factor 3 larger than the measurement. Potential issues in the simulations have been investigated, such as boundary effects (insufficient number of grating periods), or incorrect material permittivity for the ultrashort (broadband) pulse at high amplitude. None of those seem to explain a factor 3 discrepancy. As the most likely possibility, we assume that the current distribution was inaccurate, which has a strong impact on the wake strength and wake timing. Since the numerically obtained current distribution depends strongly on the slice energy spread, a quantity which itself is rather uncertain, the prediction of the strong compression result, together with space charge and potentially also coherent synchrotron radiation wakes in BC2 is a primary source of inaccuracies. Once the TDC in Athos is installed, the profiles can be measured directly and this source of error can be excluded.

4 Conclusion

4.1 Summary

In order to add novel acceleration schemes as DLA to the available accelerator equipment toolbox, pragmatic engineering approaches are necessary. Especially the length scalability of the real structures in the laboratories is one of the most crucial aspects for the performance of DLA designs. Rather than just creating a beam dynamics approach on the theoretical base, the goal of practical implementation of an accelerator on a chip obtaining high energy gain was the main focus of this work. The loop of design-fabricate-test was supplemented as design-simulate-fabricate-test-simulate, in order to carefully understand the practical issues as early as possible in the development, and to mitigate them already in the theoretical concept.

Starting from the rather naive, entirely conventional approach to beam dynamics in DLA (as being presented in Paper 5.1), it became immediately clear that the main challenge is to keep the electrons in the tiny aperture of the DLA by the laser fields themselves, without external focusing. Thus, a simulation approach, allowing quick access to the involved phase-dependent dynamics was required and could be realized by the DLAttrack6D code conceived in Paper 5.2. Later, this code was re-implemented and equipped with a wake field module, in order to assess collective effects (Paper 5.10). The symplectic scheme of DLAttrack6D also gave rise to a Hamiltonian for DLA, in which the DLA cell properties and the synchronous phase can parametrically change. With this powerful tool, analytic design of APF lattices could be approached and the APF for DLA scheme could be conceived. Analytical and manual optimizations were verified immediately by quick DLAttrack6D simulations. Finally, also full-field frequency domain and subsequent particle tracking simulations were performed, confirming the models within their design limitations.

However, running the 2D-designed models with the real 3D structures that are supposed to attain invariance in one transverse direction resulted in insufficient performance. Furthermore, also other 3D simulations and experiments suggested that the 2D assumption cannot be held in length-scalable devices. Thus, the necessity of generalizing the APF for DLA scheme to 3D became obvious. The 3D APF for DLA scheme as conceived in Paper 5.11 has advantages over the 2D scheme both at high and at low energy. At low energy it is the vertical confinement itself and the enhanced structure constants due to the additional edge in the third dimension, which increase the scheme's performance. The 3D structures do not require any kind of external focusing components such

as the outlined single quadruple magnet at all. Further simplicity is attained by implementing the scheme in the device layer of a SOI wafer and illuminating from the top (see Paper 5.13), which requires only one laser beam and the fabrication can be done by standard procedures in nanophotonics. Using this approach, also an APF-type buncher was presented, which in full 3D start-to-end simulation meets the energy spread constraint for the injection into a scalable accelerator implemented on the same SOI wafer.

The advantages of the 3D APF scheme at high energy are also decisive. Since only the sum of the two transverse focusing wavenumbers must vanish in the ultrarelativistic limit, there is always a counter-phase focusing scheme (see Paper 5.11) that attains high focusing gradients, even at high energy. As a consequence of the stronger focusing, the focusing periods become shorter. The synchronous acceleration is completely unaffected by the improvement of the focusing gradient. Thus, by keeping a single, high damage threshold material, the record peak gradients can be converted into average acceleration gradients on the same order of magnitude. In order to preserve the symmetry of the structures, the fabrication process is however rather involved, including hydrofluoric etching and direct bonding.

As an intermediate step on the high energy side, DLA structures scaled to the THz range have been investigated for their wakefield properties. These wakefields can be used for shaping of the energy spectrum of the high energy beam. The principle of this process is well understood and an extensive measurement campaign was conducted at SwissFEL. Qualitatively, the results match the expectations, however the strength of the wakefield is obtained as a factor 3 discrepancy between measurement and simulation. This mostly accounted to uncertainties in the longitudinal profile of the ultrashort bunch. We are confident, that a direct profile measurement close to the ACHIP chamber will be possible soon and resolve this discrepancy in a new measurement campaign.

The injector remains an open challenge for a low energy DLA attaining large energy gain. Due to the small aperture, geometric injection emittances of about 10-30 pm are required. The requirement can be relaxed proportionally, when resorting to longer drive laser wavelength. Moreover, at $\lambda = 6 \mu\text{m}$, injection energies as low as 2.5 keV were considered (see Paper 5.11 Supplement). Potentially, such a chip could even use an on-chip electron gun [94, 95], however, the over-proportionally harder emittance requirement renders this rather unfeasible. The geometric emittances obtained from the sources available in ACHIP are on the order of 300 pm for the SEM and 150 pm for the immersion lens setups. In future, we hope to be able to improve the immersion lens setup by better understanding and optimizing the spherical and chromatic aberrations, in order to achieve the goal of injection into a scalable 3D APF DLAs without emittance filtering.

4.2 Applications of DLA

A key application of a scalable low energy DLA is ultrafast electron diffraction (UED) [96, 97]. Usually, UED is mentioned in conjunction with ultrafast electron microscopy (UEM) [98], however, the use of time-dependent acceleration fields necessarily leads to larger energy spread. Together with the inevitable chromatic aberrations in the cylindrically symmetric setup, this leads to a large spot on the specimen, negating the advantage of DLA in UEM. For UED, the electron beam is projected onto the specimen in parallel fashion, with as small as possible angle spread, which can be easier achieved by a DLA based setup. The purpose of UED is similar to X-ray diffraction e.g. in crystallography, in order to determine the structure of (crystallized) molecules. If coherence and ultrashort pulses are required, X-ray diffraction is carried out in large scale x-ray FEL facilities. While replacing X-ray by electrons already leads to a huge advantage in size and cost, studies also suggest advantages in the analysis of radiation-damage-sensitive samples [99]. Medium scale facilities, based on RF accelerators have been built for this purpose [100, 101, 102]. The idea of DLA in UED is to provide high energy, on the order of 1 MeV, in instruments of the size of conventional electron diffractometers [103]. Moreover, the timing precision intrinsically available in DLAs can be put directly on the specimen, since at higher energy the intrinsic dispersion is significantly reduced. Thus, UED with DLA output beams can be conceived as a pump-probe setup, where the electron source, the DLA, and the pumping of the specimen are driven by the same laser, allowing intrinsic, ultra-precise synchronization.

An interesting topic of DLA applications was already outlined in Fig. 1.3, namely to inject the naturally fitting electron beam in laser driven DLA based undulators [48, 49, 50]. These tilted DLA grating structures allow to deflect the beam phase-dependently. It is under consideration, to create undulators with significantly shorter periods than their conventional magnetic counterparts. Therefore, with the same beam energy shorter radiated wavelength, or the same wavelength with lower electron beam energy can be obtained. However, there are still some hurdles to be taken. One is to keep the beam focused on a sinusoidal trajectory, which in principle can be obtained by an APF configuration of the tilted DLA structures. The second hurdle is to obtain sufficiently high electron current to convert into a reasonable amount of radiation power. This will, as all other DLA applications, hinge on the available electron source brightness and brightness preservation along the beam channel.

High energy and high gradient DLAs are of course a consideration for a long term project such as a high energy electron-positron linear collider for elementary particle physics experiments. The highest interest is on the production of Higgs bosons by lepton collisions below 1 TeV, but also longer term goals on the order of 30 TeV are formulated, requiring multiple kilometer ranging linacs [104]. Such a linac must provide a high gradient to be competitive in length to other advanced acceleration schemes. It must also be competitive in energy efficiency, which requires that the laser energy from the pulse must be largely depleted, i.e., converted to electron kinetic energy. Nowadays, the

electrons take only a tiny fraction out of the energy of the laser and the rest is wasted. There are schemes to recycle the laser energy by running a laterally driven DLA in the laser cavity loop [105]. On the long run, however, one will have to resort to traveling wave schemes with matched group velocity, such that the electron pulse and the laser pulse completely overlap over a long travel distance. Nonlinear optics, in particular the generation of hyperbolic-secant shaped solitons might be employed to preserve the pulse shape in electron-beam-dynamically engineered acceleration structures over long distances in the future.

Another interesting high energy goal of DLA is the injection into an electron storage ring. Continuous injection at the top energy of a synchrotron (so-called top-up injection, see e.g. [106, 107]) can make use of the intensity-limited beam of a DLA. In contrast to ion synchrotrons, Liouville's theorem does not prevent injection into already occupied phase space entirely, since the final beam emittance is obtained from an equilibrium defined by the radiation cooling process rather than by the injector. Thus, the beam intensity can be accumulated over long time, or technically more interesting, the beam losses in a synchrotron can be compensated by a continuously running DLA top-up injector.

4.3 Outlook

It is planned to continue this research in the TU Darmstadt DLA group, in order to facilitate experimental demonstration of an accelerator from sub-100 keV to about 1 MeV. This will have to be a multi-stage 3D APF DLA and can be implemented in the device layer of a SOI chip. Intermediate steps, especially two-digit keV energy gain in sub-100 keV silicon structures is to be expected soon, preliminary results of the structures designed in Darmstadt are already available. Although current DLA equipment is unsuitable in terms of energy efficiency, it serves well in the realm of ultra-precise metrology, as e.g. the aforementioned UED application.

The start-to-end design and simulation of such a UED beamline boosted in energy with a DLA is outlined at TU Darmstadt in a project funded by LOEWE-Exploration, where the hardware construction is outlined at Stanford. This requires considerable improvements of multiple parts of the Shoebox/Glassbox injector systems. The new injector will be based on larger, highly-doped silicon nanotip emitters inside the successful SiC immersion lens setup. However, eventually a second SiC electrode might be added. This serves to remove the solenoid and still not fully focus the beam into the DLA with a single immersion lens, which has been shown to create too strong aberrations. Next, the multistage accelerator on a chip needs to be designed completely with minimizing the beam losses between the stages. A simplified simulation of such a setup in DLATRACK6D alongside with full-start-to-end simulation can be done as described in Paper 5.14. However, for the extensive parameter studies required for a multistage setup optimization, this is expected to be too slow. Lastly, a UED beamline also requires a lensing system

to shine the electron beam parallel to the optical axis onto the specimen, followed by another lensing system after the specimen to project on a MCP screen.

In the near future we will finish the tracking code "FemtoTrack", which tackles all these issues of the UED beamline in a computationally efficient manner, such that the extensive parameter scans for the design can be combined with a start-to-end simulation of the entire beamline. A flowchart of the outlined code is shown in the Appendix in Fig. B.1. It is currently being tested and documented and will be published as open-source for the scientific community soon, alongside with a research paper reiterating the results of Papers 5.13 and 5.15 as test cases, with a projected 100 times speedup compared to the previous results.

There are plenty of future projects, which are however tentative in character, since their funding applications are currently under review. One of these projects focuses on computation of radiation generation in nanophotonic or nanoplasmonic structures when being traversed by electron beams. The coherence parameters of Cherenkov/Smith-Purcell radiation from novel nanostructure based sources shall be investigated by self-consistent PIC simulation as well as by simplified models. Another project aims to demonstrate ultrafast (femtosecond) streaking by means of split ring resonators [108] in the THz realm, driven by optical rectification of the same laser that drives the electron source. One of the most interesting future projects involves the variable shaping of the laser pulses for DLA (tilted [20], bent [24], modulated [61], etc.) and online control thereof on an electron-beam-dynamical basis. Due to lack of electron beam diagnostics on the DLA chip, one has to rely on "virtual diagnostics" based on a surrogate model. The parameters of the surrogate model can be obtained by machine learning methods, based on both numerical and experimental training data. This allows to optimize the input laser and electron beam parameters based on the complete knowledge of the beam dynamics from the surrogate model, while keeping the outputs of the numerical and experimental accelerators matched by continuous adaption of the model parameters.



5 Selected Paper Contributions (chronological order)

The following 15 papers are reproduced with permission of the publisher. See table of contents for the titles and direct links. All rights remain with the publisher, i.e.,

- Paper 1: ©Institute of Physics Publishing
- Paper 2-4,7,8,10-13: ©American Physical Society
- Paper 5: ©World Scientific Publishing Company
- Paper 6: ©Optical Society of America. Due to publisher request, the accepted manuscript rather than the appeared paper is reprinted here. The paper appeared in Optics Letters: <https://doi.org/10.1364/OL.44.001520>
- Paper 9,14: ©Nature Research
- Paper 15: ©American Institute of Physics

The papers 1-3, 10-13, and 15 are available as open access from the journal website. The papers 2 and 4 have been selected as editor's suggestion. Papers 4 and 15 have been selected as "featured".

Designing a Dielectric Laser Accelerator on a Chip

Uwe Niedermayer, Oliver Boine-Frankenheim, and Thilo Egenolf

TEMF, TU-Darmstadt, Schlossgartenstr. 8, 64289 Darmstadt, Germany

E-mail: niedermayer@temf.tu-darmstadt.de

Abstract. Dielectric Laser Acceleration (DLA) achieves gradients of more than 1GeV/m, which are among the highest in non-plasma accelerators. The long-term goal of the ACHIP collaboration is to provide relativistic (>1 MeV) electrons by means of a laser driven microchip accelerator. Examples of "slightly resonant" dielectric structures showing gradients in the range of 70% of the incident laser field (1 GV/m) for electrons with $\beta=0.32$ and 200% for $\beta=0.91$ are presented. We demonstrate the bunching and acceleration of low energy electrons in dedicated ballistic buncher and velocity matched grating structures. However, the design gradient of 500 MeV/m leads to rapid defocusing. Therefore we present a scheme to bunch the beam in stages, which does not only reduce the energy spread, but also the transverse defocusing. The designs are made with a dedicated homemade 6D particle tracking code.

1. Introduction

The Accelerator on a Chip (ACHIP) collaboration [1] aims to construct a source of relativistic electrons out of a shoe-box size Dielectric Laser Accelerator (DLA). Furthermore, the collaboration also aims at radiation generation by means of laser driven undulators. Beyond the acceleration of relativistic electrons [2], recent experiments also addressed DLA for subrelativistic electrons [3, 4]. Since only the evanescent near field which decays as $\exp(-\omega y/(\beta\gamma c))$ contributes to acceleration, both the gradients and the apertures are smaller in subrelativistic structures. In Figure 1 we present a novel DLA structure that contains both features of a side-coupled grating accelerator and a Bragg-waveguide accelerator. This structure is "slightly resonant" and thus presents a compromise between filling time and acceleration gradient. The structure constant is the ratio between the gradient and the incident laser field and can be conveniently expressed by the normalized resonant spatial Fourier coefficient \underline{e}_m as

$$SC = \frac{\max_{\varphi} \{\Delta W\}}{eE_{z0}\lambda_g} = |\underline{e}_m|, \quad (1)$$

where E_{z0} is the incident (z-polarized) laser field and $\varphi = 2\pi s/\lambda_g$ is the phase of a particle at a distance s behind a design particle. The resonant integer m fulfills the Wideroe condition $\lambda_g = m\beta\lambda_0$, where λ_g is the structure period. Usually the fundamental $|\underline{e}_1|$ is the largest coefficient so we will restrict ourselves to $m = 1$ in the following. The thickness of the Bragg reflection layers is $d = (1/4 + n/2)\lambda_0/\sqrt{\epsilon_r}$, where the integer n can be chosen according to practical requirements of the fabrication aspect ratio and the required height. The structure constant can be determined using time domain simulations (here: CST MWS [5]), evaluated at the center frequency of the broadband spectrum. Alternatively, we developed a dedicated finite element (FEM) code in the frequency domain [6], which was also used to optimize the $\beta = 0.91$ version of the Bragg structure.



Content from this work may be used under the terms of the [Creative Commons Attribution 3.0 licence](https://creativecommons.org/licenses/by/3.0/). Any further distribution of this work must maintain attribution to the author(s) and the title of the work, journal citation and DOI.

Published under licence by IOP Publishing Ltd

1

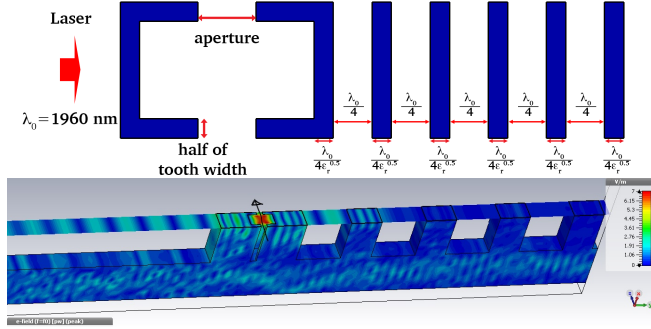


Figure 1. Bragg mirror cavity structure (Silicon $\epsilon_r = 11.63$, length $\lambda_g = 620\text{nm}$ for $n=0$ (top) and 3D simulation for $n=3$ and height $3\mu\text{m}$ (bottom). The black arrow indicates the electron trajectory at which the structure is periodic.

2. Accelerator Design

We propose a structure that comprises ballistic bunching followed by velocity matched acceleration, see Figure 2. For simplicity we assume that the structure is driven from both lateral sides with a cw laser. In the choice of initial electron beam parameters we follow [3], i.e. $\beta = 0.3165$, $\sigma_E = 10\text{ eV}$ and the transverse emittance is disregarded at first. The parameters of the structure are summarized in Table 1 and shall be discussed in detail in the following.

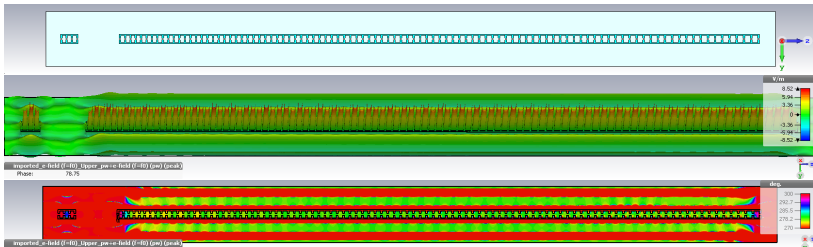


Figure 2. Chirped accelerator structure with 100 periods (top), longitudinal electric field amplitude (center), and phase (bottom) along the chirp.

2.1. Velocity bunching

Velocity bunching is well known for both ion and electron beams. The idea is to modulate a coasting beam such that it has a sinusoidal correlated energy spread pattern. A following drift section for subrelativistic beams (or a dispersive chicane for relativistic beams) will transform the energy modulation into a phase modulation of $\Delta\varphi = \pi/2$, at which the longitudinal focus is

Table 1. Accelerator parameters

Laser strength	1 GV/m
Aperture	200 nm
Buncher periods	3
Buncher period length λ_{g0}	620 nm
ΔW_{corr} (incl. fringe)	≈ 1.6 keV
L_{Drift} (total)	5.06 μm
$L_{\text{Drift,int}}$	8 λ_{g0}
$L_{\text{Drift,frac}}$ (incl. ph. corr.)	0.16 λ_{g0}
Accelerator $ \underline{e}_1 $	0.73 (initial)
Linear chirp Δz	3.2 nm/cell
Chirp decrement $\Delta\Delta z$	16 pm/cell
Synchronous phase φ_s	47°
Acceptance ΔE_{max}	2 keV
Synchrotron frequency f_s	4.53 THz (initial)
Gradient	500MeV/m (initial)

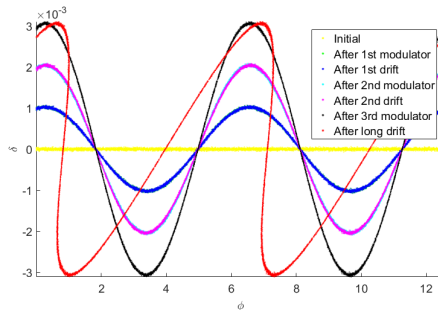
reached. This happens in $T = \lambda_g / (4\Delta\beta c)$ and thus the length needs to be

$$L_{\text{int}} = \beta c T = \frac{\lambda_g}{4} \frac{\beta}{\Delta\beta} = \frac{\beta^2 \gamma^3}{4} \frac{m_e c^2}{\Delta W_{\text{kin}}} \lambda_g, \quad (2)$$

where the energy-velocity differential is $d\beta = d\gamma / (\beta\gamma^3)$. The energy modulation can be realized with more than one grating cell, since the drift between the cells is negligible, see Figure 3. The particles pile up at the zero crossing of the modulator phase and can be injected exactly at the designed synchronous phase φ_s by a fractional period drift

$$L_{\text{frac}} = \lambda_{g0} \frac{\pi/2 - \varphi_s + \Delta\varphi_B}{2\pi}, \quad (3)$$

where $\Delta\varphi_B$ is a phase correction due to the buncher fringe fields, see Figure 2 bottom. The total length of the drift is $L_{\text{Drift}} = \lambda_{g0}[L_{\text{int}}/\lambda_{g0}] + L_{\text{frac}}$, where the square brackets denote integer rounding.

**Figure 3.** Buncher longitudinal phase space

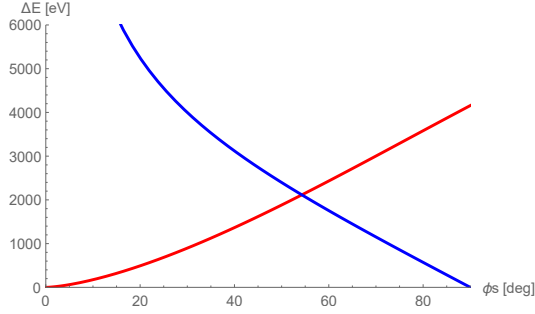


Figure 4. Energy spread acceptance (red) and energy gain per quarter synchrotron period (blue) as function of the synchronous phase φ_s

2.2. Energy spread acceptance

The energy spread acceptance and the initial synchrotron frequency are determined similarly to ordinary RF accelerators. The tracking equations can be approximated by differential equations cast in the form of Hamilton's equations, which can be integrated in the conjugate variables $\tau = \varphi/\omega_0$ and $\Delta W = \gamma m_e c^2 \delta$ to find the Hamiltonian as

$$H(\varphi, \delta) = \frac{m_e c^2}{2\beta^2 \gamma} \delta^2 - e E_{z0} |\underline{\mathcal{E}}_1| \frac{\lambda_g}{2\pi} (\sin \varphi - \varphi \cos \varphi_s). \quad (4)$$

The separatrix is found by the value of H at the saddle point $\varphi_{\text{saddle}} = -\varphi_s$ as

$$\delta_{\text{sep}}(\varphi) = \pm \sqrt{\frac{2\beta^2 \gamma}{m_e c^2} [H(-\varphi_s, 0) - H(\varphi, 0)]}. \quad (5)$$

The bucket height gives the energy spread acceptance $\Delta E_{\text{max}} = \gamma m_e c^2 \delta_{\text{sep}}(\varphi_s)$ as depicted in Figure 4. Moreover, from the Hamiltonian in Equation (4) the second order differential equation

$$\frac{\partial^2 \varphi}{\partial t^2} = \frac{2\pi}{\gamma^3} \frac{e E_{z0} |\underline{\mathcal{E}}_1|}{m_e \lambda_g} [\cos(\varphi) - \cos(\varphi_s)] \quad (6)$$

can be derived. Assuming $\varphi = \varphi_s + \Delta\varphi$ the small amplitude synchrotron frequency is found as

$$f_s = \frac{\omega_s}{2\pi} = \sqrt{\frac{e E_{z0} |\underline{\mathcal{E}}_1|}{2\pi \gamma^3 m_e \lambda_g} \sin(\varphi_s)}. \quad (7)$$

2.3. Chirped grating

In order to trap the particles with energy spread and phase spread in the bucket and accelerate, the phase of the accelerating Fourier coefficient needs to be as constant as possible along the chirped grating. This is achieved in the same manner as tuning RF cavities, namely by adjusting a geometry parameter that is still free. Here, the tooth width t is taken as

$$t = t^{(0)} \left(\frac{\lambda_g / \lambda_g^{(0)} - 1}{\xi} + 1 \right), \quad (8)$$

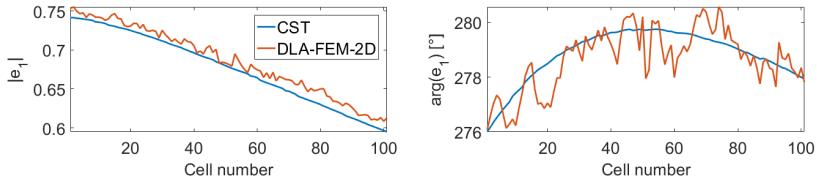


Figure 5. Establishing (almost) constant phase (4 deg jitter) by adjusting the tooth width

with $t^{(0)} = 200$ nm and optimal phase flatness for $\xi \approx 2.7$, see Figure 5. Once phase stability is established, the design of the entire structure can proceed according to the scheme in Figure 6. The linear chirp $\Delta z^{(n)} = \lambda_g^{(n+1)} - \lambda_g^{(n)}$ is given by

$$\Delta z^{(n)} = \lambda_0 \Delta \beta = \frac{\lambda_0 \Delta \gamma}{\gamma^3 \beta} = \left[\frac{\lambda_0}{\beta \gamma^2} \frac{\Delta W(\varphi_s)}{\gamma m_e c^2} \right]^{(n)}, \quad (9)$$

where $\Delta W^{(n)} = m_e c^2 \Delta \gamma^{(n)}$ is the energy gain in the n -th grating period. The decreasing amplitude of e_1 is taken into account by writing $\Delta z^{(n)} = \Delta z^{(1)} - (n-1)\Delta \Delta z$. Note that Δz and $\Delta \Delta z$ are averages and are thus not requirements for the fabrication precision. The slight change in the phase of the Fourier coefficients (Figure 5) leads to an identical change of the synchronous phase, causing a small additional energy spread increase. The acceleration ramp obtained by a CST tracking simulation is shown in Figure 7, where 72 particles represent a uniform distribution. The synchrotron motion is clearly visible, its initial period agrees roughly with $\lambda_s^{\text{init}} = 21 \mu\text{m}$ calculated by Equation (7).

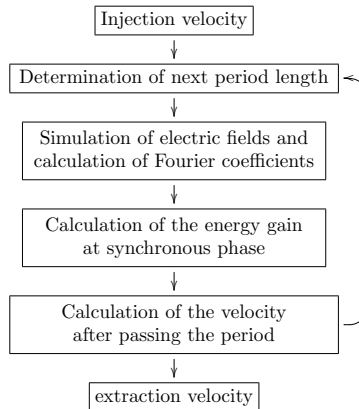


Figure 6. Iteration process for the design of a chirped grating

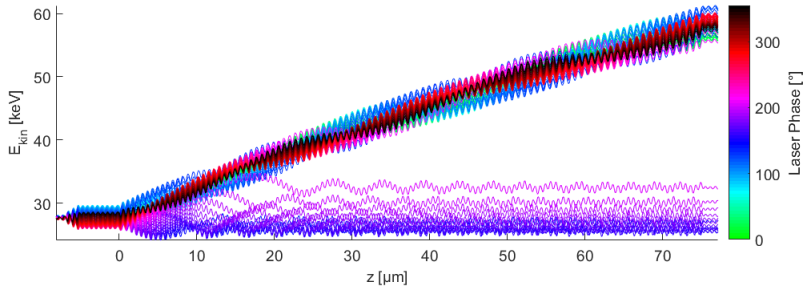


Figure 7. Energy gain along the structure for 72 particles launched at $t = 0$ sweeping over the laser phase in steps of 5 degrees. The fraction of trapped particles is 81%.

3. Optimized bunching

When taking into account finite transverse emittance, the acceleration defocusing plays a decisive role. Already in the modulator the electrons are strongly focused or defocused, depending on their arrival wrt. the laser phase. Adding a demodulator (same structure as the modulator but half a period displaced) at the end of the drift section will decrease the energy spread and the initially defocused particles will be focused and vice versa, see Figure 8. The headline of the transverse plots gives the percentage of particles that survived the aperture.

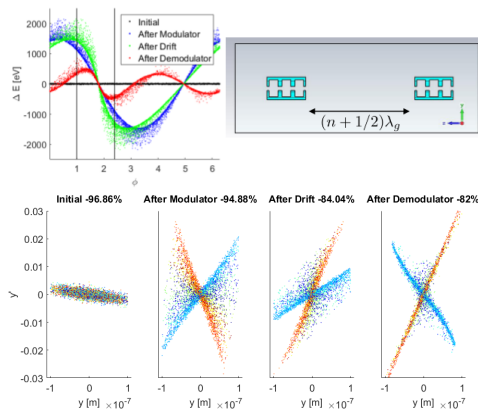


Figure 8. Longitudinal phase space and grating setup (top) and transverse phase space ($y' = \gamma\beta_y$), where the color indicates the particle phase φ (bottom).

4. Conclusion and Outlook

We introduced a novel "slightly resonant" DLA structure that combines Bragg waveguides and symmetric grating structures. We showed that the longitudinal dynamics in DLAs for low energy can be well controlled, in a similar manner as for conventional accelerators. The acceleration defocusing due to the high gradient can however not be compensated by solenoid or quadrupole magnets. Thus in future dedicated laser driven focusing schemes as outlined in the last section and approaches to the transverse dynamics have to be developed.

5. Acknowledgment

This work is funded by the Gordon and Betty Moore Foundation (Grant GBMF4744 to Stanford) and the German Federal Ministry of Education and Research (Grant FKZ:05K16RDB).

References

- [1] ACHIP website: <https://achip.stanford.edu>
- [2] Peralta E A *et al.* 2013 Demonstration of electron acceleration in a laser-driven dielectric microstructure *Nature* **503** 91–94
- [3] Breuer J and Hommelhoff P 2013 Laser-Based Acceleration of Nonrelativistic Electrons at a Dielectric Structure *Phys. Rev. Lett.* **111** 134803
- [4] Leedle K J *et al.* 2015 Laser acceleration and deflection of 96.3keV electrons with a silicon dielectric structure, *Optics Letters* **40** 18
- [5] CST Microwave Studio www.cst.com
- [6] Egenolf T, Boine-Frankenheim O and Niedermayer U 2017 Simulation of DLA grating structures in the frequency domain *Proc. 8th Int. Particle Accelerator Conf. (May 14–19 Copenhagen)* WEPVA002 (this issue)



Beam dynamics analysis of dielectric laser acceleration using a fast 6D tracking scheme

Uwe Niedermayer,^{*} Thilo Egenolf, and Oliver Boine-Frankenheim[†]

*Institut für Theorie elektromagnetischer Felder, Technische Universität Darmstadt,
Schlossgartenstr. 8 D-64289 Darmstadt, Germany
(Received 31 July 2017; published 3 November 2017)*

A six-dimensional symplectic tracking approach exploiting the periodicity properties of dielectric laser acceleration (DLA) gratings is presented. The longitudinal kick is obtained from the spatial Fourier harmonics of the laser field within the structure, and the transverse kicks are obtained using the Panofsky-Wenzel theorem. Additionally to the usual, strictly longitudinally periodic gratings, our approach is also applicable to periodicity chirped (subrelativistic) and tilted (deflection) gratings. In the limit of small kicks and short periods we obtain the 6D Hamiltonian, which allows, for example, to obtain matched beam distributions in DLAs. The scheme is applied to beam and grating parameters similar to recently performed experiments. The paper concludes with an outlook to laser based focusing schemes, which are promising to overcome fundamental interaction length limitations, in order to build an entire microchip-sized laser driven accelerator.

DOI: 10.1103/PhysRevAccelBeams.20.111302

I. INTRODUCTION

Dielectric laser acceleration (DLA) provides highest gradients among nonplasma accelerators. In 2013, the acceleration of relativistic electrons was demonstrated at SLAC with a gradient of more than 250 MeV/m [1], which was recently increased to 690 MeV/m [2]. Low energy electrons (27.7 keV) were accelerated by the group in Erlangen [3] with a gradient of 25 MeV/m using a single grating structure. The group at Stanford University used a dual pillar structure to accelerate 96 keV electrons with a gradient of more than 200 MeV/m [4]. In principle, the gradient of a DLA is only limited by the structure damage threshold fluence, which is roughly two orders of magnitude higher for dielectrics than for metals. The reason for the rediscovery of this rather old concept of inverse Smith-Purcell or inverse Cherenkov effects for particle acceleration (see, e.g., [5]) is that nowadays both the ultrashort laser pulse control techniques as well as the nano-fabrication have significantly improved. Summaries of the recent developments can be found in [6,7].

Although the experimentally demonstrated gradients in DLA structures are very promising, there are still crucial challenges to create a miniaturized DLA-based particle accelerator. So far the experimentally achieved gradients

could only be used to increase the beam's energy spread and not for coherent acceleration. Moreover, the interaction length with present DLA structures is limited to the Rayleigh range (see Appendix) of the incident electron beam. For low energy electrons, due to the high gradient, the acceleration defocusing even leads to interaction distances significantly shorter than the Rayleigh range.

Thus, in order to use DLA for a real accelerator, focusing schemes have to be developed. One option would be alternating phase focusing (APF) as outlined in Fig. 1. Here, drift sections between grating cells lead to jumps in the synchronous phase, which can be designed to provide net focusing. Such schemes can be a way to increase the interaction length in DLAs and make an accelerator on a microchip feasible.

A challenge in the creation of a DLA based optical accelerator is related to the complex 3D beam dynamics in DLA structures, which has not been treated systematically

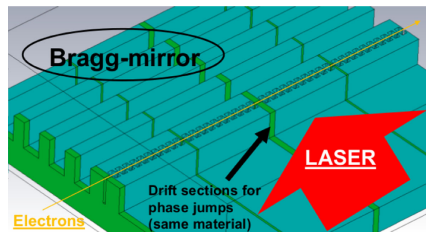


FIG. 1. Example Bragg cavity grating with a Bragg mirror on one side.

^{*}niedermayer@temf.tu-darmstadt.de

[†]Also at GSI Helmholtzzentrum für Schwerionenforschung, Planckstr. 1, D-64291 Darmstadt, Germany.

Published by the American Physical Society under the terms of the Creative Commons Attribution 4.0 International license. Further distribution of this work must maintain attribution to the author(s) and the published article's title, journal citation, and DOI.

in the existing literature yet. In order to facilitate front to end simulations and identify optimized DLA structures, we employ a simple and efficient numerical tracking scheme, which does not require a large amount of computing power, it runs in MATLAB [8] on an ordinary PC.

Due to the periodicity of a DLA grating, only one spatial Fourier harmonic contributes to the kick of the beam. In a simplified approach, where fringe fields are neglected, the entire laser field can be represented by a set of such Fourier coefficients, where only one complex number represents each grating cell. By means of the Panofsky-Wenzel theorem [9], this single complex number also allows to determine the transverse kicks experienced by a particle while traveling through one grating period.

When the three-dimensional kicks are applied to the beam particles in a symplectic scheme (we use symplectic Euler, which is equivalent to Leap Frog) the tracking becomes phase space volume preserving. Thus, with no numerical (artificial) emittance increase, the physical emittance increase due to the nonlinear fields in the DLA interaction can be calculated. Moreover, since the equations of motion are coupled, there is also emittance exchange between the different planes which can be analyzed.

In the present study we neglect all intensity dependent effects as space charge, wakes, and radiation emission. The number of particles is chosen such that smooth spectra are obtained, a reasonable value is 10^6 , at which the computational time is about one second per grating cell.

With no loss of generality, we restrict ourselves to symmetric grating structures driven from both lateral sides. This makes sure that the axis of symmetry is in the center and the fields have a cosh profile. In the case of non-symmetric structures or nonsymmetric driving, the fields will have an exponential or an off-axis cosh profile. However, single driver systems can be combined with Bragg mirrors in order to obtain a good approximation to an on-axis cosh profile with a single side driver (see again Fig. 1). Another option is to reshape the structure as e.g., presented in [4], or, just to accept the asymmetry which then leads to a smaller effective aperture. Furthermore, we restrict ourselves to linear dielectrics. Driving the dielectric into its nonlinear regime is discussed in [10] (experimental), whereas the theoretical reader [11] particularly covers quantum aspects of high fields.

As it is usually done, e.g., for the synchrotron motion in ion synchrotrons, we take the limit from the tracking difference equations to differential equations. Since the three-dimensional kick must be irrotational due to the Panofsky-Wenzel theorem, it can be derived from a scalar potential. This potential directly allows to determine the 6D Hamiltonian which completely describes the single particle dynamics analytically.

Both the numerical and the analytical approach can be generalized from ordinary DLA gratings to tilted DLA gratings, which have been proposed as deflectors or laser

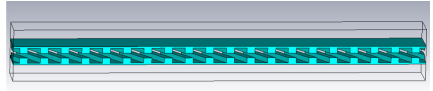


FIG. 2. Tilted Bragg cavity grating, where the dual drive laser comes from top and bottom and is polarized in the electron beam direction (left to right).

driven undulators [12–14]. Such a grating is depicted in Fig. 2. However, since our code does not include the radiation fields, a dedicated code as, e.g., [15] can be used to treat the dynamics self-consistently. The analytical kicks reported here can serve as input quantities. Our approach aims at maximal simplicity such that studies of fundamental questions, as, e.g., transverse focusing and deflection, are quickly possible.

The paper is organized as follows. Section II presents the determination of the longitudinal and transverse fields and kicks in a single grating period. Here we use CST Studio Suite [16] to calculate the longitudinal kick at the center of the structure. The dependence on the transverse coordinates as well as the transverse kicks are modeled analytically. In Sec. III we present a symplectic 6D tracking method based on one kick per grating period. Analytical descriptions of the coupled longitudinal and transverse beam dynamics as well as the full 6D Hamiltonian are given in Sec. IV. Simplifications and beam matching in linearized fields are also discussed in this section. In Sec. V we address the three crucial examples: subrelativistic acceleration, relativistic acceleration, and deflection by means of DLA gratings. The paper concludes with a summary and an outlook to DLA focusing channels in Sec. VI.

II. FIELDS AND KICKS IN PERIODIC STRUCTURES

Usual particle tracking algorithms solve Maxwell's equations with a predefined time step. Instead of that, we make use of the periodicity of the structure and apply only the kicks which are known not to average out *a priori*. The other field harmonics are neglected. The validity of this neglect depends on the effect of transients which is effectively suppressed when the structure period is matched to the beam velocity. With no loss of generality we restrict ourselves here to an infrared laser with $\lambda_0 = 1.96 \mu\text{m}$ and structures made of Silicon ($\epsilon_r = 11.63$). A single cell of a symmetrically driven Bragg mirror cavity structure is shown in Fig. 3.

A. Analysis of the longitudinal field

A coordinate system is applied such that the electron beam propagates in positive z -direction and the z -polarized laser propagates in y -direction. The unit cell of a periodic dielectric structure has dimensions λ_{yx} and λ_{yz} . In order to

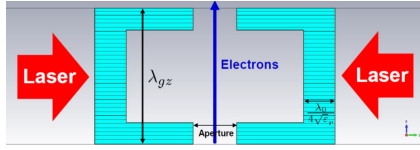


FIG. 3. One period of a symmetric Bragg mirror cavity structure.

allow the laser field to escape the structure, open boundaries in positive and negative y -direction are assumed. The energy gain of a particle in one cell is

$$\Delta W(x, y, s) = q \int_{-\lambda_{gc}/2}^{\lambda_{gc}/2} E_z(x, y, z; t = (z+s)/v) dz \quad (1)$$

$$= q \int_{-\lambda_{gc}/2}^{\lambda_{gc}/2} \text{Re}\{E_z(x, y, z) e^{i\omega(z+s)/v}\} dz, \quad (2)$$

where the underlined electric field is a phasor at the fixed frequency $\omega = 2\pi c/\lambda_0$ of the laser, and q is the charge ($q = -e$ for electrons). The variable s denotes the relative position of the particle behind an arbitrarily defined reference particle moving at $z = vt$. Thus z is the absolute position in the laboratory frame, while s denotes the phase shift with respect to z . Due to the z -periodicity, the laser field can be expanded in spatial Fourier series

$$\underline{E}_z(x, y, z) = \sum_{m=-\infty}^{\infty} \underline{e}_m(x, y) e^{-im\frac{2\pi}{\lambda_{gc}}z} \quad (3)$$

$$\underline{e}_m(x, y) = \frac{1}{\lambda_{gc}} \int_{-\lambda_{gc}/2}^{\lambda_{gc}/2} \underline{E}_z(x, y, z) e^{im\frac{2\pi}{\lambda_{gc}}z} dz, \quad (4)$$

which allows us to compute the energy gain integral [Eq. (2)] as

$$\Delta W(x, y, s) = q \text{Re} \left[e^{\frac{2\pi i s}{\beta \lambda_0}} \sum_{m=-\infty}^{\infty} \underline{e}_m(x, y) \lambda_{gc} \text{sinc} \left(\frac{\lambda_{gc}}{\beta \lambda_0} - m \right) \right], \quad (5)$$

where $\text{sinc}(\cdot) = \sin(\pi \cdot)/(\pi \cdot)$. The electric field phasor and its spatial Fourier coefficients for the structure in Fig. 3 are plotted in Fig. 4. It has a small real part, which is coincidental, and a strong first and weak second harmonic. If the round braces in Eq. (5) is non-integer, the energy gain averages to zero, if it is integer other than zero, it directly vanishes. Thus we have the phase synchronicity condition

$$\lambda_{gc} = m\beta\lambda_0 \quad (6)$$

and the particle's energy gain simplifies to

$$\Delta W(x, y, s) = q\lambda_{gc} \text{Re} \left\{ e^{\frac{2\pi i s}{\beta \lambda_0}} \underline{e}_m(x, y) \right\} = q\lambda_{gc} |\underline{e}_m| \cos \left(2\pi \frac{s}{\beta \lambda_0} + \varphi_m \right), \quad (7)$$

where $\varphi_m = \arctan \text{Im}\{\underline{e}_m\} / \text{Re}\{\underline{e}_m\}$ is the phase of the Fourier coefficient. The energy gain is maximal at $s_{\text{opt}} = -\varphi_m \beta \lambda_0 / 2\pi$ for positively charged particles and $s_{\text{opt}} = -(\varphi_m + \pi) \beta \lambda_0 / 2\pi$ for electrons. Zero acceleration is found at $s_0 = -(\varphi_m \pm \pi/2) \beta \lambda_0 / 2\pi$, where all these expressions are to be taken modulo $\beta \lambda_0 / m$. The integer spatial harmonic m has the same meaning as the harmonic number in conventional accelerators, i.e., the number of buckets per grating period and Eq. (6) resembles the Wideroe condition.

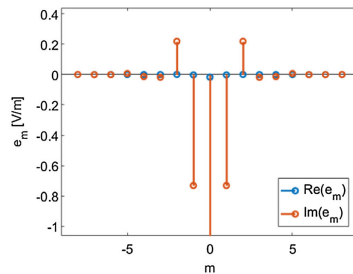
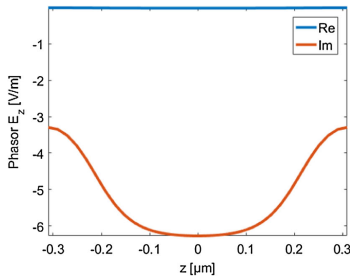


FIG. 4. Longitudinal electric field on the beam axis for the Bragg mirror structure in Fig. 3 and spatial Fourier harmonics for incident laser field normalized to 1 V/m.

As shown in Eq. (5), the higher nonsynchronous harmonics average out. It can be shown, that their second order (ponderomotive) contribution is also small. However, the lower non-synchronous (sub-) harmonics can provide ponderomotive focusing, as discussed in [17]. In our code, they can be represented by modifying the synchronous Fourier coefficient $\underline{e}_1(n)$ along the grating cells n , which however is beyond the scope of this paper.

For subrelativistic accelerators, the grating needs to be chirped in period length in order to always fulfill Eq. (6) on the energy ramp. The change of period length is given by the energy velocity differential

$$\frac{\Delta z}{\lambda_{gz}} = \frac{1}{\beta^2 \gamma^2} \frac{\Delta W}{W} \quad (8)$$

and is in the range of $\lesssim 1\%$ for $W_{\text{kin}} = 30$ keV and $\Delta W/\lambda_{gz} = 1$ GeV/m. The thus created ‘‘quasiperiodic’’ grating can be seen in good approximation as periodic, however, phase drifts have to be compensated in the structure design [18].

B. Analysis of the transverse field

The transverse field probed by a rigidly moving charge can be obtained using the Panofsky-Wenzel theorem [9], which holds for either vanishing fields at infinity or periodic boundary conditions as

$$\begin{aligned} \nabla' \times \Delta \vec{p}(\vec{r}_\perp, s) &= \int_{-T/2}^{T/2} dt [\nabla \times \vec{F}(\vec{r}_\perp, z, t)]_{z=vt-s} \\ &= \vec{B}'_{-T/2} = 0. \end{aligned} \quad (9)$$

Here the ‘‘relative gradient’’ is defined as $\nabla' = (\partial_x, \partial_y, -\partial_s)^T$ and $\lambda_{gz} = \beta c T$. The transverse kick per cell can be written as

$$\begin{aligned} \Delta \vec{p}_\perp(x, y, s) &= - \int ds \nabla_\perp \Delta p_\parallel(x, y, s) \quad (10) \\ &= - \frac{\lambda_{gz}}{2\pi m} q \frac{1}{\beta c} \nabla_\perp \int_{-\lambda_{gz}/2}^{\lambda_{gz}/2} \text{Im}\{E_z(x, y, z) e^{i\omega(z+s)/v}\} dz, \quad (11) \end{aligned}$$

where the energy momentum differential $\Delta p_\parallel = \Delta W/(\beta c)$ was applied. Moreover, if the phase-synchronicity condition [Eq. (6)] is fulfilled, the kick becomes

$$\Delta \vec{p}_\perp(x, y, s) = - \frac{\lambda_{gz}^2}{2\pi m} q \frac{1}{\beta c} \nabla_\perp \text{Im}\{e^{2\pi i \frac{s}{\lambda_{gz}}} \underline{e}_m(x, y)\} \quad (12)$$

$$= - \frac{\lambda_{gz}}{m} q \frac{1}{\beta c} \text{Im}\{e^{2\pi i \frac{s}{\lambda_{gz}}} \vec{f}_m(x, y)\}, \quad (13)$$

where $\vec{f}_m(x, y) = \lambda_{gz} \nabla_\perp \underline{e}_m(x, y)/2\pi$. In the following, the structure under investigation is generalized to a tilted grating as visible in Fig. 5, which reproduces the ordinary grating with tilt angle $\alpha = 0$. The tilted grating is periodic in z and x direction. Thus for any function $F(x, y, s)$ must hold

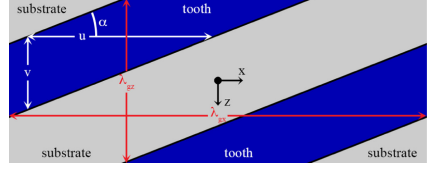


FIG. 5. Tilted grating with periodic boundary conditions in x and z direction and $\tan \alpha = \lambda_{gz}/\lambda_{gx} = v/u$.

$$\frac{\partial F}{\partial x} = \frac{\partial F}{\partial s} \frac{\partial s}{\partial z} \frac{\partial z}{\partial x} = \frac{\partial F}{\partial s} \tan \alpha. \quad (14)$$

The s -derivative can be calculated in the Fourier representation by Eq. (7) as

$$\frac{\partial \underline{e}_m(x, y)}{\partial x} = \tan \alpha \frac{2\pi i}{\beta \lambda_0} \underline{e}_m(x, y). \quad (15)$$

The derivatives in y -direction can be determined by the dispersion relation for the synchronous mode. We have

$$k_z = \frac{\omega}{\beta c}, \quad k_x = \frac{2\pi}{\beta \lambda_0} \tan \alpha \quad \text{and} \quad k = \frac{\omega}{c} \quad (16)$$

and thus

$$k_y = \pm \sqrt{k^2 - (k_z^2 + k_x^2)} = \pm \frac{\omega}{c} \sqrt{1 - \frac{1}{\beta^2} (1 + \tan^2 \alpha)}. \quad (17)$$

For a nontilt grating ($\alpha = 0$) this is the well-known evanescent decay of the near field $k_y = i\omega/(\beta \gamma c)$. Once k_x, k_y are determined, the fields can be found from

$$\underline{e}_m(x, y) = \underline{e}_m(0, 0) \cosh(ik_y y) e^{ik_x x}, \quad (18)$$

where $\lambda_{gx} = \lambda_{gz}/\tan \alpha$.

A map of the energy gain and transverse kicks for the grating in Fig. 6 can be seen in Fig. 7 for a grating tilt angle

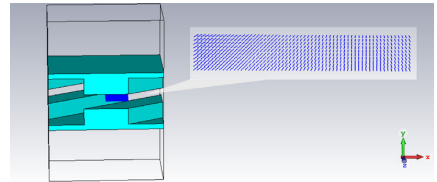


FIG. 6. Single cell of the tilted grating deflector structure and enlargement of kick integration curves array. The integrated kicks are displayed in Fig. 7.

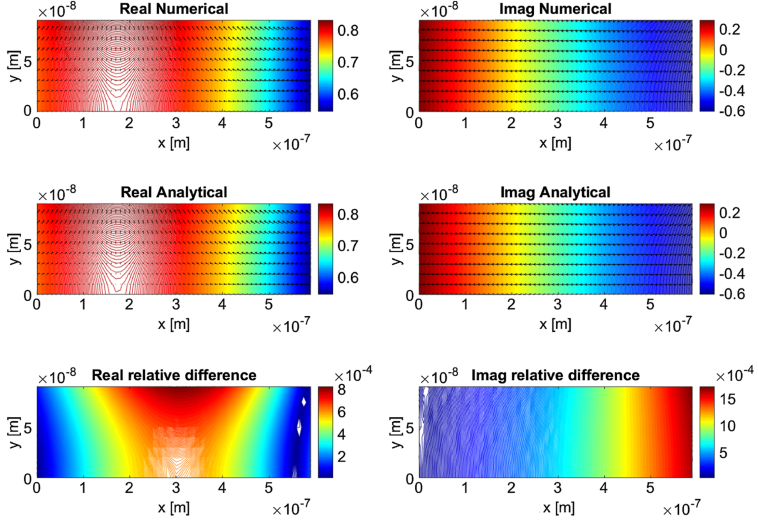


FIG. 7. Contour lines of $\underline{e}_m(x, y)$ and kick field $\underline{\vec{f}}_m(x, y)$ for the tilted grating with $\alpha = 30$ deg. The fields have been obtained both analytically and numerically, the bottom plots show the relative difference.

$\alpha = 30$ deg. The results labeled numerical are obtained by line integration [Eq. (7)] of the electric field simulated with CST MWS [16] and the analytical results correspond to Eq. (18). The transverse kicks are obtained by Eq. (13) as

$$\underline{\vec{f}}_m(x, y) = \underline{e}_m(0, 0) \cosh(ik_y y) e^{ik_x x} \tan \alpha \underline{\vec{e}}_x + \underline{e}_m(0, 0) \sinh(ik_y y) e^{ik_x x} (ik_y \lambda_{gz} / 2\pi) \underline{\vec{e}}_y \quad (19)$$

and are depicted as arrows in Fig. 7. For the numerical results, the gradient is determined by finite differences in MATLAB [8]. Note that $-ik_y \in \mathbb{R}^+$, i.e., the kick in x -direction is in phase with the acceleration while the kick in y -direction is 90 degrees shifted.

For a particle that is only slightly displaced from the beam axis by $\Delta \vec{x} = (\Delta x, \Delta y)$, the kick can be written as two-dimensional Taylor expansion

$$\underline{\vec{f}}_m(x, y) = \underline{\vec{f}}_m(x_0, y_0) + (\nabla_{\perp} \underline{\vec{f}}_m(x_0, y_0)) \Delta \vec{x} + O(\|\Delta \vec{x}\|^2) = \frac{\lambda_{gz}}{2\pi} (\nabla_{\perp} \underline{e}_m(x_0, y_0) + (\nabla_{\perp} \nabla_{\perp}^T) \underline{e}_m(x_0, y_0) \Delta \vec{x}) + O(\|\Delta \vec{x}\|^2), \quad (20)$$

where

$$\nabla_{\perp} \nabla_{\perp}^T = \begin{pmatrix} \partial_x^2 & \partial_x \partial_y \\ \partial_x \partial_y & \partial_y^2 \end{pmatrix} \quad (21)$$

is the Hessian. The expansion Eq. (20) about $x_0 = 0$, $y_0 = 0$ of Eq. (18) results in

$$\underline{\vec{f}}_m(\Delta x, \Delta y) = \frac{\lambda_{gz}}{2\pi} \underline{e}_m(0, 0) \begin{pmatrix} ik_x - k_x^2 \Delta x \\ -k_y^2 \Delta y \end{pmatrix}, \quad (22)$$

i.e., a position independent (coherent) kick component in x -direction, vanishing for $\alpha = 0$. Using this abstract derivation, the results of several papers proposing DLA undulators [12–14] can be recovered.

III. TRACKING EQUATIONS

In order to study the motion of particles in the fields of periodic gratings we approximate the forces by one kick per grating period and track with the symplectic Euler method. In spite of the very high gradients in DLA structures, the energy can still be seen as an adiabatic variable, as it is the case in conventional linacs. Tracking the full time dependence of γ , as required for example in plasma accelerators, can be avoided due to the shortness of the periods. For simplicity, we restrict ourselves to $m = 1$ from this point and introduce normalized variables in the paraxial approximation

$$\begin{aligned}
x' &= \frac{p_x}{p_{z0}}, & \Delta x' &= \frac{\Delta p_x(x, y, \varphi)}{p_{z0}}, \\
y' &= \frac{p_y}{p_{z0}}, & \Delta y' &= \frac{\Delta p_y(x, y, \varphi)}{p_{z0}}, \\
\varphi &= 2\pi \frac{s}{\lambda_{gz}}, & \delta &= \frac{W - W_0}{W_0}, \\
\Delta\delta &= \frac{\Delta W(x, y, \varphi) - \Delta W(0, 0, \varphi_s)}{W_0},
\end{aligned} \quad (23)$$

where $W_0 = \gamma m_e c^2$ and $p_{z0} = \beta \gamma m_e c$. The particle at the synchronous phase φ_s has $\Delta\delta = 0$, i.e., its energy gain is entirely described by the acceleration ramp. The energy gain ΔW is given by Eq. (7) and thus the energy gain of the synchronous particle is

$$\Delta W(0, 0, \varphi_s) = q \lambda_{gz} \text{Re}\{e^{i\varphi_s} \underline{e}_1\}, \quad (24)$$

where we write $\underline{e}_1 = \underline{e}_1(x=0, y=0)$ for brevity. Note that the synchronous phase and the phase of each

particle always refer to the laser phase. The sum of the kicks

$$W(N) = W_{\text{init}} + \sum_{n=1}^N \Delta W^{(n)}(0, 0, \varphi_s^{(n)}) \quad (25)$$

describes the acceleration ramp, where the synchronous phase φ_s can be chosen arbitrarily in each grating cell. The variables $\underline{e}_1, \lambda_{gz}, W_0, \beta, \gamma, \varphi_s$ and all variables in Eq. (24) are stored as arrays indexed by the grating cell number. The kicks are obtained using Eqs. (7), (18), (19), and (13) and read

$$\Delta x' = -\frac{q \lambda_0}{p_{z0} c} \tan(\alpha) \cosh(ik_y y) \text{Re}\{\underline{e}_1 e^{i\varphi + i\frac{2\pi x}{\lambda_{gz}}}\}, \quad (26a)$$

$$\Delta y' = \frac{-ik_y \lambda_0^2 q \beta}{2\pi p_{z0} c} \sinh(ik_y y) \text{Im}\{\underline{e}_1 e^{i\varphi + i\frac{2\pi x}{\lambda_{gz}}}\}, \quad (26b)$$

$$\Delta\delta = \frac{q \lambda_{gz}}{\gamma m_e c^2} \text{Re}\{\underline{e}_1 (\cosh(ik_y y) e^{i\varphi + i\frac{2\pi x}{\lambda_{gz}}} - e^{i\varphi_s})\}, \quad (26c)$$

where k_y is given by Eq. (17). The tracking equations are

$$\begin{pmatrix} x \\ x' \\ y \\ y' \\ \varphi \\ \delta \end{pmatrix}^{(n+1)} = \begin{pmatrix} x \\ Ax' + \Delta x'(x, y, \varphi) \\ y \\ Ay' + \Delta y'(x, y, \varphi) \\ \varphi \\ \delta + \Delta\delta(x, y, \varphi; \varphi_{\text{sync}}) \end{pmatrix}^{(n)} + \begin{pmatrix} \lambda_{gz} x'(x, y, \varphi) \\ 0 \\ \lambda_{gz} y'(x, y, \varphi) \\ 0 \\ -\frac{2\pi}{\beta^2 \gamma^2} \delta(x, y, \varphi) \\ 0 \end{pmatrix}^{(n+1)}, \quad (27)$$

where an explicit scheme is obtained by applying first the “kicks” and then the “pushes”. The adiabatic damping in the transverse planes is described by

$$A^{(n)} = \frac{(\beta\gamma)^{(n+1)}}{(\beta\gamma)^{(n)}} = 1 + \left[\frac{\lambda_0 q \text{Re}\{e^{i\varphi_s} \underline{e}_1\}}{\beta \gamma m_e c^2} \right]^{(n)}. \quad (28)$$

Symplecticity of the scheme is confirmed by calculating

$$\det \frac{\partial(x, x', y, y', \varphi, \delta)^{(n+1)}}{\partial(x, x', y, y', \varphi, \delta)^{(n)}} = A^{(n)2}, \quad (29)$$

which holds independently of the realization of the kick functions $\Delta x'(x, y, \varphi)$, $\Delta y'(x, y, \varphi)$ and $\Delta\delta(x, y, \varphi)$. Equations (27) contain the full nonlinear kicks which cannot be linearized, since the usual bunch lengths and widths are not significantly smaller than the grating periods and apertures. However, in the idealized case of extremely small bunches, linearization results in a scheme equivalent to one linear R-matrix transformation per grating period.

Relevant information about the particle ensemble moving in space is given by statistical quantities such as envelope and emittance, which can be derived from the beam matrix (second order moment matrix) as function of the period number. We define the 6D coordinate vector as

$$\vec{r} = (x, p_x, y, p_y, \Delta s, \Delta P_z)^T, \quad (30)$$

where $\Delta s = (\varphi - \varphi_s) \lambda_{gz} / 2\pi$ and $\Delta P_z = \Delta p_z / \gamma = W_0 / (\beta \gamma c) \delta$. The symmetric and positive definite beam matrix reads

$$\mathbf{M} = \langle \vec{r} \vec{r}^T \rangle, \quad (31)$$

where the average is taken component-wise. In the absence of nonlinearities, particular emittances are conserved. That is in the case of coupling only the 6D emittance given by

$$\varepsilon_{6D} = \sqrt{\det \mathbf{M}}. \quad (32)$$

In case of decoupled planes, the determinants of the diagonal blocks (the emittances of the respective plane) are conserved individually. They read

$$\begin{aligned}
\epsilon_{x,n} &= \frac{1}{m_e c} \sqrt{\det \mathbf{M}_1}, \\
\epsilon_{y,n} &= \frac{1}{m_e c} \sqrt{\det \mathbf{M}_2}, \\
\epsilon_{z,n} &= \frac{1}{e} \sqrt{\det \mathbf{M}_3},
\end{aligned} \quad (33)$$

in the usual units of m rad and eVs, respectively. The analysis of emittance coupling by means of the eigen-emittances

$$\epsilon_{\text{eig},i} = \text{eigs}(\mathbf{JM}), \quad (34)$$

where \mathbf{J} is the symplectic matrix, is also possible with our code, however beyond the scope of this paper.

IV. CONTINUOUS EQUATIONS OF MOTION

In order to address the continuous motion in DLA structures we employ positions and momentum as canonically conjugate variables in all directions. The transformation for the energy is $\Delta p_z = \Delta W/(\beta c)$. We address the flat and the tilted grating separately and assume for simplicity $|\underline{\epsilon}_1|$ to be constant for all cells and $\arg(\underline{\epsilon}_1) = 0$.

A. Flat grating

Hamilton's equations can be written as

$$\dot{x} = \frac{p_x}{m_e \gamma} \quad (35a)$$

$$\dot{p}_x = 0 \quad (35b)$$

$$\dot{y} = \frac{p_y}{m_e \gamma} \quad (35c)$$

$$\dot{p}_y = -q e_1 \frac{\lambda_{gz}}{2\pi} \frac{\omega}{\beta \gamma c} \sinh\left(\frac{\omega y}{\beta \gamma c}\right) \sin\left(\frac{2\pi s}{\lambda_{gz}}\right) \quad (35d)$$

$$\dot{s} = \frac{\Delta p_z}{m_e \gamma^3} \quad (35e)$$

$$\Delta \dot{p}_z = q e_1 \left[\cosh\left(\frac{\omega y}{\beta \gamma c}\right) \cos\left(\frac{2\pi s}{\lambda_{gz}}\right) - \cos \varphi_s \right]. \quad (35f)$$

Due to Eq. (9) the force field is irrotational and can be derived from a potential as $\vec{F} = -\nabla V$, where integration yields

$$V = q e_1 \left[\frac{\lambda_{gz}}{2\pi} \cosh\left(\frac{\omega y}{\beta \gamma c}\right) \sin\left(\frac{2\pi s}{\lambda_{gz}}\right) - s \cos \varphi_s \right]. \quad (36)$$

This potential and its adiabatic change with β is illustrated in Fig. 8. The full 6D Hamiltonian reads

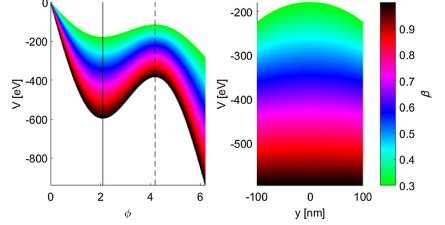


FIG. 8. The potential (Eq. (36)) as function of φ and y at the synchronous phase indicated by the solid vertical line. The longitudinally unstable fixed point (dashed line) flips the sign of the transverse potential. The color scale indicates the adiabatic change of the potential with β .

$$H = \frac{1}{2m_e \gamma} (p_x^2 + p_y^2 + \Delta P_z^2) + V, \quad (37)$$

where $\Delta p_z/\gamma$ was replaced with ΔP_z . The coupled equations of motion are

$$\ddot{x} = 0 \quad (38a)$$

$$\ddot{y} = -\frac{q e_1}{m_e \gamma^2} \sinh\left(\frac{\omega y}{\beta \gamma c}\right) \sin\left(\frac{2\pi s}{\lambda_{gz}}\right) \quad (38b)$$

$$\ddot{s} = \frac{q e_1}{m_e \gamma^3} \left(\cosh\left(\frac{\omega y}{\beta \gamma c}\right) \cos\left(\frac{2\pi s}{\lambda_{gz}}\right) - \cos \varphi_s \right). \quad (38c)$$

If the beam size is significantly smaller than the aperture ($y \ll \beta \gamma c/\omega$), the longitudinal equation decouples and becomes the ordinary differential equation of synchrotron motion. The transverse motion becomes linear in this case, however still dependent on the longitudinal motion via φ . The equation of motion,

$$\ddot{y} = \frac{-q e_1 \omega}{m_e \gamma^3 \beta c} \sin(\varphi) y, \quad (39)$$

is Hill's equation, with the synchrotron angle being the focusing function. However there is a crucial difference to ordinary magnetic focusing channels. The focusing force scales as γ^{-3} as expected for acceleration defocusing [19], rather than with γ^{-1} as would be expected for a magnetic quadrupole focusing channel. The solution to Eq. (39) as function of z for fixed $s = \lambda_{gz} \varphi_s / 2\pi$, i.e., when the bunch length is significantly shorter than the period length, is

$$y = y_0 \exp\left(\sqrt{\frac{-q e_1 \omega}{m_e \gamma^3 \beta^3 c^3} \sin \varphi_s} z\right) \quad (40)$$

and a synchronous particle with nonzero transverse offset is expected to grow to double transverse amplitude in

$$L_2 = \frac{\ln 2}{\sqrt{\frac{-qe_0\omega}{m_e\gamma^3\beta^3 c^3} \sin \varphi_s}}. \quad (41)$$

For subrelativistic particles L_2 can reach down to a few micron. However, longer interaction lengths can be achieved by focusing the beam into the DLA structure externally.

As shown in Fig. 9, the phase ranges of longitudinal and transverse focusing are disjoint. This is a consequence of Earnshaw's theorem [20] which can be directly observed in Eq. (36), i.e., V has no minima but only saddle points. Similarly as in Paul traps (see, e.g., [21]), stable motion in both the y - and z -planes can only be achieved by rotating the saddle. For an accelerator this means alternating the synchronous phase. This so called alternating-phase-focusing (APF) scheme has been developed for ion rf linacs already in the 1950s (e.g., [22]) but later rejected in favor of the RFQ [19].

For an adiabatic Hamiltonian and if stable orbits exist, a matched locally Gaussian distribution is given by

$$f = C e^{-H/(H)} \quad (42)$$

and a locally elliptic (Hofmann-Pedersen [23]) matched distribution is given by

$$f = C \sqrt{H_{\max} - H}. \quad (43)$$

The normalization constant C is determined by integration. Note that in the case of nonperiodic motion f will not be integrable. Thus, we can only write a matched distribution for the longitudinal plane if $\varphi_s \in [\pi/2, \pi]$ and for the transverse plane if $\varphi_s \in [\pi, 3/2\pi]$.

The Hamiltonian is not time independent, however its dependence on β and γ is adiabatic. Thus, if φ_s is changing at most adiabatically, the distribution will deform such that the emittance increase is bounded, i.e., also the emittance remains an adiabatic invariant. First, we consider the longitudinal plane and linearized fields. For a given bunch length $\sigma_{\Delta s}$, the matched energy spread is

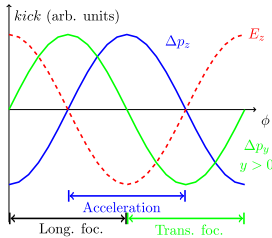


FIG. 9. Overview of electron acceleration and focusing properties for an x -invariant grating.

$$\sigma_{\Delta W} = \frac{c_0}{\lambda_0} \sqrt{-2\pi\lambda_{gr} m_e \gamma^3 q e_1 \sin \varphi_s \sigma_{\Delta s}}. \quad (44)$$

For a slow change of the potential and filling the bucket only up to a small fraction, the phase space area given by $\pi\sigma_{\Delta\varphi}\sigma_{\Delta W}$ is conserved. Moreover, using Eq. (44) a normalized bunch length and energy spread can be written as [19]

$$\sigma_{\Delta W,n} = \frac{1}{\sqrt[4]{\beta^3\gamma^3}} \sigma_{\Delta W} \quad (45a)$$

$$\sigma_{\Delta\varphi,n} = \sqrt[4]{\beta^3\gamma^3} \sigma_{\Delta\varphi}. \quad (45b)$$

Accordingly, in position and momentum coordinates, this reads

$$\sigma_{\Delta P_{z,n}} = \sqrt[4]{\frac{\beta}{\gamma}} \sigma_{\Delta P_z} \quad (46a)$$

$$\sigma_{\Delta s,n} = \sqrt[4]{\frac{\gamma}{\beta}} \sigma_{\Delta s}. \quad (46b)$$

Thus the adiabatic phase damping in DLAs behaves in the same way as in rf linacs.

As a test of the code, we plot the long time evolution of the longitudinal emittance at zero transverse emittance for 3 different setups in Fig. 10. First, we consider a bunch matched according to Eq. (44) in linearized fields. As expected, the symplectic code preserves the emittance in linear fields. However, the linearly matched bunch shows emittance growth in the non-linear fields. Even stronger emittance increase is to be expected, when there is a mismatch of the bunch length and the energy spread (here we chose 10% excess energy spread). The according result

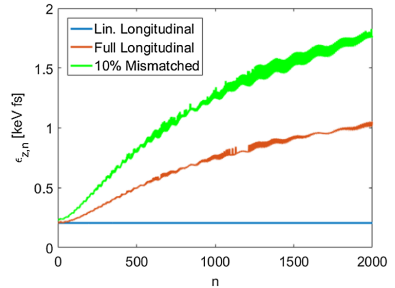


FIG. 10. Longitudinal emittance evolution for a linearly matched Gaussian beam in linearized fields, with the full fields, and with 10% excess energy spread.

is obtained for the y-emittance when setting the synchronous phase into the transverse focusing regime and taking the longitudinal emittance as zero.

The effect of adiabatic damping also appears in DLAs in the transverse plane. The linearized transverse Hamiltonian reads

$$H_{\perp} = \frac{p_y^2}{2m_e\gamma} + \frac{qe_1\omega \sin \varphi_s}{2\beta\gamma^2 c} y^2 \quad (47)$$

and the matched momentum spread is

$$\sigma_{p_y} = \sqrt{\frac{m_e q e_1 \omega \sin \varphi_s}{\beta \gamma c} \sigma_y}. \quad (48)$$

The area $\pi\sigma_y\sigma_{p_y}$ is conserved and thus we can write normalized spreads as

$$\sigma_{y,n} = \frac{1}{\sqrt{\beta\gamma}} \sigma_y \quad (49a)$$

$$\sigma_{p_y,n} = \sqrt{\beta\gamma} \sigma_{p_y}. \quad (49b)$$

One observes, that for increasing beam energy the transverse beam size increases, while the momentum spread decreases. This is in accordance with the potential becoming flatter in the transverse plane, while it becomes steeper in the longitudinal plane for increasing beam energy (cf. Fig. 8).

B. Tilted grating

The Hamiltonian for the tilted grating is obtained by modifying the potential [Eq. (36)] as

$$V = qe_1 \left[\frac{\lambda_{gz}}{2\pi} \cosh(ik_y y) \sin\left(\frac{2\pi s}{\lambda_{gz}} + \frac{2\pi x}{\lambda_{gx}}\right) - s \cos \varphi_s \right]. \quad (50)$$

The coupled equations of motion are

$$\ddot{x} = -\frac{qe_1 \lambda_{gz}}{m_e \gamma \lambda_{gx}} \cosh(ik_y y) \cos\left(\frac{2\pi s}{\lambda_{gz}} + \frac{2\pi x}{\lambda_{gx}}\right) \quad (51a)$$

$$\ddot{y} = \frac{-ik_y \lambda_{gz} qe_1}{2\pi m_e \gamma} \sinh(ik_y y) \sin\left(\frac{2\pi s}{\lambda_{gz}} + \frac{2\pi x}{\lambda_{gx}}\right) \quad (51b)$$

$$\dot{s} = \frac{qe_1}{m_e \gamma^3} \left[\cosh(ik_y y) \cos\left(\frac{2\pi s}{\lambda_{gz}} + \frac{2\pi x}{\lambda_{gx}}\right) - \cos \varphi_s \right]. \quad (51c)$$

One can observe that a bunch which is not significantly shorter than the grating period is accelerated in both positive and negative x-direction dependent on s . Therefore, a coherent deflection can only be obtained for extremely short bunches. In the following we assume no net acceleration, i.e., $\varphi_s = \pi/2$, and replace $s = \lambda_0 \varphi_s / 2\pi + \Delta s$. Since tilted gratings are outlined for the generation of wiggler radiation we restrict ourselves to the ultrarelativistic case ($\beta \rightarrow 1$) here. From Eq. (17) one finds $\pm ik_y = k_x = \omega/c \tan \alpha$, which simplifies the potential to

$$V = qe_1 \frac{\lambda_0}{2\pi} \cosh\left(\frac{\omega \tan \alpha}{c} y\right) \cos\left[\frac{\omega}{c} (\Delta s + x \tan \alpha)\right]. \quad (52)$$

The equations of motion become

$$\ddot{x} = \frac{qe_1}{m_e \gamma} \tan(\alpha) \cosh\left[\frac{\omega \tan \alpha}{c} y\right] \sin\left[\frac{\omega}{c} (\Delta s + x \tan \alpha)\right] \quad (53a)$$

$$\ddot{y} = \frac{-ik_y \lambda_{gz} qe_1}{2\pi m_e \gamma} \sinh\left[\frac{\omega \tan \alpha}{c} y\right] \cos\left[\frac{\omega}{c} (\Delta s + x \tan \alpha)\right] \quad (53b)$$

$$\ddot{\Delta s} = \frac{qe_1}{m_e \gamma^3} \cosh\left[\frac{\omega \tan \alpha}{c} y\right] \sin\left[\frac{\omega}{c} (\Delta s + x \tan \alpha)\right]. \quad (53c)$$

Injecting the beam with an offset $x_0 \ll \lambda_0/(4 \tan \alpha)$ results in a coherent oscillation around the x-axis with the longitudinal period

$$\lambda_u = \frac{2\pi c}{\sqrt{\frac{-2\pi q e_1}{m_e \gamma \lambda_0} \tan \alpha}} \quad (54)$$

for a particle with $\Delta s = y = 0$. In linearized fields, the oscillation amplitude is arbitrary. However, in the nonlinear fields, additionally to the longitudinal plane, we find “buckets” with a distance λ_{gx} also in the x-plane. These buckets split a ribbon beam which is large in x-direction into multiple beamlets, where the momentum spread acceptance is maximum at zero and vanishes at $\lambda_{gx}/2$, where integer multiples of λ_{gx} can be added.

V. APPLICATIONS

We apply our approach to similar experimental parameters as for the subrelativistic experiments at FAU Erlangen [3] and the relativistic experiments at SLAC [1,2]. Although the structures are idealized, the results are qualitatively recovered. As a next step, we show modifications and idealizations of the beam parameters, which outline the way to a microchip accelerator.

A. Subrelativistic acceleration

A subrelativistic DLA structure needs to be chirped in order to always fulfill the synchronicity condition (6) for the synchronous particle. The proper chirp for each cell and the synchronous velocity are obtained by iterating the two equations

$$\Delta z^{(n+1)} = \frac{qe_1 \lambda_0^2 \cos \varphi_s^{(n)}}{m_e c^2} \sqrt{1 - \beta^{(n)2}} \quad (55)$$

$$\beta^{(n+1)} = \beta^{(n)} + \frac{\Delta z^{(n+1)}}{\lambda_0}. \quad (56)$$

The cell length and synchronous energies are

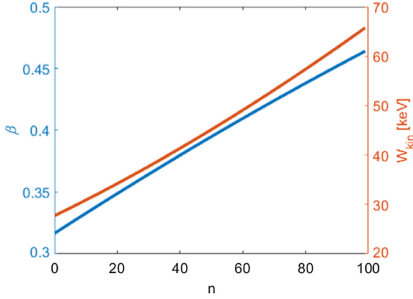


FIG. 11. Acceleration ramp according to Eqs. (56) and (58).

$$\lambda_g^{(n)} = \lambda_{g0} + \sum_{j=2}^n \Delta z^{(j-1)} \quad (57)$$

$$W_0^{(n)} = W_{\text{init}} + qe_1 \sum_{j=2}^n \cos \varphi_s^{(j-1)} \lambda_g^{(j-1)}. \quad (58)$$

In the following simulations, we assume that the construction of the grating was made such that the cells always fulfill Eq. (57). We start with very low energy electrons $W_{\text{kin}} = 27.7$ keV, i.e., $\beta = 0.3165$.

For $\lambda_0 = 1.96 \mu\text{m}$ the initial grating period is 620 nm. For simplicity we assume $e_1 = 1$ GV/m with zero phase for all cells. Aiming for a gradient of 500 MeV/m, the synchronous phase has to be 120 degree. The ramp according to these parameters is depicted in Fig. 11. Since the electron bunches in the experiments are significantly longer than the grating period, we look at initially unbunched beams with $\sigma_E = 10$ eV.

In free space, the full Rayleigh length (cf. Appendix) of the beam with assumed geometric emittance 1 nm at the aperture of $A = 200$ nm is $L_R = A^2/(4\epsilon_r) = 10 \mu\text{m}$, i.e., about 16 cells. This requires the optimal initial focusing angle of 20 mrad. However, as shown in Fig. 12, in the presence of strong acceleration defocusing forces, the waist appears earlier, i.e., in cell 4.

The particle loss and the energy spectrum are plotted in Fig. 13. The spectrum shows clearly that only a fraction of the particles is trapped in the bucket, the particles with

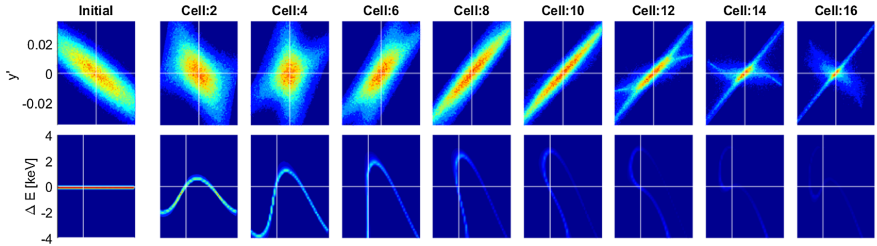


FIG. 12. Longitudinal (bottom) and transverse (top) phase space for 16 cells of the chirped grating with an initially unbunched beam, focused into the structure. The axes are $-100 \text{ nm} < y < 100 \text{ nm}$ and $0 < \varphi < 2\pi$. The color represents the phase space density, where the initial plots are normalized to their maximum and all other plots are normalized to the respective maxima of the second column.

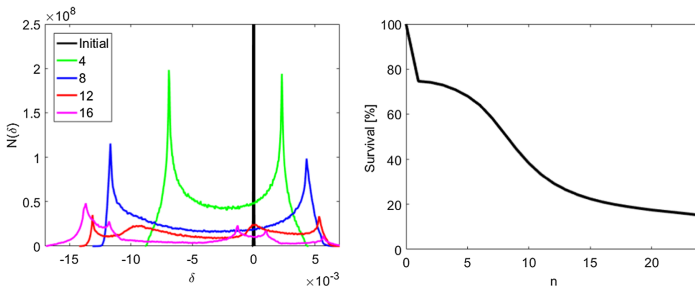


FIG. 13. Energy spectra and particle survival rate for the unbunched beam.

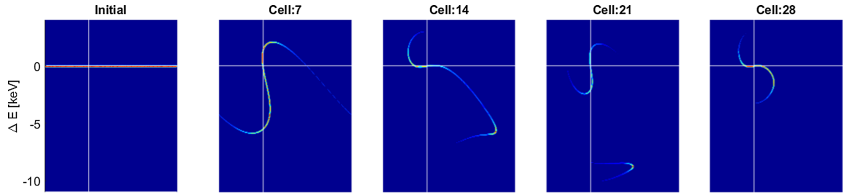


FIG. 14. Longitudinal phase space evolution for zero transverse emittance. The vertical axis is $0 < \varphi < 2\pi$.

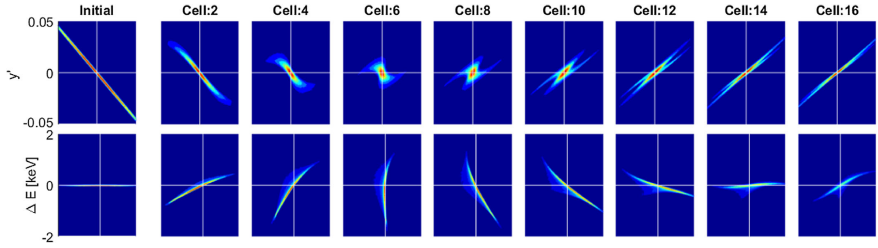


FIG. 15. Longitudinal (bottom) and transverse (top) phase space for 16 cells of the chirped grating with the beam initially focused into the structure. The axes are $-100 \text{ nm} < y < 100 \text{ nm}$ and $1.5 < \varphi < 2.6$. Again, the color represents the phase space density, normalized to the maximum of the second column.

$\delta \approx -13 \times 10^{-3}$ are lost, although they do not hit the aperture. The physical loss of particles happens when they reach the aperture in y -direction ($\pm 100 \text{ nm}$). The longitudinal bucket capture process is illustrated more clearly for zero transverse emittance in Fig. 14, where no transverse losses appear and a full synchrotron period is displayed.

As next step, we take a bunched beam with $\sigma_z = 30 \text{ nm}$ and a reduced transverse emittance of $\varepsilon_y = 0.1 \text{ nm}$. As shown in Fig. 15, the waist appears approximately at cell 7, when the beam is strongly focused initially with 45 mrad .

Without the acceleration defocusing, the Rayleigh length would be $100 \mu\text{m}$ at an initial focusing angle of 2 mrad . The bunch has initially again an energy spread of 10 eV , which is significantly smaller than the matched energy spread. Thus a coherent quadrupole oscillation appears, which is also visible in the energy spectrum in Fig. 16.

B. Relativistic acceleration

In this example we take the full aperture to be $A = 800 \text{ nm}$, $\lambda_g = \lambda_0 = 1.96 \mu\text{m}$, $|\underline{e}_1| = 1 \text{ GV/m}$, and

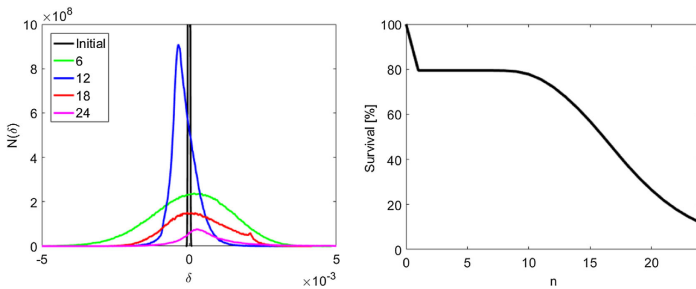


FIG. 16. Energy spectra and particle survival rate for a short low energy bunch.

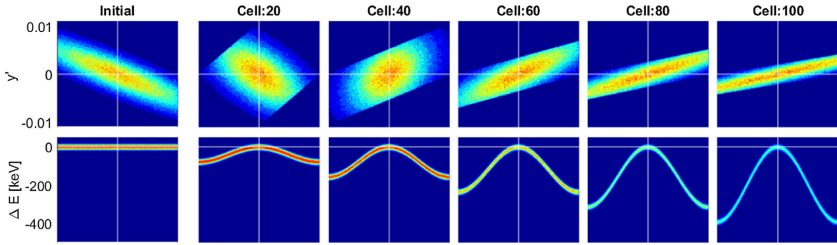


FIG. 17. Evolution of the y and z phase spaces. The axes are $-400 \text{ nm} < y < 400 \text{ nm}$ and $0 < \varphi < 2\pi$. Again, the color represents the phase space density, normalized to the second column.

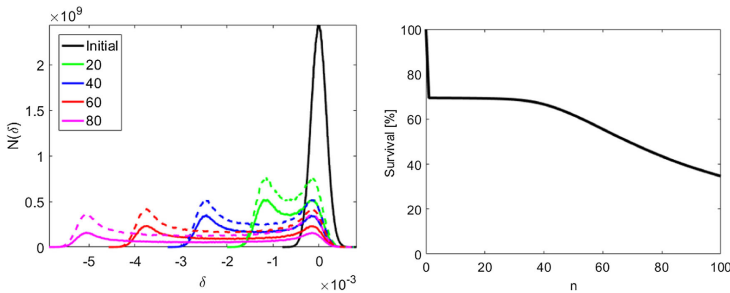


FIG. 18. Energy spectra with 1 nm (solid lines) and zero (dashed lines) transverse emittance normalized to the initial number of particles 10^6 (left) and particle survival rate (right).

the number of grating cells is 100. Taking the reference particle on-crest, i.e., $\varphi_s = \pi$, the design ramp is linear with a slope of 1 GeV/m. The incident electron beam has a bunch length significantly larger than the grating period and is again assumed as unbunched. The kinetic energy is 60 MeV and the spread is $\sigma_W = 10 \text{ keV}$. The spot size is taken as $\sigma_y = 400 \text{ nm}$ and the geometric emittance $\varepsilon_y = 1 \text{ nm}$. The full Rayleigh range is thus $L_R = A^2/(4\varepsilon_y) = 160 \mu\text{m}$, which is practically achieved when the beam is focused with 5 mrad into the structure. Figure 17 shows the evolution of the y and z phase spaces. The particle loss is monitored in Fig. 18, where the first jump is again the loss at the initial aperture. The plateau is within the Rayleigh range, however already before the end of the Rayleigh range the particles with excess momentum are being lost. Exactly at the Rayleigh range (after cell 81), the particle, that was initially the intersection of the ellipse diagonal with the aperture, is lost. The acceleration defocusing plays only a minor role for highly relativistic beams, i.e., the Rayleigh range is not significantly shortened. Figure 18 shows also the energy spectrum which becomes broader along the grating. This is due to particles being accelerated and decelerated according

to their phase. Such spectra were also practically measured in [1,2]. The dashed lines in the plot show the same spectra in the case of zero transverse emittance, where also no loss on the aperture occurs.

C. Dynamics in tilted gratings

Finally, we address the tilted grating with the same laser parameters and a bunched electron beam with parameters $\varepsilon_x = \varepsilon_y = 1 \text{ nm}$, $\sigma_x = 1 \mu\text{m}$, $\sigma_y = 0.4 \mu\text{m}$, $\sigma_z = 30 \text{ nm}$, $\sigma_W = 10 \text{ keV}$ and a focusing angle of 5 mrad in the y -direction. The grating tilt angle is 70 degrees and again $|\mathcal{E}_1| = 1 \text{ GV/m}$. Figure 19 shows the evolution of the phase space in all three planes. Evaluating Eq. (54), one finds $\lambda_d \approx 160\lambda_0$, i.e., half an oscillation period in the x -direction in the displayed 80 grating cells.

As visible in Fig. 19, the horizontal and longitudinal phase spaces are correlated. The projections of the energy spectrum can be seen in Fig. 20 together with the particle loss, which takes place at the physical aperture in y -direction at $\pm 400 \text{ nm}$. Unlike the straight grating with relativistic

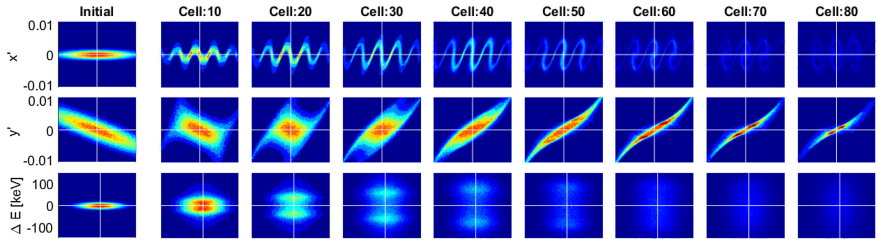


FIG. 19. Horizontal, vertical, and longitudinal phase space projection for every tenth cell. The axes are $-1.5\mu\text{m} < x < 1.5\mu\text{m}$, $-0.4\mu\text{m} < y < 0.4\mu\text{m}$ and $1.3 < \varphi < 1.8$. Again, the color represents the phase space density, normalized to the second column.

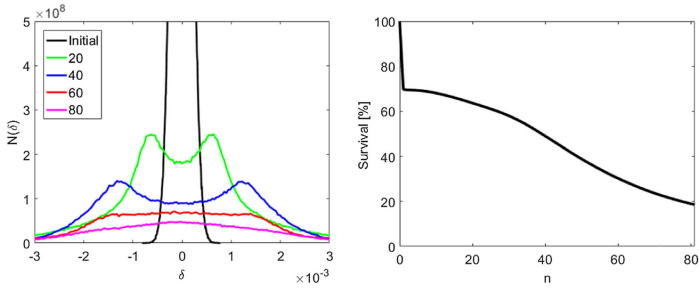


FIG. 20. Evolution of the energy spectrum and particle loss.

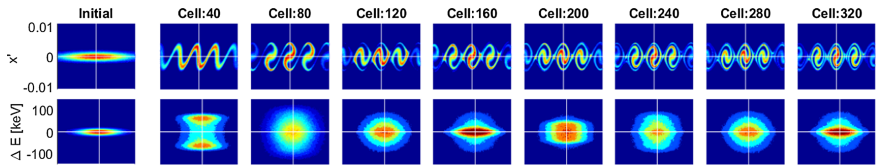


FIG. 21. Horizontal and longitudinal phase space for every fortieth cell for $\varepsilon_y = 0$. The axes are $-1.5\mu\text{m} < x < 1.5\mu\text{m}$ and $1.3 < \varphi < 1.8$. Two periods of transverse oscillations are visible [cf. Eq. (54)].

particles, the tilted grating creates a defocusing force in the y -direction which significantly decreases the Rayleigh range. The energy spread shows a breathing mode, similar to the quadrupole modes in the synchrotron motion. However, since the synchrotron motion is practically frozen due to the high γ , this mode arises entirely due to the correlation with the x -plane. Excluding the defocusing by setting $\varepsilon_y = 0$, two coherent oscillation periods are displayed in Fig. 21.

VI. CONCLUSION AND OUTLOOK

The laser fields in a periodic DLA grating can be represented by spatial Fourier harmonics, where only the resonant harmonic, which fulfills the Wideroe condition, provides a first order net kick. Exploiting this property, we showed that the entire 6D beam dynamics without collective effects can be modeled by applying kicks in all spatial directions once per grating period. These kicks are not independent, but analytically connected by the

Panofsky-Wenzel theorem. If the structure is not periodic, but slightly chirped (quasiperiodic), our approach is still applicable. However, fringe fields at the end of the structure are neglected.

As an example we introduced a novel Bragg-reflection based grating structure, which shows a particularly high first harmonic. The structure is discussed in [18,24] in more detail. Here we restrict ourselves in representing the grating structures by the one resonant Fourier coefficient, i.e., one complex number for each grating cell.

We also showed that our tracking approach still works for tilted gratings that have been proposed for beam deflection or optical undulators. However, in the case of curved gratings, which have been proposed for focusing, the fields cannot be determined analytically, since the decay constant is not uniform. In order to still use our tracking algorithm, the longitudinal kicks must be provided numerically for each pair of transverse coordinates.

Additionally to our fast, symplectic tracking approach, we also derived the Hamiltonian for the single particle motion in DLA structures. This allows analytical approaches to the 6D nonlinear and coupled equations of motion in DLA structures. In the case of constant synchronous phase, the longitudinal beam dynamics is identical to the one for conventional drift tube linacs. However, for longitudinally stable buckets, the transverse fields are always defocusing. Due to the high gradients in DLA, this strong defocusing cannot be compensated by ordinary means as magnets, which is particularly critical at low electron beam energy. At relativistic energies the full Rayleigh range of an externally focused beam can be reached, however this is also only in the range of several hundred microns.

In future a focusing scheme for DLA needs to be developed. One candidate is the proposed higher order harmonic focusing [17]. In order to simulate this with our code, the additional harmonic kicks would have to be implemented. The other candidate is alternating phase focusing (APF), which can be directly approached with our code. In this scheme the synchronous phase is alternated between longitudinally stable and unstable ranges, similarly as a FODO cell, but instead of x-y, rather in the y-z planes.

We plan to achieve such phase jumps by inserting drift sections as already outlined in Fig. 1. Other options are to modify the accelerating Fourier coefficient in each cell, e.g., by phase masking within the structure or by active phase control of individual parts of the laser pulse. In general, we believe that this paper gives a beam dynamics foundation on which DLA structures providing stable long distance beam transport schemes can be developed.

ACKNOWLEDGMENTS

The authors wish to thank Ingo Hofmann for proof-reading the manuscript. This work is funded by the Gordon and Betty Moore Foundation (Grant No. GBMF4744 to

Stanford) and the German Federal Ministry of Education and Research (Grant No. FKZ:05K16RDB).

APPENDIX: RAYLEIGH RANGE FOR LIGHT AND PARTICLE BEAMS

The Rayleigh range for a particle beam can be defined in the same way as for a light beam. The envelope of an externally focused beam is

$$w = w_0 \sqrt{1 + \left(\frac{z}{z_0}\right)^2}. \quad (\text{A1})$$

Inserting into the envelope equation

$$w'' = w^{-3} \quad (\text{A2})$$

results in $w_0 = \sqrt{z_0}$. The beam size is given by $a(z) = \sqrt{\epsilon} w(z)$ and thus the Rayleigh length is $z_0 = a_0^2/\epsilon$, where a_0 is the beam size at the waist. The beam size at the Rayleigh length, where it is limited by the aperture, is $a_1 = \sqrt{2}a_0$. The full Rayleigh range $L_R = 2z_0$ as function of the full aperture $A = 2a_1$ is thus

$$L_R = \frac{A^2}{4\epsilon}. \quad (\text{A3})$$

The same result is obtained for a light beam, where the emittance is identified with the wavelength, i.e., $\epsilon_{\text{light}} = \lambda_0/\pi$.

- [1] E. a. Peralta, K. Soong, R. J. England, E. R. Colby, Z. Wu, B. Montazeri, C. McGuinness, J. McNeur, K. J. Leedle, D. Walz, E. B. Sozer, B. Cowan, B. Schwartz, G. Travish, and R. L. Byer, Demonstration of electron acceleration in a laser-driven dielectric microstructure, *Nature (London)* **503**, 91 (2013).
- [2] K. P. Wootton, Z. Wu, B. M. Cowan, A. Hanuka, I. V. Makasyuk, E. A. Peralta, K. Soong, R. L. Byer, and R. J. England, Demonstration of acceleration of relativistic electrons at a dielectric microstructure using femtosecond laser pulses, *Opt. Lett.* **41**, 2696 (2016).
- [3] J. Breuer and P. Hommelhoff, Laser-Based Acceleration of Nonrelativistic Electrons at a Dielectric Structure, *Phys. Rev. Lett.* **111**, 134803 (2013).
- [4] K. J. Leedle, R. F. Pease, R. L. Byer, and J. S. Harris, Laser acceleration and deflection of 96.3 keV electrons with a silicon dielectric structure, *Optica* **2**, 158 (2015).
- [5] K. Shimoda, Proposal for an Electron Accelerator Using an Optical Maser, *Appl. Opt.* **1**, 33 (1962).
- [6] R. J. England *et al.*, Dielectric laser accelerators, *Rev. Mod. Phys.* **86**, 1337 (2014).
- [7] K. P. Wootton, J. McNeur, and K. J. Leedle, Dielectric Laser Accelerators: Designs, Experiments, and Applications, *Rev. Accel. Sci. Technol.* **09**, 105 (2016).
- [8] MathWorks, Matlab, (2016).

- [9] W. K. H. Panofsky and W. A. Wenzel, Some Considerations Concerning the Transverse Deflection of Charged Particles in Radio-Frequency Fields, *Rev. Sci. Instrum.* **27**, 967 (1956).
- [10] D. Cesar, S. Custodio, J. Maxson, P. Musumeci, X. Shen, E. Threlkeld, R. J. England, A. Hanuka, I. V. Makasyuk, E. A. Peralta, K. P. Wootton, and Z. Wu, arXiv:1707.02364.
- [11] H. K. Avetissian, *Relativistic Nonlinear Electrodynamics* (Springer, New York, 2016).
- [12] T. Plettner and R. L. Byer, Proposed dielectric-based microstructure laser-driven undulator, *Phys. Rev. ST Accel. Beams* **11**, 030704 (2008).
- [13] T. Plettner and R. L. Byer, Microstructure-based laser-driven free-electron laser, *Nucl. Instrum. Methods Phys. Res., Sect. A* **593**, 63 (2008).
- [14] T. Plettner, R. Byer, C. McGuinness, and P. Hommelhoff, Photonic-based laser driven electron beam deflection and focusing structures, *Phys. Rev. ST Accel. Beams* **12**, 101302 (2009).
- [15] A. Fallahi, A. Yahaghi, and F. X. Kärtner, arXiv:1612.03310.
- [16] CST, CST Studio Suite, (2016).
- [17] B. Naranjo, A. Valloni, S. Putterman, and J. B. Rosenzweig, Stable Charged-Particle Acceleration and Focusing in a Laser Accelerator Using Spatial Harmonics, *Phys. Rev. Lett.* **109**, 164803 (2012).
- [18] U. Niedermayer, O. Boine-Frankenheim, and T. Egenolf, Designing a Dielectric Laser Accelerator on a Chip, *J. Phys. Conf. Ser.* **874** 012041 (2017).
- [19] T. P. Wangler, *RF Linear Accelerators* (Wiley-VCH, Weinheim, 2008).
- [20] S. Earnshaw, On the nature of the molecular forces which regulate the constitution of the luminiferous ether, *Trans. Cambridge Philos. Soc.* **7**, 97 (1842).
- [21] F. Major, V. Gheorghie, and G. Werth, *Charged Particle Traps* (Springer, Heidelberg, 2005).
- [22] I. B. Fainberg, *Proc. CERN Symp. High Energy Accel Pion Phys.* (CERN, Geneva, 1956).
- [23] A. Hofmann and F. Pedersen, Bunches with Local Elliptic Energy Distributions, *IEEE Trans. Nucl. Sci.* **26**, 3526 (1979).
- [24] T. Egenolf, O. Boine-Frankenheim, and U. Niedermayer, Simulation of DLA grating structures in the frequency domain, *J. Phys. Conf. Ser.* **874** 012040 (2017).

Alternating-Phase Focusing for Dielectric-Laser AccelerationUwe Niedermayer,^{1,*} Thilo Egenolf,¹ Oliver Boine-Frankenheim,^{1,3} and Peter Hommelhoff²¹*Technische Universität Darmstadt, Schlossgartenstrasse 8, D-64289 Darmstadt, Germany*²*Department Physik, Friedrich-Alexander-Universität Erlangen-Nürnberg (FAU), Staudtstrasse 1, D-91058 Erlangen, Germany*³*GSI Helmholtzzentrum für Schwerionenforschung GmbH, Planckstrasse 1, D-64291 Darmstadt, Germany*

(Received 13 June 2018; published 20 November 2018)

The concept of dielectric-laser acceleration provides the highest gradients among breakdown-limited (nonplasma) particle accelerators. However, stable beam transport and staging have not been shown experimentally yet. We present a scheme that confines the beam longitudinally and in one transverse direction. Confinement in the other direction is obtained by a single conventional quadrupole magnet. Within the small aperture of 420 nm we find the matched distributions, which allow an optimized injection into pure transport, bunching, and accelerating structures. The combination of these resembles the photonics analogue of the radio frequency quadrupole, but since our setup is entirely two dimensional, it can be manufactured on a microchip by lithographic techniques. This is a crucial step towards relativistic electrons in the MeV range from low-cost, handheld devices and connects the two fields of attosecond physics and accelerator physics.

DOI: 10.1103/PhysRevLett.121.214801

Since dielectric-laser acceleration (DLA) of electrons was proposed in 1962 [1,2], the development of photonic nanostructures and the control of ultrashort laser pulses has advanced significantly (see Ref. [3] for an overview). Phase synchronous acceleration was experimentally demonstrated first in 2013 [4,5]. Damage threshold limited record gradients, more than an order of magnitude higher than in conventional accelerators, were achieved meanwhile for both relativistic [6] and low-energy electrons [7]. These gradients, so far, express themselves only in the generation of energy spread, not as a coherent acceleration. Moreover, the interaction length is limited to the Rayleigh length, after which the electron beam defocuses and hits the small (submicrometer) aperture. During synchronous acceleration, there are additional defocusing forces which cannot be overcome by magnetic focusing only [8] since equivalent magnetic focusing gradients would have to be in the MT/m range [9].

In this Letter we solve this outstanding problem with a laser-based scheme which allows transport and acceleration of electrons in dielectric nanostructures over arbitrary lengths. It is applicable to changing DLA period lengths, which is required to accelerate subrelativistic electrons. Moreover, we find the maximum tolerable emittances and beam envelopes in DLA beam channels. Another substantial advancement of our scheme is ballistic bunching of

subrelativistic electrons down to attosecond duration, while the beam remains transversely confined. Thus, our scheme makes DLA scalable, which paves the way for a low-cost accelerator on a microchip, providing electrons in the MeV range from a small-scale, potentially handheld device.

Our scheme uses only one spatial harmonic, namely, the synchronous one, but its magnitude and phase change along the DLA grating. This is interpreted as a time dependent focusing potential. A focusing concept using nonsynchronous spatial harmonics of traveling waves was presented by Naranjo *et al.* [10]. They derived stability due to retracting ponderomotive forces from the nonsynchronous spatial harmonics, while the synchronous one serves for acceleration. Our description is in the comoving real space, as compared to Naranjo's description in the spatial frequency domain. This supports changes of all grating-related quantities, while the Courant-Snyder (CS) theory [11] from conventional accelerator physics is still applicable. Stable beam confinement is achieved by alternating-phase focusing (APF), which had already been developed in the 1950s for ion acceleration [12–14]. However, the later developed radio frequency quadrupole (RFQ) cavities turned out to have better performance, especially for high current beams. Thus, APF was rejected in favor of the RFQ and was only rarely implemented [14]. In the 1980s APF was also proposed for grating-based linacs [15–18], but these three-dimensional designs are hardly feasible at optical wavelengths. Since 3D structures such as RFQs or rotated gratings are not feasible for lithographic fabrication on a microchip, we present an entirely two-dimensional APF scheme in this Letter, enabling stable and almost lossless electron transport in high-gradient DLA.

Published by the American Physical Society under the terms of the Creative Commons Attribution 4.0 International license. Further distribution of this work must maintain attribution to the author(s) and the published article's title, journal citation, and DOI.

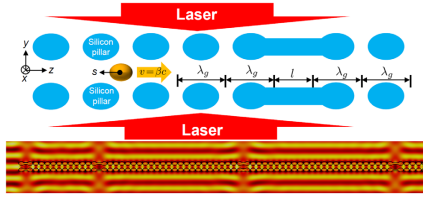


FIG. 1. (Top panel) Schematic view of a dual pillar DLA structure and a particle bunch around a reference particle and (bottom panel) simulation of the longitudinal time harmonic electric field.

We use standing wave dual pillar structures [7] as shown in Fig. 1, but our scheme can also be applied to Bragg cavity structures [19]. The z -polarized lasers, incident from both lateral sides, are modeled as plane waves with wavelength $\lambda_0 = 2 \mu\text{m}$. In practice, they can be realized as pulse-front-tilted profiles [20–23] or on-chip wave guide systems [24]; see the Supplemental Material [9] for details. The tilted pulses appear to a single or a few electron bunches as a plane wave; however, the pulse duration impinging on each pillar is significantly reduced, and thus the damage threshold field strength is increased [25,26]. The Hamiltonian for single particle motion in the DLA is [27]

$$H = \frac{1}{2m_e\gamma} [p_x^2 + p_y^2 + (\Delta p_z/\gamma)^2] + V, \quad (1)$$

where $\gamma = (1 - \beta^2)^{-1/2}$ is the reference mass factor, m_e the electron mass, p_x, p_y the transverse momenta, and Δp_z the deviation of longitudinal momentum from the reference particle at fixed laser phase (the black dot in Fig. 1). In [27] we showed by means of the Panofsky-Wenzel theorem [28] that the time dependent potential can be written as (see also the Supplemental Material [9])

$$V = q\text{Im} \left\{ e_1 \left[\frac{\lambda_y}{2\pi} \cosh\left(\frac{\omega y}{\beta\gamma c}\right) e^{2\pi i s/\lambda_y} - i s e^{i\varphi_s} \right] \right\}, \quad (2)$$

where $\omega = 2\pi c/\lambda_0$ is the laser angular frequency, q is the (negative) electron charge, and s is the distance of the particle behind the reference particle. The field strength of the resonant harmonic with the Wideroe condition $\lambda_y = \beta\lambda_0$ is e_1 ; i.e., with no loss of generality we work with the first (usually the strongest) spatial harmonic. The parameters $e_1, \varphi_s, \beta, \gamma$, and λ_y are allowed to vary with the timelike cell index n . The synchronous phase φ_s determines the energy gain of the reference particle as a function of the cell number (the acceleration ramp) as

$$W_{\text{kin}}(N) = W_{\text{kin},0} + q \sum_{n=1}^N \lambda_y^{(n)} \text{Re}\{e_1^{(n)} e^{i\varphi_s^{(n)}}\}, \quad (3)$$

where $W_{\text{kin},0} = 83 \text{ keV}$ is the injection energy. The cell lengths increase according to the Wideroe condition as

$$\frac{\lambda_y^{(n+1)} - \lambda_y^{(n)}}{\lambda_0} = \beta^{(n+1)} - \beta^{(n)} = \frac{q\lambda_0 \text{Re}\{e_1^{(n)} e^{i\varphi_s^{(n)}}\}}{m_e c^2 \gamma^{(n)^3}}.$$

For a given structure the synchronous phase is thus determined as $\varphi_s^{(n)} = \varphi_0 - \arg(e_1)^{(n)}$, where

$$\varphi_0 = \arccos\left(\frac{m_e c^2 \gamma^3 \Delta\lambda_y}{q\lambda_0 |e_1| \lambda_0}\right). \quad (4)$$

In this Letter we use optimized structures which provide φ_0 independent of n at an arbitrary chirp parameter $\Delta\lambda_y$, such that the synchronous phase φ_s can be switched by a particular drift from one grating segment to another. Tying the phase $\arg(e_1)^{(n)}$ to $\lambda_y^{(n)}$ does not avoid a small drift in the normalized amplitude $|e_1^{(n)}/E_L| \approx 0.34 \dots 0.39$ (see the Supplemental Material [9]), which is taken into account in the ramp [Eq. (3)].

Earnshaw's theorem dictates that constant focusing cannot be achieved in all three spatial directions simultaneously [29]. Thus, at least two focusing directions have to be alternating. In conventional Alvarez linacs or in synchrotrons constant focusing is applied in the longitudinal direction and alternating quadrupole lattices provide transverse confinement [30]. In our APF scheme, we apply the alternation to the disjoint focusing phase ranges of the longitudinal plane and the noninvariant transverse plane (y). Jumping the reference particle by means of a fractional cell drift between the orange circles in Fig. 2 provides stable transport at constant energy, and between the red dots we additionally obtain acceleration. The strong acceleration defocusing in y is compensated by acceleration focusing at the longitudinally unstable phase. In the invariant x direction a single conventional quadrupole magnet [9] suffices to confine the beam to an area in the center of the structure height, where the laser fields are homogeneous, i.e., do not depend on x .

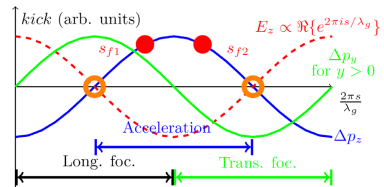


FIG. 2. Overview of electron acceleration and focusing properties as a function of phase. The circles denote the fixed points for different φ_s .

We find the fixed points of the motion by setting $\nabla V = 0$ as $s_{f1} = \varphi_s \lambda_g / 2\pi$ and $s_{f2} = -\lambda_g / 2\pi [\varphi_s + 2 \arg(e_1)]$ and define $\Delta s_1 = s - s_{f1}$ and $\Delta s_2 = s - s_{f2}$. Note that in the longitudinal plane for $\arg(e_1) = 0$ the fixed point s_{f1} is elliptic and s_{f2} is hyperbolic, and vice versa in the transverse plane. Expanding V to second order and omitting constant terms shows the APF principle:

$$V(x, y, s = s_{f1} + \Delta s) = -V(x, y, s = s_{f2} + \Delta s) \\ = \frac{q|e_1|\lambda_g}{2\pi} \left[\frac{1}{2} \left(\frac{\omega y}{\beta \gamma c} \right)^2 - \frac{1}{2} \left(\frac{2\pi}{\lambda_g} \Delta s \right)^2 \right] \sin(\varphi_0); \quad (5)$$

i.e., switching between s_{f1} and s_{f2} with $\Delta s = \Delta s_1 = \Delta s_2$ flips the sign of the potential. Only the nonaccelerating case ($\varphi_0 = \pi/2$) provides two interchangeable buckets, whereas a π -shifted version of the accelerating bucket will be decelerating and unstable due to a mismatch with the ramp. Hill's equations of the linearized motion are found from Eqs. (1) and (5) as

$$y'' + Ky = 0, \quad (6a)$$

$$\Delta s'' - K\Delta s = 0, \quad (6b)$$

where $K = |q\omega e_1 / (m_0 \beta^3 \gamma^3 c^3)| \sin(\varphi_s)$. Note that linearization leads to decoupling of the nonlinear equations of motion, which are coupled due to Eq. (2). The segments between two phase shifts are enumerated by P such that

$$\arg(e_1)(P) = \begin{cases} 0, & P \text{ odd,} \\ 2\varphi_0, & P \text{ even} \end{cases} \quad (7)$$

leads to a sign alternation in the focusing function K in Eq. (6). In order to switch between the two fixed points we take short drift sections denoted by l and model the lattice as thick lenses of lengths L^f and L^d . Each lattice cell consists of two segments and has p transverse focusing and p transverse defocusing elements; thus, its length is given by $L = L^f + l^f + L^d + l^d$, where

$$L^f = \sum_{n=1}^p \lambda_g^{(n)}, \quad L^d = \sum_{n=p+1}^{2p} \lambda_g^{(n)}, \quad (8a)$$

$$l^f = (2\pi - \varphi_s^{(p)}) \lambda_g^{(p)} / \pi, \quad l^d = (\pi - \varphi_s^{(2p)}) \lambda_g^{(2p)} / \pi. \quad (8b)$$

The solution to Eq. (6) is found by applying the CS formalism [11] to the channel of thick focusing (F) and defocusing (D) elements. We start with a nonaccelerating transport structure, i.e., $\varphi_0 = \pi/2$, where the lattice cells are strictly periodic. In a long lattice cell ($p \gg 1$) we can neglect the drift sections and represent it as [9]

$$\mathbf{M}(z, L) = \begin{cases} \mathbf{M}_f(z), & 0 < z < L/2, \\ \mathbf{M}_d(z - L/2) \mathbf{M}_f(L/2), & L/2 < z < L, \end{cases}$$

with the length $L = (2p + 1)\lambda_g$. The phase advance per cell σ is given for a strictly periodic FD -cell by

$$\cos(\sigma) = \frac{1}{2} \text{Tr}\{\mathbf{M}(L, L)\} = \cos\left(\frac{\sqrt{K}L}{2}\right) \cosh\left(\frac{\sqrt{K}L}{2}\right).$$

The CS parameters $\eta = (\hat{\beta}, \hat{\alpha}, \hat{\gamma})^T$ are mapped from one point to another by the matrix \mathbf{T} (see the Supplemental Material [9]) and fulfill the eigenvector relation $\eta_e = \mathbf{T}\eta_e$ for their initial values. For small σ the constant $\hat{\beta}$ function in the smooth approximation is found from $(\hat{\beta}) = L/\sigma$. However, the most critical issue in DLA is to match a given emittance to the tiny aperture. Thus, the maximum of the $\hat{\beta}$ function, which appears at $L/4$, needs to be minimal (see Fig. 3). The only variable parameter in an experimental setup is the laser field strength. Its tuning range from maximal admissible beam size to the structure damage threshold [25,26] is indicated by the black arrow. The evolution of the transverse phase space is shown below, where the particles were initially arranged on a Cartesian grid and only the long-term surviving ones are displayed in red. For simplicity, this simulation starts at $L/4$ in order to avoid correlations in the conjugate variables. This plot uses zero bunch length, but stability is also attained for an unbunched beam; see the video in the Supplemental Material [9]. The blue ellipses indicate the strictly periodic linear case, which is slightly smaller in area due to the cosh potential in Eq. (2) being

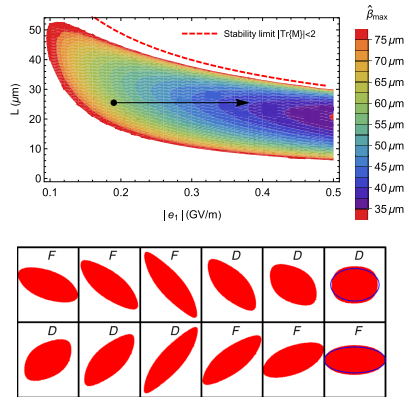


FIG. 3. (Top panel) Contours of $\hat{\beta}_{\max} = \hat{\beta}(L/4)$ in the $(|e_1|, L)$ plane. The arrow indicates the laser amplitude dependent tuning range. (Bottom panel) The transverse phase space evolution (parameters at the black dot on top) of particles, not hitting the aperture ($\pm 0.21 \mu\text{m}$) within 1200 DLA cells, is shown as every two DLA cells. The blue ellipses are the linear theory, at minimum and maximum beam size.

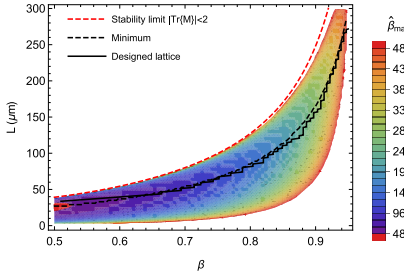


FIG. 4. Contours of $\hat{\beta}_{\max} = \hat{\beta}(L/4)$ in the (β, L) plane. The designed accelerator lattice is a trade-off between following the minimum and minimizing the mismatch at the jumps.

steeper than the square well in Eq. (5). In the linear case the single particle emittances are invariants

$$\varepsilon(y, y') = \hat{\gamma}y^2 + 2\hat{\alpha}yy' + \hat{\beta}y'^2, \quad (9a)$$

$$\varepsilon_L(\Delta s, \Delta s') = \hat{\gamma}_L\Delta s^2 + 2\hat{\alpha}_L\Delta s\Delta s' + \hat{\beta}_L\Delta s'^2, \quad (9b)$$

where $\Delta s' = \Delta W/(m_e c^3 \beta^2 c^2)$, and we introduce longitudinal CS functions as a half lattice cell shift of the transverse ones, $\eta_L(z) = \eta(z - L/2)$.

An accelerating lattice can be attained by taking the initial values from the eigenvalue solution and successively multiplying the segment maps as $\eta_N = \mathbf{T}_N \dots \mathbf{T}_1 \eta_0$ to it. In non-periodic lattices the longitudinal CS functions have to be calculated individually with the same procedure. If the change in length from one period to another is small, the $\hat{\beta}$ function can be approximated by the eigenvalue solution in each cell, which is, however, discontinuous at the boundaries. The line of increasing minimum of $\hat{\beta}_{\max}$ in Fig. 4 is followed only approximately. The increase is counteracted by

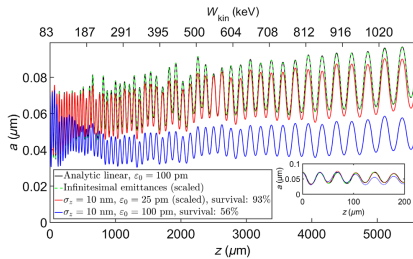


FIG. 5. Analytical [Eq. (10)] and numerical (rms) beam envelopes, scaled to identical initial beam size at $\varepsilon = 100$ pm. (Inset) Enlargement of the beginning.

adiabatic emittance damping due to momentum conservation. Altogether the beam envelope can be written as [30]

$$a(z) = \sqrt{\hat{\beta}(z) \frac{\varepsilon_0 \beta_0 \gamma_0}{\beta(z) \gamma(z)}}, \quad (10)$$

where the 0 indices denote initial values. Acceleration from 83 keV to 1 MeV at $\varphi_0 = 4\pi/3$, with an average gradient of 187 MeV/m and 500 MV/m incident laser field strength from both sides, is shown to be well confined within the physical aperture of $\pm 0.21 \mu\text{m}$ in Fig. 5. The analytical and numerical results coincide for infinitesimally low emittance. At small but achievable emittances [31,32], we obtain 56% transmission for $\varepsilon_0 = 100$ pm (see the video in the Supplemental Material [9]), and 93% for $\varepsilon_0 = 25$ pm. The phase space density at top energy is plotted in Fig. 6, where Φ_p and ΔW are the longitudinal coordinates in the comoving (Galilean) laboratory frame. As in Fig. 3, the initial particle positions in Fig. 6 (left panel) are arranged on a Cartesian grid, and only the ones that make it to 1 MeV are drawn in red. The blue ellipse corresponds to an initially matched bunch adjusted to the area of the surviving particles. Note that this size is slightly reduced at finite transverse emittance; thus, we choose $\sigma_z = 10$ nm. Below this bunch length the transmission depends only on the initial transverse emittance, i.e., is fully scalable.

The APF scheme discussed here can also be used to attain the bunching needed to inject into the accelerator structure. Creating and removing sinusoidal energy spread (see the Supplemental Material [9] and the video therein) results in extremely short (attosecond) bunch lengths at acceptably low energy spread. The phase alternation additionally provides transverse confinement, which can be matched to the initial CS functions of the accelerator. The particles not captured are defocused, while the captured ones remain at small longitudinal and transverse amplitudes, within the limits of Liouville's theorem. The phase

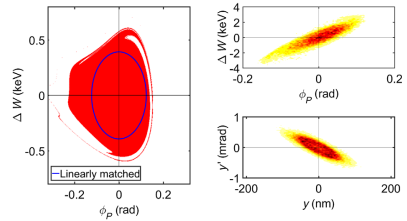


FIG. 6. (Right panels) Phase space after acceleration of a Gaussian bunch up to 1 MeV and (left panel) transmittable initial longitudinal distribution at 83 keV for $y = y' = 0$. The blue ellipse represents a linearly matched bunch with a total bunch length $4\sigma_z = 40$ nm.

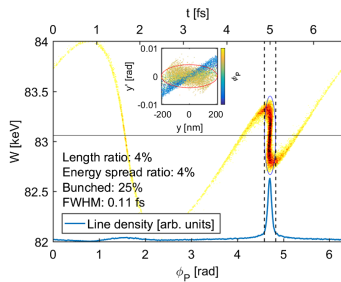


FIG. 7. Periodic longitudinal phase space after APF bunching. The initial beam parameters for the accelerator given by the ellipses are met. The small plot shows the transverse phase space, where the particle phase is color coded.

space after the buncher is plotted in Fig. 7. Both ellipses are matched for the injection into the accelerator (the blue ellipses in Figs. 7 and 6 are identical). Before the buncher the energy spread is $\sigma_{\Delta W} = 16$ eV. The initial longitudinal emittance equals the final one in the ellipse which has 25% of the particles captured. The duration is decreased to 4% (≈ 260 as), whereas the energy spread is increased by the same ratio. The initial CS functions are determined by inverse mapping of the desired final values for the accelerator. Additionally to the injection into DLAs, these short bunches are also very promising for ultrafast time-resolved electron microscopy.

In conclusion, we developed a scheme that makes DLA fully scalable. We showed for the first time how a focusing lattice, which relies on APF only, can be integrated. The entire accelerator or parts such as a single focusing stage or the buncher can now be experimentally approached. Acceleration of sub-100 keV electrons from readily available sources up to the MeV range with gradients of several 100 MeV/m works with transmission rates well above 90%. The admissible synchronous phase is determined by the available bunch length at injection. We showed that controlling this nonlinear dependence is crucial to avoiding particle loss. Our bunching scheme provides the required atosecond bunches with the matched energy spread and a reasonable capture rate of 25%. In principle, fully adiabatic bunching as in the RFQ is also possible. This would, however, require a larger total length. The APF scheme can also be scaled to higher energies, where smaller beam size and larger physical apertures due to longer roll-off of the evanescent acceleration fields will ease the requirements.

U. N. would like to thank Holger Podlech for the discussions on APF. This work is funded by the Gordon and Betty Moore Foundation (Grant No. GBMF4744) and the German Federal Ministry of Education and Research (Grant No. FKZ: 05K16RDB).

- niedermayer@temf.tu-darmstadt.de
- [1] K. Shimoda, *Appl. Opt.* **1**, 33 (1962).
 - [2] A. Lohmann, IBM Technical Note 5, 169, 1962.
 - [3] R. J. England *et al.*, *Rev. Mod. Phys.* **86**, 1337 (2014).
 - [4] E. A. Peralta, K. Soong, R. J. England, E. R. Colby, Z. Wu, B. Montazeri, C. McGuinness, J. McNeur, K. J. Leedle, D. Walz, E. B. Sozer, B. Cowan, B. Schwartz, G. Travish, and R. L. Byer, *Nature (London)* **503**, 91 (2013).
 - [5] J. Breuer and P. Hommelhoff, *Phys. Rev. Lett.* **111**, 134803 (2013).
 - [6] K. P. Wootton, Z. Wu, B. M. Cowan, A. Hanuka, I. V. Makasyuk, E. A. Peralta, K. Soong, R. L. Byer, and R. J. England, *Opt. Lett.* **41**, 2696 (2016).
 - [7] K. J. Leedle, A. Ceballos, H. Deng, O. Solgaard, R. F. Pease, R. L. Byer, and J. S. Harris, *Opt. Lett.* **40**, 4344 (2015).
 - [8] A. Ody, P. Musumeci, J. Maxson, D. Cesar, R. J. England, and K. P. Wootton, *Nucl. Instrum. Methods Phys. Res., Sect. A* **865**, 75 (2017).
 - [9] See Supplemental Material at <http://link.aps.org/supplemental/10.1103/PhysRevLett.121.214801> for mathematical/technical details and movies.
 - [10] B. Naranjo, A. Valloni, S. Putterman, and J. B. Rosenzweig, *Phys. Rev. Lett.* **109**, 164803 (2012).
 - [11] E. Courant and H. Snyder, *Ann. Phys. (N.Y.)* **3**, 1 (1958).
 - [12] I. B. Fainberg, in *Proceedings of the 1st International Conference on High-Energy Accelerators (HEACC), Geneva, 1956*, edited by E. Regenstein (CERN, Geneva, 1956).
 - [13] P. Lapostolle, Los Alamos Technical Report No. 11601, 1989.
 - [14] T. P. Wangler, *RF Linear Accelerators* (Wiley-VCH, Weinheim, 2008).
 - [15] R. B. Palmer, *Part. Accel.* **11**, 81 (1980).
 - [16] R. B. Palmer, *AIP Conf. Proc.* **91**, 179 (1982).
 - [17] K. Kim and N. Kroll, Lawrence Berkeley Laboratory Report No. LBL-14378, 1982.
 - [18] M. Pickup, Report No. CLNS-85/655, 1985.
 - [19] U. Niedermayer, O. Boine-Frankenheim, and T. Egenolf, *J. Phys. Conf. Ser.* **874**, 012041 (2017).
 - [20] Y. Wei, M. Ibsen, G. Xia, J. D. A. Smith, and C. P. Welsch, *Appl. Opt.* **56**, 8201 (2017).
 - [21] D. D. Cesar, J. Maxson, X. Shen, K. P. Wootton, S. Tan, R. J. England, and P. Musumeci, *Nucl. Instrum. Methods Phys. Res., Sect. A* (to be published).
 - [22] D. Cesar, J. Maxson, X. Shen, K. P. Wootton, S. Tan, R. J. England, and P. Musumeci, *Opt. Express* **26**, 29216 (2018).
 - [23] M. Kozák, J. McNeur, N. Schönenberger, J. Illmer, A. Li, A. Tafel, P. Yousefi, T. Eckstein, and P. Hommelhoff, *J. Appl. Phys.* **124**, 023104 (2018).
 - [24] T. W. Hughes, S. Tan, Z. Zhao, N. V. Saprà, K. J. Leedle, H. Deng, Y. Miao, D. S. Black, O. Solgaard, J. S. Harris, J. Vuckovic, R. L. Byer, S. Fan, R. J. England, Y. J. Lee, and M. Qi, *Phys. Rev. Applied* **9**, 054017 (2018).
 - [25] P. P. Pronko, P. A. Van Rompay, C. Horvath, F. Loesel, T. Juhasz, X. Liu, and G. Mourou, *Phys. Rev. B* **58**, 2387 (1998).
 - [26] K. Soong, R. L. Byer, E. R. Colby, R. J. England, and E. A. Peralta, *AIP Conf. Proc.* **1507**, 511 (2012).

- [27] U. Niedermayer, T. Egenolf, and O. Boine-Frankenheim, *Phys. Rev. Accel. Beams* **20**, 111302 (2017).
- [28] W. K. H. Panofsky and W. A. Wenzel, *Rev. Sci. Instrum.* **27**, 967 (1956).
- [29] S. Earnshaw, *Trans. Cambridge Philos. Soc.* **7**, 97 (1842).
- [30] S. Y. Lee, *Accelerator Physics* (World Scientific, Singapore, 2004).
- [31] D. Ehberger, J. Hammer, M. Eisele, M. Krüger, J. Noe, A. Högele, and P. Hommelhoff, *Phys. Rev. Lett.* **114**, 227601 (2015).
- [32] A. Feist, N. Bach, N. Rubiano da Silva, T. Danz, M. Möller, K. E. Priebe, T. Domröse, J. G. Gatzmann, S. Rost, J. Schauss, S. Strauch, R. Bormann, M. Sivis, S. Schäfer, and C. Ropers, *Ultramicroscopy* **176**, 63 (2017).

Supplemental Material

Uwe Niedermayer,^{1,*} Thilo Egenolf,¹ Oliver Boine-Frankenheim,^{1,2} and Peter Hommelhoff³

¹ *Technische Universität Darmstadt, Schlossgartenstrasse 8, D-64289 Darmstadt, Germany*

² *GSI Helmholtzzentrum für Schwerionenforschung GmbH, Planckstrasse 1, D-64291 Darmstadt, Germany*

³ *Department Physik, Friedrich-Alexander-Universität Erlangen-Nürnberg (FAU), Staudtstrasse 1, D-91058 Erlangen, Germany*

(Dated: November 12, 2018)

DERIVATION OF THE TIME-DEPENDENT POTENTIAL

We start by citing the kicks in each DLA cell from Eq. 26 in [1] as

$$\Delta x' = -\frac{q\lambda_0}{p_{z0}c} \tan(\alpha) \cosh(ik_y y) \operatorname{Re} \left\{ \varepsilon_1 e^{i\varphi + i\frac{2\pi x}{\lambda_{gx}}} \right\} \quad (1a)$$

$$\Delta y' = \frac{-ik_y \lambda_0^2 q \beta}{2\pi p_{z0} c} \sinh(ik_y y) \operatorname{Im} \left\{ \varepsilon_1 e^{i\varphi + i\frac{2\pi x}{\lambda_{gx}}} \right\} \quad (1b)$$

$$\Delta \delta = \frac{q\lambda_{gz}}{\gamma m_e c^2} \operatorname{Re} \left\{ \varepsilon_1 \left(\cosh(ik_y y) e^{i\varphi + i\frac{2\pi x}{\lambda_{gx}}} - e^{i\varphi_s} \right) \right\}, \quad (1c)$$

where $\varphi = 2\pi s/\lambda_g$. For a nontilt ($\alpha = 0$ and $\lambda_{gx} \rightarrow \infty$) DLA grating we have $k_y = i\omega/(\beta\gamma c)$ (see Eq. 17 in [1]) and the kicks simplify to

$$\Delta x' = 0 \quad (2a)$$

$$\Delta y' = \frac{2\pi q}{\omega\gamma p_{z0}} \sinh\left(\frac{\omega y}{\beta\gamma c}\right) \operatorname{Im} \left\{ \varepsilon_1 e^{2\pi is/\lambda_g} \right\} \quad (2b)$$

$$\Delta \delta = \frac{q\lambda_{gz}}{\gamma m_e c^2} \operatorname{Re} \left\{ \varepsilon_1 \left(\cosh\left(\frac{\omega y}{\beta\gamma c}\right) e^{2\pi is/\lambda_g} - e^{i\varphi_s} \right) \right\}. \quad (2c)$$

In the limit of infinitely short DLA cells and infinitely small kicks, the forces can be written as

$$\dot{p}_y \simeq \frac{\Delta p_y}{\Delta t} = \frac{cp_{z0}}{\lambda_0} \Delta y' \quad (3a)$$

$$\dot{\Delta p}_z \simeq \frac{\Delta(\Delta p_z)}{\Delta t} = \frac{W_0}{\beta\lambda_0} \Delta \delta, \quad (3b)$$

which is still a good approximation at small but finite sized DLA cells and kicks in each laser period $\Delta t = \lambda_0/c$. Inserting Eqs. 2 into Eqs. 3, manipulations and integration finally yield

$$V = q\operatorname{Im} \left\{ \varepsilon_1 \left[\frac{\lambda_g}{2\pi} \cosh\left(\frac{\omega y}{\beta\gamma c}\right) e^{2\pi is/\lambda_g} - i s e^{i\varphi_s} \right] \right\}, \quad (4)$$

which can be easily proven by calculating $\vec{F} = -\nabla V$, i.e., $\dot{p}_y = -\partial_y V$ and $\Delta p_z = \partial_s V$. This derivation follows [1], but without making any restrictions on $\arg(\varepsilon_1)$. Since the kicks in Eq. 2 can change parametrically in every DLA cell, so can the potential Eq. 4.

LASER PULSE SHAPING

The scalability of laterally coupled DLAs depends on a laser power delivery system, which has to provide short pulse lengths to each DLA cell independently of the total length of the accelerator structure. One option would be to include the laser power delivery system on the chip by means of waveguides with properly tailored delay [2], another would be to work with tilted pulses in free space. Pulse front tilt is achieved by using gratings that provide reflection with unequal incident and reflection angles and has enormous potential for DLA [3–6]. The pulse length impinging to a single structure pillar is 100 fs, depending only on the bandwidth of the structure and the number of bunches one wishes to accelerate per laser pulse. This does not only ease the damage constraint but also the laser pulse energy requirement. The damage threshold field for Silicon is about 2 GV/m for 100 fs pulses at $\lambda_0 = 1.06\ \mu\text{m}$ [7]. Since Soong et al. [8] indicate that the damage threshold does not vary more than a factor of 2 between 1 μm and 2 μm wavelength, we assume to be close but below the damage threshold when the field strength is 500 MV/m from both lateral sides. The laser pulse energy requirement is $W_L \approx 2\varepsilon_0 E_L^2 \cdot h \cdot L \cdot ct = 13.2\ \mu\text{J}$ for the parameters $E_L = 500\ \text{MV/m}$, $h = 20\ \mu\text{m}$, $t = 100\ \text{fs}$, and $L = 5\ \text{mm}$. Such pulses can be generated by optical parametric amplifiers (OPA) or directly by novel Tm- or Ho-Tm fiber laser amplifiers. The efficiency under the assumption of 10 bunches with each having the charge of 1 fC results in about $7 \cdot 10^{-4}$. If higher efficiency is required, techniques of laser radiation energy recovery can be employed [9]. Plasma based accelerators reach significantly higher bunch charges and thus also higher efficiencies, but their bunch size and repetition rate parameters are completely different such that we do not attempt a comparison here.

MATRIX FORMALISM AND EIGENVALUE PROBLEM FOR STRICTLY PERIODIC CELLS

Conjugate particle coordinates can be mapped from one point to another by [10]

$$\begin{bmatrix} y(z) \\ y'(z) \end{bmatrix} = \mathbf{M}(z|z_0) \begin{bmatrix} y(z_0) \\ y'(z_0) \end{bmatrix}, \quad (5)$$

For simplicity, we choose $z_0 = 0$ and either remove the second argument of \mathbf{M} completely, or replace it by the total length of a focusing cell L . Thick focusing, defocusing and drift elements can be written as matrices [10]

$$\mathbf{M}_f(z) = \begin{bmatrix} \cos(\sqrt{K}z) & \frac{1}{\sqrt{K}} \sin(\sqrt{K}z) \\ -\sqrt{K} \sin(\sqrt{K}z) & \cos(\sqrt{K}z) \end{bmatrix}, \quad (6a)$$

$$\mathbf{M}_d(z) = \begin{bmatrix} \cosh(\sqrt{K}z) & \frac{1}{\sqrt{K}} \sinh(\sqrt{K}z) \\ \sqrt{K} \sinh(\sqrt{K}z) & \cosh(\sqrt{K}z) \end{bmatrix}, \quad (6b)$$

$$\mathbf{M}_o(z) = \begin{bmatrix} 1 & z \\ 0 & 1 \end{bmatrix}, \quad (6c)$$

respectively. The total map of a section of an accelerator is the proper product of those, labeled by \mathbf{M} . The Courant-Snyder parameters $\eta = (\hat{\beta}, \hat{\alpha}, \hat{\gamma})^T$ can be mapped in the same manner from one point to another by [10]

$$\mathbf{T} = \begin{bmatrix} \mathbf{M}_{11}^2 & -2\mathbf{M}_{11}\mathbf{M}_{12} & \mathbf{M}_{12}^2 \\ -\mathbf{M}_{11}\mathbf{M}_{21} & \mathbf{M}_{11}\mathbf{M}_{22} + \mathbf{M}_{12}\mathbf{M}_{21} & -\mathbf{M}_{12}\mathbf{M}_{22} \\ \mathbf{M}_{21}^2 & -2\mathbf{M}_{21}\mathbf{M}_{22} & \mathbf{M}_{22}^2 \end{bmatrix},$$

where the indices denote a rearrangement of the components of \mathbf{M} . Introducing a third equation leads to a certain redundancy, which is expressed by [10]

$$\hat{\beta}\hat{\gamma} - \hat{\alpha}^2 = 1. \quad (7)$$

A periodic focusing channel requires the Courant-Snyder parameters η_e at the boundary (entry and exit of a cell) to fulfill $\eta_e = \mathbf{T}\eta_e$, i.e., they are the components of the eigenvector to the eigenvalue 1 of \mathbf{T} , which are determined by symbolic computer algebra [11]. The eigenvector scaling constant is fixed by demanding η to fulfill Eq. 7 and $\hat{\beta} > 0$. The focusing channel should be opti-

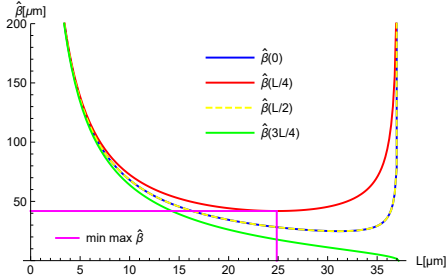


FIG. 1. Optimal length for minimal maximum of $\hat{\beta}(z)$ for $\epsilon_1 = 0.345 \times 2 \times 0.5$ GV/m. Due to the symmetry of the FD-cell, the maximum appears at $L/4$, the minimum appears at $3L/4$, and the $\hat{\beta}$ -function at 0, $L/2$, and L is identical.

mized such that the maximum with respect to z of the

$\hat{\beta}$ -function becomes minimal with respect to L . From the symmetry of a $\mathbf{M}_d(L/2)\mathbf{M}_f(L/2)$ cell, it is obvious that this maximum appears at $L/4$, thus L should be chosen such that $\hat{\beta}(L/4) \rightarrow \min$, see Fig. 1. In this way, the envelope [10]

$$a(z) = \sqrt{\hat{\beta}(z)\epsilon}, \quad (8)$$

is minimized and thus the number of particles transported from a Gaussian distribution is maximized.

Once the Courant-Snyder functions are determined, linearly matched Gaussian distributions are obtained from the Courant-Snyder invariants at any position as

$$f(y, y') = \frac{1}{2\pi\epsilon} e^{-\frac{1}{2\epsilon}(\hat{\gamma}y^2 + 2\hat{\alpha}yy' + \hat{\beta}y'^2)} \quad (9a)$$

$$f(\Delta s, \Delta s') = \frac{1}{2\pi\epsilon_L} e^{-\frac{1}{2\epsilon_L}(\hat{\gamma}_L\Delta s^2 + 2\hat{\alpha}_L\Delta s\Delta s' + \hat{\beta}_L\Delta s'^2)}. \quad (9b)$$

FOCUSING ANGLE AND ENERGY CHIRP FROM COURANT-SNYDER PARAMETERS

A bivariate Gaussian distribution can be constructed from two univariate ones by

$$Y = \sigma_y \mathcal{N}(0, 1) \quad (10a)$$

$$Y' = \frac{\alpha_f}{\sigma_y} Y + \sigma_{y'} \mathcal{N}(0, 1), \quad (10b)$$

where $\mathcal{N}(0, 1)$ is the standard normal distribution and $\sigma_y, \sigma_{y'}$ are the variances. The covariance is $\langle YY' \rangle = \alpha_f \sigma_y$ and thus the correlation coefficient is

$$\rho = \frac{\langle YY' \rangle}{\sqrt{\langle Y^2 \rangle \langle Y'^2 \rangle}} = \frac{\alpha_f}{\sigma_{y'}}. \quad (11)$$

The bivariate Gaussian distribution can be written as

$$f(y, y') = \frac{1}{2\pi\sigma_y\sigma_{y'}\sqrt{1-\rho^2}} \exp \left[-\frac{1}{2(1-\rho^2)} \left(\left(\frac{y}{\sigma_y} \right)^2 - 2\rho \frac{yy'}{\sigma_y\sigma_{y'}} + \left(\frac{y'}{\sigma_{y'}} \right)^2 \right) \right] \quad (12)$$

Comparing this equation to Eq. 9a leads to the equation system

$$\frac{\hat{\gamma}}{\epsilon} = \frac{1}{(1-\rho^2)\sigma_y^2} \quad (13a)$$

$$\frac{\hat{\alpha}}{\epsilon} = -\frac{\rho}{(1-\rho^2)\sigma_y\sigma_{y'}} \quad (13b)$$

$$\frac{\hat{\beta}}{\epsilon} = \frac{1}{(1-\rho^2)\sigma_{y'}^2} \quad (13c)$$

which can be solved for the parameters

$$\alpha_f = \varrho \sigma_{y'} = -\hat{\alpha} \sqrt{\varepsilon/\hat{\beta}} \quad (14a)$$

$$\sigma_y = \sqrt{\hat{\beta} \varepsilon} \quad (14b)$$

$$\sigma_{y'} = \sqrt{\hat{\gamma} \varepsilon}, \quad (14c)$$

where again Eq. 7 was used. The rms emittance is given by [10] $\varepsilon_{rms} = \sigma_y \sigma_{y'} \sqrt{1 - \varrho^2} = \varepsilon$, i.e. the rms-emittance equals the Courant-Snyder invariant for a particle at rms amplitude.

Choosing to start in the center of a thick focusing element, i.e., where $\hat{\beta}(z)$ has a maximum, provides $\hat{\alpha}_0 = 0$ and thus $\hat{\beta}_0 \hat{\gamma}_0 = 1$, i.e., the matching condition is completely described by a single number $\hat{\beta}_0$.

The same formalism applies to the longitudinal plane, where Eq. 9b is compared to the bivariate Gaussian. We find the system accordingly as

$$\frac{\hat{\gamma}_L}{\varepsilon_L} = \frac{1}{(1 - \varrho^2) \sigma_{\Delta s}^2} \quad (15a)$$

$$\frac{\hat{\alpha}_L}{\varepsilon_L} = -\frac{\varrho}{(1 - \varrho^2) \sigma_{\Delta s} \sigma_{\Delta s'}} \quad (15b)$$

$$\frac{\hat{\beta}_L}{\varepsilon_L} = \frac{1}{(1 - \varrho^2) \sigma_{\Delta s'}^2} \quad (15c)$$

solved as

$$\alpha_{Echirp} = \varrho \sigma_{\Delta s'} = -\hat{\alpha}_L \sqrt{\varepsilon_L / \hat{\beta}_L} \quad (16a)$$

$$\sigma_{\Delta s} = \sqrt{\hat{\beta}_L \varepsilon_L} \quad (16b)$$

$$\sigma_{\Delta s'} = \sqrt{\hat{\gamma}_L \varepsilon_L}. \quad (16c)$$

Particularly in the uncorrelated case we have

$$\alpha_{Echirp} = 0 \quad (17a)$$

$$\sigma_{\varphi} = \frac{2\pi}{\lambda_g} \sqrt{\hat{\beta}_L \varepsilon_L} \quad (17b)$$

$$\sigma_{\Delta W} = m_e c^2 \gamma^3 \beta^2 \sqrt{\varepsilon_L / \hat{\beta}_L}, \quad (17c)$$

which allows us to eliminate the longitudinal emittance to find

$$\frac{\sigma_{\varphi}}{2\pi} = \frac{\hat{\beta}_L}{\beta^3 \gamma^3 \lambda_0} \frac{\sigma_{\Delta W}}{m_e c^2} \quad (18)$$

as the linear matching condition.

SIMULATION METHODS

The simulations are performed by DLAttrack6D [1], which is written in Matlab [12]. It applies one three-dimensional kick per DLA cell, which fulfills the Panofsky-Wenzel theorem [13], conveniently written as

$$\nabla \times \Delta \vec{p} = 0. \quad (19)$$

The kicks and pushes are arranged in a symplectic manner, such that no artificial emittance increase occurs and the natural one due to the nonlinear fields can be properly calculated. The fields in individual cells are simulated in CST Microwave Studio [14] in the time domain. However, the results are exported in frequency domain, i.e., as the Fourier transform in every spatial point evaluated at the center frequency. The spatial Fourier coefficients e_1 are then calculated in an additional post-processing step. This process is repeated for each DLA cell length, where the eccentricity of the elliptical pillars is used as a tuning knob to obtain constant phase $\arg(e_1)$ independent of λ_g . The amplitude $|e_1|$ however still depends on $\beta = \lambda_g/\lambda_0$, see Fig. 2.

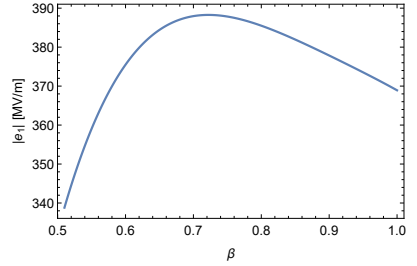


FIG. 2. Field strength of the first spatial harmonic in a DLA cell with elliptical pillars and incident laser field of 500 MV/m from both lateral sides. The cell length is given by the Wieroe condition $\lambda_g = \beta \lambda_0$.

The final structure, which accelerates over a large energy range, can also be simulated to obtain the fields and then perform the particle tracking in CST Particle Studio [14]. The simulation effort for this is however extremely large. In order to obtain convergence of the phase in each DLA cell, it needs to be discretized with about 200,000 hexahedral mesh cells leading to 600 million mesh cells for the entire 1 MeV accelerator. Tracking on a cluster computer with the full fields on this mesh is planned in the future. This will determine the effect of the drift sections on the field flatness. The more resonant the structures, the worse will be the field flatness at drifts, but the higher will be the relative acceleration field harmonic at given incident laser field strength. The dual pillar structures are a reasonable trade-off between these two optimization goals.

DESIGN OF A BUNCHER

In order to provide stable beam transport in a buncher section, the same amount of focusing and defocusing cells should be available. Starting with a longitudi-

nally focusing section (transversely defocusing) the unbunched beam is sinusoidally modulated in energy. A

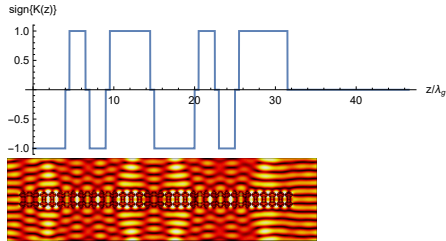


FIG. 3. Lattice function of the buncher (top) and structure design (bottom). The time harmonic longitudinal electric field from a simulation [14] with two symmetrically incident, z -polarized laser beams is shown as color code.

drift would result in bunching from this, however together with transverse defocusing. Instead of a pure drift we use an alternating gradient lattice. At the end of the stage, the energy modulation is again removed (demodulated), which also provides transverse focusing. This process can be repeated multiple times. Here, we use a lattice of two modulator/demodulator stages as

$$\mathbf{M}_b = \mathbf{M}_{b2}\mathbf{M}_{b1} \quad (20a)$$

$$\mathbf{M}_{b1} = \mathbf{M}_o\mathbf{M}_f^5\mathbf{M}_o\mathbf{M}_d^2\mathbf{M}_o\mathbf{M}_f^2\mathbf{M}_o\mathbf{M}_d^4 \quad (20b)$$

$$\mathbf{M}_{b2} = \mathbf{M}_o^{30}\mathbf{M}_f^5\mathbf{M}_o\mathbf{M}_d^2\mathbf{M}_o\mathbf{M}_f^2\mathbf{M}_o\mathbf{M}_d^5, \quad (20c)$$

where \mathbf{M}_f and \mathbf{M}_d denote transversely focusing/defocusing cells (contrarywise in the longitudinal plane) of length λ_g , and \mathbf{M}_o denotes a drift cell of length $\lambda_g/2$. The lattice function and the realization as a dual pillar DLA chip is shown in Fig. 3, where the scale of the two pictures is roughly identical. The ridges at the drift sections are inserted to improve the field flatness. The length of the long drift section at the end is $15\lambda_g$, such that the ellipse in longitudinal phase space is vertical at the end. The energy chirp before this drift depends on the laser amplitude, which can be tuned in an experiment. The number of bunches that can be created in a bunch train depends on the damage threshold of the material. In a pure buncher, the material can be changed from Silicon to Fused Silica, facilitating longer pulses at the cost of lower refractive index. The thus lower $|e_1|$ results in a lower gradient, which is acceptable for a pure buncher chip. Moreover, the number of bunches can also be increased by using a smaller laser field strength and a longer buncher structure.

FOCUSING IN THE INVARIANT TRANSVERSE DIRECTION

The focusing in the x -direction can be done with a single quadrupole magnet. Assuming an emittance of 1 nm and an aperture (good-field region within the pillar height) of $1\ \mu\text{m}$ the constant $\hat{\beta}_x$ function needs to be 1 mm. In constant focusing we have $\hat{\beta}_x = 1/\sqrt{\kappa}$, where the focusing strength of a quadrupole magnet is given by [15]

$$\kappa = \frac{|q| B_0 c}{m_e c^2 b \beta \gamma} \quad (21)$$

with the circular aperture radius b . This means that values of $B_0 \approx 1\ \text{T}$ and $b \approx 1\ \text{mm}$ are feasible. We propose to achieve this by four permanent magnets, one for each pole yoke. Additionally we outline dipole corrector coils in order to be able to slightly move the magnetic field axis in case of misalignment. Since $\kappa \ll K$ in Eq. 6 of the main paper, the defocusing effect in the y -plane can be neglected compared to the strong APF focusing. Moreover, by setting $\kappa = K$ we can determine an equivalent magnetic focusing strength for the thick APF focusing cells of about 5 MT/m, obviously much higher than achievable by quadrupole magnets as in a conventional *FODO* lattice.

ONLINE AVAILABLE VIDEO EXAMPLES

There are three videos available to show the coupled longitudinal and transverse phase space evolutions for pure transport of an unbunched beam, acceleration, and bunching.

In the transport video (Transport.mp4), the ellipses of minimal and maximal linearly matched beam size are marked in yellow and blue, respectively. As one can see at stationary state (in the end of the video), the energy spread flips according to the transverse beam size of the respective bunch parts, where phase has been color-coded in the right plot.

The buncher and accelerator videos (Buncher.gif and Accelerator.mp4) show bunching with the structure in Fig. 3 and acceleration from 83 keV to more than 1 MeV (see main text for the parameters) in a length of roughly 5 mm, respectively. Both are color-coded with the phase space density.

* niedermayer@temf.tu-darmstadt.de

- [1] U. Niedermayer, T. Egenolf, and O. Boine-Frankenheim, Phys. Rev. AB **20**, 111302 (2017).
- [2] T. W. Hughes, S. Tan, Z. Zhao, N. V. Sapro, K. J. Leedle, H. Deng, Y. Miao, D. S. Black, O. Solgaard, J. S. Harris,

- J. Vuckovic, R. L. Byer, S. Fan, R. J. England, Y. J. Lee, and M. Qi, *Physical Review Applied* **9**, 54017 (2018).
- [3] Y. Wei, M. Ibison, G. Xia, J. D. A. Smith, and C. P. Welsch, *Applied Optics* **56**, 8201 (2017).
- [4] D. Cesar, J. Maxson, P. Musumeci, X. Shen, R. J. England, and K. P. Wootton, *Nuclear Instruments and Methods in Physics Research, Section A: Accelerators, Spectrometers, Detectors and Associated Equipment* (2018), 10.1016/j.nima.2018.01.012.
- [5] D. Cesar, J. Maxson, P. Musumeci, X. Shen, R. J. England, K. P. Wootton, and S. Tan, arXiv preprint , 1804.00634 (2018).
- [6] M. Kozák, J. McNeur, N. Schönenberger, J. Illmer, A. Li, A. Tafel, P. Yousefi, T. Eckstein, and P. Hommelhoff, *Journal of Applied Physics* **124** (2018), 10.1063/1.5032093.
- [7] P. Pronko, P. V. Rompay, C. Horvath, X. Liu, T. Juhasz, and G. Mourou, *Physical Review B* **58**, 2387 (1998).
- [8] K. Soong, R. L. Byer, E. R. Colby, R. J. England, and E. A. Peralta, *AIP Conference Proceedings* **1507**, 511 (2012).
- [9] R. H. Siemann, *Physical Review Special Topics - Accelerators and Beams* **7**, 82 (2004).
- [10] S. Y. Lee, *Accelerator Physics* (World Scientific Publishing Co. Pte. Ltd., 2004).
- [11] Wolfram, “Mathematica 11.2,” (2017).
- [12] MathWorks, “Matlab,” (2016).
- [13] W. K. H. Panofsky and W. A. Wenzel, *Review of Scientific Instruments* **27**, 31 (1956).
- [14] CST, “CST Studio Suite,” (2017).
- [15] M. Reiser, *Theory and Design of Charged Particle Beams*, 2nd ed. (Wiley-VCH, Weinheim, 2008).

Laser-Driven Electron Lensing in Silicon MicrostructuresDylan S. Black,¹ Kenneth J. Leedle,¹ Yu Miao,¹ Uwe Niedermayer,² Robert L. Byer,³ and Olav Solgaard¹

(ACHIP Collaboration)

¹*Department of Electrical Engineering, Stanford University, David Packard Building, 350 Serra Mall, Stanford, California 94305-9505, USA*²*Institut für Theorie Elektromagnetischer Felder, Technische Universität Darmstadt, Schloßgartenstr. 8, 64289 Darmstadt, Germany*³*Department of Applied Physics, Stanford University, 348 Via Pueblo Mall, Stanford, California 94305-4090, USA*

(Received 24 October 2018; published 12 March 2019)

We demonstrate a laser-driven, tunable electron lens fabricated in monolithic silicon. The lens consists of an array of silicon pillars pumped symmetrically by two 300 fs, 1.95 μm wavelength, nJ-class laser pulses from an optical parametric amplifier. The optical near field of the pillar structure focuses electrons in the plane perpendicular to the pillar axes. With 100 ± 10 MV/m incident laser fields, the lens focal length is measured to be 50 ± 4 μm , which corresponds to an equivalent quadrupole focusing gradient B' of 1.4 ± 0.1 MT/m. By varying the incident laser field strength, the lens can be tuned from a 21 ± 2 μm focal length ($B' > 3.3$ MT/m) to focal lengths on the centimeter scale.

DOI: 10.1103/PhysRevLett.122.104801

The dielectric laser accelerator (DLA) is a dielectric microstructure that harnesses the large electric fields in femtosecond-pulsed lasers to produce an electron linear accelerator with acceleration gradients orders of magnitude higher than conventional metal accelerators [1,2]. The microstructure is a subwavelength grating whose optical near field is phase matched to a propagating electron beam, thereby accelerating the electron beam. The accelerator size is commensurate with its drive wavelength; while advantageous in some respects, this presents new challenges. To confine an electron beam to a μm -scale DLA channel, a lens with focusing strength many orders of magnitude higher than currently available is necessary.

In conventional accelerators, the magnetic quadrupole is the preferred lens for charged particle focusing due to its high focusing strength, low dispersion, and linear field gradient [3]. Focusing strength is defined as $k = 1/(fL)$, where f is the focal length and L the length of the lens. The magnetic quadrupole focusing strength is $k[\text{m}^{-2}] \approx 0.3B'[\text{T/m}]/p[\text{GeV}/c]$ [4]. It is common to compare lens strengths by their equivalent quadrupole field gradient B' , and this convention is adopted throughout this Letter. The required B' for DLA is between 100–1000 kT/m, set by the resonant defocusing forces of the synchronous accelerating mode [1,5,6]. Conventional quadrupoles can achieve a B' of only 500 T/m [7–9]. The other commonly employed static-field lenses, einzel lenses [10], and solenoids [11], are also far too weak to achieve effective confinement. To realize an electron linac on-chip, a new type of lens, as proposed in Ref. [6], must be designed.

The ideal lens for DLA beam confinement would be stable, high-power, tunable, and monolithically integrable into the current architecture. Monolithic integration is especially critical, as alignment tolerances for μm -scale beam lines are measured in nanometers, and such tight alignment tolerances are only realistically accessible by use of a monolithic fabrication procedure for both lens and accelerator.

Electrodynamic lenses can provide the required focusing strength. Active plasma lenses have focusing gradients exceeding 3 kT/m [12], while plasma wakefield lensing has focusing strengths on the order of 1 MT/m [13,14]. Plasma wakefield lensing fits naturally with plasma-based accelerators [15], and provides more than sufficient focusing strength. However, integration of plasma lenses with photonic accelerators would require generation of stable plasmas on-chip that are compatible with the accelerator nanofabrication processes.

Strong lensing effects can also be derived from the optical near fields of femtosecond-pulsed lasers. Recently, a laser-driven lens with a 190 μm focal length was demonstrated by McNeur *et al.* [16], which is estimated to have an equivalent B' of 85 kT/m. The evanescent fields near a curved silicon grating generate a focusing field in the plane of the wafer. However, in single gratings there are always undesirable out-of-plane deflection forces [17]. Moreover, the curvature of the grating causes undesirable coupling of the two transverse planes, which complicates the lens implementation in a multistage accelerator design.

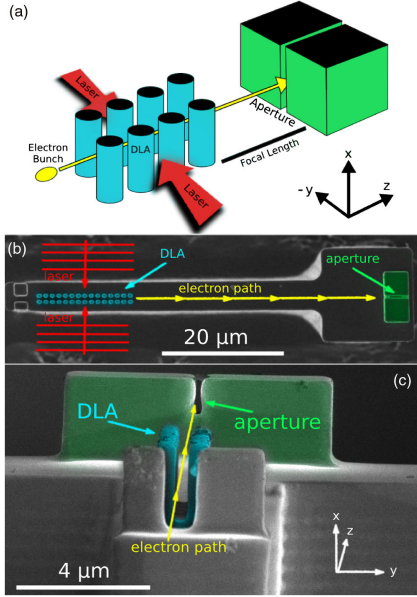


FIG. 1. (a) An electron beam passes through a DLA lens with two identical laser pulses normally incident upon it. The beam is focused, travels approximately one focal length, and is filtered by an aperture of two silicon blocks with a small gap between them. (b) An SEM of the lens and aperture, viewed from above. The lens is composed of two rows of 15 pillars each. The drift length is $39.6 \mu\text{m}$. (c) An SEM showing the aperture structure.

In this Letter, we demonstrate a laser-driven, solid-state electron lens based on the DLA architecture, which was first proposed by Pletner *et al.* in Refs. [18,19], and whose specific architecture is discussed by Leedle *et al.* in Ref. [20]. When illuminated by two laser pulses, each

with an electric field of $100 \pm 10 \text{ MV/m}$, its focal length is measured to be $50 \pm 4 \mu\text{m}$ ($B' = 1.4 \pm 0.1 \text{ MT/m}$). The lens strength is continuously tunable, and we demonstrate its tuning to a focal length below $21 \pm 2 \mu\text{m}$ ($B' = 3.3 \pm 0.3 \text{ MT/m}$). The lensing behavior agrees well with simulation, and we provide a linearized model that approximates the lens focal length. This lens architecture adds no additional complexity to the accelerator fabrication process, as it uses identical procedures and can be integrated directly into the lithographic mask. The demonstrated focusing strength is sufficient to confine an electron beam to a μm -scale beam line. We propose that this lens be used in an alternating phase focusing (APF) scheme [6], which allows stable beam confinement and acceleration over arbitrary distances.

The lens structure (Fig. 1) is fabricated from monolithic 5–10 Ωcm B:Si, and consists of 2 rows of 15 pillars, with periodicity $\Lambda = 1013$ and a 375 nm wide channel between the rows. The pillars are elliptical ($613 \times 459 \text{ nm}$), with a height of $2.7 \mu\text{m}$. The electron beam passes through the central channel, where it interacts with two $300 \pm 25 \text{ fs}$ laser pulses with a center wavelength of $1.950 \pm 0.005 \mu\text{m}$ and a $1/e^2$ radius of $20 \pm 2 \mu\text{m}$. Following the lens is $39.6 \mu\text{m}$ of drift space, then an aperture consisting of two $4 \times 4 \times 2.7 \mu\text{m}$ silicon blocks with a gap of $150 \pm 10 \text{ nm}$ between them.

The electromagnetic fields in the lens are described following Refs. [20–22]. We consider a dual-pillar structure semi-infinite in x , symmetric in y , and periodic in z . The device is illuminated by two counterpropagating z -polarized plane waves, incident from the $\pm y$ directions (Fig. 1), each with electric field E_{inc} . The electrons travel in z with velocity $\beta = v/c$. The synchronicity (or phase matching) condition between the laser field and the electron is

$$\beta\lambda_0 = \Lambda, \quad (1)$$

where λ_0 is the central laser wavelength and Λ is the structure periodicity. The Lorentz force on an electron inside the structure, assuming Eq. (1) is satisfied and non-phase-matched harmonics are negligible, is

$$\vec{F} = -\frac{qe_1}{2\gamma} \text{Re} \begin{bmatrix} 0 \\ \sin\phi[(e^{i\theta} - 1)\cosh(k_y y) + (e^{i\theta} + 1)\sinh(k_y y)] \\ \gamma \cos\phi[(e^{i\theta} + 1)\cosh(k_y y) + (e^{i\theta} - 1)\sinh(k_y y)] \end{bmatrix}, \quad (2)$$

where $\gamma = (1 - \beta^2)^{-1/2}$, $k_y = 2\pi/\beta\gamma\lambda_0$ is the wave vector of the evanescent field, q is the elementary charge, and e_1 is the magnitude of the synchronous accelerating field at $y = 0$ [21]. We assume a laser phase such that e_1 is purely real and positive, and define the structure constant $c_s = e_1/E_{\text{inc}}$. ϕ is the phase of the electron relative to the

optical cycle of the $+y$ plane wave, and θ is the relative phase between the counterpropagating waves. The force along the x coordinate is zero by the semi-infinite assumption. Previous experimental results, as well as 3D FDTD simulations, indicate that the semi-infinite approximation works well for $2.7 \mu\text{m}$ tall (or taller) pillars [20].

The magnitude of the transverse and longitudinal forces differ by a factor of γ , as expected from the Panofsky-Wenzel theorem [23].

For in-phase drive lasers ($\theta = 0$) and assuming perfect synchronicity, the focal length of a device with N periods is approximately

$$f \approx \frac{\beta^2 \gamma^3 m_e c^2}{2\pi N q e_1 \sin \phi}. \quad (3)$$

Equation (3) is valid for a sufficiently small N such that the thin-lens approximation holds. The lens strengths considered here restrict the validity of Eq. (3) to devices with $N < 18$.

Neglecting phase slippage due to acceleration, valid for short structures, the energy gain in the $\theta = 0$ mode is

$$\Delta U \approx -q e_1 N \Lambda \left(\frac{\cos \theta + 1}{2} \right) \cos \phi. \quad (4)$$

For out-of-phase drive lasers ($\theta = \pm\pi$), there exists, to first order in y , a constant deflection force whose direction varies sinusoidally with ϕ . Further discussion of the accelerator modes is contained in the Supplemental Material [24].

The electron bunch is modeled as a collection of normally distributed x , y , and ϕ values. Each electron experiences a focal length drawn from the distribution of Eq. (3), and for an electron beam much longer than an optical cycle (~ 6 fs), the electrons within the bunch stochastically sample all possible focal lengths. To measure the minimum lens focal length, a very small aperture is placed one focal length from the lens and acts as a temporal filter, biasing electron detection towards the focusing phases ($0 < \phi < \pi$) over the defocusing phases ($\pi < \phi < 2\pi$).

The electron beam used in this experiment was produced with a 300 ± 25 fs FWHM, 100 kHz, 256 nm laser pulse incident on a flat copper cathode. The electron beam has a circular Gaussian spatial profile and a 4σ width of 780 ± 63 nm at the lens entrance, measured by a knife edge scan. The geometric 1D emittance is estimated to be ~ 0.5 nm rad. The beam energy is 89.4 ± 0.1 keV, which corresponds to $\beta \approx 0.525$. The beam current is set to 730 ± 200 e^-/s to avoid energy broadening from space charge effects at the cathode. Each electron pulse at the interaction point is 740 ± 110 fs FWHM in length, measured by cross correlation with a 300 ± 25 fs laser pulse.

$43 \pm 8\%$ of electrons are transmitted through the aperture with the laser (and thus the lens) off. Leakage through the silicon blocks is small; the blocks block 95% of incident electrons. For the $\theta = 0$ focusing mode, an increase in electron transmission through the aperture is expected, with maximal transmission when the drift length is matched to the lens focal length. ‘‘Contrast,’’ the percent increase in electron transmission when the lens is turned on [Eq. (5)], quantifies this increase.

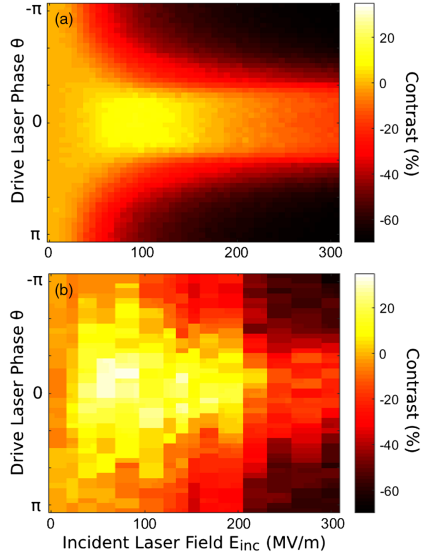


FIG. 2. (a) Simulated contrast plotted against relative drive laser phase θ and electric field E_{inc} . The simulation is a symplectic 2D particle-tracking scheme based on Ref. [21] which applies a momentum kick once per lens period equal to the time integral of Eq. (2) over one structure period. Expected contrast is calculated by a Monte Carlo approach. (b) Contrast is measured as a function of θ and E_{inc} .

$$\text{Contrast}[\%] \equiv 100 \left(\frac{T_{\text{on}}}{T_{\text{off}}} - 1 \right). \quad (5)$$

T_{on} is the electron transmission with the lens on, and T_{off} is the electron transmission with the lens off. After the aperture, the electrons travel through a magnetic spectrometer with an energy resolution of 100 eV, and are detected on a microchannel plate detector.

Electron transmission simulations were carried out for a range of incident laser fields (E_{inc}) and drive laser phases (θ) [Fig. 2(a)]. Because of the long bunch length, the increased transmission from the focusing phases is partially offset by the decreased transmission from the defocusing phases. Thus, the expected contrast in this operating mode is low, only 11%. However, for the $\theta = \pm\pi$ mode, a large transmission decrease for all values of ϕ is expected.

In Fig. 2(b), the parameter space simulated in Fig. 2(a) is measured. The experimental data agree qualitatively with the simulation. There is a small contrast peak at $E_{\text{inc}} = 100 \pm 10$ MV/m for $\theta = 0$, with a large region of strong negative contrast in the $\theta = \pm\pi$ region.

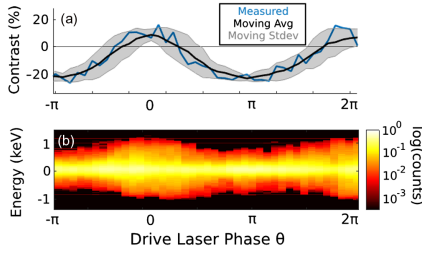


FIG. 3. (a) The measured contrast as a function of θ for $E_{\text{inc}} = 137 \pm 13$ MV/m. The blue line is measured data, the black line and gray shaded area are the moving average and standard deviation, respectively. (b) The electron energy spectrum is measured simultaneously with the phase sweep in (a). Electron counts are normalized to the maximum value.

The energy modulation and contrast as a function of drive laser phase is shown in Fig. 3. The sinusoidal variation of energy gain and contrast predicted by Eq. (4) is demonstrated, and the peak transmission and peak energy modulation occur at the same θ , in agreement with theory.

Figure 4 plots contrast in the $\theta = 0$ focusing mode as a function of E_{inc} , to aid a visual comparison between simulation and experiment. The collocation of the peak contrast for simulation and experiment is apparent. Duplicate runs omitted from Fig. 2(b) for visual clarity are included in Fig. 4.

The contrast peak at $E_{\text{inc}} = 100 \pm 10$ MV/m ($e_1 = 38$ MV/m) corresponds to a focal length of 64 ± 6 μm in the linearized approximation [Eq. (3)]. Our experimentally measured focal length, defined as the total distance from the lens principal plane to aperture center, is measured to be 50 ± 4 μm ($B' = 1.4 \pm 0.1$ MT/m). The measured focal power is greater than predicted by Eq. (3), indicating that the thin-lens approximation breaks down at these lens strengths. The simulation, which uses the forces from Eq. (2), accurately predicts the incident field which gives peak contrast. Because the measured focal length will always be less than that predicted by the linearized approximation, Equation (3) can be considered a lower bound on the lens focusing strength. The incident laser field is increased to a maximum of 306 ± 16 MV/m, corresponding to a linearized focal length of 21 ± 2 μm ($B' = 3.3 \pm 0.3$ MT/m).

The structure constant c_s was measured to be 0.38 ± 0.04 for this structure, with a maximum acceleration gradient e_1 of 111 ± 6 MeV/m. Previous work with similar structures has demonstrated $c_s = 0.27 \pm 0.03$, with $e_1 = 133 \pm 8$ MeV/m [20].

The main experimental limitation was electron beam pointing instability. The electron beam could be stably aligned to the aperture for approximately 60 s, limited by

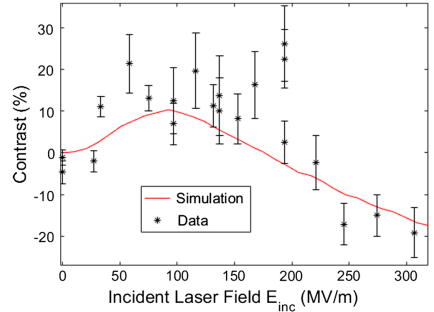


FIG. 4. This figure plots the contrast and standard deviation as a function of E_{inc} for $\theta = 0$. The simulation curve is a cross section of Fig. 2(a) at $\theta = 0$. Duplicate runs have been included.

thermal drifts. An averaging time of 3 s per data point (~ 2000 electrons) was chosen to compromise between high frequency and low frequency noise. The effects of random beam motion are partially compensated by normalizing the total number of transmitted electrons to the fraction of electrons detected at the initial beam energy of 89.4 keV. Since the laser pulse is shorter than the electron pulse, many electrons within the pulse do not interact with the laser, and these electrons are all detected at 89.4 keV. The fluctuation of the electron counts detected at 89.4 keV serves as an instantaneous measure of electron beam misalignment. The details are included in the Supplemental Material [24].

The focusing strength scales as $1/\gamma^3$, which is a less favorable scaling than the $1/\gamma^2$ scaling of solenoids or the $1/\gamma$ scaling of quadrupoles. The equivalence point is found by equating k of a quadrupole lens to k of a DLA lens and solving for γ . The equivalence point here is ~ 35 MeV. This can be increased by increasing either the electric field or the lens length. Efficient laser-electron interaction requires that the lens material refractive index n be greater than $1/\beta$ [25,26]. Silicon has $n \approx 3.45$ at $\lambda_0 = 2.0$ μm , corresponding to a lower limit of $\beta \approx 0.29$ (23 keV).

The lens focal length is continuously variable from approximately 20 microns to the centimeter scale. However, electron pulses of duration $\tau_p \ll \lambda_0/c$ are required for use as a single focal length lens. Fortunately, a pulse train created using the same DLA architecture [6,27] has the correct microbunch length and periodicity. The use of evanescent fields to focus electrons necessitates a narrow aperture, and so its emittance acceptance is small. The beam emittance in this lens is not conserved; however the emittance growth due to field nonlinearity is quite small. Achievable spot sizes are limited by third-order aberrations from the sinh focusing profile. Lens nonlinearities are treated more fully by Niedermayer *et al.* in Refs. [6,21].

We propose to use this lens in an alternating phase focusing confinement scheme. Briefly, lens stages are alternated with drift sections chosen to provide a specific phase offset between lens stages. For example, a drift length of one half period is equivalent to a π phase delay in ϕ , which reverses the sign of the lens focal length. If the phase offsets are chosen appropriately, it is possible to achieve stable confinement in both the transverse and longitudinal directions simultaneously, which can then be combined with high gradient acceleration, as detailed in Ref. [6]. The confinement requirements for DLA are set by the resonant defocusing forces [1,5,6], and since the defocusing forces are exactly those forces described by Eq. (2), the lensing forces presented here have precisely the same strength as the resonant defocusing itself. Thus, using this architecture, the focusing strength requirement for confinement in DLA is satisfied automatically, even for the large defocusing forces present in high-gradient accelerators [28].

In summary, we have demonstrated a laser-driven, continuously tunable electrodynamic lens with a focusing strength equivalent to those observed in plasmas [13,14] and which far exceeds any static-field lens. Its design is easily and monolithically integrable with current photonic accelerator architectures, and its strength is sufficient to confine an electron beam to an accelerator channel less than $1\ \mu\text{m}$ wide for an arbitrary distance [6]. This removes a major roadblock in the development of scalable on-chip electron accelerators.

The authors wish to acknowledge the entire ACHIP collaboration for their support and guidance. This work is funded by the Gordon and Betty Moore Foundation (GBMF4744).

[1] R. Joel England *et al.*, Dielectric laser accelerators, *Rev. Mod. Phys.* **86**, 1337 (2014).
 [2] K. P. Wootton *et al.*, Towards a fully integrated accelerator on a chip: Dielectric laser acceleration (DLA) from the source to relativistic electrons, *Proc. IPAC* **4744**, 2520 (2017).
 [3] D. L. Smith, Focusing properties of electric and magnetic quadrupole lenses, *Nucl. Instrum. Methods* **79**, 144 (1970).
 [4] J. Rossbach and P. Schmüser, Basic course on accelerator optics, 1993, <http://inspirehep.net/record/347558/files/Cern.pdf>; <http://cds.cern.ch/record/247501>.
 [5] A. Ody, P. Musumeci, J. Maxson, D. Cesar, R. J. England, and K. P. Wootton, Flat electron beam sources for DLA accelerators, *Nucl. Instrum. Methods Phys. Res., Sect. A* **865**, 75 (2017).
 [6] U. Niedermayer, T. Egenolf, O. Boine-Frankenheim, and P. Hommelhoff, Alternating-Phase Focusing for Dielectric-Laser Acceleration, *Phys. Rev. Lett.* **121**, 214801 (2018).
 [7] J. Strait, Very high gradient quadrupoles, in *PAC2001, Proceedings of the 2001 Particle Accelerator Conference*

(*Cat. No. 01CH37268*) (IEEE, Chicago, IL, 2002), Vol. 1, pp. 176–180.
 [8] T. Eichner, Florian Grüner, S. Becker, Matthias Fuchs, D. Habs, R. Weingartner, U. Schramm, H. Backe, Peter Kunz, and Werner Lauth, Miniature magnetic devices for laser-based, table-top free-electron lasers, *Phys. Rev. ST Accel. Beams* **10**, 082401 (2007).
 [9] S. Becker, M. Bussmann, S. Raith, M. Fuchs, R. Weingartner, P. Kunz, W. Lauth, U. Schramm, M. El Ghazaly, F. Grüner, H. Backe, and D. Habs, Characterization and tuning of ultrahigh gradient permanent magnet quadrupoles, *Phys. Rev. ST Accel. Beams* **12**, 102801 (2009).
 [10] F. H. Read, A. Adams, and J. R. Soto-Montiel, Electrostatic cylinder lenses. I. Two element lenses, *J. Phys. E* **4**, 625 (1971).
 [11] V. Kumar, Understanding the focusing of charged particle beams in a solenoid magnetic field, *Am. J. Phys.* **77**, 737 (2009).
 [12] J. van Tilborg, S. Steinke, C. G. R. Geddes, N. Mattis, B. Shaw, A. Gonsalves, J. V. Huijts, K. Nakamura, J. Daniels, C. B. Schroeder, C. Benedetti, E. Esarey, S. S. Bulanov, N. Bobrova, P. Sasorov, and W. Leemans, Active Plasma Lensing for Relativistic Laser-Plasma-Accelerated Electron Beams, *Phys. Rev. Lett.* **115**, 184802 (2015).
 [13] J. S. T. Ng, P. Chen, H. Baldi, P. Bolton, D. Cline, W. Craddock, C. Crawford, F. J. Decker, C. Field, Y. Fukui, V. Kumar, R. Iverson, F. King, R. E. Kirby, K. Nakajima, R. Noble, A. Ogata, P. Raimondi, D. Walz, and A. W. Weidemann, Observation of Plasma Focusing of a 28.5 gev Positron Beam, *Phys. Rev. Lett.* **87**, 244801 (2001).
 [14] E. Chiadroni, M. P. Anania, M. Bellaveglia, A. Biagioni, F. Bisesto, E. Brentegani, F. Cardelli, A. Cianchi, G. Costa, D. Giovenale, G. Di Pirro, M. Ferrario, F. Filippi, G. Alessandro, A. Giribono, A. Marocchino, A. Mostacci, L. Piersanti, R. Pompili, and A. Zigler, Overview of plasma lens experiments and recent results at SPARC-LAB, *Nucl. Instrum. Methods Phys. Res., Sect. A* **909**, 16 (2018).
 [15] S. Kuschel, D. Hollatz, T. Heinemann, O. Karger, M. B. Schwab, D. Ullmann, A. Knetsch, A. Seidel, C. Rödel, M. Yeung, M. Leier, A. Blinne, H. Ding, T. Kurz, D. J. Corvan, A. Sävert, S. Karsch, M. C. Kaluza, B. Hidding, and M. Zepf, Demonstration of passive plasma lensing of a laser wakefield accelerated electron bunch, *Phys. Rev. Accel. Beams* **19**, 071301 (2016).
 [16] J. McNeur, M. Kozák, N. Schönenberger, K. J. Leedle, H. Deng, A. Ceballos, H. Hoogland, A. Ruehl, I. Hartl, R. Holzwarth, O. Solgaard, J. S. Harris, R. L. Byer, and P. Hommelhoff, Elements of a dielectric laser accelerator, *Optica* **5**, 687 (2018).
 [17] K. J. Leedle, R. Fabian Pease, R. L. Byer, and J. S. Harris, Laser acceleration and deflection of 96.3 keV electrons with a silicon dielectric structure, *Optica* **2**, 158 (2015).
 [18] T. Plettner, R. L. Byer, C. McGuinness, and P. Hommelhoff, Photonic-based laser driven electron beam deflection and focusing structures, *Phys. Rev. ST Accel. Beams* **12**, 101302 (2009).
 [19] T. Plettner, R. L. Byer, and B. Montazeri, Electromagnetic forces in the vacuum region of laser-driven layered grating structures, *J. Mod. Opt.* **58**, 1518 (2011).

- [20] K. J. Leedle, D. S. Black, Y. Miao, K. E. Urbanek, A. Ceballos, H. Deng, J. S. Harris, O. Solgaard, and R. L. Byer, Phase-dependent laser acceleration of electrons with symmetrically driven silicon dual pillar gratings, *Opt. Lett.* **43**, 2181 (2018).
- [21] U. Niedermayer, T. Egenolf, and O. Boine-Frankenheim, Beam dynamics analysis of dielectric laser acceleration using a fast 6D tracking scheme, *Phys. Rev. Accel. Beams* **20**, 111302 (2017).
- [22] Y. Wei, M. Ibison, G. Xia, J. D. A. Smith, and C. P. Welsch, Dual-grating dielectric accelerators driven by a pulse-front-tilted laser, *Appl. Opt.* **56**, 8201 (2017).
- [23] W. K. H. Panofsky and W. A. Wenzel, Some considerations concerning the transverse deflection of charged particles in radiofrequency fields, *Rev. Sci. Instrum.* **27**, 967 (1956).
- [24] See Supplemental Material at <http://link.aps.org/supplemental/10.1103/PhysRevLett.122.104801> for derivations of some of the equations which appear in the main manuscript, as well as a detailed description of the data analysis methodology used to process the data that appears in the main manuscript.
- [25] T. W. Hughes, S. Tan, Z. Zhao, N. V. Sapra, K. J. Leedle, H. Deng, Y. Miao, D. S. Black, O. Solgaard, J. S. Harris, J. Vuckovic, R. L. Byer, S. Fan, R. J. England, Y. Jo Lee, and M. Qi, On-Chip Laser-Power Delivery System for Dielectric Laser Accelerators, *Phys. Rev. Applied* **9**, 054017 (2018).
- [26] M. Kozák, P. Beck, H. Deng, J. McNeur, N. Schönenberger, C. Gaida, F. Stutzki, M. Gebhardt, J. Limpert, A. Ruehl, I. Hartl, O. Solgaard, J. S. Harris, R. L. Byer, and P. Hommelhoff, Acceleration of sub-relativistic electrons with an evanescent optical wave at a planar interface, *Opt. Express* **25**, 19195 (2017).
- [27] U. Niedermayer, O. Boine-Frankenheim, and T. Egenolf, Designing a dielectric laser accelerator on a chip, *J. Phys. Conf. Ser.* **874**, 012041 (2017).
- [28] D. Cesar, S. Custodio, J. Maxson, P. Musumeci, X. Shen, E. Threlkeld, R. J. England, A. Hanuka, I. V. Makasyuk, E. A. Peralta, K. P. Wootton, and Z. Wu, High-field non-linear optical response and phase control in a dielectric laser accelerator, *Commun. Phys.* **1**, 46 (2018).

Supplemental Material for Laser-Driven Electron Lensing in Silicon Microstructures

Dylan S. Black,^{1*} Kenneth J. Leadle,¹ Yu Miao,¹ Uwe Niedermayer,³ Robert L. Byer,² Olav Solgaard¹

¹*Department of Electrical Engineering, Stanford University,*

²*Department of Applied Physics, Stanford University,*

³*Institut für Theorie Elektromagnetischer Felder, Technische Universität Darmstadt*

(ACHIP Collaboration)

(Dated: February 9, 2019)

SUMMARY

This appendix contains derivations of some equations stated in the main paper, as well as the details of the normalization scheme used to process the reported experimental data. All references refer to the bibliography in the main paper.

DLA LENS FOCAL LENGTH

For convenience, the definitions of various parameters stated in the main manuscript are restated here.

As in the main manuscript, we consider a dual-pillar structure semi-infinite in x , symmetric in y , and periodic in z (following Refs. [20-22]). The device is illuminated by two counter-propagating z -polarized plane waves, incident from the y direction. The electrons travel along z with velocity $\beta = v/c$, λ_0 is the laser center wavelength, Λ is the structure periodicity, $\gamma = (1 - \beta^2)^{-1/2}$, $k_y = 2\pi/\beta\gamma\lambda_0$ is the wavevector of the evanescent field, q is the elementary charge, e_1 is the magnitude of the synchronous accelerating field at $y = 0$, ϕ is the phase of the electron relative to the laser optical cycle of the $+y$ plane wave within the periodic structure, and θ is the relative phase between the counter-propagating waves. We assume a laser phase such that e_1 is purely real and positive.

Beginning from the Lorentz force (Eq. (2) in the main paper), the transverse force F_y seen by an electron at a given ϕ can be written as a superposition of a cosh term and a sinh term, which correspond to the deflecting and focusing modes, respectively.

$$F_y \propto \text{Re} \left[\frac{(e^{i\theta} - 1)}{2} \cosh(k_y y) + \frac{(e^{i\theta} + 1)}{2} \sinh(k_y y) \right] \quad (\text{S.1})$$

The relative drive laser phase θ controls the behavior of the device. For in-phase drive lasers ($\theta = 0$) and assuming perfect synchronicity, integrating F_y in time across one period Λ (see Ref. [21]) gives

$$\Delta p_y = -\frac{\Lambda}{\beta c} \frac{q e_1}{\gamma} \sinh\left(\frac{2\pi}{\beta\gamma\lambda_0} y\right) \sin\phi \quad (\text{S.2})$$

Applying $\beta\lambda_0 = \Lambda$ and expanding to first order in y yields

$$\Delta p_y \approx -\frac{2\pi q e_1}{c\beta\gamma^2} y \sin\phi \quad (\text{S.3})$$

The angular deviation of the electron trajectory over one DLA period $\Delta y'_1$ near the center of the channel is

$$\Delta y'_1 = \frac{\Delta p_y}{p_{z0}} \approx -\frac{2\pi q e_1 \sin\phi}{\beta^2 \gamma^3 m_e c^2} y \quad (\text{S.4})$$

For a sufficiently small number of periods N such that y is nearly constant, the total angular deflection is $\Delta y' \approx N\Delta y'_1$. In analogy with the first order approximation of lens focal length, $\Delta y' = -y/f$, the focal length of the DLA lens is approximately,

$$f \approx \frac{\beta^2 \gamma^3 m_e c^2}{2\pi N q e_1 \sin\phi} \quad (\text{S.5})$$

Eq. (S.5) is valid only for cases where the focal length f is much less than the length of the lens. For a lens of N periods, the lens length is $N\Lambda$ and the thin lens approximation holds when

$$N^2 \leq \frac{\beta^2 \gamma^3 m_e c^2}{2\pi \Lambda q e_1} \quad (\text{S.6})$$

For the lens strengths considered here, the lens can be considered “thin” if $N < 18$. Longer lenses must be modeled as thick lenses (see Ref. [6]).

ENERGY GAIN OF SHORT DLA STRUCTURES

On-axis ($y = 0$), the electron sees a longitudinal force F_z of

$$F_z = \text{Re} \left[-\frac{q e_1}{2} (e^{i\theta} + 1) \cos\phi \right] \quad (\text{S.7})$$

Since energy gain is small for small N , phase slippage due to acceleration can be neglected, and the total energy gain over N periods is found by integrating F_z over the length of the structure, yielding an on-axis energy gain of

$$\Delta U \approx -q e_1 N \Lambda \left(\frac{\cos\theta + 1}{2} \right) \cos\phi \quad (\text{S.8})$$

DEFLECTION FORCES

For $\theta = \pi$, the forces in the transverse direction are given by

$$F_y = \frac{qe_1}{\gamma} \cosh(k_y y) \sin \phi \quad (\text{S.9})$$

In the limit of small deviations from the $y = 0$ axis, F_y is

$$F_y \approx \frac{qe_1}{\gamma} \left(1 + \frac{1}{2} \left(\frac{2\pi y}{\beta\gamma\lambda_0} \right)^2 \right) \sin \phi \quad (\text{S.10})$$

For a lens with a channel width much less than λ_0 , higher order terms may be neglected and the deflection force is approximately constant in magnitude across the lens channel. The direction of the deflection force varies sinusoidally with ϕ , and the magnitude is directly proportional to the laser field strength via e_1 . Operated in this mode, the structure can be used as an optical frequency streaking element.

The angular deflection for a single period is easily calculated by integration of F_y over one period, yielding, to leading order,

$$\Delta y'_1 \approx \frac{qe_1 \Lambda}{\beta^2 \gamma^2 m_e c^2} \sin \phi \quad (\text{S.11})$$

Since the deflection force is constant to leading order in y , angular deflection for N periods is well approximated by

$$\Delta y' \approx \frac{qe_1 N \Lambda}{\beta^2 \gamma^2 m_e c^2} \sin \phi \quad (\text{S.12})$$

The same caveats that limit the applicability of the thin-lens approximation in the previous sections also apply here, with the additional constraint that a beam deflected uniformly by each period of accelerator structure will hit the channel wall after some distance, limiting the maximum angular deflection produced by this structure.

PEAK NORMALIZATION

Introduction

The electron beam misalignment caused by slow thermal drifts is the main source of experimental noise. A common technique for removing external effects from a measured signal is to compare the experiment to a simultaneous reference experiment. In light optics, for example, a beamsplitter can be used to create a reference beam against which the experiment may be compared.

An identical reference electron beam cannot be created for this experiment. However, since the laser pulse used

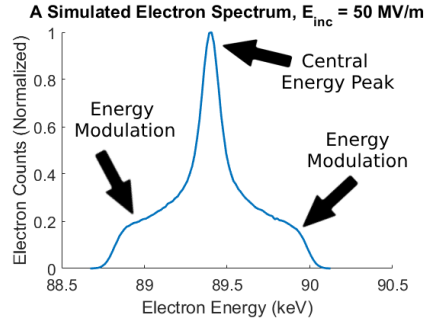


FIG. S.1. An example (simulated) energy spectrum which shows a large peak at the central beam energy of 89.4 keV. This spectrum was simulated using a 300 fs intensity FWHM laser pulse, with peak electric field values of 50 MV/m, and a 730 fs FWHM electron bunch. The large central peak, which is composed mainly of non-interacting electrons due to the long electron bunch, is contrasted by the smaller wings, which are composed of electrons accelerated and/or deflected by the laser fields.

to modulate the energy of the electron pulse is shorter than the electron pulse itself, there are many electrons detected which do not interact with the laser at all. The fluctuation of the non-interacting electron counts is not dependent on the laser fields, and can therefore be used as an instantaneous reference for beam alignment to the lens channel.

The non-interacting electrons are all detected at the initial beam energy (see Fig. S.1). Thus, by filtering the detected electrons with a magnetic spectrometer and normalizing the total electron counts to the electron counts at the initial beam energy, it is possible to partially separate the electron count fluctuations due to the laser fields from the fluctuations due to beam misalignment. In other words, the height of the central energy peak (Fig. S.1) constitutes an instantaneous pseudo-reference beam against which total electron transmission can be compared. Not all of the electrons which appear at the central energy peak are non-interacting. But, since the electron pulse used in this experiment is nearly twice as long as the laser pulse, the majority of the electrons detected at the initial beam energy are, in fact, non-interacting.

A Note on the Experimental Procedure

The independent variables in the experiment are the peak electric field of one drive laser E_{inc} , and the relative

phase between the two drive lasers θ . The dependent variable is the electron counts measured on the detector. Each data point taken in the experiment was taken as part of a “phase sweep,” which consists of holding E_{inc} constant while θ is varied linearly, and continuously measuring the electron energy spectrum as a function of phase (see Fig. 4 in the main paper or Fig. S.3 in the Supplemental Material for an example of a phase sweep). During the phase sweep, individual data points are collected, consisting of an electron energy spectrum with an averaging time of 3 s (~ 2000 electrons). After each phase sweep is completed, the laser is turned off, and the energy spectrum is again measured. Then, E_{inc} is increased by a fixed amount, and another phase sweep is taken. In this way, the entire (θ, E_{inc}) parameter space is sampled for both laser-on and laser-off conditions.

Notation

Let the total number of electron counts (“transmission”) measured at an energy ϵ for some (θ, E_{inc}) be denoted by $T_\epsilon(\theta, E_{\text{inc}})$. In order to reduce visual clutter, this quantity will be written simply as T_ϵ when the functional dependence is not relevant. This experiment depends on measuring the “Contrast” (see Eq. (5) in the main paper) between a laser-on and a laser-off condition. These two conditions will be specified by a superscript when it is necessary to distinguish them, *e.g.* T^{on} (the transmission with the laser on) or T^{off} (the transmission with the laser off), but the superscript will be omitted when the equation can be applied equally to both laser conditions, *i.e.* an equation involving T is valid for both T^{on} and T^{off} . The superscript will also be used to explicitly denote quantities which are measured or simulated when it is necessary to distinguish the two, *e.g.* $T^{\text{on, sim}}$ is the simulated transmission T for the laser-on condition.

Normalized quantities in the simplified scheme will be written with a hat, *e.g.* \hat{T} . Corrected, normalized quantities will be written with a tilde, *e.g.* \tilde{T} .

Simplified Normalization Scheme

Define the normalization factor $N(\theta, E_{\text{inc}})$ as

$$N(\theta, E_{\text{inc}}) = \frac{T_{\epsilon_0}(\theta, E_{\text{inc}})}{\langle T_{\epsilon_0}(\theta, E_{\text{inc}}) \rangle_\theta} \rightarrow N = \frac{T_{\epsilon_0}}{\langle T_{\epsilon_0} \rangle_\theta} \quad (\text{S.13})$$

where ϵ_0 is the central beam energy, and $\langle \rangle_\theta$ is the average over all drive laser phases θ for a single phase sweep. N is then a function of θ and E_{inc} , defined for each data point, whose mean over a single phase sweep is 1, and whose fluctuations are directly proportional to the electron counts detected with energy ϵ_0 .

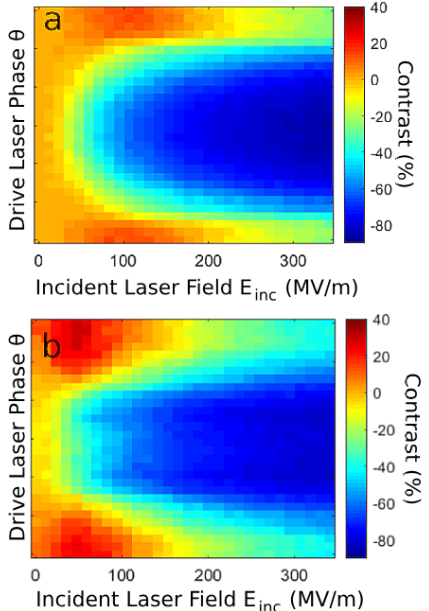


FIG. S.2. (a) An example simulation of the experimental parameter space. (b) The same parameter space with the simplified peak normalization scheme applied, showing a clear distortion of the space. Here, simulation parameters have been deliberately chosen to exaggerate the warping caused by the simplified peak normalization, but the distortion is present for any choice of parameters when the simplified normalization scheme is applied. This is then corrected to obtain the data used in the main manuscript.

Define the total electron transmission T as

$$T = \sum_{\epsilon} T_{\epsilon} \quad (\text{S.14})$$

and the normalized transmission \hat{T} as

$$\hat{T} = T/N \quad (\text{S.15})$$

Contrast C is defined as

$$C = 100 \left(\frac{T^{\text{on}}}{T^{\text{off}}} - 1 \right) \quad (\text{S.16})$$

The normalized contrast \hat{C} is then

$$\hat{C} = 100 \left(\frac{\hat{T}^{\text{on}}}{\hat{T}^{\text{off}}} - 1 \right) \quad (\text{S.17})$$

Corrected Normalization Scheme

The simplified normalization scheme above warps the parameter space (see Fig. S.2), preventing a legitimate comparison of simulated and measured data. The normalization scheme must be corrected such that the parameter space in the zero-noise case remains invariant under normalization.

To construct the corrected normalized transmission \tilde{T} , the normalization factor N is simulated for the entire parameter space, and an inverse normalization is applied to both the simulated and the measured data, *i.e.* for simulated data,

$$\tilde{T}^{\text{sim}} = N^{\text{sim}} \hat{T}^{\text{sim}} = \left(\frac{N^{\text{sim}}}{\tilde{N}^{\text{sim}}} \right) T^{\text{sim}} = T^{\text{sim}} \quad (\text{S.18})$$

and for measured data,

$$\tilde{T}^{\text{meas}} = \left(\frac{N^{\text{sim}}}{\tilde{N}^{\text{meas}}} \right) T^{\text{meas}} \quad (\text{S.19})$$

Clearly, for simulated data, the corrected, normalized transmission \tilde{T} is identical to the actual electron transmission T . For measured data, this is not necessarily true. In the following section, the desired signal, the “true” transmission T , which is assumed to be identical to the simulated value, will be explicitly separated from any undesirable random fluctuations in the real experiment, denoted by Z . Define

$$T^{\text{meas}} = T + Z \quad (\text{S.20})$$

The measured normalization factor N^{meas} is

$$N^{\text{meas}} = \frac{T_{\epsilon_0} + Z_{\epsilon_0}}{\langle T_{\epsilon_0} + Z_{\epsilon_0} \rangle_{\theta}} \quad (\text{S.21})$$

The mean value of the drift over time is uncorrelated with drive laser phase θ . Assuming that Z averages to zero over many periods of θ , it can be neglected in the denominator, giving

$$N^{\text{meas}} = \frac{T_{\epsilon_0} + Z_{\epsilon_0}}{\langle T_{\epsilon_0} \rangle_{\theta}} \quad (\text{S.22})$$

Again, to reduce visual clutter, the transmission ratios R, \hat{R} will be defined as

$$R = \frac{T^{\text{on}}}{T^{\text{off}}}, \hat{R} = \frac{\hat{T}^{\text{on}}}{\hat{T}^{\text{off}}} \quad (\text{S.23})$$

The measured, normalized transmission ratio \hat{R}^{meas} is, explicitly

$$\hat{R}^{\text{meas}} = \frac{(T^{\text{on}} + Z^{\text{on}}) \left(\frac{T_{\epsilon_0}^{\text{off}} + Z_{\epsilon_0}^{\text{off}}}{\langle T_{\epsilon_0}^{\text{off}} \rangle_{\theta}} \right)}{(T^{\text{off}} + Z^{\text{off}}) \left(\frac{T_{\epsilon_0}^{\text{on}} + Z_{\epsilon_0}^{\text{on}}}{\langle T_{\epsilon_0}^{\text{on}} \rangle_{\theta}} \right)} \quad (\text{S.24})$$

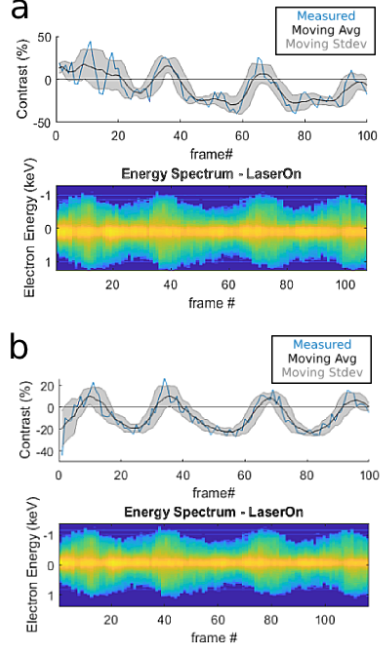


FIG. S.3. (a) A measured phase sweep, with contrast and energy spectrum plotted as a function of frame number (3 s per frame, ~ 2000 electrons). The slow drift of the electron beam away from the aperture manifests as the slow decay of the contrast curve. Shorter time scale fluctuations, seen in frames 0 - 20, are also present. The maximum energy modulation provides a good independent reference for the shape of the contrast curve, *i.e.* the contrast peaks should appear with the same frequency and at the same time as the energy modulation maxima. (b) The same measured data as in panel (a), with the corrected normalization scheme applied. The slow drift of the beam is corrected, yielding a sinusoidal curve with a constant average value over each period. The short time scale fluctuations are also corrected by the normalization scheme. The sinusoidal oscillation of contrast is well matched to the frequency and phase of the energy spectrum oscillation.

Applying the simulated correction factor according to Eq. (S.13) gives the corrected, normalized transmission ratio \hat{R}^{meas}

$$\hat{R}^{\text{meas}} = \frac{(T^{\text{on}} + Z^{\text{on}}) (T_{\epsilon_0}^{\text{off}} + Z_{\epsilon_0}^{\text{off}}) (T_{\epsilon_0}^{\text{on}})}{(T^{\text{off}} + Z^{\text{off}}) (T_{\epsilon_0}^{\text{on}} + Z_{\epsilon_0}^{\text{on}}) (T_{\epsilon_0}^{\text{off}})} \quad (\text{S.25})$$

Which can be rewritten in terms of the “true” transmission ratio $R = T^{\text{on}}/T^{\text{off}}$ as

$$\tilde{R}^{\text{meas}} = R \left(\frac{1 + Z^{\text{on}}/T^{\text{on}}}{1 + Z_{\epsilon_0}^{\text{on}}/T_{\epsilon_0}^{\text{on}}} \right) \left(\frac{1 + Z_{\epsilon_0}^{\text{off}}/T_{\epsilon_0}^{\text{off}}}{1 + Z^{\text{off}}/T^{\text{off}}} \right) \quad (\text{S.26})$$

where each quantity $R(\theta, E_{\text{inc}})$, $Z(\theta, E_{\text{inc}})$, $T(\theta, E_{\text{inc}})$ is understood to be evaluated for the same (θ, E_{inc}) . If any noise present in the measurement is a constant fraction of the signal over the whole electron energy spectrum, *i.e.* $Z/T = Z_{\epsilon_0}/T_{\epsilon_0}$, then, even for cases where $Z \neq 0$, $\tilde{R}^{\text{meas}} = R$ and the expression for the corrected, normalized contrast reduces to the true contrast,

$$\tilde{C}^{\text{meas}} = C \quad (\text{S.27})$$

An example phase sweep in unprocessed form and the correction of both slow drift and higher frequency fluctuations with the corrected peak normalization scheme is shown in Fig. S.3. As Fig. S.3 clearly shows, the corrected normalization scheme is effective in removing electron count fluctuations due to drift while preserving the general shape of the curve.

The maximum energy modulation for a given θ is robust to beam misalignment. Because the maximum en-

ergy modulation occurs at the edge of the lens channel, where the evanescent field is strongest, the maximum energy modulation for a given θ does not change with small misalignments of the electron beam - so long as the beam remains partially within the channel, some electrons from the beam experience the largest possible energy modulation provided by the optical mode. In this regime, the maximum energy modulation depends solely on the amplitude and phase of the drive lasers, whose fluctuations are small compared to the electron count fluctuations introduced by beam pointing instability.

Shown below each panel in Fig. S.3 is the electron energy spectrum as a function of frame number (time) as the laser phase θ is linearly increased. The correlation between the contrast and the energy broadening is supported by analytical considerations (See Eq. (4) in the main paper), and is clearly seen in Fig. S.3. This provides a good sanity check for our normalization scheme.

Restating the key result, if the noise is evenly distributed in electron energy space, then the corrected, normalized contrast \tilde{C} is equal to the true contrast C , and the correct (de-noised) value of contrast for each data point can be recovered through the peak normalization scheme without use of a distinct reference beam.

Challenges in simulating beam dynamics of dielectric laser acceleration

Uwe Niedermayer*[†]

*Technische Universität Darmstadt,
Institute for Accelerator Science and Electromagnetic Fields (TEMF),
Schlossgartenstrasse 8, D-64289 Darmstadt, Germany
niedermayer@temf.tu-darmstadt.de*

A. Adelman, S. Bettoni, M. Calvi, M. Dehler, E. Ferrari, F. Frei, D. Hauenstein,
B. Hermann, N. Hiller, R. Ischebeck, C. Lombosi, E. Prat, S. Reiche and L. Rivkin
Paul Scherrer Institut, CH-5232 Villigen, Switzerland

R. Aßmann, U. Dorda, I. Hartl, W. Kuroпка, F. Lemery, B. Marchetti,
F. Mayet, H. Xuan and J. Zhu
Deutsches Elektronen-Synchrotron, D-22607 Hamburg, Germany

D. S. Black, P. N. Broaddus, R. L. Byer, A. Ceballos, H. Deng, S. Fan, J. Harris,
T. Hirano, T. W. Hughes, Y. Jiang, T. Langenstein, K. Leedle, Y. Miao, A. Ody,
A. Pigott, N. Saprà, O. Solgaard, L. Su, S. Tan, J. Vuckovic, K. Yang and Z. Zhao
Stanford University, Stanford, CA 94305, USA

O. Boine-Frankenheim, T. Egenolf and E. Skär
Technische Universität Darmstadt, D-64289 Darmstadt, Germany

D. Cesar, P. Musumeci, B. Naranjo, J. Rosenzweig and X. Shen
University of California, Los Angeles, CA 90095, USA

B. Cowan
Tech-X Corporation, Boulder, CO 80303, USA

R. J. England and Z. Huang
SLAC National Accelerator Laboratory, Menlo Park, CA 94025, USA

H. Cankaya, M. Fakhari, A. Fallahi and F. X. Kärtner
*Center for Free-Electron Laser Science,
DESY and University of Hamburg, D-22607 Hamburg, Germany*

*Corresponding author.

[†]Visting postdoctoral scholar at Ginzton Lab, Stanford University (2018).

T. Feuer

Universität Bern, Switzerland

P. Hommelhoff, J. Illmer, A. Li, A. Mittelbach, J. McNeur, N. Schönenberger,
R. Shiloh, A. Tafel and P. Yousefi

Friedrich-Alexander Universität Erlangen-Nürnberg, 91058 Erlangen, Germany

M. Kozak

Charles University, 12116 Prague 2, Czech Republic

M. Qi and Y. J. Lee

Purdue University, West Lafayette, IN 47907, USA

Y.-C. Huang

Nat. Tsing Hua University, Taiwan

E. Simakov

Los Alamos National Laboratory, USA

Received 28 February 2019

Revised 15 June 2019

Accepted 17 June 2019

Published 26 November 2019

Dielectric Laser Acceleration (DLA) achieves the highest gradients among structure-based electron accelerators. The use of dielectrics increases the breakdown field limit, and thus the achievable gradient, by a factor of at least 10 in comparison to metals. Experimental demonstrations of DLA in 2013 led to the Accelerator on a Chip International Program (ACHIP), funded by the Gordon and Betty Moore Foundation. In ACHIP, our main goal is to build an accelerator on a silicon chip, which can accelerate electrons from below 100 keV to above 1 MeV with a gradient of at least 100 MeV/m. For stable acceleration on the chip, magnet-only focusing techniques are insufficient to compensate the strong acceleration defocusing. Thus, spatial harmonic and Alternating Phase Focusing (APF) laser-based focusing techniques have been developed. We have also developed the simplified symplectic tracking code DLAttrack6D, which makes use of the periodicity and applies only one kick per DLA cell, which is calculated by the Fourier coefficient of the synchronous spatial harmonic. Due to coupling, the Fourier coefficients of neighboring cells are not entirely independent and a field flatness optimization (similarly as in multi-cell cavities) needs to be performed. The simulation of the entire accelerator on a chip by a Particle In Cell (PIC) code is possible, but impractical for optimization purposes. Finally, we have also outlined the treatment of wake field effects in attosecond bunches in the grating within DLAttrack6D, where the wake function is computed by an external solver.

Keywords: Dielectric; laser; accelerator; chip; ACHIP.

1. Introduction

The Accelerator on a Chip International Program (ACHIP),¹ funded by the Gordon and Betty Moore Foundation in the period between 2015 and 2020, aims to explore

1942031-2

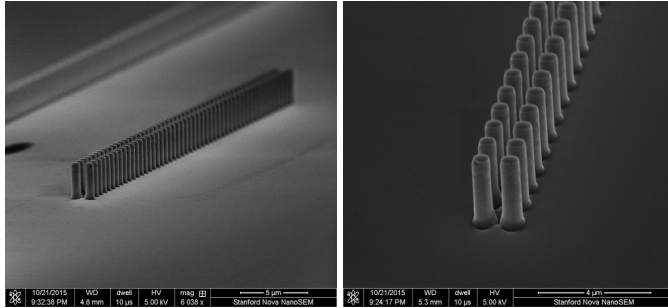


Fig. 1. Scanning Electron Microscope (SEM) pictures of a dual pillar acceleration structure.

Dielectric Laser Acceleration (DLA). This nascent acceleration scheme provides the highest gradients among structure-based (nonplasma, nonvacuum, etc.) electron accelerators and thus allows reduction of the size of high energy electron accelerators significantly. The principle of DLA relies on the inverse Smith–Purcell (or the inverse Cherenkov effect) and was first proposed in 1962.^{2,3} In 2013, the acceleration of relativistic electrons was first demonstrated at SLAC with a gradient of more than 250 MeV/m in an SiO₂ double grating structure driven by a 800 nm Ti:Sapphire laser.⁵ In the same setup, the gradient was later increased to 690 MeV/m.⁶ Also, in 2013, strongly sub-relativistic electrons (27.7 keV) were accelerated by the group at FAU Erlangen with a gradient of 25 MeV/m using a single grating structure at the third spatial harmonic.⁷ The group at Stanford University used a silicon dual pillar structure to accelerate 96 keV electrons with a gradient of more than 200 MeV/m⁸ and a similar experiment at 30 keV with few-cycle laser pulses was done at FAU Erlangen.⁹ An example of such a dual pillar structure is shown in Fig. 1. These schemes all utilize laterally incident lasers with polarization in the electron beam direction, thus the accelerating near field is a standing wave. It is also possible to use longitudinally coupled (traveling wave) structures, see Refs. 10 and 11 for details and a general overview. Another option using a quite simple structure is to excite surface waves by total internal reflection in flat dielectrics.⁴

The goal of ACHIP is to build an accelerator as sketched in Fig. 2, which can accelerate electrons from electrostatic sources (< 100 keV) to above 1 MeV. A second goal is to make use of the accelerator by exploring the options of DLA-based deflection (see e.g. Ref. 12), which can potentially lead to laser-driven undulators.^{13–15}

Different materials have been investigated for DLA.¹⁶ In order to achieve the highest gradient, the material-specific damage threshold fluence

$$F_{\text{dam}} > F = \frac{P\Delta t}{A}, \quad (1)$$

1942031-3

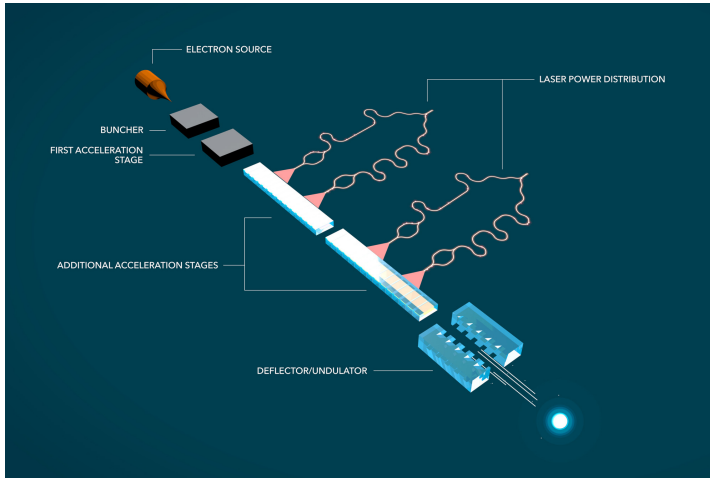


Fig. 2. Sketch of the goals of the ACHIP collaboration.

where P/A is the laser intensity and Δt is the pulse length, is approached, but must not be exceeded. Note that the dependence on the laser wavelength and pulse length can be strongly nonlinear, see e.g. Ref. 17 for an in-depth discussion and more empirical data. Moreover, if the laser travels a longer distance through the material, the nonlinear phase shift also needs to be considered.¹⁸ In general, a shorter pulse allows for a higher gradient at the same fluence. Moreover, a high band gap material as e.g. SiO_2 will have a higher damage threshold and a low band gap material such as Silicon has a lower damage threshold but a higher refractive index.

For the sub-relativistic experiments in the ACHIP collaboration, we mostly use $\lambda_0 = 2 \mu\text{m}$ femtosecond laser pulses, generated by Optical Parametric Amplifiers (OPA) or by novel Tm or Ho-Tm fiber laser amplifiers currently under development. The electron source needs to provide ultra-low emittance, particularly at low energy. For a lossless sub-100-keV injection into a DLA operating at $2 \mu\text{m}$, geometric emittances smaller than 0.1 nm are required.¹⁹ Different emitters are available to produce these low emittances, e.g. Ref. 20, or see Ref. 21 for an overview. At these emittances, the achievable charge is quite small at the moment. We hope to achieve higher average charge in the future by increasing both the repetition rate and the single microbunch charge.

2. Different Means of Laser Coupling

All the DLA experiments published so far have used free space laser coupling. At longer interaction length, it is necessary to provide symmetric fields, such that there

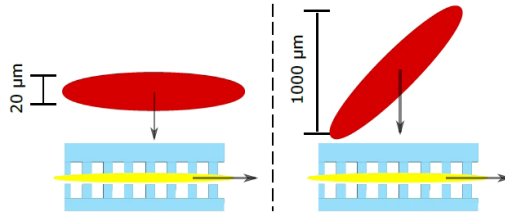


Fig. 3. Flat versus tilted laser pulse. At roughly the same pulse length for each grating cell, the interaction length is significantly increased. Picture adapted from Ref. 25.

is no coherent deflection force. There are different means to obtain symmetric fields in the acceleration channel, the simplest is to illuminate the structure symmetrically from both sides with equal phase and polarization. If this is impractical from the optics point of view, the fields of a single side drive laser can also be symmetrized by using a Bragg mirror on the chip.^{22,23}

The laser fluence on each DLA cell can be reduced by shortening the pulse and tilting the pulse front,^{25,26} such that it remains synchronous with a few electron bunches over a distance (or duration) much longer than a single DLA cell is illuminated, see Fig. 3. Practically, the pulse front tilt can be achieved, for example, by a prism or by a reflection grating with unequal incidence and reflection angles.^{24–26}

Another option to increase the interaction length in the accelerator structure is an on-chip waveguide system,²⁷ see Fig. 4. This supplies different parts of the accelerator structure with the appropriate phase and group delay. Moreover, a different higher damage threshold and lower refractive index material can be used to convey higher laser fluence in the waveguides, which can be split into many waveguides

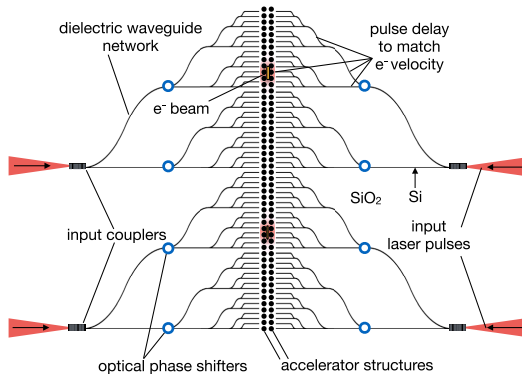


Fig. 4. On-chip waveguide laser power delivery system. Picture adapted from Ref. 27.

1942031-5

before coupling to the high refractive index accelerator structure. Using this technique, it is possible to produce a similar illumination pattern as would be obtained by pulse front tilt in free space.

3. Field Computation for a Single DLA Cell

The laser field computation of a single DLA cell using periodic boundary conditions is not a challenge, since its electrical length L/λ is on the order of one. It can be simulated by various techniques such as Finite Difference/Finite Integration Time Domain (FD/FI TD) codes,^{28,29} Finite Difference Frequency Domain (FDFD) codes,³⁰ or Finite Element Frequency Domain (FEFD) codes.^{29,31} These can be combined with various optimization techniques, in order to find structures with highest gradient, lowest field inside the material, or highest bandwidth. Of course, these optimization goals compete, such that an optimum can only be found in the sense of a Pareto-front. Simple DLA structures can also be designed from a physical point of view, such that maximum electric field modulation at the synchronous harmonic is achieved, which results in Bragg cavity structures.^{31,32} A more mathematical approach is rather to use adjoint methods to perform large-scale, gradient-based optimization of the full permittivity distribution.³⁴ However, these methods tend to generate nonintuitive device geometries and sometimes require additional constraints to create fabricable structures. Moreover, adjoint methods have also been used for other parts of the integrated DLA, such as grating couplers.³⁵

4. Beam Dynamics Simulations in DLAttrack6D

We will summarize and slightly add to DLAttrack6D, the one kick per cell tracking approach originally conceived in Ref. 32. The kicks are sufficiently described by one complex coefficient per DLA cell, where the longitudinal and transverse dependencies are derived analytically. Although the derivation holds true only for strict periodicity, small deviations can be accepted within reasonable error. Also, fringe fields are not included, even in practice they should be reduced as much as possible. The effect of fringe fields is however strongly dependent on the quality factor of the structure, usually determined by the available bandwidth.

Starting from the longitudinal energy gain, the kicks in all directions are computed and then used for symplectic tracking. The energy gain of an electron with charge $q = -e$ can be written as function of the time domain electric field E_z , its Frequency Domain (FD) phasor \underline{E}_z , or by means of spatial Fourier series in periodic DLA structures

$$\Delta W(x, y, s) = q \int_{-\lambda_{gz}/2}^{\lambda_{gz}/2} E_z(x, y, z; t = (z + s)/v) dz \quad (2)$$

$$= q \lambda_{gz} \operatorname{Re} \left\{ e^{2\pi i \frac{s}{\beta \lambda_0}} \underline{e}_m(x, y) \right\}. \quad (3)$$

1942031-6

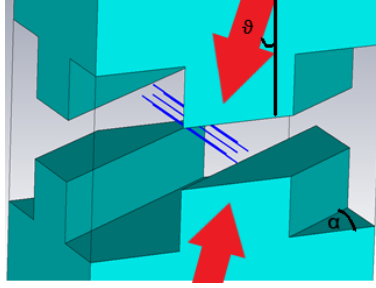


Fig. 5. Unit cell of a tilted grating (tilt angle α , where $\alpha = 0$ is a straight, infinitely wide grating). The blue lines indicate possible electron trajectories. The laser is incident from top and bottom, with polarization in electron beam direction and possible tilt angle ϑ in the plane perpendicular to the electron beam.

Here, the spatial Fourier coefficient is computed as

$$\underline{e}_m(x, y) = \frac{1}{\lambda_{gz}} \int_{-\lambda_{gz}/2}^{\lambda_{gz}/2} \underline{E}_z(x, y, z) e^{im \frac{2\pi}{\lambda_{gz}} z} dz. \quad (4)$$

The above relation holds only if the Wideroe condition $\lambda_{gz} = m\beta\lambda_0$ is fulfilled, where λ_{gz} is the grating period and β is the velocity in units of c . In the following we will restrict the arbitrary integer spatial harmonic m to $m = 1$, which usually has the strongest amplitude \underline{e}_1 . For the application of higher harmonics see e.g. Ref. 33.

The transverse kicks can be obtained by exploiting the known transverse dependency of $\underline{e}_1(x, y)$ on the transverse coordinates. From the Panofsky–Wenzel theorem,³⁶ conveniently written as

$$\nabla' \times \Delta \mathbf{p}(x, y, s) = 0, \quad (5)$$

where the relative gradient is $\nabla' = (\partial_x, \partial_y, -\partial_s)$, we obtain under the synchronicity condition³²

$$\Delta \mathbf{p}_\perp(x, y, s) = -\frac{\lambda_{gz}^2}{2\pi} q \frac{1}{\beta c} \text{Im}\{e^{2\pi i \frac{s}{\beta\lambda_0}} \nabla_\perp \underline{e}_1(x, y)\}. \quad (6)$$

For a symmetric laser illumination, the transverse dependencies can be written as

$$\underline{e}_1(x, y) = \underline{e}_1(0, 0) \cosh(ik_y y) e^{ik_x x}, \quad (7)$$

where k_x includes the option of a tilt of the grating or the laser incidence, $k_z = 2\pi/(\beta\lambda_0)$, and $k_y = \pm\sqrt{(2\pi/\lambda_0)^2 - k_z^2 - k_x^2}$. For a grating tilt angle α (see Fig. 5) we obtain³² $k_x = k_z \tan(\alpha)$ and for a laser tilt angle θ (keeping the polarization parallel to the electron beam) we obtain $k_x = k_z \sin(\theta)$. After some manipulations, we finally obtain the kicks³²

$$\Delta x' = -\frac{q\lambda_0}{p_{z0}c} \tan(\alpha) \cosh(ik_y y) \text{Re}\{\underline{e}_1 e^{i\varphi + ik_x x}\}, \quad (8a)$$

$$\Delta y' = -\frac{ik_y \lambda_0^2 q \beta}{2\pi p_{z0} c} \sinh(ik_y y) \text{Im}\{\underline{\epsilon}_1 e^{i\varphi + ik_x x}\}, \quad (8b)$$

$$\Delta \delta = \frac{q \lambda_{gz}}{\gamma m_e c^2} \text{Re}\{\underline{\epsilon}_1 (\cosh(ik_y y) e^{i\varphi + ik_x x} - e^{i\varphi_s})\}. \quad (8c)$$

In case of an anti-symmetric illumination, i.e. a π phase shift between the two laser beams, the transverse dependence is

$$\underline{\epsilon}_1(x, y) = \underline{\epsilon}_1(0, 0) \sinh(ik_y y) e^{ik_x x}, \quad (9)$$

and the kicks are accordingly

$$\Delta x' = -\frac{q \lambda_0}{p_{z0} c} \tan(\alpha) \sinh(ik_y y) \text{Re}\{\underline{\epsilon}_1 e^{i\varphi + ik_x x}\}, \quad (10a)$$

$$\Delta y' = \frac{-ik_y \lambda_0^2 q \beta}{2\pi p_{z0} c} \cosh(ik_y y) \text{Im}\{\underline{\epsilon}_1 e^{i\varphi + ik_x x}\}, \quad (10b)$$

$$\Delta \delta = \frac{q \lambda_{gz}}{\gamma m_e c^2} \text{Re}\{\underline{\epsilon}_1 \sinh(ik_y y) e^{i\varphi + ik_x x}\}. \quad (10c)$$

Note that in the sinh-mode, the energy gain of the synchronous particle is always zero, since the longitudinal electric field vanishes in the center of the channel. The sinh-mode can be used as a diagnostic, in order to convert a temporal profile into an angle distribution profile,³⁷ which is usually referred to as beam streaking.

The symplectic one-kick-per-cell tracking is independent of the realization of the kick functions and reads

$$\begin{pmatrix} x \\ x' \\ y \\ y' \\ \varphi \\ \delta \end{pmatrix}^{(n+1)} = \begin{pmatrix} x \\ Ax' + \Delta x' \\ y \\ Ay' + \Delta y' \\ \varphi \\ \delta + \Delta \delta(\varphi_s) \end{pmatrix}^{(n)} + \begin{pmatrix} \lambda_{gz} x' \\ 0 \\ \lambda_{gz} y' \\ 0 \\ -\frac{2\pi}{\beta^2 \gamma^2} \delta \\ 0 \end{pmatrix}^{(n+1)}, \quad (11)$$

with the tracking variables in paraxial approximation

$$\begin{aligned} x' &= \frac{p_x}{p_{z0}}, & \Delta x' &= \frac{\Delta p_x(x, y, \varphi)}{p_{z0}}, \\ y' &= \frac{p_y}{p_{z0}}, & \Delta y' &= \frac{\Delta p_y(x, y, \varphi)}{p_{z0}}, \\ \varphi &= 2\pi \frac{s}{\lambda_{gz}}, & \delta &= \frac{W - W_0}{W_0}, \\ \Delta \delta &= \frac{\Delta W(x, y, \varphi) - \Delta W(0, 0, \varphi_s)}{W_0}, \end{aligned} \quad (12)$$

where $W_0 = \gamma m_e c^2$ and $p_{z0} = \beta \gamma m_e c$. The adiabatic damping of the transverse emittance is described by

$$A^{(n)} = \frac{(\beta\gamma)^{(n+1)}}{(\beta\gamma)^{(n)}} = 1 + \left[\frac{\lambda_0 q \text{Re}\{e^{i\varphi_s} \underline{e}_1\}}{\beta\gamma m_e c^2} \right]^{(n)}. \quad (13)$$

While keeping the synchronicity condition by appropriately chirping the structure, the acceleration ramp can be written as

$$W(N) = W(0) + q \sum_{n=1}^N \lambda_g^{(n)} \text{Re}\{e_1^{(n)} e^{i\varphi_s^{(n)}}\}. \quad (14)$$

We note that chirping the structure length while maintaining constant phase $\arg(\underline{e}_1)$ is possible by correcting the phase drift with another parameter in the structure design.²²

DLAtrack6D is written in Matlab,³⁸ it is based on a phase space structure that allows for vectorized updates in each DLA cell. The code, together with a brief manual, is available upon request.

5. Electron Beam Focusing

Optical near field accelerators cannot rely on magnetic focusing only, since the small scale of the near field requires sub-micron beam sizes which in turn would require magnetic field strengths unachievable by conventional quadrupole magnets.³⁹ Thus, a laser-based focusing scheme is required to make DLA scalable.

Two different options have been proposed for focusing with the phase-dependent transverse laser fields. In 2012, the group at UCLA has proposed spatial harmonic focusing.⁴⁰ Stability of the electron beam could be predicted by means of retracting ponderomotive forces due to nonsynchronous harmonics, while the synchronous harmonic serves for acceleration. However, the beam envelope at given emittance could not be determined more accurately than in the smooth approximation. Moreover, the focusing harmonic needs to be quite strong (much stronger than the accelerating harmonic), which puts a constraint on the choice of materials and pulse length due to the damage threshold fluence. In particular, this scheme has been implemented with SiO₂ structures at relativistic energies.⁴¹

Recently, Niedermayer *et al.* proposed Alternating Phase Focusing (APF) for DLA.¹⁹ Here, we work only with a single spatial harmonic, i.e. \underline{e}_1 , but its phase can be changed by means of fractional period drift elements. The hereby generated longitudinal/transversal alternating focusing gradients can be integrated in the Courant–Snyder sense. Thus, a scalable scheme is obtained, where about half (dependent on the synchronous phase) of the synchronous harmonic is translated to acceleration gradient. The required pre-bunching on the optical scale can be obtained with the same scheme, see Ref. 19. Due to the exact integration of the lattice (and thus a precise determination of the beam envelope) and the efficient translation of incident field to acceleration gradient, this scheme is particularly suited

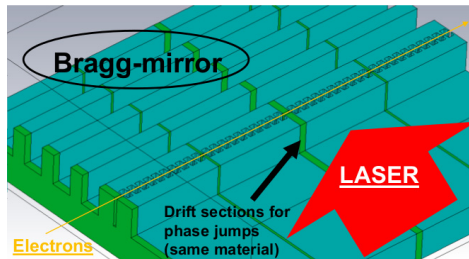


Fig. 6. Outline of an APF DLA structure, picture adapted from Ref. 32.

for sub-relativistic DLAs working with high refractive index Silicon structures that have a rather low damage threshold. An outline of such a structure is depicted in Fig. 6. Such APF-structures are capable of confining the electron beam in longitudinal and horizontal direction. The confinement in the vertical direction, where the laser fields are ideally invariant, can be achieved by enclosing the entire chip by a vertically focusing quadrupole magnet, which can be realized with Neodymium permanent magnets.

6. Full Scale Simulation Techniques

For full scale tracking and Particle In Cell (PIC) simulations, we mostly use the codes CST Studio Suite²⁹ and VSim.²⁸ A full scale PIC simulation is however numerically quite heavy, thus we prefer to do this only for finished designs and rely on DLAttrack6D for design studies. In CST, we have the convenient option to calculate the fields either in TD or FD and store them as frequency domain phasors, i.e. one complex number per mesh edge. Note that storing in FD does not necessarily mean computation in FD; in fact, FD simulations become intractable as the simulation size becomes large, so instead, TD computation can be performed along with an on-the-fly Fourier Transform.

We use VSim in cases where large scale computing is required. Moreover, including a pulse front tilted laser beam is rather involved in CST at the moment, thus we did this in VSim. The capability of VSim for electron energy loss in materials, to model experiments where part of the electron beam clips the structure, was also added and showed good agreement with experiments.⁶ In the near future, we plan to conduct high performance PIC simulations to assess the effects of fringe fields and imperfect field flatness, wake fields, and radiation emission using NERSC cluster time awarded to the ACHIP collaboration partner TechX.

7. Recently Completed and Ongoing Experiments

Simulations are conducted for the design and the evaluation of different recent DLA experiments. Recently completed were experiments for acceleration with displaced

dual pillar structures and Bragg reflectors.⁴² Moreover, the first acceleration results with waveguide driven inverse-designed DLA structures were obtained recently.⁴³

The first focusing experiment uses the intrinsic phase-dependent focusing properties of a DLA structure.⁴⁴ In this experiment, the electrons are injected at random phase, which means that they are either focused or defocused, i.e. a cross-shape is formed in transverse phase space (see also Ref. 22). An aperture lets only the focused electrons pass, the defocused ones are lost. This transmission is however still higher than in the absence of the laser, i.e. when there is no focusing at all. This experiment can also be run in deflection (sinh) mode, i.e. the electrons are deflected to the left or right, dependent on their phase. Strong deflection will reduce the transmission through the aperture accordingly, which is readily measurable.

Another ongoing focusing experiment is APF with a Bragg mirror, as outlined in Fig. 7. As discussed in detail in Ref. 19, this APF focusing channel transports particles at all phases. A pre-bunching is not required for transport only, however it would be required for acceleration. In the bottom of the figure, the longitudinal electric field is plotted. Different options for filling the half cell spaces for phase jumps have been simulated. In the end, it turned out that the spacers are only helpful in the beginning and the end of the structure and within it is sufficient to leave half a cell empty. Moreover, another crucial optimization is to tune the Bragg mirror distance such that the fields in the channel become symmetric. After the optimized fields have been determined, electron tracking can be done both in DLAttrack6D and full PIC codes. Figure 8 shows how the fraction of electrons transported through the structure is dependent on the laser field strength (DLAttrack6D). This structure has recently been fabricated (see Fig. 9) and is ready for testing at FAU Erlangen.

The minimal beta-function is obtained at roughly 200 MV/m, where maximum transmission occurs. Beyond that point, the beam is first over-focused, and eventually leaves the area of stability. The reason for the losses at the matched e_1 is the geometric emittance of 0.3 nm (Gaussian distribution initially), which is larger than

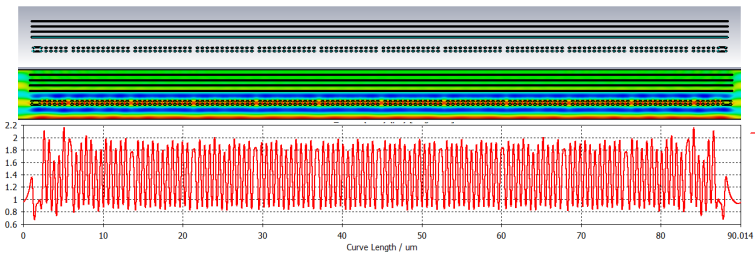


Fig. 7. (Color online) APF single laser beam transport structure (top), normalized (to 1 V/m incident laser field) longitudinal electric field phasor magnitude with laser from bottom (center) and on axis normalized field flatness plot (bottom), obtained by CST MWS in TD. The linear color scale reaches from 0 (blue) to 2 (red).

1942031-11

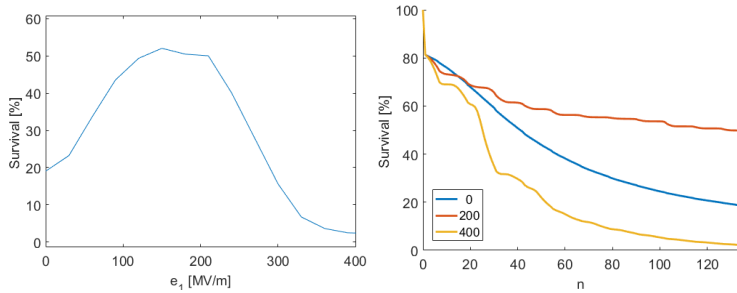


Fig. 8. Transmission rate as function of laser field strength (left) and electron loss as function of DLA cell index for $e_1 = (0, 200, 400)$ MV/m laser field strength (right).

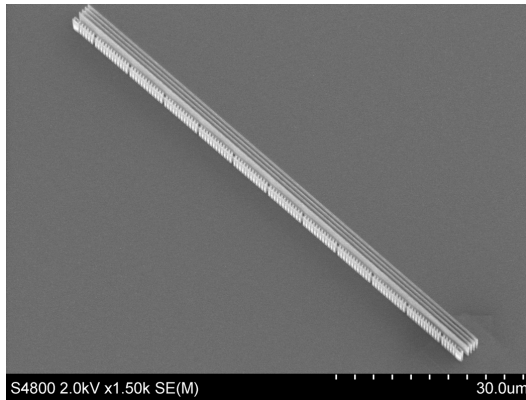


Fig. 9. SEM picture of the structure design as in Fig. 7.

the acceptance of the structure. Once saturated at about 50%, the electrons can be transported over an arbitrary distance, which is limited only by the defocusing in the direction of the pillar height. Roughly the same results are obtained by tracking in the CST PIC solver.

In succession to Refs. 37, 45 and 46, we plan a two stage buncher-accelerator or buncher-streaker experiment, see Fig. 10. Here, we use dual drive from two stages, with independent phase control and independent amplitude control of lasers 1 and 2. The first DLA stage is normally run in cosh-mode and serves as a buncher. The second stage can be either run in cosh-mode for acceleration, or in sinh-mode for streaking. Replacing the first (buncher) structure by an APF-type buncher, see Ref. 19, will allow us to obtain short bunches with low energy spread. This gives



Fig. 10. Combined buncher and accelerator/streaker DLA.

the opportunity to observe both coherent streaking and coherent acceleration at the same setup on a spectrometer screen.

Additionally to the low energy experiment, there are also high-energy experiments planned. Most prominently, we will use the 3.2 GeV beam at SwissFEL at PSI to inject into a DLA. Due to the extremely small geometric emittance at such high energy, this injection will be almost lossless. Additionally, at such energy, the deflection and acceleration defocusing is rather small. Therefore, we are restricted only by the conventional electron optics (Rayleigh length) and the available laser pulse energy, which can be cast in a tilted pulse. Details of the outlined experiments can be found in Refs. 47 and 48.

Moreover, relativistic energy experiments are also outlined at the SINBAD facility at DESY, where an inverse FEL undulator together with a chicane will be employed for optical-scale bunching of the beam before it is injected into the DLA. Driving the DLA with the same laser as is used for seeding the inverse FEL allows for the precise phase control required for coherent acceleration.⁴⁹

The group at UCLA aims for a 2-cm long DLA experiment at about 5 MeV injection energy at the Pegasus facility.⁵⁰ Challenges are that focusing of the beam is still required and also a slight chirp needs to be imprinted to account for the slightly sub-relativistic velocity. Creating both the focusing harmonics and the chirp is planned to be achieved by a strictly periodic SiO₂ grating fed by a tilted laser pulse that is modulated by a Spatial Light Modulator, see e.g. Ref. 51.

8. Current Status and Outlook

We are now able to perform start-to-end simplified simulations of larger DLA chips with DLAttrack6D. For full scale 3D PIC or tracking simulations, a cluster computer is required. The experiments performed at the moment can still be simulated well in 2D by available PIC codes. However, it is expected that the structure lengths will soon significantly increase.

One option for efficient large-scale PIC for DLA would be a moving window code, which discretizes only the co-moving environment of a few electron micro-bunches. The rest of the structure contains neither electrons nor laser energy, since we strongly restrict the interaction region by applying the pulse front tilt or other means of selective synchronized illumination.

The charge we accelerate in current DLA experiments is mostly rather low. However, at particular high energy experiments as e.g. at PSI, the entire beam is

put through the small aperture of the DLA. We expect to see wake field effects here for the first time. Simulations of wake field effects are already in place.⁵² We outline to integrate linear and nonlinear wake kicks from precomputed wake functions into DLAttrack6D as well. With this we will be able to properly predict the strength of beam loading effects and longitudinal and transverse beam instabilities in longer DLA structures.

Acknowledgments

ACHIP is funded by the Gordon and Betty Moore Foundation (Grant No. GBMF4744 to Stanford). U.N. acknowledges also the funding by the German Federal Ministry of Education and Research (Grant No. FKZ:05K16RDB). B.C. (TechX) acknowledges usage of NERSC, a U.S. Department of Energy Office of Science User Facility operated under Contract No. DE-AC02-05CH11231.

References

1. ACHIP website: <https://achip.stanford.edu>.
2. K. Shimoda, *Appl. Opt.* **1**, 33 (1962).
3. A. Lohmann, IBM Technical Note, 169 (1962).
4. M. Kozak et al., *Opt. Exp.* **25**, 19195 (2017).
5. E. A. Peralta et al., *Nature* **503**, 91 (2013), doi:10.1038/nature12664.
6. K. P. Wootton et al., *Opt. Lett.* **41**, 2696 (2016).
7. J. Breuer and P. Hommelhoff, *Phys. Rev. Lett.* **111**, 134803 (2013).
8. K. J. Leedle, A. Ceballos, H. Deng, O. Solgaard, R. Fabian Pease, R. L. Byer and J. S. Harris, *Opt. Lett.* **40**, 4344 (2015).
9. M. Kozak et al., *NIM A* **865**, 84 (2017).
10. R. J. England et al., *Rev. Mod. Phys.* **86**, 1337 (2014).
11. K. P. Wootton, J. Mcneur and K. J. Leedle, *Rev. Accel. Sci. Tech.* **09**, 105 (2016).
12. J. McNeur et al., *Optica* **5**, 687 (2018), doi:10.1364/OPTICA.5.000687.
13. T. Plettner and R. L. Byer, *Phys. Rev. ST Accel. Beam* **11**, 030704 (2008).
14. T. Plettner and R. L. Byer, *Nucl. Instrum. Methods Phys. Res. A* **593**, 63 (2008).
15. T. Plettner, R. Byer, C. McGuinness and P. Hommelhoff, *Phys. Rev. ST Accel. Beams* **12**, 101302 (2009).
16. K. Soong, R. L. Byer, E. R. Colby, R. J. England and E. A. Peralta, *AIP Conf. Proc.* **1507**, 511 (2012).
17. P. Pronko et al., *Phys. Rev. B* **58**, 2387 (1998).
18. D. Cesar et al., *Nat. Comm. Phys.* **1**, 46 (2018).
19. U. Niedermayer, T. Egenolf, O. Boine-Frankenheim and P. Hommelhoff, *Phys. Rev. Lett.* **121**, 214801 (2018).
20. D. Ehberger, J. Hammer, M. Eisele, M. Krueger, J. Noe, A. Hogege and P. Hommelhoff, *Phys. Rev. Lett.* **114**, 227601 (2015).
21. A. Feist et al., *Ultramicroscopy* **176**, 63 (2017).
22. U. Niedermayer, O. Boine-Frankenheim and T. Egenolf, *J. Phys. Conf. Ser.* **874**, 012041 (2017), doi:10.1088/1742-6596/874/1/012041.
23. P. Yousefi et al. *Nucl. Instrum. Methods A* **909**, 221 (2018).
24. Y. Wei et al., *Appl. Opt.* **56**, 8201 (2017).
25. D. Cesar, J. Maxson, P. Musumeci, X. Shen, R. J. England and K. P. Wootton, SLAC-PUB-17180 (2017).

26. M. Kozak *et al.*, *J. Appl. Phys.* **124**, 023104 (2018), doi:10.1063/1.5032093.
27. T. W. Hughes *et al.*, *Phys. Rev. Appl.* **9**, 54017 (2018).
28. VSim, www.txcorp.com.
29. CST Studio Suite 2018, www.cst.com.
30. W. Shin and S. Fan, *Opt. Express* **21**, 22578 (2013).
31. T. Egenolf, O. Boine-Frankenheim and U. Niedermayer, *J. Phys.: Conf. Ser.* **874**, 012040 (2017), doi:10.1088/1742-6596/874/1/012040.
32. U. Niedermayer, T. Egenolf and O. Boine-Frankenheim, *Phys. Rev. AB* **20**, 111302 (2017).
33. J. McNeur, M. Kozak, D. Ehberger, N. Schönenberger, A. Tafel, A. Li and P. Hommelhoff, *J. Phys. B: At. Mol. Opt. Phys.* **49**, 034006 (2016).
34. T. Hughes *et al.*, *Opt. Express* **25**, 15414 (2017), doi:10.1364/OE.25.015414.
35. N. Sapra *et al.*, *IEEE JSTQE* **25** (2019).
36. W. K. H. Panofsky and W. A. Wenzel, *Rev. Sci. Instrum.* **27**, 967 (1956), doi:10.1063/1.1715427.
37. K. J. Leedle, D. S. Black, Y. Miao, K. E. Urbanek, A. Ceballos, H. Deng, J. S. Harris, O. Solgaard and R. L. Byer, *Opt. Lett.* **43**, 2181 (2018).
38. MathWorks, Matlab (2016).
39. A. Ody, P. Musumeci, J. Maxson, D. Cesar, R. J. England and K. P. Wootton, *NIM A* **865**, 75 (2017).
40. B. Naranjo, A. Valloni, S. Putterman and J. B. Rosenzweig, *Phys. Rev. Lett.* **109**, 164803 (2012).
41. D. Cesar, J. Maxson, X. Shen, K. P. Wootton, S. Tan, R. J. England and P. Musumeci, *Opt. Express* **26**, 29216 (2018) 1804.00634.
42. P. Yousefi, N. Schönenberger, J. McNeur, M. Kozak, U. Niedermayer and P. Hommelhoff, *Opt. Lett.* **44**, 1520 (2019).
43. N. Sapra *et al.*, 1905.12822.
44. D. Black, K. Leedle, Y. Miao, U. Niedermayer, R. L. Byer and O. Solgaard, *Phys. Rev. Lett.* **122**, 104801 (2019).
45. M. Kozak *et al.*, *Nat. Comm.* **8**, 14342 (2017).
46. M. Kozak, N. Schönenberger and P. Hommelhoff, *Phys. Rev. Lett.* **120**, 103203 (2018).
47. E. Prat *et al.*, *NIM A* **865**, 87 (2017).
48. E. Ferrari *et al.*, *NIM A* **907**, 244 (2018).
49. F. Mayet *et al.*, *NIM A* **909**, 213 (2018).
50. D. Cesar, P. Musumeci and R. J. England, *2018 IEEE Advanced Accelerator Concepts Workshop (AAC)*, doi:10.1109/AAC.2018.8659380.
51. ThorLabs EXULUS-HD1 Spatial Light Modulator, www.thorlabs.com.
52. T. Egenolf, U. Niedermayer and O. Boine-Frankenheim, *2018 IEEE Advanced Accelerator Concepts Workshop (AAC)*, doi:10.1109/AAC.2018.8659426.

Dielectric-laser electron acceleration in a dual pillar grating with a distributed Bragg reflector

PEYMAN YOUSEFI,^{1,*} NORBERT SCHÖNENBERGER,¹ JOSHUA MCNEUR,¹
MARTIN KOZÁK,^{1,2} UWE NIEDERMAYER,³ AND PETER HOMMELHOFF^{1,4}

¹ Department of Physics, Friedrich Alexander University Erlangen Nuremberg, Staudtstr. 1, 91058 Erlangen, Germany

² Faculty of Mathematics and Physics, Charles University, Ke Karlovu 3, 12116 Prague 2, Czech Republic

³ Institute for Accelerator Science and Electromagnetic Fields (TEMF), Technische Universität Darmstadt, Schlossgartenstr. 8 D-64289 Darmstadt, Germany

⁴ Max Planck Institute for the Science of Light, Staudtstr. 2, 91058 Erlangen, Germany

*Corresponding author: peyman.yousefi@fau.de

Received 15 January 2019; accepted 9 February 2019; posted 20 February 2019 (Doc. ID XXXX); published 15 March 2019

We report on the efficacy of a novel design for dielectric laser accelerators by adding a distributed Bragg reflector (DBR) to a dual pillar grating accelerating structure. This mimics a double-sided laser illumination, resulting in an enhanced longitudinal electric field while reducing the deflecting transverse effects, when compared to single-sided illumination. We improve the coupling efficiency of the incident electric field into the accelerating mode by 57 percent. The 12 μm long structures accelerate sub-relativistic 28 keV electrons with gradients of up to 200 MeV/m in theory and 133 MeV/m in practice. Our work shows how lithographically produced nano-structures help to make novel laser accelerators more efficient.

<https://doi.org/10.1364/OL.44.001520>

Dielectric laser accelerators (DLAs) are enticing candidates for future particle accelerators. They can reduce the length of the current radio-frequency (RF) accelerators by 1 to 2 orders of magnitude as dielectrics can withstand peak electric fields in the GV/m regime and therefore yield higher acceleration gradients [1]. They are based on electrons interacting with laser-induced optical near-fields in close vicinity to a grating structure described by the inverse Smith-Purcell effect [2, 3]. Acceleration gradients of beyond 250 MeV/m using double sided fused-silica gratings at relativistic electron injection energies and up to 375 MeV/m for single sided fused-silica gratings at sub-relativistic energies have been already demonstrated [4–6]. Different structures from simple gratings to complex geometries have been studied [7–11]. Recent studies have shown acceleration gradients in excess of 200 MeV/m for 96.3 keV electrons and 210 MeV/m for 28 keV electrons using silicon structures [12, 13]. Even higher acceleration gradients of up to 370 MeV/m have been demonstrated by exciting a coupled-mode field profile using a silicon dual pillar grating for sub-100 keV electrons [14]. This design, first proposed by Palmer [15], is of interest as it can provide a practical structure for DLAs with a more uniform field profile in the acceleration channel, due to the symmetric design of the structure. This approach not only reduces the losses, dispersion and nonlinear

distortion of the laser pulse, as it reduces the amount of dielectric material that the pulse needs to traverse, but also facilitates the fabrication process by eliminating the need for bonding two single sided gratings.

The uniformity in field profile is crucial for DLAs as it reduces the deflection forces for electrons [16], enabling longer accelerator structures and larger energy gains. Dual side laser illumination is a favorable approach to provide field uniformity, however it introduces more complexity in the optical path for phase matching the two laser beams. To further improve such an approach, we take advantage of a distributed Bragg reflector (DBR), a highly reflective mirror consisting of alternating layers of high and low refractive index materials, each being a quarter wavelength in thickness. Adding a DBR to the dual pillar grating mimics double-sided laser illumination, which offers a better symmetry in the transverse electric field profile between the pillars where electrons are injected. It also enhances the longitudinal electric field of the accelerating mode, which in theory can lead to an acceleration gradient as high as 70% of the incident field for 28 keV electron energies [17]. Our calculations predict a 99% reflection of the incident field from the DBR to the accelerating channel. They also show a maximum amplitude for the acceleration mode by introducing half a period ($\lambda_0/2$) offset for one row of pillars with respect to the other. This offset is found to be ideal only for low electron energies whereas for higher energies of about 100 keV, dual pillar structures without an offset yield a better efficiency of excitation for the acceleration modes [18].

To optimize the geometrical parameters of the DLA structures, we utilize a combination of FDTD field simulations [19] and General Particle Tracer (GPT) [20], a 5th order Runge-Kutta motion solver, to track the electrons through the simulated electromagnetic near-fields of the accelerator. To reduce computational requirements, the simulation is performed on a single cell with periodic boundaries in 2D, assuming the direction along the pillars' height to be invariant. This allows for quick iteration over parameter sets. Field uniformity, acceleration gradient and minimized transverse deflection are used as figures of merit for determining the ideal design. Finally, the whole structure is simulated to include edge effects. The electron beam parameters are chosen to reproduce the beam used in the experiments with energies of 28.4 keV and 28.1 keV and a geometric emittance of 300 pm rad. We assume a Gaussian beam with a FWHM circular spot size of 20 nm at the entrance of the accelerator structure.

Figure 1(a, b) shows the structures fabricated from 1-5 ohm-cm phosphorus-doped Si<100>. Their patterns are written via electron beam lithography using a RAITH 150TWO. The written patterns are etched via cryogenic reactive ion etching using a Plasma lab 100 Oxford Instruments to directionally etch silicon to a depth of (3.0 ± 0.1) μm [21]. The structures are (12.0 ± 0.1) μm long with a period of (630 ± 5) nm, a pillar diameter of (320 ± 5) nm and an acceleration channel aperture of (200 ± 5) nm. The DBR consists of four layers of silicon with a thickness of (145 ± 5) nm equivalent to $\lambda/4n$, with n the refractive index of silicon at the incident wavelength of $\lambda=2$ μm . The layers are separated by vacuum layers with a distance of (530 ± 5) nm, which is approximately equal to a quarter of the designed incident wavelength. We fabricated two sets of structures one with-and one without a DBR to determine the DBR effect on the acceleration. The relative difference between geometrical dimensions of the fabricated structures is 0.8 %. Such a similarity is crucial to exclusively study the DBR effect on the electron dynamics. A 1930 nm laser pulse with a pulse duration of 650 fs is incident on the pillars with an incident angle of approximately 5° to the zy plane, exciting the optical near-fields. Alignment apertures are etched in front of the structures for easier alignment of the electron beam in the accelerating channel between the pillars.

Since the geometrical parameters of the fabricated structures deviate about 6% from the ideal simulated parameters, limited by the

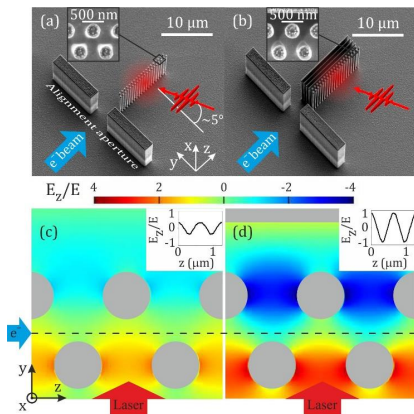
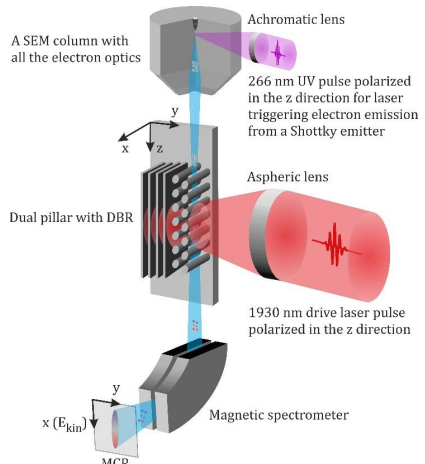


Figure 1. Silicon dual pillar gratings. (a) without DBR, and (b) with DBR. More details of the structures are shown in the insets. The structures are (12.0 ± 0.1) μm long (in the z direction) and (3.0 ± 0.1) μm tall (in the x direction). Apertures are for easier alignment of the electron beam in the channel between the pillars. The red and blue arrows indicate the directions of the laser beam and the electron beam, respectively. The laser pulse is polarized parallel to the z direction and it is incident on the structure with an angle of $\sim 5^\circ$ to the zy plane. Electron pulses

Figure 2. Experimental setup. Electron pulses are emitted from a UV laser-triggered Schottky emitter installed inside a SEM column. The emitted electrons traverse a dual pillar grating with DBR illuminated by 1930 nm, 650 fs drive laser pulses polarized in the z direction. After the electron pulse has interacted with the excited near-fields in between the pillars, it enters a magnetic spectrometer for energy analysis.

fabrication precision, we performed 2D-FDTD simulations for the structures with the fabricated geometrical parameters. The simulations are performed on the whole structure. Figure 1(c, d) shows the simulated longitudinal electric field (E_z) profile normalized by the incident electric field (E) for dual pillars without a DBR and with a DBR, respectively. A Gaussian laser beam with a central wavelength of 1930 nm and a pulse duration of 650 fs is chosen, in accordance with the values used in the experiment. It is evident from the field profiles that adding a DBR enhances the longitudinal electric field. The inset plots show the cross-sectional slice of the normalized longitudinal electric field at the dashed line. As they indicate, the field amplitude inside the accelerating channel is doubled when the DBR is added. This occurs as the phase shift between the incident field and the reflected field from the DBR is zero, $\Delta\phi=0$, which leads to a constructive interference of the two fields.

Our experimental setup is depicted in Figure 2. We employ a Phillips XL30 scanning electron microscope (SEM) equipped with a standard Schottky emitter. A Ti:Sapphire regenerative amplifier with a repetition rate of 1 kHz, combined with an optical parametric amplifier (OPA) generates infrared (IR) pulses with a central wavelength of 1930 nm and a pulse duration of 100 fs. The IR pulses with a polarization parallel to the z axis illuminate the dual pillars from one side exciting the optical near-fields (see Figure 1d). An ultraviolet (UV) beam with a central wavelength of $\lambda_U=266$ nm is generated via second harmonic generation and subsequent sum frequency generation of the fundamental and second harmonics of the Ti:Sapphire laser. The UV pulses are focused onto the Schottky tip, with a filament current below the DC emission threshold. Thus, electron pulses are emitted via single photon absorption. The resulting pulse train has an initial energy of 28



keV ($\beta=0.32$) and an initial energy spread of ~ 0.5 eV. After propagation through the electron optics, the electron pulses have a temporal length of ≥ 400 fs, measured via cross correlation with the laser pulses at the accelerator structure [22]. The electron pulses are focused to the entrance of the dual pillar channel. In order to increase the temporal overlap between the electrons and the near-fields, the IR pulses' length

is stretched from 100 fs to 650 fs using a Fabry-Perot bandpass filter. This allows all electrons to interact with the excited near-fields. We temporarily overlap the electron pulses with the laser illuminating the structure by controlling the arrival time of the IR pulses with a delay stage. After the electrons have interacted with the near-fields, they enter a magnetic spectrometer with a resolution of ~ 30 eV. The spectrally dispersed electrons are incident onto a micro-channel plate (MCP). Spectra are acquired from the phosphor screen of the MCP via a CCD camera and integrated over many iterations for each measurement to improve the signal-to-noise ratio. The spectral resolution of the detection system in the presented study is limited to ~ 200 eV.

Figure 3 shows the measured electron energy spectra for two structures, with- and without a DBR. The peak electric field over a $9.0 \mu\text{m}$ waist radius for both structures is 0.5 GV/m . We observe a maximum energy gain of $(0.44 \pm 0.05) \text{ keV}$ for the structure without the DBR and $(0.69 \pm 0.05) \text{ keV}$ for the structure with the DBR. This corresponds to 1.57 times higher energy gain when the DBR is added. This result implies the existence of a non-zero phase shift, $\Delta\phi \sim 0.3\pi$, between the incident field and the reflected field from the DBR. The ideal design had targeted a $\Delta\phi = 0$ to double the field amplitude in the accelerating channel. This however was not exactly achieved experimentally due to the fabrication tolerances.

To measure the maximum achievable acceleration gradient, we examined a different set of dual pillar gratings with DBR whose geometrical parameters are the same as the structures used earlier. This time we used 28.4 keV electrons for different pulse energies. We observed partial structural damage at a peak electric field of $(1.4 \pm 0.1) \text{ GV/m}$. Figure 4 shows the measured electron energy spectra for different incident peak electric fields nearly up to the structure's damage threshold. The energy spectra broaden as the peak field increases, meaning that electrons are gaining or losing more energy as the peak field increases. At 1.4 GV/m peak electric field, a maximum energy gain of $(1.6 \pm 0.1) \text{ keV}$ is achieved. The acceleration gradient (G_{acc}) is calculated by the longitudinal energy gain (ΔE) over the structure's length (L), $G_{acc} = \Delta E/L$. We achieved a maximum acceleration gradient of $(133 \pm 9) \text{ MeV/m}$ for a $(12 \pm 0.1) \mu\text{m}$ long structure.

To determine the efficacy of DBR in theory and the acceleration gradient limit for our current structures, we performed particle tracking simulations for structures with the same geometrical parameters as the

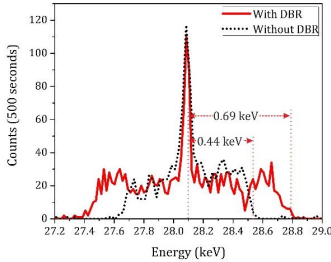


Figure 3. Energy spectra of 28.1 keV electrons modulated by the excited near-fields between the two rows of pillars. The dotted line shows the spectrum taken from the dual pillar grating without a DBR and the solid line denotes the structure with a DBR. Both structures are illuminated by a 1930 nm , 650 fs laser beam with a peak field amplitude of $(0.50 \pm 0.1) \text{ GV/m}$. The structure with DBR shows 57% more energy gain for the same laser and electron beam parameters. This corresponds to a phase shift of $\sim 0.3\pi$ between the incident field and the reflected field from the DBR.

fabricated ones. Figure 5 shows the calculated electron energy spectra as the incident peak electric field varies up to 1.4 GV/m limited by the structure's damage threshold observed experimentally. Here, 28.4 keV electrons are chosen to stay synchronized with the near-fields' phase velocity. Electrons are transmitted through the simulated electromagnetic field shown in figure 1(c,d). At 0.5 GV/m , a maximum energy gain of $(0.4 \pm 0.1) \text{ keV}$ for the structure without DBR and $(0.8 \pm 0.1) \text{ keV}$ for the structure with DBR have been calculated. The energy gain is doubled when the DBR is added, which occurs as $\Delta\phi = 0$ (see Figure 1(c,d)). This is an ideal condition to achieve a maximum field amplitude in the acceleration channel.

According to our simulations an energy gain of up to 2.4 keV at 1.4 GV/m peak electric field is achievable for the dual pillars with DBR, which corresponds to an acceleration gradient of 200 MeV/m for a $12 \mu\text{m}$ long structure. This is 1.5 times higher than the measured value

Figure 4. Measured energy spectra of 28.4 keV electrons after interacting with the near-fields excited by a 1930 nm laser beam with a pulse duration of 650 fs inside the acceleration channel of a dual pillar grating structure with a DBR. The maximum peak electric field of 1.4 GV/m is limited by the laser damage threshold of the structure. The inset plot shows the maximum longitudinal energy gain (ΔE) as a function of the peak electric field. A maximum energy gain of $(1.6 \pm 0.1) \text{ keV}$ is achieved for the $(12 \pm 0.1) \mu\text{m}$ long structure.

which suggests room for further optimizations. This could be due to multiple factors such as imperfections of the fabricated structures in terms of not having perfectly round pillars or a slight alternation in the geometrical parameters from pillar to pillar. The etching process may have also roughened the pillars causing field distortions during the experiment. Moreover, the laser beam is incident with an angle which could lower the effective peak electric field in the acceleration channel, thereby lowering the energy gain.

In conclusion, we have studied the effect of distributed Bragg reflectors on the electron energy modulation using a dual pillar grating. A DBR improves the acceleration gradient by 57% for 28 keV electrons indicating a phase shift of $\Delta\phi \sim 0.3\pi$ between the incident field and the reflected field from the DBR. Such structures can excite a symmetric near-field profile providing up to 200 MeV/m gradient in theory and up to 133 MeV/m gradient in practice under 1930 nm , 650 fs laser illumination. Dual pillar gratings with DBR are good candidates for a miniaturized dielectric laser accelerator as they can mimic dual laser illumination on chip for a better transverse control of electrons. Since the structures are etched in one step, it offers more reproducibility in terms of geometry from structure to structure. The final DLA structure

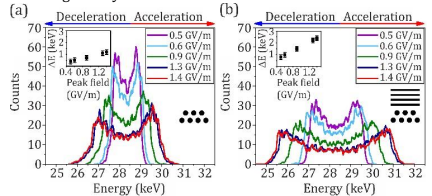


Figure 5. Simulated energy spectra of 28.4 keV electrons modulated by different peak electric fields for a) Dual pillars without DBR and b) Dual pillars with DBR. The peak fields are chosen in accordance to the experiment. The energy gain is doubled when the DBR is added (see the inset plots). At 1.4 GV/m a maximum energy gain of $(2.4 \pm 0.1) \text{ keV}$ is calculated which corresponds to a gradient of $(200 \pm 9) \text{ MeV/m}$.

for sub-relativistic energies needs to be tapered to prevent electrons dephasing. A full particle accelerator indeed needs other elements such as pre-buncher and focusing elements [23], which can all be implemented with the DBR approach. This concept could ultimately lead to a compact laser-driven particle accelerator for variety of applications from low energy radiation therapy devices to high energy particle colliders.

Funding. Gordon and Betty Moore Foundation, Acceleration on a Chip International Project (ACHIP) (GBMF4744); German Federal Ministry for Education and Research (BMBF) via the project e-fs (05K16WEC); European Research Council (ERC) via the project Near Field Atto.

Acknowledgment. We thank F. Gannott, O. Lohse and I. Harder for assistance in structure fabrication and the ACHIP collaboration members for fruitful discussions.

REFERENCES

- R. J. England, R. J. Noble, K. Bane, D. H. Dowell, C.-K. Ng, J. E. Spencer, S. Tantawi, Z. Wu, R. L. Byer, E. Peralta, K. Soong, C.-M. Chang, B. Montazeri, S. J. Wolf, B. Cowan, J. Dawson, W. Gai, P. Hommelhoff, Y.-C. Huang, C. Jing, C. McGuinness, R. B. Palmer, B. Naranjo, J. Rosenzweig, G. Travish, A. Mizrahi, L. Schachter, C. Sears, G. R. Werner, and R. B. Yoder, "Dielectric laser accelerators," *Reviews of Modern Physics* **86**, 1337-1389 (2014).
- A. Lohmann, "Electron Acceleration by Light Waves," IBM Technical Note TN5, San Jose, CA (1962).
- K. Shimoda, "Proposal for an Electron Accelerator Using an Optical Maser," *Appl. Opt.* **1**, 33-35 (1962).
- E. A. Peralta, K. Soong, R. J. England, E. R. Colby, Z. Wu, B. Montazeri, C. McGuinness, J. McNeur, K. J. Leele, D. Walz, E. B. Sozer, B. Cowan, B. Schwartz, G. Travish, and R. L. Byer, "Demonstration of electron acceleration in a laser-driven dielectric microstructure," *Nature* **503**, 91-94 (2013).
- J. Breuer and P. Hommelhoff, "Laser-based acceleration of nonrelativistic electrons at a dielectric structure," *Physical review letters* **111**, 134803 (2013).
- D. Cesar, S. Custodio, J. Maxson, P. Musumeci, X. Shen, E. Threlkeld, R. J. England, A. Hanuka, I. V. Makasyuk, and E. A. Peralta, "High-field nonlinear optical response and phase control in a dielectric laser accelerator," *Communications Physics* **1**, 46 (2018).
- C.-M. Chang and O. Solgaard, "Silicon buried gratings for dielectric laser electron accelerators," *Applied Physics Letters* **104**, 184102 (2014).
- Z. Wu, R. J. England, C.-K. Ng, B. Cowan, C. McGuinness, C. Lee, M. Qi, and S. Tantawi, "Coupling power into accelerating mode of a three-dimensional silicon woodpile photonic band-gap waveguide," *Physical Review Special Topics-Accelerators and Beams* **17**, 081301 (2014).
- M. Kozák, P. Beck, H. Deng, J. McNeur, N. Schönenberger, C. Gaida, F. Stutzki, M. Gebhardt, J. Limpert, and A. Ruehl, "Acceleration of sub-relativistic electrons with an evanescent optical wave at a planar interface," *Optics Express* **25**, 19195-19204 (2017).
- E. A. Peralta, E. Colby, R. J. England, C. McGuinness, B. Montazeri, K. Soong, Z. Wu, and R. L. Byer, "Design, fabrication, and testing of a fused-silica dual-layer grating structure for direct laser acceleration of electrons," *AIP Conference Proceedings* **1507**, 169-177 (2012).
- J. McNeur, M. Kozák, N. Schönenberger, K. J. Leele, H. Deng, A. Ceballos, H. Hoogland, A. Ruehl, I. Hartl, and R. Holzwarth, "Elements of a dielectric laser accelerator," *Optica* **5**, 687-690 (2018).
- K. J. Leele, R. F. Pease, R. L. Byer, and J. S. Harris, "Laser acceleration and deflection of 96.3 keV electrons with a silicon dielectric structure," *Optica* **2**, 158-161 (2015).
- M. Kozák, M. Förster, J. McNeur, N. Schönenberger, K. Leele, H. Deng, J. S. Harris, R. L. Byer, and P. Hommelhoff, "Dielectric laser acceleration of sub-relativistic electrons by few-cycle laser pulses," *Nuclear Instruments and Methods in Physics Research Section A: Accelerators, Spectrometers, Detectors and Associated Equipment* **865**, 84-86 (2017).
- K. J. Leele, A. Ceballos, H. Deng, O. Solgaard, R. F. Pease, R. L. Byer, and J. S. Harris, "Dielectric laser acceleration of sub-100 keV electrons with silicon dual-pillar grating structures," *Opt Lett* **40**, 4344-4347 (2015).
- R. B. Palmer, "Open accelerating structures," (CERN, 1996).
- J. Breuer, J. McNeur, and P. Hommelhoff, "Dielectric laser acceleration of electrons in the vicinity of single and double grating structures—theory and simulations," *Journal of Physics B: Atomic, Molecular and Optical Physics* **47**, 234004 (2014).
- U. Niedermayer, O. Boine-Frankenheim, and T. Egenolf, "Designing a Dielectric Laser Accelerator on a Chip," *Journal of Physics: Conference Series* **B74**, 012041 (2017).
- K. J. Leele, D. S. Black, Y. Miao, K. E. Urbanek, A. Ceballos, H. Deng, J. S. Harris, O. Solgaard, and R. L. Byer, "Phase-dependent laser acceleration of electrons with symmetrically driven silicon dual pillar gratings," *Optics letters* **43**, 2181-2184 (2018).
- Lumerical FDTD Solutions, Version 8.21.1781.
- General Particle Tracer, Version 3.35.
- P. Yousefi, J. McNeur, M. Kozák, U. Niedermayer, F. Gannott, O. Lohse, O. Boine-Frankenheim, and P. Hommelhoff, "Silicon dual pillar structure with a distributed Bragg reflector for dielectric laser accelerators: Design and fabrication," *Nuclear Instruments and Methods in Physics Research Section A: Accelerators, Spectrometers, Detectors and Associated Equipment* **909**, 221-223 (2018).
- M. Kozák, J. McNeur, N. Schönenberger, J. Illmer, A. Li, A. Tafel, P. Yousefi, T. Eckstein, and P. Hommelhoff, "Ultrafast scanning electron microscope applied for studying the interaction between free electrons and optical near-fields of periodic nanostructures," *Journal of Applied Physics* **124**, 023104 (2018).
- U. Niedermayer, T. Egenolf, O. Boine-Frankenheim, and P. Hommelhoff, "Alternating-Phase Focusing for Dielectric-Laser Acceleration," *Physical Review Letters* **121**, 214801 (2018).

Net Acceleration and Direct Measurement of Attosecond Electron Pulses in a Silicon Dielectric Laser Accelerator

Dylan S. Black,¹ Uwe Niedermayer,³ Yu Miao,¹ Zhexin Zhao,¹ Olav Solgaard,¹ Robert L. Byer² and Kenneth J. Leedle¹

¹Department of Electrical Engineering, Stanford University, 350 Serra Mall, Stanford, California 94305-9505, USA

²Department of Applied Physics, Stanford University, 348 Via Pueblo Mall, Stanford, California 94305-4090, USA

³Technische Universität Darmstadt, Institut für Teilchenbeschleunigung und Elektromagnetische Felder (TEMF), Schloßgartenstr. 8, 64289 Darmstadt, Germany

 (Received 25 June 2019; revised manuscript received 3 August 2019; published 26 December 2019)

Net acceleration of attosecond-scale electron pulses is critical to the development of on-chip accelerators. We demonstrate a silicon-based laser-driven two-stage accelerator as an injector stage prototype for a Dielectric Laser Accelerator (DLA). The first stage converts a 57-keV (500 ± 100 -fs (FWHM) electron pulse into a pulse train of 700 ± 200 as (FWHM) microbunches. The second stage harnesses the tunability of dual-drive DLA to perform both a net acceleration and a streaking measurement. In the acceleration mode, the second stage increases the net energy of the electron pulse by 200 eV over $12.25 \mu\text{m}$. In the deflection mode, the microbunch temporal profile is analyzed by a direct streaking measurement with 200 as resolution. This work provides a demonstration of a novel, on-chip method to access the attosecond regime, opening new paths towards attosecond science using DLA.

DOI: 10.1103/PhysRevLett.123.264802

Combining the GV/m fields of femtosecond lasers with the high damage thresholds of dielectric materials and the nanofabrication expertise of the semiconductor industry has enabled construction of the highest-gradient nonplasma particle accelerators that currently exist [1]. However, previous demonstrations of Dielectric Laser Accelerators (DLAs) [2,3] have almost exclusively performed *energy modulation* experiments, with equal numbers of accelerated and decelerated particles. Net acceleration requires bunch compression to a fraction of an optical cycle, similar to conventional radio frequency injector stages [4,5]. A DLA injector which can achieve net acceleration with femtosecond optical cycles must therefore produce attosecond-scale bunches.

Attosecond electron pulses are the subject of recent pioneering research [6–11]. For example, ultrafast electron diffraction (UED) uses ultrashort electron pulses to resolve molecular dynamics on femtosecond time scales [12–14]. Attosecond-scale UED would allow sufficient resolution to resolve intramolecular electronic dynamics. Attosecond-scale electron pulses could also provide superradiant enhancement to Smith-Purcell radiators for wavelengths in the VUV-XUV range [15].

Recently, microbunched pulse trains using dielectric structures have been investigated in the THz regime, using charge-dependent self-modulation to achieve microbunching [16]. Laser-driven attosecond-scale microbunching of relativistic electron beams has also been achieved in an inverse free-electron laser, using a magnetic chicane as the dispersive element [17]. However, in a fully on-chip DLA injector, it is simpler to use a velocity bunching scheme while the beam is subrelativistic [18,19].

In this Letter, we generate attosecond-scale microbunched pulse trains by velocity bunching in a subrelativistic, on-chip DLA. We inject this pulse train into a second DLA stage at a tunable injection phase, and observe net acceleration by 200 eV over $12.25 \mu\text{m}$. By tuning the optical mode of the second stage, we characterize the microbunch duration by a direct streaking measurement with an estimated temporal resolution of 200 as. The microbunches produced are measured to be as short as 700 ± 200 as FWHM. The streaking resolution achieved is on par with state-of-the-art direct measurement techniques (~ 100 as resolution) [20–23].

The theory of dual-drive DLA is detailed in [24–26]. We choose a coordinate system $(x, x', y, y', \varphi \equiv \omega \Delta t, E)$, where x and y are the transverse offsets from the beam axis (z) passing through the center of the pillars, x' and y' are the corresponding trajectory angles relative to the z axis, φ is the longitudinal injection phase of an electron relative to the laser field in the structure, Δt is the time delay of an electron relative to a reference particle, ω is the laser angular frequency, and E is the electron energy.

The dual-drive DLA has symmetric and antisymmetric modes, determined by the relative (dual-drive) laser phase: $\theta_1 - \theta_2 = 0, \pm\pi$ for symmetric and antisymmetric modes, respectively [Fig. 1(a)]. In the symmetric mode, the energy gain of a phase-matched particle over N periods of length Λ is

$$\Delta E = -qe_1 N \Lambda \cosh\left(\frac{\omega}{\beta c \gamma} y\right) \cos \omega \Delta t, \quad (1)$$

where β is the normalized electron velocity v_e/c , $\gamma = (1 - \beta^2)^{-1/2}$, and e_1 is defined as the synchronous on axis accelerating field [24]. Experimentally, e_1 is measured by observation of the accelerating gradient of the on axis electrons, visible as the peak of the double-horns energy spectrum (see the Supplemental Material [27]). For clarity, we define the elementary charge q to be 1 and quote all measurements of e_1 in units of MeV/m.

The electron bunch energy is modulated according to Eq. (1) by the first DLA stage. Electrons with injection phase $\omega\Delta t \in [-(\pi/2), (\pi/2)]$ lose energy, and electrons with $\omega\Delta t \in [(\pi/2), (3\pi/2)]$ gain energy. For on axis particles, the faster electrons intersect the slower ones after a distance f_i to create maximally short microbunches spaced by one optical period (Fig. 1). In the limit of linear chirp,

$$f_i \approx \frac{m_e c^2 \beta^2 \gamma^3}{\zeta q e_1 N}, \quad (2)$$

where m_e is the electron mass, and $\zeta = 2\pi$ if the intrinsic energy spread limits the microbunch duration [29]. If the energy spread is negligible, $\zeta = 4$ [19]. When $\zeta = 2\pi$, this “temporal focal length” is equal to the spatial focal length of a DLA lens [30].

In the antisymmetric mode, the particle angular deflection $\Delta y'$ over N periods is

$$\Delta y' \approx \frac{q e_1 N \Lambda}{\beta^2 \gamma^2 m_e c^2} \sin \omega \Delta t, \quad (3)$$

see Ref. [30].

The antisymmetric mode allows direct measurement of the average microbunch duration within the pulse train. In this mode, the deflection force is proportional to $\sin \omega \Delta t$ [Eq. (3)]. When $\omega \Delta t$ is small, the deflection angle has a linear dependence on the electron time delay given by

$$\Delta y' \approx D \Delta t, \quad (4)$$

where D (mrad/fs) is the “streaking speed” [20] or “shear parameter”. The time delay Δt of an electron entering an antisymmetric-mode DLA is therefore linearly mapped onto $\Delta y'$ in the linear region of the laser field.

The electron beam has intrinsic divergence derived from its emittance—in a streaking measurement, the duration of the microbunch manifests as a broadening of the intrinsic deflection spectrum. The microbunch temporal profile can be recovered by deconvolving the lasers-on (streaked) bunch profile with the lasers-off (unstreaked) profile.

DLATRACK6D simulations [24] predict that for intrinsic energy spreads < 1 eV, single-digit attosecond bunches occur exactly at the longitudinal focus, but rapidly broaden with larger energy spreads. For energy spread dominated beams, microbunch duration scales approximately linearly with energy spread [29].

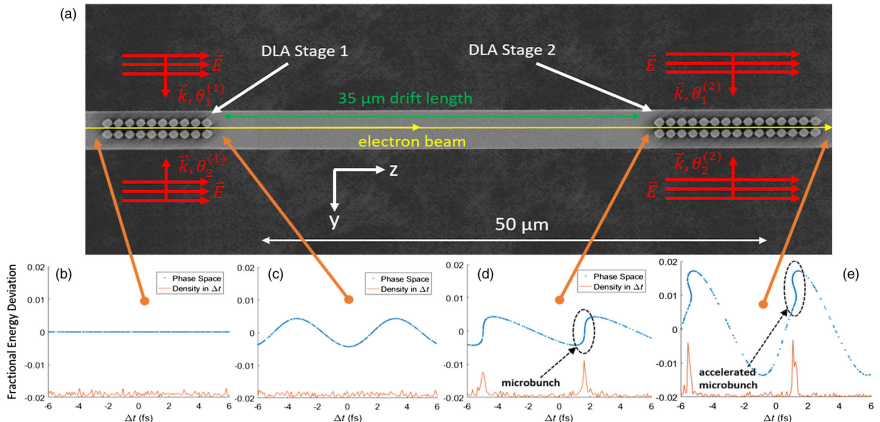


FIG. 1. (a) An electron beam travels through two DLA stages separated by a $35 \mu\text{m}$ drift length, each driven by two laser pulses. All four pulses are identical and phase locked, with phases given by $\theta_1^{(1)}, \theta_2^{(1)}$ and $\theta_1^{(2)}, \theta_2^{(2)}$. (b) An example particle distribution with average kinetic energy 57 keV. The electron density is initially uniform over Δt . (c) The bunching stage modulates the electron energy. (d) The drift shears the phase space and modulates the electron density. Pulse train formation by microbunching is visible. (e) The pulse train is injected into an accelerating stage, and its net energy increases.

The energy spread produced by the bunching stage causes significant microbunch evolution over the length of the streaker. The recovered temporal profiles should therefore be understood as the *average* microbunched pulse train profile over the length of the streaker. The recovered microbunch duration is not strongly affected by the minimum bunch duration for durations below ~ 200 as FWHM, instead being dominated by the bunch evolution.

Two stages of dual-pillar DLAs like those in [26,30] are fabricated from monolithic 5–10 Ω cm B:Si (Fig. 1). Pairs of elliptical pillars 2.7 μm in height with a channel gap of 300 nm are spaced by a periodicity Λ of 875 nm. The first DLA stage has ten pillars (thus nine active periods, length 7.88 μm) followed by a 35 μm drift length, then a second DLA stage with fifteen pillars (14 periods, 12.25 μm length) (Fig. 1).

A fraction of a 1 μm , 100 kHz, 300 fs regenerative amplifier pulse is used to generate the initial 500 ± 100 fs FWHM electron pulse from a silicon nanotip photocathode [31]. It has a central energy of 57 keV and energy spread < 10 eV. The electron pulse is focused to a 120 ± 25 nm RMS spot at the DLA, and its divergence is set to 1 mrad half-angle by an aperture, giving a geometric emittance of 120 ± 25 pm-rad. Electron currents of $< 1e^-/\text{pulse}$ (at the cathode) ensure that space-charge-induced temporal broadening is minimal. Electron current at the DLA is limited by the aperture to roughly $1000 e^-/s$. Beam transmission through the DLA is further limited by suboptimal matching to the transverse structure acceptance [32]. The transmitted current is approximately $300 e^-/s$ (30%).

The remainder of the regenerative amplifier pulse pumps an OPA which generates a 1980 nm, 605 ± 5 fs pulse. This pulse is split into four accelerator drive pulses—two per stage (Fig. 1). Each identical drive pulse, having energy between 20 and 45 nJ depending on the desired e_1 , is focused to a $1/e^2$ radius of $20 \pm 1 \mu\text{m}$.

The first accelerator stage is operated in the symmetric mode, which produces a microbunched pulse train at the second stage. The temporal focal length of the first stage is matched to the drift length between stages (35 μm) for $e_1 = 60$ MeV/m. The second stage is operated in symmetric mode for net acceleration (Fig. 2), or tuned to the antisymmetric mode for streaking (Fig. 3). The experimental setup is otherwise identical.

The electron beam then passes through a sector magnet spectrometer and hits a microchannel plate detector where its energy and deflection spectra are analyzed with 100 eV and 0.36 mrad resolution, respectively. Roughly 2500 electrons are averaged to create one data frame.

Figure 2(a) shows a simulation of the two-stage net acceleration experiment for $e_1 = 58$ MeV/m using a symplectic tracking code based on DLATrack6D [24]. Both stages are operated symmetrically, the injection phase $\omega\Delta t$ is linearly varied, and the energy spectrum is monitored. Figure 2(b) shows the experimentally measured

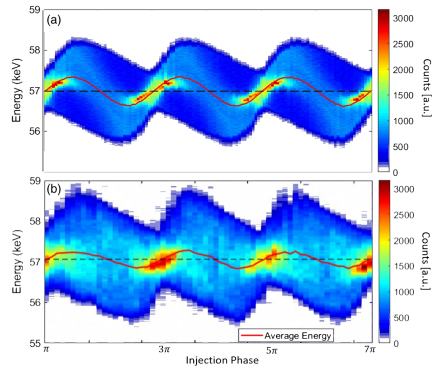


FIG. 2. (a) A two-stage accelerator simulation where the injection phase is linearly varied. $e_1 = 58$ MeV/m. The net energy gain is 350 eV, and the peak energy modulation is slightly over 1 keV. (b) The measured spectrogram for $e_1 = 58 \pm 5$ MeV/m. The net energy gain is 200 ± 10 eV, and the peak energy modulation is 1.3 keV.

spectrogram. Accurate e_1 measurement in the bunching stage is desirable, but was impeded by the presence of the second stage. e_1 in the second stage was measured to be 58 ± 5 MeV/m, and e_1 in both stages assumed to be the same. The simulated peak energy modulation is slightly over 1 keV, and the measured peak modulation is 1.3 keV, indicating that the measurement of $e_1 = 58 \pm 5$ MeV/m slightly underestimates the true e_1 . However, the measured net acceleration (200 ± 10 eV) is smaller than the simulated net acceleration (350 eV). The main error source is likely to be dual-drive phase error (see the Supplemental Material [27]).

The features present in simulation are well reproduced by the experiment, and the sinusoidal variation of net energy gain is clear evidence of both microbunching and coherent control of the pulse train injection phase. Net energy gain is sharply limited by the evolution of the microbunches through the second stage—without a particle-capture mechanism, the large energy spread produced by the buncher causes the microbunches to “wash out” during acceleration. This can be significantly improved by the scheme proposed in [32], which can produce equally short microbunches with sufficiently small energy spread for injection into a monoenergetic DLA device.

By tuning the second stage to the antisymmetric mode, a streaking measurement of the microbunch duration was made by linearly varying the injection phase $\omega\Delta t$ while monitoring the deflection spectrum. e_1 was measured by measuring the energy gain in the symmetric mode of the second stage. At the optimum bunching condition, e_1 was

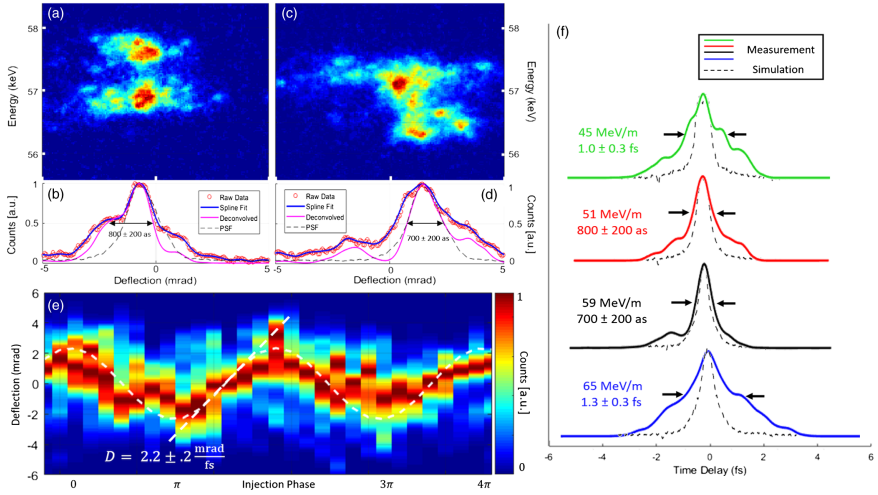


FIG. 3. (a) An MCP image of a streaked, microbunched pulse train taken from (e), showing the characteristic double-horns energy spectrum. (b) The spline fit of the deflection spectrum with the point-spread function (PSF). Their deconvolution yields the bunch temporal profile. (c) Another representative bunch from (e). (d) Its spline fit, PSF, and recovered profile. (e) A measured deflectogram as injection phase $\omega\Delta t$ is varied from 0 to 4π . e_1 is measured in the second stage to be 59 ± 5 MeV/m. The electron bunch is deflected by a total of 5 mrad over $1/2$ optical cycle. The streaking speed $D = 2.2 \pm 0.2$ mrad/fs. (f) The simulated, recovered microbunch profiles (from DLATrack6D), are overlaid with the measured, averaged profiles as a function of e_1 . The measured e_1 values and mean FWHM are listed next to the measured traces.

measured to be 59 ± 5 MeV/m. In this condition, 5 mrad of total deflection was observed over $1/2$ optical period [Fig. 3(e)], however, this is roughly half of the value predicted by Eq. (3) using the measured e_1 value. The relative weakness of the antisymmetric mode is partially attributable to dual-drive phase error, however, 3D effects and low dual-pillar reflectivity may also play a role (see the Supplemental Material [27]).

The amplitude of the deflectogram shown in Fig. 3(e) yields a streaking speed $D = 2.2 \pm 0.2$ mrad/fs. Selected images of microbunched pulse trains from Fig. 3(e) are displayed in Figs. 3(a) and 3(c), along with their temporal profiles [Figs. 3(b) and 3(d)] after Lucy-Richardson deconvolution [33,34] with the unstreaked bunch profile (PSF). Figure 3(a) shows a clear double-horn energy spectrum characteristic of an energy modulator, and the temporal correlation of the two energy lobes, indicating microbunching. The electrons are contained within a fraction of the optical cycle corresponding to 800 ± 200 as FWHM [Fig. 3(b)] and 700 ± 200 as FWHM [Fig. 3(d)].

Figure 3(f) shows measurements of microbunch durations vs e_1 . Streaking speeds for each e_1 are calculated from deflectograms analogous to Fig. 3(e), and range between 2.0 and $2.8(\pm 0.2)$ mrad/fs. All recovered microbunch

temporal profiles within the deflectogram linear region (50% streaking amplitude) are clustered by a kernel density estimation (KDE) [35,36] algorithm, producing an average bunch duration and standard error for each cluster. The temporal profiles within each cluster are then averaged, and the minimum-duration cluster averages are shown in Fig. 3(f). Because bunch profiles are taken from all zero-crossing regions of the deflectogram, their temporal orientation (i.e., leading vs lagging edge) is not preserved after averaging, resulting in an artificial symmetrization of the bunch profile which accurately reflects the microbunch FWHM, but not the true temporal profile as in Figs. 3(b) and 3(d).

A trend is visible in Fig. 3(f)—the bunch duration is minimized as e_1 approaches the matched value (60 MeV/m), though the difference in microbunch duration between $e_1 = 59 \pm 5$ MeV/m and 51 ± 5 MeV/m is not statistically significant. The structures began to damage at higher e_1 , corresponding to ~ 50 nJ laser pulses (~ 8 mJ/cm² peak fluence).

The minimum resolvable bunch duration is determined by the minimum measurable broadening of the deflection spectrum, approximately 200 as for $D = 2.2 \pm 0.2$ mrad/fs. The measurement uncertainty is primarily

limited by shot noise and dual-drive laser timing jitter—these produce a standard error in measurement between 200 and 300 as, depending on the data run. Better phase stability and more electron current would significantly improve the standard error (see the Supplemental Material [27] for a discussion of measurement resolution and measurement noise).

This work demonstrates an injector prototype for a DLA composed of two dual-drive, dual-pillar stages. We demonstrate the creation of microbunched pulse trains with microbunch durations of 700 ± 200 as from a macrobunch 500 ± 100 fs in duration, and their net acceleration by 200 eV. By tuning the optical mode in the structure, we also characterize the microbunch duration with a direct streaking measurement, whose resolution is estimated to be 200 as, which is on par with the state-of-the-art for direct time-domain measurements of electron bunches.

The primary limitation of this DLA injector prototype is the energy spread produced by the bunching stage. The energy modulation necessary for μm -scale temporal focal lengths is of order 100 eV, and thus the bunch washes out after a very short distance. For bunch injection into an Alternating-Phase-Focusing (APF) DLA [32] or high-gradient DLA [1], the injector must produce a bunch with ultra-short temporal duration and small energy spread that fits inside the “accelerating bucket” in phase space. An APF DLA has longitudinal acceptance of order 10^{-13} eV s [32], which corresponds to roughly 500 eV in 300 as. A silicon APF injector is capable of producing such a beam, and this work constitutes the first step towards its realization.

The authors wish to acknowledge the entire ACHIP collaboration for their support and guidance, as well as the staff from the Stanford Nanofabrication Facility (SNF) and Stanford Nanofabrication Shared Facilities (SNSF), supported by the National Science Foundation under Grant No. ECCS-1542152. The authors also wish to acknowledge helpful discussions with R. J. England. This work is funded by the Gordon and Betty Moore Foundation (GBMF4744). U. N. additionally acknowledges funding by the German Federal Ministry of Education and Research (Grant No. FKZ: 05K16RDB).

Note added.—Similar results are reported by other members of the ACHIP collaboration in the companion Letter [37].

- [1] D. Cesar, S. Custodio, J. Maxson, P. Musumeci, X. Shen, E. Threlkeld, R. J. England, A. Hanuka, I. V. Makasyuk, E. A. Peralta, K. P. Wootton, and Z. Wu, *Commun. Phys.* **1**, 46 (2018).
 [2] K. P. Wootton *et al.*, *Proc. IPAC* **4744**, 2520 (2017).
 [3] R. J. England *et al.*, *Rev. Mod. Phys.* **86**, 1337 (2014).
 [4] S. Kuschel, D. Hollatz, T. Heinemann, O. Karger, M. B. Schwab, D. Ullmann, A. Knetsch, A. Seidel, C. Rödel,

- M. Yeung, M. Leier, A. Blinne, H. Ding, T. Kurz, D. J. Corvan, A. Siverst, S. Karsch, M. C. Kaluza, B. Hidding, and M. Zepf, *Phys. Rev. Accel. Beams* **19**, 071301 (2016).
 [5] P. McIntosh, R. Akre, R. Boyce, P. Emma, A. Hill, and C. Rago, in *Proceedings of the IEEE Particle Accelerator Conference (IEEE, 2005)*, Vol. 2005, pp. 2753–2755.
 [6] D. M. Villeneuve, *Contemp. Phys.* **59**, 47 (2018).
 [7] F. Calegari, G. Sansone, S. Stagira, C. Vozzi, and M. Nisoli, *J. Phys. B: At., Mol. Opt. Phys.* **49**, 062001 (2016).
 [8] K. E. Priebe, C. Rathje, S. V. Yalunin, T. Hohage, A. Feist, S. Schäfer, and C. Ropers, *Nat. Photonics* **11**, 793 (2017).
 [9] M. V. Tsarev and P. Baum, *New J. Phys.* **20**, 033002 (2018).
 [10] A. Feist, N. Bach, N. Rubiano da Silva, T. Danz, M. Möller, K. E. Priebe, T. Domröse, J. G. Gatzmann, S. Rost, J. Schauss, S. Strauch, R. Bormann, M. Sivis, S. Schäfer, and C. Ropers, *Ultramicroscopy* **176**, 63 (2017).
 [11] O. Lundh, C. Reichatn, J. Lim, V. Malka, and J. Faure, *Phys. Rev. Lett.* **110**, 065005 (2013).
 [12] M. Chergui and A. H. Zewail, *ChemPhysChem* **10**, 28 (2009).
 [13] A. H. Zewail, *Annu. Rev. Phys. Chem.* **57**, 65 (2006).
 [14] X. Wang and Y. Li, *Chin. Phys. B* **27**, 076102 (2018).
 [15] H. L. Andrews, C. H. Boulware, C. A. Brau, and J. D. Jarvis, *Phys. Rev. ST Accel. Beams* **8**, 110702 (2005).
 [16] F. Lemery, P. Piot, G. Amatuini, P. Boonpraprasert, Y. Chen, J. Good, B. Grigoryan, M. Groß, M. Krasilnikov, O. Lishilin, G. Loisch, A. Oppelt, S. Philipp, H. Qian, Y. Renier, F. Stephan, and I. Zagorodnov, *Phys. Rev. Lett.* **122**, 044801 (2019).
 [17] C. M. Sears, E. Colby, R. Ischebeck, C. McGuinness, J. Nelson, R. Noble, R. H. Siemann, J. Spencer, D. Walz, T. Plettner, and R. L. Byer, *Phys. Rev. ST Accel. Beams* **11**, 061301 (2008).
 [18] S. Di Mitri and M. Venturini, Velocity bunching & more on magnetic-chicane bunch compression, U.S. Particle Accelerator School, http://uspas.fnal.gov/materials/13CSU/Velocity_Bunching.pdf (retrieved 2013).
 [19] U. Niedermayer, O. Boine-Frankenheim, and T. Egenolf, *J. Phys. Conf. Ser.* **874**, 012041 (2017).
 [20] C. Kealhofer, W. Schneider, D. Ehberger, A. Ryabov, F. Krausz, and P. Baum, *Science* **352**, 429 (2016).
 [21] P. Ecker, M. Smolarski, P. Schlup, J. Biegert, A. Staudte, M. Schöffler, H. G. Müller, R. Dörner, and U. Keller, *Nat. Phys.* **4**, 565 (2008).
 [22] J. Itatani, F. Quéré, G. L. Yudin, M. Y. Ivanov, F. Krausz, and P. B. Corkum, *Phys. Rev. Lett.* **88**, 173903 (2002).
 [23] Y. Morimoto and P. Baum, *Nat. Phys.* **14**, 252 (2018).
 [24] U. Niedermayer, T. Egenolf, and O. Boine-Frankenheim, *Phys. Rev. Accel. Beams* **20**, 111302 (2017).
 [25] U. Niedermayer *et al.*, *JMPA*, 10.18429/JACoW-ICAP2018-MOPLG01 (2019).
 [26] K. J. Leedle, D. S. Black, Y. Miao, K. E. Urbanek, A. Ceballos, H. Deng, J. S. Harris, O. Solgaard, and R. L. Byer, *Opt. Lett.* **43**, 2181 (2018).
 [27] See the Supplemental Material at <http://link.aps.org/supplemental/10.1103/PhysRevLett.123.264802> for a detailed discussion of the experimental error in the microbunch duration measurement, as well as a description of the forces inside a dual-grating structure, specifically high-

- lighting a correction term proportional to the dual-pillar reflectivity which may explain discrepancies between theory and experiment. It also contains representative energy and deflection spectra from the modulator (stage 1) and streaker (stage 2) stages, operated individually and in the symmetric mode. The Supplemental Material includes Ref. [28].
- [28] R. J. England, A. Ody, and Z. Huang, Report No. SLAC-PUB-17450 (SLAC, 2019).
- [29] D. Nguyen, J. Lewellen, and L. Duffy, Bunch Compression—RF Linacs for High-Gain FEL, U.S. Particle Accelerator School, http://uspas.fnal.gov/materials/14UNM/E_Bunch_Compression.pdf (retrieved 2014).
- [30] D. S. Black, K. J. Leedle, Y. Miao, U. Niedermayer, R. L. Byer, and O. Solgaard, *Phys. Rev. Lett.* **122**, 104801 (2019).
- [31] A. Ceballos (to be published).
- [32] U. Niedermayer, T. Egenolf, O. Boine-Frankenheim, and P. Hommelhoff, *Phys. Rev. Lett.* **121**, 214801 (2018).
- [33] L. B. Lucy, *Astron. J.* **79**, 745 (1974).
- [34] W. H. Richardson, *J. Opt. Soc. Am.* **62**, 55 (1972).
- [35] E. Parzen, *Ann. Math. Stat.* **33**, 1065 (1962).
- [36] M. Rosenblatt, *Ann. Math. Stat.* **27**, 832 (1956).
- [37] N. Schöenberger, A. Mittelbach, P. Yousefi, J. McNeur, and P. Hommelhoff, following Letter, *Phys. Rev. Lett.* **123**, 264803 (2019).

Generation and Characterization of Attosecond Microbunched Electron Pulse Trains via Dielectric Laser Acceleration

Norbert Schönenberger,^{1,*} Anna Mittelbach,¹ Peyman Yousefi¹, Joshua McNeur,¹
Uwe Niedermayer,² and Peter Hommelhoff^{1,3}

¹*Department of Physics, Friedrich-Alexander Universität Erlangen-Nürnberg (FAU), Staudtstraße 1, 91058 Erlangen, Germany*

²*Technische Universität Darmstadt, Institut für Teilchenbeschleunigung und Elektromagnetische Felder (TEMF)
Schlossgartenstraße 8, 64289 Darmstadt, Germany*

 (Received 25 June 2019; revised manuscript received 28 October 2019; published 26 December 2019)

Dielectric laser acceleration is a versatile scheme to accelerate and control electrons with the help of femtosecond laser pulses in nanophotonic structures. We demonstrate here the generation of a train of electron pulses with individual pulse durations as short as 270 ± 80 attoseconds (FWHM), measured in an indirect fashion, based on two subsequent dielectric laser interaction regions connected by a free-space electron drift section, all on a single photonic chip. In the first interaction region (the modulator), an energy modulation is imprinted on the electron pulse. During free propagation, this energy modulation evolves into a charge density modulation, which we probe in the second interaction region (the analyzer). These results will lead to new ways of probing ultrafast dynamics in matter and are essential for future laser-based particle accelerators on a photonic chip.

DOI: 10.1103/PhysRevLett.123.264803

Ultrashort electron pulses find various applications in research and technology, including ultrafast diffraction [1–3], ultrafast electron microscopy [4–7], as well as ultrafast photon generation [8]. Many of these techniques operate with electron pulse durations in the realm of femtoseconds.

In order to resolve processes taking place on atomic time scales in atoms or molecules or on electronic time scales in solids, electron pulses with attosecond duration are highly sought after. The temporal resolution of laser-triggered electron sources is usually limited by the temporal duration of the electron-releasing laser pulses and subsequent dispersive broadening of the electron pulses. Typical electron pulse durations at the sample are in the range of 30 fs to 1 ps [1–9]. Schemes have been proposed and demonstrated to compress the electron pulses at the sample, see e.g., [10,11]. The shortest pulse duration demonstrated this way is 6 fs so far [12].

The temporal resolution can be increased significantly by utilizing directly the optical carrier field of ultrashort laser pulses. Energy modulation of the free electrons via optical fields, for example, can be accomplished in several different schemes, leading to electron pulse trains with suboptical cycle bunchlet duration. One such method is to utilize ponderomotive forces [13,14]. Recently, microbunches as short as 260 as have been realized this way [15,16]. In another scheme, the inverse free electron laser (IFEL) process has been used, where microbunch durations as short as 410 as have been demonstrated [17]. Finally, optical nearfields can be used to transfer momentum from a light field to free electrons. With nearfields generated by

(metallic) plasmonic nanostructures, pulse durations as short as 655 as have been reached [18].

We here use dielectric (transparent) nanophotonic structures made from silicon. They are extremely versatile and easy to produce, even in large numbers. These structures are utilized to generate an optical nearfield allowing efficient momentum transfer from the lightfield into the electron beam over a prolonged interaction distance, which other schemes cannot provide. Because these structures only vary the phase of the optical field on suboptical cycle dimensions, the interaction of the light field with the structure can be modeled as a purely dispersive effect. Hence, light absorption hardly takes place in these structures, allowing us to reach high laser damage thresholds in excess of 2 GV m^{-1} , corresponding to peak intensities of $5 \times 10^{11} \text{ W cm}^{-2}$. In addition to this high damage threshold, these structures are highly advantageous over other schemes and structures because of their broad functionality that can be encoded into the nanostructure.

Various dielectric structures for laser-driven particle acceleration have been proposed ([19,20], and references therein). In 2013, dielectric laser acceleration was shown experimentally, demonstrating phase-synchronous acceleration of charged particles with light fields [21,22]. Quickly thereafter, various other functionalities have been realized based on this scheme of phase-synchronous interaction of nearfields generated in dielectric structures and fast electron pulses, both at relativistic and nonrelativistic energies. Examples include the deflection, focusing, and streaking of an electron beam [23–26]. With all these individual

building blocks available, and with the demonstration of two concatenated structures [24], the concept of a particle accelerator on a photonic chip is now within reach. Importantly, acceleration of electrons in infinitely long structures with negligible electron loss has recently been demonstrated numerically based on alternating phase focusing [27]. In this Letter, we show that by carefully controlling

the phase space dynamics of a pulsed electron beam, suboptical cycle bunching and attosecond bunch generation can be achieved [28]. For this, we imprint an energy modulation periodic with the driving optical period of 6.45 fs on each 400 fs-long electron pulse in a first nearfield interaction section called the modulator [Fig. 1(a)]. This nearfield can be described by the following formula [29]:

$$E(x, z) = c \begin{bmatrix} -\frac{1}{\beta\gamma^2} [C_s \sinh(k_x x) + C_c \cosh(k_x x)] \cos(k_z z - \omega t) \\ 0 \\ \frac{1}{\beta\gamma} [C_s \cosh(k_x x) + C_c \sinh(k_x x)] \sin(k_z z - \omega t) \end{bmatrix} \quad (1)$$

where $C_c = 0$ and C_s is proportional to the field amplitude, x is the transverse coordinate, and z is the electron propagation direction.

After this, the energy-modulated electron pulse propagates freely to the second nearfield interaction section called the analyzer [structure and field is identical to the modulator field shape in Eq. (1)]. During this drift, the energy modulation develops into a density modulation,

probed in the analyzer section and diagnosed with the a dipole magnet electron spectrometer. We obtain feature-rich electron spectrograms, which show the electron energy versus the time delay (up to an offset) between modulator and analyzer laser pulses. By comparing these spectrograms to numerically obtained ones, we can clearly show the suboptical cycle, attosecond electron pulse duration.

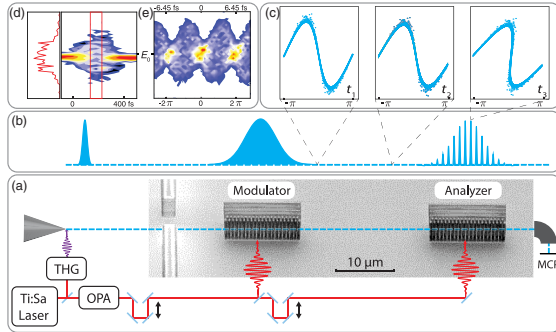


FIG. 1. Sketch of the experimental setup with modulator and analyzer structure and sketches of the electron phase space behavior. (a) Laser-emitted electrons are focused into the center of the channel of the first dielectric laser acceleration structure, comprised of two rows of pillars, the modulator. An SEM image of modulator and analyzer structure can be seen in the background of this sketch. After the electrons have propagated through the analyzer structure, their energy is measured with a magnetic deflection spectrometer. (b) Sketch of the evolution of the electron pulse duration. At the source, the electron pulse duration resembles that of the triggering UV laser pulse (~ 100 fs). During propagation through the electron column, trajectory effects increase the electron pulse duration to roughly 400 fs at the modulator. The pulsed laser beam acting on each arriving electron pulse modulates the energy of the electrons. During subsequent propagation, the energy modulation leads to a density modulation. At the temporal focus, the minimum electron pulse duration of each bunchlet is reached. The position of the temporal focus depends on the amplitude of the energy modulation in the modulator. Here microbunching at the position of the analyzer is shown. (c) Sketch of the phase space evolution during the electron drift. The vertical axis denotes the energy of the electrons plotted over one cycle ($-\pi \cdot \cdot \cdot \pi \equiv 6.45$ fs). The faster higher energy electrons catch up with the slower electrons, forming the microbunched pulse train. (d) Example spectrogram of the electrons after interaction in the modulator only (laser intensity of 3×10^{11} W cm $^{-2}$). The red curve shows the homogeneous broadening inside the red region. (e) Example spectrogram with modulator and analyzer structure illuminated (1.5×10^{10} W cm $^{-2}$ in the modulator, 2.5×10^{10} W cm $^{-2}$ in the analyzer). The periodicity with the optical period of 6.45 fs and suboptical cycle duration features are clearly visible.

The experiments are performed in an ultrafast scanning electron microscope (USEM). Laser pulses from an amplified titanium:sapphire laser with pulse durations of 100 fs and a repetition rate of 1 kHz are fed into an optical parametric amplifier (OPA). A part of the fundamental output is used to generate the third harmonic to photoemit electrons from the Schottky-type emitter in a modified commercial electron microscope, which serves as the electron source. The dielectric structures are illuminated by laser pulses generated in the OPA with a wavelength of 1932 nm and a pulse duration of 650 fs, obtained via a Fabry Perot filter. The relative phases or time differences of the pulsed laser beams impinging on the modulator and analyzer structure as well as on the electron source are precisely adjusted via delay stages. The electron microscope is operated at $\beta = (v_e/c) = 0.32$ corresponding to an energy of 28.4 keV. The spot size is approximately 50 nm, with a divergence angle of approximately 1 to 2 mrad. The focus of the electron beam is adjusted to be as close as possible to the center of the structure. Since the electron pulses experience temporal broadening due mainly to trajectory effects inside of the electron column, the pulses have a duration of ~ 400 fs when they reach the dielectric structure [9]. It is mainly because of the small laser repetition rate and the use of a commercial SEM as electron source that the electron count rate is only 1–10 electrons per second here, implying that one 400 fs-long electron pulse contains less than one electron on average. This is because the SEM is optimized for high resolution and image quality, so the (usually DC) electron beam is heavily filtered by various apertures. More details of the setup can be found in [9].

We chose dual pillar structures etched into silicon as building blocks of the dielectric structures for their ease of manufacturing and laser in-coupling [30]. Modulator and analyzer structure are identical and $13.2 \mu\text{m}$ long. The distance from the end of the modulator to the center of the analyzer constitutes the drift section, which was chosen to be $30 \mu\text{m}$. More details about the structure are included in the Supplemental Material [31]. After the analyzer structure, the electrons propagate into a magnetic deflection spectrometer with an energy resolution of ~ 40 eV [9]. This way, we record spectrograms by plotting electron spectra versus the time delay between the pulsed laser beams impinging on modulator and analyzer structure (Fig. 1). The pulsed laser beams are focused on the structures down to a spot size of roughly $(14 \pm 0.5) \mu\text{m}$ ($1/e^2$ intensity radius). With average laser powers of 30 to $100 \mu\text{W}$, we generate peak intensities of 1.5×10^{10} to $4.7 \times 10^{10} \text{ W cm}^{-2}$, corresponding to peak optical fields of 340 to 600 MV m^{-1} on the modulator. With a structure factor of ~ 0.1 [32], which determines the conversion of incident field to the synchronous mode, the resulting peak acceleration gradient acting on the electrons is 34 to 60 MeV m^{-1} . Damage usually sets in at a field strength of

around 2 GV m^{-1} , corresponding to peak intensities of $5 \times 10^{11} \text{ W cm}^{-2}$. The structure has been designed for an intermediate gradient of 20 to 25 MeV m^{-1} corresponding to a longitudinal focal length of $30 \mu\text{m}$. This is a compromise between defocusing, energy spread and the ability to properly separate the two laser spots. The longitudinal focal length,

$$L = \frac{\lambda_g}{2\pi} \beta^2 \gamma^3 m c^2 \frac{1}{\Delta E}, \quad (2)$$

with λ_g the periodicity of the structure, β the speed of the electrons in units of the speed of light and γ the Lorentz factor, is defined as the distance from the end of the first structure to the plane where of shortest micropulse duration, i.e., the plane in which the imprinted velocity modulation has evolved until the fast electrons have caught up with the slow ones [28].

Figure 2 shows experimental data, simulation results, retrieved time traces, and phase space diagrams for various laser intensities in the modulator. The measured spectrograms include effects from both the modulator and analyzer, rendering a direct extraction of the electron time structure at the analyzer position difficult. For this reason, we compare the measured spectrograms with numerically obtained ones to indirectly measure the micropulse length. The numerical spectrograms are based on a finite difference time domain (FDTD) simulation of the optical nearfields inside of the nanophotonic structures [33], while the electron tracking was performed with a Runge-Kutta motion solver [34]. From the simulation results, we also obtain the electron density and the phase space distribution shown in the two rightmost columns in Fig. 2.

From top to bottom, the laser intensity in the modulator structure increases. In the first two cases, Figs. 2(a) and 2(b), the laser intensity in the modulator is below the intensity needed to produce fully bunched electrons at the analyzer structure. Hence, the temporal focus of the microbunches lies after the center of the analyzer. For the parameters shown in Fig. 2(c), the laser intensity is almost ideally matched to the drift length so that the electron pulses are close to the minimal pulse duration. The onset of overbunching is, however, already discernible. When we increase the laser intensity in the modulator even further [Figs. 2(d)–2(f)], the temporal focus shifts closer to the modulator, resulting in clear overbunching at the position of the analyzer.

To find the best matching numerical spectrograms, we have simulated various parameter sets close to the experimental ones. This process and the concomitant pulse duration extraction are detailed in the Supplemental Material [31]. Importantly, the length of the electron microbunch duration can not be directly inferred from features contained in the recorded spectrograms. This is because the relatively high energy spread induced in the

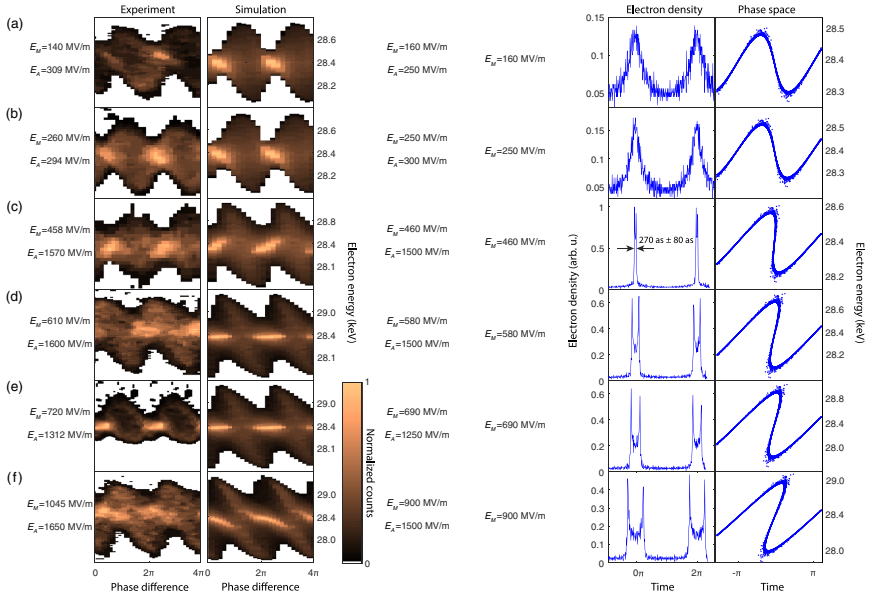


FIG. 2. Spectrograms, electron density and phase space at the analyzer structure. The left column shows experimental data, next to it we show simulated spectrograms, and the third and fourth column show the electron density distribution and phase space at the position of the analyzer, respectively. The color scale of the first two columns shows electron counts, normalized to the maximum count of electrons for each data set individually. Peak fields are given next to the spectra. Underbunching is clearly visible in the first two rows, where the temporal focus lies behind the analyzer. Shortest micropulses are shown in (c), with a pulse duration of (270 ± 80) as. Various degrees of overbunching are displayed in the last three rows. The fourth column shows the phase space distribution of the microbunches: the vertical axes represent the electrons' energy. When the maximum and minimum of the modulation coincide in time, the temporal focus is reached. After that the characteristic overbunching shape is formed, when the high energy electrons have passed the slow electrons in the analyzer and the temporal focus lies in front of it.

modulator structure causes significant bunch evolution even in the analyzer structure since the temporal depth of focus is so narrow. A unique best matching solution for the spectrogram in Fig. 2(c) is found for these parameters: $E_M = 460 \text{ MV m}^{-1}$, the incident field strength on the modulator structure, and $E_A = 1500 \text{ MV m}^{-1}$, the incident field on the analyzer. The resulting microbunch duration (full width at half maximum, FWHM) is (270 ± 80) as. The error is derived from the comparison with adjacent simulation results. In the vicinity of our shortest measured microbunches, a variation of $\pm 20 \text{ MV m}^{-1}$ in the modulator results in a change of ± 80 as in the analyzer structure. Hence, we conservatively estimate the measurement error to be 80 as. An extensive sweep, which was performed with step sizes of 40 to 300 MV m^{-1} for the modulator fields and 250 MV m^{-1} for the analyzer can be found in the

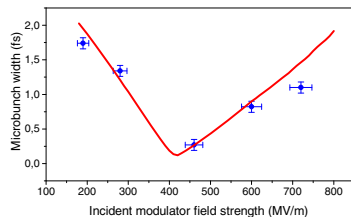


FIG. 3. Microbunch duration versus incident field strength on the modulator after a fixed drift length of $30 \mu\text{m}$. The blue datapoints show the measurements with their respective microbunch lengths, while the red curve shows the simulation results, with a minimum of 125 as.

Supplemental Material [31]. Within this grid of simulations we can uniquely identify the simulated spectrum that matches the experiment best.

The experimentally achieved microbunch duration in the almost ideally bunched case of (270 ± 80) as corresponds to just 4% or 270 mrad of the optical driving period. In the simulation, we find that a minimal electron microbunch duration of 125 as should be feasible with the scheme and laser pulse parameters employed here (Fig. 3). With incident fields close to the damage threshold and shorter drift spaces, one might even consider reaching the single digit attosecond range. Simulations indicate that the structures used here would produce 7 as (FWHM) microbunches with an incident field on the modulator of 1.5 GV m^{-1} after a drift space of $2 \mu\text{m}$, when the initial energy spread is small ($< 1 \text{ eV}$). Note that spectra approaching a double hump structure resulting from a sinusoidal modulation have been observed [32]. This indicated that we can observe the required beam dynamics.

To summarize, we have demonstrated attosecond microbunch train generation with individual bunchlet durations as short as (270 ± 80) as. Simulations show that the shortest microbunch duration with the current nanostructure could reach 125 as. Even shorter bunches can be achieved by reducing the drift section and using higher field strengths in the modulator section. The resulting microbunch trains could already be utilized to probe coherently pumped processes in a stroboscopic fashion. An increase in the available currents by orders of magnitude is straightforward by going to higher repetition rate laser sources (commercially available) and to better matched mini- or even microelectron optics. Furthermore, advances in the fields of optical field-driven particle accelerators require suboptical cycle-bunched electrons to be injected into the proper phase space region for the acceleration to be efficient and lossless. The precisely defined injection phase demonstrated here paves the way to matched injection into the acceptance of a scaleable DLA using technologies like the aforementioned alternating phase focusing. This enables to not only modulate electron energy, i.e., to have a beam with a big energy spread, comprised of accelerated and decelerated electrons, but to produce a net accelerated beam, where a substantial portion of the electrons is shifted to a higher energy with an energy spread significantly lower than that of a purely modulated beam. Our work will hence enable both new time-resolved electron-based imaging as well as building new and efficient optical particle accelerators.

This work was funded by the Gordon and Betty Moore Foundation (GBMF) through Grant No. GBMF4744 “Accelerator on a Chip International Program-ACHIP” and BMBF via 05K16WEC and 05K16RDB.

Note added.—Similar results are reported in the companion Letter [35].

*norbert.schoenenberger@fau.de

†peter.hommelhoff@fau.de

- [1] B. J. Siwick, J. R. Dwyer, R. E. Jordan, and R. J. D. Miller, An atomic-level view of melting using femtosecond electron diffraction, *Science* **302**, 1382 (2003).
- [2] P. Baum, D.-S. Yang, and A. H. Zewail, 4d visualization of transitional structures in phase transformations by electron diffraction, *Science* **318**, 788 (2007).
- [3] Y. Morimoto and P. Baum, Diffraction and microscopy with attosecond electron pulse trains, *Nat. Phys.* **14**, 252 (2018).
- [4] L. Zhao *et al.*, Terahertz Streaking of Few-Femtosecond Relativistic Electron Beams, *Phys. Rev. X* **8**, 021061 (2018).
- [5] K. B. Schliep, P. Quarterman, J. P. Wang, and D. J. Flannigan, Picosecond Fresnel transmission electron microscopy, *Appl. Phys. Lett.* **110**, 222404 (2017).
- [6] N. Rubiano Da Silva, M. Möller, A. Feist, H. Ulrichs, C. Ropers, and S. Schäfer, Nanoscale Mapping of Ultrafast Magnetization Dynamics with Femtosecond Lorentz Microscopy, *Phys. Rev. X* **8**, 031052 (2018).
- [7] G. Berruto, I. Madan, Y. Murooka, G. M. Vanacore, E. Pomarico, J. Rajeswari, R. Lamb, P. Huang, A. J. Kruchkov, Y. Togawa, T. LaGrange, D. McGrouther, H. M. Ronnow, and F. Carbone, Laser-Induced Skyrmion Writing and Erasing in an Ultrafast Cryo-Lorentz Transmission Electron Microscope, *Phys. Rev. Lett.* **120**, 117201 (2018).
- [8] S. Ackermann *et al.*, Generation of Coherent 19- and 38-nm Radiation at a Free-Electron Laser Directly Seeded at 38 nm, *Phys. Rev. Lett.* **111**, 114801 (2013).
- [9] M. Kozák, J. McNeur, N. Schönenberger, J. Illmer, A. Li, A. Tafel, P. Yousefi, T. Eckstein, and P. Hommelhoff, Ultrafast scanning electron microscope applied for studying the interaction between free electrons and optical near-fields of periodic nanostructures, *J. Appl. Phys.* **124**, 023104 (2018).
- [10] C. Kealhofer, W. Schneider, D. Ehberger, A. Ryabov, F. Krausz, and P. Baum, All-optical control and metrology of electron pulses, *Science* **352**, 429 (2016).
- [11] G. Sciaini and R. J. D. Miller, Femtosecond electron diffraction: Heralding the era of atomically resolved dynamics, *Rep. Prog. Phys.* **74**, 096101 (2011).
- [12] L. Zhao *et al.*, Terahertz Streaking of Few-Femtosecond Relativistic Electron Beams, *Phys. Rev. X* **8**, 021061 (2018).
- [13] P. Baum and A. H. Zewail, Attosecond electron pulses for 4d diffraction and microscopy, *Proc. Natl. Acad. Sci. U.S.A.* **104**, 18409 (2007).
- [14] S. A. Hilbert, C. Uiterwaal, B. Barwick, H. Batelaan, and A. H. Zewail, Temporal lenses for attosecond and femtosecond electron pulses, *Proc. Natl. Acad. Sci. U.S.A.* **106**, 10558 (2009).
- [15] M. Kozák, T. Eckstein, N. Schönenberger, and P. Hommelhoff, Inelastic ponderomotive scattering of electrons at a high-intensity optical travelling wave in vacuum, *Nat. Phys.* **14**, 121 (2018).
- [16] M. Kozák, N. Schönenberger, and P. Hommelhoff, Ponderomotive Generation and Detection of Attosecond Free-Electron Pulse Trains, *Phys. Rev. Lett.* **120**, 103203 (2018).
- [17] C. M. S. Sears, E. Colby, R. Ischebeck, C. McGuinness, J. Nelson, R. Noble, R. H. Siemann, J. Spencer, D. Walz, T. Plettner, and R. L. Byer, Production and characterization of

- attosecond electron bunch trains, *Phys. Rev. ST Accel. Beams* **11**, 061301 (2008).
- [18] K. E. Priebe, C. Rathje, C. V. Yalunin, T. Hohage, A. Feist, S. Schäfer, and C. Ropers, Attosecond electron pulse trains and quantum state reconstruction in ultrafast transmission electron microscopy, *Nat. Photonics* **11**, 793 (2017).
- [19] R. J. England *et al.*, Dielectric laser accelerators, *Rev. Mod. Phys.* **86**, 1337 (2014).
- [20] K. P. Wootton, J. McNeur, and K. J. Leedle, Dielectric laser accelerators: Designs, experiments, and applications, *Rev. Accel. Sci. Technol.* **09**, 105 (2016).
- [21] E. Peralta, K. Soong, E. R. England, R. J. and Colby, Z. Wu, B. Montazeri, C. McGuinness, J. McNeur, K. J. Leedle, D. Walz, E. Sozer, B. Cowan, B. Schwartz, G. Travish, and R. L. Byer, Demonstration of electron acceleration in a laser-driven dielectric microstructure, *Nature (London)* **503**, 91 (2013).
- [22] J. Breuer and P. Hommelhoff, Laser-Based Acceleration of Nonrelativistic Electrons at a Dielectric Structure, *Phys. Rev. Lett.* **111**, 134803 (2013).
- [23] K. P. Wootton, D. B. Cesar, C. Lee, I. V. Makasyuk, J. Maxson, P. Musumeci, and R. J. England, Dielectric laser acceleration and focusing using short-pulse lasers with an arbitrary laser phase distribution, in *AIP Conference Proceedings* (2017), Vol. 1812, p. 060001.
- [24] M. Kozák, J. McNeur, K. J. Leedle, H. Deng, N. Schönenberger, A. Ruehl, I. Hartl, J. S. Harris, R. L. Byer, and P. Hommelhoff, Optical gating and streaking of free electrons with sub-optical cycle precision, *Nat. Commun.* **8**, 14342 (2017).
- [25] J. McNeur, M. Kozák, N. Schönenberger, K. J. Leedle, H. Deng, A. Ceballos, H. Hoogland, A. Ruehl, I. Hartl, R. Holzwarth, O. Solgaard, J. S. Harris, R. L. Byer, and P. Hommelhoff, Elements of a dielectric laser accelerator, *Optica* **5**, 687 (2018).
- [26] D. S. Black, K. J. Leedle, Y. Miao, U. Niedermayer, R. L. Byer, and O. Solgaard, Laser-Driven Electron Lensing in Silicon Microstructures, *Phys. Rev. Lett.* **122**, 104801 (2019).
- [27] U. Niedermayer, T. Egenolf, O. Boine-Frankenheim, and P. Hommelhoff, Alternating-Phase Focusing for Dielectric-Laser Acceleration, *Phys. Rev. Lett.* **121**, 214801 (2018).
- [28] U. Niedermayer, O. Boine-Frankenheim, and T. Egenolf, Designing a dielectric laser accelerator on a chip, *J. Phys. Conf. Ser.* **874**, 012041 (2017).
- [29] J. Breuer, J. Mcneur, and P. Hommelhoff, Dielectric laser acceleration of electrons in the vicinity of single and double grating structures-theory and simulations, *J. Phys. B* **47**, 234004 (2014).
- [30] K. J. Leedle, A. Ceballos, H. Deng, O. Solgaard, R. Fabian Pease, R. L. Byer, and J. S. Harris, Dielectric laser acceleration of sub-100 keV electrons with silicon dual-pillar grating structures, *Opt. Lett.* **40**, 4344 (2015).
- [31] See the Supplemental Material at <http://link.aps.org/supplemental/10.1103/PhysRevLett.123.264803> for further discussion on the structure, data retrieval and theoretical limits for the achievable microbunch duration.
- [32] P. Yousefi, N. Schönenberger, J. McNeur, M. Kozák, U. Niedermayer, and P. Hommelhoff, Dielectric laser electron acceleration in a dual pillar grating with a distributed Bragg reflector, *Opt. Lett.* **44**, 1520 (2019).
- [33] <https://www.lumerical.com/>.
- [34] <http://www.pulsar.nl/gpt/index.html>.
- [35] D. S. Black, U. Niedermayer, Y. Miao, O. Solgaard, R. L. Byer, and K. J. Leedle, preceding Letter, Generation, acceleration, and direct measurement of attosecond electron pulse trains in silicon nanostructures, *Phys. Rev. Lett.* **123**, 264802 (2019).

Supplemental Materials to Generation and Characterization of Attosecond Micro-Bunched Electron Pulse Trains via Dielectric Laser Acceleration

Norbert Schöenberger,^{1,*} Anna Mittelbach,¹ Peyman Yousefi,¹
Joshua McNeur,¹ Uwe Niedermayer,² and Peter Hommelhoff^{1,†}

¹Department of Physics, Friedrich-Alexander Universität Erlangen-Nürnberg (FAU),
Staudtstraße 1, 91058 Erlangen, Germany

²Technische Universität Darmstadt, Institut für Teilchenbeschleunigung und Elektromagnetische Felder (TEMF)
Schlossgartenstraße 8, 64289 Darmstadt, Germany

STRUCTURE

The used structure, as seen in Fig. 1 and 2, is comprised of two rows of pillars paired with a distributed Bragg reflector. The structure parameters are optimized via full FDTD simulations and charged particle tracing. The resulting structure has a channel width of 200 nm, pillar diameters of (385 ± 7) nm and a periodicity of 640 nm. A more detailed accounting of the manufacturing process and typical structure parameters is provided in [1].

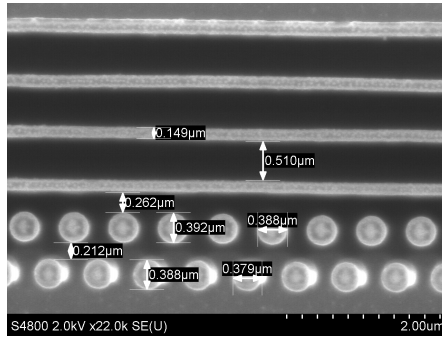


FIG. 1. Close-up and measurements of one of the used structures. At the bottom of the picture, the two rows of pillars forming the accelerator are visible. The pillars have diameters of (385 ± 7) nm and have a periodicity of 640 nm. The electrons propagate between the two rows of pillars, in the gap of 212 nm, where the nearfield modulates their energy. Furthermore a distributed Bragg reflector is included. The parameters were optimized in simulations to achieve the suitable phase offset to create an accelerating mode and to provide the highest reflectivity at a center wavelength of 1932 nm. This is influenced by the distance of the Bragg reflector and the pillar structure, here 262 nm.

The laser is incident on the structure from the bottom (Fig. 2), and is reflected from the Bragg reflector at the top of the structure to mimic double sided pumping of the structure. This greatly reduces the field asymmetry compared to single sided pumping. Nevertheless, the reflected part of the beam will not provide the same peak field as the laser pulse was already transmitted through the pillars since some losses will have occurred, reducing field symmetry. Furthermore the phase offset of the reflected portion can not be adjusted and is subject to manufacturing errors. An analysis of this provided in [1] shows that the effect is noticeable but not very severe.

The structure has a geometrical limit in the acceptable divergence angle of 2 mrad given by the aperture of the electron channel and the length of the structure. This figure does not take into account any transverse effects inherent to these photonic accelerators, reducing the acceptable input divergence. Therefore, the electrons would ideally be focused as close to the center of the drift space as possible to provide the smallest possible beam diameter across the whole structure. However, due to experimental reasons, this is not feasible and the electrons are focused to the center of the first structure. This acceptance problem is alleviated by the newly developed adaptation of the classical mechanism of alternating phase focusing to dielectric laser accelerators [2], since it provides transverse guiding mechanisms.

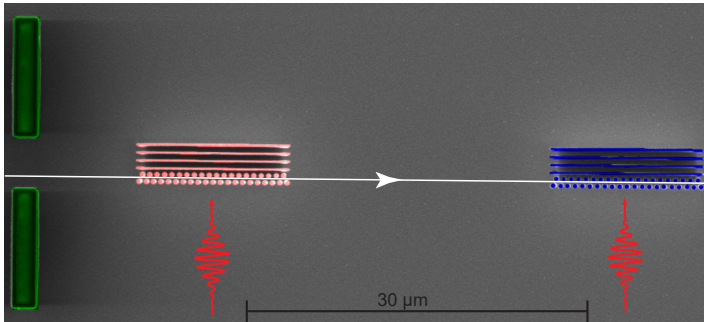


FIG. 2. Top view of the used structure. The electron propagation path is shown in white. Shown in red is the modulator structure. On the right hand side after a defined drift distance the modulator, shown in blue, is reached by the electrons. The green alignment marks are used to find the structure in the laser triggered operation mode of the scanning electron microscope. Since imaging is not possible due to the low average current, the transmitted electrons can be used as an indicator of where the electrons are relative to the structure.

SIMULATIONS AND DATA RETRIEVAL

Since direct measurement of the duration of the microbunches is not possible in the experimental arrangement presented in this paper, we retrieve the microbunch length from simulations that are matched to the experimental parameters. The structures are reproduced as a CAD-model, in the simulation package FDTD Solutions by Lumerical, with fabricated structure parameters measured with an electron microscope, like shown in Fig 1. The FDTD simulation is conducted with a transform limited pulse with a central wavelength of 1932 nm and a pulse length of 650 fs. The validity of these parameters was confirmed via a frequency-resolved optical gating (FROG) measurement. The laser pulses also form a Gaussian beam in the simulation and are focused to the spot size measured in the experiment of $7 \mu\text{m}$ ($1/e^2$ radius).

The resulting time dependent fields are exported and used in the charged particle tracker software General Particle Tracer (GPT). The custom code necessary to use this field data in GPT has been carefully vetted with simpler structures. The initial electron pulse conditions are chosen to be as close to the experiment as possible, with a pulse of 400 fs FWHM normally distributed, 10 nm spot size and a divergence of 1 mrad.

Since we operate in a regime of one electron per pulse, the simulations are executed without space charge forces and typically contain thousands of electrons per simulation to provide good statistics.

The overlap of the fields and electrons is adjusted so that the electrons experience the maximum amplitude in both interactions, like in the experiment. The relative phase between the interactions is tuned via a time offset of the second interaction. Since the structures are identical, the same simulated fields are used. The electron spectrum for each phase delay is recorded at a distance greater than $40 \mu\text{m}$ from the end of the analyzer, where the fields have decayed almost completely.

In Fig. 3 we show the data retrieval exemplary for the simulation and measurement of our shortest microbunches. This happens at an incident modulator field of 460 MV m^{-1} and an incident analyzer field of 1500 MV m^{-1} . In a first step, we find the center line of the high density electron region, located at the nodes of the modulation. The region around this center line is integrated, perpendicular to the center line, to average out noise from the measurement and help with the low resolution in both measurement and simulation. Finally the projection on the x-axis, which is the axis of phase difference, is fitted with a normal distribution. The slope, given in eV/fs, and the width on the phase axis fully characterize the spectrograms. Lastly, to determine the actual microbunch duration, a simulation excluding the analyzer is performed, which gives the electron phasespace and density at the position of the analyzer.

Due to the Gaussian temporal shape of the laser pulse and the electron pulse being of similar duration as the laser pulse, the longitudinal focal length varies depending on the amplitude of the laser field the electrons experience. Therefore, microbunches that are further from the temporal center of the whole electron pulse are under bunched in the chosen temporal focus. This can be rectified by either stretching the laser pulse further or utilizing flat top

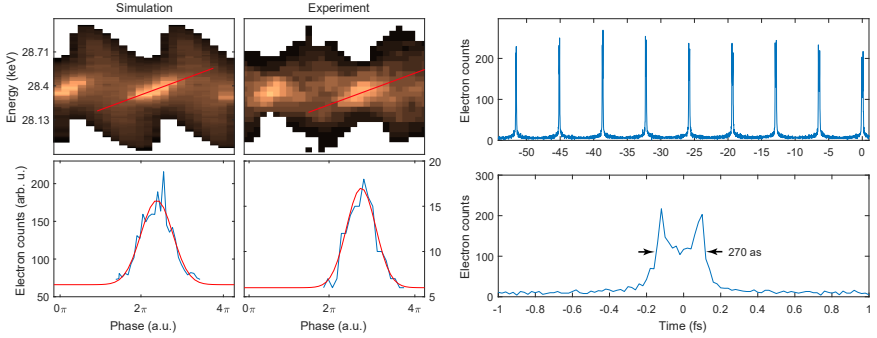


FIG. 3. The top row shows simulation and experimental data for the parameters $E_M = 460 \text{ MeV m}^{-1}$ and $E_A = 1500 \text{ MeV m}^{-1}$ where the shortest microbunch duration was measured. Also included is the fitted center line of the high density region at the nodes of the modulation, shown in red. This center line has a slope of $(46.94 \pm 6.10) \text{ eV fs}^{-1}$ in the case of the simulation and $(48.52 \pm 18.70) \text{ eV fs}^{-1}$ for the experimental data. This center line is used to sum up the relevant data perpendicularly to the line. Finally this summed distribution is projected to the phase-axis and fitted with a normal distribution to retrieve the width. The widths are $\sigma = (1.64 \pm 0.27) \text{ fs}$ and $\sigma = (1.645 \pm 0.490) \text{ fs}$ respectively. On the right hand side, we show an excerpt of the pulse train, where time zero denotes where the measurement was performed. The overbunching increases towards our measurement time. The lower graph shows the bunches at the interaction point of the analyzer with their length of 270 as. The temporal profile shows the double horn typical for overbunched pulses.

laser pulses, so each electron interacts with the same field amplitude. Therefore, we give the FWHM of the center microbunch as the duration and don't average over all 100 microbunches in the pulse train.

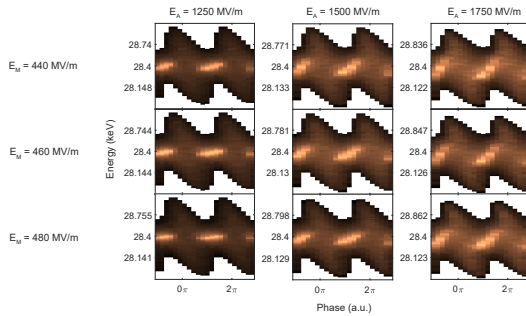


FIG. 4. Map of simulations around the parameter set matching to the shortest measured bunch duration. From this we conclude the parameters that fit the measurements best. Furthermore, we estimate the error of our data retrieval via these simulations. The step size of 20 MV m^{-1} in the modulator leads to a difference of 80 as in bunch duration. We therefore assume ± 80 as a conservative error.

Additional simulations were performed once the rough location of each measurement was established on the map of simulations to determine the exact interaction, since the structure factor for each individual section can vary due to manufacturing tolerances. Furthermore, we estimate the error according to these neighboring simulations. One such set is shown in Fig. 4. It shows the simulation of the shortest experimentally measured microbunches, with adjacent

TABLE 1. Table of slopes and widths, collected from the simulations in Fig. 3. Due to the comparatively big variation of these values for the different input parameters, with respect to the deviation between measurement and simulation, we conclude that the chosen simulation and the error are valid. The given errors are not due to statistical uncertainty but due to the model of a line and Gaussian fit not being the perfect choice here.

		Analyzer peak fields (MV/m)		
		1250	1500	1750
Modulator peak fields (MV/m)	440		$m = (61.44 \pm 7.40) \text{ eV fs}^{-1}$ $w = (1.653 \pm 0.203) \text{ fs}$	
	460	$m = (11.71 \pm 4.30) \text{ eV fs}^{-1}$ $w = (1.464 \pm 0.129) \text{ fs}$	$m = (46.94 \pm 6.10) \text{ eV fs}^{-1}$ $w = (1.642 \pm 0.276) \text{ fs}$	$m = (93.05 \pm 8.00) \text{ eV fs}^{-1}$ $w = (1.773 \pm 0.242) \text{ fs}$
	480		$m = (19.33 \pm 7.40) \text{ eV fs}^{-1}$ $w = (1.628 \pm 0.209) \text{ fs}$	

simulations with a spacing of 20 MV m^{-1} in the modulator peak field and 250 MV m^{-1} in the analyzer peak field. At this step size, differences are already visible to the eye. The retrieved parameters are listed in Table 1. The performed measurement can unambiguously be matched to one simulation, within this grid of simulations. Therefore, we assume the deviation in microbunch length of 80 as, resulting from a shift of 20 MV m^{-1} in the modulator peak field, to be a conservative estimate of our error.

SUB-10 ATTOSECOND PULSES

To find the limit of achievable bunch duration, we perform simulations, based on the same full fields and of increasing peak field in the modulator structure, while tracking the temporal focal distance. We find that the minimal microbunch length is ≈ 7 as (FWHM), shown in Fig. 5. The peak of this width contains 8% of the initial electrons per optical cycle.

From a simple phasespace argument, when we assume just linear interactions, the shortest bunches are reached when the linearly modulated portion of the initial electrons is exactly vertical. The sinusoidal energy modulation

$$\Delta E = -qe_1 \lambda_g N \sin\left(\frac{2\pi t}{T}\right) \quad (1)$$

with λ_g the structure period, N the number of periods, e_1 the peak field in the accelerating mode and T the period of the sinusoidal modulation, can be linearized when only considering the region around $t = 0$. Using $\Delta\beta(t) = \frac{\Delta E(t)}{mc^2\beta\gamma^3}$ to convert from electron energy to β this yields

$$\Delta\beta(t) = -qe_1 \frac{2\pi}{T} t \frac{\lambda_g N}{mc^2\beta\gamma^3}.$$

With $\Delta s(t) = \frac{t}{\beta} \lambda_g$ we get the time it takes the electrons to reach the temporal focus

$$\tau = \frac{\Delta s}{\delta\beta c} = \frac{\lambda_g \beta \gamma^3}{2\pi \frac{qe_1 \lambda_g N c}{mc^2}}$$

and finally arrive at the longitudinal focal length:

$$L_0 = \beta c \tau = \frac{\lambda_g}{2\pi} \frac{\beta^2 \gamma^3 mc^2}{\Delta E}$$

with $\Delta E = q_1 \lambda_g N$ the width of the energy modulation. Finally we can define the micro bunch length as the time difference between the fastest and slowest electrons to reach the longitudinal focus:

$$\Delta\tau = \frac{L_0}{v_{min}} - \frac{L_0}{v_{max}} = L_0 \frac{\delta v}{v^2} = L_0 \frac{\delta\beta c}{\beta^2 c^2} = \frac{L_0}{c\beta^3\gamma^3} \frac{\delta E}{mc^2}$$

with $\delta\beta = \frac{1}{\beta\gamma^3} \frac{\delta E}{mc^2}$ being the velocity spread due to the initial energy spread. Finally using L_0 we arrive at

$$\frac{\Delta\tau}{T} = \frac{1}{2\pi} \frac{\delta E}{\Delta E}, \quad (2)$$

where T is the laser period, $\Delta\tau$ is the FWHM of the microbunch, δE is the FWHM of the initial energy spread and ΔE is the peak value of the energy modulation. The final phase space area of the bunch is $\Delta E\Delta\tau$, which is equal to the initial phase space area $\delta E T$ divided by 2π . This means that the fraction of electrons that end up in the bunch is $\frac{1}{2\pi} = 16\%$, which is the fraction of electrons that are linearly modulated by the sinusoidal fields in Eq. 1. This confirms that Liouville's theorem, which is only valid for linear interaction, is satisfied in the linear range of about 16% of a period.

With this relation of the micro bunch length, the length of the optical cycle, the initial energy spread and the induced sinusoidal energy spread and using the values $\delta E = 0.5$ eV, $\Delta E = 1700$ eV and $T = 6.45$ fs gives a theoretical bunch length of 0.3 as. This result does however not include transverse effects occurring in the structure, manufacturing tolerances and so on.

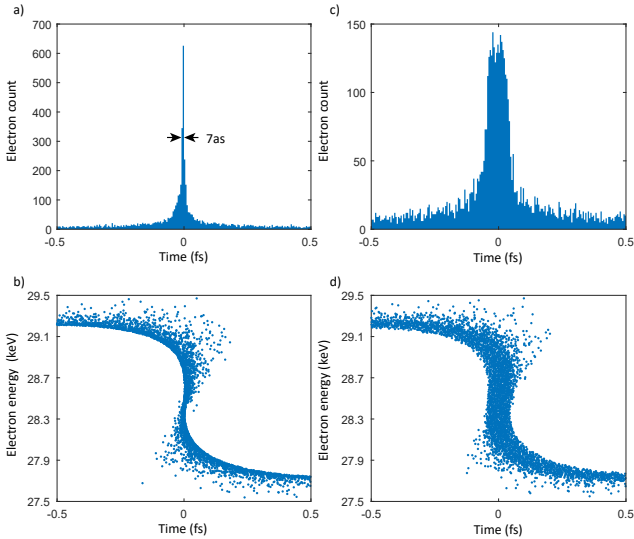


FIG. 5. a) Histogram of the 7 as bunch. b) Corresponding phasespace with initial energy spread of 0.5 eV. c) bunch histogram for an initial energy spread of 50 eV leading to a bunch duration of ≈ 100 as. This exaggerated energy spread was chosen to more easily visualize the dependence of the final bunchlength on the initial energy spread d) The corresponding phasespace shows the increased energy spread, that contributes significantly to the increased microbunch duration after the phasespace rotation.

Figure 5 shows simulations which include the transverse effects, real structure parameters and the non zero emittance of the initial electron beam. The longer microbunch duration of 7 as is caused by these effects. Figures 5 c) and d) show an exaggerated example to more easily visualize this dependence on the initial energy spread. The interaction is the same as in a) and b) except for the increased initial energy spread of 50 eV. Figure 5 c) clearly shows the increased energy spread in the center of the vertical part, after the phasespace rotation has taken place. This greater energy spread leads to the increased pulse length of approximately 0.1 fs.

Furthermore, we can estimate the achievable microbunch length from the imparted energy spread and the spectral shape [3, 4]. In the simulations the energy spread was 1700 eV. Experimentally measured spectra showed achievable energy spreads of up to 2400 eV while also showing spectra approaching the characteristic double hump shape [1], associated with sinusoidal energy modulation. Therefore, the applied fields are of reasonable quality. Otherwise the spectral shape would be different. Using these energy spreads with $\Delta t \Delta E \approx 5h[4]$, minimal bunch lengths of 1.94 as in the simulation and 1.4 as for the experimentally achieved energy spread should be achievable. These calculations

assume no initial energy spread and a perfect double hump spectrum as specified in equation D1 of [4]. In the experiment, neither of these conditions is satisfied. The initial energy spread is assumed to be 0.5 eV. The spectrum is a blurred out double hump spectrum, due to the non zero emittance of the used electron beam and transverse effects in the structures, allowing different electrons to sample different fields. Furthermore the non perfect structure causes not fully symmetric fields. While the two explored models show much shorter possible bunch durations, the numerically derived values include most of these imperfections inherent to any experiment, including manufacturing variations, they more closely represent what would actually be achievable. With higher induced energy spreads, even sub attosecond micro bunch durations might be possible.

* norbert.schoenberger@fau.de

† peter.hommelhoff@fau.de

- [1] P. Yousefi, N. Schöenberger, J. McNeur, M. Kozák, U. Niedermayer, and P. Hommelhoff, “Dielectric laser electron acceleration in a dual pillar grating with a distributed Bragg reflector,” *Optics Lett.* **44**, 1520–1523 (2019).
- [2] U. Niedermayer, T. Egenolf, O. Boine-Frankenheim, and P. Hommelhoff, “Alternating-Phase Focusing for Dielectric-Laser Acceleration,” *Phys. Rev. Lett.* **121**, 214801 (2018).
- [3] Peter Baum, “Quantum dynamics of attosecond electron pulse compression,” *Journal of Applied Physics* (2017), 10.1063/1.5006864.
- [4] Yuya Morimoto and Peter Baum, “Attosecond control of electron beams at dielectric and absorbing membranes,” *Physical Review A* (2018), 10.1103/PhysRevA.97.033815.

OPEN Laser-Driven Modulation of Electron Beams in a Dielectric Micro-Structure for X-Ray Free-Electron Lasers

Benedikt Hermann^{1,2*}, Simona Bettoni¹, Thilo Egenolf³, Uwe Niedermayer³, Eduard Prat³ & Rasmus Ischebeck¹

We describe an application of laser-driven modulation in a dielectric micro-structure for the electron beam in a free-electron laser (FEL). The energy modulation is transferred into longitudinal bunching via compression in a magnetic chicane before entering the undulator section of the FEL. The bunched electron beam comprises a series of enhanced current spikes separated by the wavelength of the modulating laser. For beam parameters of SwissFEL at a total bunch charge of 30 pC, the individual spikes are expected to be as short as 140 as (FWHM) with peak currents exceeding 4 kA. The proposed modulation scheme requires the electron beam to be focused into the micrometer scale aperture of the dielectric structure, which imposes strict emittance and charge limitations, but, due to the small interaction region, the scheme is expected to require ten times less laser power as compared to laser modulation in a wiggler magnet, which is the conventional approach to create a pulse train in FELs.

Free-electron lasers (FELs) make use of a highly compressed relativistic electron beam to generate electromagnetic radiation in a magnetic undulator. They are the brightest sources of radiation from the VUV^{1,2} to the X-ray regime³⁻⁷. The emission of radiation in a so-called self-amplification of spontaneous emission (SASE) FEL grows exponentially from noise and critically depends on the local properties of the electron beam. A technique proposed to generate an individual or a train of sub-femtosecond X-ray pulses with well-defined separation is the energy modulation of the electron bunch with a laser in the magnetic field of a resonant undulator. This “enhanced SASE” (ESASE) method has been proposed by Zholents⁸, and is being implemented at LCLS⁹ and planned at other facilities such as SwissFEL¹⁰.

In this paper, we present and compare an alternative method to the conventional undulator modulation scheme. We show, that by modulating the electron bunch in a laser-driven dielectric micro-structure, similar modulation strength can be achieved with significantly lower laser power. The beamline required for the proposed scheme is sketched in Fig. 1. Key elements are the strong focusing and matching quadrupole triplets, the chicane for bunching and the FEL undulator section with interleaved chicanes acting as phase shifters. The intrinsic synchronization of the FEL pulses to an external laser, which is achieved in both schemes, naturally gives rise to pump-probe experiments. The CHIC scheme in the soft X-ray beamline in SwissFEL (Athos) makes use of magnetic chicanes between the undulator segments to delay the electron beam with respect to the X-Rays^{10,11}. Athos is planned to deliver FEL radiation for wavelengths ranging from 0.65 nm to 5 nm from 2020 and user operation starting in 2021¹⁰. Adjusting these chicanes to form overlap between each X-ray pulse with the subsequent slice of the electron bunch, the longitudinal coherence is transferred along the bunch, and the X-ray pulses become phase-locked¹². The chamber for the interaction with the laser and dielectric structure is installed in the switchyard to Athos and is currently being commissioned. It is also planned to demonstrate GV/m gradients in these dielectric laser acceleration (DLA) structures with a length of 1 mm at a laser wavelength of 2 μm ^{13,14}.

¹Paul Scherrer Institut, 5232, Villigen PSI, Switzerland. ²Institute of Applied Physics, University of Bern, 3012, Bern, Switzerland. ³Institute for Accelerator Science and Electromagnetic Fields (TEMF), TU Darmstadt, 64289, Darmstadt, Germany. *email: benedikt.hermann@psi.ch

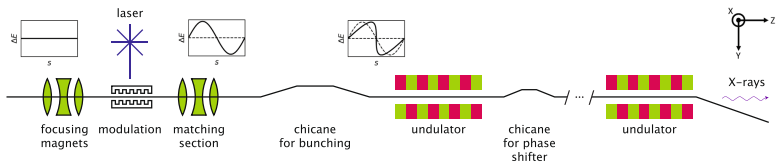


Figure 1. Schematic overview of the proposed scheme. Strong focusing is required to match the beam into the micrometer scale aperture of the dielectric grating. The longitudinal phase-space is modulated by the optical near fields in the dielectric structure excited by a laser. The energy modulation is converted into longitudinal bunching by a magnetic chicane. Three inset plots illustrate the longitudinal phase-space evolution. The resulting pulse train emits a series of homogeneously spaced x-ray pulses which can be mode-locked by small chicanes between undulator modules acting as phase shifters.

Modulation of Electron Beams in a Laser-Driven Dielectric Double Grating

Illuminating a dielectric grating with a laser creates evanescent waves which travel inside the gap of the structure with a phase velocity defined by the periodicity of the structure and the wavelength of the illuminating laser. For a laser incident normal onto a straight grating a net interaction with a charged particle traveling along the gap is achieved if the resonance condition is fulfilled: $\lambda_S = \lambda_L \beta n$ ¹⁵. Here, λ_S denotes the periodicity of the dielectric structure, λ_L is the wavelength of the laser, β is the normalized electron velocity and n is the order of the spatial harmonic of the evanescent wave. To sustain the interaction over distances greater than the laser pulse length, a pulse-front tilt setup for the laser has to be employed^{16–18}. Due to the optical phase dependence of the interaction, net-acceleration of electrons can be achieved only for bunches significantly shorter than the wavelength of the driving laser. The momentum distribution of an electron beam longer than the laser wavelength will be modulated sinusoidally. The amplitude of the longitudinal interaction with the evanescent waves inside the channel of a straight grating is proportional to $\cosh(2\pi y/(\lambda_L \beta \gamma))$ and the transverse component of the interaction is proportional to $\sinh(2\pi y/(\lambda_L \beta \gamma))$ ¹⁹. As a result, the modulation amplitude becomes homogeneous over the entire gap and the transverse component vanishes for ultra-relativistic particles ($\gamma \gg 1$). Therefore, a straight grating illuminated by a laser polarized along the direction of the electrons creates an almost purely longitudinal momentum modulation. A resonant transverse momentum component can be added by tilting the grating²⁰. In principle, the transverse momentum modulation can be used to bunch the beam by an appropriate compression setup using R_{32} (transfer matrix element relating transverse momentum changes to temporal deviations). However, compression of the transversely modulated beam leads to a slice emittance increase within the spikes. Since the SASE process strongly depends on the transverse slice emittance²¹, we focus on longitudinal modulation only to avoid emittance growth after compression.

Results

Modulation and compression. The particle distribution for this study is optimized with ASTRA²² to obtain a low emittance and a low energy spread for a bunch charge of 30 pC and an energy of 3 GeV to achieve a final peak current which is sufficient to drive the SASE FEL process. This working point is covered by the parameter range of the SwissFEL accelerator at the location of the ACHIP interaction chamber in the switchyard of the Athos beamline. At this location, the optimized distribution has a peak current of 300 A and a length of around 100 fs. The tracking of the modulated electron beam through the switchyard is done with ELEGANT²³ including longitudinal space charge and coherent synchrotron radiation effects. The electromagnetic field distribution created in a laser excited structure is modeled with CST Studio²⁴. We observe that the longitudinal and transverse component of the interaction follow the analytical solution derived in¹⁹. The remaining transverse modulation amplitude is 500 times smaller than the transverse momentum spread for the case of the 3 GeV electron beam in Athos at SwissFEL. Detailed information about the field simulations with CST are given in section Methods - We conclude, that the interaction of an ultra-relativistic electron bunch ($\gamma \approx 6000$) inside the channel of a double grating structure with the fields of a normally incident laser can be modeled as a homogeneous sinusoidal momentum modulation. The transverse kicks and the transverse dependence of the longitudinal kick vanish for a straight grating and ultra-relativistic electrons¹⁹. The symmetry of the field can be even further enhanced by illuminating the structure from both sides or by using a distributed Bragg mirror (DBR) behind the structure^{25,26}. The DBR consists of dielectric layers with well-defined thicknesses to reflect the laser and mimic double-sided illumination. The modulated electron beam is bunched in a subsequent magnetic chicane. Naturally, the achievable peak current after optimal compression depends on the slice energy spread and increases with the modulation strength, up to a certain limit. To illustrate the concept we use a modulation amplitude of 0.5 MeV, which leads to an optimal R_{32} around 2 mm. This modulation amplitude corresponds to an average acceleration gradient of 0.5 GV/m in a 1 mm long structure. Such gradients have recently been demonstrated in a DLA experiment for relativistic electrons at the Pegasus facility at UCLA in 0.5 mm to 1 mm long structures²⁷. The interaction length was limited to 21.5 μm due to the temporal overlap with the laser pulse since no pulse-front tilt for the laser was used in this experiment. The simulation results for the DLA modulation, transport through the Athos switchyard of SwissFEL and optimal bunching are summarized in Fig. 2. In the first row (sub-figures a–d) projections of the

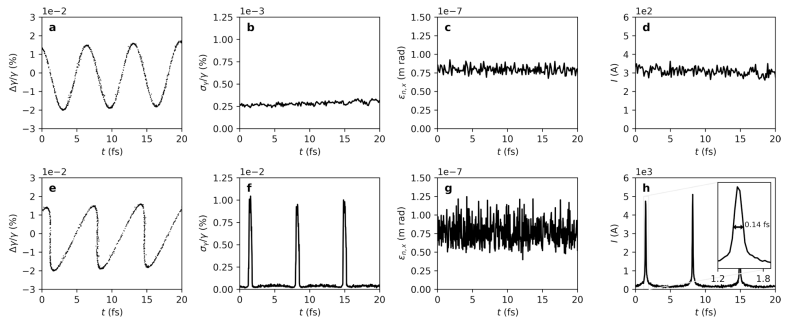


Figure 2. Simulated phase-space of the 3 GeV electron beam of SwissFEL at two locations: after the DLA interaction (first row, **a–d**) and after the propagation through the switchyard to the Athos beamline and optimal compression (second row, **e–h**). A strong increase in slice energy spread is observed, compare sub-figure (**b** and **f**), whereas the slice emittance remains unchanged (sub-figure (**c** and **g**)). The noise in (**g**) appears larger than in (**c**), as the bin width is reduced to resolve the short spikes. After optimal compression peak currents of up to 5 kA are predicted by this simulation (**h**).

phase-space just after the DLA interaction are shown, whereas the second row (sub-figures **e–h**) depicts the bunched particle distribution after the magnetic chicane. After compression a strong increase of the slice energy spread ($\sigma_s/\gamma = 1 \times 10^{-4}$) within the current spikes is observed, where γ is the relativistic mass factor. For SASE FELs the energy spread has to be much smaller than the FEL Pierce parameter ρ , see for instance⁴⁸. In case of the Athos beamline at SwissFEL, ρ is in the order of 1×10^{-3} , this condition is fulfilled. Since the transverse modulation is negligible, we assume the slice emittance ($\varepsilon_{s,e}$) to be conserved. Peak currents of up to 5 kA are achievable in this configuration, which corresponds to a current enhancement by a factor of 16. Similarly as for the conventional scheme, the spike heights inherit the Gaussian envelope from the original macro-bunch shape. The length of the individual spikes is expected to be around 140 as (FWHM). We observe 14 individual spikes with peak currents exceeding 2.5 kA spaced by 6.7 fs corresponding to the laser wavelength of 2 μm .

Comparison with undulator modulation. The conventional ESASE scheme uses an undulator magnet to resonantly transfer energy from a co-propagating optical laser to the electron beam to achieve a net-modulation of the electron beam⁸. Here, we compare our proposed DLA modulation scheme to the conventional approach in terms of electron beam and laser requirements.

Emittance and charge limitations. Typical apertures of wiggler magnets are in the order of 10 mm. Typical electron beam sizes at the end of FEL accelerators are far below 1 mm. Thus, no special focusing elements for the electron beam are needed and the charge which can be transported through the modulating structure is not limited by the geometry of the wiggler. In comparison, the DLA modulation scheme requires the GeV electron beam to be focused into the micrometer scale channel of the dielectric structure. This can be achieved with strong quadrupole focusing in combination with low transverse emittance. The beam size is determined by the emittance and the Twiss parameter $\bar{\beta}$ at the interaction point by $\sigma = (\varepsilon_{s,e} \bar{\beta} / \gamma)^{1/2}$. Since emittance scales with the charge for photo-injectors used at FELs, the charge which can be modulated in this scheme is limited. To estimate the charge limit, we assume a grating aperture of 1.2 μm , a beam energy of 3 GeV, and a $\bar{\beta}$ -function of 5 mm at the interaction point. These parameters can be achieved with the existing permanent magnet quadrupoles in the ACHIP chamber in the Athos branch at SwissFEL¹⁴. The in-vacuum quadrupole magnets are 10 cm long and provide a geometric strength (K -value) of 26 m^{-2} and 39 m^{-2} at a beam energy of 3 GeV¹³. For the parameters described above, the beam size and charge are plotted against emittance in Fig. 3. The emittance of the electron beam in SwissFEL has been optimized for different charges according to the procedure explained in Methods. For a maximum beam size of $\sigma = 0.3 \mu\text{m}$, corresponding to a 4 σ -aperture of 1.2 μm , a normalized emittance smaller than 100 nm rad is required, which limits the charge to approximately 50 pC.

Modulation effectiveness. The total modulation amplitude $\Delta\gamma$ obtained from a laser with a peak power P_{pk} and a spot size $\sigma_{L,x}, \sigma_{L,z}$ (distance from the center at which the intensity drops to $e^{-1/2}$ of the maximum), in a dielectric grating of length L_g is calculated by

$$\Delta\gamma = e \frac{e}{m_e c^2} \left(\frac{P_{pk}}{c \varepsilon_0 \pi \sigma_{L,x} \sigma_{L,z}} \right)^{1/2} \int_{-L_g/2}^{L_g/2} \exp\left(-\frac{z^2}{4\sigma_{L,z}^2}\right) dz. \quad (1)$$

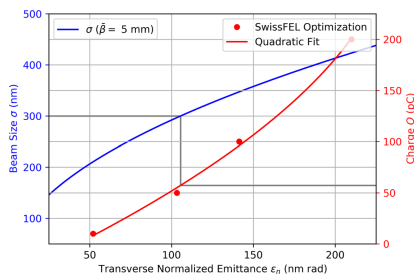


Figure 3. The transverse beam size (σ) for a fixed β -function (5 mm) and the maximum charge are plotted as a function of emittance. The emittance has been optimized for the SwissFEL injector at 4 different working points. We observe that a maximum charge of 50 pC can be focused to a beam size of $0.3\ \mu\text{m}$ using the existing magnets in the ACHIP chamber installed in the Athos switchyard of SwissFEL.

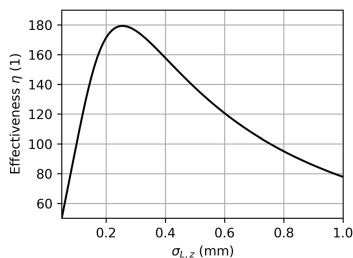


Figure 4. Dependency of the DLA modulation effectiveness on the laser focal spot size $\sigma_{L,z}$ for a 1 mm long structure.

Here, e_1 denotes the structure factor being the ratio of the effective acceleration gradient to the required incident electric field strength, which corresponds to the Fourier coefficient of the first spatial harmonic of the laser field inside the structure¹⁹. This formula is derived by integration of the electric field along the structure, and from the relation between the electric field vector \vec{E} and the intensity I of an electromagnetic wave, $I = c\epsilon_0 E^2/2$, where the vacuum permittivity is denoted by ϵ_0 . Considering that the modulation amplitude is proportional to the square root of the laser power, it is useful to define the unit-less modulation effectiveness η as

$$\eta = \frac{c\epsilon_0 (m_e c^2 \Delta\gamma)^2}{e^2 P_{pk}}. \tag{2}$$

This quantity describes the effectiveness of the modulating process and can be applied to any laser driven modulation scheme. It is a measure for the laser power which is required to achieve a certain modulation amplitude. The effectiveness depends on the laser focal spot size as described by Eqs. 1 and 2. Due to the Gaussian integral involving the shape of the laser in z , the dependence is not monotonous and an optimum value can be found. To illustrate this, we plot the effectiveness against $\sigma_{L,z}$, see Fig. 4. For a 1 mm long structure, the maximum effectiveness is achieved for $\sigma_{L,z} \approx 250\ \mu\text{m}$. In practice, it can be favorable to use a larger laser spot size to reduce the peak electric field strength in the dielectric material and accept the reduced effectiveness. For the comparison, we assume a laser focal spot size of $\sigma_{L,x} = 4\ \mu\text{m}$ by $\sigma_{L,z} = 500\ \mu\text{m}$. The effectiveness is approximately 20% lower as compared to the optimal case, see Fig. 4. The Rayleigh length in x for a Gaussian laser beam is $z_{r,x} = 4\pi\sigma_{L,x}^2/\lambda_D$, which is around $100\ \mu\text{m}$ in this case. The structure factor e_1 for a relativistic DLA made of fused silica is typically in the order of 1, which is what we use for the calculation, but can be higher (2–3) for a smaller gap size²⁰. Higher e_1 however goes along with more resonant structures, prohibiting short pulse operation. Based on these parameters and the formula above we calculate an effectiveness of the DLA modulation technique of around 140. The ESASE scheme proposed for LCLS at Stanford uses a modulation at a wavelength of $2.2\ \mu\text{m}$ with a modulation amplitude of 7 MeV. The required laser peak power is estimated to be $10.7\ \text{GW}$ ³⁰. The corresponding effectiveness,

Parameter	Symbol	DLA Modulation	ESASE Undulator	Unit
Required transverse electron beam size	σ_{x0}	0.3	—	μm
Structure Period (grating/wiggler magnet)	λ_S	2×10^{-6}	0.3	m
Number of periods	N_S	500	8	1
Structure length	L_S	1×10^{-3}	2.4	m
Laser wavelength	λ_L	2	2.2	μm
Laser spot size, x	$\sigma_{L,x}$	4	250	μm
Laser spot size, z	$\sigma_{L,z}$	500	250	μm
Modulation effectiveness	η	140	12	1

Table 1. Comparison of the requirements for the electron beam and the laser for DLA modulation and conventional undulator modulation for ESASE. The parameters for the ESASE scheme are taken from the proposal for LCLS³⁰.

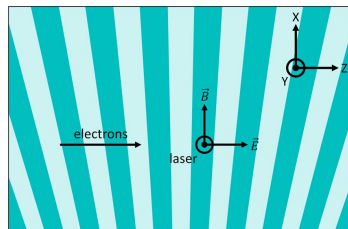


Figure 5. Conceptual drawing of the diverging grating structure. The periodicity can be scanned by moving the grating along x with respect to the electron beam. The dimensions and especially the slope of the changing periodicity need to be chosen, such that the periodicity changes not significantly within the beam size. As a consequence, the length of the chirped grating along the open direction (x) follows from the required tunability range. For a homogeneous interaction within the transverse beam shape we limit the periodicity change within $10 \mu\text{m}$ to $0.01 \lambda_S \equiv 20 \text{ nm}$. The resulting slope of the periodicity change along x equals 2×10^{-5} . For a tunability range of $1.5 \mu\text{m}$ to $2.5 \mu\text{m}$ a structure length along the open direction (x) is given by wavelength range/slope = 0.5 mm .

as previously defined, for this setup is around 12. In comparison, the proposed DLA modulation scheme is around ten times more effective, in terms of required laser power for a fixed modulation amplitude. The requirements for the electron beam and the laser pulse for both schemes are summarized in Table 1.

Tunability. Another important aspect for both schemes is the tunability of the modulation period. In both scenarios a change of the laser wavelength λ_L is required. In an experiment, this can be realized by a tunable optical parametric amplifier (OPA) in combination with reflective optics for the laser transport to avoid chromatic effects, for example in lenses. Regarding the undulator modulation scheme, the wiggler parameter K_W needs to be modified such that $\lambda_L = \lambda_W(1 + K_W^2/2)/2\gamma^2$, where λ_W is the wiggler period⁸. This is typically achieved by adjusting the gap between the magnetic arrays of the wiggler. In order to change the modulation period in the DLA scheme, the periodicity of the structure needs to be modified according to the resonance condition $\lambda_S = \lambda_L \beta n$. We propose to realize this with a chirped (diverging) grating, where the periodicity slowly changes along the open direction, see Fig. 5. The resulting tilt of the grating will not degrade the transverse emittance since the transverse momentum modulation acquired in the first half of the structure is canceled in the second half as the tilt angle is inverted. In comparison to a series of different structures, the chirped grating approach would provide fast and continuous scanning capabilities by positioning the grating along its open direction (x). In principle, fused silica can be used for wavelengths ranging from $0.4 \mu\text{m}$ to $4 \mu\text{m}$. In this window, the refractive index at room temperature varies between 1.4 and 1.6 and the absorption index is close to zero. To enhance the modulation effectiveness other grating parameters, such as the grating tilt width, could be optimized for the desired wavelength interval. For larger wavelengths, the absorption rises strongly and peaks at around $10 \mu\text{m}$ ³¹. The length of the individual current spikes can be tuned in both schemes by adjusting the modulation amplitude and the compression factor R_{co} of the magnetic chicane. For the DLA modulation scheme the modulation amplitude is limited by the damage threshold of the dielectric structure. Irreversible damage of fused silica DLAs has been observed for incident electric fields of around 9 GV/m ²⁷, which would limit the modulation amplitude to around 9 MeV for a 1 mm long structure. This boundary is more than one order of magnitude higher than the modulation amplitude we use for the bunching simulation presented above.

Discussion

We investigated a scheme which uses the fields in a dielectric micro-structure excited by a laser to modulate the ultra-relativistic electron beam of an FEL with the purpose of creating a pulse train for the ESASE scheme. Beam dynamics simulations using parameters of the SwissFEL accelerator predict the generation of 140 as (FWHM) electron spikes with peak currents up to 5 kA from a bunch with a total charge of 30 pC and an initial current of 0.3 kA. These beam parameters are suitable to drive the SASE process and create pulsed FEL radiation. Investigation of the properties of the radiation created in the Athos undulators at SwissFEL, through time-dependent FEL simulations, can be subject of a future study. Especially, the undulator tapering to increase the pulse energy while keeping the FEL pulses short and phase shifters between the undulator sections to create phase-locked pulses need to be optimized in detail.

The micrometer scale aperture of the dielectric structure implies strict limitations for beam focusing and transverse emittance. For the case of the Athos beamline at SwissFEL, the estimated charge limit is around 50 pC. Losses created by the tails of the beam limit the achievable repetition rate. The conventional undulator modulation scheme has no such limitations and is favourable in a high charge, emittance and repetition rate machine. Based on our estimation, dielectric laser modulation for ultra-relativistic electron beams is around a factor of ten more effective than undulator modulation, meaning that only a tenth of laser power is required to achieve the same modulation amplitude of the longitudinal phase-space. Since the laser system is one of the main cost drivers of the ESASE scheme, the proposed DLA modulation scheme presents a significant economic advantage. This aspect is particularly important for future, more compact and less expensive X-ray FEL facilities which will operate at lower charge and emittance than existing facilities. Both schemes allow continuous scanning of the modulation period, by changing the wavelength of the laser and properties of the modulating structure: in the undulator modulation scheme the wiggler parameter needs to be changed; in the DLA modulation scheme the periodicity of the grating needs to be adapted. We propose to use a diverging grating for continuous scanning capabilities.

Methods

Emittance optimization for swissFEL. SwissFEL can run at different bunch charges to accommodate the requests of the users. For each case, the emittance and the optics mismatch along the slices of the beam have been optimized at the injector to maximize the uniformity of the properties along the bunch, and therefore the lasing intensity. The main parameters included in the optimization are the first focusing at the exit of the radio-frequency gun, along the first accelerating structure, and the transverse size of the laser at the cathode. These parameters are determined starting from the layout corresponding to the 200 pC design case of SwissFEL and finely tuned using a simplex optimizer³². In the simulations the assumed intrinsic emittance is 550 nm/mm, accordingly to what was measured at the SwissFEL injector test facility^{33,34}. Downstream of the injector the beam is compressed in two stages. We optimized the compression parameters to have an optimum balance between the intrinsic energy spread, the peak current and the residual chirp. We simulated 2×10^9 macro-particles for the tracking with ELEGANT³⁵ of the 30 pC-distribution which is used in this study.

Electron optics for high current beams. Operating the proposed DLA modulation scheme with a high current initial electron beam will induce strong wakefields inside the dielectric structure that may lead to heating and destruction of the device. The electron optics can be adapted to achieve a strongly asymmetric focus to reduce the current density inside the structure to reduce short-range wakefields. This can be achieved with a strong quadrupole doublet. We used the focusing strengths of the existing permanent magnets inside the ACHIP chamber at SwissFEL and optimized their position with ELEGANT³⁵. Due to the ultra-relativistic energy (3 GeV) transverse space charge effects at the focus can be neglected and the particle tracking code ELEGANT can be applied. The laminarity parameter, as defined for instance in³⁵, must not exceed unity in order to neglect space charge forces. For the parameters of this study the laminarity parameter at the interaction point is indeed around 1×10^{-3} . The Twiss parameters ($\bar{\beta}_x$ and $\bar{\beta}_y$) along the beamline and the transverse beam profile at the interaction point for a normalized slice emittance at the core of the beam of 80 nm rad are shown in Fig. 6. The particle distribution for this simulation was optimized with ASTRA³² at a charge of 30 pC for the SwissFEL injector. The compression settings were optimized using ELEGANT. With the optimized permanent magnet configuration a ratio $\bar{\beta}_x/\bar{\beta}_y$ of around 1600 can be achieved ($\bar{\beta}_x = 10$ m, $\bar{\beta}_y = 5$ mm). The aspect ratio of the electron beam is given by $(\bar{\beta}_x/\bar{\beta}_y)^{1/2} \approx 40$. A larger transverse electron beam size at the interaction point requires an even larger laser spot to maintain a homogeneous interaction. As a result, the laser power requirement would increase.

Structure optimization and transverse effects. The geometry of the dielectric double grating is optimized to achieve a structure factor of about 1. We used CST Microwave Studio³⁴ to calculate the electromagnetic fields of a single grating period in the frequency domain. The incident laser field is modeled as a plane wave coupled into the dielectric structure. The Fourier coefficient of the first spatial harmonic is given by¹⁹

$$\epsilon_1(y) = \frac{1}{\lambda_s E_0} \int_{-\lambda_s/2}^{\lambda_s/2} \underline{E}_z(y, z) \exp\left(i \frac{2\pi}{\lambda_s} z\right) dz \quad (3)$$

with the longitudinal electric field $\underline{E}_z(y, z)$ inside the channel and the amplitude E_0 of the incident laser field. The absolute value of the complex Fourier coefficient as the structure factor describes the ratio of the acceleration gradient to the incident laser field. To achieve the desired structure factor in the center of the channel, we optimized the teeth and also the base thickness for a given aperture. The resulting parameters are shown in Fig. 7. Since the transverse dependence of the Fourier coefficient is analytically given as $\epsilon_1(y) = \epsilon_1(y=0) \cosh(2\pi y / (\lambda_s \beta \gamma))$ ¹⁹, the modulation amplitude is almost independent of the transverse position in the gap. This is confirmed by numerically evaluating the structure

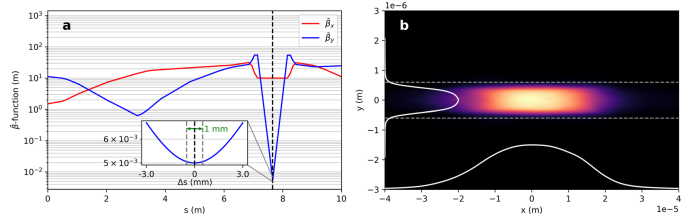


Figure 6. (a) Electron optics for asymmetric focusing with 2 strong permanent magnet quadrupoles. The Twiss parameters β_x and β_y are plotted around the interaction region. A ratio β_x/β_y of around 1600 is achieved with a permanent magnet quadrupole doublet. The inset shows the evolution of β_x in the vicinity of the interaction point (black dashed line). We observe that the beam size does not change significantly within a propagation distance of 1 mm (green arrow). (b) Simulated electron beam profile at the interaction point. The two dashed lines indicate the gap of the dielectric double grating (1.2 μm).

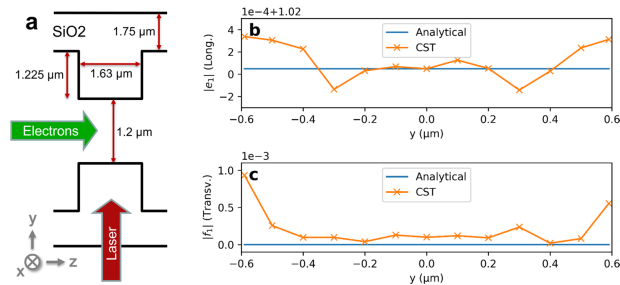


Figure 7. (a) Parameters of the optimized double grating. (b) Longitudinal structure factor $e||$, plotted along the 1.2 μm wide gap of the structure. The numerical noise of the constant structure factor of 1.02 is in the order of 1×10^{-4} . (c) Transverse structure factor f_t . Transverse forces (including numerical noise) across the gap are 3 orders of magnitude smaller than longitudinal forces.

factor along the gap, see Fig. 7. The transverse fields can be analytically obtained using the Panofsky-Wenzel theorem. For a straight grating, the transverse kick becomes $f_t(y) = \lambda_y/(2\pi)\partial \epsilon_y/\partial y = \epsilon_y(y=0) \sinh(2\pi y/(\lambda_y \beta \gamma))/\gamma^{19}$ and therefore vanishes for ultra-relativistic electrons. Numerically the transverse kick can be calculated by integrating the transverse electric and magnetic fields inside the channel as

$$f_t(y) = \frac{1}{\lambda_y E_0} \int_{-\lambda_y/2}^{\lambda_y/2} (\mathbf{E}_y(y, z) + \beta c \mathbf{B}_x(y, z)) \exp\left(i \frac{2\pi}{\lambda_y} z\right) dz. \quad (4)$$

The evaluation of this integral along the gap using the fields simulated by CST Microwave Studio confirmed the analytical description, i.e. that the transverse effect vanishes, see Fig. 7. Note that the numerical noise arises especially from the interpolation of the magnetic field, which is not allocated at the same mesh entity as the electric field and thus needs to be interpolated. This is the reason why the numerical transverse kicks, which are close to zero, do not fulfill the Panofsky-Wenzel theorem. To estimate the effect of the remaining transverse component we compare f_t to the transverse momentum spread of the electron beam at the interaction point. Over the entire gap the transverse amplitude is more than a factor of 1000 smaller than the longitudinal modulation component. For the case of the longitudinal modulation amplitude used in this study (0.5 MeV) the transverse modulation is expected to be smaller than 0.5 keV. The rms transverse momentum spread at the interaction point is calculated to be around 260 keV, which is a factor of 500 larger than the transverse modulation effect. The large transverse momentum spread is a result of the strong focusing. Hence, the degradation of the slice emittance by transverse forces in the structure can be neglected for an ultra-relativistic electron beam.

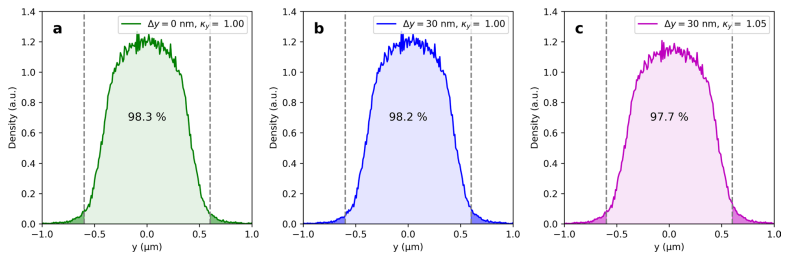


Figure 8. Transverse beam profiles for different combinations of position offset (Δy) and beam size factor (κ_y): (a) ideal case $\Delta y = 0$ nm, $\kappa_y = 1.00$, (b) $\Delta y = 30$ nm, $\kappa_y = 1.00$, (c) worst case $\Delta y = 30$ nm, $\kappa_y = 1.05$. The aperture of the dielectric grating structure is shown in gray, dashed.

Jitter and stability considerations. Good stability of beam position and size is required for the DLA modulation scheme, due to its micro-meter sized aperture. The electromagnetic field simulation for the proposed structure shows good homogeneity of the modulation strength ($<0.05\%$) and negligible transverse forces across the channel gap. Therefore, beam position and size jitter will not affect the modulation strength but only the number of particles hitting the boundary of the dielectric grating. In the following, we estimate the fraction of particles being transmitted through the structure geometry defined above. An upper limit for the position jitter of the electron beam in the accelerator of SwissFEL is 10% of the beam size. The beam size measured along the machine typically shows jitter in the order of 3%. In the proposed strong focusing setup, energy jitter adds significantly to the beam size due to chromatic effects of the permanent magnet quadrupoles. Simulations using ELEGANT²³ show an increase of the spot size by 1% for a typical energy error of 0.1%. For the calculation of the transmitted fraction we consider a maximum position offset of $\Delta y = 30$ nm and a beam size scaled by the factor $\kappa_y = 1.05$. The beam profile distribution is shown in Fig. 8 for three different combinations: (a) $\Delta y = 0$ nm, $\kappa_y = 1.00$, (b) $\Delta y = 30$ nm, $\kappa_y = 1.00$, (c) $\Delta y = 30$ nm, $\kappa_y = 1.05$. In the worst case scenario (c) a fraction of 2.3 of the electrons will scatter in the dielectric material of the structure. Towards high repetition rates above 100 Hz, radiation protection of the machine may become an issue. In this case, it might be required to increase the structure gap and sacrifice efficiency. The small loss of scattered particles in the tail of the electron beam do not reduce the stability of the FEL output power since the core of the beam is dominantly driving the SASE FEL process.

Data availability

The simulation data that support the findings of this study are available from the corresponding author upon reasonable request.

Received: 9 August 2019; Accepted: 9 December 2019;

Published online: 24 December 2019

References

- Ackermann, W. A. *et al.* Operation of a free-electron laser from the extreme ultraviolet to the water window. *Nature photonics* **1**, 336 (2007).
- Allaria, E. *et al.* The fermi free-electron lasers. *Journal of synchrotron radiation* **22**, 485–491 (2015).
- Emma, P. *et al.* First lasing and operation of an ångström-wavelength free-electron laser. *Nature photonics* **4**, 641 (2010).
- Ishikawa, T. *et al.* A compact x-ray free-electron laser emitting in the sub-ångström region. *Nature photonics* **6**, 540 (2012).
- Altarelli, M. *et al.* The european x-ray free-electron laser. *Technical design report*, DESY **97**, 1–26 (2006).
- Kang, H.-S. *et al.* Hard x-ray free-electron laser with femtosecond-scale timing jitter. *Nature Photonics* **11**, 708 (2017).
- Milne, C. *et al.* Swissfel: the swiss x-ray free electron laser. *Applied Sciences* **7**, 720 (2017).
- Zholents, A. A. Method of an enhanced self-amplified spontaneous emission for x-ray free electron lasers. *Physical Review Special Topics-Accelerators and Beams* **8**, 040701 (2005).
- Coffe, R. N. *et al.* Development of ultrafast capabilities for x-ray free-electron lasers at the linac coherent light source. *Philosophical Transactions of the Royal Society A* **377**, 20180386 (2019).
- Abela, R. *et al.* The swissfel soft x-ray free-electron laser beamline: Athos. *Journal of Synchrotron Radiation* **26** (2019).
- Prat, E. *et al.* Undulator beamline optimization with integrated chicane for x-ray free-electron-laser facilities. *Journal of synchrotron radiation* **23**, 861–868 (2016).
- Thompson, N. & McNeil, B. Mode locking in a free-electron laser amplifier. *Physical review letters* **100**, 203901 (2008).
- Prat, E. *et al.* Outline of a dielectric laser acceleration experiment at swissfel. *Nuclear Instruments and Methods in Physics Research Section A: Accelerators, Spectrometers, Detectors and Associated Equipment* **865**, 87–90 (2017).
- Ferrari, E. *et al.* The achip experimental chambers at the paul scherrer institut. *Nuclear Instruments and Methods in Physics Research Section A: Accelerators, Spectrometers, Detectors and Associated Equipment* **907**, 244–247 (2018).
- England, R. J. *et al.* Dielectric laser accelerators. *Reviews of Modern Physics* **86**, 1337 (2014).
- Wei, Y., Ibbson, M., Xia, G., Smith, J. & Welsch, C. Dual-grating dielectric accelerators driven by a pulse-front-tilted laser. *Applied optics* **56**, 8201–8206 (2017).
- Kozák, M. *et al.* Ultrafast scanning electron microscope applied for studying the interaction between free electrons and optical near-fields of periodic nanostructures. *Journal of Applied Physics* **124**, 023104 (2018).

18. Cesar, D. *et al.* Optical design for increased interaction length in a high gradient dielectric laser accelerator. *Nuclear Instruments and Methods in Physics Research Section A: Accelerators, Spectrometers, Detectors and Associated Equipment* **909**, 252–256 (2018).
19. Niedermayer, U., Egenolf, T. & Boine-Frankenheim, O. Beam dynamics analysis of dielectric laser acceleration using a fast 6d tracking scheme. *Physical Review Accelerators and Beams* **20**, 111302 (2017).
20. Niedermayer, U. *et al.* Challenges in simulating beam dynamics of dielectric laser acceleration. In *13th Int. Computational Accelerator Physics Conf. (ICAP'18), Key West, FL, USA, 20–24 October 2018*, 120–126 (JACOW Publishing, Geneva, Switzerland, 2019).
21. Prat, E. *et al.* Emittance measurements and minimization at the swissfel injector test facility. *Physical Review Special Topics-Accelerators and Beams* **17**, 104401 (2014).
22. Floettmann, K. Astra, <http://www.desy.de/~mppyflo/> (2000).
23. Borland, M. Elegant: A flexible sdds-compliant code for accelerator simulation. Tech. Rep., Argonne National Lab., IL (US) (2000).
24. CST, CST studio suite (2019).
25. Niedermayer, U., Boine-Frankenheim, O. & Egenolf, T. Designing a dielectric laser accelerator on a chip. In *Journal of Physics: Conference Series*, vol. 874, 012041 (IOP Publishing, 2017).
26. Yousefi, P. *et al.* Dielectric laser electron acceleration in a dual pillar grating with a distributed bragg reflector. *Optics letters* **44**, 1520–1523 (2019).
27. Cesar, D. *et al.* High-field nonlinear optical response and phase control in a dielectric laser accelerator. *Communications Physics* **1**, 46 (2018).
28. Huang, Z. & Kim, K.-J. Review of x-ray free-electron laser theory. *Physical Review Special Topics-Accelerators and Beams* **10**, 034801 (2007).
29. Wootton, K. P. *et al.* Demonstration of acceleration of relativistic electrons at a dielectric microstructure using femtosecond laser pulses. *Optics letters* **41**, 2696–2699 (2016).
30. Zholents, A. A. *et al.* Current-enhanced sase using an optical laser and its application to the lcls. In *Presented at, SLAC-PUB-10713*, 582–585 (2004).
31. Kitamura, R., Pilon, L. & Jonas, M. Optical constants of silica glass from extreme ultraviolet to far infrared at near room temperature. *Applied optics* **46**, 8118–8133 (2007).
32. Bettoni, S., Pedrozzi, M. & Reiche, S. Low emittance injector design for free electron lasers. *Physical Review Special Topics-Accelerators and Beams* **18**, 123403 (2015).
33. Divall, M. C. *et al.* Intrinsic emittance reduction of copper cathodes by laser wavelength tuning in an rf photoinjector. *Physical Review Special Topics-Accelerators and Beams* **18**, 033401 (2015).
34. Prat, E., Bettoni, S., Braun, H.-H., Ganter, R. & Schietinger, T. Measurements of copper and cesium telluride cathodes in a radio-frequency photoinjector. *Physical Review Special Topics-Accelerators and Beams* **18**, 043401 (2015).
35. Ferrario, M., Migliorati, M. & Palumbo, L. Space charge effects. In *Proceedings of the CAS-CERN Accelerator School: Advanced Accelerator Physics, Trondheim, Norway, 19–29 August 2013*, vol. CERN-2014-009 (2014).

Acknowledgements

We would like to thank Eugenio Ferrari for his design work related to ACHIP at PSI prior to this project. We wish to express our gratitude to the members of the ACHIP collaboration, as well as Thomas Feuer and Sven Reiche for helpful discussions, support and guidance. We are thankful to the reviewers whose detailed comments helped to enhance this manuscript. This work is funded by the Gordon and Betty Moore Foundation (GBMF4744).

Author contributions

B.H., U.N., E.P. and R.L. designed the concept. S.B. simulated the generation of suitable electron bunches in the SwissFEL accelerator. E.P. and B.H. implemented the beam dynamics simulation for the transport of the beam along Atheros. T.E. modeled the electromagnetic fields in the structure and optimized the structure geometry. U.N. and B.H. developed the notion of modulation effectiveness. All authors contributed to the manuscript.

Competing interests

The authors declare no competing interests.

Additional information

Correspondence and requests for materials should be addressed to B.H.

Reprints and permissions information is available at www.nature.com/reprints.

Publisher's note Springer Nature remains neutral with regard to jurisdictional claims in published maps and institutional affiliations.

 **Open Access** This article is licensed under a Creative Commons Attribution 4.0 International License, which permits use, sharing, adaptation, distribution and reproduction in any medium or format, as long as you give appropriate credit to the original author(s) and the source, provide a link to the Creative Commons license, and indicate if changes were made. The images or other third party material in this article are included in the article's Creative Commons license, unless indicated otherwise in a credit line to the material. If material is not included in the article's Creative Commons license and your intended use is not permitted by statutory regulation or exceeds the permitted use, you will need to obtain permission directly from the copyright holder. To view a copy of this license, visit <http://creativecommons.org/licenses/by/4.0/>.

© The Author(s) 2019

Tracking with wakefields in dielectric laser acceleration grating structures

Thilo Egenolf[✉], Uwe Niedermayer[✉], and Oliver Boine-Frankenheim[†]*Institut für Teilchenbeschleunigung und Elektromagnetische Felder (TEMF),
Technische Universität Darmstadt, Schlossgartenstrasse 8, D-64289 Darmstadt, Germany*

(Received 11 November 2019; accepted 27 April 2020; published 7 May 2020)

Due to the tiny apertures of dielectric laser acceleration grating structures within the range of the optical wavelength, wakefields limit the bunch charge for relativistic electrons to a few femtocoulomb. In this paper, we present a wakefield upgrade of our six-dimensional tracking scheme DLAtack6D in order to analyze these limitations. Simulations with CST Studio Suite provide the wake functions to calculate the kicks within each tracking step. Scaling laws and the dependency of the wake on geometrical changes are calculated. The tracking with wakefields is applied to beam and structure parameters following recently performed and planned experiments. We compare the results to analytical models and identify intensity limits due to the transverse beam breakup and strong head-tail instability. Furthermore, we reconstruct phase advance spectrograms and use them to analyze possible stabilization mechanisms.

DOI: 10.1103/PhysRevAccelBeams.23.054402

I. INTRODUCTION

Dielectric laser acceleration (DLA) structures accelerate electrons in the optical near-fields of periodic gratings [1,2]. Powered by ultrafast lasers, they are a promising concept for compact accelerators due to tenfold higher gradients as compared to conventional rf accelerators [3,4]. Recently, accelerating gradients of 850 MeV m⁻¹ were demonstrated at UCLA [5] using 45 fs laser pulses. Reviews of DLA theory and experiments can be found in [6–8]. The optimization of the beam dynamics in DLA is dominated by the question of how to fit a finite emittance beam into the sub-micrometer apertures of the grating structures over a length of several thousand periods. A scheme to confine a beam in the longitudinal as well as in one transverse plane by alternating the synchronous phase (APF-scheme) was proposed recently [9], wherein we described the single electron dynamics of an accelerator, which is fully scalable in length and energy. However, intensity effects were not included, yet. These intensity effects play a major role in relativistic DLA experiments, where conventional photoinjectors and booster-linacs are used.

Coherent DLA acceleration requires bunch lengths significantly shorter than the optical wavelength. Together with

the small apertures in DLAs, this leads to a strong short-range wakefield compared to the laser fields. As an example, Fig. 1 shows the wakefield in a dielectric dual pillar structure. Previous work on wake effects in DLAs has concentrated on longitudinal effects such as beam loading. This has been described by simplified analytical models of the structures, namely an azimuthal symmetrical and longitudinally flat structure and pointlike bunch distributions [10–15]. The analysis of metallic periodically corrugated structures like flat grating-dechirpers [16] has shown that the geometrical parameters influence the wakefields of particles close to the structure. Similar outcomes are expected for dielectric structures, however, additionally to the Smith-Purcell effect also the Cherenkov effect is present. Distinguishing between these two is not trivial and depends on geometrical as well as material parameters of the structure. The effects creating the Cherenkov wakes can be seen for example in the Cherenkov cone and the reflections within the Bragg layers in Fig. 1. They are intensively studied within the context of driving wakefields in dielectric wakefield accelerators (DWAs) [17–19]. One of the key findings of the work on DWAs is that the use of flat beams suppresses the transverse wake. Since the height of most DLA structures, e.g. pillars, is limited by the achievable etching depth to a few micron, the use of flat beams is impractical. Thus, we focus our study in the following on transversely almost circular bunch distributions.

Due to the finite emittance of available sources for round highly relativistic beams, the small apertures of a DLA grating are almost completely filled by particles. In order to analyze intensity effects in arbitrary DLA grating structures, we expand our tracking scheme DLAtack6D [20] by kicks due to the charge-distribution dependent wake in this paper.

[✉]egenolf@temf.tu-darmstadt.de[†]Also at GSI Helmholtzzentrum für Schwerionenforschung GmbH, Planckstrasse 1, D-64291 Darmstadt, Germany.

Published by the American Physical Society under the terms of the Creative Commons Attribution 4.0 International license. Further distribution of this work must maintain attribution to the author(s) and the published article's title, journal citation, and DOI.

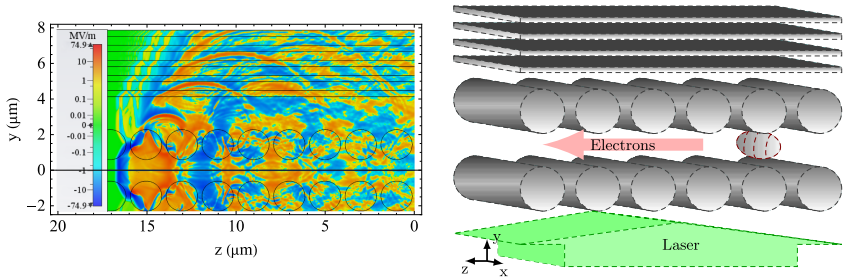


FIG. 1. Left: Longitudinal electric field of a 50 nm bunch (at $z = 16.565 \mu\text{m}$) with 1 fC bunch charge (left) propagating through a dielectric dual pillar structure with $2 \mu\text{m}$ period length (right). The dimensions of the structure can be found in Appendix A.

DLAtrack6D is based on calculating the longitudinal kicks from the spatial Fourier harmonics of the laser field and deriving the transverse kicks by means of the Panofsky-Wenzel theorem [21]. Subsequently, the kicks are applied to each particle of a bunch and the tracking is performed by the symplectic Euler (or leap frog) method. In this paper, we add wake kicks in a similar way as the external laser kicks. The paper is organized as follows: The calculation of the wake kicks is summarized in Sec. II, which is followed by a description of the simulated grating structures and scaling laws in Sec. III. Section IV shows tracking results for different energy ranges and links them to simplified analytical models of transverse instabilities. Stabilization mechanisms and intensity limits are also given in this section. The paper concludes with a summary and an outlook in Sec. V.

II. WAKE KICKS

The calculation of wake kicks requires solving Maxwell's equations in a given structure. Starting from a periodic grating structure, which is translation invariant in x -direction, we simulate the wake potential by the time-domain wakefield solver in CST Studio Suite [22] (cf. Fig. 1) using open boundary conditions in y - and z -direction and electric boundary conditions in x -direction. The number of DLA periods and the spacing to the boundaries is chosen such that the short range wakefield per DLA period converges. From the CST simulation we obtain the wake potential of a longitudinally Gaussian shaped moving line charge with a predefined bunch length. In order to get a three-dimensional map of the wake potential, the wakefield-integration paths are arranged on a rectangular grid in the gap region and the beam path is varied along the locations of the integration path in y -direction (cf. Fig. 2). The simulation is performed for each position of the source beam. Due to the translation symmetry of the structure in x -direction, it is sufficient to have all beam paths at only one x -position.

In order to calculate the wake potential of an arbitrary bunch distribution, the Green's function wake \vec{w} , i.e., the wake of a single particle excitation is required. However, if the length of a Gaussian excitation signal is much shorter than the length of the later used arbitrary bunch distribution, the wake potential of the corresponding CST simulation is a good approximation of the Green's function $\vec{w}(x - \bar{x}, y, \bar{y}, \bar{s})$, where \bar{x} and \bar{y} are the coordinates of the beam path, x and y are the coordinates of the integral path, and \bar{s} is the longitudinal coordinate with $\bar{s} = 0$ at the position of the charge. The convolution with the arbitrary bunch distribution on an arbitrary transverse position in the gap results in the wake potential

$$\vec{W}(x, y, s) = \int_{-\infty}^{\infty} \int_{-\infty}^{\infty} \int_{-\infty}^{\infty} [\vec{w}(x - \bar{x}, y, \bar{y}, \bar{s}) \times \lambda(\bar{x}, \bar{y}, s - \bar{s})] d\bar{x} d\bar{y} d\bar{s}, \quad (1)$$

where the bunch distribution is normalized as $\int_V \lambda(x, y, s) dV = 1$. For simplicity, we assume an uncorrelated distribution $\lambda(\bar{x}, \bar{y}, s - \bar{s}) = \lambda_x(\bar{x}) \lambda_y(\bar{y}) \lambda_s(s - \bar{s})$. This splits the integral in Eq. (1) in three parts, which can be evaluated independently. The wake potential is the result of a convolution over the longitudinal coordinate

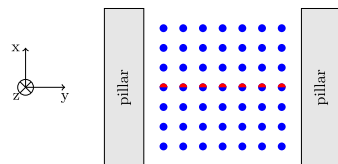


FIG. 2. Integration paths (blue dots) and beam paths (red dots) in the CST simulation. For each beam path the simulation is performed and the resulting wakefields are recorded in every integration path.

$$\bar{W}(x, y, s) = \int_{-\infty}^{\infty} \bar{W}^{\lambda_x \lambda_y}(x, y, \bar{s}) \lambda_s(s - \bar{s}) d\bar{s}, \quad (2)$$

where the integrals over the transverse coordinates are

$$\bar{W}^{\lambda_x \lambda_y}(x, y, \bar{s}) = \int_{-\infty}^{\infty} \bar{W}^{\lambda_y}(x - \bar{x}, y, \bar{s}) \lambda_x(\bar{x}) d\bar{x} \quad (3)$$

and

$$\bar{W}^{\lambda_y}(x - \bar{x}, y, \bar{s}) = \int_{-\infty}^{\infty} \bar{w}(x - \bar{x}, y, \bar{y}) \lambda_y(\bar{y}) d\bar{y}. \quad (4)$$

We will now discretize the above integrals, i.e., approximate them as sums. The integral over the transverse coordinate \bar{y} is, for example, approximated as

$$\bar{W}^{\lambda_y}(x - \bar{x}, y, \bar{s}) \approx \Delta \bar{y} \sum_{n_y} [\bar{w}(x - \bar{x}, y, n_y \Delta \bar{y}, \bar{s}) \times \lambda_y(n_y \Delta \bar{y})]. \quad (5)$$

The sum can be interpreted as a tensor product with all coordinates replaced by representative indices

$$\bar{W}^{\lambda_y}(x - \bar{x}, y, \bar{s}) \approx \bar{W}_{n_x, n_y, n_s}^{\lambda_y} \quad (6a)$$

$$= \Delta \bar{y} \sum_{n_y} \bar{w}_{n_x, n_y, n_s, n_y}^{\lambda_y}. \quad (6b)$$

The discrete representation of Eq. (1) follows as

$$\begin{aligned} \bar{W}(n_x, n_y, n_s) \\ = \Delta \bar{s} \Delta \bar{x} \Delta \bar{y} \sum_{n_x} \sum_{n_y} \sum_{n_s} \bar{w}_{n_x, n_y, n_s, n_y}^{\lambda_x} \lambda_x^s \lambda_s^s, \end{aligned} \quad (7)$$

which can be implemented in a very efficient manner.

The calculation of the wake kicks in each grating period starts with particle binning to determine the bunch distribution. Three tensor products as shown in Eq. (6b) yield the position dependent discrete wake potential for the bunch passing through one grating period. Evaluating the wake potential at the particle coordinates (x_p, y_p, s_p) , the wake kicks for each particle can be calculated as

$$\Delta x'(x_p, y_p, s_p) = \frac{q q_{\text{bunch}}}{p_{z0} \beta_{\text{ref}} c_0} W_x(x_p, y_p, s_p), \quad (8a)$$

$$\Delta y'(x_p, y_p, s_p) = \frac{q q_{\text{bunch}}}{p_{z0} \beta_{\text{ref}} c_0} W_y(x_p, y_p, s_p), \quad (8b)$$

$$\Delta \delta(x_p, y_p, s_p) = \frac{q q_{\text{bunch}}}{E_{0, \text{ref}}} W_s(x_p, y_p, s_p) \quad (8c)$$

with the particle charge q , the bunch charge q_{bunch} , the speed of light c_0 , the reference energy $E_{0, \text{ref}}$, the reference velocity β_{ref} , and the reference momentum p_{z0} . The changes in transverse and longitudinal momenta can be combined by the Panofsky-Wenzel theorem [21]

$$\partial_s \Delta \vec{p}_{\perp} = -\nabla_{\perp} \Delta p_s, \quad (9)$$

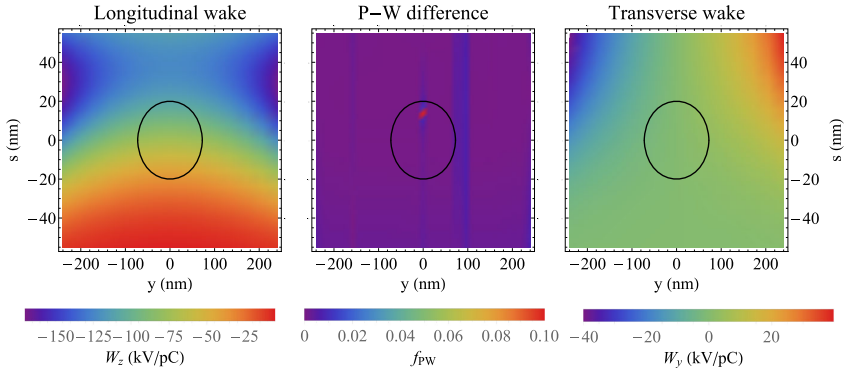


FIG. 3. Longitudinal and transverse wake potential per grating period in the left and right plot, respectively. The plot in the center shows the normalized difference between the left and the right-hand side of the Panofsky-Wenzel theorem [Eq. (11)] calculated for the simulated data of a Gaussian bunch distribution with standard deviation given by the black ellipse.

which is applicable under periodic boundary conditions [20]. Inserting the kicks [Eq. (8)] with $\Delta x' = \Delta p_x/p_{z0}$, $\Delta y' = \Delta p_y/p_{z0}$ and $\Delta\delta = \Delta p_s\beta c/E_{0,\text{ref}}$, Eq. (9) becomes

$$\partial_s \bar{W}_\perp = -\nabla_\perp W_s, \quad (10)$$

i.e. the same property as for the laser kicks also holds for the wake kicks. Equation (10) is a generally known result in wakefield research (see, e.g., [23]); here we use it as validation of Eqs. (8) and also of the numerical simulations and postprocessing steps. The relative error in fulfilling Eq. (9) is written as

$$f_{\text{PW}}(x, y, s) = \frac{\left| \frac{\partial W_s}{\partial y}(x, y, s) + \frac{\partial W_s}{\partial s}(x, y, s) \right|}{\left| \frac{\partial W_s}{\partial x}(x, y, s) \right| + \left| \frac{\partial W_s}{\partial y}(x, y, s) \right|} \quad (11)$$

with $f_{\text{PW}}(x, y, s) \ll 1$, which is plotted in Fig. 3. The plot in the center shows that the numerical difference in the Panofsky-Wenzel theorem is well below 1% except for one spot where both derivatives of the wake are zero and thus artifacts of the finite differences blow up the relative error.

The wake kicks [Eqs. (8)] are added to the kicks by the external laser field (cf. Eq. (23) in [20]). The prior implementation of DLAttrack6D runs in MATLAB [24]. For the presented extension, DLAttrack6D was migrated to PYTHON [25]. All convolutions are implemented as matrix multiplications, which makes the calculation fast and efficient, such that it can run on an ordinary PC.

III. STRUCTURES AND SCALING

Equipped with the simulation tools to calculate the wakefields and the resulting kicks we investigate an example of a relativistic DLA structure as shown in Fig. 1. It consists of two rows of pillars made of fused silica ($\epsilon_r = 2.13$) with a Bragg mirror on one side to symmetrize the external accelerating fields [26]. The vacuum gap as channel for the electrons between the two pillar rows has a width of $1.2 \mu\text{m}$. The period length equals the laser wavelength of $2 \mu\text{m}$, i.e. the structure is matched to $\beta = 1$. The dimensions of the pillars are optimized in terms of acceleration gradient and can be found in Appendix A.

If we change the geometric parameters of a structure, we have to repeat the expensive wakefield simulations for each parameter change. This effort can be significantly reduced by using scaling laws. If all dimensions of the grating structure are modified by a scaling factor α , i.e., $\bar{s} = \alpha s$, the Green's function wake per period scales as α^{-1} [27], i.e., $\bar{w}(\bar{s}) = \alpha^{-1} w(s)$. For a longitudinal bunch distribution, which is also scaled as $\tilde{\lambda}(\bar{s}) = \alpha^{-1} \lambda(s)$, the wake potential scales the same as the Green's function wake. This follows from the convolution

$$\bar{W}(\bar{s}) = \int_{-\infty}^{\infty} \tilde{\lambda}(\bar{s} - \hat{s}) \bar{w}(\hat{s}) d\hat{s} \quad (12a)$$

$$= \alpha^{-1} \int_{-\infty}^{\infty} \lambda(s - \hat{s}) w(\hat{s}) d\hat{s} \quad (12b)$$

$$= \alpha^{-1} W(s). \quad (12c)$$

Scaling the period length of a grating structure and the laser wavelength for $\beta \approx 1$ is almost equivalent to modifying all dimensions since a change in period length causes a change in acceptable bunch length for coherent acceleration and also a change in the decay length of the evanescent fields in the channel. We will use this to scale the wakefields of DLA experiments performed at $\lambda_0 = 800 \text{ nm}$ to the same structure at $\lambda_0 = 2 \mu\text{m}$, i.e., $\alpha^{-1} = 2.5$. The loss factor is defined as

$$k_{\text{loss}} = \int_{-\infty}^{\infty} \int_{-\infty}^{\infty} \int_{-\infty}^{\infty} W_s(x, y, s) \lambda(x, y, s) dx dy ds. \quad (13)$$

An increase of the gap width lowers the wakefield and thus the loss factor significantly. However, the acceleration gradient expressed by the first Fourier coefficient e_1 of the external field \underline{E}_z in the center of the gap [20],

$$e_1 = \frac{1}{\beta_{\text{ref}} \lambda_0} \int_{-\beta_{\text{ref}} \lambda_0/2}^{\beta_{\text{ref}} \lambda_0/2} E_z(z) e^{i \frac{2\pi z}{\beta_{\text{ref}} \lambda_0}} dz, \quad (14)$$

also decreases with the gap width. Figure 4 shows the loss factor indicating the strength of wake effects in comparison to $|e_1|$ for the grating described previously as function of the gap width. The plateau in the first Fourier coefficient represents a robust optimum for the vacuum gap in the range of the previously chosen value of $1.2 \mu\text{m}$. Values, that fulfill a Bragg condition are resonant, as e.g. at a gap of $0.6 \mu\text{m}$. Thus, they are not robust and also impede the use of short laser pulses due to the limited bandwidth.

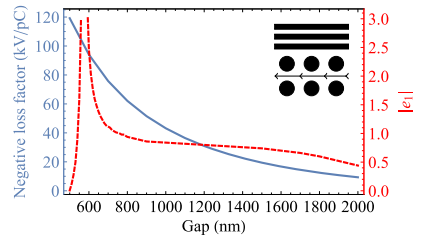


FIG. 4. Loss factor indicating the strength of wake effects as function of the vacuum gap compared to the absolute value of the first Fourier coefficient indicating the accelerating gradient in the center of a fused silica dual pillar structure with $2 \mu\text{m}$ period length for a given external field strength.

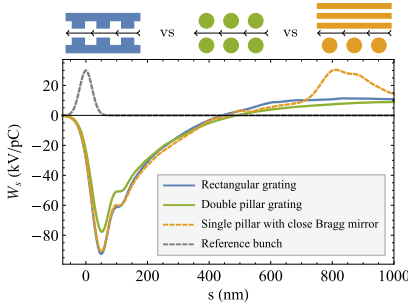


FIG. 5. Longitudinal wake per grating period of a Gaussian bunch distribution passing on-axis through a dual-layer rectangular grating structure (blue), a dual pillar structure (green) and a single-row pillar structure, where the second row is replaced by a Bragg mirror (yellow). The reference bunch distribution is shown in dashed gray.

In contrast to geometrical changes, modifications in the relative permittivity only slightly affect the loss factor, since it constitutes an average over a large frequency band. The narrow-band external laser drive, however, is very sensitive to material changes, which in turn requires geometrical optimization.

Recent experiments use different dual-layer rectangular grating structures [5,28]. If we optimize the teeth of a fused-silica dual-layer rectangular grating with the same vacuum gap as the analyzed dual pillar structure in terms of acceleration gradient, we reach a gradient 40% lower than for the dual pillar structure. The dimensions of the optimized structure are given in Appendix A. Figure 5

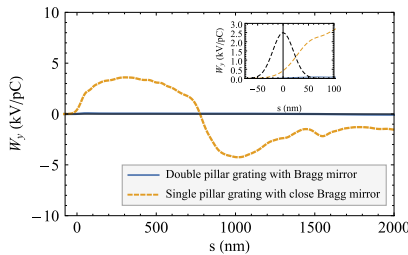


FIG. 6. Transverse wake per grating period of a Gaussian bunch distribution passing a dual pillar structure with a Bragg mirror (blue) and a single-row pillar structure, where the second row is replaced by a Bragg mirror (yellow) on-axis. The inset shows an enlargement of the short-range wake and the reference bunch distribution in black.

compares the short range longitudinal wake of both grating structures for a Gaussian shaped line charge, where good agreement between the curve shapes is visible. However, in contrast to the acceleration gradient, the wake of the dual pillar structure is slightly weaker. Furthermore, an additional Bragg mirror breaks the symmetry of the grating structure. If the distance of the Bragg mirror is much larger than the vacuum gap, it does not affect the short-range wake and can thus have only multibunch effects. If the Bragg mirror is located near to the vacuum gap or one pillar row is even replaced by the Bragg mirror, it affects also the short-range wake. In this case, the short-range wake is almost equal to the rectangular grating but additional effects in the long-range wake occur. Breaking the symmetry generates especially a nonvanishing transverse wake deflecting an on-axis bunch (cf. Fig. 6).

IV. TRANSVERSE WAKE EFFECTS

A. Previous estimations

In [29] we have calculated the wakefields and the beam loading limit for the dual pillar structure described previously. The tracking results of a transversely small bunch verify these results in the range of a few femtocoulombs. However we have also shown that the wake of bunches which fill the whole aperture of the structure depends strongly on the transverse position of each source particle. That has created the demand to add 3D wakefields to DLAttrack6D in order to analyze transverse instabilities.

B. Beam breakup

Caused by the potential at constant synchronous phase, the particles in a bunch undergo synchrotron motion. The synchrotron frequency is [28]

$$\Omega_s = \sqrt{\frac{-2\pi eG \sin(\phi_s)}{\lambda_0 \beta^3 \gamma^3 m_e}}, \quad (15)$$

where G is the accelerating peak gradient, ϕ_s the synchronous phase, λ_0 the laser wavelength, β and γ the relativistic factors and m_e the electron rest mass. Consider parameters achievable at the DLA experiment at SwissFEL [30,31], i.e. a 3 GeV electron beam accelerated with a peak gradient of $G = 1 \text{ GeV m}^{-1}$ and a synchronous phase $\phi_s = 135^\circ$, the synchrotron frequency is $\Omega_s \approx 43.9 \times 10^6 \text{ s}^{-1}$. The synchrotron period is thus $\lambda_s \approx 42.87 \text{ m}$. On the other hand, the DLA grating is outlined to be only up to 1.5 mm long. Thus the synchrotron motion can be considered frozen within the DLA grating. Using the APF-scheme to confine the beam, the frequencies of longitudinal motion and transverse betatron motion are equal by construction [9]. This distinguishes a DLA from conventional high energy linacs and also from synchrotrons, where the transverse betatron frequency is significantly larger than the

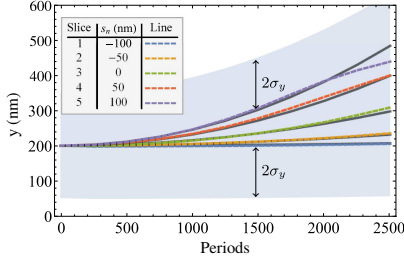


FIG. 7. Comparison of slice center of mass for a tracked bunch divided into five slices (dashed lines) with the analytical description (black solid lines). The gray area shows the 2σ distance to the minimum and maximum curve. The aperture of the dual pillar structure with $2\ \mu\text{m}$ period length is at $y = 600\ \text{nm}$.

longitudinal synchrotron frequency. Consequently, the betatron motion can also be considered frozen in the 1.5 mm long DLA grating. However, transverse wakes can cause particle loss by defocusing or deflection. This can be described analytically by dividing the bunch distribution $\lambda(s)$ in N slices with a center at s_n and a width Δs . For a given initial offset \hat{y}_0 of the whole bunch, a deflecting force acts on each slice given by

$$y_n'' = \frac{q_e q_{\text{bunch}}}{p_{z0} \beta_{\text{ref}} c_0 \lambda_z} W_y(s_n, \hat{y}_0). \quad (16)$$

The n th slice has an offset of

$$y_n(z) = \hat{y}_0 + \frac{q_e q_{\text{bunch}}}{2 p_{z0} \beta_{\text{ref}} c_0 \lambda_z} W_y(s_n, \hat{y}_0) z^2 \quad (17)$$

with the longitudinal position z of the bunch. This is equal to Chao's two-particle model [32] in the limit $k_\beta z = 2\pi z/\lambda_\beta = 2\pi z/\lambda_s \ll 1$. Figure 7 shows the tracking results of a 16 fC Gaussian bunch with $\sigma_s = 50\ \text{nm}$ and $\sigma_y = \sigma_x = 75\ \text{nm}$ injected with an offset of 200 nm and the corresponding analytical solutions given by Eq. (17) which fit quite well. For this, the bunch is divided into five slices and each is plotted separately. As long as the bunch (pictured by the width of two standard deviations as gray area in the plot) is within the aperture, in this example up to about 4.72 mm (2360 periods) grating length, the analytical description indicates negligible particle loss. This maximal interaction length is proportional to $\sqrt{p_{z0} \beta_{\text{ref}} / q_{\text{bunch}}}$. However, particle loss starts earlier as visible in the decreasing slope of the maximum tracked curve in Fig. 7. This is caused by an increasing standard deviation of the bunch distribution due to defocusing of the macroparticle slices which is not included in the analytical description. Figure 8

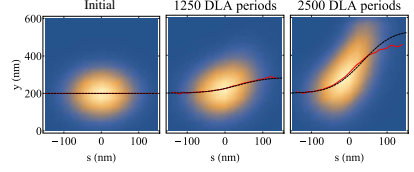


FIG. 8. Initial bunch distribution and bunch distribution after 1250 and 2500 DLA grating periods. The red curves show the means of transverse slices in comparison to the analytical estimates (black curves).

shows the initial and resulting bunch distributions after 1250 and 2500 DLA grating periods. If the transverse width of a bunch is small compared to the aperture, the analytical description gives a good estimate for the transverse deflection of the bunch tail. However, if the bunch fills most of the aperture, tracking covers also the effect of the incoherent wake defocusing forces.

To reduce the deflection and defocusing particle loss, one knob would be to avoid an injection offset as good as possible. However, this is technically difficult to ensure and helps only in symmetric structures. Generally, mitigation can only be obtained by reduced bunch charge, geometrical wake optimization, or simply by a more stiff beam at higher energy.

C. Strong head-tail instability

Considering a lower energy beam, for example a 6.5 MeV beam accelerated with a gradient of $0.56\ \text{GeV m}^{-1}$ corresponding to the experimental parameters at PEGASUS [33], the synchrotron period length is in the range of a few millimeters, i.e., in the same order of magnitude as the interaction length or below. Therefore, we have to take the longitudinal and transverse motion into account. For a validation of the tracking results including wake effects, we adapt the analytical description of the strong head-tail instability, in particular Chao's two-particle model for synchrotrons [32], to these assumptions (see Appendix B 1). In smooth approximation, the stability criterion given by the two-particle model is [cf. Eq. (B11)]

$$\frac{q_e q_{\text{bunch}}}{p_{z0} \beta_{\text{ref}} c_0 \lambda_z \hat{y}_0} W_y(\sigma_s, \hat{y}_0) \leq \frac{16\pi}{L_\beta} \quad (18)$$

with the betatron period length L_β and assuming a wake which depends linearly on the transverse offset. The betatron period length is $L_\beta = 2\pi L/\mu$, where L is the length of an APF FD-cell and

$$\mu = \arccos \left[\cos \left(\frac{k_\beta L}{2} \right) \cosh \left(\frac{k_\beta L}{2} \right) \right] \quad (19)$$

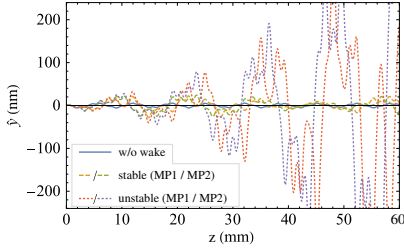


FIG. 9. Two-particle model using the APF transfer matrices with the wake of a dual pillar APF grating with 0.8 μm period length. The y -offsets of both macroparticles (MP1 and MP2) are plotted respectively. The initial excitation without wake is shown for comparison (blue).

is the corresponding phase advance per APF cell [9]. Note that the betatron wave number k_β scaled with the square root of the accelerating gradient. For the PEGASUS parameters with a gradient of 0.56 GeV m^{-1} [33], a FD-cell length of 1808 DLA periods (1.44 mm) with the structure in Fig. 1 scaled to a laser wavelength of 0.8 μm and a bunch length of 20 nm, the maximal bunch charge is about 0.3 fC. According to the APF design procedure in [9], the FD-cell length is chosen such that the maximal beta function (without wake) is minimized. Following Eq. (18), a further minimization of the betatron period length would increase the maximal bunch charge. It would, however, increase the maximal beta function at the same time and thus decrease the initial acceptance.

Using the smooth approximation, the coherent oscillation of a transversely stable bunch in y has a sinusoidal envelope whereas the oscillation amplitude of an unstable bunch grows exponentially. In comparison, Fig. 9 shows the y -offset of the macroparticles calculated with the

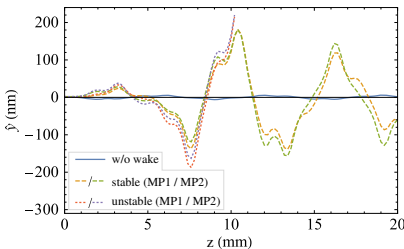


FIG. 10. Bunch distribution divided in two halves (MP1 and MP2) and tracked through a dual pillar APF grating with a 0.8 μm period length. The betatron motion without wake is shown for comparison (blue).

full APF transfer matrices given in Eqs. (B7) and (B13). The alternating sign of the focusing function reduces the stability threshold in this numerical example and for the analyzed interaction length roughly by half. The full tracking results shown in Fig. 10 confirm these semi-analytical estimates. Thus, the two-particle model in smooth approximation can be seen as an upper limit for the estimation of the stability threshold. The more precise limit for a given APF grating with given interaction length is, however, smaller and can be estimated numerically using the presented tracking scheme.

D. Acceleration

So far, we have not considered coherent acceleration of a bunch. A linear energy gain $\gamma(z) = \gamma_0(1 + G \cos \phi_s / (m_e c_0^2) z)$ is usually provided for an ultrarelativistic accelerator design, i.e., peak acceleration gradient G and synchronous phase ϕ_s are constant. The focusing strength decreases proportional to $\gamma^{-3/2}(z)$ [9] as compared to $\gamma^{-1/2}$ for a magnetic quadrupole lattice. To keep the phase advance per APF-cell constant, the length of the cell needs to be increased accordingly. This is equivalent to keeping the maximal beta function minimal, as was described in [9].

The corresponding equations of motion for the two-particle model are solved in Appendix B 2 and the solutions are compared to Chao's two-particle model of a conventional linac. In Chao's model, the magnetic focusing strength is increased proportionally to the bunch energy to get a constant betatron wave number [32]. Increasing the focusing strength in an APF lattice is only possible at the price of increasing the laser field strength limited by material damage or playing with the synchronous phase. The adiabatic damping is being counteracted by the increase in the beta function due to reduced focusing strength and thus a coherent offset of a bunch already increases without deflection by the wake [cf. Eq. (B18)]. Therefore, the adiabatic damping of an initial coherent offset in a conventional linac which leads to a prediction of an increased stability threshold [34] does not help for DLA. Instead, the stability threshold is decreased compared to an APF transport channel.

We confirmed that by tracking simulations, which are stable in the simulated interaction length in the case of transport and unstable for an accelerated bunch. For an acceleration from 6.5 MeV up to 17 MeV, the numerical simulations show a reduction of the threshold roughly by half as compared to an APF transport channel at constant energy.

E. Analysis of the phase advance

The nonlinear spatial dependence of the fields in the dielectric grating leads to a phase advance depending on the particle's amplitude ("tune-spread"). The linear phase advance ("set-tune") is given analytically by Eq. (19).

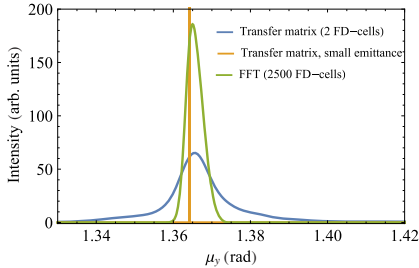


FIG. 11. Transverse phase advance for a negligible emittance in complete agreement with the analytical $\mu_y = 1.3642$ and a distribution with 20 nm bunch length and 100 nm transverse size. The latter is obtained by both FFT and the transfer matrix reconstruction method. The narrowing of the FFT curve originates from high amplitude particle losses over the long (2500 cells) transport distance.

Numerically, the phase advance can be determined by reconstructing the transfer matrix of a FD-cell from the tracking result for each particle using the transfer matrix reconstruction algorithm presented in [35]. Figure 11 shows the distributions of the transverse phase advance for a particle distribution with negligible emittance, which exactly confirms the analytical value $\mu_y = 1.3642$, and a realistic emittance, where the distribution shows the expected broadening. Note that we calculate only two-dimensional transfer matrices neglecting coupling between planes. Therefore, we require only two subsequent FD-cells for the transfer matrix calculations. Calculating the phase advance by a fast Fourier transform (FFT) of particle tracking data along 2500 FD-cells yields the same mean value of the phase advance spectrum. Such a large number of FD-cells is required to achieve a sufficient resolution in the spectrum. However, one has to account for the enhanced particle losses during this long timescale. In particular, particles with large amplitudes have a large tune deviation and are likely to be lost, which leads to a narrowing of the spectrum.

Physically, the spread is explained as follows: A larger longitudinal emittance leads to a weaker focusing and thus to a spread toward smaller phase advances. A larger transverse emittance, on the other hand, leads to a stronger focusing and thus to a spread toward larger phase advances.

Furthermore, the calculation of the phase advance as trace of the transfer matrix allows a moving window approach to obtain a tune-spectrogram, in order to analyze the temporal variation of the phase advance, e.g. in case of acceleration. As described in Sec. IV D, the length of a FD-cell varies over the structure length to keep the phase advance per FD-cell constant and thus the beam envelope bounded. The left plot in Fig. 12 shows the spectrum of the

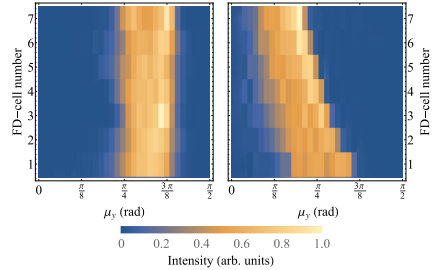


FIG. 12. Spectrograms of the transverse phase advance for a particle distribution accelerated in a dual pillar APF structure with 0.8 μm period length. Increasing the FD-cell length along the structure in accordance to the increasing energy keeps the phase advance distribution almost constant (left). A constant FD-cell length, however, leads to a decreasing phase advance (right).

transverse phase advance for an accelerator design with increasing FD-cell length such that the designed linear phase advance on the acceleration ramp remains constant. The right plot shows the spectrum for a constant FD-cell length, where the phase advance decreases over time. The width of the distributions is composed of both the intrinsic width of the particle distribution and the numerical error that results from the calculation of the transfer matrix using two subsequent FD-cells, which are only approximately but not exactly identical.

F. Damping mechanisms

The upper bunch charge limit due to longitudinal wake effects of the analyzed structure is in the range of a few femtocoulombs [29], where the beam loading cancels the laser field with 1 GeV acceleration gradient completely. As the stability criterion of the strong head-tail instability, however, is below a femtocoulomb for the same peak gradient, the bunch intensity is thus limited by the transverse effects. To raise the limits, a damping mechanism is required.

BNS-damping [36] as routinely used in relativistic rf linacs is not applicable, as it requires a chirp in phase advance depending on the longitudinal position of the particles within the bunch. Due to the longitudinal motion in APF, the particle positions change continuously and a constant chirp in phase advance as function of longitudinal coordinate cannot be achieved.

Another stabilizing mechanism is based on phase mixing [37], i.e., the incoherent betatron frequencies spread could possibly stabilize the bunch against the strong head-tail instability. Thus, the bunch charge limit given by Eq. (18) is increased at larger emittances. In order to confirm that, tracking simulations through a 5 cm long dual pillar APF

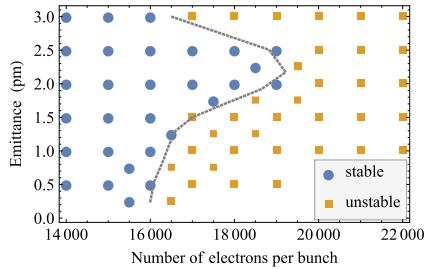


FIG. 13. Stability diagram of bunch distribution with varying transverse geometric emittance and bunch charge passing through a dual pillar APF structure with $0.8 \mu\text{m}$ period length. The energy of the particles is 6.5 MeV . Simulation settings with stable behavior are colored yellow and settings with unstable behavior are colored blue. The dotted line displays the interpolated limit between stable and unstable settings.

grating with varying initial transverse emittances are performed. The matched Gaussian bunch distribution has an initial longitudinal length of 20 nm , a constant width of 400 nm in x -direction, and a particle energy of 6.5 MeV . The FD-cell length is chosen so that the maximum of the Twiss beta parameter is minimal, i.e., $\hat{\beta}_{y,\text{max}} = 0.69 \text{ mm}$, and the assumed peak acceleration gradient is 5 GeV m^{-1} . The stable and unstable distributions as functions of the transverse emittance and bunch charge are shown in Fig. 13. In the limit of zero transverse emittance the limit of stability is already larger than described by the analytical stability criterion in Eq. (18) ($q_{\text{bunch,max}} \approx 1.8 \text{ fC}$), since stabilization is already provided by the finite longitudinal emittance. Moreover, the nonzero width in the x -direction weakens the wake. For increasing transverse emittance, the stability limit is shifted to higher bunch charges, which indicates a stabilization by phase mixing is really present here. Due to the finite aperture of the grating, a further increase of the emittance leads to particle loss before the stabilization by phase mixing can be efficacious. Stable beam transport with larger charge and larger emittance is, however, possible with an increased aperture. This reduces on the other hand again the acceleration gradient, or requires more laser power, which is however limited by the material damage threshold.

V. CONCLUSION

We have successfully integrated wake kicks in our DLA particle tracker DLAtack6D and presented for the first time tracking results with wakefields in nanophotonic electron acceleration structures. The wake functions themselves originate from electromagnetic simulations by the CST Particle Studio wakefield solver. When excited by a

sufficiently short bunch, the obtained wake potential is a good approximation of the Green's function wake. We showed, that scaling laws can be applied to vary geometric parameters of the dielectric grating structures without complete recalculation of the wake.

The tracking results showed, that transverse wake effects limit the bunch charge stronger than longitudinal effects. In the simulated example at 6.5 MeV , the strong head-tail instability limits the bunch charge of an almost round Gaussian bunch for stable beam transport to a few femtocoulomb for a reasonable peak gradient. At higher energies, 3 GeV in the example, the synchrotron motion is too slow to have any stabilizing effect. The transverse wake deflects a noncentered bunch and the length before it hits the wall can be calculated upon the wake and the bunch charge. In both regimes (with or without longitudinal motion), the description of the transverse effects by analytical models, in particular by Chao's two-particle model, was confirmed by tracking simulations.

We also calculated the spread in phase advance of a particle distribution moving through an APF DLA grating and numerically showed that phase mixing stabilizes the bunch in a DLA against transverse wake instabilities. Increasing the bunch charge further is only possible if the structure geometry is changed to make room for a larger emittance or if the focusing strength is increased.

An increase of the vacuum gap would lower the wake-field but also the acceleration gradient. A more significant reduction of the wake would be the increase of the grating period length to the wavelength of CO lasers [38], that is $10 \mu\text{m}$, or to the Terahertz range [39], where however the availability of efficient power sources represents the bottleneck.

In case of acceleration, the adiabatic damping of a coherent offset in a conventional rf linac with a magnetic focusing lattice increases the stability threshold of transverse instabilities. We showed that in an APF DLA adiabatic damping is counteracted by an increasing beta function and a coherent offset increases. Thus, the stability threshold decreases for acceleration compared to a pure guiding structure.

So far, we have not considered the particle motion in the x -direction which is assumed to be invariant in most DLA gratings. The transverse quadrupole wake leads to a focusing force in this direction depending on the width of the bunch. This has to be analyzed in more detail in the future, where also possible confinement methods in this direction have to be taken into account.

ACKNOWLEDGMENTS

This work is funded by the Gordon and Betty Moore Foundation (Grant No. GBMF4744) and the German Federal Ministry of Education and Research (Grant No. FKZ: 05K16RDB).

APPENDIX A: STRUCTURE DIMENSIONS

The dimensions of the analyzed DLA structures made of fused silica are optimized for highest gradient at given incoming laser peak field. Fixed dimensions are the vacuum gap and the period length, optimization parameters are the pillar dimensions for the dual pillar structure and the tooth dimensions for the dual-layer rectangular grating structure. If a Bragg mirror is used, the distance between

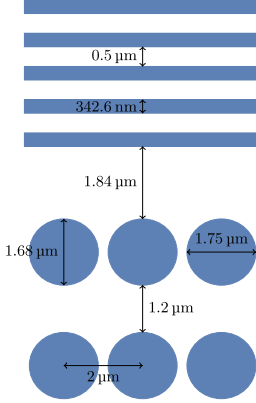


FIG. 14. Dimensions of the dual pillar structure. The structure is made of fused silica ($\epsilon_r = 2.13$).

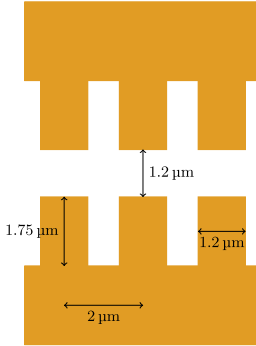


FIG. 15. Dimensions of the dual-layer rectangular grating structure. The structure is made of fused silica ($\epsilon_r = 2.13$) and the height of the substrate is much larger than the period length to avoid effects of a defined substrate thickness on the short-range wake.

the pillars and the first layer is an additional optimization parameter, the layer thickness and the distance between the layers are, however, given by the relative permittivity of the dielectric. The dimensions of the optimized structures are summarized in Figs 14 and 15. For wakefield studies with a laser wavelength of 800 nm, the dimensions of the dual pillar structure are scaled by a factor of 0.4.

APPENDIX B: TWO-PARTICLE MODEL

1. Beam transport

The strong head-tail instability for a bunch passing a circular accelerator is analytically described by Chao's two-particle model [32]. The simplified model in smooth approximation consider a bunch which is made of two macroparticles executing synchrotron oscillations with equal amplitude but opposite phase. During the first half of the synchrotron period, the leading particle has the index 1, the trailing particle the index 2. Chao's derivation assumes that the synchrotron frequency is much smaller than the transverse betatron frequency. According to the APF scheme [9], both frequencies are indeed the same and we adapt the model in the following.

The equations of motion for the two macroparticles in a focusing lattice are

$$y_1'' + k_\beta^2 y_1 = 0 \quad (\text{B1a})$$

$$y_2'' + k_\beta^2 y_2 = C_W y_1, \quad (\text{B1b})$$

with

$$C_W = \frac{qq_{\text{bunch}}}{p_{z0}\beta_{\text{ref}}c_0\lambda_0} W_y', \quad (\text{B2})$$

the betatron wave number k_β , the particle charge q , the bunch charge q_{bunch} , the reference momentum of the bunch p_{z0} , the reference velocity β_{ref} , the speed of light c_0 , the laser wavelength λ_0 and the slope $W_y' = \partial W_y / \partial y$ of the transverse wake per grating cell. We assume the wake is a constant longitudinally and linear in the transverse offset. A solution of Eq. (B1a) for the leading particle is the unperturbed (betatron) oscillation

$$y_1(z) = y_1(0) \cos(k_\beta z) + \frac{y_1'(0)}{k_\beta} \sin(k_\beta z). \quad (\text{B3})$$

The solution of Eq. (B1b) for the trailing particle is

$$y_2(z) = \cos(k_\beta z) \left(y_2(0) - \frac{y_1'(0)}{2k_\beta^2} C_W z \right) + \sin(k_\beta z) \left(\frac{y_2'(0)}{k_\beta} + \frac{y_1'(0)}{2k_\beta^3} C_W + \frac{y_1(0)}{2k_\beta} C_W z \right). \quad (\text{B4})$$

The first terms in the brackets describe the unperturbed (betatron) oscillation of the trailing particle and the second

terms, growing linearly with z , describe the perturbation by the wake. The solutions (B3) and (B4) can be combined to a matrix form

$$\begin{pmatrix} y_1 \\ y_1' \\ y_2 \\ y_2' \end{pmatrix} = \begin{pmatrix} M_\beta^f(z) & 0 \\ M_W^f(z) & M_\beta^f(z) \end{pmatrix} \begin{pmatrix} y_1 \\ y_1' \\ y_2 \\ y_2' \end{pmatrix}_{z=0}, \quad (\text{B5})$$

where the entries in the matrix are themselves 2×2 matrices given by

$$M_\beta^f(z) = \begin{pmatrix} \cos(k_\beta z) & \frac{1}{k_\beta} \sin(k_\beta z) \\ -k_\beta \sin(k_\beta z) & \cos(k_\beta z) \end{pmatrix} \quad (\text{B6})$$

and

$$M_W^f(z) = \begin{pmatrix} \frac{C_W}{2k_\beta} z \sin(k_\beta z) & \frac{C_W}{2k_\beta^3} \sin(k_\beta z) - \frac{C_W}{2k_\beta^2} z \cos(k_\beta z) \\ \frac{C_W}{2k_\beta} \sin(k_\beta z) + \frac{C_W}{2} z \cos(k_\beta z) & \frac{C_W}{2k_\beta} z \sin(k_\beta z) \end{pmatrix}. \quad (\text{B7})$$

Evaluating Eqs. (B6) and (B7) after half a longitudinal oscillation period and taking into account that the longitudinal oscillation period equals the transverse betatron period, the transfer matrices become

$$M_\beta^f\left(\frac{L_\beta}{2}\right) = \begin{pmatrix} -1 & 0 \\ 0 & -1 \end{pmatrix} \quad (\text{B8})$$

and

$$M_W^f\left(\frac{L_\beta}{2}\right) = \begin{pmatrix} 0 & \frac{C_W L_\beta^3}{16\pi} \\ -\frac{C_W}{4} L_\beta & 0 \end{pmatrix}. \quad (\text{B9})$$

The results for the second half oscillation period where the particles change their position can be obtained by exchanging the indices in Eq. (B5). The transfer matrix of a full oscillation period is then given by

$$\begin{pmatrix} y_1 \\ y_1' \\ y_2 \\ y_2' \end{pmatrix}_{z=L_\beta} = \begin{pmatrix} 1 + M_W^f\left(\frac{L_\beta}{2}\right)^2 & M_W^f\left(\frac{L_\beta}{2}\right) \\ M_W^f\left(\frac{L_\beta}{2}\right) & 1 \end{pmatrix} \begin{pmatrix} y_1 \\ y_1' \\ y_2 \\ y_2' \end{pmatrix}_{z=0}. \quad (\text{B10})$$

We can now eigenanalyze the resulting transfer matrix according to Chao's stability analysis. Stability requires that for all solutions of the eigenvalues λ the function $\lambda + 1/\lambda$ is real and its value is between -2 and 2. This gives the stability criterion

$$C_W \leq \frac{16\pi}{L_\beta^3}, \quad (\text{B11})$$

which can be used as an estimation for the maximum bunch charge in an APF grating (cf. Sec. IV C and Fig. 16).

Calculating the full APF transfer matrices without the smooth approximation requires also knowledge of the transfer matrices for the defocusing sections in an APF grating. The equations of motion in these sections are equal to the Eqs. (B1) except that the sign changes. This results in exchanging the trigonometric functions in Eqs. (B6) and (B7) by hyperbolic functions which yields

$$M_\beta^d(z) = \begin{pmatrix} \cosh(k_\beta z) & \frac{1}{k_\beta} \sinh(k_\beta z) \\ k_\beta \sinh(k_\beta z) & \cosh(k_\beta z) \end{pmatrix} \quad (\text{B12})$$

and

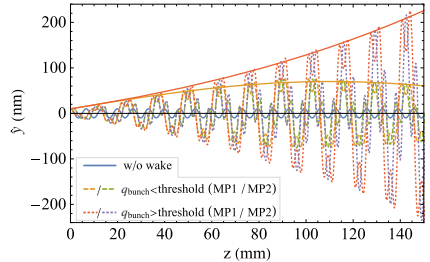


FIG. 16. Two-particle model in smooth approximation. For a small initial offset, a transversely stable bunch has a sinusoidal envelope (yellow line) and an unstable bunch has an exponentially growing amplitude (red line). The y -offsets of both macro-particles (MP1 and MP2) are plotted respectively. The initial excitation without wake is shown for comparison (blue).

$$M_W^d(z) = \begin{pmatrix} \frac{C_w}{2k_\beta} z \sinh(k_\beta z) & \frac{C_w}{2k_\beta} z \cosh(k_\beta z) - \frac{C_w}{2k_\beta} \sinh(k_\beta z) \\ \frac{C_w}{2k_\beta} \sinh(k_\beta z) + \frac{C_w}{2} z \cosh(k_\beta z) & \frac{C_w}{2k_\beta} z \sinh(k_\beta z) \end{pmatrix}. \quad (\text{B13})$$

Tracking with these transfer matrices describes the stability behavior significantly better than with the smooth approximation (cf. Sec. IV C and Fig. 9). Calculating an analytical stability threshold as in Eq. (B11) is, however, not possible.

2. Acceleration

Considering coherent acceleration of a bunch the bunch energy is a function of time, thus equivalently of the longitudinal position in the grating. Using again a two-particle model, the transverse equations of motion for the two macroparticles are given by

$$\frac{d}{dz} \left(\gamma(z) \frac{dy_1}{dz} \right) + \gamma(z) k_\beta(z)^2 y_1 = 0 \quad (\text{B14a})$$

$$\frac{d}{dz} \left(\gamma(z) \frac{dy_2}{dz} \right) + \gamma(z) k_\beta(z)^2 y_2 = \gamma(z) C_w(z) y_1, \quad (\text{B14b})$$

where the Lorentz factor $\gamma(z)$ and thus also the wake term on the right-hand side are functions of the longitudinal position z . For a constant phase advance per FD-cell, the FD-cell length has to be proportional to $\gamma^{3/2}$ according to the energy dependence of the focusing strength. This means

$$k_\beta(z) = \frac{k_{\beta,0}}{\gamma(z)^{3/2}} \gamma_0^{3/2}. \quad (\text{B15})$$

If we consider a linear energy gain $\gamma(z) = \gamma_0(1 + G \cos \phi_s / (m_e c_0^2) z)$ and apply the transformation $u = 1 + \alpha z$ with $\alpha = G \cos \phi_s / (m_e c_0^2)$, the equations of motion become

$$\frac{d^2 y_1}{du^2} + \frac{1}{u} \frac{dy_1}{du} + \frac{k_y^2}{u^3} y_1 = 0 \quad (\text{B16a})$$

$$\frac{d^2 y_2}{du^2} + \frac{1}{u} \frac{dy_2}{du} + \frac{k_y^2}{u^3} y_2 = \frac{C_{w,0}}{\alpha^2 u} y_1, \quad (\text{B16b})$$

with $k_y = k_{\beta,0}/\alpha$. A solution of Eq. (B16a) is

$$y_1(u) = c_1 J_0 \left(\frac{2k_y}{\sqrt{u}} \right) + c_2 N_0 \left(\frac{2k_y}{\sqrt{u}} \right), \quad (\text{B17})$$

where $J_0(x)$ and $N_0(x)$ are Bessel and Neumann functions. Using the asymptotic expressions and the initial conditions $y_1(u=1) = y_0$ and $y_1'(u=1) = y_0'$, the solution of the first macroparticle becomes

$$y_1(u) = \sqrt[4]{u} \left[y_0 \cos \left(2k_y \left(1 - \frac{1}{\sqrt{u}} \right) \right) - \frac{\alpha y_0 - 4y_0'}{4\alpha k_y} \sin \left(2k_y \left(1 - \frac{1}{\sqrt{u}} \right) \right) \right]. \quad (\text{B18})$$

Equation (B18) shows that the betatron oscillations in a DLA grating are not damped adiabatically compared to a conventional magnetic focusing lattice. An increase of the stability threshold as described by Chao for the conventional magnetic focusing lattice can thus not be expected and numerical tracking simulations confirm this statement (cf. Sec. IV D). For the sake of completeness, Eq. (B16b) can be solved as

$$y_2(u) = y_1(u) + \frac{C_{w,0}}{\alpha^2} \int_1^u G(u, \bar{u}) y_1(\bar{u}) d\bar{u}, \quad (\text{B19})$$

where the Green's function is given by

$$G(u, \bar{u}) = -\pi \left[J_0 \left(\frac{2k_y}{\sqrt{\bar{u}}} \right) N_0 \left(\frac{2k_y}{\sqrt{u}} \right) - N_0 \left(\frac{2k_y}{\sqrt{\bar{u}}} \right) J_0 \left(\frac{2k_y}{\sqrt{u}} \right) \right] \quad (\text{B20a})$$

$$\approx \frac{\sqrt{u\bar{u}}}{k_y} \sin \left(2k_y \left(\frac{1}{\sqrt{u}} - \frac{1}{\sqrt{\bar{u}}} \right) \right). \quad (\text{B20b})$$

- [1] K. Shimoda, Proposal for an electron accelerator using an optical maser, *Appl. Optics* **1**, 33 (1962).
- [2] A. Lohmann, Electron acceleration by light waves, IBM Technical Note 5, 169 (1962).
- [3] E. A. Peralta *et al.*, Demonstration of electron acceleration in a laser-driven dielectric microstructure, *Nature (London)* **503**, 91 (2013).
- [4] K. P. Wootton, Z. Wu, B. M. Cowan, A. Hanuka, I. V. Makasyuk, E. A. Peralta, K. Soong, R. L. Byer, and R. J. England, Demonstration of acceleration of relativistic electrons at a dielectric microstructure using femtosecond laser pulses, *Opt. Lett.* **41**, 2696 (2016).
- [5] D. Cesar *et al.*, High-field nonlinear optical response and phase control in a dielectric laser accelerator, *Commun. Phys.* **1**, 46 (2018).
- [6] R. J. England *et al.*, Dielectric laser accelerators, *Rev. Mod. Phys.* **86**, 1337 (2014).
- [7] J. McNeur, M. Kozak, N. Schönenberger, A. Li, A. Tafel, and P. Hommelhoff, Laser-driven acceleration of subrelativistic electrons near a nanostructured dielectric

- grating: From acceleration via higher spatial harmonics to necessary elements of a dielectric accelerator, *Nucl. Instrum. Methods Phys. Res., Sect. A* **829**, 50 (2016).
- [8] U. Niedermayer *et al.*, Challenges in simulating beam dynamics of dielectric laser acceleration, *Int. J. Mod. Phys. A* **34**, 1942031 (2019).
- [9] U. Niedermayer, T. Egenolf, O. Boine-Frankenheim, and P. Hommelhoff, Alternating-Phase Focusing for Dielectric-Laser Acceleration, *Phys. Rev. Lett.* **121**, 214801 (2018).
- [10] L. Schächter, Energy recovery in an optical linear collider, *Phys. Rev. E* **70**, 016504 (2004).
- [11] R. H. Siemann, Energy efficiency of laser driven, structure based accelerators, *Phys. Rev. Accel. Beams* **7**, 061303 (2004).
- [12] A. Hanuka and L. Schächter, Bragg accelerator optimization, *High Power Laser Sci. Eng.* **2**, E24 (2014).
- [13] A. Hanuka and L. Schächter, Optimized operation of dielectric laser accelerators: Multi bunch, *Phys. Rev. Accel. Beams* **21**, 064402 (2018).
- [14] A. Hanuka and L. Schächter, Optimized operation of dielectric laser accelerators: Single bunch, *Phys. Rev. Accel. Beams* **21**, 054001 (2018).
- [15] A. Hanuka and L. Schächter, Operation regimes of a dielectric laser accelerator, *Nucl. Instrum. Methods Phys. Res., Sect. A* **888**, 147 (2018).
- [16] K. Bane, G. Stupakov, and I. Zagorodnov, Analytical formulas for short bunch wakes in a flat dechirper, *Phys. Rev. Accel. Beams* **19**, 084401 (2016).
- [17] A. Tremaine, J. Rosenzweig, and P. Schoessow, Electromagnetic wake fields and beam stability in slab-symmetric dielectric structures, *Phys. Rev. E* **56**, 7204 (1997).
- [18] D. Mihalcea, P. Piot, and P. Stoltz, Three-dimensional analysis of wakefields generated by flat electron beams in planar dielectric-loaded structures, *Phys. Rev. Accel. Beams* **15**, 081304 (2012).
- [19] P. D. Hoang, G. Andonian, I. Gadjev, B. Naranjo, Y. Sakai, N. Sudar, O. Williams, M. Fedurin, K. Kusche, C. Swinson, P. Zhang, and J. B. Rosenzweig, Experimental Characterization of Electron-Beam-Driven Wakefield Modes in a Dielectric-Woodpile Cartesian Symmetric Structure, *Phys. Rev. Lett.* **120**, 164801 (2018).
- [20] U. Niedermayer, T. Egenolf, and O. Boine-Frankenheim, Beam dynamics analysis of dielectric laser acceleration using a fast 6D tracking scheme, *Phys. Rev. Accel. Beams* **20**, 111302 (2017).
- [21] W. K. H. Panofsky and W. A. Wenzel, Some considerations concerning the transverse deflection of charged particles in radio-frequency fields, *Rev. Sci. Instrum.* **27**, 967 (1956).
- [22] Dassault Systemes Deutschland GmbH, CST Studio Suite 2019 (2019).
- [23] L. Palumbo, V. G. Vaccaro, and M. Zobov, Wake fields and impedance, *Proceedings of the CERN Accelerator School* (1994), pp. 331–390, <https://doi.org/10.5170/CERN-1995-006.331>.
- [24] MathWorks, MATLAB (2016).
- [25] PYTHON Software Foundation, PYTHON3.7 (2018).
- [26] P. Yousefi, N. Schönenberger, J. Meneur, M. Kozák, U. Niedermayer, and P. Hommelhoff, Dielectric laser electron acceleration in a dual pillar grating with a distributed Bragg reflector, *Opt. Lett.* **44**, 1520 (2019).
- [27] K. Bane, Wakefield effects in a linear collider, in *AIP Conf. Proc.* **153**, 971 (1987).
- [28] U. Niedermayer, O. Boine-Frankenheim, and T. Egenolf, Designing a dielectric laser accelerator on a chip, *J. Phys. Conf. Ser.* **874**, 012041 (2017).
- [29] T. Egenolf, U. Niedermayer, and O. Boine-Frankenheim, Intensity limits by wakefields in relativistic dielectric laser acceleration grating structures, in *Proc. of 2018 IEEE Advanced Accelerator Concepts Workshop, AAC 2018, Breckenridge, CO, USA* (2019), <https://doi.org/10.1109/AAC.2018.8659426>.
- [30] E. Prat *et al.*, Outline of a dielectric laser acceleration experiment at SwissFEL, *Nucl. Instrum. Methods Phys. Res., Sect. A* **865**, 87 (2017).
- [31] B. Hermann, S. Bettoni, T. Egenolf, U. Niedermayer, E. Prat, and R. Ischebeck, Laser-Driven Modulation of Electron Beams in a Dielectric Micro-Structure for X-Ray Free-Electron Lasers, *Sci. Rep.* **9**, 19773 (2019).
- [32] A. Chao, *Physics of Collective Beam Instabilities in High Energy Accelerators* (John Wiley & Sons, New York, 1993).
- [33] D. Cesar, J. Maxson, P. Musumeci, X. Shen, R. J. England, K. P. Wootton, and S. Tan, Enhanced energy gain in a dielectric laser accelerator using a tilted pulse front laser, *Opt. Express* **26**, 29216 (2018).
- [34] A. W. Chao, Coherent instabilities of a relativistic bunched beam, Stanford Linear Accelerator Center Report No. SLAC-PUB-2946, 1982.
- [35] A. Luccio and N. D’Imperio, Eigenvalues of the one-turn matrix, Brookhaven National Laboratory Technical Report No. C-A/AP#126, 2003.
- [36] V. E. Balakin, A. V. Novokhatsky, and V. P. Smirnov, VLEPP transverse beam dynamics, in *Proc. of the 12th Intern. Conf. on High-Energy Accelerators* (FERMILAB, Batavia, 1983), p. 119.
- [37] A. Hofmann, Landau damping, in *CAS—CERN Accelerator School: Intermediate Course on Accelerator Physics* (Zeuthen, Germany, 2006), pp. 271–304.
- [38] W. D. Kimura and I. V. Pogorelsky, CO₂-Laser-Driven Dielectric Laser Accelerator, in *Proc. of 2018 IEEE Advanced Accelerator Concepts Workshop, AAC 2018, Breckenridge, CO, USA* (2019), <https://doi.org/10.1109/AAC.2018.8659403>.
- [39] E. A. Nanni, W. R. Huang, K. H. Hong, K. Ravi, A. Fallahi, G. Moriena, R. J. D. Miller, and F. X. Kärtner, Terahertz-driven linear electron acceleration, *Nat. Commun.* **6**, 8486 (2015).

Three Dimensional Alternating-Phase Focusing for Dielectric-Laser Electron Accelerators

Uwe Niedermayer^{1*}, Thilo Egenolf¹, and Oliver Boine-Frankenheim^{1,2}

¹Technische Universität Darmstadt, Schlossgartenstrasse 8, D-64289 Darmstadt, Germany

²GSI Helmholtzzentrum für Schwerionenforschung GmbH, Planckstrasse 1, D-64291 Darmstadt, Germany

 (Received 11 April 2020; revised 21 August 2020; accepted 9 September 2020; published 13 October 2020)

The concept of dielectric-laser acceleration (DLA) provides the highest gradients among breakdown-limited (nonplasma) particle accelerators and thus the potential of miniaturization. The implementation of a fully scalable electron accelerator on a microchip by two-dimensional alternating phase focusing (APF), which relies on homogeneous laser fields and external magnetic focusing in the third direction, was recently proposed. In this Letter, we generalize the APF for DLA scheme to 3D, such that stable beam transport and acceleration is attained without any external equipment, while the structures can still be fabricated by entirely two-dimensional lithographic techniques. In the new scheme, we obtain significantly higher accelerating gradients at given incident laser field by additionally exploiting the new horizontal edge. This enables ultralow injection energies of about 2.5 keV ($\beta = 0.1$) and bulky high voltage equipment as used in previous DLA experiments can be omitted. DLAs have applications in ultrafast time-resolved electron microscopy and diffraction. Our findings are crucial for the miniaturization of the entire setup and pave the way towards integration of DLAs in optical fiber driven endoscopes, e.g., for medical purposes.

DOI: 10.1103/PhysRevLett.125.164801

Dielectric laser acceleration (DLA) was already proposed in 1962 [1,2], however, first experiments came 50 years later [3,4] by means of femtosecond laser pulses and lithographic nanofabrication. Recent advances in ultrashort laser pulses have enabled demonstrations of damage-threshold and self-phase modulation limited record peak gradients approaching the GeV/m milestone for relativistic electrons [5,6]. At subrelativistic energies, driven by a tabletop electrostatic preaccelerator, peak gradients of 133 [7] and 370 MeV/m [8] were achieved in silicon pillar structures. In order to create a functioning accelerator out of these impressive gradients, the interaction length needs to be increased while maintaining a stable 6D phase space confinement. Such a miniaturized accelerator has applications in attosecond science [9,10], ultrafast electron microscopy and diffraction (UEM/UED) [11–15], lithography [16], and it would be possible to provide relativistic electrons within (e.g., medical) endoscopes [17].

First approaches to beam dynamics in grating linacs were already made in the 1980s [18–20]. In 2012, Naranjo *et al.* [21] showed that the nonsynchronous spatial (sub)harmonics can provide a ponderomotive focusing force, which was later turned into an accelerator design for medium energy [22].

Our approach starts from showing that a periodic grating provides phase dependent forces which can be concentrated in one kick per grating cell [23]. Per Panofsky-Wenzel theorem [24], this three-dimensional kick is irrotational, and can thus be modeled as a (time-dependent) potential in the Hamiltonian. Removing the time dependence is achieved by lattice integration of the linearized fields according to the Courant-Snyder (CS) theory [25]. An accelerator lattice design providing stable motion in the longitudinal and one transverse direction is obtained by an alternating phase focusing (APF) arrangement of grating segments treated as thick lenses [26]. Full scalability of the APF DLA is achieved by using a pulse-front-tilted laser [27–29] or an on-chip photonic waveguide system [30], which in principle allows us to work with arbitrary short pulses.

The equivalent magnetic focusing strength of an individual APF segment was predicted [26] and experimentally demonstrated to be in the MT/m range [31]. Moreover, the energy modulation of a subrelativistic DLA can also be turned into ballistic bunching [10,32–34]; however, the hereby created energy spread is too large to inject into a scalable APF DLA accelerator. A proposed APF-based segmented buncher [26] solves this problem and is currently being experimentally tested. Another ongoing experiment is the demonstration of a periodically segmented APF transport channel [35], which is however limited in length by the Rayleigh range of the electron beam in the invariant direction. In [26], we proposed to overcome this limit by installing an external quadrupole magnet which constantly focuses the beam in the vertical

Published by the American Physical Society under the terms of the Creative Commons Attribution 4.0 International license. Further distribution of this work must maintain attribution to the author(s) and the published article's title, journal citation, and DOI.

direction. A major challenge in the experimental realization of a fully scalable APF DLA is the alignment of this external magnet and the sufficient homogeneity of the laser fields in the invariant vertical direction of the structure.

In this Letter, we generalize the APF-based confinement to both transverse directions. This enables to completely eliminate external focusing devices in scalable DLAs of arbitrary length. Moreover, since the additional dimension provides an additional edge, the accelerating near-field is increased, which results in either higher gradient, or allows us to push for lower injection energy at given aperture. Previously reported minimal injection energies of 9.6 keV [36] required using higher harmonics (in [36] the fifth) and confinement was not attained. Here, we intend to stay at the first harmonic since it provides the slowest dropoff from the grating surface and thus the highest center gradient. We show, that injection energies of 16.75 and 2.5 keV are attainable at laser wavelengths of 2 and 6 μm , respectively. Thus, bulky high voltage feedthroughs in the experimental chambers can be entirely omitted.

The 3D APF-based DLA can still be fabricated by 2D lithographic techniques. The key idea is to work with two materials, exhibiting an as high as possible refractive index contrast, see Fig. 1. Such technology is already commercially available in nanoelectronics and -photonics, e.g., as silicon-on-insulator (SOI) wafers [37], and has been used to demonstrate a waveguide driven DLA recently [38]. The refractive indices at 2 μm are [39] $n_{\text{Si}} = 3.67$ and $n_{\text{SiO}_2} = 1.44$, respectively. At first, we make the approximation of $n_{\text{SiO}_2} \approx 1$, which will be later refined. In other words, the oxide serves as just a building brick to

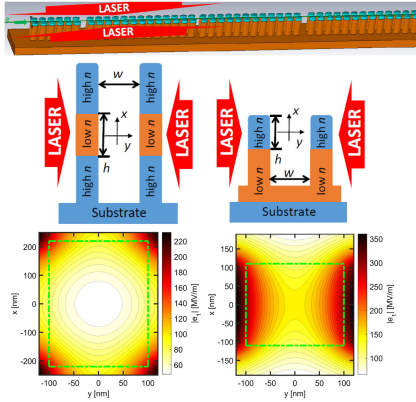


FIG. 1. Top: 3D APF DLA based on SOI dual pillars. Bottom: cross sections and $|e_1(x, y)|$ therein for in-phase APF (left) and counterphase APF (right), with approximation of $n_{\text{SiO}_2} \approx 1$ and the beam channel $w \times h$ in green.

construct 3D silicon structures by 2D lithography, where the layer thickness h and the pillar semiaxis radii can attain single digit nanometer precisions.

To model the electromagnetic fields in the (quasi) periodic structures, we first look at the Helmholtz wave equation, in temporal frequency domain and Fourier series expanded in the longitudinal direction (see the Supplemental Material [40]),

$$[\Delta_{\perp} - k_z^2 + \omega^2/c^2]e_1(x, y) = 0, \quad (1)$$

where Δ_{\perp} is the transverse Laplacian, $k_z = \omega/(\beta c)$ is the longitudinal wave number of the synchronous mode e_1 to an electron traveling at speed βc and $\omega = 2\pi c/\lambda$. Equation (1) is valid only in the vacuum of the beam channel. In contrast to conventional metallic accelerators, boundary conditions, necessary to solve Eq. (1), are not available. We can however determine the dispersion relation from Eq. (1) by $\partial_x \rightarrow -ik_x$, $\partial_y \rightarrow -ik_y$, and $\gamma^2 = 1/(1 - \beta^2)$ as

$$k_x^2 + k_y^2 = \frac{\omega^2}{c^2} - k_z^2 = -\frac{\omega^2}{\beta^2 \gamma^2 c^2} =: -\kappa^2, \quad (2)$$

which is plotted in Fig. 2. Instead of solving Eq. (1), we only need to determine $e_{10} = e_1(0, 0)$ and one transverse wave number, which can be done numerically (see the Supplemental Material [40]), for each individual grating cell. The transverse dependence of e_1 can then be written analytically as

$$e_1(x, y) = e_{10} \cosh(ik_x x) \cosh(ik_y y), \quad (3)$$

which is numerically confirmed within 5% in the channel $w \times h$ and plotted in Fig. 1 over a slightly larger range. The assumption that the oxide can be neglected is cross-checked in Fig. 3 (top), where $|e_{10}|$, k_x , and k_y are

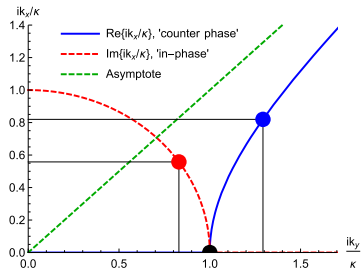


FIG. 2. Relation of ik_x and ik_y . The black dot represents the two-dimensional APF scheme ($k_x = 0$) as introduced in [26]. The red and blue dots are examples of the in-phase and counterphase APF scheme, respectively.

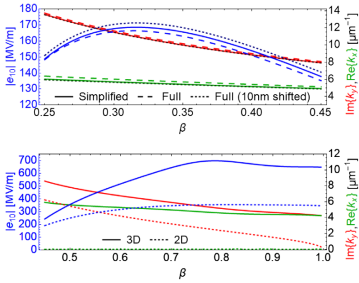


FIG. 3. Comparison of peak acceleration gradient and focusing strength of counterphase structures: (top panel) low energy for simplified vs full pillars and (bottom panel) high energy 3D vs 2D ($k_x = 0$).

compared for a free-floating simplified pillar, a full pillar with the origin centered in h , and a full pillar with the origin slightly shifted towards the substrate. Since the curves agree to sufficient accuracy, we will continue with the simplified pillars for brevity. Figure 3 (bottom) shows a direct comparison of the peak gradient and focusing strength to the 2D case [26] for higher velocity, where an up to twofold gradient enhancement is visible. The enhancement is even larger at lower β , where the dropdown of e_1 renders the 2D scheme unfeasible.

For the laser traveling in $\pm y$ direction and polarized in z direction, ik_x is always a purely real number. However, ik_x can either be purely real or purely imaginary, see Fig. 2. We will refer to these cases as in-phase and counterphase scheme, indicating whether or not both transverse planes are simultaneously focused.

With no loss of generality, we continue with the counterphase scheme only, since the structures are straightforward to fabricate on SOI wafers. The dependence of the wave numbers $k_{x/y}$ as well as e_{10} on the height h of a free-floating pillar is plotted in Fig. 4. The oscillation of $|e_{10}|$ is due to eigenmodes arising in the x direction. Subsequently, the 2D case holds only for discrete values of h . These roots (and the corresponding maxima) of k_x are not robust with respect to perturbations such as attaching the pillar to the oxide or to the substrate. Robust counterphase focusing behavior is found below the first root of k_x and we choose $h = 0.22 \mu\text{m}$ (commercially available [37], vertical black line in Fig. 4), slightly below this first maximum.

In contrast to [26], the pillar shape is kept constant, i.e., $r_z = 200 \text{ nm}$ and $r_y = 100 \text{ nm}$ for Fig. 3 (top) and $r_z = 400 \text{ nm}$ and $r_y = 300 \text{ nm}$ for Fig. 3 (bottom), which set the minimum β to roughly 0.25 and 0.45, respectively. The occurring phase drift as function of $\beta = \lambda_g/\lambda$ is compensated by shifting the pillar center off the cell center by $\Delta z^{(n)} = \lambda_g^{(n)} [\arg(e_{10}^{(n)}) - \arg(e_{10}^{(1)})]/2\pi$, see the

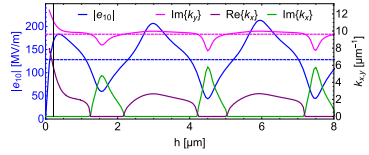


FIG. 4. Height scan for a free-floating dual pillar (counter-phase) setup at $\beta = 0.31$. Periodically reoccurring vertical eigenmodes make the 2D case (dashed lines) exceptional.

Supplemental Material [40]. The gradient can be further optimized by using a few additional pillar designs at different β . Moreover, fabrication errors for identical pillars are systematic and thus correctable, which decisively simplifies the fabrication and error estimation processes.

With the above knowledge of the electromagnetic field, we proceed to the Hamiltonian $H = \Delta \vec{P}^2 / (2m_e \gamma) + V$, where $\Delta \vec{P} = (p_x, p_y, \Delta p_z / \gamma)^T$ is the momentum deviation from the reference particle and m_e is the electron rest mass. The time-dependent potential V reads generally (same procedure as in [26]) as

$$V(x, y, s) = q \text{Im} \{ k_z^{-1} e_1(x, y) e^{ik_x s} - i s e_{10} e^{i\varphi_s} \}, \quad (4)$$

where q is the (negative) electron charge, s is the relative longitudinal coordinate with respect to the laser phase, and φ_s is the synchronous phase at which the reference particle gains energy according to the design acceleration ramp. Tracking with the nonlinear kicks according to Eq. (4) is performed by DLAttrack6D [23]. Expanding Eq. (4) to second order, Hamilton's equations provide Hill's equations

$$\Delta s'' + K_s \Delta s = 0, \quad (5a)$$

$$y'' + K_y y = 0, \quad (5b)$$

$$x'' + K_x x = 0, \quad (5c)$$

where $\Delta s = s - \lambda_g \varphi_s / 2\pi$. Due to the absence of first order terms in V , the linearized motion is decoupled. The focusing functions are

$$K_s = -\frac{k_z^2}{\gamma^2} \frac{|q e_{10}|}{m_e \beta \gamma c \omega} \sin(\varphi_s), \quad (6a)$$

$$K_y = (ik_y)^2 \frac{|q e_{10}|}{m_e \beta \gamma c \omega} \sin(\varphi_s), \quad (6b)$$

$$K_x = (ik_x)^2 \frac{|q e_{10}|}{m_e \beta \gamma c \omega} \sin(\varphi_s), \quad (6c)$$

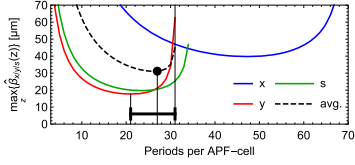


FIG. 5. Maximum of each $\hat{\beta}$ function for different APF cell lengths. The bar indicates the Pareto front of the multimimization, where the minimum of the arithmetic average is taken as initial guess for every cell length in the design.

and fulfill $K_x + K_y + K_s = 0$ according to Eq. (2), which reflects Earnshaw's theorem [44]. Note that K_s is the same as K in the 2D scheme [26] and the s and y planes are alternately focused by switching φ_s using fractional period drifts. The numerical value of K_y is however different from the 2D case and thus all three frequencies and phase advances are disparate. As compared to 2D, the 3D APF provides significantly higher values of e_{10} , k_x , and k_y , which allows us to push for lower injection energy while the confinement is maintained. Moreover, for $\beta \rightarrow 1$, K_x and K_y scale as γ^{-1} since k_x and k_y remain constant, whereas in the 2D scheme a faster γ^{-3} decay occurs (cf. Fig. 3).

This general description of the motion is now turned into a functioning accelerator that provides 3D particle confinement by individual CS lattice integration [25] in each plane x , y , s . As in [26], the lattice functions in Eqs. (6) are converted to CS-functions (also called Twiss parameters)

$\eta = (\hat{\beta}, \hat{\alpha}, \hat{\gamma})^T$ by solving the Twiss map eigenvector problem $\eta_0 = \mathbf{T}\eta_0$ for the initial values and subsequently mapping them to any other position.

The maxima of the $\hat{\beta}$ functions for a strictly periodic APF cell at $\beta = 0.25$ are plotted in Fig. 5. To avoid electron loss at the aperture, the cell length of choice should minimize these three maxima at given laser amplitude. A suitable (not unique) multiobjective optimal cell length, i.e., an element of the Pareto front, is given by the minimum of the arithmetic average of these three maxima-curves.

At given injection energy we pick the synchronous phase as a compromise between desired acceleration gradient and required longitudinal focusing strength. The laser field strength is picked as slightly below the damage threshold fluence for a (curved-tilted) 100 fs pulse. A laser amplitude of 500 MV/m from each side and a synchronous phase of $\pm 60^\circ$ off crest are chosen, leading to an average gradient of $G \approx \cos(\varphi_s) \langle |e_{10}| \rangle \approx 73$ MeV/m. Laser pulse shape and exact average gradient are detailed in the Supplemental Material [40].

The periodic solutions and their Twiss maps $\mathbf{T}_p^{x,y,s}$ for the optimal cell length as indicated in Fig. 5 are determined for a continuum of velocities β . Usually, a lattice obtained by simple matrix mapping of η_0 will exhibit growing $\hat{\beta}$ functions, due to cumulation of the small mismatch between two APF cells. Smooth and slowly growing $\hat{\beta}$ functions, such that the envelopes $a = (\hat{\beta}\varepsilon)^{1/2}$ are non-growing, are obtained by manual correction of the segment lengths, which slightly squeezes the beam in one direction at the expense of another. Note that a slight growth of $\hat{\beta}$ is tolerable, since the emittance decreases by adiabatic

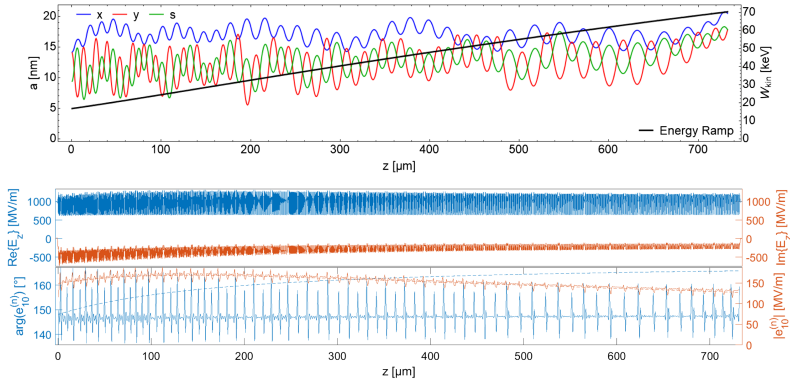


FIG. 6. Upper panel (design): envelopes for $\varepsilon_n = 2.5$ pm and kinetic energy ramp. Lower panel (3D analysis): complex electric field $E_z(0, 0, z)$ and spatial Fourier coefficients $e_{10}^{(n)}$ calculated from the full field windowed in each DLA cell n . The dashed lines represent the individually computed values of e_{10} under periodic boundary conditions, which were used for the design.

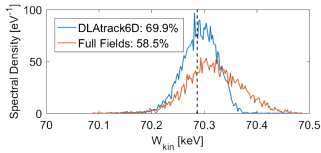


FIG. 7. Comparison of the final energy spectrum and throughput from a DLAttrack6D [23] simulation vs tracking simulation in the full laser fields using CST [45]. The dashed vertical line is the design top energy.

damping according to $\varepsilon = \varepsilon_n / (\beta\gamma)$, where the normalized emittance ε_n is an invariant of the linearized motion.

The resulting energy ramp and envelopes for a structure that accelerates from 16.75 keV ($\beta = 0.25$) to 70.29 keV ($\beta = 0.48$), consisting of 945 cells and 74 APF jumps, are plotted in Fig. 6 (top). After a full 3D field simulation [45], the complex field result along the channel is plotted below. Windowing this global field for each DLA cell allows a comparison between the $e_{10}^{(n)}$ in the entire accelerator to the individual $e_{10}^{(n)}$ initially computed under periodic boundary conditions (cf. Fig. 3). As visible, the phase drift compensation keeps $\arg(e_{10}^{(n)})$ constant, but at the φ_s jumps a Gibbs phenomenon occurs. This is the main source of excess emittance growth and particle loss (cf. Fig 7).

The injection parameters were chosen as Gaussian distributions with geometric emittances $\varepsilon_x = 12$ pm, $\varepsilon_x = 7$ pm, and bunch length $\sigma_s = 5$ nm with matched energy spread. These values are at the most sensitive beam loss clipping point and beam loss occurs in the lowest energy section of the accelerator. The throughput and energy spread is shown in Fig. 7 for one kick per cell vs 3D full field tracking. Similar results for 2.5 keV ($\beta = 0.1$) to 16.75 keV ($\beta = 0.25$) using $\lambda = 6$ μ m are discussed in the Supplemental Material [40] and in principle, one could even start at a few eV only, by using a Terahertz driver. However, lowering the injection energy poses a challenge to the robustness. Structure bandwidth, fabrication tolerances, and injection energy mismatch have to be controlled more precise. Normalized emittances in the single digit picometer range are available [46,47], however, after the electrostatic preaccelerator mostly higher values are reported (e.g., [48,49]). This is due to nonlinear aberrations in the electrostatic lensing system. Our findings ease this problem significantly, since aberrations scale with the overall size of the system, which can be significantly reduced at lower injection energy. As confirmed by full 3D simulation, the 3D APF DLA scheme on SOI wafers is ready for experimental testing in different energy ranges. Moreover, DLAs with 6D confinement improve our ability to keep the energy spread small over long distance, e.g., to observe and control electron matter waves [50–54].

More detailed theoretical studies are required to assess the effects of nonlinear and coupled tune spread and emittance evolution, e.g., with the extended DLAttrack6D [55].

U. N. would like to thank Peyman Yousefi, Payton Broadus, and Olav Solgaard for the discussions on SOI wafer processing. This work is funded by the Gordon and Betty Moore Foundation under Grant No. GBMF4744 (ACHIP).

*niedermayer@temf.tu-darmstadt.de

- [1] A. Lohmann, Electron acceleration by light waves, IBM Tech. Note 5, 169 (1962).
- [2] K. Shimoda, Proposal for an electron accelerator using an optical maser, *Appl. Opt.* **1**, 33 (1962).
- [3] J. Breuer and P. Hommelhoff, Dielectric laser acceleration of 28 keV electrons with the inverse Smith-Purcell effect, *Nucl. Instrum. Methods Phys. Res., Sect. A* **740**, 114 (2013).
- [4] E. A. Peralta, K. Soong, R. J. England, E. R. Colby, Z. Wu, B. Montazeri, C. McGuinness, J. McNeur, K. J. Leedle, D. Walz, E. B. Sozer, B. Cowan, B. Schwartz, G. Travish, and R. L. Byer, Demonstration of electron acceleration in a laser-driven dielectric microstructure, *Nature (London)* **503**, 91 (2013).
- [5] K. P. Wootton, Z. Wu, B. M. Cowan, A. Hanuka, I. V. Makasyuk, E. A. Peralta, K. Soong, R. L. Byer, and R. J. England, Demonstration of acceleration of relativistic electrons at a dielectric microstructure using femtosecond laser pulses, *Opt. Lett.* **41**, 2696 (2016).
- [6] D. Cesar, S. Custodio, J. Maxson, P. Musumeci, X. Shen, E. Threlkeld, R. J. England, A. Hanuka, I. V. Makasyuk, E. A. Peralta, K. P. Wootton, and Z. Wu, High-field nonlinear optical response and phase control in a dielectric laser accelerator, *Commun. Phys.* **1**, 46 (2018).
- [7] P. Yousefi, J. McNeur, M. Kozák, U. Niedermayer, F. Gannott, O. Lohse, O. Boine-Frankenheim, and P. Hommelhoff, Silicon dual pillar structure with a distributed Bragg reflector for dielectric laser accelerators: Design and fabrication, *Nucl. Instrum. Methods Phys. Res., Sect. A* **909**, 221 (2018).
- [8] K. J. Leedle, R. Fabian Pease, R. L. Byer, and J. S. Harris, Laser acceleration and deflection of 963 keV electrons with a silicon dielectric structure, *Optica* **2**, 158 (2015).
- [9] F. Krausz and M. Ivanov, Attosecond physics, *Rev. Mod. Phys.* **81**, 163 (2009).
- [10] Y. Morimoto and P. Baum, Diffraction and microscopy with attosecond electron pulse trains, *Nat. Phys.* **14**, 252 (2018).
- [11] A. H. Zewail and J. M. Thomas, *4D Electron Microscopy* (Wiley-VCH Verlag GmbH & Co. KGaA, Weinheim, 2010).
- [12] R. K. Li and C. X. Tang, Temporal resolution of MeV ultrafast electron diffraction based on a photocathode RF gun, *Nucl. Instrum. Methods Phys. Res., Sect. A* **605**, 243 (2009).
- [13] S. P. Weathersby *et al.*, Mega-electron-volt ultrafast electron diffraction at SLAC National Accelerator Laboratory, *Rev. Sci. Instrum.* **86**, 073702 (2015).

- [14] N. Rubiano Da Silva, M. Möller, A. Feist, H. Ulrichs, C. Ropers, and S. Schäfer, Nanoscale Mapping of Ultrafast Magnetization Dynamics with Femtosecond Lorentz Microscopy, *Phys. Rev. X* **8**, 031052 (2018).
- [15] R. F. Egerton, Outrun radiation damage with electrons?, *Adv. Struct. Chem. Imaging* **1**, 5 (2015).
- [16] E. Slot, M. J. Wieland, G. de Boer, P. Kruit, G. F. ten Berge, A. M. C. Houkes, R. Jager, T. van de Peut, J. J. M. Peijster, S. W. H. K. Steenbrink, T. F. Teepen, A. H. V. van Veen, and B. J. Kampherbeek, MAPPER: High throughput maskless lithography, *Emerging Lithogr. Technol.* **XII** **6921**, 69211P (2008).
- [17] R. J. England *et al.*, Dielectric laser accelerators, *Rev. Mod. Phys.* **86**, 1337 (2014).
- [18] R. B. Palmer, A laser driven grating linac, *Part. Accel.* **11**, 375 (1980), <http://cds.cern.ch/record/1107986/files/p81.pdf>.
- [19] K. Kim and N. Kroll, Some effects of the transverse-stability requirement on the design of a grating linac, Report No. LBL-14378, Cornell University, Ithaca, NY, 1982.
- [20] M. Pickup, A grating linac at microwave frequencies, Report No. CLNS-85/655, Lawrence Berkeley Laboratory, UC Berkeley California, 1985.
- [21] B. Naranjo, A. Valloni, S. Putterman, and J. B. Rosenzweig, Stable Charged-Particle Acceleration and Focusing in a Laser Accelerator using Spatial Harmonics, *Phys. Rev. Lett.* **109**, 164803 (2012).
- [22] D. Cesar, P. Musumeci, and J. England, All optical control of beam dynamics in a DLA, in *2018 IEEE Advanced Accelerator Concepts Workshop (AAC)*, Breckenridge, CO, USA (IEEE, Breckenridge, 2018), pp. 1–5.
- [23] U. Niedermayer, T. Egenolf, and O. Boine-Frankenheim, Beam dynamics analysis of dielectric laser acceleration using a fast 6D tracking scheme, *Phys. Rev. Accel. Beams* **20**, 111302 (2017).
- [24] W. K. H. Panofsky and W. A. Wenzel, Some considerations concerning the transverse deflection of charged particles in radio-frequency fields, *Rev. Sci. Instrum.* **27**, 967 (1956).
- [25] E. Courant and H. Snyder, Theory of the alternating-gradient synchrotron, *Ann. Phys. (N.Y.)* **3**, 1 (1958).
- [26] U. Niedermayer, T. Egenolf, O. Boine-Frankenheim, and P. Hommelhoff, Alternating-Phase Focusing for Dielectric-Laser Acceleration, *Phys. Rev. Lett.* **121**, 214801 (2018).
- [27] Y. Wei, M. Ibsion, G. Xia, J. D. A. Smith, and C. P. Welsch, Dual-grating dielectric accelerators driven by a pulse-front-tilted laser, *Appl. Opt.* **56**, 8201 (2017).
- [28] D. Cesar, J. Maxson, P. Musumeci, X. Shen, R. J. England, and K. P. Wootton, Optical design for increased interaction length in a high gradient dielectric laser accelerator, *Nucl. Instrum. Methods Phys. Res., Sect. A* **909**, 252 (2018).
- [29] M. Kozák, J. McNeur, N. Schönenberger, J. Illmer, A. Li, A. Tafel, P. Yousefi, T. Eckstein, and P. Hommelhoff, Ultrafast scanning electron microscope applied for studying the interaction between free electrons and optical near-fields of periodic nanostructures, *J. Appl. Phys.* **124**, 023104 (2018).
- [30] T. W. Hughes, S. Tan, Z. Zhao, N. V. Saprà, K. J. Leedle, H. Deng, Y. Miao, D. S. Black, O. Solgaard, J. S. Harris, J. Vuckovic, R. L. Byer, S. Fan, R. J. England, Y. J. Lee, and M. Qi, On-Chip Laser-Power Delivery System for Dielectric Laser Accelerators, *Phys. Rev. Applied* **9**, 054017 (2018).
- [31] D. S. Black, K. J. Leedle, Y. Miao, U. Niedermayer, R. L. Byer, and O. Solgaard, Laser-Driven Electron Lensing in Silicon Microstructures, *Phys. Rev. Lett.* **122**, 104801 (2019).
- [32] U. Niedermayer, O. Boine-Frankenheim, and T. Egenolf, Designing a dielectric laser accelerator on a chip, *J. Phys. Conf. Ser.* **874**, 012041 (2017).
- [33] D. S. Black, U. Niedermayer, Y. Miao, Z. Zhao, O. Solgaard, R. L. Byer, and K. J. Leedle, Net Acceleration and Direct Measurement of Attosecond Electron Pulses in a Silicon Dielectric Laser Accelerator, *Phys. Rev. Lett.* **123**, 264802 (2019).
- [34] N. Schönenberger, A. Mittelbach, P. Yousefi, J. McNeur, U. Niedermayer, and P. Hommelhoff, Generation and Characterization of Attosecond Microbunched Electron Pulse Trains via Dielectric Laser Acceleration, *Phys. Rev. Lett.* **123**, 264803 (2019).
- [35] U. Niedermayer *et al.*, Challenges in simulating beam dynamics of dielectric laser acceleration, *Int. J. Mod. Phys. A* **34**, 1942031 (2019).
- [36] J. McNeur, M. Kozák, D. Ehberger, N. Schönenberger, A. Tafel, A. Li, and P. Hommelhoff, A miniaturized electron source based on dielectric laser accelerator operation at higher spatial harmonics and a nanotip photoemitter, *J. Phys. B* **49**, 034006 (2016).
- [37] www.order.universitywafer.com, 2019.
- [38] N. V. Saprà, K. Y. Yang, D. Vercrucysee, K. J. Leedle, D. S. Black, R. J. England, L. Su, R. Trivedi, Y. Miao, O. Solgaard, R. L. Byer, and J. Vuckovic, On-chip integrated laser-driven particle accelerator, *Science* **367**, 79 (2020).
- [39] www.refractiveindex.info, 2019.
- [40] See the Supplemental Material at <http://link.aps.org/supplemental/10.1103/PhysRevLett.125.164801> for details on structure constant, laser pulse shaping, an ultralow injection energy design, and video examples, which contains Refs. [41–43].
- [41] P. Pronko, P. V. Rompay, C. Horvath, X. Liu, T. Juhasz, and G. Mourou, Avalanche ionization and dielectric breakdown in silicon with ultrafast laser pulses, *Phys. Rev. B* **58**, 2387 (1998).
- [42] K. Soong, R. L. Byer, E. R. Colby, R. J. England, and E. A. Peralta, Laser damage threshold measurements of optical materials for direct laser accelerators, *AIP Conf. Proc.* **1507**, 511 (2012).
- [43] B. Sun, P. S. Salter, and M. J. Booth, Pulse front adaptive optics: a new method for control of ultrashort laser pulses, *Opt. Express* **23**, 19348 (2015).
- [44] S. Earnshaw, On the nature of the molecular forces which regulate the constitution of the luminiferous ether, *Trans. Cambridge Philos. Soc.* **7**, 97 (1842).
- [45] CST, CST Studio Suite (2019).
- [46] D. Ehberger, J. Hammer, M. Eisele, M. Krüger, J. Noe, A. Högele, and P. Hommelhoff, Highly Coherent Electron Beam from a Laser-Triggered Tungsten Needle Tip, *Phys. Rev. Lett.* **114**, 227601 (2015).
- [47] A. Feist, N. Bach, N. Rubiano da Silva, T. Danz, M. Möller, K. E. Priebe, T. Dornöse, J. G. Gatzmann, S. Rost, J. Schauss, S. Strauch, R. Bornmann, M. Sivis, S. Schäfer, and C. Ropers, Ultrafast transmission electron microscopy using a laser-driven

- field emitter: Femtosecond resolution with a high coherence electron beam, *Ultramicroscopy* **176**, 63 (2017).
- [48] A. Tafel, S. Meier, J. Ristein, and P. Hommelhoff, Femtosecond Laser-Induced Electron Emission from Nanodiamond-Coated Tungsten Needle Tips, *Phys. Rev. Lett.* **123**, 146802 (2019).
- [49] T. Hirano, K. E. Urbanek, A. C. Ceballos, D. S. Black, Y. Miao, R. Joel England, R. L. Byer, and K. J. Leedle, A compact electron source for the dielectric laser accelerator, *Appl. Phys. Lett.* **116**, 161106 (2020).
- [50] B. Barwick, D. J. Flannigan, and A. H. Zewail, Photon-induced near-field electron microscopy, *Nature (London)* **462**, 902 (2009).
- [51] O. Keller, *Quantum Theory of Near Fields* (Springer, Berlin-Heidelberg, 2011).
- [52] E. Jones, M. Becker, J. Luiten, and H. Batelaan, Laser control of electron matter waves, *Laser Photonics Rev.* **10**, 214 (2016).
- [53] G. M. Vanacore, I. Madan, G. Berruto, K. Wang, E. Pomarico, R. J. Lamb, D. McGrouther, I. Kaminer, B. Barwick, F. J. García De Abajo, and F. Carbone, Attosecond coherent control of free-electron wave functions using semi-infinite light fields, *Nat. Commun.* **9**, 2694 (2018).
- [54] S. Nehemia, R. Dahan, M. Shentcis, O. Reinhardt, Y. Adiv, K. Wang, O. Beer, Y. Kurman, X. Shi, M. H. Lynch, and I. Kaminer, Observation of the stimulated quantum Cherenkov effect, [arXiv:1909.00757](https://arxiv.org/abs/1909.00757).
- [55] T. Egenolf, U. Niedermayer, and O. Boine-Frankenheim, Tracking with wakefields in dielectric laser acceleration grating structures, *Phys. Rev. Accel. Beams* **23**, 054402 (2020).

Supplemental Material

Uwe Niedermayer,* Thilo Egenolf, and Oliver Boine-Frankenheim
Technische Universität Darmstadt, Schlossgartenstrasse 8, D-64289 Darmstadt, Germany
 (Dated: September 9, 2020)

This Supplemental Material to *Three-Dimensional Alternating-Phase Focusing for Dielectric-Laser Electron Accelerators* details (1) the determination of the individual structure constants and their dependencies on various parameters, (2) the shaping of the required laser pulses, (3) the accelerator design for 2.5 keV injection energy, and (4) a summary of the available video files.

I. STRUCTURE CONSTANT AND BANDWIDTH

We assume a monochromatic laser excitation of wavelength λ and angular frequency $\omega = 2\pi c/\lambda$, polarized in z -direction. The electric field within the DLA structure can be written as

$$\vec{E}_t(x, y, z, t) = \text{Re} \{ \vec{E}(x, y, z) e^{i\omega t} \}, \quad (1)$$

where \vec{E} is the complex phasor of the electric field. The structure is (piecewise) periodic in the z -direction with periodicity λ_g , thus, the longitudinal component of the phasor can be written as Fourier series

$$E_z(x, y, z) = \sum_{m=-\infty}^{\infty} e_m(x, y) e^{-im \frac{2\pi}{\lambda_g} z}. \quad (2)$$

As shown in [1], only one coefficient, which fulfills the Wideroe synchronicity condition $\lambda_g = m\beta\lambda$, contributes to the sum in an average over many periods. With no loss of generality, we choose $m = 1$, i.e., the first harmonic for which the Fourier coefficient reads

$$e_1(x, y) = \frac{1}{\lambda_g} \int_{-\lambda_g/2}^{\lambda_g/2} E_z(x, y, z) e^{-i \frac{2\pi}{\lambda_g} z} dz. \quad (3)$$

This expansion can be performed for every transverse coordinate pair (x, y) , and we define the particular value at the origin $e_{10} = e_1(0, 0)$. The value $|e_{10}|$ is the peak gradient and $|e_{10}^{(\text{norm})}| = |e_{10}|/E_L$, where E_L is the incident laser amplitude, is commonly referred to as structure constant. The "global" gradient in a confined system is reduced by an off-crest synchronous phase as $|e_{10}| \cos \varphi_s$, where $\varphi_s = \pm 60^\circ$ results in half the peak gradient. Due to the drifts in an APF system, there is a further slight gradient reduction of about 5% before the average gradient $\Delta W_{\text{total}}/L_{\text{total}}$ is obtained. Note that the structure constant $|e_{10}^{(\text{norm})}|$ is strongly dependent on the reference velocity β and the aperture of the structure. The exact acceleration ramp, necessary to determine the average gradient, is determined by adding up the exact energy gains $|e_{10}^{(n)}| \lambda_g^{(n)} \cos(\varphi_s)$ for each DLA cell n .

Since the electric field \vec{E}_t fulfills the wave equation $[\Delta - c^{-2}\partial_t^2] \vec{E}_t = 0$, the transverse distribution of $e_1(x, y)$ must fulfill the corresponding Helmholtz equation

$$\left[\Delta_{\perp} - \left(\frac{2\pi}{\lambda_g} \right)^2 + \frac{\omega^2}{c^2} \right] e_1(x, y) = 0, \quad (4)$$

which is Eq. 1 of the main manuscript. Here, $\Delta_{\perp} = \partial_x^2 + \partial_y^2$ represents the transverse part of the Laplacian Δ . Throughout this work, \vec{E} is used in the frequency domain, and the time dependent signal $\vec{E}_t(x, y, z, t)$ is omitted. We use numerical determination of e_1 by the commercial Software CST Studio Suite [2] throughout this work. As it is practically feasible, we use time domain simulation with on-the-fly Fourier transform to obtain the frequency domain field $\vec{E}(x, y, z)$. For single-cell optimization or single-cell parameter sweeps, periodic boundary conditions in the z -direction are applied. All other boundaries are modeled as open, i.e. with perfectly matched layers (PMLs),

* niedermayer@temf.tu-darmstadt.de

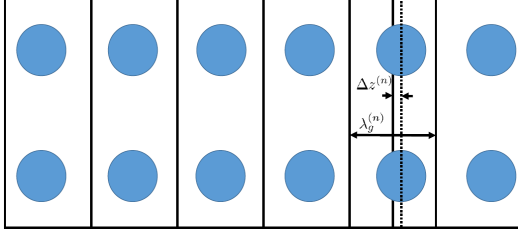


FIG. 1: Correcting the phase shift due to the cell length chirp allows to keep the pillar shape identical. The correction is obtained by moving the pillar within the cell, which leads to a predictable phase shift according to the shift theorem of the Fourier transform.

at sufficient distance. Two-dimensional simulations are obtained by removing this distance and replacing the open boundary conditions by periodic boundary conditions in the x -direction. The spatial Fourier integral Eq. 3 is evaluated as a post-processing step, either for a single point to obtain e_{10} or on a grid to obtain the entire $e_1(x, y)$ distribution. The values of k_x and k_y are determined using Eq. 3 of the main manuscript with particular values of $e_1(x, y)$.

We adjust the transverse coordinate system such that $\nabla_{\perp} e_{10}(0, 0) = 0$, i.e., the origin is at the saddle point for the *counter-phase* scheme and at the minimum for the *in-phase* scheme. Knowledge of the phase of e_{10} is required to precisely inject the electron beam at proper time, i.e. to design an attosecond buncher [3–6] that can inject the electron beam at the synchronous phase. Phase adjustments in $\arg(e_{10})$ can be performed by moving the pillar away from the DLA cell center by $\Delta z^{(n)} = \lambda_g \Delta \arg(e_{10}) / 2\pi$, i.e., the phase is adjusted by using the shift theorem of the Fourier transform, see Fig. 1. This allows in particular to compensate for phase drifts when using the identical pillar shapes for a continuum of values of $\lambda_g^{(n)} = \lambda \beta^{(n)}$. The effect of the phase correction can be seen in Fig. 6 (bottom panel) of the main paper. The maximum correction of 50 nm fits easily into the remaining free space within the DLA cell.

In order to allow deviations from a strictly λ_g -periodic grating, in particular for the APF phase jumps, each grating cell has to support a certain bandwidth Δf . This means we have to optimize the structures for a *low* quality factor Q and a high $|e_{10}|$, similar to the geometry optimizations in conventional RF accelerator cavities, where first the geometry is optimized to maximize R/Q (R is the shunt impedance) and later the surface is optimized to obtain highest Q . In this way, maximal $R = (R/Q)Q$ is obtained. For DLAs, only the geometry is subject to optimization and $|e_{10}|/Q$ is pragmatically optimized by first maximizing $|e_{10}|$ and then simply checking if sufficient bandwidth is supported, i.e. if Q is sufficiently small.

We determine the bandwidth of a particular structure by fitting $e_{10}(f)$ to a Lorentzian peak, while the Wideroe condition $\lambda_g = \beta \lambda$ is always fulfilled. Thus, while sweeping the frequency, the particle velocity has to be adjusted according to $\beta = \lambda_g f / c$ and the proper frequency dependent definition of e_{10} reads

$$e_{10}(f) = \frac{1}{\lambda_g} \int_{-\lambda_g/2}^{\lambda_g/2} E_z(0, 0, z; f) e^{-i \frac{2\pi}{\lambda_g} z} dz. \quad (5)$$

The resonance frequency f_r , the peak amplitude $|e_{10}(f_r)|$ and the quality factor Q are determined by fitting the frequency sweep to the Lorentzian

$$|e_{10}(f)| = \frac{|e_{10}(f_r)|}{\sqrt{1 + Q^2 \left(\frac{f-f_r}{f_r}\right)^2}}. \quad (6)$$

The resulting resonance curves and quality factors are plotted in Fig. 2. As examples, we compare a structure made of individual pillars and a structure which is topologically connected. Both structures have been geometrically optimized to maximize e_{10} at $f_0 = 150$ THz. Note that some structures might exhibit multiple resonances, that have to be fitted individually to Lorentzian peaks, however, here we look only on those close to the excitation center laser frequency f_0 . Moreover, especially at high bandwidth, f_r and f_0 might differ significantly.

We observe, that the connected structure does not provide sufficient bandwidth to support APF phase jumps. A smooth curve for $|e_{10}|$, as in Fig. 6 of the main manuscript, is not attained for the connected structure, since the

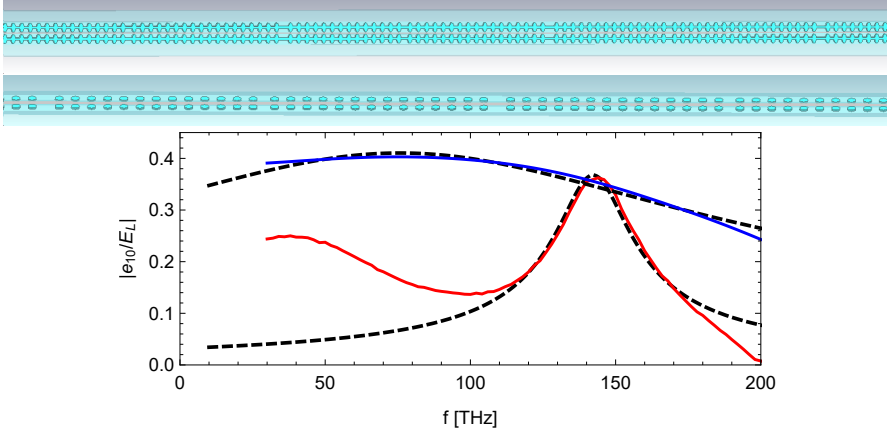


FIG. 2: Comparison of the bandwidth $\Delta f = f_0/Q$ of a connected (upper drawing, red curve) and not connected structure (lower drawing, blue curve). For the connected structure the quality factor is $Q = 11.5$, resulting in 12.4 THz bandwidth. For the individual pillars, we find $Q = 0.7$ and 104.8 THz bandwidth. The displaced resonance frequency ($f_r \approx 75$ THz) is not an issue due to the large bandwidth.

phase jumps induce wild oscillations. Thus we reject the connected structures and keep the individual pillars. As a coarse criterion for a single cell that supports APF phase jumps we formulate $Q \lesssim 1$.

The individual pillars however cannot be bulk grounded and require metal atomic layer deposition (ALD) to slowly remove charge that accumulated due to electron beam loss. The calculation of $e_{10}(f)$ can be performed either as a frequency sweep and point-wise evaluation of Eq. 5 or at once as a time domain broadband pulse excitation with simultaneous evaluation of multiple frequencies.

II. LASER PULSE SHAPE

A fully scalable DLA requires a tilted laser pulse, such that the time of interaction of the laser pulse with the electron beam becomes independent of the time of interaction with a particular pillar of the structure. The tilt angle is given by (see e.g. [7])

$$\alpha = \arctan \frac{1}{\beta} \quad (7)$$

and can be implemented e.g. by a diffraction grating. The laser field amplitude follows a bi-Gaussian distribution as

$$E_z \propto \exp -\frac{1}{2} \left[\left(\frac{(z - z^*) \cos \alpha + (y - \tilde{y}) \sin \alpha}{\sigma_z} \right)^2 + \left(\frac{(z - z^*) \sin \alpha - (y - \tilde{y}) \cos \alpha}{\sigma_y} \right)^2 \right], \quad (8)$$

where $\sigma_y = c\sigma_t$ is the pulse length and σ_z is the pulse width, which has to cover the entire DLA structure. The polarization is in z -direction and the phase fronts are flat xz -planes. For constant reference velocity β , the laser pulse can be arbitrary short. However, when the electron is accelerated, its trajectory within the laser pulse will not be linear anymore. Ideally, the tilted pulse would be replaced by a "banana"-shaped pulse, in order to exactly follow the acceleration ramp. A constantly tilted pulse can however approximate the "banana" if the interaction is over a finite length L . The drawback of this is that a minimum length of the pulse is required.

In order to calculate the minimal pulse length and the optimal tilt angle, we have to compute the trajectory $y(z)$

of the electron within the laser pulse. Its derivative provides

$$\frac{dy}{dz} = \tan \alpha(z) = \frac{1}{\beta(z)} \Rightarrow y(z) = \int_0^z \frac{d\tilde{z}}{\beta(\tilde{z})}. \quad (9)$$

A secant to this trajectory is

$$y_s(z) = \frac{y(L)}{L} z \quad (10)$$

where L is the length of the accelerator. The optimal tilt angle $\alpha^* = \arctan \frac{1}{\beta(z^*)}$ of a linearly tilted pulse is now found at the position where the difference between the "banana" and its secant is maximal, i.e.

$$z^* = \operatorname{argmax} y(z) - y_s(z). \quad (11)$$

An estimate of the required pulse length, such that at perfect timing the laser amplitude has dropped not more than to $\exp(-\xi^2/2)$ of the peak value, is

$$\sigma_y = \frac{\cos(\alpha^*)}{\xi} \max y(z) - y_s(z) \quad (12)$$

under the condition $\sigma_z \gg \sigma_y$. The proper value for \tilde{y} is found as the middle between $y(z^*)$ and $y_s(z^*)$ as $\tilde{y} = \frac{1}{2} [y(z^*) + y_s(z^*)]$.

In the following we take $\xi = 1$ and a linear energy ramp, i.e., $W(z) = \gamma_0 m_e c^2 + Gz$, with γ_0 being the initial Lorentz factor and G being the constant gradient. The integral 9 is solved as

$$y(z) = \frac{m_e c^2}{G} \left[\sqrt{\left(\gamma_0 + \frac{Gz}{m_e c^2} \right)^2 - 1} - \sqrt{\gamma_0^2 - 1} \right] = \frac{m_e c^2}{G} [\beta(z)\gamma(z) - \beta_0\gamma_0] \quad (13)$$

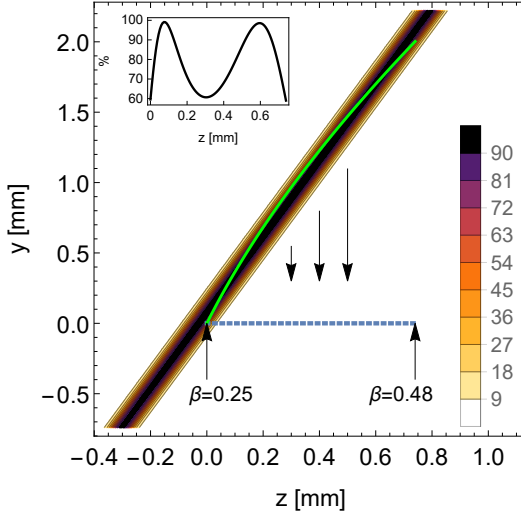


FIG. 3: Contours of E_z as Eq. 8 for the values $\alpha^* = 69.72^\circ$, $\sigma_t = 179$ fs, $\sigma_z = 1$ cm in percent. The dashed blue line represents the accelerator structure. The green line shows the trajectory of the electron within the pulse according to Eq. 13. The inset is a parametric evaluation of the laser amplitude on the electron trajectory.

and $\beta(z^*) = L/y(L)$. The optimal center point z^* is obtained by setting $W(z^*) = m_e c^2 \gamma^*$ as

$$z^* = \frac{m_e c^2}{G} (\gamma^* - \gamma_0). \quad (14)$$

The pulse length is thus explicitly

$$\sigma_y = \frac{m_e c^2}{G} \frac{\cos(\alpha^*)}{\xi} [\beta^* \gamma^* - \beta_0 \gamma_0 - (\gamma^* - \gamma_0)/\beta^*]. \quad (15)$$

The pulse parameters for the accelerator in the main paper, i.e. for $\beta = 0.25$ to $\beta = 0.48$ in $740 \mu\text{m}$ (73 MeV/m average gradient), are depicted in Fig 3. The optimal tilt angle is $\alpha^* = 69.72^\circ$ and a pulse duration of $\sigma_t = 179$ fs is required. The damage threshold for Silicon is about 2 GV/m for 100 fs pulses at $\lambda = 1.06 \mu\text{m}$ [8]. Soong et al. [9] indicate that the damage threshold does not vary more than a factor of 2 between $1 \mu\text{m}$ and $2 \mu\text{m}$, therefore we assume to be close but below the damage threshold when the amplitude is 500 MV/m from both lateral sides. We furthermore assume that SOI structures have the damage threshold of silicon, since the one of the oxide is significantly higher.

This damage threshold fluence constraint requires pulses as short as 100 fs, which in turn requires creating the "banana"-shape as described by Eq. 13. A possible technique for this is given by the combination of a Spatial Light Modulator (SLM) and a Deformable Mirror (DM), see [10]. Another option would be to split the pulse in parts with individual tilt angles, such that the "banana" is approximated by linear pieces.

The 40% lower amplitudes at the electron trajectory can be compensated by increasing the overall laser power within the damage constraint. In contrast to lower than nominal laser amplitudes, slightly higher amplitudes do not lead to electron beam loss, since increased K values lead to decreased β functions. On the other hand, however, the $\hat{\gamma}$ function is increased, leading to a larger energy spread (and also angle spread) of the outgoing electron beam. The reference output energy is not affected by slight laser amplitude changes, since it is hard-coded into the accelerator lattice design by the periodicity chirp.

III. ULTRA-LOW INJECTION ENERGY DESIGN

Similarly to the design in the main paper, we show another accelerator design here at ultra-low injection energy of 2.574 keV ($\beta = 0.1$). We choose a wavelength of $\lambda = 6 \mu\text{m}$, at which silicon is still transparent, and the first period $\lambda_y^{(1)} = 600$ nm is not too small for fabrication. The aperture is chosen as 500 nm and the dimensions of the identical pillars are $r_y = 100$ nm and $r_z = 250$ nm. The silicon layer height is 440 nm and the laser amplitude is again 500 MV/m from both lateral sides. The design as well as the analysis of the 3D field results are shown in Fig. 4.

Due to decreased bandwidth at low β , the deviation of the full 3D field amplitude and phase from the design values (periodic boundaries) is quite substantial. Thus, further structure optimization is required in the future. Moreover, at such low injection energy, energy and phase mismatch have a large impact on the total particle transmission.

The particle tracking simulation was performed both with DLAttrack6D [1] using $e_{10}^{(n)}$ and with CST [2] taking into account the full fields. The emittance was taken as $\varepsilon_x = 10$ pm, $\varepsilon_y = 20$ pm and the bunch length was $\sigma_z = 5$ nm with matched energy spread. The expected throughput should be on the order of 94%, see Fig. 5, however with CST we obtain only about 20%. We account this to two issues. First, the insufficient field quality especially at the lower end of the accelerator. Second, and likely more decisive, the CST simulation in full 3D frequency domain fields creates an artificial energy offset at injection.

When the particles are released from a window within the computational domain, they see the already present fields immediately. This violates the conditions of the Lawson-Woodward theorem, which states that a plane wave cannot produce first order net acceleration [11]. However even a plane wave (e_0 mode) can do a net transfer of energy to the particles if they suddenly appear out of a window. This ends up in a significant injection energy error on the order of 100 eV. In order to study this effect, we have artificially included it in a DLAttrack6D simulation. The effect of a 25 eV (1%) offset is shown in Fig. 5, right panel. A coherent oscillation arises, which strongly probes the nonlinearities of the fields. This leads to emittance growth in all 3 planes and eventually beam loss, i.e. we obtain only 35% throughput in the example. Manual correction (fine-tuning) of the injection energy is possible up to an estimated residual of 10 to 20 eV. We note, that this is only an issue of the simulation, not the design.

In general, a lower limit for the injection energy is found by practical considerations. These are in particular related to fitting the envelope a into the aperture A of the structure. The scaling laws for the envelope are

$$a = \sqrt{\beta \varepsilon} \propto \sqrt{\frac{1}{K} \frac{\varepsilon_n}{\beta \gamma}} \propto \frac{\beta \gamma}{\sqrt{|e_{10}|}}, \quad (16)$$

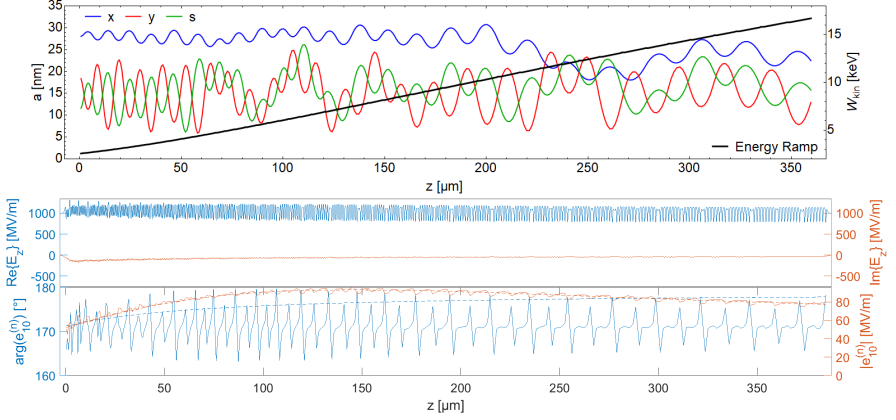


FIG. 4: Upper panel (design): envelopes for $\varepsilon_n = 2.5$ pm and kinetic energy ramp. Lower Panel (3D analysis): complex electric field $E_z(0, 0, z)$ and spatial Fourier coefficients $e_{10}^{(n)}$ calculated from the full field windowed in each DLA cell n . The dashed lines represent the individually computed values of e_{10} under periodic boundary conditions, which were used for the design.

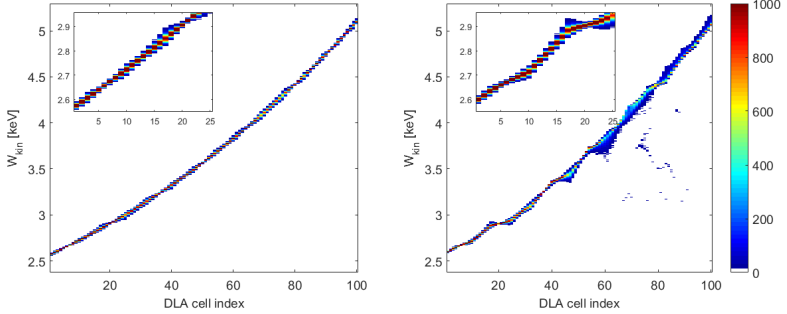


FIG. 5: Spectrograms for the first 100 cells of the $\beta = 0.1$ to $\beta = 0.25$ accelerator from DLAttrack6D simulation. The left panel is at design injection energy and produces 94% total throughput, the right panel is at +25 eV injection energy offset and produces only 35% total throughput. The insets are enlargements of the first 25 cells.

i.e. due to the strong K values at low energy, an at most quadratic drop of the structure constant with β is tolerable (without changing the aperture).

IV. ONLINE AVAILABLE VIDEO EXAMPLES

Three videos are online available with this supplemental material to be downloaded. They represent DLTrack6D simulations for the case in the main paper, the ultra-low energy example in this supplement, and the +25 keV injection energy offset example of the latter. Scatter plots are intended to draw the reader's attention to the high amplitude particles, which perform three-dimensionally coupled nonlinear oscillations.

-
- [1] U. Niedermayer, T. Egenolf, and O. Boine-Frankenheim, Beam Dynamics Analysis of Dielectric Laser Acceleration using a Fast 6D Tracking Scheme, *Physical Review Accelerators and Beams* **20**, 111302 (2017).
 - [2] CST, CST Studio Suite (2019).
 - [3] U. Niedermayer, O. Boine-Frankenheim, and T. Egenolf, Designing a Dielectric Laser Accelerator on a Chip, *Journal of Physics: Conference Series* **874** (2017).
 - [4] U. Niedermayer, T. Egenolf, O. Boine-Frankenheim, and P. Hommelhoff, Alternating-Phase Focusing for Dielectric-Laser Acceleration, *Physical Review Letters* **121**, 214801 (2018).
 - [5] D. S. Black, U. Niedermayer, Y. Miao, Z. Zhao, O. Solgaard, R. L. Byer, and K. J. Leadle, Net Acceleration and Direct Measurement of Attosecond Electron Pulses in a Silicon Dielectric Laser Accelerator, *Physical Review Letters* **123**, 264802 (2019).
 - [6] N. Schönenberger, A. Mittelbach, P. Yousefi, J. McNeur, U. Niedermayer, and P. Hommelhoff, Generation and Characterization of Attosecond Microbunched Electron Pulse Trains via Dielectric Laser Acceleration, *Physical Review Letters* **123**, 264803 (2019).
 - [7] Y. Wei, M. Ibson, G. Xia, J. D. A. Smith, and C. P. Welsch, Dual-grating dielectric accelerators driven by a pulse-front-tilted laser, *Applied Optics* **56**, 8201 (2017).
 - [8] P. Pronko, P. V. Rompay, C. Horvath, X. Liu, T. Juhasz, and G. Mourou, Avalanche ionization and dielectric breakdown in silicon with ultrafast laser pulses, *Physical Review B* **58**, 2387 (1998).
 - [9] K. Soong, R. L. Byer, E. R. Colby, R. J. England, and E. A. Peralta, Laser damage threshold measurements of optical materials for direct laser accelerators, *AIP Conference Proceedings* **1507**, 511 (2012).
 - [10] B. Sun, P. S. Salter, and M. J. Booth, Pulse front adaptive optics: a new method for control of ultrashort laser pulses, *Optics Express* **23**, 19348 (2015).
 - [11] R. J. England, R. J. Noble, K. Bane, D. H. Dowell, C.-K. Ng, J. E. Spencer, S. Tantawi, Z. Wu, R. L. Byer, E. Peralta, K. Soong, C.-M. Chang, B. Montazeri, S. J. Wolf, B. Cowan, J. Dawson, W. Gai, P. Hommelhoff, Y.-C. Huang, C. Jing, C. McGuinness, R. B. Palmer, B. Naranjo, J. Rosenzweig, G. Travish, A. Mizrahi, L. Schachter, C. Sears, G. R. Werner, and R. B. Yoder, Dielectric laser accelerators, *Reviews of Modern Physics* **86**, 34 (2014).

Low-Energy-Spread Attosecond Bunching and Coherent Electron Acceleration in Dielectric Nanostructures

Uwe Niedermayer^{1,*}, Dylan S. Black^{2,†}, Kenneth J. Leedle², Yu Miao², Robert L. Byer³, and Olav Solgaard²

¹*Technische Universität Darmstadt, Institut für Teilchenbeschleunigung und Elektromagnetische Felder (TEMF), Schlossgartenstrasse 8, Darmstadt D-64289, Germany*

²*Department of Electrical Engineering, Stanford University, 350 Serra Mall, Stanford, California 94305-9505, USA*

³*Department of Applied Physics, Stanford University, 348 Via Pueblo Mall, Stanford, California 94305-4090, USA*

 (Received 7 August 2020; revised 16 November 2020; accepted 13 January 2021; published 11 February 2021)

We demonstrate a compact technique to compress electron pulses to attosecond length, while keeping the energy spread reasonably small. The technique is based on dielectric laser acceleration (DLA) in nanophotonic silicon structures. Unlike previous ballistic optical microbunching demonstrations, we use a modulator-demodulator scheme to compress phase space in the time and energy coordinates. A second DLA device on the same chip coherently accelerates these pulses by 1.5 ± 0.1 keV, which is significantly larger than the remaining energy spread of $0.88^{+0.0}_{-0.2}$ keV FWHM. We show that by linearly sweeping the phase between the two stages, the energy spectrum can be coherently moved in a periodic manner, while keeping the energy spread roughly constant. After leaving the buncher, the electron pulse is also transversely focused and can be matched into a following accelerator lattice. Thus, this setup is the prototype injector into a scalable DLA based on alternating-phase focusing (APF).

DOI: [10.1103/PhysRevApplied.15.L021002](https://doi.org/10.1103/PhysRevApplied.15.L021002)

Dielectric laser acceleration (DLA) provides the highest gradients among structure-based particle accelerators by utilizing GV/m femtosecond-laser damage thresholds of nanostructured dielectric materials. After the initial proposals [1,2], it took 50 years for the experimental DLA demonstrations to be realized [3,4]. Recently, the gradients have been further pushed to 690 MeV/m [5] and 850 MeV/m [6] for relativistic electrons and to 133 MeV/m [7] and 370 MeV/m [8] for their low-energy counterparts. While the relativistic setups use rf photoinjectors, sub-relativistic experiments require ultralow-emittance nanotip emitters [9–13] and electrostatic preaccelerators to obtain suitable electron beams. Especially at low injection energies, a beam confinement and bunching scheme [14–16] is required to scale DLAs up to megaelectronvolt energy gain for applications [17] as, e.g., ultrafast electron microscopy and diffraction [18–20], attosecond science [21], or studies of quantum effects [22,23].

When injected electron pulses are significantly longer than one DLA period, the energy spectra show the typical symmetric shoulder modulation [3,5,7,24], which can be analytically modeled using probability theory [25].

Combined with on-chip ballistic bunching, net acceleration and steering in a downstream DLA stage has recently been demonstrated [26,27]. However, the large energy spread created in the buncher stage quickly dissolves the microbunch phase coherence. Here, we demonstrate an optical modulator-demodulator that compresses first the bunch length and then the energy spread. The resulting simultaneously ultrashort and low-energy-spread electron pulses can be captured in an optical potential well and accelerated in a lossless and scalable fashion. Due to the short bunches, the phase-dependent acceleration does not create a large additional energy spread. Due to the low energy spread from the buncher, this can be observed on the spectrum. Thus, this letter presents an experimental observation of *coherent* electron acceleration on a chip.

At low injection energies from typical nanotip electron sources [9,10,13], the alternating-phase-focusing (APF) scheme [15] is well suited to confine and accelerate the beam, since it is flexible in focusing cell design and economic in field strength to acceleration-gradient conversion, which constitutes the performance bottleneck of a scalable accelerator [16]. However, as compared to constant longitudinal focusing [28], which does not provide any transverse confinement, the temporal acceptance of APF is slightly smaller. The structure presented here is an APF-based buncher, which is suitable for injection

*niedermayer@temf.tu-darmstadt.de

†These authors contributed equally to this work.

into an APF-based accelerator, due to matching of both the subfemtosecond bunch length and the low energy spread.

Attosecond pulses of subrelativistic electron beams can be created by ballistic bunching [20,26–28], i.e., a sinusoidal energy modulation ΔW is turned to bunching after reaching the longitudinal focal length of

$$L = \frac{\lambda_g \beta^2 \gamma^3 m_e c^2}{2\pi \Delta W}, \quad (1)$$

where λ_g is the period length of the modulation, β is the injection velocity in units of c , γ is the mass factor, and $m_e c^2$ is the electron rest energy. Note that if the modulation is produced by a laser of wavelength λ in a DLA grating, the Wideroe condition $\lambda_g = \beta \lambda$ has to be fulfilled, where λ_g is the grating period.

The motion toward the focus is linear in the vicinity of the fixed point(s) and strongly nonlinear elsewhere. Thus, longer dispersive drift after the modulation produces more irreversible longitudinal emittance growth. Since the modulation is essentially longitudinal focusing, according to Earnshaw's theorem [29] transverse defocusing is created. Here, we introduce a grating segment that removes these drawbacks by removing the energy modulation after a certain drift length, which is shorter than the focal length. The final longitudinal focus is then reached with a significantly smaller energy spread and transversely focused.

The phase acceptance of a scalable APF-DLA depends on the choice of the accelerator synchronous phase, i.e., in an overall design, one has to trade off temporal acceptance and the resulting average gradient. At $\pm 60^\circ$ off crest, where the gradient is half the peak gradient, the full temporal acceptance in a longitudinal focus is about 5% of an optical cycle [15], which is $\delta t = 0.33$ fs for the 1980-nm driver laser that we use here. The matched energy spread in an APF lattice is [15]

$$\delta W = m_e c^2 \beta^3 \gamma^3 \frac{c}{\hat{\beta}_L} \delta t, \quad (2)$$

where $\hat{\beta}_L$ is the longitudinal beta function at the beginning of the accelerator. The minima of $\hat{\beta}_L$ can reach down to 10–20 μm , depending on the driver amplitude. At a reference energy of 57 keV, the resulting full energy-spread acceptance is 286–572 eV and can be filled by an injector as presented here.

Numerical simulations in DLAttrack6D [30] are performed to describe the nonlinear dynamics of the experiment; however, the design follows analytic considerations. In each DLA cell, the energy gain is

$$\Delta W = q e_1 \lambda_g \cosh\left(\frac{\omega y}{\beta \gamma c}\right) \sin(\phi_P - \phi_S), \quad (3)$$

where $\omega = 2\pi c/\lambda$, $q = -e$, $\phi_P = \omega \Delta t$ is the particle phase, and ϕ_S is the synchronous phase. The laser-field amplitude is characterized by the synchronous mode coefficient e_1 , designed to be 50 MV/m. Note that $q e_1$ is the on-crest gradient in the center of the channel. During n DLA cells, the phase of an off-energy particle will slip as [30]

$$\Delta \phi_P = \frac{2\pi n}{\beta \gamma^3 m_e c^2} \Delta W. \quad (4)$$

By means of a fractional period drift of l_d , the synchronous phase can be changed as

$$\Delta \phi_S = 2\pi \frac{l_d}{\lambda_g}, \quad (5)$$

while the change in the particle phase is negligible due to the shortness of this drift. We use $l_d = \lambda_g/2$ here, i.e., a π shift of ϕ_S ; see Fig. 1 for the design of the synchronous phase and Fig. 2 for the evolution of the longitudinal phase space as computed by DLAttrack6D. The bunch profiles and energy spectra are plotted in Fig. 3. The device is designed as shown in Fig. 1, which modulates the beam first, then transports it from (b) to (f), where alternating modulation and demodulation is employed for the purpose of transverse confinement. Then the segment (f)–(g) demodulates the beam, such that only a small residual energy spread remains. This remaining small energy spread finally compresses the already prebunched beam to a minimum bunch length roughly at the beginning of the second stage (h). Simulation predicts that the bunch at point (h) is on the order of 230 as in length, with an energy spread of about 237 eV, which would be suitable for injection into an APF accelerator [cf. Eq. (2)]. We only implement one segment of 28- μm length as the second stage here, which extends up to point (i). A slightly longer second stage would reduce the output energy spread to 165 eV at point (j), but this is not implemented in the experiment.

The transverse focus of the bunched electrons is roughly in the center of stage (2). The 35- μm drift between the

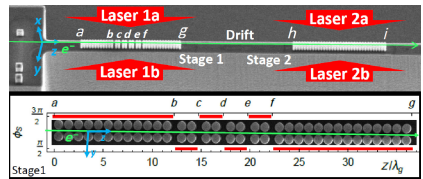


FIG. 1. A scanning-electron-microscope image of the structure. The inset shows an enlarged top view of the buncher stage with the designed distribution of the synchronous phase.

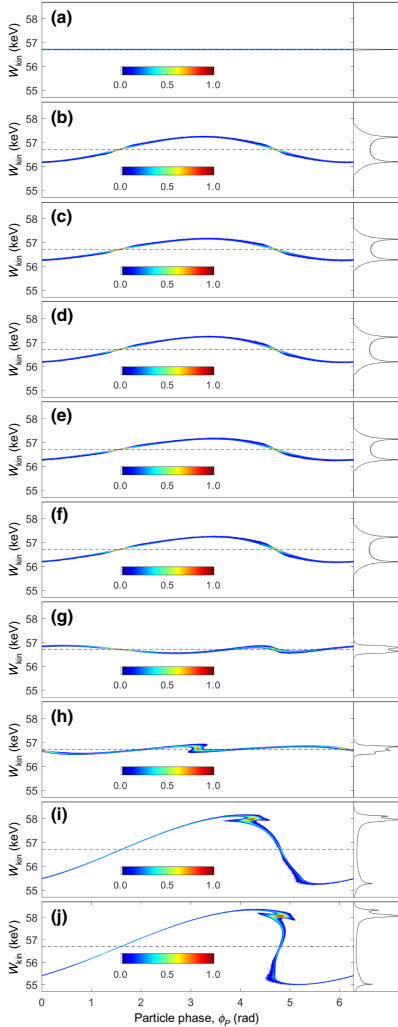


FIG. 2. The longitudinal-phase-space density in arbitrary linear units scaled to the maximum after each part of the structure (a)–(i) as indicated in Fig. 1. Panel (j) shows a slightly longer accelerator stage. The insets show the projected energy spectra.

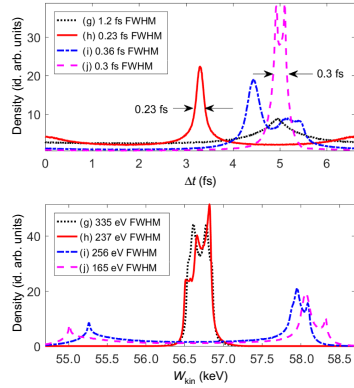


FIG. 3. The simulated bunch lengths (top panel) and energy spreads (bottom panel) in identical units. The arrival-time difference $\Delta t = \phi_p/\omega$ is plotted for one laser period $T = \lambda/c = 6.6$ fs. The energy spectrum (h) is one cell into the second stage; the difference from (g) is mainly due to clipping particles at the edge of stage (2).

stages is chosen as sufficiently large to spatially separate the laser beams (1) and (2) to avoid crosstalk. The phase difference between stages (1) and (2), i.e., the synchronous phase of stage (2), can be chosen arbitrarily. In Fig. 2, it is chosen such that a maximal energy gain of about 1.3 keV is produced by slipping over the crest. Without this phase slippage, the energy gain would be $|qe_1|L = 1.4$ keV.

The experimental setup and the 5–10- Ω -cm B-Si structures are similar to those of Ref. [26]. The elliptical pillars have dimensions of roughly $r_z = 690$ nm, $r_y = 830$ nm, and $h = 2.7$ μ m and the channel gap is 300 nm. The electron macrobunch is produced by illumination of a silicon-nanotip cathode [12] with a $\lambda = 1$ μ m laser with a roughly 300-fs pulse length. The repetition rate is 100 kHz and the electron pulse length is 730 ± 100 fs, measured by cross-correlation with the DLA drive laser. The electron beam is focused to a circular Gaussian spot of width 230 ± 30 nm rms at the beginning of the structure (a).

The outgoing electron beam is analyzed by a sector-magnet spectrometer with a roughly 100-eV point-spread function. The injection reference energy can be set in a range between 56 keV and 60 keV, with a spread less than 10 eV; more precisely, we expect about 1 V ripple at 60 keV from the power supply. The current is approximately 300 electrons per second, i.e., negligible space charge. Current fluctuations, however, prevent accurate determination of the transmission percentage through the structure.

The DLA structures are pumped with a commercial OPA system, driven by the same laser that drives the cathode. The pulse length is 605 ± 5 fs intensity FWHM at $\lambda = 1980$ nm. The four DLA drive beams (see Fig. 1) are focused to a $1/e^2$ intensity radius of $22 \pm 1 \mu\text{m}$ and provide up to approximately 50 nJ each. The phase of each branch is differentially controlled by piezo delay stages with a stability better than $\lambda/10$ over short time scales (< 1 s). The total averaging time per frame is limited by larger slow drifts.

Both DLA stages are operated in the symmetric drive configuration, i.e., zero relative phase between (a) and (b) sides. The injection phase of the electron into the second stage is controlled by symmetrically delaying stage (2) versus stage (1). The first stage does not produce a net energy gain, so accurate measurement of e_1 is only possible in stage (2) and we have to assume the same power level at stage (1). Together with the phase error (1a) versus (1b), this is the main source of driver errors. The amplitude measured via the energy gain in stage (2) is also used in the comparative simulations.

Two example experimental spectra are shown in Fig. 4, where the electrons are coherently accelerated or decelerated depending on the stage-(2) injection phase. The increase of the transverse spot size is small, since the captured electrons spend roughly the same time on focusing and defocusing synchronous phases. The energy gain of the bunch center is determined by the difference between the edge of the spectrum and the injection energy, minus

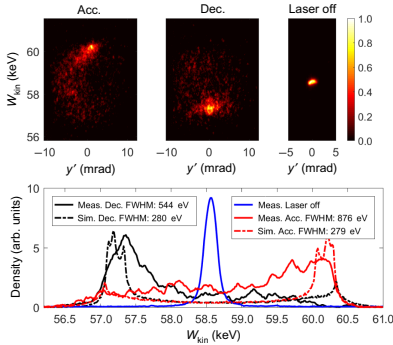


FIG. 4. Top panel: the data as recorded on the microchannel plate (MCP) for different synchronous phases in stage (2). The speckles are electrons that are not captured but that still make it to the MCP. Bottom panel: a comparison of the respective spectra to simulation. The maximum energy gain of the bunch is 1.5 ± 0.1 keV with a spread of $0.88^{+0.0}_{-0.2}$ keV FWHM.

half the (simulated) energy spread minus half the point-spread function. The resulting 1.5 ± 0.1 keV indicates a slight overpower of $e_1 = 56 \pm 5$ MV/m. The energy spreads are $0.88^{+0.0}_{-0.2}$ keV and $0.54^{+0.0}_{-0.2}$ keV FWHM at maximum acceleration and deceleration, respectively.

The main measurement error is the spectrometer point-spread function, which shows a broader spectrum on the screen than in reality. This is visible in Fig. 4 in the laser-off curve, which exhibits a close-to-Gaussian shape of about 0.2 keV FWHM. However, the energy spread is still larger than predicted by the simulations after accounting for the spectrometer point-spread function. This excess energy spread is caused primarily by three-dimensional (3D) geometry effects such as the finite height of the pillars and the mesa structure, leading to a possibly strong $e_1(x)$ dependency (see Ref. [16]). Consequently, there can be underbunching, overbunching, and deflection in the same measurement.

A complete phase-sweep measurement is shown in Fig. 5 with $e_1 = 53 \pm 5$ MV/m, close to the design gradient. A clear sinusoidal spectral dependence is visible, i.e., the energy gain can be continuously selected by the inter-stage phase. Again, the source for the excess energy spread is the vertical spread of e_1 and, due to the lower energy

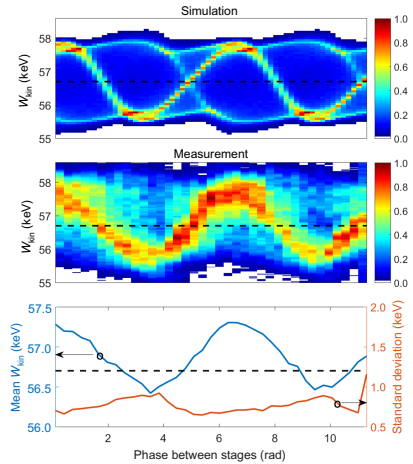


FIG. 5. The sinusoidal spectrogram shows excellent agreement with simulation, albeit with a higher energy spread, which can be attributed to a vertical spread of $e_1(x)$ and the spectrometer point-spread function. The bottom panel shows the mean and standard deviation of the data. The energy gain of the bunch is observable in the spectrograms (center) as 1.3 ± 0.1 keV.

gain, there is significant background from nontrapped electrons. The background and the point-spread function are the reasons why the simulated rather than the measured energy spread is used to calculate the energy gain in the experiment and the accompanying simulations. Figure 5 (bottom panel) shows the mean and standard deviation of the entire spectrum (including the decelerated tail) for each phase. The tail causes the mean to be 0.6 keV above the injection energy as compared to the 1.3-keV bunch-energy gain near the edge of the spectrum. Crucially, the standard deviation stays constant at 800 ± 200 eV, with a slight increase at maximum deceleration, where some of the electrons are lost.

Together with the streaking experiment presented in Ref. [26], we are now able to coherently move the electron beam in both dimensions (energy and deflection) on the microchannel plate (MCP) screen by changing the relative phase of the two stages. The observable small-angle spread indicates that the beam is not defocused. For streaking, it is advantageous to have a shorter second stage, which reduces errors due to phase slippage. For acceleration, a longer second stage [cf. Fig. 2(j)] leads to higher energy gain and thus better relative resolution. Moreover, after slipping over the crest, the energy spread is additionally compressed at the expense of an increased bunch length. The bunch length can be inferred from the measured energy spectra via comparison to simulations [27], which we do not attempt here due to the large uncertainty for that measurement with our parameters.

In conclusion, we demonstrate small-energy-spread optical bunching in a DLA, based on a modulation-demodulation APF scheme. The resulting subfemtosecond electron pulses are injected into a second stage for coherent acceleration. Good agreement with simulation results is achieved, with the increased experimental energy spread accounted for by 3D field nonuniformity. This nonuniformity can be quite strong but can also be exploited to confine the beam vertically, enabling a scalable APF DLA accelerator [16]. Preliminary 3D tracking simulations indicate that APF buncher structures with vertical confinement would achieve similar energy spreads as predicted in the two-dimensional simulations presented here.

ACKNOWLEDGMENTS

This work is funded by the Gordon and Betty Moore Foundation (Grant No. GBMF4744).

- [1] K. Shimoda, Proposal for an electron accelerator using an optical maser, *Appl. Opt.* **1**, 33 (1962).
- [2] A. Lohmann, Electron acceleration by light waves, IBM Technical Note 5, 169 (1962).
- [3] E. A. Peralta, K. Soong, R. J. England, E. R. Colby, Z. Wu, B. Montazeri, C. McGuinness, J. McNeur, K. J. Leedle,

- D. Walz, E. B. Sozer, B. Cowan, B. Schwartz, G. Travish, and R. L. Byer, Demonstration of electron acceleration in a laser-driven dielectric microstructure, *Nature* **503**, 91 (2013).
- [4] J. Breuer and P. Hommelhoff, Dielectric laser acceleration of 28 keV electrons with the inverse Smith-Purcell effect, *Nucl. Instrum. Methods Phys. Res. Sec. A: Accelerators, Spectrometers, Detectors Associated Equipment* **740**, 114 (2013).
- [5] K. P. Wootton, Z. Wu, B. M. Cowan, A. Hanuka, I. V. Makasyuk, E. A. Peralta, K. Soong, R. L. Byer, and R. J. England, Demonstration of acceleration of relativistic electrons at a dielectric microstructure using femtosecond laser pulses, *Opt. Lett.* **41**, 2696 (2016).
- [6] D. Cesar, S. Custodio, J. Maxson, P. Musumeci, X. Shen, E. Threlkeld, R. J. England, A. Hanuka, I. V. Makasyuk, E. A. Peralta, K. P. Wootton, and Z. Wu, High-field nonlinear optical response and phase control in a dielectric laser accelerator, *Commun. Phys.* **1**, 1 (2018).
- [7] P. Yousefi, N. Schönenberger, J. Mcneur, M. Kozák, U. Niedermayer, and P. Hommelhoff, Dielectric laser electron acceleration in a dual pillar grating with a distributed Bragg reflector, *Opt. Lett.* **44**, 1520 (2019).
- [8] K. J. Leedle, R. Fabian Pease, R. L. Byer, and J. S. Harris, Laser acceleration and deflection of 963 keV electrons with a silicon dielectric structure, *Optica* **2**, 158 (2015).
- [9] D. Ehberger, J. Hammer, M. Eisele, M. Krüger, J. Noe, A. Högele, and P. Hommelhoff, Highly Coherent Electron Beam from a Laser-Triggered Tungsten Needle Tip, *Phys. Rev. Lett.* **114**, 227601 (2015).
- [10] A. Feist, N. Bach, N. Rubiano da Silva, T. Danz, M. Möller, K. E. Priebe, T. Domröse, J. G.atzmann, S. Rost, J. Schauss, S. Strauch, R. Bormann, M. Sivis, S. Schäfer, and C. Ropers, Ultrafast transmission electron microscopy using a laser-driven field emitter: Femtosecond resolution with a high coherence electron beam, *Ultramicroscopy* **176**, 63 (2017).
- [11] A. Tafel, S. Meier, J. Ristein, and P. Hommelhoff, Femtosecond Laser-Induced Electron Emission from Nanodiamond-Coated Tungsten Needle Tips, *Phys. Rev. Lett.* **123**, 146802 (2019).
- [12] Andrew Ceballos, Ph.D. thesis, Stanford University, 2019.
- [13] T. Hirano, K. E. Urbanek, A. C. Ceballos, D. S. Black, Y. Miao, R. Joel England, R. L. Byer, and K. J. Leedle, A compact electron source for the dielectric laser accelerator, *Appl. Phys. Lett.* **116**, 161106 (2020).
- [14] B. Naranjo, A. Valloni, S. Putterman, and J. B. Rosenzweig, Stable Charged-Particle Acceleration and Focusing in a Laser Accelerator Using Spatial Harmonics, *Phys. Rev. Lett.* **109**, 164803 (2012).
- [15] U. Niedermayer, T. Egenolf, O. Boine-Frankenheim, and P. Hommelhoff, Alternating-Phase Focusing for Dielectric-Laser Acceleration, *Phys. Rev. Lett.* **121**, 214801 (2018).
- [16] U. Niedermayer, T. Egenolf, and O. Boine-Frankenheim, Three-dimensional Alternating-Phase Focusing for Dielectric-Laser Electron Accelerators, *Phys. Rev. Lett.* **125**, 164801 (2020).
- [17] R. J. England *et al.*, Dielectric laser accelerators, *Rev. Mod. Phys.* **86**, 34 (2014).
- [18] A. H. Zewail and J. M. Thomas, *4D Electron Microscopy* (Imperial College Press, Weinheim, 2010).

- [19] R. F. Egerton, Outrun radiation damage with electrons?, *Adv. Struct. Chem. Imaging* **1**, 5 (2015).
- [20] Y. Morimoto and P. Baum, Diffraction and microscopy with attosecond electron pulse trains, *Nat. Phys.* **14**, 252 (2018).
- [21] F. Krausz and M. Ivanov, Attosecond physics, *Rev. Mod. Phys.* **81**, 163 (2009).
- [22] E. Jones, M. Becker, J. Luiten, and H. Batelaan, Laser control of electron matter waves, *Laser Photonics Rev.* **10**, 214 (2016).
- [23] G. M. Vanacore, I. Madan, G. Berruto, K. Wang, E. Pomarico, R. J. Lamb, D. McGrouther, I. Kaminer, B. Barwick, F. J. García De Abajo, and F. Carbone, Attosecond coherent control of free-electron wave functions using semi-infinite light fields, *Nat. Commun.* **9**, 2694 (2018).
- [24] N. V. Sapra, K. Y. Yang, D. Verduyck, K. J. Leedle, D. S. Black, R. J. England, L. Su, R. Trivedi, Y. Miao, O. Solgaard, R. L. Byer, and J. Vuckovic, On-chip integrated laser-driven particle accelerator, *Science* **367**, 79 (2020).
- [25] T. Egenolf and U. Niedermayer, Analytical energy spectra and wake effects for relativistic dielectric laser accelerators, *J. Phys.: Conf. Ser.* **1596**, 012017 (2020).
- [26] D. S. Black, U. Niedermayer, Y. Miao, Z. Zhao, O. Solgaard, R. L. Byer, and K. J. Leedle, Net Acceleration and Direct Measurement of Attosecond Electron Pulses in a Silicon Dielectric Laser Accelerator, *Phys. Rev. Lett.* **123**, 264802 (2019).
- [27] N. Schönenberger, A. Mittelbach, P. Yousefi, J. McNeur, U. Niedermayer, and P. Hommelhoff, Generation and Characterization of Attosecond Microbunched Electron Pulse Trains via Dielectric Laser Acceleration, *Phys. Rev. Lett.* **123**, 264803 (2019).
- [28] U. Niedermayer, O. Boine-Frankenheim, and T. Egenolf, Designing a dielectric laser accelerator on a chip, *J. Phys.: Conf. Ser.* **874**, 012041 (2017).
- [29] S. Earnshaw, On the nature of the molecular forces which regulate the constitution of the luminiferous ether, *Trans. Camb. Phil. Soc.* **7**, 97 (1842).
- [30] U. Niedermayer, T. Egenolf, and O. Boine-Frankenheim, Beam dynamics analysis of dielectric laser acceleration using a fast 6D tracking scheme, *Phys. Rev. Accel. Beams* **20**, 111302 (2017).

Design of a Scalable Integrated Nanophotonic Electron Accelerator on a Chip

Uwe Niedermayer[Ⓞ],^{1,*} Jan Lautenschläger[Ⓞ],¹ Thilo Egenolf[Ⓞ],² and Oliver Boine-Frankenheim[Ⓞ]^{1,2}

¹*Institut für Teilchenbeschleunigung und Elektromagnetische Felder, Technische Universität Darmstadt, Schlossgartenstrasse 8, 64289 Darmstadt, Germany*

²*GSI Helmholtzzentrum für Schwerionenforschung GmbH, Planckstrasse 1, 64291 Darmstadt, Germany*



(Received 9 June 2021; accepted 21 July 2021; published 12 August 2021)

A simple way of implementing a scalable laser-driven nanophotonic electron accelerator on a chip is presented. The design requires only a single incident laser pulse and can be fabricated straightforwardly on commercial silicon-on-insulator wafers. We investigate the low-energy regime of tabletop electron microscopes where the silicon structures safely allow peak gradients of about 150 MeV/m. By means of a three-dimensional alternating-phase-focusing scheme, we obtain about half of the peak gradient as the average gradient with six-dimensional confinement and full-length scalability. The structures are completely designed within the device layer of the wafer and can be arranged in stages. We choose the stages as energy doublers and outline how errors in the handshake between the stages can be corrected by on-chip steerers. Since the electron pulse length in the attosecond realm is preserved, our chip is the ideal energy booster for ultrafast-electron-diffraction machines, opening the megaelectronvolt scale on tabletop setups.

DOI: 10.1103/PhysRevApplied.16.024022

I. INTRODUCTION

Dielectric laser accelerators (DLAs) were proposed as long ago as 1962 [1,2]. However, experimental demonstrations of the high acceleration gradients due to short pulses and high material damage thresholds came 50 years later [3,4] by means of modern femtosecond lasers and lithographic nanofabrication. Recent advances have further pushed the peak gradients in nanophotonic structures for relativistic electrons to 690 MeV/m [5] and 850 MeV/m [6] and to 133 MeV/m [7] and 370 MeV/m [8] for their subrelativistic counterparts. While DLAs in high-energy accelerator facilities are an emerging subject of study [9,10], there are already many imaginable applications of subrelativistic DLAs in electron microscopy and diffraction [11–13]. Especially an electron diffractometer [14,15] could be equipped with a DLA to allow working at significantly higher energy, while the entire setup, including the laser, would still be tabletop-sized. Higher energy in electron diffraction translates to higher spatial resolution [16] and is nowadays restricted to extremely large electrostatic setups or bulky rf systems with issues of their own, e.g., jitter [17].

To enable scalable DLAs for these use cases, the setup has to be made simple and robust in operation. The amount of external equipment has to be reduced as much as possible. For example, on-chip waveguides [18,19], which might increase the efficiency of an already-working accelerator, are also avoided here for robustness reasons. In the long run, we imagine a setup and a timeline oriented on the history of the integrated circuit, which first needed much external equipment but nowadays is a stand-alone device working with nearly 100% reliability. Pursuing this goal, we deem robustness and scalability as more critical than efficiency or the number of features and thus construct the accelerator according to the beam dynamics necessities to minimize beam losses for given injector parameters.

The accelerating near fields in a DLA decay exponentially from the grating surface, and thus such accelerators have only tiny (subwavelength) apertures. Keeping the electrons in this aperture cannot be achieved by magnets, since tremendous focusing gradients on the order of several million teslas per meter would be required [20–22]. A solution to this problem is to use the evanescent fields from the nanophotonic structures themselves and arrange them such that they keep the electron beam in the channel without external focusing being required. This is achieved by the alternating-phase-focusing (APF) technique [21,23], which presents a design recipe for the chip as a composition of individual cells, to which periodic boundary conditions can be applied in a good approximation.

*niedermayer@temf.tu-darmstadt.de

Published by the American Physical Society under the terms of the Creative Commons Attribution 4.0 International license. Further distribution of this work must maintain attribution to the author(s) and the published article's title, journal citation, and DOI.

To use most of the small physical aperture (i.e., to maximize the dynamic aperture), the three-dimensional- (3D) APF scheme [23] requires the synchronous electric field to be symmetric in both transverse planes. When driven with two lasers from both lateral sides, this results in a rather strict requirement for the two lasers to have exactly the same phase, as otherwise the working point is laterally dislocated from the channel center. Moreover, dual lateral illumination requires a significant amount of experimental complexity, especially when an independently driven on-chip buncher is used [24,25].

In this paper we present how the symmetric fields required for a scalable APF DLA can be produced in a simple manner, entirely encoded in the chip. The chip itself can be fabricated by a standard process of nanophotonics—namely, etching of solely the top layer of commercially available silicon-on-insulator (SOI) wafers by electron-beam lithography and/or photolithography. By shining the laser from the top, the partial reflection from the silicon substrate is used to create a symmetric quadrupolar synchronous field to enable a stable 3D lattice design [23] on an asymmetrically (single pulse) illuminated chip.

Additionally to the structure and accelerator lattice design, we present computationally heavy full 3D start-to-end simulations of the setup, exposing the imperfections of the structure, which eventually lead to emittance increase and beam losses. For these heavy simulations we use CST Particle Studio [26] and we compare the results with those of lightweight simulations in DLATrack6D [27].

We find that due to the imperfect vertical symmetry, a deflection force is exerted, which can be partially compensated by the structure design. The remaining vertical deflection is sufficiently small in a single-stage setup. For a multistage setup, it can be compensated by on-chip steerers located between the stages. Multiple stages can be constructed on a single SOI chip, enabling full scalability. Because of the lithographic fabrication process, the lateral and longitudinal alignment is perfect. Vertical misalignment can be corrected by electrostatic deflectors, which can be fabricated as silicon “bridges” on a silicon-on-glass wafer that is mounted from the top. The required steering voltages can be connected by pads on the device layer of the SOI wafer far from the laser spot.

This paper is organized as follows: Sec. II presents the top-illuminated SOI structures that are crucial for the entire setup and explains how they are combined into a scalable accelerator using the 3D-APF segmentation technique introduced in Ref. [23]. This procedure is performed and a full start-to-end simulation of the resulting energy doubler for electron microscopes is shown in Sec. III. In Sec. IV, we show how the issue of a coherent deflection force, which leads to partial beam loss, can be overcome. Section V outlines a full integration of the setup, including staging of multiple energy doublers and beam steering

between the stages. Finally, Sec. VI concludes with an outlook of controlling the remaining few external parameters by a digital-twin model and enabling ultrafast electron diffraction on the megaelectronvolt level with tabletop setups based on the chips introduced here.

II. TOP-ILLUMINATED 3D-APF STRUCTURES ON SOI WAFERS

The principle of the setup is shown in Fig. 1. A laser pulse of wavelength $\lambda = 2 \mu\text{m}$ impinges as a plane wave from the top (i.e., in the negative x direction), with the polarization in the z direction. The structures are quasi-periodic, with period lengths $\lambda_g = \beta\lambda$, where $\beta = v/c$ is the synchronous electron velocity. The cells are arranged in APF-type segments [21], acting as accelerators and thick focusing lenses. As in many other photonic devices produced on SOI wafers, it is crucial here that the oxide layer (brown in Fig. 1) has a refractive index $n_{\text{SiO}_2} = 1.45$ [28] that differs as much as possible from that in the silicon device layer and substrate ($n_{\text{Si}} = 3.41$ [28]). The former is important for the structures to stand alone and produce a vertically symmetric field as if the pillars were free-floating, and the latter is necessary for a high reflection factor. Throughout this work we use a commercially available SOI wafer made of a $700\text{-}\mu\text{m}$ silicon substrate, a $3\text{-}\mu\text{m}$ buried oxide layer, and a 220-nm silicon device layer [29]. At higher energy, thicker device layers and wider channels would also be feasible, allowing larger emittances and higher particle throughput.

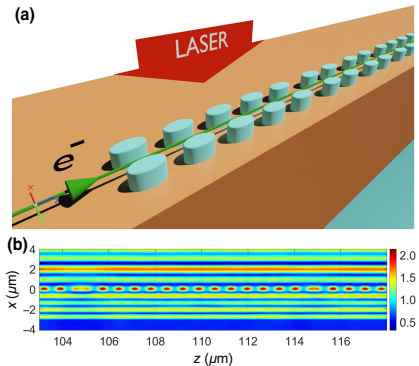


FIG. 1. Acceleration structures created by etching only the device layer of a SOI wafer (a) and longitudinal electric field magnitude normalized to the incident laser field strength in a longitudinal cut ($y = 0$ plane) (b).

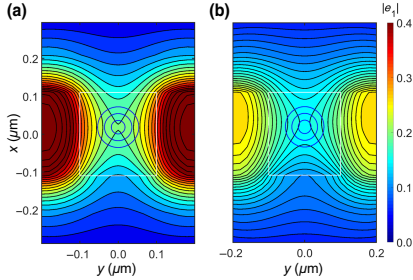


FIG. 2. Normalized synchronous longitudinal electric field distribution for $\beta = 0.31$ (a) and uncorrected $\beta = 0.5$ (b). The white box indicates the beam channel (note the refraction of the potential lines at the bottom). The blue circles indicate 1σ , 2σ , and 3σ of the beam size at injection.

The structure cells are characterized by the first spatial harmonic of the longitudinal electric field

$$e_1(x, y) = \frac{1}{\lambda_g} \int_{-\lambda_g/2}^{\lambda_g/2} E_z(x, y, z) e^{2\pi iz/\lambda_g} dz, \quad (1)$$

where $E_z(x, y, z)$ is the electric field in the frequency domain, which we however determine from a time-domain simulation and on-the-fly Fourier transform. This is particularly efficient, since the speed of explicit time-domain simulation is exploited, while not saving the entire time dependence of the three-dimensional field. The higher (nonsynchronous) spatial harmonics can be ignored [21]. By our determining e_1 in each cell and fixing the synchronous phase ϕ_s as $\pm 60^\circ$ off-crest, the acceleration ramp and the 3D focusing channel are designed [23] such that half the peak gradient is available as the average gradient within one segment.

The structures shown in Fig. 1 locally create a quadrupolar distribution (see Fig. 2) as $e_1(x, y) = e_{10} \cosh(k_y y) \cos(k_x x)$, which refers to the “counterphase” APF scheme. Since we deal only with this scheme throughout this paper, we take k_x and k_y as purely real. From Ref. [23], the identification $k_x = \text{Re } k_x$ and $k_y = \text{Im } k_y$ has to be made, yielding $k_x^2 - k_y^2 + \omega^2/(\beta\gamma c)^2 = 0$, with $\omega = 2\pi c/\lambda$ being the laser angular frequency.

III. DESIGN OF AN ENERGY DOUBLER FOR ELECTRON MICROSCOPES

For the design of a scalable accelerator, the fields as shown in Fig. 1 (bottom) can be calculated for each individual cell of length λ_g , where periodic boundary conditions are used in the longitudinal direction and open boundary conditions are used in the x direction, in which

the z -polarized laser beam travels. The wave impedance of the open boundary condition at the bottom is matched to that of silicon. Because the wafer substrate is much thicker than the laser pulse length, reflections at the very bottom (which also has high surface roughness) can be neglected. Laterally, at $y = 0$ and $y = 6 \mu\text{m}$, magnetic boundary (symmetry) conditions are used. The magnitude of the synchronous harmonic is plotted in Fig. 2 for two different beam velocities. As desired, the structure cells produce a quadrupolelike field between the pillars. To enable the design procedure as outlined in Ref. [23], the vertical drift of the working point $x_0(\beta)$ needs to be compensated. Insignificant compensation of this drift results in a coherent oscillation of the beam, leading to emittance increase and beam loss.

The periods are elliptic cylinders of the device-layer height $h = 220 \text{ nm}$ and radii $r_y = 100 \text{ nm}$ and variable r_z . By changing $r_z = r_{z0} + \Delta r_z$, one can change the working-point position exactly such that the drift with β is compensated:

$$\Delta x_0 = \frac{\partial x_0}{\partial r_z} \Delta r_z + \frac{\partial x_0}{\partial \beta} \Delta \beta = 0. \quad (2)$$

Since the drift of the working point is not too large and continuously depends on β and r_z , we can linearize this numerically determined dependency and obtain $r_z = r_{z0} - \xi(\beta - \beta_0)$, with $\xi = \partial_{\beta} x_0 / \partial_{r_z} x_0 = -1.7 \mu\text{m}$ at a linearization point $\beta_0 = 0.42$ and $r_{z0} = 0.35 \mu\text{m}$. A comparison of the corrected and uncorrected single-cell parameters is shown in Fig. 3. Moreover, this plot also contains a comparison between sharp top edges and realistically rounded top edges. As one can see, the effect in e_1 is small and the shift in x_0 is constant (i.e., correctable).

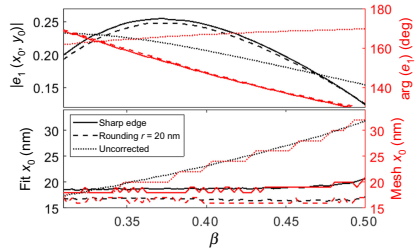


FIG. 3. Synchronous electric field and position of the working point x_0 versus β . The solid lines show the corrected [Eq. (2)] cells, as compared with the uncorrected ones (dotted lines). The dashed line shows the effect of applying a realistic rounding (20 nm) to the top edge of the elliptical cylinders. The working-point position x_0 is determined in two well-agreeing ways: taking the numerical maximum of the data (mesh x_0) and fitting a parabola to the data (fit x_0).

We design an accelerator with injection energy $W_{\text{inj}} = 26.478$ keV ($\beta_{\text{inj}} = 0.31$), which doubles the energy to 53 keV, or $\beta = 0.4233$. Continuation to triple energy ($\beta = 0.5$) is possible straightforwardly; however, simulation of this entire setup currently exceeds our computational capabilities. The designed stage has a length of $381 \mu\text{m}$ and an average gradient of 69.3 MeV/m at a design incident laser field strength E_L of 600 MV/m. To stay below the damage threshold of silicon (the damage threshold for SiO_2 is significantly higher), the laser pulse needs to be in the subpicosecond realm. This can be achieved by pulse-front tilting (PFT) [30–32], where the phase fronts and the polarization remain parallel to the wafer. However, since the electron velocity increases, the PFT angle $\alpha = \arctan(1/\beta)$ has to decrease accordingly. Since our structure has a finite length, the required curved pulse front can be approximated by one linear PFT per stage, which however requires a finite (minimum) pulse length [23]. We find the optimum $\alpha = 69.8^\circ$ and a pulse length of 430 fs, which keeps the local laser amplitude above 95% of the maximum; see Fig. 4. The pulse width is chosen here to be $\sigma_z = 6$ mm, and σ_y should be larger than several tens of micrometers for practical alignment purposes. The fluence of this pulse is about 200 J/m^2 , which is almost an order of magnitude below the damage threshold of silicon [33,34].

To match the needs of cylindrical symmetric electron-microscope setups, the beam spot at the input is designed

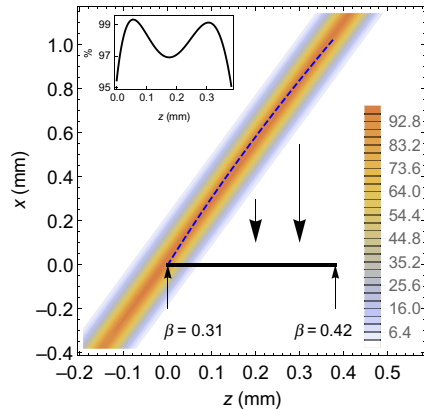


FIG. 4. Electric field amplitude as a percentage of the maximum for the tilted laser pulse. The accelerator structure is indicated by the thick black line and the phase fronts are parallel to it. The dashed blue line describes the position in the laser pulse that is synchronous with an electron in the accelerator. The inset shows the laser amplitude on this curve.

to be circular ($\hat{\beta}_x = \hat{\beta}_y = 32 \mu\text{m}$). Moreover, by use of half segments, the beam can be made uncorrelated at the input ($\hat{\alpha} = 0$) and output ($\hat{\alpha} \approx 0$). From a DLAttrack6D [27] simplified simulation, we expect a Gaussian beam with geometric emittances $\varepsilon_x = \varepsilon_y = 10$ pm and bunch length $\sigma_z = 10$ nm (matched energy and angle spreads) to have an energy-doubling throughput of about 50%. In modern electron microscopes such low emittances are available [35] and the bunching can be achieved by on-chip bunchers [25]. By further lowering of the emittances, the throughput of the accelerator structures can be increased toward 100%. Animations of the DLAttrack6D simulations are available in Supplemental Material [36].

Before running a complete 3D tracking simulation of the entire setup, we first calculate the fields in the entire setup (approximately 350×10^6 hexahedral mesh cells) and retrieve the channel position and the focusing wave numbers k_x and k_y , as well as e_1 from them. As seen in Fig. 5, the agreement with the calculation for the individual cells with use of periodic boundary conditions is excellent. At the APF phase jumps, an unavoidable Gibbs phenomenon is however visible, which among other effects might degrade the throughput.

The designed envelopes as well as the tracking results are shown in Figs. 6 and 7. In the bottom plots, the acceleration ramp and a loss comparison of the tracking in the full fields and in DLAttrack6D are shown. The envelopes relate to the lattice functions as $a_{x,y,\Delta z} = (\hat{\beta}_{x,y,z} \varepsilon_{x,y,z})^{1/2}$ and $a_{x',y',\Delta z'} = (\hat{\gamma}_{x,y,z} \varepsilon_{x,y,z})^{1/2}$, where the

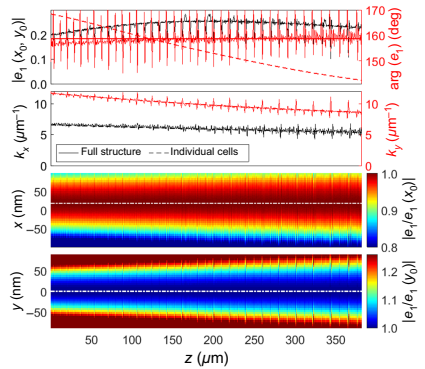


FIG. 5. Comparison of the field quality for single cells with periodic boundaries and the whole structure. The phase drift is corrected by our displacing the pillars within the cell [23] and thus follows a straight line. The two bottom plots show the channel position, which is almost perfectly straight at $x_0 = 18$ nm and $y_0 = 0$.

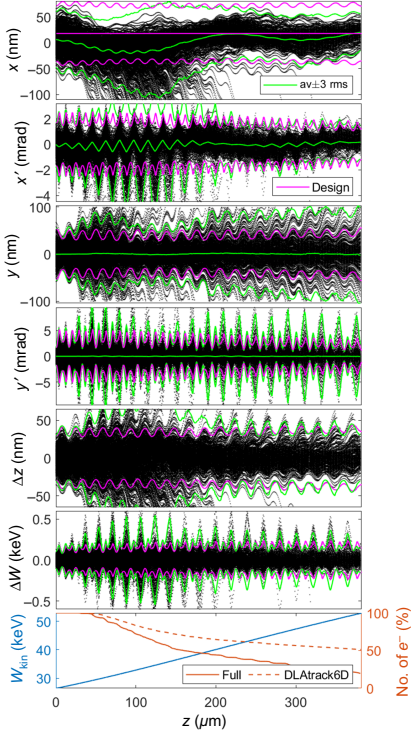


FIG. 6. Phase-space evolution in the elliptical-cell structure without a correction field. The black dots show individual particle positions and the lines show the averages and the averages with 3 times the rms value added or subtracted. Magenta is for the design, whereas green is for the statistics obtained from the black-dot data. The slight off-axis injection increases the throughput to 19.8%, as compared with the very poor transmission for on-axis injection.

geometric emittances undergo adiabatic damping as $\varepsilon = \varepsilon_0 \beta_0 \gamma_0 / \beta \gamma$ and the longitudinal emittance is obtained from the initial bunch length as $\varepsilon_z = \sigma_z^2 / \beta_z$. The matched energy spread reads $\Delta W = mc^2 \beta^2 \gamma^3 a_{\Delta z}$. The same initial six-dimensional bunch distributions are used in the fast DLAttrack6D simulation and in the full-field tracking simulation, where the bunch is released at $z = 0$ and appropriate time to hit the synchronous phase. In both simulations the particles are treated independently; we choose 1000 (for unbunched 10 000) electrons to obtain good statistics. In

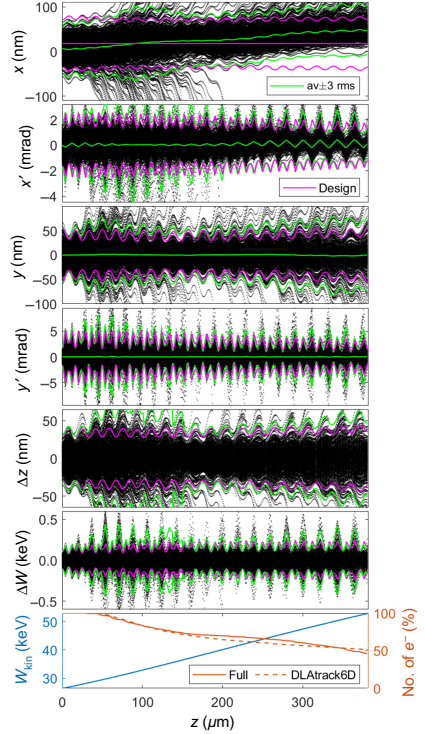


FIG. 7. Phase-space evolution in the elliptical-cell structure with 14 mT correction field. The black dots show individual particle positions and the lines show the averages and the averages with 3 times the rms value added or subtracted. Magenta is for the design, whereas green is for the statistics obtained from the black-dot data. The throughput can be increased to 46.1%, almost as high as anticipated by the fast DLAttrack6D simulation. For small particle amplitudes, the DLAttrack6D simulation produces the same envelopes as the design [21,23] (not shown here).

reality there is only one electron per bucket at most, however there are many buckets per pulse and a high pulse repetition rate. This renders collective effects entirely irrelevant for subrelativistic DLAs, unlike in relativistic DLAs, where collective effects were recently investigated by an extension of DLAttrack6D [37].

As seen in the top panel in Fig. 6, the electron beam experiences a strong deflection force in the negative x direction. After a length of 100 μm and some beam loss,

the focusing is however able to catch the beam and move it back to the designed trajectory. Coherent motion due to mismatch in the x direction might also lead to emittance increase and beam loss in the y or z direction, since the aperture-filling high particle amplitudes probe the coupled nonlinearities of the fields [27].

The origin of the deflecting force is the gradient of the phase across x , i.e., $\nabla \arg e_1(x, y)$, leading to a deflection ramp similar to the acceleration ramp. Following Eq. (12) in Ref. [27], the transverse acceleration can be written as

$$x'' = -\frac{qE_L \lambda_g}{m\gamma \beta^2 c^2} |e_1| \cos \phi_s \partial_x \arg(e_1)|_{x_0}, \quad (3)$$

where $\partial_x \arg(e_1)|_{x_0}$ is the linearized phase gradient on the reference beam axis. The resulting effect is similar to that of a homogeneous magnetic field, which leads to a deflection $x'' = qB_y/m\gamma\beta c$. Therefore, with $T = \lambda/c$, the magnetic field required to correct for the deflection reads

$$B_{\text{corr}} = E_L T |e_1| \cos \phi_s \partial_x \arg(e_1)|_{x_0}, \quad (4)$$

which is only implicitly dependent on the beam velocity via $|e_1| \partial_x \arg(e_1)|_{x_0}$. Figure 8 shows the required correction field as a function of β . The inset shows the worst case for injection at $\beta = 0.31$, where the phase change across the beam size is roughly 2° , resulting in a required correction field of more than 100 mT.

A correcting external magnetic field cannot however be applied to each cell as would be required; it can be applied only homogeneously over the entire chip. Therefore, the correction needs to be a compromise between

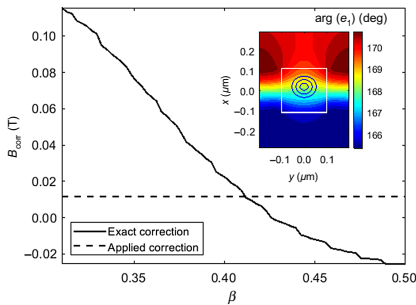


FIG. 8. Required correction field due to the phase gradient. The inset shows the phase distribution across the channel at the injection energy ($\beta = 0.31$). Since the correction field can be applied only in a homogeneous manner, a compromise has to be found, which is $B = 14$ mT, and a slightly displaced injection uses the focusing channel for further correction.

the different values along the channel. Additionally, an off-axis injection can be used to counteract the initially strong deflection. An example of doing this is shown in Fig. 7, where a 14-mT field is applied and the injection is chosen at $x_{0,\text{inj}} = 6$ nm, 12 nm below the design value. With this, the throughput is more than doubled from 19.8% to 46.1%, which is however still slightly lower than the prediction by DLTrack6D of 50.8% disregarding the deflection.

IV. COMPROMISE BETWEEN STRAIGHT CHANNEL AND LOW COHERENT DEFLECTION

As seen in Fig. 8, the coherent deflection and the required correction field are strongest at the lowest beam velocity, where also most of the channel correction is applied. However, modification of the ellipse-semiaxis radii does not lead to a sufficient reduction. Especially at low energy, the phase gradient can rather be reduced by reshaping the pillars as rectangles ($\Delta Y = 440$ nm by $\Delta Z = 460$ nm and $R = 40$ nm corner rounding for fabrication feasibility), reducing the phase gradient to about a tenth of the value for the elliptical pillars at injection, which is plotted in Fig. 9. In the plot we also investigate lateral grounding traces to remove lost electrons from the pillars. The lateral grounding traces even further reduce the

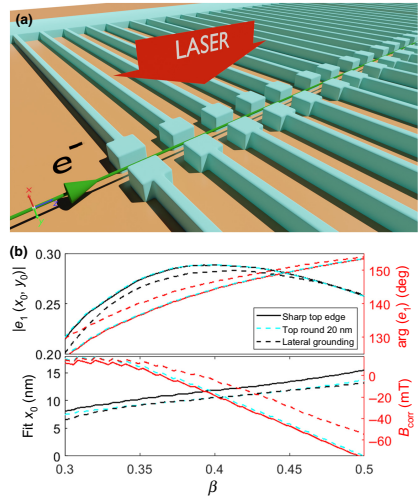


FIG. 9. Rectangular acceleration structures with lateral grounding (a) and velocity scan (b). The sharp-top-edge structures without grounding are compared with ones with lateral grounding and with top rounding.

phase gradient–induced deflection. Moreover, in Fig. 9 we once again verify that the effect of a realistic top rounding of 20 nm is small. In the full simulation that follows, we keep nongrounded structures with sharp top edges for simplicity.

The lattice is redesigned in the same way as for the elliptical structures. The working-point drift for the rectangular structures is only 5 nm over the entire length of the energy-doubler structure. Correction of this slight drift would lead to an increase in deflection force and is therefore not attempted. In the field-flatness analysis shown in Fig. 10 this drift is hardly visible. Because of the higher ϵ_1 , the length is reduced to 344 μm (average gradient 77.7 MeV/m) and the throughput predicted by DLAttrack6D is 57.3%.

The full simulation as shown in Fig. 11 results in a throughput of 44.6%, without any correction magnetic field. Further optimization can be done by slightly changing the injection angle x'_0 , injection position x_0 , and injection phase. Moreover, another tuning parameter is the laser amplitude, which gives the highest throughput at about 3% above the nominal value (i.e., 618 MV/m). Increasing the laser amplitude does not lead to higher output energy since the ramp is hard-coded in the lattice. However, it leads to a steeper potential well and thus to a smaller but hotter beam. Since this however appears nonuniformly, it leads to a “sweet spot” being close to the design incident field.

In the simulations here, we assume a bunched beam, which can be readily created by APF buncher structures [25]. These bunchers can also be created with 3D confinement on the same SOI chip. Depending on how “adiabatic” the buncher is designed to be (i.e., how long it is in the end), a bunching efficacy of 50% can be achieved

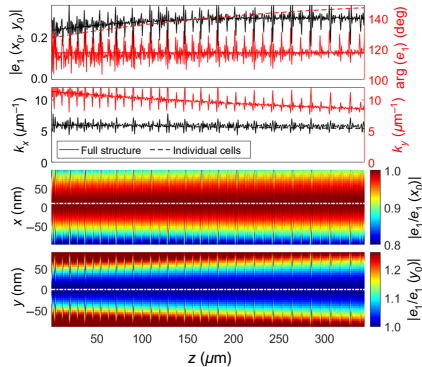


FIG. 10. Field-flatness analysis as in Fig. 5 for the rectangular-cell structure. The 5-nm drift of x_0 is too small to be visible.

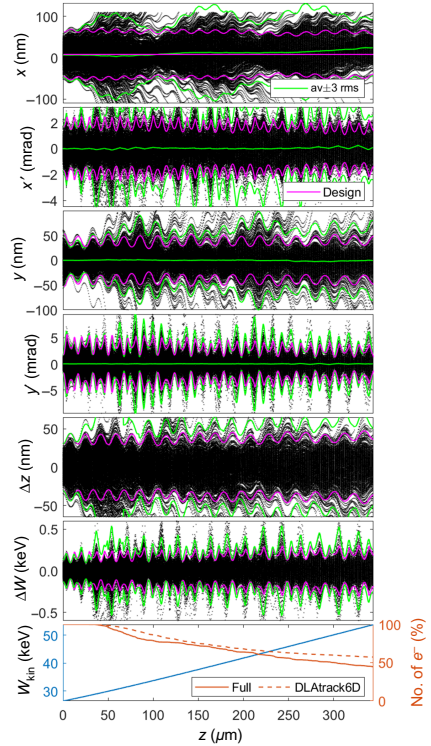


FIG. 11. Evolution of the electron beam in the design with rounded rectangular structures. The expected transmission can almost be reached without any correcting external field.

with bunch lengths of several hundreds of attoseconds and matched energy spreads. For an unbunched beam, DLAttrack6D predicts transmission of 5.1%, and the full simulation results in 4.0%. Thus, one would expect a combined transmission of about 20% with a buncher as compared with 4% without a buncher for the 10-pm emittance beam. Video files of the DLAttrack6D and CST Particle Studio simulations are available in Supplementary Material [36].

V. VERTICAL STEERERS AND STAGING THE DESIGN ON A SINGLE CHIP

We have seen that structures can be made that achieve decent energy-doubling throughput without any correcting field for available beam emittances of 10 pm at $\beta = 0.31$.

To obtain higher energy, the setup can be staged, where each stage can be run with its own constant PFT angle. At the output of each stage, the beam might however be vertically displaced and inclined. For injection into the next stage, the vertical injection angle and position need to be controlled. For that purpose we exploit the fact that the substrate is grounded and thus constitutes an electrode of an electrostatic deflector. The device layer can act as a connection platform for the other electrode. Moreover, the device layer can also be equipped with lateral traces so as to ground the acceleration structures (see Fig. 9). This allows us to remove lost charges. Lateral grounding is more preferable than connecting the pillars longitudinally, since longitudinal connections decrease the bandwidth, therefore strongly increasing the field deviations at the phase jumps [23].

A mock-up layout for the device layer with the connections is shown in Fig. 12. Both the acceleration structures and the large areas with the crosses are connected to pads located far from the laser spots. They can be contacted by metallic wires or needle contacts. The crosses are alignment marks to align a second chip from the top. The

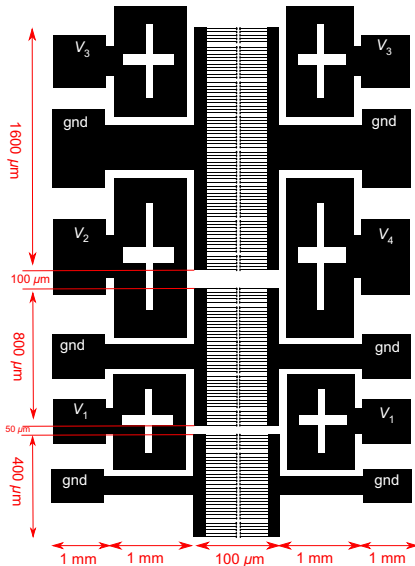


FIG. 12. Layout of the device layer for a staged accelerator chip. The dimensions are mock-up parameters for a three-stage setup with four steering voltages. The drawing is not to scale.

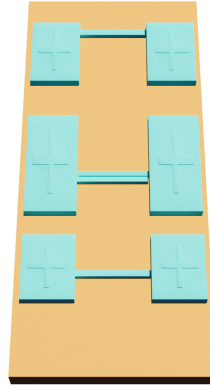


FIG. 13. Deflection electrodes etched on a silicon-on-glass wafer. The large areas with the crosses are supposed to be aligned with and touching the SOI wafer's device layer.

upper chip as shown in Fig. 13 is made on a thicker silicon-on-glass wafer, where all the silicon is removed except for some bridges, which constitute the second electrode of the deflectors.

The deflection strength is calculated from the dc breakdown strength of glass, which is 10 MV/m [38], as $x'' = qE_x/m\gamma\beta^2c^2 = E_x/(W/q)/\beta^2$. For 53 keV, this results in 50 m^{-1} , leading to a kick of $\Delta x' = x''L = 2.5 \text{ mrad}$ and a displacement of $\Delta x = x''L^2/2 = 62.5 \text{ nm}$ in a deflector of length $L = 50 \text{ }\mu\text{m}$. The required voltage on the pads is only 30 V when a $3\text{-}\mu\text{m}$ gap is maintained for the beam, and half of the breakdown field strength is used as deflection field. For fused silica the dielectric strength is about 500 MV/m [38], which would reduce the required length significantly. In the design of the deflector lengths, other quantities also play a role. For example, the beam defocuses during that drift (i.e., its rms size will increase by $\sigma_x L \approx 20 \text{ nm}$), which has to be matched to the next stage. Moreover, the two laser spots for the two stages should be designed for constructive interference of the two pulses in the interface region of the two respective stages.

Two deflectors can also be combined to create a dogleg. This can be used to send the beam above the acceleration structures to bypass a subsequent stage. In this manner, the stages can be subsequently tested and aligned from the lowest energy to the highest energy, where all stages are on the same chip. Since longitudinal and lateral alignment between the stages is already perfect due to the high accuracy of the lithographic fabrication of the device layer, the

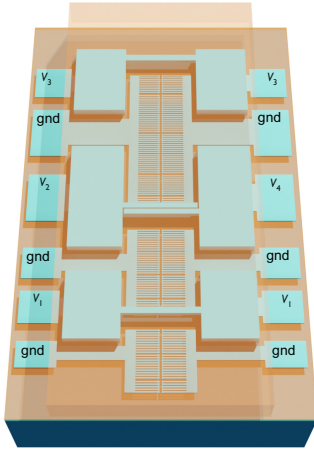


FIG. 14. Final assembly of a three-stage acceleration chip. Each stage is driven by an individually tilted laser pulse from the top.

vertical steerers should suffice to align the beam for a controlled energy boost above 1 MeV in four or five stages with a total length of about 1 cm. The complete assembly of 3 such stages is shown in Fig. 14.

VI. CONCLUSION AND OUTLOOK

In summary, we show two different designs of nanophotonic linear electron accelerators, which double the energy of tabletop electron microscopes. The chips are less than 400 μm in length and contain about 500 DLA cells. The cells are organized by an optimized 3D-APF scheme, which produces smooth and small envelope functions in all directions of the six-dimensional phase space. By means of illuminating the structures from the top and exploiting the partial reflection due to the refractive-index contrast in the SOI wafer, we can drive the energy doubler by a single, linearly tilted laser pulse of 430-fs length. The experimental complexity is significantly reduced, which also practically enables multistage setups, fabricated on a single chip with perfect longitudinal and lateral alignment. The vertical alignment can be controlled by on-chip electrostatic steerers, which also allow the bypassing of entire stages. The alignment of the top electrodes needs only to be in the single-digit micrometer range longitudinally and in the two-digit micrometer range laterally. The voltage supply of the deflectors as well as grounding of the laser-driven accelerator structures themselves can be achieved

by metallic contacting on the SOI device layer far from the laser spot.

We simulate the two single-stage designs both in the simplified, one-kick-per-cell DLA simulator DLATRACK6D [27] and with the full fields in CST Particle Studio [26]. The full simulations reveal that due to the small phase gradient across the beam channel, there is a coherent force deflecting the beam vertically. We find that the impact of this parasitic force is stronger than the effect of the working-point drift with changing beam velocity. To compensate for this force, an external homogeneous magnetic field can be applied; however, complete compensation is obtained only for a particular beam velocity. A better approach is to eliminate the phase gradient in the individual cell design. We find that the phase gradient can be significantly reduced by choosing rectangular rather than elliptical structures at low energy. For fabrication reasons the rectangles must have rounded corners though. With these structures, a small channel drift of 5 nm however remains. Correction of this drift using Eq. (2) leads to a stronger phase gradient, which is not favorable. The excess beam losses found in the full simulations are rather due to the remaining coherent deflection appearing at high energy ($\beta \approx 0.4$). At this higher energy, the elliptical structures produce zero phase gradient. Thus, to compensate for the phase gradient for the entire ramp, hyperelliptical structures, parameterized by $(y/r_y)^p + (z/r_z)^p = 1$ (with $p = p(\beta) > 2$ not necessarily an integer), can be used. Varying p smoothly allows us to design structures that look like rectangles at low energy and smoothly translate into ellipses at higher energy when p approaches 2.

The full simulations performed in this study are heavy for twofold reasons. First, the stages themselves have an electrical length (length in the unit of the wavelength) equal to the number of DLA cells. Second, the channel is transversely much smaller than the entire setup and the beam is very sensitive to its initial parameters within the channel. Although in experiments the shots can come with a repetition rate above 100 kHz, a single shot requires about 17 h for simulation in the full 3D fields. Thus, scanning the sensitive injection parameters (i.e., x_0, x'_0 , injection phase, and laser amplitude) and eventually also correction fields is extremely time-consuming. In the future one could apply a surrogate model to optimize these parameters with fewer evaluations of the full 3D model (“Bayesian optimization”), as was recently done for plasma accelerators [39]. The numerous shots in the experiments come however with the drawback of only little diagnostic equipment available so far. Essentially, in the experiment one can see the beam on a spectrometer screen only after the accelerator. The laser distribution over the accelerator structure is unknown to sufficient accuracy, without even considering the phase-space evolution within the structures. The advantages of quick results and the observability of all parameters are combined in

the fast one-kick-per-cell simulation tool DLAttrack6D. In the future, one could imagine using it as a “digital twin” running in parallel with experiments. Of course, the modeling in DLAttrack6D would have to be refined to match input and output data of the experiment. Especially modeling the phase-gradient kick as introduced here would be crucial. The necessary parameters could be obtained from machine learning [40], especially so-called transfer learning, where the training data are obtained by a cheaper process (e.g., numerous DLAttrack6D runs or experimental data). With such a “digital twin” an experimenter could get live insights into otherwise-hidden parameters (e.g., the position in the chip where beam losses occur). This would especially allow tuning of the injection parameters such that the beam is matched and envelope oscillations are largely avoided so as to obtain maximal charge throughput.

To reduce experimental complexity in the first place, the single-stage energy doublers presented here can be elongated to an energy tripler or even longer, depending on the laser pulse length. If greater energy gains at such low energy are desired, a curved pulse-front-tilt is necessary. The curved pulse can be circumvented by approximating it by linear pieces, resulting in a staged setup, where each stage is driven by an individual pulse of the respective linear tilt angle. Fabricating four or five such stages on a common chip allows the energy to be boosted into the megaelectronvolt realm. At the output, the 3D-APF lattice can be designed such that the beam is uncorrelated and can be magnified by a cylindrical electrostatic lens (or *Einzel* lens) to a larger spot size and to be parallel to the optical axis at the specimen. In this manner, the way is paved to high-energy electron diffraction on tabletop setups.

We have submitted a patent application for the above structures to the German patent office under DE 102020119875.2, priority date July 28, 2020.

ACKNOWLEDGMENTS

This work is funded by the Gordon and Betty Moore Foundation under Grant No. GBMF4744 (ACHIP) and the German Federal Ministry of Education and Research (Grant No. 05K19RDE).

- [1] A. Lohmann, Electron acceleration by light waves, *IBM Tech. Note* **5**, 169 (1962).
- [2] K. Shimoda, Proposal for an electron accelerator using an optical maser, *Appl. Opt.* **1**, 33 (1962).
- [3] J. Breuer and P. Hommelhoff, Dielectric laser acceleration of 28 keV electrons with the inverse Smith-Purcell effect, *Nucl. Instrum. Methods Phys. Res., Sect. A: Accel. Spectrom. Detect. Assoc. Equip.* **740**, 114 (2013).
- [4] E. A. Peralta, K. Soong, R. J. England, E. R. Colby, Z. Wu, B. Montazeri, C. McGuinness, J. McNeur, K. J. Leedle, D. Walz, E. B. Sozer, B. Cowan, B. Schwartz, G. Travish, and R. L. Byer, Demonstration of electron acceleration in a laser-driven dielectric microstructure, *Nature* **503**, 91 (2013).
- [5] K. P. Wootton, Z. Wu, B. M. Cowan, A. Hanuka, I. V. Makasyuk, E. A. Peralta, K. Soong, R. L. Byer, and R. J. England, Demonstration of acceleration of relativistic electrons at a dielectric microstructure using femtosecond laser pulses, *Opt. Lett.* **41**, 2696 (2016).
- [6] D. Cesar, S. Custodio, J. Maxson, P. Musumeci, X. Shen, E. Threlkeld, R. J. England, A. Hanuka, I. V. Makasyuk, E. A. Peralta, K. P. Wootton, and Z. Wu, High-field nonlinear optical response and phase control in a dielectric laser accelerator, *Commun. Phys.* **1**, 46 (2018).
- [7] P. Yousefi, J. McNeur, M. Kozák, U. Niedermayer, F. Gannott, O. Lohse, O. Boine-Frankenheim, and P. Hommelhoff, Silicon dual pillar structure with a distributed Bragg reflector for dielectric laser accelerators: Design and fabrication, *Nucl. Instrum. Methods Phys. Res., Sect. A: Accel. Spectrom. Detect. Assoc. Equip.* **909**, 221 (2018).
- [8] K. J. Leedle, R. Fabian Pease, R. L. Byer, and J. S. Harris, Laser acceleration and deflection of 963 keV electrons with a silicon dielectric structure, *Optica* **2**, 158 (2015).
- [9] B. Hermann, S. Bettoni, T. Egenolf, U. Niedermayer, E. Prat, and R. Ischebeck, Laser-driven modulation of electron beams in a dielectric micro-structure for X-ray free-electron lasers, *Sci. Rep.* **9**, 19773 (2019).
- [10] B. Marchetti, *et al.*, SINBAD-ARES—a photo-injector for external injection experiments in novel accelerators at DESY, *J. Phys.: Conf. Ser.* **1596**, 012036 (2020).
- [11] B. J. Siwick, J. R. Dwyer, R. E. Jordan, and R. J. Miller, An atomic-level view of melting using femtosecond electron diffraction, *Science* **302**, 1382 (2003).
- [12] R. F. Egerton, Outrun radiation damage with electrons? *Adv. Struct. Chem. Imaging* **1**, 5 (2015).
- [13] T. Gruene, J. T. Wennmacher, C. Zaubitzer, J. J. Holstein, J. Heidler, A. Fecteau-Lefebvre, S. De Carlo, E. Müller, K. N. Goldie, I. Regeni, T. Li, G. Santiso-Quinones, G. Steinfeld, S. Handschin, E. van Genderen, J. A. van Bokhoven, G. H. Clever, and R. Pantelic, Rapid structure determination of microcrystalline molecular compounds using electron diffraction, *Angew. Chem. - Int. Ed.* **57**, 16313 (2018).
- [14] J. Heidler, R. Pantelic, J. T. Wennmacher, C. Zaubitzer, A. Fecteau-Lefebvre, K. N. Goldie, E. Müller, J. J. Holstein, E. van Genderen, S. De Carlo, and T. Gruene, Design guidelines for an electron diffractometer for structural chemistry and structural biology, *Acta Crystallogr. Section D: Struct. Biol.* **75**, 458 (2019).
- [15] M. Warren, “Why didn’t we think to do this earlier?” Chemists thrilled by speedy atomic structures, *Nature* **563**, 16 (2018).
- [16] J. Yang, *et al.*, Diffractive Imaging of Coherent Nuclear Motion in Isolated Molecules, *Phys. Rev. Lett.* **117**, 153002 (2016).
- [17] R. K. Li and C. X. Tang, Temporal resolution of MeV ultrafast electron diffraction based on a photocathode RF gun, *Nucl. Instrum. Methods Phys. Res., Sect. A: Accel. Spectrom. Detect. Assoc. Equip.* **605**, 243 (2009).
- [18] T. W. Hughes, S. Tan, Z. Zhao, N. V. Saprà, K. J. Leedle, H. Deng, Y. Miao, D. S. Black, O. Solgaard, J. S.

- Harris, J. Vuckovic, R. L. Byer, S. Fan, R. J. England, Y. J. Lee, and M. Qi, On-Chip Laser-Power Delivery System for Dielectric Laser Accelerators, *Phys. Rev. Appl.* **9**, 54017 (2018).
- [19] N. V. Sapra, K. Y. Yang, D. Verduyck, K. J. Leadle, D. S. Black, R. J. England, L. Su, R. Trivedi, Y. Miao, O. Solgaard, R. L. Byer, and J. Vuckovic, On-chip integrated laser-driven particle accelerator, *Science* **367**, 79 (2020).
- [20] A. Ody, P. Musumeci, J. Maxson, D. Cesar, R. J. England, and K. P. Wootton, Flat electron beam sources for DLA accelerators, *Nucl. Instrum. Methods Phys. Res., Sect. A: Accel. Spectrom. Detect. Assoc. Equip.* **865**, 75 (2017).
- [21] U. Niedermayer, T. Egenolf, O. Boine-Frankenheim, and P. Hommelhoff, Alternating-Phase Focusing for Dielectric-Laser Acceleration, *Phys. Rev. Lett.* **121**, 214801 (2018).
- [22] D. S. Black, K. J. Leadle, Y. Miao, U. Niedermayer, R. L. Byer, and O. Solgaard, Laser-Driven Electron Lensing in Silicon Microstructures, *Phys. Rev. Lett.* **122**, 104801 (2019).
- [23] U. Niedermayer, T. Egenolf, and O. Boine-Frankenheim, Three-dimensional Alternating-Phase Focusing for Dielectric-Laser Electron Accelerators, *Phys. Rev. Lett.* **125**, 164801 (2020).
- [24] D. S. Black, U. Niedermayer, Y. Miao, Z. Zhao, O. Solgaard, R. L. Byer, and K. J. K. Leadle, Net Acceleration and Direct Measurement of Attosecond Electron Pulses in a Silicon Dielectric Laser Accelerator, *Phys. Rev. Lett.* **123**, 264802 (2019).
- [25] U. Niedermayer, D. S. Black, K. J. Leadle, Y. Miao, R. L. Byer, and O. Solgaard, Low Energy Spread Attosecond Bunching and Coherent Electron Acceleration in Dielectric Nanostructures, *Phys. Rev. Appl.* **15**, L021002 (2021).
- [26] www.cst.com CST Studio Suite (2021).
- [27] U. Niedermayer, T. Egenolf, and O. Boine-Frankenheim, Beam dynamics analysis of dielectric laser acceleration using a fast 6D tracking scheme, *Phys. Rev. Accel. Beams* **20**, 111302 (2017).
- [28] www.refractiveindex.info (2020).
- [29] www.order.universitywafer.com (2020).
- [30] D. Cesar, J. Maxson, P. Musumeci, X. Shen, R. J. England, and K. P. Wootton, Optical design for increased interaction length in a high gradient dielectric laser accelerator, *Nucl. Instrum. Methods Phys. Res., Sect. A: Accel. Spectrom. Detect. Assoc. Equip.* **909**, 252 (2018).
- [31] M. Kozák, J. McNeur, N. Schönenberger, J. Illmer, A. Li, A. Tafel, P. Yousefi, T. Eckstein, and P. Hommelhoff, Ultrafast scanning electron microscope applied for studying the interaction between free electrons and optical near-fields of periodic nanostructures, *J. Appl. Phys.* **124**, 023104 (2018).
- [32] Y. Wei, M. Ibson, G. Xia, J. D. A. Smith, and C. P. Welsch, Dual-grating dielectric accelerators driven by a pulse-front-tilted laser, *Appl. Opt.* **56**, 8201 (2017).
- [33] P. Pronko, P. V. Rompay, C. Horvath, X. Liu, T. Juhasz, and G. Mourou, Avalanche ionization and dielectric breakdown in silicon with ultrafast laser pulses, *Phys. Rev. B* **58**, 2387 (1998).
- [34] K. Soong, R. L. Byer, E. R. Colby, R. J. England, and E. A. Peralta, Laser damage threshold measurements of optical materials for direct laser accelerators, *AIP Conf. Proc.* **1507**, 511 (2012).
- [35] A. Feist, N. Bach, N. Rubiano da Silva, T. Danz, M. Möller, K. E. Priebe, T. Domröse, J. G. Gatzmann, S. Rost, J. Schauss, S. Strauch, R. Bormann, M. Sivis, S. Schäfer, and C. Ropers, Ultrafast transmission electron microscopy using a laser-driven field emitter: Femtosecond resolution with a high coherence electron beam, *Ultramicroscopy* **176**, 63 (2017).
- [36] U. Niedermayer, J. Lautenschläger, T. Egenolf, and O. Boine-Frankenheim, See Supplemental Material at <http://link.aps.org/supplemental/10.1103/PhysRevApplied.16.024022> for videos of the DLAttrack6D and CST simulations, without a correction field and without initial bunching (2021).
- [37] T. Egenolf, U. Niedermayer, and O. Boine-Frankenheim, Tracking with wakefields in dielectric laser acceleration grating structures, *Phys. Rev. Accel. Beams* **23**, 54402 (2020).
- [38] J. Rumble, *CRC Handbook of Chemistry and Physics* (CRC Press, Boca Raton, FL, 2020), 101st ed.
- [39] S. Jalas, M. Kirchen, P. Messner, P. Winkler, L. Hübner, J. Dirkwinkel, M. Schnepf, R. Lehe, and A. R. Maier, Bayesian Optimization of a Laser-Plasma Accelerator, *Phys. Rev. Lett.* **126**, 104801 (2021).
- [40] A. Edelen, N. Neveu, M. Frey, Y. Huber, C. Mayes, and A. Adelman, Machine learning for orders of magnitude speedup in multiobjective optimization of particle accelerator systems, *Phys. Rev. Accel. Beams* **23**, 44601 (2020).

Electron phase-space control in photonic chip-based particle acceleration

<https://doi.org/10.1038/s41586-021-03812-9>

Received: 29 January 2021

Accepted: 7 July 2021

Published online: 22 September 2021

 Check for updates

R. Shiloh^{1,4,5}, J. Illmer^{1,4,5}, T. Chlouba^{1,4}, P. Yousefi¹, N. Schönenberger^{1,2}, U. Niedermayer³, A. Mittelbach¹ & P. Hommelhoff^{1,2,5}

Particle accelerators are essential tools in science, hospitals and industry^{1–6}. Yet their costs and large footprint, ranging in length from metres to several kilometres, limit their use. The recently demonstrated nanophotonics-based acceleration of charged particles can reduce the cost and size of these accelerators by orders of magnitude^{7–9}. In this approach, a carefully designed nanostructure transfers energy from laser light to the particles in a phase-synchronous manner, accelerating them. To accelerate particles to the megaelectronvolt range and beyond, with minimal particle loss^{10,11}, the particle beam needs to be confined over extended distances, but the necessary control of the electron beam's phase space has been elusive. Here we demonstrate complex electron phase-space control at optical frequencies in the 225-nanometre narrow channel of a silicon-based photonic nanostructure that is 77.7 micrometres long. In particular, we experimentally show alternating phase focusing^{10–13}, a particle propagation scheme for minimal-loss transport that could, in principle, be arbitrarily long. We expect this work to enable megaelectronvolt electron-beam generation on a photonic chip, with potential for applications in radiotherapy and compact light sources⁹, and other forms of electron phase-space control resulting in narrow energy or zeptosecond-bunched beams^{14–16}.

Particle accelerators have enabled the discovery of the fundamental constituents of matter, exemplified by the recent identification of the Higgs particle^{1,2}. In addition, they drive modern light sources such as synchrotrons and free electron lasers, which allow unrivalled insights into structural biology and material science^{3,4}. Metre-long versions of accelerators provide radiation in modern hospitals for cancer treatment^{5,6}.

Accelerators accelerate charged particles while, at the same time, confining them transversally. This is challenging because the larger the acceleration, the larger the forces that disperse the beam, reflecting Earnshaw's theorem^{10,17}. In the radiofrequency (RF) accelerators currently used, methods have been found to accelerate and confine the particle beam¹⁰.

Recently, laser-based electron acceleration has been demonstrated based on efficient momentum transfer from strong optical nearfields generated at nanophotonic dielectric structures^{7,8}—first proposed in 1962^{18,19} and today termed dielectric laser acceleration (DLA)⁹. This is the counterpart of classical RF acceleration but at a factor of ~10,000 larger driving frequencies and hence in a structure with feature sizes smaller by the same factor. Intriguingly, at optical frequencies, dielectric structures can withstand peak fields roughly a factor of 100 larger than their metallic RF cavities counterparts. A damage threshold of 9 GV m⁻¹ and an accelerating field of 1.8 GV m⁻¹ have already been demonstrated in DLA²⁰. Similarly, all functional elements required in any particle accelerator have been demonstrated in DLA, including

acceleration^{7,8,20,21}, deflection^{22,23} and focusing^{23–25} with purely optical forces, as well as waveguide-fed DLA²⁶.

The small size of DLA features also reflects DLA's largest limitation: the acceleration channel aperture is orders of magnitudes smaller than that of RF accelerators. Hence, DLA bunch charges will always be much smaller than RF accelerator bunch charges. Yet, mainly because of high-repetition-rate lasers powering future dielectric laser accelerators, they are now even being discussed in the context of future linear colliders with their demanding luminosity and (average) current demands²⁷. Clearly, a greatly increased pulse charge will be needed for DLA to succeed, in addition to the extended beam control discussed here.

To our knowledge, the longest DLA structure hitherto used for sub-relativistic electrons was 13.2 μm long¹⁸. To greatly increase the acceleration length, active control schemes need to be devised to confine a beam and prevent particle loss²⁸. We show here that with complex phase-space control, we can transport a beam through a 77.7-μm-long structure. Without experiencing net acceleration, electrons are actively propagated through the DLA structure with the help of optical near-field forces. Low-loss transport is essential because without it the best acceleration will not lead to noticeable electron currents, let alone to a power-efficient accelerator⁹. For transport, too, Earnshaw's theorem imposes severe limitations: continuous focusing in all spatial directions is prohibited. Alternating phase focusing (APF) circumvents this by repeatedly alternating the focusing directions and allowing defocusing in the other direction^{10,12,13,19,29}.

¹Physics Department, Friedrich-Alexander-Universität Erlangen-Nürnberg (FAU), Erlangen, Germany. ²Max Planck Institute for the Science of Light, Erlangen, Germany. ³Technische Universität Darmstadt, Institute for Accelerator Science and Electromagnetic Fields (EMF), Darmstadt, Germany. ⁴These authors contributed equally: R. Shiloh, J. Illmer, T. Chlouba. ⁵e-mail: roy.shiloh@fau.de; johannes.illmer@fau.de; peter.hommelhoff@fau.de

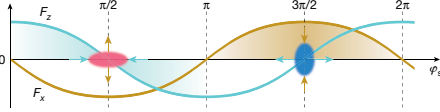


Fig. 1 | Forces acting as a function of the synchronous phase φ_s . The forces acting on a charged particle copropagating with the optical nearfield mode according to equation (1), as a function of the particle's position inside of the mode, the synchronous phase φ_s . The longitudinal force F_z is shown in cyan. The orange curve shows the transverse force F_x , acting on a particle at negative transverse (x) position. The force is flipped for positive x values, leading to focusing or defocusing behaviour, indicated by the arrows. Around $\varphi_s = \pi/2$, the pulse is transversally defocused but longitudinally focused (D phase), around $\varphi_s = 3\pi/2$, it is transversally focused but longitudinally defocused (F phase). The colour gradient indicates the strength of the respective focusing force.

The force on the synchronous electron can be written as^{13,23}

$$\mathbf{F} = \frac{q\mathbf{c}}{\beta\gamma} C_c \left(\hat{\mathbf{x}} \frac{1}{\gamma} \sinh(k_x x) \sin \varphi_s + \hat{\mathbf{z}} \cosh(k_x x) \cos \varphi_s \right) \quad (1)$$

where q is the electron charge, c the speed of light, β the velocity of the electron in units of c , γ the Lorentz factor, C_c the excitation coefficient of the driving mode, k_x the fundamental wavenumber of the DLA structure and φ_s the synchronous phase (Fig. 1). The particles propagate in the $\hat{\mathbf{z}}$ -direction, where $\hat{\mathbf{x}}$ is the transverse direction parallel to the substrate (Fig. 2, 3), and the particle velocity and the optical mode velocity are identical, that is, the system operates in the phase-synchronous regime¹⁰. For this reason, no explicit time dependence shows up in equation (1), although it is implicitly reflected by the synchronous phase φ_s . The synchronous electron experiences a constant synchronous force, which depends strongly on the time the electron is injected into the optical mode (Fig. 1). The synchronous phase and the incident laser phase have a fixed phase relation for purely periodic synchronous transport structures. However, the synchronous phase can be changed easily and almost instantaneously by introducing a gap in the periodic nanostructure, leading to a jump in the optical phase of the nearfield mode acting on the propagating electrons.

For an electron close to the central axis ($x=0$), we can plot the force components depending on φ_s as depicted in Fig. 1. For $\varphi_s = 3\pi/2$, the electron experiences a transversely focusing, longitudinally defocusing force (F phase for short), whereas for $\varphi_s = \pi/2$, the electron experiences a transversely defocusing, longitudinally focusing force (D phase). By variation of φ_s , we can repeatedly switch between the F and D phases (Fig. 2). The DLA structure is thus separated into F and D macro cells, realizing a FODO lattice, where O stands for no force (drift). It is well known that FODO lattices may lead to full confinement of the electron pulses¹⁴. Here, we choose the narrow transverse and the longitudinal direction as two directions out-of-phase by $\pi/2$. Because the nanophotonic pillars are 3 μm high (Fig. 3), we do not require forces along the y -direction (see Methods). Extension to a full three-dimensional (3D) confinement can be readily achieved if needed²⁹.

Figure 2 shows the behaviour of electrons in transverse phase space ($x-x'$) and longitudinal phase space ($\Delta s-\Delta s'$) for one FODO lattice period. Here, x describes the particle position transversally off the centre line, and x' is the electron's angle with respect to straight propagation. Δs describes the deviation from the synchronous particle (which propagates at the synchronous phase), and $\Delta s'$ the longitudinal momentum of change. Figure 2a–d shows that when the electron is focused transversally, it is debunched (defocused) longitudinally, and

vice versa: Starting at $z=0$ ($\varphi_s = \pi/2$ in Fig. 2), the transverse size of the beam (x) decreases because x' is negative for positive x and vice versa (Fig. 2b) – the beam is converging. Simultaneously, the forces in this D macro cell counter this momentum, allowing the beam to reach a minimum at the centre of the macro cell before diverging again. After the phase jump to $\varphi_s = 3\pi/2$, the beam size (x) continues to grow, owing to x' being negative for negative x and vice versa. However, the optical force again counters this behaviour, allowing the beam to reach a point of maximum size in x before starting to focus again. This procedure repeats in each FODO lattice period. In parallel, the same happens in the longitudinal direction, but shifted by half a period (Fig. 2c, d).

So far, we have discussed the behaviour of an electron bunch occupying a small phase section to illustrate the dynamics. The experimental situation is more complex because the electrons arrive at the structure in an unbunched fashion³⁰; hence all phases are occupied. However, the APF effect in a pure transport structure works for all initial phases¹³.

The photonic nanostructures used in the experiment consist of 3- μm -high pillar pairs etched in monocrystalline silicon with an open channel width of 225 nm (Fig. 3). The high-contrast structure (Fig. 3a) comprises 10 macro cells, each consisting of 12 silicon pillar pairs. The required phase jump is realized with a 589-nm-long drift gap between the macro cells. With this structure, we show successful beam transport over a total structure length of 77.7 μm , entailing 10 π -phase jumps, 10 macro cells and thus 5 FODO lattice periods.

The experimental set-up is described under Methods. Briefly, a 28.4-keV pulsed electron beam is generated in a modified commercial scanning electron microscope (SEM). The ~600-fs-long electron pulses are focused into the channel of the photonic nanostructure. After the interaction, the electron beam energy is measured with a magnetic spectrometer. The nanostructure is driven with femtosecond laser pulses of 1.93 μm central wavelength and 680 fs pulse duration, focused cylindrically to a spot size of 94 μm ($1/e^2$ radius) along the nanostructure channel and 14 μm along the pillar height. The laser field polarization points along the travel direction of the electrons, and the temporal overlap between laser and electron pulses is controlled by a delay stage in the laser beamline.

We measure the normalized electron current (see Methods) through the high-contrast structure as a function of the peak optical field strength. With increasing laser intensity, more electrons are guided, and the current increases steadily (Fig. 4a). At a peak field strength of 727 $\text{MV m}^{-1} \pm 76 \text{ MV m}^{-1}$, a factor of 2.67 ± 0.05 more electrons are transported through than without laser, where the current decreases along the structure (Fig. 4e). Numerical particle tracking simulations, explained in detail in the Methods section, fit the experimental behaviour well (solid line in Fig. 4a).

To show that too large a field strength leads to over-focusing and hence an electron current that again decreases, we would need to increase the field strength to above 800 MV m^{-1} in this structure, but for such large field strengths laser-induced damage sets in. We can design a structure with longer macro-cell dimension so that optimal transport is achieved at a smaller field strength, at the cost of decreased total current transmission. This over-focusing structure is shown in Fig. 4f and Extended Data Fig. 3. Here we use 24 pillar pairs per macro cell such that the electrons experience the same phase (D or F) for twice as long. This second type of APF structure contains four macro cells and two half cells at the beginning and the end, with a total length of 76.2 μm . The optimal transport field strength is 325 MV m^{-1} . For larger field strengths, the electrons are over-focused, resulting in a loss of electrons, as observed in Fig. 4c. For peak fields larger than 550 MV m^{-1} , the normalized current falls below 1, indicating that now the laser fields actively destroy the beam rather than preventing it from crashing into the channel walls.

In Fig. 4b we show an electron energy spectrum as a function of the temporal overlap between laser pulses and electron pulses in the high-contrast structure. For maximum overlap, the largest electron

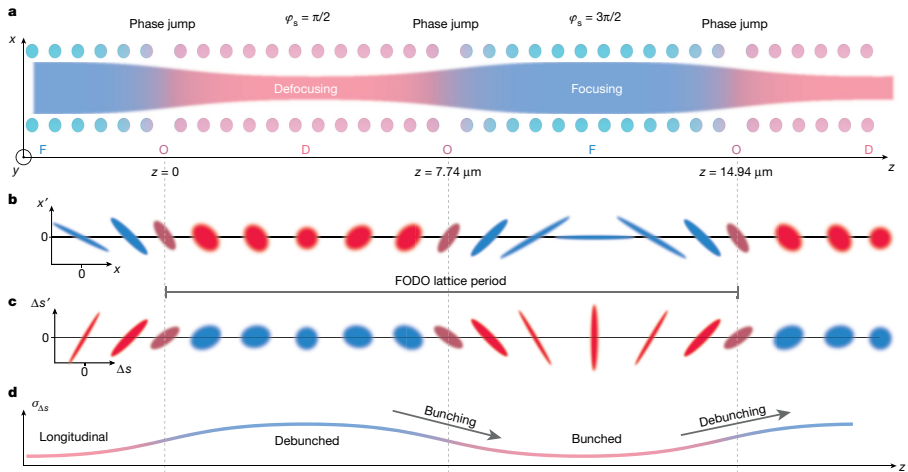


Fig. 2 | Complex optical electron phase-space control in alternating phase focusing. **a**, Sketch of the electron-beam envelope (coloured band) under the influence of the optical nearfield generated by the dielectric nanostructure. Filled circles indicate nanopillars extruded out of plane (y -direction). **a**, **b**, Evolution of a particle ensemble in transverse phase space relative to the structure layout: The electron distribution at $z=0$ is compressed in transverse phase space (x extent decreasing), while in this D cell transversally defocusing forces already act on the electrons. The point of minimum transverse size is reached in the middle of the first macro cell ($z=3.87 \mu\text{m}$). At $z=7.74 \mu\text{m}$, a gap in

the structure leads to a jump in the synchronous phase ϕ_s between electrons and optical nearfield so that the particles now experience transverse focusing forces (F cell). **c**, **d**, The longitudinal forces, 90° out of phase relative to the transverse forces, act similarly on the longitudinal phase-space distribution: the pulse length ($\sigma_{\Delta s}$) maximum in the longitudinal direction coincides with the minimal extent in the transverse direction and vice versa. The net effect is a confinement of the beam both transversally and longitudinally. For illustration purposes, the particles depicted occupy a small initial phase volume.

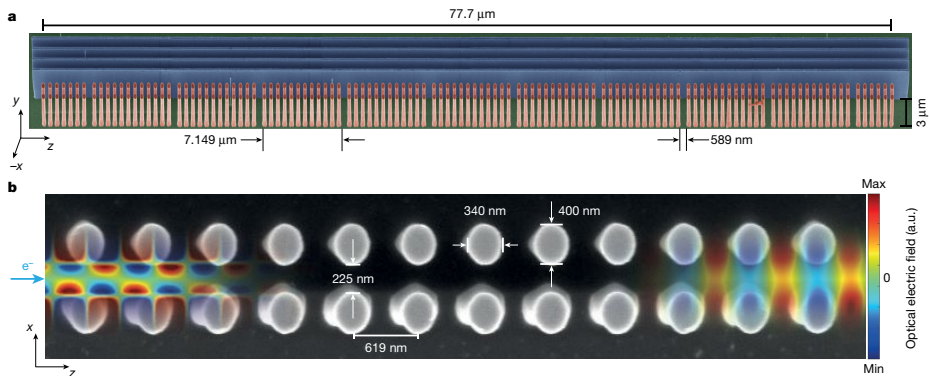


Fig. 3 | Silicon photonic nanostructure for phase-space control. **a**, SEM image of the 10 macro cell APF structure (high-contrast structure), coloured for clarity. Each full macro cell is $7.149 \mu\text{m}$ long and is separated from its neighbour by a 589-nm -wide gap. The two half cells at the beginning and end ensure that an unbunched beam is optimally coupled in and out of the structure (see Methods). The total structure length is $77.7 \mu\text{m}$. The pulsed laser beam impinges on the nanostructure along the x -direction. A distributed Bragg reflector (blue) placed behind the pillar structure reflects the laser light back

to create a symmetric field distribution³¹. **b**, Top view of one macro cell. The pillars consist of elliptical silicon cylinders with axes 400 nm and 340 nm long, and a height of $3 \mu\text{m}$. The distance between pillars is 619 nm . Dimensions have to be accurate to 20 nm for efficacy of the structure (see Methods). Electrons (light blue arrow) are injected from the side. The colour superimposed on the left shows a snapshot of the electric field component exerting transverse forces (along x) on the electrons, while the colour on the right displays the electric field component in longitudinal z -direction.

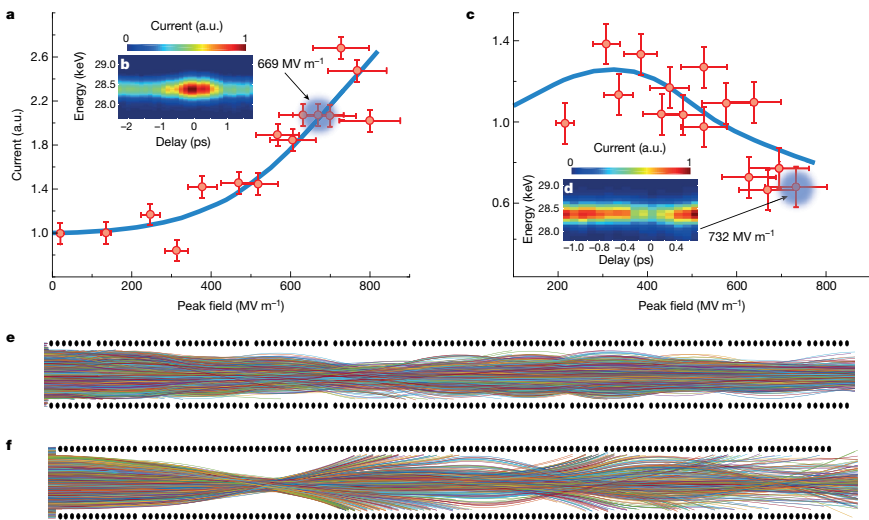


Fig. 4 | Experimental verification of the APF scheme. a, Current after the high-contrast structure as function of the peak optical field. Red points, experimental data; blue curve, particle tracking simulation results. The current increases from 1 (laser off) with increasing field strength up to a maximum value of 2.67 ± 0.05 . **b**, Time delay scan between electron and laser pulses of the spectrally resolved current at $669 \text{ MV m}^{-1} \pm 70 \text{ MV m}^{-1}$. Clearly, the largest current is observed for maximum temporal overlap (zero time delay). **c**, As in a but now for the over-focusing structure. Over-focusing sets in for fields larger

than 300 MV m^{-1} . The current drops to below 1 for fields larger than 550 MV m^{-1} . **d**, Same as in **b** for the over-focusing structure at $732 \text{ MV m}^{-1} \pm 76 \text{ MV m}^{-1}$. Now, the largest electron loss happens at maximum overlap. **e, f**, Example particle trajectories in the high-contrast structure, **e**, and in the over-focusing structure, **f**. Excellent beam transport is observed in **e**, while over-focusing is visible in **f**. The colours in **e** and **f** are chosen to discern individual trajectories for presentation purposes. Error bars mark the measured value $\pm 1 \text{ s.d.}$ —see Methods for details.

count rate is observed, and this drops with decreasing temporal overlap. The spectral width remains minimal as predicted by our numerical simulations. Figure 4d shows the same temporal overlap scan for the overfocusing structure at $732 \text{ MV m}^{-1} \pm 76 \text{ MV m}^{-1}$ peak electric field. Here we observe a minimum in the electron count rate. The advantage of the APF scheme is apparent: particles can be transported while confined in these narrow channels, all the while keeping the energy spread minimal.

Figure 4e depicts simulated example particle trajectories in the case of optimal guiding in the high-contrast structure. Some particles are lost at in-coupling, but then the forces acting on the remaining particles are ideal to transport all of them through the structure. The simulated electron beam parameters are consistent with the experimental ones: The normalized input emittance was determined previously as $100 \text{ pm-rad}^{30,31}$. In contrast, Fig. 4f shows an example of particle trajectories for the over-focusing case. Because the transverse forces acting on the particles are too strong, the focusing force is no longer matched to the phase-jump intervals, so the electrons gain too large a transverse momentum, and minimal-loss guiding cannot be maintained.

For both structure types, experimental results agree well with our particle tracking simulations. In addition to the transverse dynamics, the APF scheme inevitably also induces longitudinal phase-space effects. These result from the selective energy modulation that the electrons undergo as they are transported through the structure and manifest as bunching (Fig. 2c, d). Because this is periodic with the pillar period of 619 nm , a train of sub-optical short bunches of electrons is generated every 3.23 fs (half an optical period). The generation of bunch trains of electrons can also be attained after propagation through a

simpler uniform energy modulation structure plus ballistic propagation^{14,15}. In that case, the electrons first gain a large energy spread and are then merely rotated by 90° in phase space. Specially designed APF bunchers can compensate the created energy spread^{13,16}.

In conclusion, we have experimentally demonstrated ten-in-a-row well-controlled coupled transverse and longitudinal phase-space rotations—at optical frequencies in a nanophotonic structure on a chip. In our alternating phase focusing scheme, we were able to transport an electron beam over a length of $77.7 \mu\text{m}$ in a 225-nm -wide channel. Refinement of the FODO cell design will allow combined confinement and net acceleration^{18,29}. Because this scheme is scalable, we can now extend dielectric laser acceleration to long photonic structures. In particular, one could start with electrons at 30 keV and accelerate them up to 1 MeV (see Methods). Assuming an average acceleration gradient of 1 GeV m^{-1} , 1 MeV is achievable on a 1-mm -long chip. Such a particle accelerator on a chip could result in compact light sources³², potentially even compact free-electron lasers²⁸ and high-energy particle colliders²⁷, and could also be used in miniature catheterized radiation therapy devices. Similarly, the high degree of phase-space control will open the door to extreme electron-beam parameters including narrow-energy beams¹⁶ as well as bunching down into the zeptosecond realm¹⁴.

Online content

Any methods, additional references, Nature Research reporting summaries, source data, extended data, supplementary information, acknowledgements, peer review information; details of author contributions

and competing interests; and statements of data and code availability are available at <https://doi.org/10.1038/s41586-021-03812-9>.

- Aad, G. et al. A particle consistent with the Higgs boson observed with the ATLAS detector at the large hadron collider. *Science* **338**, 1576–1582 (2012).
- Chatrchyan, S. et al. A new boson with a mass of 125 GeV observed with the CMS experiment at the large hadron collider. *Science* **338**, 1569–1575 (2012).
- Focus: Synchrotron techniques. *Nat. Rev. Mater.* <https://www.nature.com/collections/vjmzctbvzy> (2018).
- Bucksbaum, P., Möller, T. & Ueda, K. Frontiers of free-electron laser science. *J. Phys. At. Mol. Opt. Phys.* **46**, 160201 (2013).
- Karzmark, C. J. Advances in linear accelerator design for radiotherapy. *Med. Phys.* **11**, 105–128 (1984).
- Podgorsak, E. B. *Radiation Oncology Physics: A Handbook for Teachers and Students* (International Atomic Energy Agency, 2005).
- Breuer, J. & Hommelhoff, P. Laser-based acceleration of nonrelativistic electrons at a dielectric structure. *Phys. Rev. Lett.* **111**, 134803 (2013).
- Peralta, E. A. et al. Demonstration of electron acceleration in a laser-driven dielectric microstructure. *Nature* **503**, 91–94 (2013).
- England, R. J. et al. Dielectric laser accelerators. *Rev. Mod. Phys.* **86**, 1337–1389 (2014).
- Wangler, T. P. *RF Linear Accelerators* 2nd edition (Wiley-VCH, 2008).
- Chao, A. W., Mess, K. H., Tigner, M. & Zimmermann, F. *Handbook of Accelerator Physics and Engineering* 2nd edition (2013).
- Courant, E. D. & Snyder, H. S. Theory of the alternating-gradient synchrotron. *Ann. Phys.* **3**, 1–48 (1958).
- Niedermayer, U., Egenolf, T., Boine-Frankenheim, O. & Hommelhoff, P. Alternating-phase focusing for dielectric-laser acceleration. *Phys. Rev. Lett.* **121**, 214801 (2018).
- Schönenberger, N. et al. Generation and characterization of attosecond microbunched electron pulse trains via dielectric laser acceleration. *Phys. Rev. Lett.* **123**, 264803 (2019).
- Black, D. S. et al. Net acceleration and direct measurement of attosecond electron pulses in a silicon dielectric laser accelerator. *Phys. Rev. Lett.* **123**, 264802 (2019).
- Niedermayer, U. et al. Low-energy-spread attosecond bunching and coherent electron acceleration in dielectric nanostructures. *Phys. Rev. Appl.* **15**, L021002 (2021).
- Panofsky, W. K. H. & Wenzel, W. A. Some considerations concerning the transverse deflection of charged particles in radio-frequency fields. *Rev. Sci. Instrum.* **27**, 967 (1956).
- Shimoda, K. Proposal for an electron accelerator using an optical maser. *Appl. Opt.* **1**, 33–35 (1962).
- Lohmann, A. Electron acceleration by light waves. *IBM Tech. Note* **5**, 169–182 (1962).
- Cesar, D. et al. High-field nonlinear optical response and phase control in a dielectric laser accelerator. *Commun. Phys.* **1**, 46 (2018).
- Leadle, K. J., Fabian Pease, R., Byer, R. L. & Harris, J. S. Laser acceleration and deflection of 96.3 keV electrons with a silicon dielectric structure. *Optica* **2**, 158–161 (2015).
- Kozák, M. et al. Optical gating and streaking of free electrons with sub-optical cycle precision. *Nat. Commun.* **8**, 14342 (2017).
- Leadle, K. J. et al. Phase-dependent laser acceleration of electrons with symmetrically driven silicon dual pillar gratings. *Opt. Lett.* **43**, 2181 (2018).
- McNeur, J. et al. Elements of a dielectric laser accelerator. *Optica* **5**, 687–690 (2018).
- Black, D. S. et al. Laser-driven electron lensing in silicon microstructures. *Phys. Rev. Lett.* **122**, 104801 (2019).
- Sapra, N. V. et al. On-chip integrated laser-driven particle accelerator. *Science* **367**, 79–83 (2020).
- Shiltsev, V. & Zimmermann, F. Modern and future colliders. *Rev. Mod. Phys.* **93**, 015006 (2021).
- Naranjo, B., Valloni, A., Putterman, S. & Rosenzweig, J. B. Stable charged-particle acceleration and focusing in a laser accelerator using spatial harmonics. *Phys. Rev. Lett.* **109**, 164803 (2012).
- Niedermayer, U., Egenolf, T. & Boine-Frankenheim, O. Three dimensional alternating-phase focusing for dielectric-laser electron accelerators. *Phys. Rev. Lett.* **125**, 164801 (2020).
- Kozák, M. et al. Ultrafast scanning electron microscope applied for studying the interaction between free electrons and optical near-fields of periodic nanostructures. *J. Appl. Phys.* **124**, 023104 (2018).
- Yousefi, P. et al. Dielectric laser electron acceleration in a dual pillar grating with a distributed Bragg reflector. *Opt. Lett.* **44**, 1520 (2019).
- Roques-Carmes, C. et al. Towards integrated tunable all-silicon free-electron light sources. *Nat. Commun.* **10**, 3176 (2019).

Publisher's note Springer Nature remains neutral with regard to jurisdictional claims in published maps and institutional affiliations.

© The Author(s), under exclusive licence to Springer Nature Limited 2021

Methods

Experimental set-up

A commercial SEM (Philips XL-30) was used as an electron-beam source. In our system, the Schottky emitter in the electron gun is triggered by ~150-fs-long (full-width half-maximum, FWHM) ultraviolet laser pulses at 257 nm with an energy of 6 nJ and polarized parallel to the electron propagation direction with a repetition rate of 167 kHz. The released electrons are then accelerated in the microscope column to 28.4 keV. Owing to trajectory effects³⁰, at the interaction point with the nanostructures, the electron pulses are estimated to be roughly 600 fs long (FWHM). The electron beam is focused to the structure entrance with a transverse beam size of ~10 nm (FWHM, measured in the normal, continuous-imaging mode). The electron energy is measured using a home-built magnetic spectrometer and a Chevron-type microchannel plate (MCP) (Extended Data Fig. 1).

The photonic structure is driven by 1.93- μ m infrared laser pulses with 680-fs FWHM duration. The beam is linearly polarized along the particle propagation direction and has a cylindrical shape in order to illuminate the whole structure with $1/e^2$ radius of 94 μ m and 9 μ m (over-focusing structure) or 14 μ m (high-contrast structure). The overlap between electron and laser pulses is achieved by using a delay stage (Extended Data Fig. 1).

In the experiment, the structure is spatially aligned using the continuous-wave imaging mode of the SEM to both laser and electron beam, such that the structure's channel and first set of pillars, along with the input aperture, are in focus. The structure is also rotated around the vector normal to the substrate to make sure that the electrons pass through the channel throughout the structure length. Slight deviations from perfect angular alignment are unavoidable, since this alignment is based on observing the electron signal scattered from the channel and picked up by the secondary electron detector of the SEM. Owing to the geometry of the dual-pillar structure and its extremely narrow channel and aspect ratio, this signal is fairly low. Specifically, for a 78- μ m-long structure with a 225-nm-wide channel, using geometrical considerations we estimate that the electron beam's angle of incidence could deviate by up to 8 mrad.

Fabrication of the photonic nanostructures

The structures were fabricated by means of electron-beam lithography from highly doped (1–5 Ω cm) <100>-oriented silicon wafers. First, the wafer was spin-coated with a 400-nm-thick negative resist (Micro Resist Technology ma-N 2405), which was patterned by a 100-kV lithography machine (Raith EBPG 5200). After the resist development, the silicon wafer was etched anisotropically to a depth of 3 μ m at cryogenic conditions (Oxford Instruments Plasmalab100). This procedure produced the high-contrast structures directly on the wafer substrate (Extended Data Fig. 2), which, owing to geometrical considerations, required the laser beam to have a small incidence angle (5°) to reach the structure itself (Extended Data Fig. 1b).

During the later experiments, we improved our fabrication process, with the goal of eliminating the non-zero incidence angle. With this feature the laser beam can be aligned to the structure in a much easier and more precise manner. Therefore, for the over-focusing structure we used additional fabrication steps to create a mesa (Extended Data Fig. 3), which followed the process described above for the nanophotonic structure fabrication. A 6- μ m-thick layer of positive photoresist (MicroChemicals AZ4562) was deposited on the wafer and patterned using a laser lithography system (Heidelberg instruments DWL66). Following resist-development, the wafer was etched by a Bosch process to a depth of about 60 μ m, and consequently the structures were then elevated by the same height above the substrate (Extended Data Fig. 3). To clean the structures from the photo-resist, the wafer is immersed in a Piranha solution for 5 min.

Structure tolerances

During these experiments, we found that the structure dimensions were critical. A variation of the thickness of all structure features of more than ± 20 nm completely cancelled the desired guiding effect in terms of transmission and energy spread. This is in contrast to previous DLA measurements, where no such sensitivity was found. The strict tolerances are due to the very nature of this exceptionally long structure: The optical nearfields in the experiment have to match the expected nearfields, otherwise errors can accumulate in such a long structure and jeopardize its efficacy.

Particle tracking simulations

The electromagnetic fields were calculated using the Ansys Lumerical FDTD software in 2D. In this simulation, the Gaussian laser beam waist radius was set to 90 μ m ($1/e^2$), and the Gaussian pulse length to 680 fs (FWHM) at 1.93 μ m central wavelength. The beam is incident perpendicular to the nanostructure, and the waist was set to intersect with the channel symmetry axis ($x = 0$ in the main text; see Fig. 3, for instance).

The numerically obtained fields were then loaded into the full 3D particle tracking software General Particle Tracer (Pulsar Physics). The electron-beam parameters were transverse normalized emittance 100 pm-rad, beam diameter 655 nm FWHM and a duration of 400 fs (FWHM). The pulse length chosen in simulation gave the best fit to the experimental data; it is reasonable to assume that in experiment, unlike in simulation, the electron pulse shape is not strictly Gaussian and instead depends heavily on trajectory effects³⁰. The beam divergence half-angle was measured in experiment (using a knife-edge) to be roughly 0.5–1 mrad. We have used 0.5 mrad in our simulations.

For illustrative purposes, the trajectories shown in Fig. 4e, f depict electron pulses that are 0.001 fs in duration. With this illustration the trajectories simulated can be directly related to the schematic explanation of the transverse APF behaviour shown in Fig. 2a. In Extended Data Fig. 4, we show more trajectory simulations. Details are discussed in the caption of that figure. We emphasize that the details of the APF scheme and hence the complex phase-space control at optical frequencies can also be clearly seen here when the trajectories are analysed as shown in the figure.

Half cells at the beginning and the end of the structure

The half macro cells appearing at the beginning and end of each of the structures are a result of the design of the FODO cell, where the incident beam is assumed to have the maximum transverse width at the input of the macro cell (see supplementary material of ref. ¹³). When the FODO lattice period matches the beam envelope's period, maximum transmission of current is achieved for one specific phase. Qualitatively, and regardless of the input transverse size, the effect of the half-cells can also be understood as follows. Assuming that the structure would start with a full lattice cell and an unbunched beam, all phases relative to the laser phase would be occupied. This would result in the lattice cell acting as a full F cell for one half of all phases and a full D cell for the other. Hence, while one part of the beam would be mostly confined, the other would be mostly lost to the pillars. Instead, half a cell only applies half the effect of an F cell on one part and half the effect of a D cell on the other, resulting in a practically more symmetric particle loss, or ideally no particle loss for all phases. The half cell at the end of the structure ensures symmetry and is important for matching the resulting electron bunches to additional stages envisaged in the accelerator on a chip scheme.

Independence of guiding from the injection phase

As stated in the main text, the APF effect in a pure transport structure works for all initial injection phases¹³. The lattice is designed in a similar fashion as the usual FODO scheme³³, where in each cell the maximum beam size is located at its entrance, and the minimum is in the

Article

middle of the FODO cell. APF works for all initial phases, where half of the phases would begin by focusing and the complementary half by defocusing in the transverse plane. Therefore, the lattice acceptance is phase-dependent, and the actual beam size must be smaller than the minimum acceptance of the lattice in order to transport all phases without losses.

In our experimental (and corresponding simulation) case, the beam is not matched to the acceptance of the structure, but is larger. Hence, some particle loss is unavoidable. This can be seen in the simulation in Fig. 4e, f, and in more detail in Extended Data Fig. 4a (the loss due to defocus is particularly seen in subcell 1a).

Comparison between simulation and experimental data

In the 2D simulation, we assumed normal-angle side-illumination. Therefore, to account for the 5° laser incidence angle on the high-contrast structure, the incident peak field observed in the experiment was multiplied by a factor of 1.53 (Fresnel reflection coefficient of silicon at 5° from the substrate). This incorporates the effect of interference on the structure of one part of the incident wave and another reflected from the substrate, and leads to good agreement between simulation and experimental results.

For the electron beam, an angle of 2.8 mrad relative to the z-axis was used to produce the simulation curve in Fig. 4a of the main text, as it agreed best with the experimental results for the high-contrast structure. These 2.8 mrad are well within the experimental angular alignment uncertainty, as discussed under ‘Experimental set-up’ above. With an input of zero angle, the simulation curve shows a similar behaviour but at a lower contrast. The over-focusing structure results match well for zero incidence angle.

Beam current

The normalized beam current is the current flowing through the structure with laser on divided by the current exiting the structure without laser illumination. With a laser repetition rate of 167 kHz and 0.005 electrons per pulse on average here, the beam current roughly equals 133 A. For this work, the total current was of hardly any interest. Importantly, and as shown in previous work³⁰, the tip can emit up to 1,000 electrons per pulse, leading to potentially 10 electrons per pulse in the structure and resulting in currents up to hundreds of femtoamperes in this SEM-based set-up. Currents orders of magnitude larger can be achieved with a more specialized source set-up³⁴ not based on a commercial SEM as used here. Moreover, parallelization schemes are expected to increase the current throughput by an order of magnitude for 10 channels, or by two orders of magnitude for 100 channels, for example³⁵. Because of the lithographic nature of the nanophotonic structure fabrication, multichannel structures are straightforward to produce in the cleanroom. Even 3D structures have been considered and can be produced for DLA³⁶. We further note that collective instabilities such as wakefield effects in these structures have recently been thoroughly investigated³⁷: Even for bunch charges of up to 18,000 electrons at relativistic energies, stable modes of operation can be found. For larger bunch charges, the electron bunch will be driven apart. This can be potentially countered with the forces discussed here but is beyond the scope of this work.

In the main text, we mentioned the possibility of applying DLAs in free-electron lasers, because we see intriguing ways to increase the peak current by many orders of magnitude. Several methods could all be combined to reach peak currents in excess of 1 kA: (1) temporal pulse compression down to 1 fs or below (demonstrated in ref. ^{34,35}), (2) a larger nanophotonic structure driven at a larger wavelength such as 10 μm (ref. ³⁸), with (3) an elliptical beam shape, which can be large in the direction parallel to the pillar height, and (4) the combination of the output beams of, say, 10 nanophotonics-based accelerators, all printed on the same chip (or even 10×10). (5) Most importantly, we expect a large increase in electron number by going to miniaturized

and custom-built electron optics, including the source³⁴. Discussions of these challenges and their potential workarounds are outside the scope of this work, although many of the points discussed above are included in ref. ⁹.

Error calculation

In Fig. 4a, c, the uncertainty of the normalized current (vertical axis) measurement is dominated by statistical noise inherent in our optical acquisition set-up of reading the MCP (see ‘Experimental set-up’ above). From repeated calibration measurements, we estimated and placed a constant standard deviation of ± 0.05 on the value of the normalized current.

The peak field uncertainty (horizontal axis) is derived from the measured elliptical spot size on the structure, and the incident power. These are related through the peak field E_{peak} .

$$E_{\text{peak}} = \left(\frac{8 \sqrt{\ln 2}}{\pi^{3/2}} \frac{Z_0}{\tau_p f_{\text{rep}}} \frac{P_{\text{avg}}}{w_{0z} w_{0y}} \right)^{1/2}, \quad (2)$$

where Z_0 is the impedance of free space, τ_p the duration (FWHM) of the driving laser pulse, f_{rep} the repetition rate of the laser, P_{avg} the average incident power, and w_{0z} and w_{0y} are the elliptical Gaussian beam waists intersecting the structure along the nanostructure channel (z) and the vertical (y) direction. The beam sizes on the structure are deduced by observing the reflected beam from the structure with an auxiliary camera. However, the illumination wavelength is large relative to the structure features and most of them cannot be resolved. w_{0z} can hence be estimated with good accuracy using the phase jumps and structure edges. w_{0y} is much larger than the pillar height and is estimated by moving the sample stage and reconstructing the beam intensity profile. From this, we estimate the measurement and uncertainty $w_{0z} \pm \Delta w_{0z}$ to be $94 \mu\text{m} \pm 4.7 \mu\text{m}$ and accordingly $w_{0y} \pm \Delta w_{0y}$ to be $9 \mu\text{m} \pm 1.8 \mu\text{m}$ (over-focusing structure) and $14 \mu\text{m} \pm 2.8 \mu\text{m}$ (high-contrast structure). The average laser power fluctuations ΔP_{avg} during the experiments are roughly $\pm 3\%$ of the power. This uncertainty is then propagated to yield the peak field and error $E_{\text{peak}} \pm \Delta E_{\text{peak}}$.

Electron acceleration from sub-relativistic to 1 MeV energy

An appropriately designed FODO cell will allow net acceleration of a design range of injection phases. In particular, the macro-cell length and the gap size need to be changed from those used here. Given that the electron velocity increases, the parameters have to vary along the structure. Initial structure designs for acceleration in combination with APF have been published^{13,29}. For an accelerating structure with large energy gain and large particle throughput, however, extending the APF confinement to 3D is needed²⁹. Then, considering the observed record accelerating field of 1.8 GV m^{-1} in DLA³⁹, an accelerator providing 1 MeV over 1 mm is already within reach, opening up venues to several proposed applications either near³⁹ or further in the future^{27,40}.

Accelerator beam parameters

At our subrelativistic electron energy of 28.4 keV and the given laser parameters (same as in Fig. 4e), the theoretically expected β -function⁴⁰ is roughly $42 \mu\text{m}$, which agrees well with the simulation results and the discussion around Extended Data Fig. 4. A similar result was obtained for 1 GV m^{-1} laser field in the supplementary of ref. ¹³. In our example here, as previously discussed, we transport our beam using five FODO cells and roughly $80 \mu\text{m}$, but this length can in principle be extended indefinitely, provided that some form of refocusing is used in the vertical direction²⁹. It is interesting to note that CERN’s Large Hadron Collider uses 23 FODO cells over 2,450 m in each arc. The horizontal and vertical β -functions switch between maximum values of 180 m or 30 m in a complementary fashion, depending on the beam position in the accelerator’s circumference⁴¹.

Data availability

Source data for Fig. 4a, c are provided with the paper. The data in Fig. 4b, d that support the findings of this study are available in Zenodo with the identifier <https://doi.org/10.5281/zenodo.4446542>. Source data are provided with this paper.

33. Wiedemann, H. *Particle Accelerator Physics* (Springer, 2015).
34. Hirano, T. et al. A compact electron source for the dielectric laser accelerator. *Appl. Phys. Lett.* (2020).
35. Zhao, Z. et al. Design of a multichannel photonic crystal dielectric laser accelerator. *Photon. Res.* **8**, 1586–1598 (2020).
36. Staude, I. et al. Waveguides in three-dimensional photonic bandgap materials for particle-accelerator on a chip architectures. *Opt. Express* **20**, 5607–5612 (2012).
37. Egenolf, T., Niedermayer, U. & Boine-Frankenheim, O. Tracking with wakefields in dielectric laser acceleration grating structures. *Phys. Rev. Accel. Beams* **23**, 054402 (2020). <https://doi.org/10.1103/PhysRevAccelBeams.23.054402>
38. Kimura, W. D., Pozorelsky, I. V & Schächter, L. CO₂-laser-driven dielectric laser accelerator. In *2018 IEEE Advanced Accelerator Concepts Workshop (AAC)* <https://doi.org/10.1109/AAC.2018.8659403> (2018).
39. Egerton, R. F. Outrun radiation damage with electrons? *Adv. Struct. Chem. Imaging* **1**, 5 (2015).

40. Cros, B. & Muggli, P. Input to the European Particle Physics Strategy Update. in *Advanced Linear Collider Study Group (ALEGRO collaboration)* (2018).
41. Brüning, O. S. et al. *LHC Design Report CERN-2004-003-V1* (2004).

Acknowledgements We acknowledge discussions with the members of the Accelerator on a Chip International Program (ACHIP). We thank the clean-room facility staff at the Max Planck Institute for the Science of Light for continued assistance. We acknowledge funding by the Gordon and Betty Moore Foundation (#GBMF4744), ERC grants NearFieldAtto (#616823) and AccelOnChip (#684217) and BMBF projects 05K19WEB and 05K19RDE.

Author contributions T.C. and J.I. measured the data. R.S. and U.N. designed the structures and performed simulations. P.Y. fabricated the structures. J.I., R.S. and T.C. analysed the data. N.S. and A.M. inferred stringent tolerance requirements from initial measurements. J.I., R.S. and P.H. wrote the manuscript. P.H. supervised the experiment.

Competing interests The authors declare no competing interests.

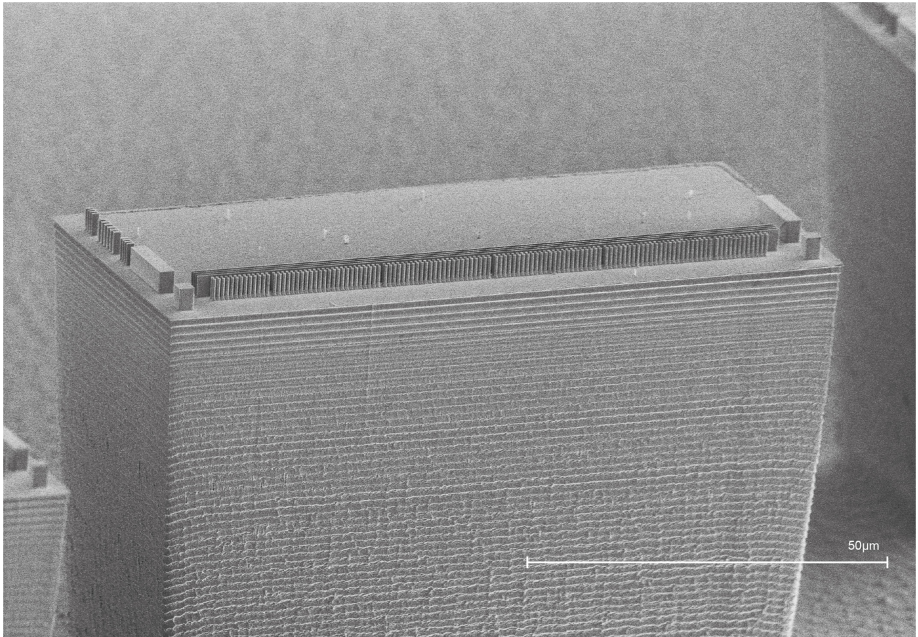
Additional information

Supplementary information The online version contains supplementary material available at <https://doi.org/10.1038/s41586-021-03812-9>.

Correspondence and requests for materials should be addressed to R. Shiloh, J. Illmer or P. Hommelhoff.

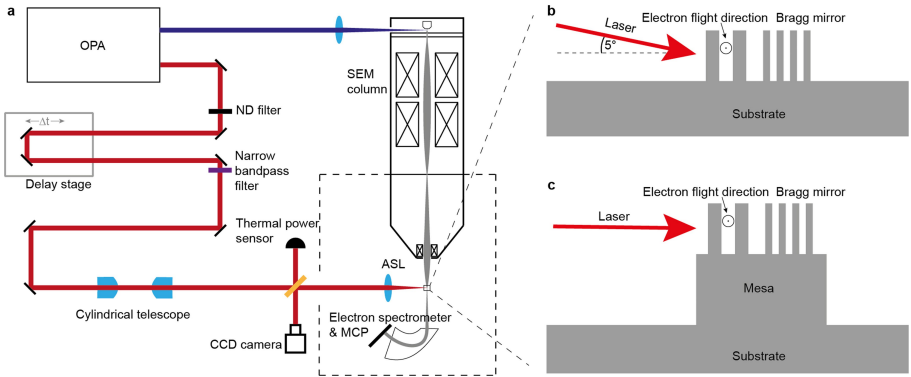
Peer review information Nature thanks James Rosenzweig, Yelong Wei and the other, anonymous, reviewer(s) for their contribution to the peer review of this work.

Reprints and permissions information is available at <http://www.nature.com/reprints>.



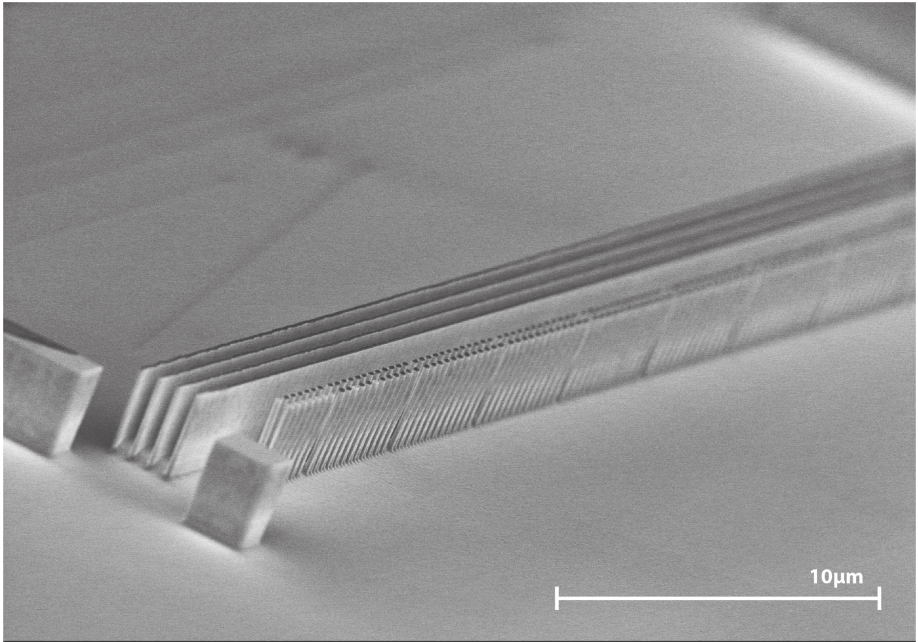
Extended Data Fig. 1 | Photonic nanostructure on top of a mesa: over-focusing structure. This SEM image shows a structure fabricated on top of a 60 μm -high mesa. The photonic structure for the over-focusing measurement is visible atop the mesa. The five gaps between the macro cells are also clearly visible. Here, 24 pillar pairs build one macro cell. Input (left) and

output (right) apertures (thick blocks) are used for alignment during experiment. Additional pillars to the left of the input aperture act as markers that identify the specific structure during the experiment. The mesa allows us to focus the laser beam under 0° incidence angle from the side (see also Extended Data Fig. 1c).



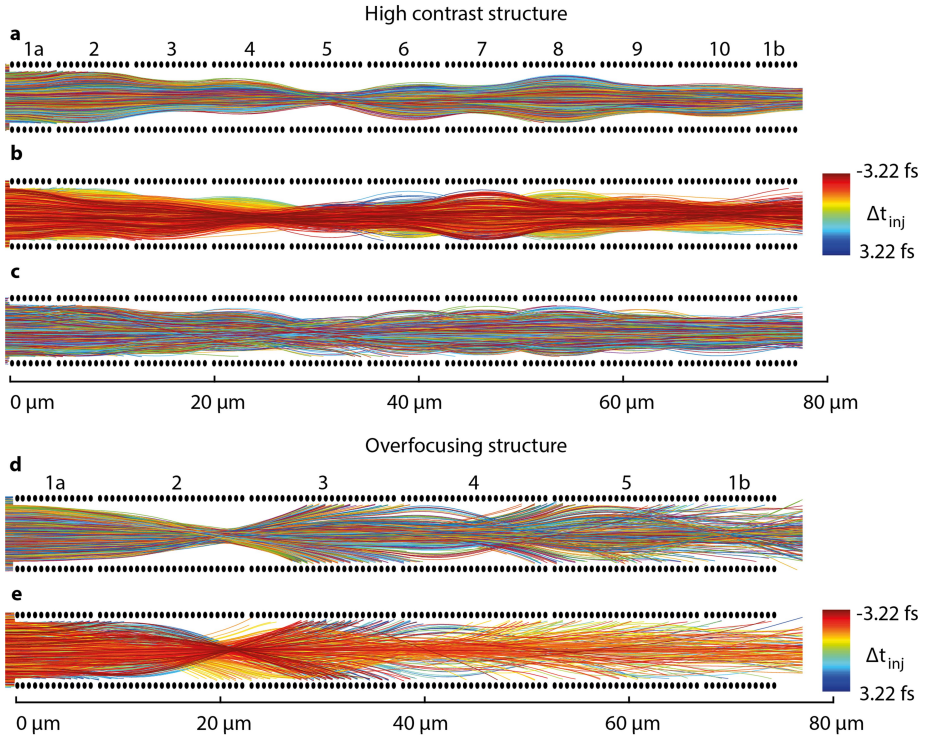
Extended Data Fig. 2 | Schematic of the experimental set-up. (a) Both IR (red) and UV (blue) laser pulses are generated with the help of an optical parametric amplifier (OPA). The UV pulses are focused onto the Schottky emitter of the SEM, where they release electron pulses. The electron pulses pass through the electron column and are focused into the nano-photonic channel. The IR pulses first pass a neutral-density (ND) filter for variable optical power attenuation before they traverse a delay stage, where the time delay between IR laser pulses and electron pulses is set. A bandpass filter limits the IR spectrum so that the laser pulses are stretched to a duration of 680 fs (FWHM).

A cylindrical telescope is used to generate an elliptic laser beam with a 1:6 ratio. The beam is then split into two parts, where one part is used to monitor the power during measurements and the other is focused on the structure via an aplanatic lens (ASL). The back reflection from the sample is used to align the laser beam to the structure. The electron energy is measured with a magnetic deflection spectrometer and an MCP detector with a phosphor screen, viewed from outside the vacuum chamber (indicated by the dashed line) with a CCD camera (not shown). For structures without a mesa (b) the incident angle of the laser beam is 5°, while for structures on top of the mesa (c) this angle is 0°.



Extended Data Fig. 3 | Photonic nanostructure on flat substrate: high contrast structure. The scanning electron microscope (SEM) image shows the dual pillar transport structure for high contrast measurements. The dual pillar transport channel can be seen on the right as a colonnade structure. The four solid slabs left-above of the colonnades structure are a distributed Bragg

mirror³¹. An alignment aperture is placed at the input of the structure (thick blocks). Electrons are focused into the colonnade structure, that is, into the channel between the rows of pillars. The laser beam impinges on the structure from the side, from bottom-right here, perpendicular to the pillars and with a 5° angle to the substrate (see also Extended Data Fig. 1b).



Extended Data Fig. 4 | Particle tracking simulation: One optical phase vs. all optical phases. (a) Example particle trajectories for the optimal guiding field strength. The differently colored curves in between the pillars denote individual particle trajectories. The APF behaviour is clearly visible in the breathing of the envelope of the particle trajectories. For illustrative purposes the simulation was conducted with an electron pulse length of 0.001 fs. This way, the APF effect is apparent because electrons only sample fields of a small random fraction of the optical cycle, away from the crest. The lattice periodicity of $2 \times (7.149 \mu\text{m} + 0.589 \mu\text{m}) = 15.47 \mu\text{m}$ (see Fig. 3), which is equal to the beta function periodicity, can be directly seen in the envelope of the trajectories, where the phase jump is manifested as a bending of the curve. Hence we can here directly assign F to macro cell 2, D to macro cell 3, and so on repeatedly (see numbering at the top of each macro cell, macro cell 1 consists of 2 half cells at the beginning and the end of the structure). (b) Same as (a) but with all optical phases uniformly sampled. The electron pulse (flat-hat) here is one optical period long. Evidently, the existence of the two fixed points in phase, $\pi/2$ and $3\pi/2$, cannot be easily discerned close to the entrance of the structure, meaning that F and D cannot be uniquely assigned to each cell. Halfway through the structure, however, the lattice oscillations become visible again in the form of two “modes”, namely two trajectory classes, each directly

linked to the lattice period again. The evolution into this two-mode structure is a consequence of the electrons accumulating around the two fixed points in phase space separated by π^{13} . The result is an overlapping of two breathing motions in the trajectories shifted by one macro cell. (c) Same as (b) though the flat-hat electron pulse is here 400 fs long, the APF scheme still leads to particle propagation with hardly any loss, and the overall envelope nearly matches that of the single-cycle pulse in (b) (same as Fig. 4e of the main text). (d) Example particle trajectories with the over-focusing behaviour visible (same as Fig. 4f of the main text). Again, we only show particle trajectories of an electron pulse with a duration of 0.001 fs. Particles are obviously lost, where the lost particles’ deviation from the design axis exceeds the aperture of the structure. (e) Same as in (d) but with all phases sampled. A similar effect as depicted in (b) takes place, where the loss of particles at the structure boundary occurs at multiple locations. The reason is, again, that macro cells act differently depending on where the electron is with respect to the optical phase, and hence experience forces shifted in phase. Most importantly, the overall performance of the APF scheme is maintained, if not for the limitation of the beam size due to the structure aperture. The colours in b and e indicate the injection time of the electron (see colour bar).

High gradient silicon carbide immersion lens ultrafast electron sources



Cite as: J. Appl. Phys. 131, 134501 (2022); doi: 10.1063/5.0086321

Submitted: 24 January 2022 · Accepted: 1 March 2022 ·

Published Online: 4 April 2022



Kenneth J. Leedle,^{1,a)} Uwe Niedermayer,² Eric Skär,² Karel Urbanek,³ Yu Miao,¹ Payton Broadus,¹ Olav Solgaard,¹ and Robert L. Byer³

AFFILIATIONS

¹Department of Electrical Engineering, Stanford University, Stanford, California 94305, USA

²Technical University Darmstadt, Institute for Accelerator Science and Electromagnetic Fields, Schlossgartenstraße 8, 64289 Darmstadt, Germany

³Department of Applied Physics, Stanford University, Stanford, California 94305, USA

^{a)} Author to whom correspondence should be addressed: kleedle@stanford.edu

ABSTRACT

We present two compact ultrafast electron injector designs with integrated focusing that provide high peak brightness of up to 1.9×10^{12} A/m² Sr² with 10's of electrons per laser pulse using silicon carbide electrodes and silicon nanotip emitters. We demonstrate a few centimeter scale 96 keV immersion lens electron source and a 57 keV immersion lens electron source with a 19 kV/mm average acceleration gradient, nearly double the typical 10 kV/mm used in DC electron sources. The brightness of the electron sources is measured alongside start-to-end simulations including space charge effects. These sources are suitable for dielectric laser accelerator experiments, ultrafast electron diffraction, and other applications, where a compact high brightness electron source is required.

© 2022 Author(s). All article content, except where otherwise noted, is licensed under a Creative Commons Attribution (CC BY) license (<http://creativecommons.org/licenses/by/4.0/>). <https://doi.org/10.1063/5.0086321>

I. INTRODUCTION

High brightness ultrafast electron sources are critical for a large variety of applications including microscopy, diffraction, and dielectric laser accelerator (DLA) devices, such as free electron lasers. These applications require both a bright electron source and subsequent electron optics to deliver a nanometer size beam to a downstream interaction point. The key electron source figure of merit is the normalized peak brightness $B_{p,n} = J_p / 4\pi^2 \epsilon_n^2$ for peak current J_p and normalized rms emittance ϵ_n in the beam focus.¹ Research efforts have focused on improving performance from metal tips, coated metal tips, silicon tips, or nanowires in various forms with great success.²⁻⁵ When combined with a meter-scale transmission electron microscope (TEM) column for beam shaping, a laser-triggered tungsten cold field emission source can deliver a $\epsilon_n = 10$ pm-rad beam with a normalized peak brightness of $\sim 4 \times 10^{13}$ A/m² Sr² with 0.5 electrons per pulse after filtering out 97% of the electrons.⁶ Such a TEM source meets the injection emittance requirements for a scalable dielectric laser accelerator,^{7,8} but the current is too low for many applications that require multiple electrons per pulse.^{9,10} DC sources with flat cathodes can provide

1000's of electrons per pulse with a downstream brightness of $\sim 2 \times 10^{11}$ A/m² Sr², but typically have a normalized emittance in the 10 nm-rad range, unsuitable for many applications without emittance filtering.¹¹⁻¹³ Without compression, the beam brightness delivered to a downstream interaction point from DC biased photocathode sources is limited by space-charge effects in the low maximum accelerating field of 10–12 kV/mm.^{11,12} Radio-frequency electron guns, on the other hand, can offer accelerating gradients in excess of 100 kV/mm, greatly reducing the influence of space-charge effects on the beam, but generate beam emittances similar to flat DC photocathodes.¹⁴ There have been several demonstrations of very high 50–130 kV/mm DC fields with a flat cathode and hemispherical anode, but these are not commonly used outside of field demonstration experiments, and have not been used in a complete electron source with a nanotip cathode.^{15,16}

In this paper, we present a compact 96 keV immersion lens¹⁷ electron source that fits within a 25 mm radius footprint with no additional focusing elements and a more flexible high gradient 57 keV immersion lens electron source that includes a separate solenoid lens so that spot size and beam divergence can be optimized

for different applications. These sources deliver sub-100-pm-rad normalized emittance beams with peak brightness of up to 1.9×10^{12} A/m² Sr² at a downstream interaction point, and they preserve the full current of the tip source with no emittance filtering. These sources build upon the prototype 30 keV immersion lens source,¹⁷ scaling to higher gradients, energy, and beam brightness. Silicon carbide electrodes are used to enable robust turn-key operation at high DC fields, and silicon nanotip cathodes are used to provide an easily integratable nanotip source. Silicon carbide has a high DC breakdown field of 300 kV/mm and is widely used in power electronics for that reason.¹⁸ It is also extremely hard and resistant to heat and many chemicals. Silicon carbide has previously been used in low energy field emission sources and thermionic converters,^{19,20} but it has not been evaluated as a material for electron gun assemblies to the best of our knowledge. The immersion lens electron beams are injected into silicon dual pillar dielectric laser accelerators to characterize their brightness and demonstrate their compatibility with applications that require sub-micron beams with many electrons per pulse.^{9,10}

II. EXPERIMENTAL DESCRIPTION

In these experiments, 4H 0.02 Ω cm nitrogen doped silicon carbide electrodes were laser cut to size and the edges were shaped with diamond abrasive tools and mechanically polished to 0.1 μm finish with diamond lapping film. The maximum field that the silicon carbide electrodes can handle is limited by subsurface defects from the mechanical polishing process. Subsurface defects result in degraded local material properties and are the initiation sites of breakdown. Using chemical-mechanical polishing or similar methods would enable even higher surface breakdown fields. In testing, the SiC electrodes were stable (below 1 fA field emission) in fields of over 100 kV/mm in a simple diode configuration and at peak surface fields of approximately 70 kV/mm for two months of operation in a full immersion lens assembly (failure was caused by mechanical shock to the vacuum system while in operation). The maximum operating gradients in our device were limited by the need for cathode drive laser clearance and the field limits on the silicon cathode from the focusing voltage. The silicon cathode breaks down at surface fields of approximately 40 kV/mm and was the primary source of electron gun failure once most surface defects in the SiC electrodes were eliminated. The high hardness of silicon carbide also facilitated handling and cleaning procedures after polishing compared to metal and silicon electrodes. Unlike conventional high voltage electrodes, these silicon and silicon carbide components will be stable up to their breakdown field without conditioning and require re-polishing after a breakdown event in the high field region.

Figure 1 shows the 96 keV “Glassbox” immersion lens constructed with a conventional average accelerating gradient of 8.4 kV/mm. The objective for this configuration was to create a ~100 keV DLA electron injector that was as compact as possible, fitting inside of a 25 mm radius “Glassbox.” The immersion lens is mounted in a stainless-steel housing suspended inside a 50 mm diameter tube and faces a 316LN stainless-steel anode at 12 mm distance. A stainless-steel anode was chosen for simplicity with the lower accelerating gradient in this design. The silicon nanotip

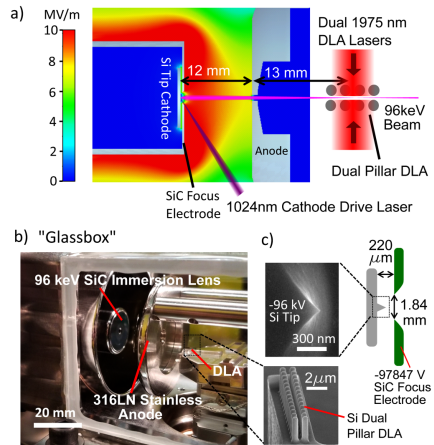


FIG. 1. (a) Schematic of the “Glassbox” 96 keV immersion lens experiment showing electric field magnitude. (b) Image of the Glassbox 96 keV immersion lens experiment. (c) Closeup of the Glassbox immersion lens geometry and scanning micrograph images of the silicon nanotip and dual pillar silicon DLA.

cathodes are mounted on an adjustable ceramic standoff with a vacuum gap between cathode and the focusing electrode. The immersion lens focus is 13 mm behind the front of the anode, for a total working distance of 25 mm from source to the dual pillar DLA structure. This is slightly longer than the 15 mm working distance for an unfocused 100 keV beam presented in Ref. 11, but it provides a beam of 100× smaller emittance.

The Glassbox immersion lens used a 360 μm thick silicon carbide focusing electrode with a tapered 1.84 mm diameter aperture and a cathode to focusing electrode gap of 220 μm as shown in Fig. 1(c). The silicon nanotips used are similar to those used in Ref. 17, with a tip height of ~400 nm above the silicon surface and a tip radius of ~20 nm. The cathode chip has an array of nearly identical silicon tips in a 20 μm spaced isometric grid, and the one closest to the center axis is used. The 20 μm tip spacing was chosen such that a tip will always be within 12 μm of the center axis, and an individual tip can be addressed with a 10 μm 1/e² radius laser spot. Figure 1(c) shows an image of the silicon nanotip and the silicon dual pillar DLA used for cross-correlation bunch length measurements.

Figure 2 shows the 57 keV “Shoebbox” immersion lens source that was designed to provide higher acceleration gradients and a reconfigurable focus size and divergence using the immersion lens together with a separate solenoid. This reconfigurability enabled the immersion lens to be optimized for maximum DLA interaction

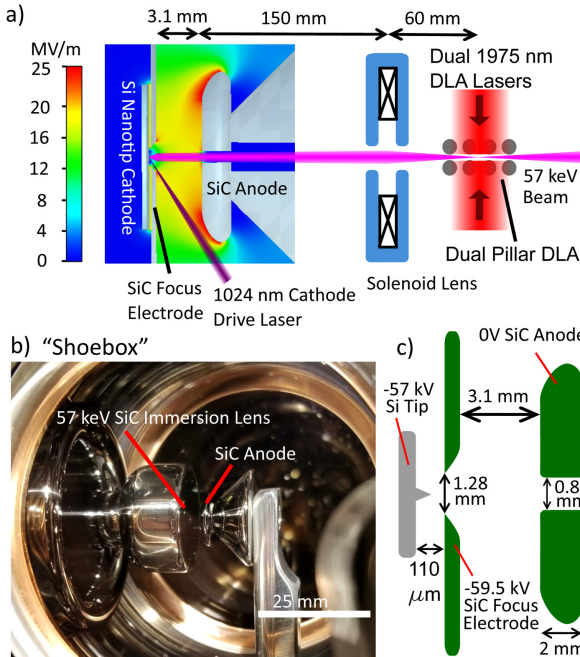


FIG. 2. (a) Schematic of the “Shoobox” 57 keV experiment showing electric field magnitude in the immersion lens. (b) Image of the 57 keV SiC immersion lens. (c) Illustration of the 57 keV immersion lens geometry (not to scale).

point brightness. Figure 2(a) shows that the peak surface field on the silicon carbide electrodes was ~ 33 kV/mm, which is less than half the breakdown field of these electrodes and resulted in turn-key operation with excellent stability. The 57 keV beam energy was chosen over a 100 keV beam energy primarily because of the reduced electrical and radiation hazards during electron gun failure and is a sufficiently high energy for DLA and ultrafast electron diffraction experiments. The immersion lens in this system is used to set the beam divergence going into the solenoid, and hence the beam’s focus size and divergence can be optimized for maximum brightness. The electrical feedthrough for the 57 keV immersion lens was a 40 mm ceramic break, for an overall system size of a shoobox, not including radiation shielding and vacuum pumps. The total working distance for the Shoobox was 213 mm from the cathode to the DLA interaction point, significantly smaller than a typical transmission electron microscope column.

The 57 keV immersion lens was constructed with a $360\ \mu\text{m}$ thick silicon carbide focus electrode with a tapered 1.28 mm diameter aperture and a 2 mm thick silicon carbide anode with a

0.85 mm diameter bore as shown in Fig. 2(c). The silicon cathode was mounted $110\ \mu\text{m}$ behind the back surface of the SiC focusing electrode. The separation between the SiC focus electrode and the SiC anode was 3.1 mm for these measurements, for a bulk accelerating field of 19 kV/mm. The same geometry silicon nanotips are used as in the Glassbox system, with the closest tip to the center axis used for these measurements.

The silicon nanotips were triggered using five-photon emission with a 1024 nm, 280 fs FWHM laser with a peak intensity of $1\text{--}2 \times 10^{10}$ W/cm² at a 30° angle to the substrate as illustrated in Figs. 1(a) and 2(a). This multi-photon emission process suppresses emission from the cathode substrate as compared to one- or two-photon emission, but it results in a larger electron energy spread.²¹ The laser repetition rate was 925 kHz for average electron beam currents of up to 7 pA or 47 electrons per pulse as measured with a Faraday cup and electrometer. Tip emission was stable over 100 h at up to 20 electrons per pulse, but it did slowly degrade at above 30 electrons per pulse. Typical emission stability was about 2% rms at 20 electrons per pulse, which is in line with the <0.5% rms

stability of the laser trigger. With the isometric tip grid, there are typically several tips that are close enough to the immersion lens center axis to provide adequate performance to prolong the life of the source to several hundred hours before the cathode needs to be replaced. There is some variation in emission properties between adjacent tips, typically requiring slightly different laser intensities for a given electron yield. The beam profile is determined by the tip radius and height, which is usually very uniform for oxidatively sharpened silicon tips.⁴ Each immersion lens was built twice with similar performance both times. The operating vacuum was 2×10^{-9} Torr for the Glassbox due to the permeability of the epoxy window seals and 5×10^{-10} Torr for the Shoebox system. Silicon tips have shown stable operation in vacuums as poor as 10^{-8} Torr, so efforts were not made to bake out the systems to improve the vacuum.³

III. RESULTS

Figure 3 shows the raw data collected from the immersion lens sources. First, the unfocused beam profile for <1 electron per

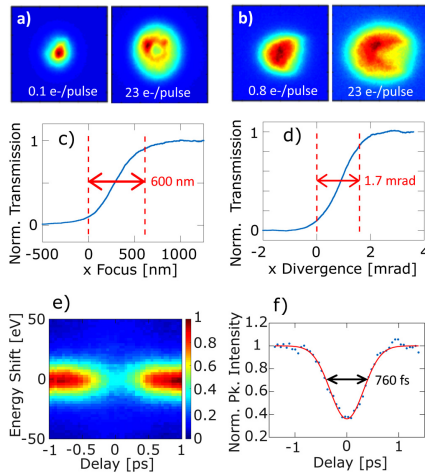


FIG. 3. (a) Profile of the 96 keV Glassbox beam at a low intensity and 23 electrons per pulse with immersion lens turned off ($0 \text{ V}_{\text{focus}}$). (b) Profiles of the 57 keV Shoebox beam at a low intensity and 23 electrons per pulse with immersion lens and solenoid lens off. (c) and (d) show example x_{10-30} knife edge focus and divergence measurements from the 57 keV shoebox at the DLA and 26 cm downstream for $1 \text{ e}^-/\text{pulse}$. Similar measurements were performed for both immersion lens designs. (e) Shoebox DLA interaction cross-correlation spectrum vs delay. (f) Peak depletion bunch length measurement at the DLA for the beam shown in (c)–(e).

laser pulse and 23 electrons per laser pulse were taken for each system using a microchannel plate detector as shown in Figs. 3(a) and 3(b). At higher electron yields, the emission cone from the tip grows and often forms a ring or crescent moon beam depending on the exact tip parameters. These ring and crescent moon shapes are caused by off-apex electron emission.²² The focusing voltage and solenoid current were then optimized and the beam emittance was measured by performing knife edge measurements at the focus of the beam on a DLA structure and at a knife edge 26 cm downstream to measure the beam divergence. The knife edge 10%–90% normalized transmission width was converted to rms width by dividing by 2.56 for an assumed Gaussian beam shape. Figures 3(c) and 3(d) show example knife edge scans from the 57 kV Shoebox immersion lens. The x and y emittance were within 10% of each other for all the data collected. At the immersion lens focus a combination of aberrations and space-charge effects will produce a Gaussian-like circle of least confusion profile, so an initial ring or crescent distribution at the tip will not significantly affect suitability for most applications.

A dual pillar silicon DLA in the beam focus was used to perform a cross-correlation acceleration experiment to measure the electron bunch length for both systems.¹⁸ Figure 3(e) shows an example DLA spectrum as a function of delay for the Shoebox system at 1 electron per pulse. Note that the DLA modulates the electrons more than 1 keV so the accelerated electrons are not resolved in this scan. The magnetic spectrometer has a point spread function of 25 eV FWHM. The center peak intensity vs delay from Fig. 3(e) is shown in Fig. 3(f) and is used to measure the electron bunch length. The Gaussian fit FWHM of the center peak depletion is deconvolved with the 310 fs electric field FWHM of the DLA drive lasers to obtain the electron bunch length. Center peak depletion is a more robust bunch length measurement than the width of accelerated electron signal as used in Ref. 17 and will usually give longer bunch length measurements. Typical focus intensities for the 1975 nm DLA drive lasers were $6 \text{ mJ}/\text{cm}^2$ from each side.

Table I summarizes the performance of the SiC immersion lenses. The Glassbox 96 keV immersion lens focused the beam

TABLE I. Low charge beam properties.

System	Glassbox	Shoebox
Beam energy (keV)	96.0	57.0
Acceleration gap (mm)	12	3.1
Total working distance (mm)	25	213
Focus voltage, V_f (V)	1847	2500
Average cathode field (kV/mm)	1.44	5.13
Average field to anode (kV/mm)	8.4	19.2
Min RMS focus (μm) (sim)	0.41 (0.42)	0.23 (0.21)
Min RMS div (μrad) (sim)	390 (346)	680 (1000)
Min normalized emittance (pm rad) (simulation)	97 (94)	77 (102)
Min FWHM bunch length (fs) (simulation)	830 (993)	700 (587)

onto the DLA at a 25 mm working distance with no additional focusing elements. This source produced a focus size of 410 nm rms, a 0.39 mrad rms divergence angle, a 97 pm-rad normalized emittance, and a bunch duration of 830 fs at low charge. The Glassbox immersion lens produced a maximum peak brightness of $B_{p,n} = J_p/4\pi^2 e_n^2 = 9.3 \times 10^{11} \text{ A/m}^2 \text{ Sr}^2$ at $N_e = 23$ electrons per pulse ($J_p = N_e q_e/t_p$ for electron charge q_e and $t_p = 1230$ fs FWHM bunch length) with a 290 pm-rad normalized emittance ϵ_n . This normalized peak brightness was similar to the $8.6 \times 10^{11} \text{ A/m}^2 \text{ Sr}^2$ at 28 electrons per pulse obtained with the 30 keV immersion lens prototype¹⁷ which informed the design of the Shoebox system to support higher gradients and better optimization. The maximum average normalized brightness of the Glassbox beam was $B_{avg,n} = J_{avg}/4\pi^2 e_n^2 = 1.05 \times 10^6 \text{ A/m}^2 \text{ Sr}^2$ in the beam focus for average current $J_{avg} = 3.4 \text{ pA}$ ($N_e = 23$ at 925 kHz) and normalized rms emittance ϵ_n .

The Shoebox 57 keV system was designed to be more flexible, with an adjustable gap between the focusing electrode and grounded anode and a separate solenoid lens to focus the nearly collimated electron beam from the immersion lens onto the DLA device. The Shoebox system had optimal performance with a beam divergence of 0.68 mrad rms, delivering 230 nm rms spot sizes, 77 pm-rad normalized emittance, and 700 fs FWHM bunch lengths at low charge. The maximum normalized peak brightness measured was $1.9 \times 10^{12} \text{ A/m}^2 \text{ Sr}^2$ at 12 electrons per pulse with a 170 pm-rad normalized emittance and a 950 fs FWHM bunch length. This corresponded to a maximum measured average brightness of $1.66 \times 10^6 \text{ A/m}^2 \text{ Sr}^2$ at 1.8 pA ($N_e = 12$ at 925 kHz). This lower maximum electron current was due to tip deterioration after testing at high electron yields. The Shoebox average brightness is comparable to or better than a CW laser triggered Schottky emitter transmission electron microscope without emittance filtering.¹

Figure 4 shows the beam brightness vs beam current for the immersion lenses. The beam brightness tends to saturate above a

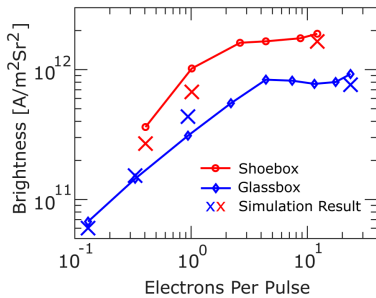


FIG. 4. Immersion lens normalized peak brightness vs beam current for the 96 keV Glassbox and 57 keV Shoebox systems. Simulation results in the single electron and maximum brightness case are marked with "x" for each experiment.

few electrons per pulse due to space charge. The Glassbox system showed a large focus size increase with space charge, but the divergence and bunch length increased more slowly. Focus size, beam divergence, and bunch length all increased more evenly with space charge for the Shoebox. The bulk accelerating gradient did not have a strong effect on the Shoebox beam brightness, since the source brightness was largely limited by the low cathode field in the immersion lens. The performance of the 57 keV immersion lens was similar at 16.5 and 18.4 kV/mm bulk gradients with similar immersion lens focal lengths. The improved brightness of the Shoebox source over the Glassbox source can largely be attributed to its higher cathode field in the immersion lens (5.1 kV/mm vs 1.4 kV/mm, respectively), which was part of the motivation for using a separate solenoid for the DLA interaction point focus.

The SiC immersion lens devices were modeled using finite element analysis and particle-in-cell tracking simulations in CST Studio to confirm the influence of the bulk accelerating field and cathode extraction field on the source brightness. The computational domain was divided into three parts: the emitter simulation, the immersion lens simulation, and the solenoid simulation in the case of the 57 keV Shoebox system. Figure 5 shows the emitter simulation in a $60 \mu\text{m}$ ($30 \mu\text{m}$ for the shoebox) long cylindrical region with the boundary potential obtained from the immersion lens simulation. After running through the emitter field, the electrons are injected into the immersion lens simulation at $z = 60 \mu\text{m}$ and $z = 30 \mu\text{m}$, respectively. Finally, for the Shoebox, there is also magnetostatic simulation performed for the solenoid focus into the DLA.

The tips in both the Glassbox and Shoebox are modeled as a cone of 400 nm height with a base radius of 200 nm and hemispherical apex of 20 nm radius. This results in a field enhancement factor (apex field divided by cathode average field) of 17.5. This enhanced field drops off over 10 s of nanometers to the baseline cathode field. The modest 10^{16} cm^{-3} doping of the silicon tips may also reduce the DC field enhancement somewhat due to field penetration.²³ Note that the maximum DC fields on the nanotips are far from the $\sim\text{GV/m}$ fields required for cold field emission.

The initial electron distribution is prepared in spherical coordinates with uniform longitude and cosine latitude. The cosine angular distribution is scaled to match the experimental emittance in the absence of space charge. The fitted electron distribution had

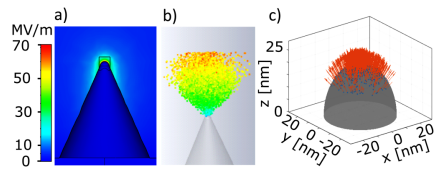


FIG. 5. Simulation of silicon tip emission in the CST studio. (a) DC fields on the tip. (b) Emitted electrons (energy color coded) (c) Prepared initial distribution (no space charge).

mean energy of 1.5 eV with a 14.2° rms cosine dependence. The rms energy spread was a fitting parameter to match the bunch length in the absence of space charge and was 0.3 eV for the Glassbox and 1.5 eV for the Shoebox. These are in line with the expected range accounting for multi-photon effects²¹ and other noise sources. Unfortunately, the magnetic spectrometer used could not resolve below 25 eV for a direct measurement of the energy spread. Displacing the tip off-center to model alignment error results in strongly asymmetric beam shapes that were not found experimentally, suggesting that the tips used were within 10 μm of the beam axis.

The initial electron temporal profile is taken as Gaussian with 140 fs FWHM, i.e., the length of the laser pulse divided by the square root of the emission photon order. This initial bunch length broadens from 140 fs to ~90% of the final bunch length by the time the electrons reach the focusing electrode due to the starting energy spread and trajectory effects even without space-charge. This bunch lengthening can be reduced by increasing the electric field in the cathode region and reducing the electron energy spread from the laser triggering process to mitigate chromatic and geometrical broadening when the electrons have low energy. This was also verified experimentally by operating the 57 keV Shoebox immersion lens with zero focusing voltage to increase the cathode field from 5.1 kV/mm at 2500 V_f to 9.3 kV/mm at 0 V_f. This decreased the experimental single electron bunch length from 700 to 630 fs FWHM, but the emittance and brightness were significantly worse due to aberrations in the solenoid lens.

The simulations were performed at low-charge and at the peak brightness point for each configuration since the full 3D simulations became prohibitively expensive computationally with space-charge dynamics included. The simulated emittance increase had to account for the larger emission cone with increasing current in addition to space charge effects. Increasing the cosine scaling to 18.2° rms matched the experimental peak brightness well for the Glassbox and Shoebox.

IV. DISCUSSION

The performance of the immersion lenses stays relatively constant over a wide range of device parameters. This is due in large part to the sensitivity of these systems to spherical and chromatic aberrations and coma in the immersion lens itself. Even small shifts of 10 μm of the cathode nanotip from the optic axis cause increases in the achievable focus size. Spherical aberration also strongly increases the achievable focus size downstream of the immersion lens, and hence the nanotip emission spatial profile strongly influences the source emittance. The ~400 nm tall silicon nanotips also need to be driven with fourth or fifth order multiphoton excitation to prevent substrate emission. This large photon order contributes to a larger energy spread for the electron source, which is higher than other needle based tip emitters that can be driven at the material work function.²⁴ Additionally, for a given immersion lens geometry and focal length, changing the bulk dc gradient does not significantly affect the relatively low electric field on the nanotip cathode. A taller nanotip with larger DC field enhancement factor could potentially provide higher performance and less sensitivity to space-charge effects. Reducing the electron

energy spread and increasing the field at the cathode would reduce the electron bunch length significantly. Shortening the cathode laser pulses from 140 fs to sub-30 fs would provide a modest improvement to the bunch lengths for single electron pulses, but would increase space-charge effects in multi-electron pulses.

V. CONCLUSION

The reported SiC immersion lenses enable very compact sources of sub-picosecond electron bunches with excellent beam parameters for dielectric laser accelerator, ultrafast electron diffraction, and other measurements with up to 23 electrons per pulse. We measured normalized emittances smaller than 100 pm-rad and peak brightness larger than 10¹² A/m²/Sr². The measurements were confirmed by multi-scale simulations in the full 3D fields. For planned scalable DLA experiments with transverse confinement and large energy gain,²⁵ these emittances are still about a factor of four too high and further improvement is needed to prevent beam loss. Currently, the sources are limited by the extra energy spread of the silicon emitter in this geometry, as well as spherical and chromatic aberrations. Future designs using different geometry nanotips could take advantage of high extraction field, low energy spread emitters and the high operating gradients enabled by silicon carbide electrodes. Furthermore, silicon and silicon carbide electron source components could be readily integrated into a high-performance accelerator on a chip platform.

ACKNOWLEDGMENTS

This work was funded by the Gordon and Betty Moore Foundation (No. GBMF4744). We wish to thank T. Hirano and P. Hommelhoff for their fruitful discussions.

AUTHOR DECLARATIONS

Conflict of Interest

The authors have no conflicts of interest to disclose.

DATA AVAILABILITY

The data supporting the findings of this manuscript are available from the corresponding author upon reasonable request.

REFERENCES

- ¹A. Feist, N. Bach, N. R. da Silva, T. Danz, M. Möller, K. E. Priebe, T. Domröse, J. Gregor Gatzmann, S. Rost, J. Schauss, S. Strauch, R. Bormann, M. Sivas, S. Schäfer, and C. Ropers, "Ultrafast transmission electron microscopy using a laser-driven field emitter: Femtosecond resolution with a high coherence electron beam," *Ultramicroscopy* **176**, 63–73 (2017).
- ²P. Hommelhoff, J. Sortais, A. Aghajani-Talesh, and M. A. Kasevich, "Field emission tip as a nanometer source of free electron femtosecond pulses," *Phys. Rev. Lett.* **96**, 077401 (2006).
- ³H. Zhang, J. Tang, J. Yuan, Y. Yamauchi, T. T. Suzuki, N. Shinya, K. Nakajima, and Lu.-C. Qin, "An ultrabright and monochromatic electron point source made of a LaB₆ nanowire," *Nat. Nanotechnol.* **11**, 273–279 (2016).
- ⁴M. E. Swanwick, P. D. Keathley, A. Fallahi, P. R. Kroger, G. Laurent, J. Moses, F. X. Kärtner, and L. F. Velásquez-García, "Nanostructured ultrafast silicon-tip optical field-emitter arrays," *Nano Lett.* **14**(9), 5035–5043 (2014).

- ⁵A. Tafel, S. Meier, J. Ristein, and P. Hommelhoff, "Femtosecond laser-induced electron emission from nanodiamond-coated tungsten needle tips," *Phys. Rev. Lett.* **123**, 146802 (2019).
- ⁶F. Houdellier, G. M. Caruso, S. Weber, M. Kociak, and A. Arbouet, "Development of a high brightness ultrafast transmission electron microscope based on a laser-driven cold field emission source," *Ultramicroscopy* **186**, 128–138 (2018).
- ⁷U. Niedermayer, T. Egenolf, O. Boine-Frankenheim, and P. Hommelhoff, "Alternating-phase focusing for dielectric-laser acceleration," *Phys. Rev. Lett.* **121**, 214801 (2018).
- ⁸U. Niedermayer, J. Lautenschläger, T. Egenolf, and O. Boine-Frankenheim, "Design of a scalable integrated nanophotonic electron accelerator on a chip," *Phys. Rev. Appl.* **16**, 024022 (2021).
- ⁹R. J. England, R. J. Noble, K. Bane, D. H. Dowell, C.-K. Ng, J. E. Spencer, S. Tantawi, Z. Wu, R. L. Byer, E. Peralta, K. Soong, C.-M. Chang, B. Montazeri, S. J. Wolf, B. Cowan, J. Dawson, W. Gai, P. Hommelhoff, Y.-C. Huang, C. Jing, C. McGuinness, R. B. Palmer, B. Naranjo, J. Rosenzweig, G. Travish, A. Mizrahi, L. Schachter, C. Sears, G. R. Werner, and R. B. Yoder, "Dielectric laser accelerators," *Rev. Mod. Phys.* **86**, 1337 (2014).
- ¹⁰A. Gover and A. Yariv, "Free-electron-bound-electron resonant interaction," *Phys. Rev. Lett.* **124**, 064801 (2020).
- ¹¹L. Waldecker, R. Bertoni, and R. Ernstorfer, "Compact femtosecond electron diffractometer with 100 keV electron bunches approaching the single-electron pulse duration limit," *J. Appl. Phys.* **117**, 044903 (2015).
- ¹²T. van Oudheusden, P. L. E. M. Pasmans, S. B. van der Geer, M. J. de Loos, M. J. van der Wiel, and O. J. Luiten, "Compression of subrelativistic space-charge-dominated electron bunches for single-shot femtosecond electron diffraction," *Phys. Rev. Lett.* **105**, 264801 (2010).
- ¹³K. J. Leadle, D. S. Black, Yu. Miao, K. E. Urbanek, A. Ceballos, H. Deng, J. S. Harris, O. Solgaard, and R. L. Byer, "Phase-dependent laser acceleration of electrons with symmetrically driven silicon dual pillar gratings," *Opt. Lett.* **43**, 2181–2184 (2018).
- ¹⁴J. B. Rosenzweig, A. Cahill, V. Dolgashev, C. Emma, A. Fukasawa, R. Li, C. Limborg, J. Maxson, P. Musumeci, A. Nause, R. Pakter, R. Pompili, R. Roussel, B. Spataro, and S. Tantawi, "Next generation high brightness electron beams from ultrahigh field cryogenic rf photocathode sources," *Phys. Rev. Accel. Beams* **22**, 023403 (2019).
- ¹⁵F. Le Pimpec, C. Gough, M. Paraliiev, R. Ganter, C. Hauri, and S. Ivkovic, "Vacuum breakdown limit and quantum efficiency obtained for various technical metals using dc and pulsed voltage sources," *J. Vac. Sci. Technol. A* **28**, 1191–1202 (2010).
- ¹⁶F. Furuta, T. Nakanishi, S. Okumi, T. Gotou, M. Yamamoto, M. Miyamoto, M. Kuwahara, N. Yamamoto, K. Naniwa, K. Yasui, H. Matsumoto, M. Yoshioka, and K. Togawa, "Reduction of field emission dark current for high-field gradient electron gun by using a molybdenum cathode and titanium anode," *Nucl. Instrum. Methods Phys. Res. Sect. A* **538**(1–3), 33–44 (2005).
- ¹⁷T. Hirano, K. E. Urbanek, A. C. Ceballos, D. S. Black, Y. Miao, R. Joel England, R. L. Byer, and K. J. Leadle, "A compact electron source for the dielectric laser accelerator," *Appl. Phys. Lett.* **116**, 161106 (2020).
- ¹⁸M. E. Levinshstein, S. L. Rumyantsev, and M. S. Shar, in *Properties of Advanced Semiconductor Materials* (Wiley, NY, 2001).
- ¹⁹S. Chen, P. Ying, L. Wang, G. Wei, and W. Yang, "Temperature-dependent field emission of flexible n-type silicon carbide nanoneedle emitters," *Appl. Phys. Lett.* **105**, 133106 (2014).
- ²⁰J. H. Lee, I. Bargatin, T. O. Gwinn, M. Vincent, K. A. Littau, R. Maboudian, Z.-X. Shen, N. A. Melosh, and R. T. Howe, "Microfabricated silicon carbide thermionic energy converter for solar electricity generation," in *2012 IEEE 25th International Conference on Micro Electro Mechanical Systems (MEMS)* (IEEE, 2012), pp. 1261–1264.
- ²¹M. Schenk, M. Krüger, and P. Hommelhoff, "Strong-field above-threshold photoemission from sharp metal tips," *Phys. Rev. Lett.* **105**, 257601 (2010).
- ²²R. Bornmann, S. Strauch, S. Schäfer, and C. Ropers, "An ultrafast electron microscope gun driven by two-photon photoemission from a nanotip cathode," *J. Appl. Phys.* **118**, 173105 (2015).
- ²³M. Ding, H. Kim, and A. I. Akinwande, "Observation of valence band electron emission from n-type silicon field emitter arrays," *Appl. Phys. Lett.* **75**, 823–825 (1999).
- ²⁴G. M. Caruso, F. Houdellier, S. Weber, M. Kociak, and A. Arbouet, "High brightness ultrafast transmission electron microscope based on a laser-driven cold-field emission source: Principle and applications," *Adv. Phys.* **4**(1), 1660214 (2019).

Acknowledgements

First of all I would like to thank Prof. Oliver Boine-Frankenheim for leading me through many parts of my scientific career, already since more than 10 years in total now. I am particularly grateful for the last 6 years, in which guidance and independence to establish my own research group were always well in balance. I also thank Prof. Sascha Preu for agreeing to be the second referent for this Habilitation thesis. Special thanks also to Profs. Peter Hommelhoff and Bob Byer for introducing me to the ACHIP collaboration and for giving me the opportunity to lead the "Beam Dynamics and Simulations" group in ACHIP. I am grateful that ACHIP was funded and that we had opportunities to reach out for further funding in this research field. Very special thanks to the Gordon and Betty Moore Foundation and to Gary Greenburg in particular.

I spent a great time as a guest scientist at UCLA in 2017, for which I thank Prof. Jamie Rosenzweig and Prof. Pietro Musumeci. Special thanks to Brian Naranjo for teaching me about ponderomotive focusing. Special thanks also to Prof. Holger Podlech for many discussions (also the lengthy political ones), and a particularly inspiring one about Alternating Phase Focusing. I spent another 6 weeks in 2018 at Stanford as postdoctoral scholar, and I am grateful to Prof. Byer for inviting me and to the many people I had great time at Ginzton Lab. Particularly, I thank Prof. Olav Solgaard, Prof. Shanhui Fan, Tyler Hughes, Zhenxin Zhao, Prof. Jelena Vuckovic, Neil Sapro, Ken Leedle, Dylan Black, Yu Miao, Alex Ody, and Payton Broddus.

I thank my colleagues at TEMF, which gave me a great time at my "Home" institute and always enabled me to learn new aspects of electrodynamics and the other things done at university. Among all TEMF employees I would like to especially mention Prof. em. Thomas Weiland, Prof. Herbert De Gerssem, Prof. Harald Klingbeil, Prof. Stefan Kurz, Prof. Sebastian Schöps, Prof. Irina Munteanu, Erion Gjonaj, Wolfgang Müller, Wolfgang Ackermann, Ulrich Römer, Dragos Munteanu, Heike Koch, and Achim Wagner.

I thank all the members of ACHIP for more than 6 years of productive collaboration. It was, and hopefully continues to be, a great endeavor. The list of individuals would be too long, so I only mention those I had lots of interaction with and those who are not mentioned above: Benedikt Hermann, Nicole Hiller, Rasmus Ischebeck, Ralph Assmann, Ulrich Dorda, Frank Mayet, Willi Kuroopka, Prof. Franz Kärtner, Huseyin Cancaya, Arya Fallahi, Ben Cowan, Johannes Illmer, Norbert Schönenberger, Roy Shiloh, Joel England, Tom Langenstein, Tomohiko Hirano, Peyman Yousefi, and Martin Kozak. Many many thanks for the last 6 years!

A very special thanks must definitely go to the present and former members of my research group, whose results were partly included in this treatise: Thilo Egenolf, Aamna Khan, Laura Bagnale, Steffen Schmid, Anna Becken, and Jan Lautenschläger. I also

would like to thank my present and former students: Lewin Eidam, Patrick Krkotic, Furkan Ucar, Stefan Patsch, Eric Skär, Magdalena Schone, and Daniel Dewitt.

I am particularly grateful to Steffen Schmid and Thilo Egenolf for proofreading this work.

Last but not least, I wish thank my family and friends for the support during a difficult time, with all the crises we had recently. Anju, you are a catastrophe, but I love you anyway!

A List of Acronyms

ACHIP	Accelerator on a CHip International Program
AOM	Acousto-Optic Modulator
APF	Alternating Phase Focusing
ARES	Accelerator Research Experiment at SINBAD
CAD	Computer Aided Design
CFL	Courant Friedrichs Lewy criterion
CRT	Cathode Ray Tube
DBR	Distributed Bragg Reflector
DESY	Deutsches Elektronensynchrotron
DLA	Dielectric Laser Acceleration
EDM	Electric Discharge Machining
EQUUS	Equidistant Multigap Structure
FD	Frequency Domain
FDFD	Finite Differences in Frequency Domain
FDTD	Finite Differences in Time Domain
FEL	Free Electron Laser
FEM	Finite Element Method
FIT	Finite Integration Technique
FWHM	Full Width at Half Maximum
KONUS	Kombinierte Null-Grad Struktur (combined zero-degree structure)
Laser	Light amplification by stimulated emission of radiation
Linac	Linear accelerator
LPS	Longitudinal Phase Space
MCP	Micro Channel Plate
MEMS	Microelectromechanical System
OPA	Optical Parametric Amplifier
PFT	Pulse Front Tilt
PIC	Particle-In-Cell
PITZ	Photo Injector Test facility at DESY in Zeuthen
PML	Perfectly Matched Layer
PMQ	Permanent Magnet Quadrupole
PSI	Paul Scherrer Institut
RF	Radio Frequency
RFQ	Radiofrequency Quadrupole
RMS	Root of Mean Square

SEM	Scanning Electron Microscope
SINBAD	Short and INovative Bunches At DESY
SLAC	Stanford Linear Accelerator Center
SLM	Spatial Light Modulator
SOI	Silicon-On-Insulator wafer
STEM	Scanning Transmission Electron Microscope
TD	Time Domain
TDC	Transverse Deflecting Cavity
TEM	Transmission Electron Microscope
UCLA	University of California at Los Angeles
UED	Ultrafast Electron Diffraction
UEM	Ultrafast Electron Microscopy

B Outline of the FemtoTrack Code

FemtoTrack is a dedicated tracker for few-electron bunches and many shots at variable energy. While the program is particularly designed for low energy electrons (also in the limit $W_{\text{kin}} \rightarrow 0$), it is also relativistically correct to be able to work at high energy. Its primary purpose is to track ultrashort electron bunches by using a moving window, such that only the fields in the channel need to be imported and only the field in the window need to be interpolated. The nanophotonic or electro/magneto-static structures creating the fields may be much larger than the size of the bunches, which only matters for the external field simulation, but not for the particle simulation. In order to numerically efficiently determine the (statistical) results of many shots, they are all comprised in

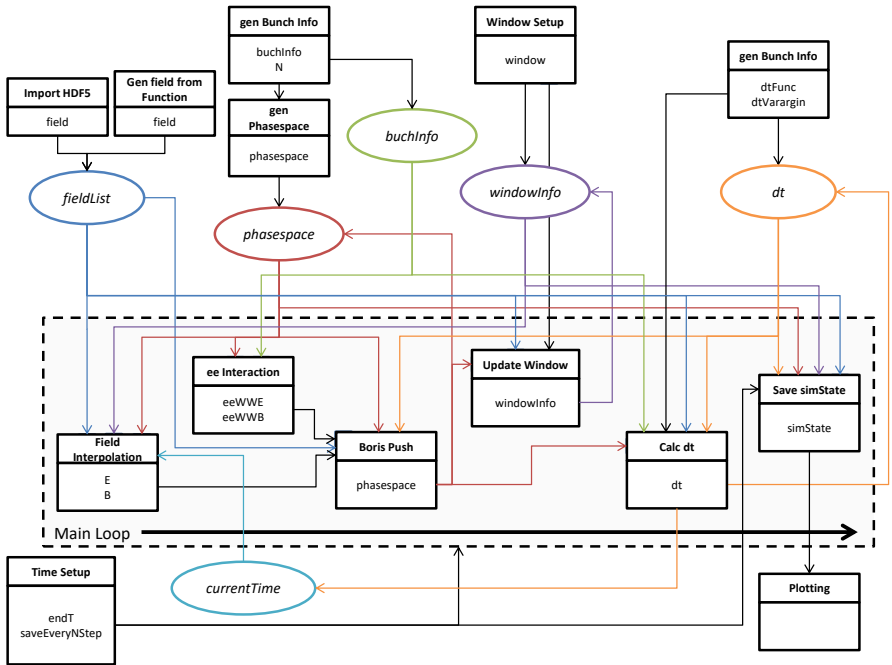


Figure B.1.: Flowchart of the outlined FemtoTrack code. Courtesy of J. Lautenschläger.

a single vector. Without space charge, this is obviously given by the ergodic theorem, i.e., ensemble average and temporal average are equal. With space charge, the tracking shall still be done for all shots simultaneously in common fields, while the particle vector is clustered. Each cluster of particles undergoes direct particle-particle space charge interaction internally, while all particle clusters independent except sharing the same external fields and the same moving window. FemtoTrack is written in Matlab [45] and uses any kind of external fields provided as hdf5 files, e.g. by export from CST Studio [44] or any other field solver. As compared to the tracking with CST Particle Studio in Papers 5.13 and 5.15, we project already a (practical) speedup of a factor 100. The code is however also outlined to be parallelized such that extensive parameter studies of start-to-end simulations of entire beamlines including multiple static and dynamic fields can be conducted.

Bibliography

- [1] H. Wiedemann, *Particle Accelerator Physics*, 3rd ed. Heidelberg: Springer, 1993. (cit. on p. 1)
- [2] K. Wille, *The Physics of Particle Accelerators*. New York: Oxford University Press, 2000. (cit. on p. 1)
- [3] J. B. Rosenzweig, *Fundamentals of Beam Physics*. Oxford University Press, 2003. (cit. on pp. 1, 10, and 26)
- [4] T. P. Wangler, *RF Linear Accelerators*. Weinheim: Wiley-VCH, 2008. (cit. on pp. 1, 11, and 20)
- [5] M. Reiser, *Theory and Design of Charged Particle Beams*, 2nd ed. Weinheim: Wiley-VCH, 2008. (cit. on pp. 1 and 37)
- [6] Wikipedia, “Linear particle accelerator.” [Online]. Available: https://en.wikipedia.org/wiki/Linear_particle_accelerator (cit. on p. 2)
- [7] W. D. Kilpatrick, “Criterion for vacuum sparking designed to include both rf and dc,” *Review of Scientific Instruments*, vol. 28, no. 10, pp. 824–826, 1957. (cit. on p. 3)
- [8] A. D. Cahill, J. B. Rosenzweig, V. A. Dolgashev, S. G. Tantawi, and S. Weathersby, “High gradient experiments with X-band cryogenic copper accelerating cavities,” *Physical Review Accelerators and Beams*, vol. 21, no. 10, p. 102002, 2018. [Online]. Available: <https://doi.org/10.1103/PhysRevAccelBeams.21.102002> (cit. on p. 3)
- [9] B. Hidding, M. Geissler, G. Pretzler, K. U. Amthor, H. Schwoerer, S. Karsch, L. Veisz, K. Schmid, and R. Sauerbrey, “Quasimonoenergetic electron acceleration in the self-modulated laser wakefield regime,” *Physics of Plasmas*, vol. 16, no. 4, 2009. (cit. on p. 3)
- [10] “ACHIP website.” [Online]. Available: www.achip.stanford.edu (cit. on p. 4)
- [11] “Gordon and Betty Moore Foundation.” [Online]. Available: <https://www.moore.org/grant-detail?grantId=GBMF4744.01> (cit. on p. 4)

-
- [12] S. J. Smith and E. M. Purcell, "Visible light from localized surface charges moving across a grating [12]," *Physical Review*, vol. 92, no. 4, p. 1069, 1953. (cit. on p. 7)
- [13] A. Lohmann, "Electron Acceleration by Light Waves," *IBM Technical Note*, vol. 5, pp. 169–182, 1962. (cit. on p. 7)
- [14] K. Shimoda, "Proposal for an Electron Accelerator Using an Optical Maser," *Applied Optics*, vol. 1, no. 1, p. 33, 1962. (cit. on p. 7)
- [15] K. Soong, R. L. Byer, E. R. Colby, R. J. England, and E. A. Peralta, "Laser damage threshold measurements of optical materials for direct laser accelerators," *AIP Conference Proceedings*, vol. 1507, no. 2012, pp. 511–515, 2012. (cit. on p. 7)
- [16] E. A. Peralta, K. Soong, R. J. England, E. R. Colby, Z. Wu, B. Montazeri, C. McGuinness, J. McNeur, K. J. Leedle, D. Walz, E. B. Sozer, B. Cowan, B. Schwartz, G. Travish, and R. L. Byer, "Demonstration of electron acceleration in a laser-driven dielectric microstructure." *Nature*, vol. 503, no. V, pp. 91–94, 2013. [Online]. Available: <http://www.ncbi.nlm.nih.gov/pubmed/24077116> (cit. on pp. 7, 8, 34, and 52)
- [17] J. Breuer and P. Hommelhoff, "Dielectric laser acceleration of 28 keV electrons with the inverse Smith-Purcell effect," *Nuclear Instruments and Methods in Physics Research, Section A: Accelerators, Spectrometers, Detectors and Associated Equipment*, vol. 740, pp. 114–116, 2013. [Online]. Available: <http://dx.doi.org/10.1016/j.nima.2013.10.078> (cit. on pp. 7 and 42)
- [18] R. J. England, R. J. Noble, K. Bane, D. H. Dowell, C.-K. Ng, J. E. Spencer, S. Tantawi, Z. Wu, R. L. Byer, E. Peralta, K. Soong, C.-M. Chang, B. Montazeri, S. J. Wolf, B. Cowan, J. Dawson, W. Gai, P. Hommelhoff, Y.-C. Huang, C. Jing, C. McGuinness, R. B. Palmer, B. Naranjo, J. Rosenzweig, G. Travish, A. Mizrahi, L. Schachter, C. Sears, G. R. Werner, and R. B. Yoder, "Dielectric laser accelerators," *Reviews of Modern Physics*, vol. 86, no. 4, pp. 34–6861, 2014. (cit. on pp. 7 and 16)
- [19] E. Hemsing, G. Stupakov, D. Xiang, and A. Zholents, "Beam by design: Laser manipulation of electrons in modern accelerators," *Reviews of Modern Physics*, vol. 86, no. 3, pp. 897–941, 2014. (cit. on p. 7)
- [20] J. Hebling, "Derivation of the pulse front tilt caused by angular dispersion," *Optical and Quantum Electronics*, vol. 28, no. 12, pp. 1759–1763, 1996. (cit. on pp. 8 and 61)
- [21] Y. Wei, M. Ibison, G. Xia, J. D. A. Smith, and C. P. Welsch, "Dual-grating dielectric accelerators driven by a pulse-front-tilted laser," *Applied Optics*, vol. 56, no. 29, p. 8201, 2017. (cit. on p. 8)

-
- [22] K. P. Wootton, Z. Wu, B. M. Cowan, A. Hanuka, I. V. Makasyuk, E. A. Peralta, K. Soong, R. L. Byer, and R. J. England, “Demonstration of acceleration of relativistic electrons at a dielectric microstructure using femtosecond laser pulses,” *Opt. Lett.*, vol. 41, no. 12, pp. 2696–2699, 2016. [Online]. Available: <http://ol.osa.org/abstract.cfm?URI=ol-41-12-2696> (cit. on pp. 8 and 52)
- [23] M. Kozák, J. McNeur, N. Schönenberger, J. Illmer, A. Li, A. Tafel, P. Yousefi, T. Eckstein, and P. Hommelhoff, “Ultrafast scanning electron microscope applied for studying the interaction between free electrons and optical near-fields of periodic nanostructures,” *Journal of Applied Physics*, vol. 124, no. 2, p. 023104, 2018. (cit. on pp. 8, 10, and 42)
- [24] L. Wang, U. Niedermayer, J. Ma, W. Liu, D. Zhang, and L. Qian, “Spatio-temporal coupling controlled laser for electron acceleration,” *Communications Physics*, vol. 5, no. 175, 2022. (cit. on pp. 9 and 61)
- [25] T. W. Hughes, S. Tan, Z. Zhao, N. V. Saprà, K. J. Leedle, H. Deng, Y. Miao, D. S. Black, O. Solgaard, J. S. Harris, J. Vuckovic, R. L. Byer, S. Fan, R. J. England, Y. J. Lee, and M. Qi, “On-Chip Laser-Power Delivery System for Dielectric Laser Accelerators,” *Physical Review Applied*, vol. 9, no. 5, p. 54017, 2018. [Online]. Available: <https://doi.org/10.1103/PhysRevApplied.9.054017> (cit. on p. 9)
- [26] N. V. Saprà, K. Y. Yang, D. Verduyck, K. J. Leedle, D. S. Black, R. J. England, L. Su, R. Trivedi, Y. Miao, O. Solgaard, R. L. Byer, and J. Vuckovic, “On-chip integrated laser-driven particle accelerator,” *Science*, vol. 367, no. January, pp. 79–83, 2020. (cit. on pp. 9, 18, 19, and 42)
- [27] D. Cesar, S. Custodio, J. Maxson, P. Musumeci, X. Shen, E. Threlkeld, R. J. England, A. Hanuka, I. V. Makasyuk, E. A. Peralta, K. P. Wootton, and Z. Wu, “High-field nonlinear optical response and phase control in a dielectric laser accelerator,” *Communications Physics*, vol. 1, p. 46, 2018. (cit. on p. 9)
- [28] D. Cesar, J. Maxson, P. Musumeci, X. Shen, R. J. England, and K. P. Wootton, “Optical design for increased interaction length in a high gradient dielectric laser accelerator,” *Nuclear Instruments and Methods in Physics Research, Section A: Accelerators, Spectrometers, Detectors and Associated Equipment*, vol. 909, no. January, pp. 252–256, 2018. (cit. on p. 9)
- [29] W. K. H. Panofsky and W. A. Wenzel, “Some Considerations Concerning the Transverse Deflection of Charged Particles in Radio-Frequency Fields,” *Review of Scientific Instruments*, vol. 27, pp. 31–34, 1956. (cit. on pp. 9 and 14)
- [30] B. Naranjo, A. Valloni, S. Putterman, and J. B. Rosenzweig, “Stable charged-particle acceleration and focusing in a laser accelerator using spatial harmonics,” *Physical Review Letters*, vol. 109, no. 16, p. 164803, 2012. (cit. on pp. 10 and 26)

-
- [31] H. H. Rose, “Optics of high-performance electron microscopes,” *Science and Technology of Advanced Materials*, vol. 9, no. 1, 2008. (cit. on p. 10)
- [32] —, *Geometrical Charged Particle Optics*. Heidelberg: Springer, 2009, vol. 158. (cit. on pp. 10 and 41)
- [33] O. Scherzer, “Über einige Fehler von Elektronenlinsen (some defects of electron lenses),” *Optik*, vol. 101, no. 9-10, pp. 593–603, 1936. (cit. on pp. 11 and 41)
- [34] D. Ehberger, J. Hammer, M. Eisele, M. Krüger, J. Noe, A. Högele, and P. Hommelhoff, “Highly Coherent Electron Beam from a Laser-Triggered Tungsten Needle Tip,” *Physical Review Letters*, vol. 114, no. 22, p. 227601, 2015. (cit. on pp. 11 and 41)
- [35] T. Hirano, K. E. Urbanek, A. C. Ceballos, D. S. Black, Y. Miao, R. Joel England, R. L. Byer, and K. J. Leedle, “A compact electron source for the dielectric laser accelerator,” *Applied Physics Letters*, vol. 116, no. 16, p. 161106, 2020. (cit. on pp. 11, 41, and 49)
- [36] P. Musumeci, J. Moody, and G. Gatti, “Ultrafast beam research at the PEGASUS laboratory,” *Proceedings of the IEEE Particle Accelerator Conference*, pp. 2751–2753, 2007. (cit. on pp. 11 and 52)
- [37] J. Jackson, *Classical Electrodynamics*. Singapore: Wiley, 1999. (cit. on p. 13)
- [38] C. F. Klingshirn, *Semiconductor Optics*. Heidelberg: Springer, 2012. (cit. on p. 13)
- [39] H. Zeng, *Ultrafast nonlinear optics*. Heidelberg: Springer, 2015, vol. 3. (cit. on p. 13)
- [40] T. Weiland and R. Wanzenberg, “Wake fields and impedances,” *Frontiers of Particle Beams: Intensity Limitations*, pp. 39–79, 1992. (cit. on p. 14)
- [41] W. Shin and S. Fan, “Accelerated solution of the frequency-domain Maxwell’s equations by engineering the eigenvalue distribution of the operator,” *Optics Express*, vol. 21, no. 19, p. 22578, 2013. [Online]. Available: <https://www.osapublishing.org/oe/abstract.cfm?uri=oe-21-19-22578> (cit. on p. 17)
- [42] T. Egenolf, O. Boine-Frankenheim, and U. Niedermayer, “Simulation of DLA grating structures in the frequency domain,” *Journal of Physics: Conference Series*, vol. 874, no. 1, 2017. (cit. on pp. 17 and 18)

-
- [43] J. P. Berenger, “A perfectly matched layer for the absorption of electromagnetic waves,” *Journal of Computational Physics*, vol. 114, no. 2, pp. 185–200, 1994. (cit. on p. 17)
- [44] Dassault-Systems, “CST Studio Suite,” 2021. [Online]. Available: www.cst.com (cit. on pp. 17, 24, 25, 30, 32, 39, 50, 51, and 222)
- [45] MathWorks, “Matlab,” 2016. [Online]. Available: www.mathworks.com (cit. on pp. 17 and 222)
- [46] T. Hughes, G. Veronis, K. P. Wootton, R. Joel England, and S. Fan, “Method for computationally efficient design of dielectric laser accelerator structures,” *Optics Express*, vol. 25, no. 13, p. 15414, 2017. (cit. on p. 18)
- [47] Y. Miao, “Design and Fabrication Improvements for the Dielectric Laser Accelerators,” Ph.D. dissertation, Stanford University, 2020. [Online]. Available: <http://purl.stanford.edu/hk823qg0346> (cit. on pp. 18, 35, and 42)
- [48] T. Plettner and R. L. Byer, “Microstructure-based laser-driven free-electron laser,” *Nuclear Instruments and Methods in Physics Research, Section A: Accelerators, Spectrometers, Detectors and Associated Equipment*, vol. 593, no. 1-2, pp. 63–66, 2008. (cit. on pp. 18 and 59)
- [49] —, “Proposed dielectric-based microstructure laser-driven undulator,” *Physical Review Special Topics - Accelerators and Beams*, vol. 11, no. 3, pp. 1–10, 2008. (cit. on pp. 18 and 59)
- [50] T. Plettner, R. Byer, C. McGuinness, and P. Hommelhoff, “Photonic-based laser driven electron beam deflection and focusing structures,” *Physical Review Special Topics - Accelerators and Beams*, vol. 12, pp. 1–9, 2009. (cit. on pp. 18 and 59)
- [51] T. Egenolf, “Intensity Effects in Dielectric Laser Accelerator Structures,” Ph.D. dissertation, TU Darmstadt, 2020. (cit. on pp. 18, 36, 37, and 38)
- [52] U. Ratzinger, H. Hähnel, R. Tiede, J. Kaiser, and A. Almomani, “Combined zero degree structure beam dynamics and applications,” *Physical Review Accelerators and Beams*, vol. 22, no. 11, p. 114801, 2019. [Online]. Available: <https://doi.org/10.1103/PhysRevAccelBeams.22.114801> (cit. on p. 21)
- [53] S. Minaev, U. Ratzinger, H. Podlech, M. Busch, and W. Barth, “Superconducting, energy variable heavy ion linac with constant β , multicell cavities of CH-type,” *Physical Review Special Topics - Accelerators and Beams*, vol. 12, no. 12, pp. 1–10, 2009. (cit. on p. 21)

-
- [54] S. Earnshaw, “On the nature of the molecular forces which regulate the constitution of the luminiferous ether,” *Trans. Camb. Phil. Soc.*, vol. 7, pp. 97–112, 1842. (cit. on p. 21)
- [55] F. Major, V. Gheorghe, and G. Werth, *Charged Particle Traps*. Heidelberg: Springer, 2005. (cit. on p. 21)
- [56] E. Courant and H. Snyder, “Theory of the alternating-gradient synchrotron,” *Annals of Physics*, vol. 3, no. 1, pp. 1–48, 1958. [Online]. Available: <http://linkinghub.elsevier.com/retrieve/pii/0003491658900125> (cit. on p. 22)
- [57] S. Y. Lee, *Accelerator Physics*. World Scientific Publishing Co. Pte. Ltd., 2004. (cit. on pp. 22 and 27)
- [58] Wolfram, “Mathematica 11.2,” 2017. [Online]. Available: <https://www.wolfram.com/mathematica/> (cit. on p. 22)
- [59] J. Rosenzweig and L. Serafini, “Transverse particle motion in radio-frequency linear accelerators,” *Physical Review E*, vol. 49, no. 2, pp. 1599–1602, 1994. (cit. on p. 26)
- [60] S. Reiche, J. B. Rosenzweig, S. Anderson, P. Frigola, M. Hogan, A. Murokh, C. Pellegrini, L. Serafini, G. Travish, and A. Tremaine, “Experimental confirmation of transverse focusing and adiabatic damping in a standing wave linear accelerator,” *Physical Review E - Statistical Physics, Plasmas, Fluids, and Related Interdisciplinary Topics*, vol. 56, no. 3, pp. 3572–3577, 1997. (cit. on p. 26)
- [61] D. Cesar, P. Musumeci, and J. England, “All Optical Control of Beam Dynamics in a DLA,” *2018 IEEE Advanced Accelerator Concepts Workshop (AAC)*, pp. 1–5, 2018. (cit. on pp. 26, 52, and 61)
- [62] A. Ody, S. Crisp, P. Musumeci, D. Cesar, and R. J. England, “SHaRD: A beam dynamics simulation code for dielectric laser accelerators based on spatial harmonic field expansion,” *Nuclear Instruments and Methods in Physics Research, Section A: Accelerators, Spectrometers, Detectors and Associated Equipment*, vol. 1013, no. April, p. 165635, 2021. [Online]. Available: <https://doi.org/10.1016/j.nima.2021.165635> (cit. on pp. 26 and 52)
- [63] U. Niedermayer, K. J. Leedle, P. Musumeci, and S. Schmid, “Beam Dynamics in Dielectric Laser Accelerators,” *Accepted in JINST*, 2022. (cit. on pp. 26 and 50)
- [64] F. Krausz and M. Ivanov, “Attosecond physics,” *Reviews of Modern Physics*, vol. 81, no. 1, pp. 163–234, 2009. (cit. on p. 28)

-
- [65] S. Crisp, A. Ody, P. Musumeci, and R. J. England, “Resonant phase matching by oblique illumination of a dielectric laser accelerator,” *Physical Review Accelerators and Beams*, vol. 24, no. 12, p. 121305, 2021. [Online]. Available: <https://doi.org/10.1103/PhysRevAccelBeams.24.121305> (cit. on p. 34)
- [66] A. W. Chao, *Physics of Collective Beam Instabilities in High Energy Accelerators*. New York: Wiley, 1993. (cit. on p. 37)
- [67] B. Hermann, “ACHIP at SwissFEL - Electron Beam Shaping with Dielectric Micro Structures Examiners,” Ph.D. dissertation, University Bern, 2021. (cit. on pp. 38, 39, 53, 55, and 56)
- [68] K. Bane, G. Stupakov, and I. Zagorodnov, “Analytical formulas for short bunch wakes in a flat dechirper,” *Physical Review Accelerators and Beams*, vol. 19, no. 8, pp. 1–11, 2016. (cit. on p. 37)
- [69] K. Bane and G. Stupakov, “Dechirper wakefields for short bunches,” *Nuclear Instruments and Methods in Physics Research, Section A: Accelerators, Spectrometers, Detectors and Associated Equipment*, vol. 820, pp. 156–163, 2016. (cit. on p. 37)
- [70] M. Dohlus, T. Limberg, and P. Emma, “Bunch Compression for Linac-based FELs,” *ICFA Beam Dynamics Newsletter*, no. 38, pp. 15–50, 2005. (cit. on p. 37)
- [71] M. Schreck and P. Wesolowski, “Analytical bunch compression studies for a linac-based electron accelerator,” *Physical Review Special Topics - Accelerators and Beams*, vol. 18, no. 10, pp. 1–26, 2015. (cit. on p. 37)
- [72] M. Timm, “Wake Fields of Short Ultra-Relativistic Electron Bunches,” Ph.D. dissertation, TU Darmstadt, 2000. (cit. on p. 39)
- [73] M. Haider, S. Uhlemann, E. Schwan, G. Rose, B. Kabius, and K. Urban, “Electron microscopy image enhanced [7],” *Nature*, vol. 392, no. 6678, pp. 768–769, 1998. (cit. on p. 41)
- [74] J. Thomas and T. Gemming, *Analytische Elektronenmikroskopie - Eine Einführung für den Praktiker*. Heidelberg: Springer, 2013. (cit. on p. 41)
- [75] L. Reimer and H. Kohl, *Transmission Electron Microscopy*. Heidelberg: Springer, 2003, vol. 50, no. 52. (cit. on p. 41)
- [76] A. Feist, N. Bach, N. Rubiano da Silva, T. Danz, M. Möller, K. E. Priebe, T. Domröse, J. G. Gatzmann, S. Rost, J. Schauss, S. Strauch, R. Bormann, M. Siviš, S. Schäfer, and C. Ropers, “Ultrafast transmission electron microscopy using a laser-driven field emitter: Femtosecond resolution with a high coherence

electron beam,” *Ultramicroscopy*, vol. 176, no. November 2016, pp. 63–73, 2017. [Online]. Available: <http://dx.doi.org/10.1016/j.ultramic.2016.12.005> (cit. on p. 41)

- [77] K. J. Leedle, R. Fabian Pease, R. L. Byer, and J. S. Harris, “Laser acceleration and deflection of 963 keV electrons with a silicon dielectric structure,” *Optica*, vol. 2, no. 2, p. 158, 2015. [Online]. Available: <http://www.opticsinfobase.org/abstract.cfm?URI=optica-2-2-158> (cit. on p. 42)
- [78] K. J. Leedle, A. Ceballos, H. Deng, O. Solgaard, R. Fabian Pease, R. L. Byer, and J. S. Harris, “Dielectric laser acceleration of sub-100 keV electrons with silicon dual-pillar grating structures,” *Optics Letters*, vol. 40, no. 18, p. 4344, 2015. [Online]. Available: <https://www.osapublishing.org/abstract.cfm?URI=ol-40-18-4344> (cit. on p. 42)
- [79] P. Yousefi, “Novel Silicon Nano-Structures for Dielectric Laser Accelerators,” Ph.D. dissertation, FAU Erlangen-Nuremberg, 2019. (cit. on p. 42)
- [80] P. Yousefi, J. McNeur, M. Kozák, U. Niedermayer, F. Gannott, O. Lohse, O. Boine-Frankenheim, and P. Hommelhoff, “Silicon dual pillar structure with a distributed Bragg reflector for dielectric laser accelerators: Design and fabrication,” *Nuclear Instruments and Methods in Physics Research, Section A: Accelerators, Spectrometers, Detectors and Associated Equipment*, vol. 909, no. November 2017, pp. 221–223, 2018. [Online]. Available: <https://doi.org/10.1016/j.nima.2018.01.065> (cit. on p. 42)
- [81] O. Iupikov, “TCST Interface,” 2022. [Online]. Available: <https://github.com/korvin011/CSTMWS-Matlab-Interface> (cit. on p. 50)
- [82] B. Marchetti, R. Assmann, R. Brinkmann, F. Burkart, U. Dorda, K. Floettmann, I. Hartl, W. Hillert, M. Huening, F. Jafarinia, S. Jaster-Merz, M. Kellermeier, W. Kuropka, F. Lemery, D. Marx, F. Mayet, E. Panofski, S. Pfeiffer, H. Schlarb, T. Vinatier, P. A. Walker, L. Winkelmann, and S. Yamin, “SINBAD-ARES - A Photo-Injector for external Injection Experiments in novel Accelerators at DESY,” *Journal of Physics: Conference Series*, vol. 1596, no. 012036, p. 012036, 2020. (cit. on p. 52)
- [83] J. Zhu, R. W. Assmann, M. Dohlus, U. Dorda, and B. Marchetti, “Sub-fs electron bunch generation with sub-10-fs bunch arrival-time jitter via bunch slicing in a magnetic chicane,” *Physical Review Accelerators and Beams*, vol. 19, no. 5, pp. 1–13, 2016. (cit. on p. 52)
- [84] U. Dorda, B. Marchetti, J. Zhu, F. Mayet, W. Kuropka, T. Vinatier, G. Vashchenko, K. Galaydych, P. A. Walker, D. Marx, R. Brinkmann, R. Assmann, N. H.

- Matlis, A. Fallahi, and F. X. Kaertner, “Status and objectives of the dedicated accelerator R&D facility “SINBAD” at DESY,” *Nuclear Instruments and Methods in Physics Research, Section A: Accelerators, Spectrometers, Detectors and Associated Equipment*, vol. 909, no. January, pp. 239–242, 2018. [Online]. Available: <https://doi.org/10.1016/j.nima.2018.01.036> (cit. on p. 52)
- [85] T. Egenolf and U. Niedermayer, “Analytical energy spectra and wake effects for relativistic dielectric laser accelerators,” in *Journal of Physics: Conference Series*, vol. 1596, no. 1, 2020, p. 012017. [Online]. Available: <http://arxiv.org/abs/1911.08396> (cit. on p. 52)
- [86] F. Mayet, “Acceleration and Phase Space Manipulation of Relativistic Electron Beams in Nano- and Micrometer-Scale Dielectric Structures Dissertation zur Erlangung des Doktorgrades an der Fakultät für Mathematik , Informatik und Naturwissenschaften Fachbereich Physik,” Ph.D. dissertation, University Hamburg, 2019. (cit. on p. 52)
- [87] N. Sudar, P. Musumeci, I. Gadjev, Y. Sakai, S. Fabbri, M. Polyanskiy, I. Pogorelsky, M. Fedurin, C. Swinson, K. Kusche, M. Babzien, and M. Palmer, “Demonstration of Cascaded Modulator-Chicane Microbunching of a Relativistic Electron Beam,” *Physical Review Letters*, vol. 120, no. 11, p. 114802, 2018. [Online]. Available: <https://doi.org/10.1103/PhysRevLett.120.114802> (cit. on p. 52)
- [88] E. Hemsing and D. Xiang, “Cascaded modulator-chicane modules for optical manipulation of relativistic electron beams,” *Physical Review Special Topics - Accelerators and Beams*, vol. 16, no. 1, pp. 1–11, 2013. (cit. on p. 52)
- [89] P. Craievich, M. Bopp, H. H. Braun, A. Citterio, R. Fortunati, R. Ganter, T. Kleeb, F. Marcellini, M. Pedrozzi, E. Prat, S. Reiche, K. Rolli, R. Sieber, A. Grudiev, W. L. Millar, N. Catalan-Lasheras, G. McMonagle, S. Pitman, V. D. P. Romano, K. T. Szypula, W. Wuensch, B. Marchetti, R. Assmann, F. Christie, B. Conrad, R. D’Arcy, M. Foese, P. G. Caminal, M. Hoffmann, M. Huening, R. Jonas, O. Krebs, S. Lederer, D. Marx, J. Osterhoff, M. Reukauff, H. Schlarb, S. Schreiber, G. Tews, M. Vogt, A. D. Z. Wagner, and S. Wesch, “Novel X-band transverse deflection structure with variable polarization,” *Physical Review Accelerators and Beams*, vol. 23, no. 11, p. 112001, 2020. [Online]. Available: <https://doi.org/10.1103/PhysRevAccelBeams.23.112001> (cit. on p. 53)
- [90] B. Hermann, V. A. Guzenko, O. R. Hürzeler, A. Kirchner, G. L. Orlandi, E. Prat, and R. Ischebeck, “Electron beam transverse phase space tomography using nanofabricated wire scanners with submicrometer resolution,” *Physical Review Accelerators and Beams*, vol. 24, no. 2, p. 22802, 2021. [Online]. Available: <https://doi.org/10.1103/PhysRevAccelBeams.24.022802> (cit. on p. 53)

-
- [91] “FEMTOprint SA.” [Online]. Available: <http://www.femtoprint.ch/> (cit. on p. 53)
- [92] “www.refractiveindex.info,” 2020. (cit. on p. 53)
- [93] M. Borland, “elegant: A Flexible SDDS-Compliant Code for Accelerator Simulation,” in *Proceedings of the 6th International Computational Accelerator Physics Conference*, Darmstadt, 2000. (cit. on p. 55)
- [94] G. Storeck, S. Vogelgesang, M. Siviş, S. Schafer, and C. Ropers, “Nanotip-based photoelectron microgun for ultrafast LEED,” *Structural Dynamics*, vol. 4, no. 4, 2017. [Online]. Available: <http://dx.doi.org/10.1063/1.4982947> (cit. on p. 58)
- [95] Andrew Ceballos, “Silicon Photocathodes for Dielectric Laser Accelerators,” Ph.D. dissertation, Stanford University, 2019. (cit. on p. 58)
- [96] J. C. Williamson, M. Dantus, S. B. Kim, and A. H. Zewail, “Ultrafast diffraction and molecular structure,” *Chemical Physics Letters*, vol. 196, no. 6, pp. 529–534, 1992. (cit. on p. 59)
- [97] B. J. Siwick, J. R. Dwyer, R. E. Jordan, and R. J. Miller, “An Atomic-Level View of Melting Using Femtosecond Electron Diffraction,” *Science*, vol. 302, no. 5649, pp. 1382–1385, 2003. (cit. on p. 59)
- [98] A. H. Zewail and J. M. Thomas, *4D Electron Microscopy*. Imperial College Press, 2010. (cit. on p. 59)
- [99] R. F. Egerton, “Outrun radiation damage with electrons?” *Advanced Structural and Chemical Imaging*, vol. 1, p. 5, 2015. (cit. on p. 59)
- [100] S. P. Weathersby, G. Brown, M. Centurion, T. F. Chase, R. Coffee, J. Corbett, J. P. Eichner, J. C. Frisch, A. R. Fry, M. Gühr, N. Hartmann, C. Hast, R. Hettel, R. K. Jobe, E. N. Jongewaard, J. R. Lewandowski, R. K. Li, A. M. Lindenberg, I. Makasyuk, J. E. May, D. McCormick, M. N. Nguyen, A. H. Reid, X. Shen, K. Sokolowski-Tinten, T. Vecchione, S. L. Vetter, J. Wu, J. Yang, H. A. Dürr, and X. J. Wang, “Mega-electron-volt ultrafast electron diffraction at SLAC National Accelerator Laboratory,” *Review of Scientific Instruments*, vol. 86, no. 7, p. 073702, 2015. (cit. on p. 59)
- [101] R. Li, W. Huang, Y. Du, J. Shi, and C. Tang, “Simulation optimization of single-shot continuously time-resolved MeV ultra-fast electron diffraction,” *Nuclear Instruments and Methods in Physics Research, Section A: Accelerators, Spectrometers, Detectors and Associated Equipment*, vol. 637, no. 1 SUPPL., pp. S15–S19, 2011. [Online]. Available: <http://dx.doi.org/10.1016/j.nima.2010.02.012> (cit. on p. 59)

-
- [102] R. K. Li and C. X. Tang, “Temporal resolution of MeV ultrafast electron diffraction based on a photocathode RF gun,” *Nuclear Instruments and Methods in Physics Research, Section A: Accelerators, Spectrometers, Detectors and Associated Equipment*, vol. 605, no. 3, pp. 243–248, 2009. (cit. on p. 59)
- [103] “Eldico Scientific,” 2022. [Online]. Available: <https://www.eldico-scientific.com> (cit. on p. 59)
- [104] ALEGRO collaboration, “Towards an Advanced Linear International Collider,” 2019. [Online]. Available: <http://arxiv.org/abs/1901.10370> (cit. on p. 59)
- [105] R. H. Siemann, “Energy efficiency of laser driven, structure based accelerators,” *Physical Review Special Topics - Accelerators and Beams*, vol. 7, no. 6, pp. 82–91, 2004. (cit. on p. 60)
- [106] H. Ohkuma, “Top-up operation in light sources,” *EPAC 2008 - Contributions to the Proceedings*, pp. 36–40, 2008. (cit. on p. 60)
- [107] H. Tanaka, M. Adachi, T. Aoki, T. Asaka, A. Baron, S. Daté, K. Fukami, Y. Furukawa, H. Hanaki, N. Hosoda, T. Ishikawa, H. Kimura, K. Kobayashi, T. Kobayashi, S. Kohara, N. Kumagai, M. Masaki, T. Masuda, S. Matsui, A. Mizuno, T. Nakamura, T. Nakatani, T. Noda, T. Ohata, H. Ohkuma, T. Ohshima, M. Oishi, S. Sasaki, J. Shimizu, M. Shoji, K. Soutome, M. Suzuki, S. Suzuki, Y. Suzuki, S. Takano, M. Takao, T. Takashima, H. Takebe, A. Takeuchi, K. Tamura, R. Tanaka, Y. Tanaka, T. Taniuchi, Y. Taniuchi, K. Tsumaki, A. Yamashita, K. Yanagida, Y. Yoda, H. Yonehara, T. Yorita, M. Yoshioka, and M. Takata, “Stable top-up operation at SPring-8,” *Journal of Synchrotron Radiation*, vol. 13, no. 5, pp. 378–391, 2006. (cit. on p. 60)
- [108] J. Fabianska, G. Kassier, and T. Feurer, “Split ring resonator based THz-driven electron streak camera featuring femtosecond resolution,” *Scientific Reports*, vol. 4, pp. 1–6, 2014. (cit. on p. 61)